Shun-Hsyung Chang
Ivan A. Parinov
Vitaly Yu. Topolov   *Editors*

Advanced Materials

Physics, Mechanics and Applications

Springer

Springer Proceedings in Physics

Volume 152

Shun-Hsyung Chang · Ivan A. Parinov
Vitaly Yu. Topolov

Editors

Advanced Materials

Physics, Mechanics and Applications

Springer

Editors

Shun-Hsyung Chang
Department of Microelectronics
    Engineering
National Kaohsiung Marine University
Kaohsiung
Taiwan

Vitaly Yu. Topolov
Department of Physics
Southern Federal University
Rostov-on-Don
Russia

Ivan A. Parinov
Research Institute of Mechanics and
    Applied Mathematics
Southern Federal University
Rostov-on-Don
Russia

Printed on acid-free paper

Preface

The Advanced materials and composites are based on achievements of modern theoretical, experimental, and computational methods, which ensure research and development of numerous processing techniques. By using the last attainments of Material Science, Condensed Matter Physics, and Mechanics of Deformable Solids, novel materials and structures have found broad applications in modern science, techniques, and technologies working in ranges from nanoscale to macroscale. The continuous rise in requirements for improvement of material properties and extension of possibilities of devices, created on their base, support tremendous interest to fast development of the theoretical, experimental, and numerical methods. These methods allow us to obtain new knowledge and are capable to provide control and forecast on development of critical phenomena and improvement of very fine processes (for example, nanostructure and microstructure transformations during processing, loading, and working modern materials and composites in critical conditions, aggressive media, and wide types of physical and mechanical treatments). Practical applications demand from modern devices and constructions very high accuracy, reliability, longevity, and extended possibilities to work on broad temperature and pressure ranges. It is evident that the device characteristics are directly defined by used materials and composites opening new possibilities in the study of various physical processes, in particular transmission and receipt of signals under water.

This collection of 30 papers presents selected reports of the 2013 International Symposium on "Physics and Mechanics of New Materials and Underwater Applications" (PHENMA-2013), which took place in Kaohsiung, Taiwan, on June 5–8, 2013 (http://phenma.math.sfedu.ru) and was sponsored by the Russian Foundation for Basic Research, National Science Council of Taiwan, South Scientific Center of Russian Academy of Sciences, New Century Education Foundation (Taiwan), Ocean & Underwater Technology Association, Unity Opto Technology Co., EPOCH Energy Technology Corp., Fair Well Fishery Co., Formosa Plastics Co., Woen Jinn Harbor Engineering Co., Lorom Group, Longwell Co., Taiwan International Ports Co., Ltd.

The theme of the PHENMA-2013 and the Springer Proceedings continues the ideas of the previous symposium PMNM-2012 (http://pmnm.math.rsu.ru), whose results have been published in the edited book "Physics and Mechanics of New

Materials and Their Applications," Ivan A. Parinov, Shun Hsyung-Chang (Eds.), Nova Science Publishers, New York, 2013, 444 p. ISBN: 978-1-62618-535-7.

The presented papers are divided into four scientific directions: (i) processing techniques of advanced materials, (ii) physics of advanced materials, (iii) mechanics of advanced materials, and (iv) applications of advanced materials.

Into framework of the first theme are considered, in particular, the nanotechnology approaches and novel methods in processing of a wide class of ferroelectric materials and multiferroics, preparation methods, and studies of ZnO nanorod arrays. Moreover, there are also presented investigations of Cu_2ZnSnS_4 solar cell materials manufactured on Mo/SLG substrates and processing technology of sapphire crystals. The first section ends by considering issues of optimization of the resin transfer molding process for curing large composite structures.

The second direction opens by theoretical studies of relations between domain states and phase contents in ferroelectrics, and also investigations of ferroelectric and magnetic phase transitions in multiferroics. Moreover, there are presented characteristics of Schottky tunneling barrier InP MOSFET and research results of the magnetic field effect on thermoelectric coefficient and Peltier factor in InSb.

From the viewpoint of mechanics are studied elastic and dissipative properties of solids on the base of finite-element modeling, and also piezo-excited Lamb waves in laminated composites. Moreover, there are studies of stress–strain state in layered anisotropic constructions at pulsed loading, problems of vibration acoustics of shells, and mechanical testing of polymeric composites for aircraft applications. The third section ends by investigations of interaction of the circular plate with elastic inhomogeneous layer and study of dependencies between displacements and elastic properties in solids of complex shape.

In the main, the presented applications are directly connected with underwater devices and issues of transmission and receipt of signals under water. In particular, the book discusses the study of underwater acoustic projector with active elements made from porous piezoceramics, digital frequency synthesizer for underwater systems, digital channels, and circuits for underwater communication including required models and algorithms. Other applied directions cover zinc oxide applications, investigations and use of cantilever-type piezoelectric generators, and closed axisymmetric shells.

The book is addressed to students, post-graduate students, scientists, and engineers taking part in R&D of nano-materials, ferro-piezoelectrics, and other advanced materials and composites presented in the book, and also in manufacture of different devices that have broad applications in different areas of modern science and technique, in particular in underwater communication.

Kaohsiung, Taiwan   Shun-Hsyung Chang
Rostov-on-Don, Russia   Ivan A. Parinov
                                                                                      Vitaly Yu. Topolov

Contents

Contributors

A. G. Abubakarov Research Institute of Physics, Southern Federal University, Rostov-on-Don, Russia 344090

V. A. Alyoshin Research Institute of Physics, Southern Federal University, Rostov-on-Don, Russia 344090

V. A. Akopyan Vorovich Mechanics and Applied Mathematics Research Institute, Southern Federal University, Rostov-on-Don, Russia, e-mail: akop@math.rsu.ru

K. P. Andryushin Research Institute of Physics, Southern Federal University, Rostov-on-Don, Russia 344090

I. N. Andryushina Research Institute of Physics, Southern Federal University, Rostov-on-Don, Russia 344090

E. G. Avvakumov Institute of Solid State Chemistry and Mechanochemistry SB RAS, Novosibirsk, Russia

A. V. Blazhevich Faculty of Physics, Research Institute of Physics, Southern Federal University, Rostov-on-Don, Russia

Ian Yi-yu Bu Department of Microelectronics Engineering, National Kaohsiung Marine University, Kaohsiung, Republic of China (Taiwan), e-mail: ianbu@webmail.nkmu.edu.tw

Herng-Hua Chang Department of Engineering Science and Ocean Engineering, National Taiwan University, 1 Sec. 4, Roosevelt Road, Daan, Taipei 10617, Republic of China (Taiwan), e-mail: herbertchang@ntu.edu.tw

Shun-Hsyung Chang Department of Electrical Engineering, National Taiwan Ocean University, 2 Pei-Ning Road, Keelung 202, Republic of China (Taiwan); Department of Microelectronics Engineering, National Kaohsiung Marine University, 142 Haichuan Road, Nantzu, Kaohsiung 811, Republic of China (Taiwan), e-mail: stephenshchang@me.com

Chung-Cheng Chen Department of Electrical Engineering, Hwa Hsia Institute of Technology, 111 Gong Jhuan Road, Chung Ho, New Taipei 235, Republic of China (Taiwan)

H. Chen University of Macau, Macau, China

Po-Fang Chen Department of Engineering Science and Ocean Engineering, National Taiwan University, 1 Sec. 4, Roosevelt Road, Daan, Taipei 10617, Republic of China (Taiwan)

Shang yang Chen Department of Microelectronics Engineering, National Kaohsiung Marine University, Kaohsiung, Republic of China (Taiwan)

Hao Cheng Department of Electrical Engineering, National Sun Yat-sen University, Kaohsiung 80424, Republic of China (Taiwan)

Nan-Hui Chiang Department of Electronic Engineering, National Kaohsiung University of Applied Sciences, 415 Chien Kung Rd, Kaohsiung 807, Taiwan, People's Republic of China

Levon Chinchan Rostvertol Helicopters, Rostov-on-Don, Russia, e-mail: levon-rostvert@yandex.ru

C.-C. Chou National Taiwan University of Science and Technology, Taipei 10607, Republic of China (Taiwan)

V. G. Dneprovski Vorovich Mechanics and Applied Mathematics Research Institute, Southern Federal University, 200/1, Stachki Ave, Rostov-on-Don, Russia 344090

Y. E. Drobotov Vorovich Mechanics and Applied Mathematics Research Institute, Southern Federal University, Rostov-on-Don, Russia 344090, e-mail: yuedrobotov@sfedu.ru

S. I. Dudkina Research Institute of Physics, Southern Federal University, Rostov-on-Don, Russia 344090

E. V. Eremin Kirensky Institute of Physics, SB RAS, Krasnoyarsk, Russia

M. B. Flek Rostvertol Helicopters, Rostov-on-Don, Russia

V. V. Gershenovich Research Institute of Physics, Southern Federal University, Rostov-on-Don, Russia 344090

N. D. T. Giang Department of Strength of Materials, Don State Technical University, Rostov-on-Don, Russia 344000; Department of Information Technology, Vietnam Maritime University, HaiPhong, Vietnam

E. Gorshkova Kuban State University, Krasnodar, Russia

Jun-Kai Guo Department of Engineering Science and Ocean Engineering, National Taiwan University, 1 Sec. 4, Roosevelt Road, Daan, Taipei 10617, Republic of China (Taiwan)

A. A. Gusev Institute of Solid State Chemistry and Mechanochemistry SB RAS, Novosibirsk, Russia

Wen-Kong Horng Department of Marine Engineering, National Koahsiung Marine University, 142, Haichuan Rd., Kaohsiung, Nantzu, Taiwan

K. J. Hsiao Department of Electrical Engineering, National Taiwan Ocean University, Keelung, Republic of China (Taiwan)

Hsi-Chin Hsin Department of Computer Science and Information Engineering, National United University, Miaoli City 360-03, Taiwan, e-mail: hsin@nuu.edu.tw

Ting-hao Hu Department of Microelectronics Engineering, National Kaohsiung Marine University, Kaohsiung, Republic of China (Taiwan)

Cheng-Liang Huang Department of Microelectronics Engineering, National Kaohsiung Marine University, No.142, Haijhuan Rd., Nanzih Dist., Kaohsiung 81157, Republic of China (Taiwan)

Jiun-Ping Huang National Kaohsiung Marine University, Kaohsiung, Rupublic of China (Taiwan); Formoza Plastics Co, Taipei, Republic of China (Taiwan), e-mail: jas3-3@hotmail.com

V. P. Isupov Institute of Solid State Chemistry and Mechanochemistry SB RAS, Novosibirsk, Russia

Ying-Shen Juang Department of Business Administration, Chung Hua University, Hsinchu 300-12, Taiwan, e-mail: ysjuang@chu.edu.tw

E. M. Kaidashev Vorovich Mechanics and Applied Mathematics Research Institute, Southern Federal University, 200/1, Stachki Ave, Rostov-on-Don, Russia 344090, e-mail: kaidashev@mail.ru

Wen-Jin Kao Department of Electrical Engineering, Hwa Hsia Institute of Technology, 111 Gong Jhuan Road, Chung Ho, New Taipei 235, Republic of China (Taiwan)

G. Ya. Karapetyan Vorovich Mechanics and Applied Mathematics Research Institute, Southern Federal University, 200/1, Stachki Ave, Rostov-on-Don, Russia 344090, e-mail: jorichkaka@yandex.ru

A. Karmazin Department of Applied Mathematics, RheinMain University of Applied Sciences, Kurt-Schumacher-Ring 18, 76185 Wiesbaden, Germany

E. Kirillova Department of Applied Mathematics, RheinMain University of Applied Sciences, Kurt-Schumacher-Ring 18, 76185 Wiesbaden, Germany, e-mail: evgenia.kirillova@hs-rm.de

Yu V. Klunnikova Southern Federal University, Taganrog, Russia

Cheng-Yuan Ko Department of Marine Engineering, National Koahsiung Marine University, 142, Haichuan Rd., Kaohsiung, Nantzu, Taiwan

S. P. Kubrin Faculty of Physics, Research Institute of Physics, Southern Federal University, Rostov-on-Don, Russia

Jung-Chan Lee Department of Electrical Engineering, National Sun Yat-sen University, Kaohsiung 80424, Republic of China (Taiwan)

Jenny Chih-Yu Lee Department of Microelectronics Engineering, National Kaohsiung Marine University, 142 Haichuan Road, Nantzu, Kaohsiung 811, Republic of China (Taiwan)

Ming-Kwei Lee Department of Electronic Engineering, Chung Yuan Christian University, Chung Li 32023, Republic of China (Taiwan), e-mail: mklee@cycu.edu.tw

Yu-Jheng Liao Department of Microelectronics Engineering, National Kaohsiung Marine University, No.142, Haijhuan Rd., Nanzih Dist., Kaohsiung 81157, Republic of China (Taiwan)

Chin-Feng Lin Department of Electrical Engineering, National Taiwan Ocean University, 2 Pei-Ning Road, Keelung 202, Republic of China (Taiwan), e-mail: lcf1024@mail.ntou.edu.tw

Yong-Cheng Lu Department of Electronic Engineering, Chung Yuan Christian University, Chung Li 32023, Republic of China (Taiwan)

N. V. Lyanguzov Vorovich Mechanics and Applied Mathematics Research Institute, Southern Federal University, 200/1, Stachki Ave, Rostov-on-Don, Russia 344090, e-mail: n.lianguzov@mail.ru

M. A. Malitskaya Faculty of Physics, Research Institute of Physics, Southern Federal University, Rostov-on-Don, Russia

S. P. Malyukov Southern Federal University, Taganrog, Russia, e-mail: malyukov@fep.tsure.ru

A. I. Miller Research Institute of Physics, Southern Federal University, Rostov-on-Don, Russia 344090

I. P. Miroshnichenko Don State Technical University, Rostov-on-Don, Russia, e-mail: ipmir@rambler.ru

S. V. Misjul Siberian Federal University, Krasnoyarsk, Russia

M. S. Molokeev Kirensky Institute of Physics, SB RAS, Krasnoyarsk, Russia

Andrey Nasedkin Southern Federal University, Rostov-on-Don, Russia, e-mail: andrey.nasedkin@gmail.com

D. G. Nesvetaev Vorovich Mechanics and Applied Mathematics Research Institute, Southern Federal University, 200/1, Stachki Ave, Rostov-on-Don, Russia 344090

Quoc-Minh Nguyen Department of Electronic Engineering, National Kaohsiung University of Applied Sciences, 415 Chien Kung Rd, Kaohsiung 807, Taiwan, People's Republic of China

A. L. Nikolaev Vorovich Mechanics and Applied Mathematics Research Institute, Southern Federal University, 200/1, Stachki Ave, Rostov-on-Don, Russia 344090

I. A. Parinov Vorovich Mechanics and Applied Mathematics Research Institute, Southern Federal University, Rostov-on-Don, Russia, e-mail: ppr@math.rsu.ru

A. A. Pavelko Research Institute of Physics, Southern Federal University, Rostov-on-Don, Russia 344090

A. A. Pavlenko Research Institute of Physics, Southern Federal University, Rostov-on-Don, Russia 344090

A. M. Pugachev Institute of Automation and Electrometry, SB RAS, Novosibirsk, Russia

S. I. Raevskaya Faculty of Physics, Research Institute of Physics, Southern Federal University, Rostov-on-Don, Russia, e-mail: sveta.raevskaya@mail.ru; igorraevsky@gmail.com

I. P. Raevski Research Institute of Physics, and Physical Faculty, Southern Federal University, Rostov-on-Don, Russia

L. A. Reznichenko Research Institute of Physics, Southern Federal University, Rostov-on-Don, Russia 344090

E. V. Rozhkov Vorovich Mechanics and Applied Mathematics Research Institute, Southern Federal University, Rostov-on-Don, Russia

V. G. Safronenko Vorovich Mechanics and Applied Mathematics Research Institute, Southern Federal University, 200/1, Stachki Ave, Rostov-on-Don, Russia 344090, e-mail: safron@math.rsu.ru

D. A. Sarychev Faculty of Physics, Research Institute of Physics, Southern Federal University, Rostov-on-Don, Russia

S. N. Shevtsov South Center of Russian Academy of Science, Rostov-on-Don, Russia, e-mail: aeroengdstu@list.ru

Maria Shevtsova Southern Federal University, Rostov-on-Don, Russia; Southern Scientific Center of Russian Academy of Sciences, Rostov-on-Don, Russia, e-mail: mariamarcs@bk.ru

M. S. Shevtsova Department of Mechanics of Active Materials, South Scientific Centre of Russian Academy of Sciences, Rostov-on-Don, Russia; Department of Mathematics, Mechanics and Computer Sciences, Southern Federal University, Rostov-on-Don, Russia

Varvara Shevtsova Don State Technical University, Rostov-on-Don, Russia

L. A. Shilkina Research Institute of Physics, Southern Federal University, Rostov-on-Don, Russia 344090

T. V. Sigaeva Department of Mathematics, Mechanics and Computer Sciences, Southern Federal University, Rostov-on-Don, Russia

E. I. Sitalo Faculty of Physics, Research Institute of Physics, Southern Federal University, Rostov-on-Don, Russia

A. N. Soloviev Department of Strength of Materials, Don State Technical University, Rostov-on-Don, Russia 344000; Vorovich Mechanics and Applied Mathematics Research Institute, Southern Federal University, Rostov-on-Don, Russia; Department of Mathematics, Mechanics and Computer Sciences, Southern Federal University, Rostov-on-Don, Russia; Department of Mechanics of Active Materials, Southern Scientific Centre of Russian Academy of Sciences, Rostov-on-Don, Russia, e-mail: solovievarc@gmail.com

V. V. Stashenko Faculty of Physics, Research Institute of Physics, Southern Federal University, Rostov-on-Don, Russia

H. A. Sudykov Research Institute of Physics, Southern Federal University, Rostov-on-Don, Russia 344090

Chia-Chi Sung Department of Engineering Science and Ocean Engineering, National Taiwan University, 1 Sec. 4, Roosevelt Road, Daan, Taipei 10617, Republic of China (Taiwan)

Tze-Yun Sung Department of Electronics Engineering, Chung Hua University, Hsinchu 300-12, Taiwan, e-mail: bobsung@chu.edu.tw

P. Syromyatnikov South Scientific Center of Russian Academy of Sciences, Rostov-on-Don, Russia

M. V. Talanov Research Institute of Physics, Southern Federal University, Rostov-on-Don, Russia 344090

Tzu-Hsien Tang Department of Electrical Engineering, National Sun Yat-sen University, Kaohsiung 80424, Republic of China (Taiwan)

Hsiao-Wen Tin Department of Electrical Engineering, National Taiwan Ocean University, 2 Pei-Ning Road, Keelung 202, Republic of China (Taiwan)

V. V. Titov Research Institute of Physics, and Physical Faculty, Southern Federal University, Rostov-on-Don, Russia

V. Yu. Topolov Department of Physics, Southern Federal University, 5 Zorge Street, Rostov-on-Don, Russia 344090; Scientific Design and Technology Institute "Piezopribor", Southern Federal University, 10 Milchakov Street, Rostov-on-Don, Russia 344090, e-mail: vutopolov@sfedu.ru

A. S. Vasiliev Vorovich Mechanics and Applied Mathematics Research Institute, Southern Federal University, Rostov-on-Don, Russia; Research and Education Center "Materials", Don State Technical University, Rostov-on-Don, Russia, e-mail: andre.vasiliev@gmail.com

I. A. Verbenko Research Institute of Physics, Southern Federal University, Rostov-on-Don, Russia 344090, e-mail: ilich001@yandex.ru

S. S. Volkov Research and Education Center "Materials", Don State Technical University, Rostov-on-Don, Russia

Fu-Tai Wang Department of Electrical Engineering, Hwa Hsia Institute of Technology, 111 Gong Jhuan Road, Chung Ho, New Taipei City 235, Republic of China (Taiwan), e-mail: wft@cc.hwh.edu.tw

Hung-Yu Wang Department of Electronic Engineering, National Kaohsiung University of Applied Sciences, 415 Chien Kung Rd, Kaohsiung 807, Taiwan, People's Republic of China, e-mail: hywang@kuas.edu.tw

C. C. Wen Department of Shipping Technology, National Kaohsiung Marine University, Kaohsiung, Republic of China (Taiwan), e-mail: wencc@webmail. nkmu.edu.tw

Jiing-Kae Wu Department of Marine Engineering, National Koahsiung Marine University, 142, Haichuan Rd., Kaohsiung, Nantzu, Taiwan, e-mail: kirkwu@ webmail.nkmu.edu.tw

P. C. Wu Nanoscience and Nanotechnology Center, National Chung Hsing University, Taichung, Taiwan

Dong-Sing Wuu Department of Materials Science and Engineering, National Chung Hsing University, 250, Kuo Kuang Rd., Taichung 40227, Republic of China (Taiwan)

Chih Chin Yang Department of Microelectronics Engineering, National Kaohsiung Marine University, Kaohsiung, Republic of China (Taiwan)

Chong-He Yang Department of Marine Engineering, National Koahsiung Marine University, 142, Haichuan Rd., Kaohsiung, Nantzu, Taiwan

Chyi-Da Yang Department of Microelectronics Engineering, National Kaohsiung Marine University, No.142, Haijhuan Rd., Nanzih Dist., Kaohsiung 81157, Republic of China (Taiwan)

T. C. Yang Institute of Applied Marine Physics and Undersea Technology, National Sun Yat-sen University, Kaohsiung 80424, Taiwan, e-mail: tsihyang @gmail.com

Min Yen Yeh Department of Microelectronics Engineering, National Kaohsiung Marine University, No.142, Haijhuan Rd., Nanzih Dist., Kaohsiung 81157, Republic of China (Taiwan), e-mail: minyen@webmail.nkmu.edu.tw

Chih-Feng Yen Department of Electronic Engineering, Chung Yuan Christian University, Chung Li 32023, Republic of China (Taiwan)

A. S. Yudin Vorovich Mechanics and Applied Mathematics Research Institute, Southern Federal University, Rostov-on-Don, Russia, e-mail: yudin@math. sfedu.ru

S. A. Yudin Vorovich Mechanics and Applied Mathematics Research Institute, Southern Federal University, Rostov-on-Don, Russia, e-mail: ysergey@mail.ru

I. N. Zakharchenko Faculty of Physics, Research Institute of Physics, Southern Federal University, Rostov-on-Don, Russia

Yu. N. Zakharov Physics Research Institute, Southern Federal University, Rostov-on-Don, Russia

D. A. Zhilin Vorovich Mechanics and Applied Mathematics Research Institute, Southern Federal University, 200/1, Stachki Ave, Rostov-on-Don, Russia 344090

I. V. Zhilyaev South Center of Russian Academy of Science, Rostov-on-Don, Russia

G. A. Zhuravlev Vorovich Mechanics and Applied Mathematics Research Institute, Southern Federal University, Rostov-on-Don, Russia 344090, e-mail: zhuravl@math.rsu.ru

Part I
Processing Techniques of Advanced Materials

Chapter 1
Highly Effective Ferroelectric Materials and Technologies for Their Processing

L. A. Reznichenko, I. A. Verbenko, I. N. Andryushina,
K. P. Andryushin, A. A. Pavelko, A. A. Pavlenko, L. A. Shilkina,
S. I. Dudkina, H. A. Sudykov, A. G. Abubakarov, M. V. Talanov,
V. V. Gershenovich, A. I. Miller and V. A. Alyoshin

The basis of most commonly ferroelectric ceramic materials (FECMs) used in the modern industry is solid solutions of complex lead oxides. It should be noted that due to significant toxicity of lead compounds there has been an intensive search for alternative materials in recent years. Such efforts resulted from the introduction of a new legislative base aiming at environmental protection [Directive 2002/95/EC of the European Parliament and Council by 27 January 2003 on the restriction of the use of certain hazardous substances in electronic equipment]. In the Research Institute of Physics of SFedU much work has been done for about 30 years to investigate and develop of the environmentally friendly FECMs on the basis of alkali niobate metals. Nowadays such materials are finding more applications in the defense industry rather than other industries. Therefore it is extremely important to promote the production of lead low-cost materials and develop new FECMs.

1.1 Introduction

Most of ferroelectric ceramic materials used in production at present are based on solid solutions (SSs) of Pb-containing systems $PbTiO_3$–$PbZrO_3$ (PZT), $Pb(Nb_{2/3}Mg_{1/3})O_3$–$PbTiO_3$ (PMN-PT) and others. The conventional technology of their manufacturing includes a solid-state synthesis and sintering at high temperatures.

Intensive studies on the search, designing and investigations of such materials have been conducting at the Research Institute of Physics of Southern Federal University for over 40 years. With the assistance of the present authors, more than 30 thousands of multicomponent complex oxides of different structural families

L. A. Reznichenko (✉) · I. A. Verbenko · I. N. Andryushina · K. P. Andryushin ·
A. A. Pavelko · A. A. Pavlenko · L. A. Shilkina · S. I. Dudkina · H. A. Sudykov ·
A. G. Abubakarov · M. V. Talanov · V. V. Gershenovich · A. I. Miller · V. A. Alyoshin
Research Institute of Physics, Southern Federal University, Rostov-on-Don,
Russia 344090
e-mail: ilich001@yandex.ru

were synthesized. The crystallochemical conditions of their existence were established. A new approach was worked out which enabled one to consider the problems of stability of structure and ferro-, antiferroelectric states in the above oxides from single positions. The regular relationships between composition, structure and properties were determined that allowed the prediction of characteristics of novel materials. On this basis, a methodology of their purposeful search was developed.

About 200 types of ferro- piezoelectric ceramic materials were engineered and the methods of their preparation were patented. These materials belong to 9 groups which distinguish themselves by a set of electrophysical parameters and, as a consequence, the fields of their application "overlapping", practically, all the known piezotechnical directions. The materials designed are as follows:

(1) Electrically and mechanically stable materials (group 1) designated for devices operating in force regimes (piezotransformers, piezoelectric motors, ultrasonic radiators, high-voltage generators). These materials possess the following parameters: $T_C = (505–625)$ K, $\varepsilon_{33}^T/\varepsilon_0 = 900–2300$, $K_p = 0.57–0.66$, $|d_{31}| = (85–195)$ pC/N, $|g_{31}| = (8.4–11.7)$ mV m/N, $\tan \delta \times 10^{-2}$ ($E = 50$ V/cm) = 0.3–0.85, $\tan \delta \times 10^{-2}$ ($E = 1$ kV/cm) = 0.4–1.0, $Q_m = 630–2000$, where T_C is the Curie temperature, $\varepsilon_{33}^T/\varepsilon_0$ is the relative dielectric permittivity of poled samples, K_p is the electromechanical coupling factor of the radial mode of vibration, $|d_{31}|$ is the piezoelectric modulus, $|g_{31}|$ is the piezoelectric voltage constant (piezoelectric response), $\tan \delta$ is the dielectric loss tangent, E is the strength of electric field, and Q_m is the mechanical quality factor.

(2) Materials having a high dielectric permittivity (group 2) designated for using in low-frequency receiving devices (hydrophones, microphones, seismoreceivers). Their main characteristics are as follows: $T_C = (430–555)$ K, $\varepsilon_{33}^T/\varepsilon_0 = 2800–6000$, $K_p = 0.68–0.71$, $K_{33} = 0.72–0.78$, $|d_{31}| = (245−380)$ pC/N, $\tan \delta \times 10^{-2}$ ($E = 50$ V/cm) = 1.2–2.9, $Q_m = 35–80$, where K_{33} is the electromechanical coupling factor of the longitudinal mode of vibration.

(3) High-sensitive materials (group 3) being effectively used in accelerometers, ultrasonic flaw detectors, devices for nondestructive controlling the objects by the method of acoustic emission, and ultrasonic medical diagnostic equipment. Their main characteristics are as follows: $T_C = (620–630)$ K, $\varepsilon_{33}^T/\varepsilon_0 = 650–1400$, $K_p = 0.62–0.68$, $|d_{31}| = (95−170)$ pC/N, $|g_{31}|= (13.7–16.5)$ mV m/N, $\tan \delta \times 10^{-2}$ ($E = 50$ V/cm) = 1.6–2.0, $Q_m = 90–105$.

(4) Materials with the medium dielectric permittivity (group 4) designated for transducers operating in a receiving mode. They possess the following characteristics: $T_C = (590–595)$ K, $\varepsilon_{33}^T/\varepsilon_0 = 1900–2200$, $K_p = 0.65–0.67$, $|d_{31}| = (205–210)$ pC/N, $|g_{31}| = (10.7–12.1)$ mV m/N, $\tan \delta \times 10^{-2}$ ($E = 50$ V/cm) = 1.4–1.6, $Q_m = 70–75$.

(5) Materials with the high anisotropy of piezoelectric parameters (group 5) designated for ultrasonic flaw detectors, thickness gauges, medical diagnostic equipment, accelerometers, piezoelectric indicators with the abnormal sensitivity to hydrostatic pressure. Their main characteristics are as follows:

$T_c = (600-715)$ K, $\varepsilon_{33}^T/\varepsilon_0 = 120-180$, $K_p = 0-0.07$, $K_{15} = 0.44-0.64$, $|d_{31}| = (0-5)$ pC/N, $d_{33} = (52-114)$ pC/N, $|g_{31}| = (0-3.2)$ mV m/N, $g_{33} = (33-108)$ mV m/N, tan $\delta \times 10^{-2}$ $(E = 50$ V/cm$) = 1.0-2.2$, $Q_m = 8-2000$, where K_{15} is the electromechanical coupling factor of the shear mode of vibration.

(6) Materials with the high stability of resonance frequency (group 6) having a broad application in filter devices. Their main characteristics are: $T_C = (575-640)$ K, $\varepsilon_{33}^T/\varepsilon_0 = 400-1400$, $K_p = 0.10-0.53$, $|d_{31}| = (6-100)$ pC/N, $\delta f_\theta/f_r$ $((213-358)$ K$) = (0.15-0.25)$ %, tan $\delta \times 10^{-2}$ $(E = 50$ V/cm$) = 0.2-2.0$, $Q_m = 300-12000$, where f_θ is the resonance frequency in the above temperature range, and f_r is the resonance frequency at room temperature.

(7) Materials with the low dielectric permittivity (group 7) designated for the use in high-frequency acoustoelectric transducers. They possess the following characteristics: $T_c = (515-595)$ K, $\varepsilon_{33}^T/\varepsilon_0 = 260-510$, $K_p = 0.20-0.54$, $|d_{31}| = (16-70)$ pC/N, $|g_{31}| = (7.0-15.5)$ mV m/N, tan $\delta \times 10^{-2}$ $(E = 50$ V/cm$) = 0.3-1.0$, $Q_m = 200-4500$, $V_R = (3.60-4.20)$ km/s.

(8) Pyroelectric materials (group 8) being applied as the operating elements of indicators of pyroelectric radiant (thermal) energy detectors with the long-distance measurement of temperature of the heated bodies, including the moving ones. Their main characteristics are: $\varepsilon_{33}^T/\varepsilon_0 = 290-420$, $|d_{31}| = (27-49)$ pC/N, $\gamma \times 10^4 = (5.0-5.5)$ C/(m^2·K̇), $(\gamma \cdot \varepsilon_{33}^T/\varepsilon_0) \times 10^6 = (1.3-1.7)$ C/(m^2·K̇), $(\gamma \cdot d_{31}) \times 10^6 = (10.4-18.5)$ N/(m^2·K̇), where γ is the pyroelectric coefficient, $(\gamma \cdot \varepsilon_{33}^T/\varepsilon_0)$ is the coefficient proportional to the V–Wt sensitivity, and $(\gamma \cdot d_{31})$ is the product that characterizes the vibrational-noise stability of the piezoelectric.

(9) High-temperature materials (group 9) which distinguish themselves by the high values of the Curie point and operating temperatures. They may effectively used, in particular, as a base for indicators of controlling the processes proceeding at the extreme conditions in different industrial power-plants (internal combustion engines and heated pipelines). They possess the following main characteristics: $T_C = (675-1475)$ K, $T_{oper} = (575-1225)$ K, $\varepsilon_{33}^T/\varepsilon_0 = 48-455$, $K_p = 0.015-0.32$, $K_t = 0.29-0.46$, $|d_{31}| = (0.51-35)$ pC/N, $d_{33} = (12-100)$ pC/N, $g_{33} = (19.0-33.0)$ mV m/N, tan $\delta \times 10^{-2}$ $(E = 50$ V/cm$) = 0.1-1.0$, $Q_m = 100-4000$ (K_t is the electromechanical coupling factor of the thickness mode of vibration). All these materials were based on the PZT system and prepared by the hot-pressing method.

Due to significant toxicity of lead compounds there has been an intensive search for alternative materials in recent years. Such efforts resulted from the introduction of a new legislative base aimed on environmental protection [Directive 2002/95/EC of the European Parliament and Council by 27 January 2003 on the restriction of the use of certain hazardous substances in electronic equipment]. In the Research Institute of Physics of SFedU great work has been conducted for about 30 years to R&D the environmentally friendly ferroelectric ceramic materials on the basis of

alkali niobate metals. Nowadays such materials are finding more applications in the defense industry rather than other industries. Therefore it is extremely important to promote the production of lead low-cost materials, develop new ferroelectric ceramic materials and other high-performance piezoelectric materials.

1.2 Research Results

In the course of our search we have developed a new technique which allows obtaining a number of lead-free and other high-performance piezoelectric materials by a common technology, which were previously made using hot pressing (HP) or exotic methods applicable only in a laboratory such as topochemical texturing and synthesis in plasma discharge. An attempt has been made to obtain new lead-free ceramics, using complex scheme of modification and various methods of additional activation of chemical agent. Recently we have obtained and examined the materials on the basis of multicomponent system $[(Na_{0.5}K_{0.5})_{1-x}Li_x]$ $(Nb_{1-y-z}Ta_ySb_z)O_3$ with the following electrophysical parameters $\varepsilon_{33}^T/\varepsilon_0 = 330$, $K_p = 0.34$, $|d_{31}| = 58.3$ pC/N, $Q_m = 100$, $V_1^E = 4.5$ km/s; high-performance PCR-35 on the basis of $NaNbO_3$–$LiNbO_3$ (with almost zero displacement of resonant frequency) and PCR-61 on the base $LiNbO_3$ (which have record work-temperature ≥ 1000 °C) with parameters $\varepsilon_{33}^T/\varepsilon_0 = 155$, $K_p = 0.19$, $|d_{31}| = 11$ pC/N, $V_1^E = 5.5$ km/s and $\varepsilon_{33}^T/\varepsilon_0 = 48$, $K_p = 0.068$, $|d_{31}| = 3$ pC/N, $K_t = 0.31$, respectively. In fact, to produce these materials a new technology was developed which does not require HP. This group of materials can be used in flaw detectors, leak detectors and control processes in the critical nodes of power plants under-water vehicles.

Due to the growing need for high-precision piezoelectric materials, the piezo-electric transducers used in sonar, ultrasonic flaw detection, and a number of other devices on the one hand, and the transition to environmentally sound technologies, on the other hand, is the actual direction of a new generation of lead free materials with high piezoelectric sensitivity ($g_{33} \sim 30$ mV m/N and more). Piezoelectric sensitivity of industrial materials meets the requirements of modern technology. The purpose of the work was to establish the influence of ions of the transition 3D-metals to form electrical properties of the selected lead-free systems and the creation of polycrystalline materials with high piezoelectric sensitivity. The objects of study were selected on the basis of solid solutions (Na, Li)NbO_3 and (Na, K)NbO_3, overstoichiometric modified (1.0–3.0) masses %MnO_2, CuO, MnO_2 + CuO and Bi_2O_3 + Fe_2O_3 (Fig. 1.1).

The work shows that the modification of solid solutions of $(Na_{1-x}Li_x)NbO_3$ microstructures are formed with a "cementing" nature of intergranular layers using liquid phase rich in Cu, Mn and Bi. The growth of Q_m, g_{33}, as well as reducing $\varepsilon_{33}^T/\varepsilon_0$, tan δ and electrical conductivity in the modified ceramic based on $(Na_{1-x}Li_x)NbO_3$ caused partial embedding cation modifier Cu^{2+} and Ni^{2+} to A^-, and Mn^{4+} in the B-sublattice of the perovskite structure with the formation of non-stoichiometric
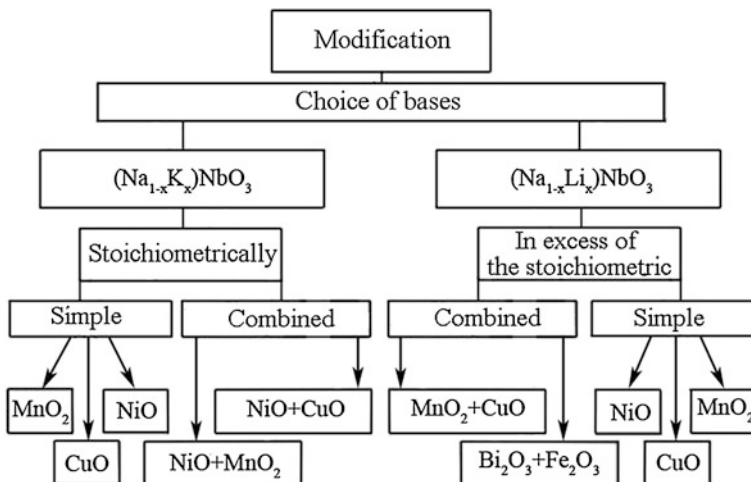
Fig. 1.1 Schematic of ceramic modification

solid solutions with increased ferroelectric hardness. Increase of piezoelectric anisotropy in modified TP associated with the formation of textures of the inter-crystalline layers that hinder the movement of their boundaries along certain directions. It was found that the growth of $\varepsilon_{33}^{T}/\varepsilon_0$, $\tan \delta$, as well as reducing the piezoelectric anisotropy in solid solutions based on $(Na_{1-x}K_x)NbO_3$ modification caused by crystal-chemical characteristics of major ions Na^+ and K^+. It is forced out into intergranular layer modifier that contributes to the process of hydrolysis and prevents the formation of anisotropic structures and texturing. It was found that a promising basis for the development of materials with high Q_m, g_{33}, anisotropic piezoelectric coefficients and low electrical conductivity while maintaining suffi-cient piezoelectric activity, $K_p \sim 0.2$, were solid solutions of the $(Na_{1-x}Li_x)NbO_3$. Developed materials with 1.5 wt% $(Bi_2O_3 + Fe_2O_3)$, having $Q_m > 700$ and $K_p \sim 0.2$, are promising for use in power ultrasonic transducer, with 2.0 wt% $(MnO_2 + 0.5\ CuO)$, of high $g_{33} \sim 40$ mV·m/H and $d_{33}/|d_{31}| > 5$, promising to sonar.

Currently, materials with properties of high absorption of microwave (MW), electromagnetic (EM) radiation are widely used in industrial applications in microwave technology (phase shifters, filters, communicators), as well as a variety of radar absorbing coatings. In context of this search, study of such materials is important.

In this paper the absorption spectra of microwave energy EM field of ferro-electrics (FE) $Sr_2Nb_2O_7$ and $Ca_2Nb_2O_7$ with layered perovskite structure as well as their solid solutions (TP) with antiferroelectric $NaNbO_3$ in $(1 - x)NaNbO_3 - xSr_2(Ca_2)Nb_2O_7$ ($0 \leq x \leq 1.0$) were studied.

X-ray studies were carried out by powder diffraction using a DRON-3 and ADP (FeK_{α}-radiation; FeK_{β}-radiation, scheme focusing on the Bragg–Brentano).

Crushed ceramic samples were studied. It is possible to eliminate the influence of surface effects, stress and texture that occur during the production of ceramics.

Set up for measurements of $L(f)$ consists of a generator swept frequency, broadband microstrip line, operating in the traveling wave and the panorama measuring voltage standing wave ratio and reducing P2-61 in the frequency range 7.8–11.8 GHz.

It is shown that in the absorption of microwave energy by $NaNbO_3$ solid solutions in areas of co-existence and the layered perovskite phase, and in the latter case—structures with different multiplicity of cells, there are large (more than 40 dB) typical absorption maxima. It is observed due to both the crystal-chemical characteristics of the studied ferroelectric compounds (layering of the structure and, as a consequence, the well-known fragility of chemical bonds), and increased defectiveness of solid solutions, characterized by structural instability of the areas of reconstructive and morphotropic phase transitions. These results suggest that the studied compositions may be a promising basis for radar absorbing materials used in particular for underwater applications.

Multiferroics, representing a broad class of materials that combine ferroelectric, ferromagnetic and ferroelastic properties are currently being studied in detail in connection with the potential for their use in new devices based on mutual control of magnetic and electric fields [1].

Bismuth ferrite is one of the most studied ferroelectric. He has a higher temperature ferroelectric ($T_C = 810$ °C) and magnetic ($T_N \sim 370$ °C) ordering. But its wide application prevents the structural instability (Fig. 1.2). It is a consequence of the boundary position in the perovskite structure type, high conductivity and thermal instability, connected to the proximity of sintering temperatures (T_{sp}) and incongruent melting, as well as the spin-modulated structure that prevents magnetoelectric interaction. The structure of the bismuth ferrite is critically dependent on the thermodynamic history (processing conditions). It is due to a narrow concentration range of a phase $BiFeO_3$, a very wide range of crystallization of compounds, volatility of $Bi_2Fe_4O_9$, $Bi_{25}FeO_{39}$, Bi_2O_3 and complexity of the reaction in equimolar mixture Bi_2O_3/Fe_2O_3. This leads to the formation during its synthesis and sintering quite significant (~ 10 %) difficult-"ballast" phases, including unreacted starting components. Laboratory methods for single-phase $BiFeO_3$ cannot be applied in the industry. The dielectric properties of $BiFeO_3$ are also unstable with respect to temperature. Thus, identification of the causes of this instability and search of possible ways to fix it in the processing methods that allow scaling of production in the industrial environment is the goal of this work.

Analysis of the results showed that «$BiFeO_3$» is based on a minimum of five Bi- and Fe-containing compounds. That is why, all bifurcations (unstable states) are inherent to them, and it is applied to macroproperties of the analyzed multiferroic. Determine the mode of processing $BiFeO_3$ with stable dielectric properties at high temperatures. It is suggested that the use of mechanical activation, is directed to reducing the size and increasing the volume area of the reactants. "Hardening" is able to "freeze" the defects and to eliminate the effect of incongruent melting.
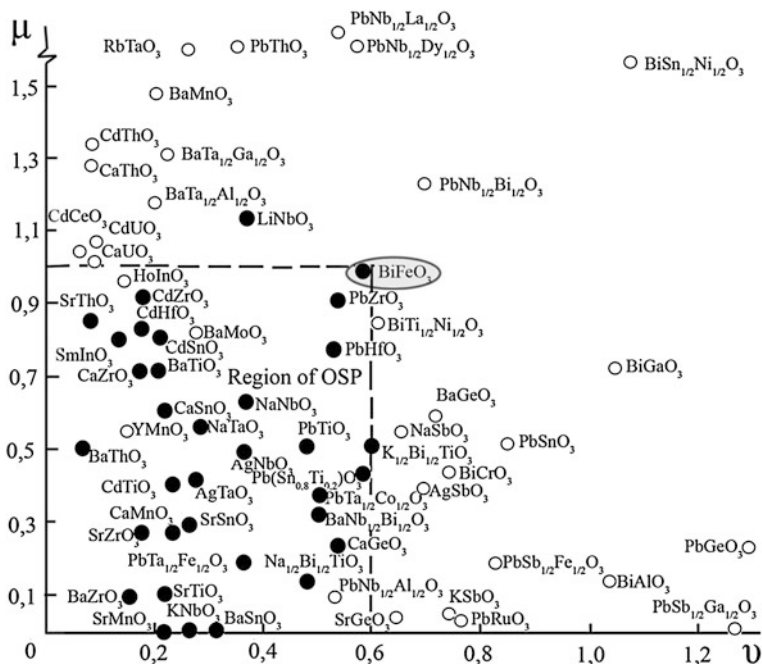
Fig. 1.2 Diagram of parameters based on orientation υ and intensity μ dependences and the existence region of OSP (oxides with a perovskite structure) [2]

Thus an increase of the amount of material enters into a full response and it does not fall out in the form of amorphous phases.

The data obtained can be used for development of spintronics, used in underwater acoustics.

As the components of these compounds often serve the rare earth elements (REEs), which help to stabilize the structure of $BiFeO_3$ and optimize its properties. The present study is aimed to identification of regularities in the formation of a polycrystalline (grain) structure of the $BiFeO_3$ samples with some REEs and their correlation with the macroscopic physical properties of the objects.

The objects of the study were TP binary systems of $Bi_{1-x}Re_xFeO_3$ (where Re = Tb, Dy, Ho, Er, Yb, Tm, Lu, x = 0.05–0.20, Δx = 0.05). The samples were obtained by conventional ceramic technology, including a two-step synthesis, followed by sintering without the application of pressure.

Bismuth-lanthanum manganite $Bi_{1/2}La_{1/2}MnO_3$ (BLM) is a multiferroic in which the electric and magnetic orders coexist [3]. Earlier, when studying the BLM ceramics at the temperature of 80 K, we detected non-Debye retardation of the complex dielectric constant $\varepsilon = \varepsilon' - i\varepsilon''$ with mean relaxation frequency $f_r^\varepsilon = (2.5–3) \times 10^3$ Hz and non-Debye relaxation of the conductivity $\gamma = \gamma' + i\gamma''$ with relaxation frequency $f_r^\gamma \approx 5 \times 10^5$ Hz. $f_r^\gamma \gg f_r^\varepsilon$ due to an increasing in the
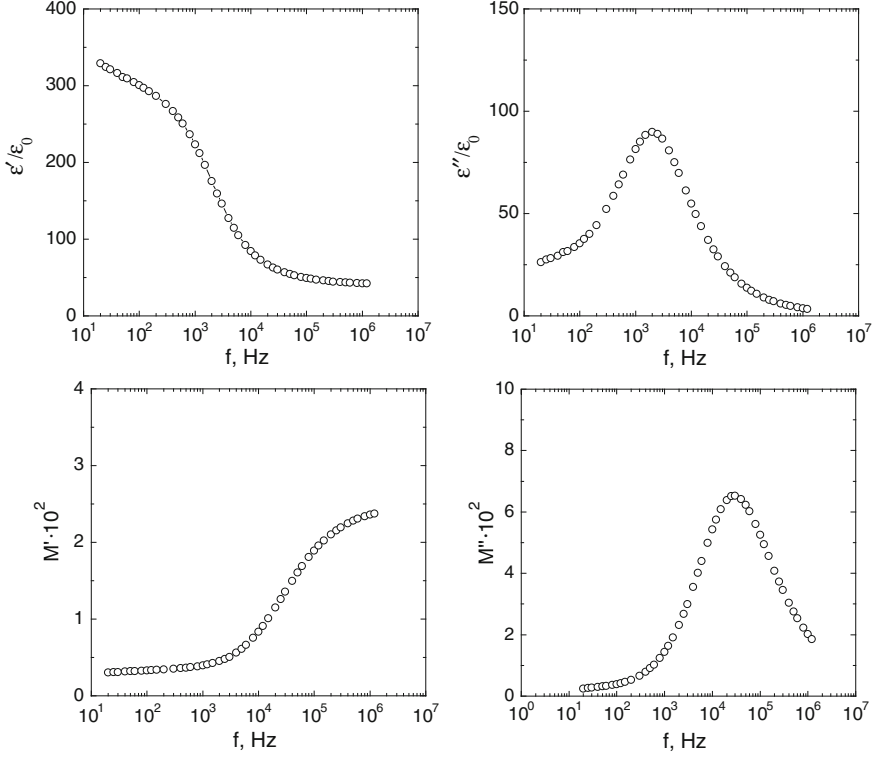
Fig. 1.3 Dependences $\varepsilon'/\varepsilon_0(f), \varepsilon''/\varepsilon_0(f), M'(f)$ and $M''(f)$ of the BLM ceramics measured at the temperature of 80 K

conductivity spectra statistical weight of the relaxation processes with short relaxation times [4].

The aim of this work is to expand researches of the BLM ceramics using a method of impedance spectroscopy for measurements of the frequency dependence and the relaxation of the complex electric modulus $M = 1/\varepsilon = M' + iM''$. The ratio of the average relaxation and retardation frequencies is represented as $f_r^M/f_r^\varepsilon = \varepsilon_s/\varepsilon_\infty$, where ε_s and ε_∞ are the static dielectric constant and high-frequency dielectric constant, respectively [5, 6]. This relation is strictly valid only for Debye-type dielectrics, semiconductors and ferrites. However, for non-Debye materials, the aforementioned relation can appear incorrect and, therefore, should be checked.

It has appeared (Fig. 1.3) that in BLM ceramics there are two non-Debye retardation and relaxation ranges, namely low-frequency and high-frequency ones. And for both these ranges $f_r^M/f_r^\varepsilon = \varepsilon_s/\varepsilon_\infty$. We have revealed that the high-frequency spectrum of the BLM ceramics can be approximated with the rectangular distribution function $f(\tau)$ of the relaxation times, where $f(\tau) = h = \mathrm{const}$ within the interval $\tau_1 \le \tau \le \tau_2$ and $f(\tau) = 0$ at $\tau < \tau_1$ and $\tau > \tau_2$. Here $f(\tau)d\tau$ is the

probability that the relaxation time be into interval from τ to $\tau + d\tau$ [4]. A relaxation oscillator in such a material can be described at a microscopic level by the model of a deep potential well with two equilibrium positions divided by a potential barrier (so-called the Fröhlich oscillator [5]). Due to a wide range of distribution of relaxation times the high-frequency dielectric spectrum of BLM ceramics has non-Debye character. Just the non-Debye character of the high-frequency dielectric spectra consists in the large distinction between the dielectric retardation (f_r^ε) and dielectric relaxation (f_r^M) frequencies.

The binary solid solutions (SSs) of the composition $(1 - x)PbZrO_3 - xPbTiO_3$ (PZT) have hitherto retained their uniqueness and practical value. Multicomponent systems with their participation became the basis of the most of the industrially produced ferro-piezoelectric materials (FPM). The aim of the present work is the determination of correlation bonds "composition—structure—electrophysical properties" in the whole concentration range of the PZT system.

This work is concerned with the specific features of sintering of SSs. The microstructure of the ceramics has been found to be a fairly homogeneous, mosaic, sufficiently close packing of isometric crystallites with a range of section from 3 to 11 μm, but there are a number of special features related to the component and phase composition of the objects. The sequence of phase transformations in the system is determined and the real phase diagram of SSs is built. The observed periodicity of phase formation processes in the rhombohedral (Rh) and tetragonal (T) regions is explained by the real (defective) structure of ceramics, which is in many aspects related to the variable valence of Ti ions and, as a result, to formation, accumulation, and ordering of point defects (oxygen vacancies) and their elimination by crystallographic shifts. Based on high temperature X-ray diffraction studies the complete $(x - T)$-phase diagram of system is built, which exhibits peculiar properties due to the real structure of ceramics: irregularity of the phase transition line to the paraelectric state, which is more pronounced in the Rh–T transition region; appearance of intermediate "region of indistinct symmetry" at $0.2 \leq x \leq 1.0$, which forestalls the transition to the non-polar cubic phase at temperature increase; formation of two morphotropic regions, contracting (rhombic—Rh) and expanding (Rh–T) at temperature increase; richness of single-symmetry phase diagram fragments by regions of coexistence of phase states.

Macro-properties of the system were studied in broad ranges of temperature ($10 \leq T \leq 1000$ K), frequency (10^{-2} Hz $\leq f \leq 10^7$ Hz) and strengths of direct and alternating electric field (0 kV/cm $\leq E \leq 30$ kV/cm). Several groups of SSs were distinguished, which differed by non-monotonic behavior of dielectric parameters in the cryogenic temperature range and at $T > 300$ K, which results both from the defective state and from the polymorphism of SSs.

On the basis of the studies, the "soft" ferroelectric compositions from Rh region close to the morphotropic one are most compliant for devices of underwater applications.

Materials based on $Pb(Mg_{1/3}Nb_{2/3})O_3$ and $Pb(Zn_{1/3}Nb_{2/3})O_3$ ferroelectric relaxor solid solutions and ferroelectric $PbTiO_3$ are of considerable interest for

Table 1.1 Principal electrical parameters of the ceramics and their known analogs

Solid solution	$\varepsilon/\varepsilon_0$	$\varepsilon_{33}^T/\varepsilon_0$	$\tan\delta \times 10^{-2}$	K_p	$|d_{31}|$, pC/N	V_1^E, km/s	Q_m
Modified	7750	9100	3.10	0.57	230	2.85	39
Unmodified	3690	4300	3.26	0.52	210	3.00	37
PCR-7	2150	3500	1.50	0.68	280	2.68	80
PCR-7 M	2800	5000	2.00	0.71	350	2.69	60
PCR-73	3200	6000	2.90	0.70	380	2.64	30
PZT-5H	–	3400	2.00	0.65	274	–	65
PZTSB-1	–	2200	1.900	0.54	205	–	70

practical applications in sonars and actuators. Materials with compositions near the morphotropic phase boundary between rhombohedral and tetragonal phases offer excellent dielectric and electromechanical properties [7].

Piezoelectric material for use in underwater devices, in particular, in sonars, must have a set of defined parameters:

(i) high values of the hydrostatic piezoelectric coefficient, d_h, and hydrostatic figure of merit, $d_h g_h$, to increase the sensitivity of the devices;
(ii) rather high relative dielectric permittivity, $\varepsilon_{33}^T/\varepsilon_0$, to simplify the signal preamplifier system and improve transducer agreement with the load;
(iii) low values of the mechanical quality factor, Q_m, to suppress spurious oscillations.

One of the most promising candidates for materials for underwater applications are solid solutions of systems based on relaxor ferroelectrics (RF) $Pb(Mg_{1/3}Nb_{2/3})O_3$ (PMN), $Pb(Zn_{1/3}Nb_{2/3})O_3$ (PZN) and classical ferroelectric $PbTiO_3$(PT), near the morphotropic phase boundary. They are characterized by the ultrahigh values of piezoelectric responses that are higher than those in the ceramics of $Pb(Ti, Zr)O_3$ (for instance, PZT-5H) [7].

In order to find new materials for underwater applications, we used the above RF and PT as a basic component in combination with another RF ($Pb(Ni_{1/3}Nb_{2/3})O_3$) [8]. Table 1.1 summarizes the room temperature basic electrical parameters of the ceramics studied and some their analogs (from PCR group) [9] prepared by hot pressing, and expensive technique. The barium modified ceramics are seen to be superior in $\varepsilon/\varepsilon_0$ and $\varepsilon_{33}^T/\varepsilon_0$ compared to both the unmodified solid solutions and the commercially available foreign analogs. Moreover, barium doping allowed us to improve the piezoelectric performance (K_p and $|d_{31}|$) of the material by 10 % and reduce $\tan\delta$, whereas its Q_m remained not very high.

The most promising compositions for further research have been recognized those with the content of PT (30–35) mol. %. They are characterized by high values of piezoelectric coefficients: $d_{33} = (450–530)$ pC/N, $d_h = (50–110)$ pC/N, $d_h g_h = (200–350) \times 10^{-15}$ m^2/h and $\varepsilon_{33}^T/\varepsilon_0 = (3000–7000)$, and low Q_m (≈ 30). Thus, we have developed materials that also superior the widespread industrial

analog PZT-5H on set of key parameters. The studied ceramics were obtained by using the most accessible and commercially adapted conventional ceramic technology, no hot pressing (as it was done previously), that significantly reduced the cost of the final product.

References

1. A.K. Zvezdin, A.S. Loginov, G.A. Meshkov, A.P. Pyatakov, Proc Russ Acad Sci Phys **71**, 1604 (2007)
2. E.G. Fesenko, A.J. Danziger, O.N. Razumovskaja, *New Piezoceramic Materials* (Rostov State University Press, Rostov-on-Don, 1983). (in Russian)
3. A.V. Pavlenko, A.V. Turik, L.A. Reznitchenko, L.A. Shilkina, G.M. Konstantinov, Tech. Phys. Lett. **39**, 78 (2013)
4. A.V. Turik, A.S. Bogatin, E.V. Andreev, Solid State Physics **53**, 1194 (2011)
5. H. Fröhlich, *Theory of Dielectrics* (Clarendon, Oxford, 1958)
6. J. Jäckle, R. Richert, Phys. Rev. E **77**, 031201 (2008)
7. S.-E. Park, T.R. Shrout, J. Appl. Phys. **82**, 804 (1997)
8. M.V. Talanov, I.A. Verbenko, L.A. Shilkina et al., Inorg. Mat. **48**, 386 (2012)
9. A.Ya. Dantsiger, O.N. Razumovskaya, L.A. Reznichenko et al., *Multicomponent Systems of Ferroelectric Mixed Oxides: Physics, Crystal Chemistry, and Technology, in Design Aspects of Piezoelectric Materials*, vol. 2. (Novaya Kniga, Rostov-on-Don, 2002) (in Russian)

Chapter 2
The Effect of Mechanical Activation on the Synthesis and Properties of Multiferroic Lead Iron Niobate

A. A. Gusev, I. P. Raevski, E. G. Avvakumov, V. P. Isupov, S. P. Kubrin, H. Chen, C.-C. Chou, D. A. Sarychev, V. V. Titov, A. M. Pugachev, S. I. Raevskaya and V. V. Stashenko

The present work studies the effect of high-energy mechanical activation using the planetary-centrifugal ball mill AGO-2 and subsequent annealing on the synthesis and magnetic properties of $PbFe_{0.5}Nb_{0.5}O_3$ (PFN). This technique enables one to perform the mechanically activated synthesis of PFN at much shorter time. The results of X-ray phase analysis, electron microscopic studies and transmission Mössbauer ^{57}Fe spectra measurement are presented and discussed. Mössbauer studies show that the temperature of magnetic phase transition in $PbFe_{0.5}Nb_{0.5}O_3$ powders can be changed by mechanical activation and subsequent annealing.

2.1 Introduction

Lead iron niobate $PbFe_{0.5}Nb_{0.5}O_3$ (PFN) is a ternary perovskite oxide possessing both ferroelectric (ferroelectric Curie temperature $T_C \approx 380$ K) and magnetic (temperature of antiferomagnetic phase transition, i.e. Neél temperature, $T_N \approx 150$ K) properties [1]. PFN is a promising basic material for multilayer

A. A. Gusev · E. G. Avvakumov · V. P. Isupov
Institute of Solid State Chemistry and Mechanochemistry SB RAS, Novosibirsk, Russia

I. P. Raevski · S. P. Kubrin · D. A. Sarychev · V. V. Titov · S. I. Raevskaya (✉) ·
V. V. Stashenko
Research Institute of Physics and Physical Faculty, Southern Federal University,
Rostov-on-Don, Russia
e-mail: sveta.raevskaya@mail.ru

H. Chen
University of Macau, Macau, China

C.-C. Chou
National Taiwan University of Science and Technology, Taipei 10607,
Republic of China (Taiwan)

A. M. Pugachev
Institute of Automation and Electrometry, SB RAS, Novosibirsk, Russia

capacitors, pyroelectric sensors, piezoelectric ceramics and electrostrictive actuators [2–6]. It is also a component of some novel room-temperature multiferroic magnetoelectrics [7].

The temperature of magnetic phase transition in Fe-containing oxides is believed to depend on the number of possible Fe–O–Fe linkages in a crystal lattice [8]. In ternary $PbFe_{0.5}B_{0.5}O_3$ perovskites this number can be governed, e.g. by changing the degree S of B-cation ordering, as the ordering changes the number of magnetic ions in the neighboring unit cells and thus reduces the possible number of Fe–O–Fe linkages. However in contrast to $PbB^{3+}_{0.5}B^{5+}_{0.5}O_3$ perovskites with $B^{3+} = Sc, Yb; B^{5+} = Nb, Ta$, [9, 10], no superstuctural reflections on X-ray diffraction patterns due to B-cation ordering have been reported for PFN [8, 11]. At the same time, the experimental value of T_N, for PFN (≈ 150 K) is located approximately half-way between calculated values of this temperature for the fully ordered ($T_N = 0$ K) and completely disordered ($T_N \approx 400$ K) states [8]. This fact is usually interpreted as an evidence of a partial ordering of Fe^{3+} and Nb^{5+} cations [8]. The possible reason of the absence of superstuctural reflections on X-ray diffraction patterns is a local character of ordering in PFN, i.e. mesoscopic domains of several nanometers in size with different values of S coexist in a crystal. Another evidence of the chemically inhomogeneous nature of PFN was obtained from the studies of magnetization [1, 11], ^{93}Nb and ^{17}O NMR [12] and Mössbauer ^{57}Fe spectra [13], diffuse neutron scattering [11] as well as from the results of the first-principal calculations [13]. Long range AFM order seems to develop in Fe-rich-Nb-poor regions while, a short-range ordered spin-glass-like state can arise at low ($T \approx 10$–20 K) temperatures from the Fe-poor-Nb-rich regions. AFM and spin-glass states can coexist in a wide temperature range [14]. Magnetic phase transition temperature in PFN is more than 100 K higher as compared to lead-free $AFe_{0.5}Nb_{0.5}O_3$ ($A = $ Ca, Sr, Ba) perovskites [15, 16]. This dramatic difference is attributed to the possibility of magnetic super-exchange via an empty $6p$ state of Pb^{2+} ions [15, 16] as well as for the clastering of iron ions in the lattice [13]. Both the degree of B-cation compositional ordering and clastering of iron ions are known to be influenced by mechanical activation, which has been successfully used for the synthesis and preparation of ternary lead-based perovskite ferroelectrics [17, 18]. This method enables one to obtain nanodispersed powders with high sintering ability thus lowering substantially the sintering temperature of ceramic materials. We have found in the literature two works devoted to the application of the mechanical activation method for synthesis of PFN [19, 20]. However, the effect of mechanical activation on magnetic properties of PFN has not been studied yet. Moreover, the energy of mechanical activation, used in [19, 20], was rather modest and the activation time varied from 20 to 30 h. Recently the planetary-centrifugal ball mill AGO-2 enabling activation with much higher energy than in [19, 20] was designed [17]. The aim of the present work was to study the effect of high-energy mechanical activation using AGO-2 mill and subsequent annealing on the synthesis and magnetic properties of PFN.

2.2 Experimental

In order to compare the effect of high-energy milling on PFN synthesis, two batches were used: stoichiometric mixture of PbO, Fe_2O_3 and Nb_2O_5 oxide powders (**I**) and stoichiometric mixture of PbO and preliminary synthesized $FeNbO_4$ precursor (**II**). The starting oxides were Nb_2O_5 (the American Society for Testing Materials (ASTM) code 16-53, 37-1468), monoclinic modification, space group P2 (no. 3), OSCh reagent grade (high pure); Fe_2O_3 (ASTM code 85-599) hematite, rhombohedral modification, space group R-3C (no. 167), ChDA reagent grade (pure for analysis); PbO (ASTM code 72-93) massicot, orthorhombic modification, space group Pbcm (no. 57), ChDA reagent grade (pure for analysis), with Pb_3O_4 admixture (ASTM code 41-1493) minium, tetrahedral modification, space group P42/mbc (no. 135). The mechanical activation was carried out using the high-energy planetary-centrifugal ball mill AGO-2 under a ball acceleration of 40 g. A mixture of powdered reagents (10 g) was placed into steel cylinder together with 200 grams of steel balls 8 mm in diameter. Activation was carried out for 5, 10 and 15 min. After each 5 min of activation, the mill was stopped, the cylinders were opened, the powder was taken out and mixed then it was put back into the cylinders for further mechanical activation. The samples for subsequent annealing were pressed at 1000 kg/cm^2 without a plasticizer. Annealing of the samples, placed into a closed alumina crucible, was carried out in an electric oven at different temperatures for 2 h. Heating rate was 10 deg/min. The samples were cooled together with the furnace after it was switched off. X-ray phase analysis was performed using DRON-3 diffractometer and Cu–K_α radiation. Electron microscopic studies were carried out with a transmission electron microscope (TEM) JEM-2000FX II (JEOL) at the accelerating voltage of 200 kV. Transmission Mössbauer ^{57}Fe spectra were measured with the aid of MS-1104EM rapid spectrometer and analyzed using the original computer program UNIVEM. The sample holder was attached to the closed-cycle helium cryostat-refrigerator Janis Ccs-850 operating in the 12–320 Ǩ range.

2.3 Results and Discussion

The diffraction patterns of the samples of stoichiometric mixture of PbO, Fe_2O_3 and Nb_2O_5 oxide powders (**I**) before activation (a) and after activation for 5, 10, and 15 min (b)–(d), respectively, are shown in Fig. 2.1. Amorphization process indicated by the broadening of the diffraction reflexes and the initial stage of the formation of perovskite structure of PFN are well seen even after 5 min of activation. After 15 min of activation, only the lines corresponding to the perovskite structure are well seen in the diffraction pattern. It is worth noting that the diffraction pattern of the mixture **I** activated for 15 min using the high-energy planetary-centrifugal ball mill AGO-2 is very similar to the patterns reported in

Fig. 2.1 Diffraction patterns illustrating the effect of mechanical activation on the stoichiometric mixture of PbO, Fe_2O_3 and Nb_2O_5 (mixture **I**): **a** initial mixture, **b** after mechanical activation for 5 min, **c** after mechanical activation for 10 min, **d** after mechanical activation for 15 min; ▼—Nb_2O_5; +—PbO; ●—Fe_2O_3; *—PFN
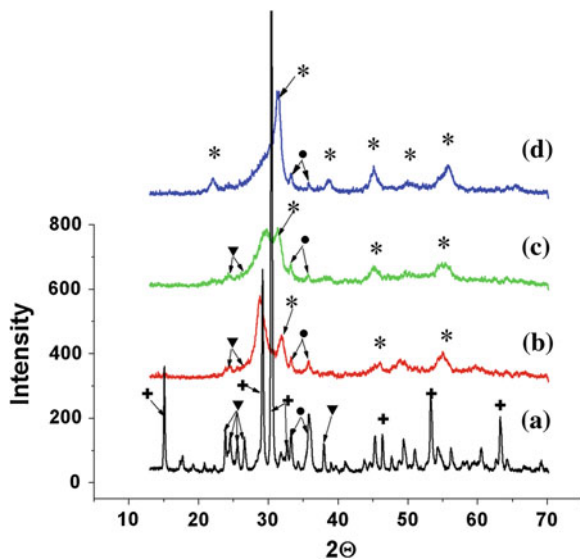
Fig. 2.2 X-ray diffraction patterns illustrating the stages of the $FeNbO_4$ synthesis: **a** initial mixture of Fe_2O_3 and Nb_2O_5, ●—Fe_2O_3, other reflections belong to Nb_2O_5; **b** after mechanical activation for 15 min, O—reflections of $FeNbO_4$; **c** after annealing at 1000 °C, ●—Fe_2O_3, other reflections belong to $FeNbO_4$−; **d** mixture of $FeNbO_4$ and PbO, +—basic reflections of PbO, †—basic reflections of Pb_3O_4, other reflections belong to $FeNbO_4$
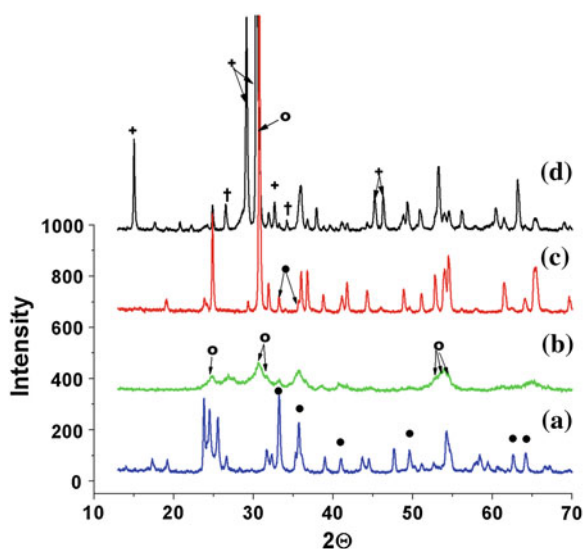
[19, 20] for the same mixtures activated in a shaker mill for 30 h or in a SPEX 8000D vibrating mill for 20 h, respectively.

One can see in Fig. 2.1d that besides the PFN reflexes, there are also two minor reflexes corresponding to Fe_2O_3 indicating that the synthesis of PFN is not complete. One can also expect that some amount of $FeNbO_4$ is present, because it appears in the activated mixture of Fe_2O_3 and Nb_2O_5 (Fig. 2.2b). However, due to a considerable widening of reflexes on the diffraction pattern, no PbO, Nb_2O_5, and $FeNbO_4$
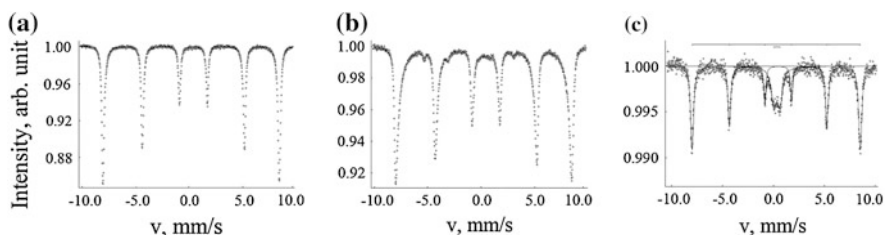
Fig. 2.3 Room-temperature Mössbauer ^{57}Fe spectra: **a** initial mixture of PbO, Fe_2O_3 and Nb_2O_5 (mixture **I**); **b** Fe_2O_3 powder after mechanical activation for 15 min; **c** mixture of PbO, Fe_2O_3 and Nb_2O_5 after mechanical activation for 15 min

reflexes could be unequivocally identified. The mean size of X-ray coherent scattering blocks, estimated using the Scherrer formula for the mixture **I** activated for 15 min, is about 13–20 nm. This value correlates well with the TEM images of the same powder. To have a deeper insight into the phase content of the mechanically activated mixture **I** we studied its room-temperature Mössbauer spectra before and after the activation (Fig. 2.3).

The spectrum of the initial mixture **I** is a sextet corresponding to Fe_2O_3 with a hyperfine field of 51.4 T. After mechanical activation of Fe_2O_3 powder for 15 min the mean size of X-ray coherent scattering blocks decreased from 35 to 14 nm and the sextet lines have become lower and broader (Fig. 2.3b). After mechanical activation of the initial mixture **I** for 15 min in the room-temperature Mössbauer spectra, besides sextet with a hyperfine field of 51.7 T, there it appears a doublet corresponding to PFN with admixture of $FeNbO_4$. The analysis of Mössbauer spectrum shows that 71.5 % of Fe remains in the Fe_2O_3 phase while 27.5 % occurs in the PFN or $FeNbO_4$ phase. Similar ratio of the Fe_2O_3 and PFN/$FeNbO_4$ phases was reported for the stoichiometric mixture of PbO, Fe_2O_3 and Nb_2O_5 activated in SPEX 8000D vibrating mill for 20 h [20].

The diffraction patterns of the disk samples pressed from the mixture **I** activated for 15 min and annealed for 2 h at different temperatures within 400–1000 °C range are shown in Fig. 2.4. After annealing at 400 °C, the diffraction patterns recorded from this sample exhibit almost no difference as compared to the patterns of unannealed mechanically activated sample (Fig. 2.1d). Only after annealing at 500 °C diffraction patterns start to differ from each other noticeably. One can see in Fig. 2.4a that the growth of $Pb_2Fe_4Nb_4O_{21}$ phase is prevailing. After annealing at 600 °C, the PFN phase starts to prevail (Fig. 2.4b), and after annealing at 800 °C its amount becomes much larger (Fig. 2.4c). However, after annealing at 900 °C again the growth of the amount of the $Pb_2Fe_4Nb_4O_{21}$ phase starts to dominate (Fig. 2.4d). After annealing at 1000 °C this phase is the major one (Fig. 2.4e) with small reflections of the PFN phase. Even after polishing (Fig. 2.4f) this is not pure PFN, but it contains noticeable amount of $Pb_2Fe_4Nb_4O_{21}$, that is, there is obviously a lack of lead oxide in the samples. Thus it seems that for obtaining the pure perovskite phase using the mechanical activation of the PbO,

Fig. 2.4 X-ray diffraction
patterns of the samples
pressed from the mixture
of PbO, Fe_2O_3 and Nb_2O_5
(mixture **I**) activated for
15 min, after annealing for
2 h at different temperatures:
a 500 °C, **b** 600 °C,
c 800 °C, **d** 900 °C,
e 1000 °C, **f** 1000 °C,
polished sample; *—
$Pb(Fe_{0.5}Nb_{0.5})O_3$,
◆—$Pb_2Fe_4Nb_4O_{21}$
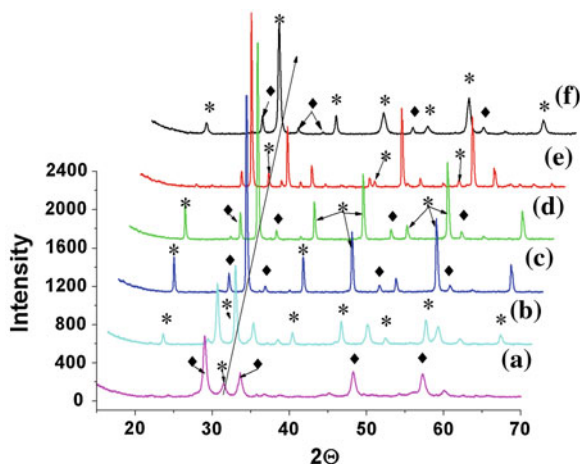
Fe_2O_3 and Nb_2O_5 oxides one needs to add an excess of PbO to the initial stoi-
chiometric mixture.

To synthesize $FeNbO_4$ precursor, necessary for obtaining the mixture **II**, a
stoichiometric mixture of Fe_2O_3 and Nb_2O_5 corresponding to $FeNbO_4$ composition
(Fig. 2.2a) was activated for 15 min. One can see in Fig. 2.2b that after such
activation the reflexes on the diffraction pattern become substantially diffused and
chemical interaction between initial components occurs, that is, reflexes corre-
sponding to $FeNbO_4$ appear. The powder activated for 15 min was annealed at
1000 °C for 2 h. Iron niobate $FeNbO_4$ of monoclinic modification with space
group P*/a (no. 13) was formed, but a small amount of unreacted initial Fe_2O_3 still
remained (Fig. 2.2c).

Then sintered $FeNbO_4$ was crumbled and mixed with lead oxide β-PbO. It is
known that the compositions of lead oxides may differ from the stoichiometry.
One can see in the diffraction patterns (Fig. 2.1d) that a small amount of red
tetragonal β-Pb_3O_4 is present in yellow rhombic lead oxide β-PbO. $FeNbO_4$ and
PbO were averaged in a mortar, and then activated in the mill for 15 min. One can
see in the diffraction patterns (Fig. 2.5a) that the product formed at once as a result
of mechanical activation is single-phase cubic modification of PFN (ASTM code
32-522), space group Pm3 m (no. 221).

During annealing the mechanically activated mixture of PbO and $FeNbO_4$
within temperature range 400–700 °C, along with PFN, a small amount of the
cubic phase $Pb_2Fe_4Nb_4O_{21}$ (ASTM code 50-445), space group F, (no. 0) is formed
in the product (Fig. 2.5b). After annealing at 800 °C, the traces of this phase
disappear from the diffraction pattern (Fig. 2.5c). The samples annealed at
1000 °C (Fig. 2.5d) exhibit the appearance of magnetoplumbite phase $PbFe_{12}O_{19}$
(ASTM code 84-2046) of hexagonal modification with space group P63/mmc (no.
194). The nucleation of this phase starts at a temperature about 900 °C and
increases with an increase in annealing temperature. However, this phase is formed
predominantly on the surface of the samples. After grinding off the surface layer of
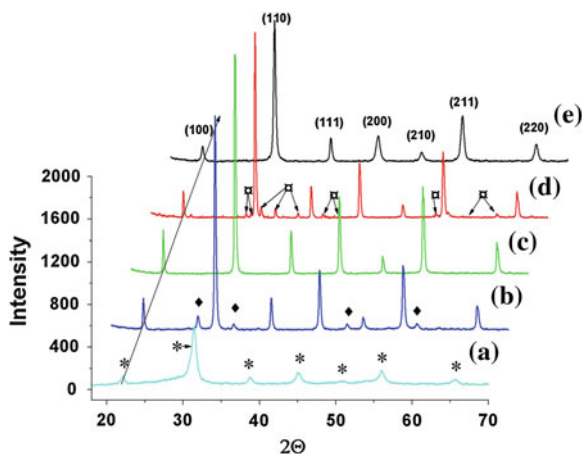
Fig. 2.5 X-ray diffraction patterns illustrating the effect of annealing on the mechanically activated stoichiometric mixture of PbO and FeNbO$_4$ (mixture **II**): **a** mixture of PbO and FeNbO$_4$ mechanically activated for 15 min, **b** after annealing at 700 °C, **c** after annealing at 800 °C (pure PFN), **d** after annealing at 1000 °C, **e** after annealing at 1000 °C and subsequent polishing the sample (pure PFN); ◆—Pb$_2$Fe$_4$Nb$_4$O$_{21}$, ¤—PbFe$_{12}$O$_{19}$, *—PFN

0.1 mm thick, no traces of this phase are observed in the diffraction patterns (Fig. 2.5e).

After mechanical activation for 15 min, the both mixtures **I** and **II** have rather small mean size D of the X-ray coherent scattering blocks (10–20 nm) and their X-ray diffraction patterns are diffused. Annealing at 400 °C and 500 °C does not change substantially neither the D values nor the degree of X-ray diffraction reflexes' diffusion. Annealing at higher temperatures leads to a fast growth of D values (Fig. 2.6) and sharpening of the X-ray diffraction reflexes with an increase of annealing temperature T_a. However above approximately 800 °C the $D(T_a)$ dependence saturates. At room temperature, Mössbauer ^{57}Fe spectra of all compositions studied appear to be doublets with the isomer shift of ≈ 0.4 mm/s (relative to the metallic iron). This value corresponds to the Fe^{3+} ions occupying the octahedral sites of the perovskite lattice. The quadrupole splitting in PFN can be caused by the asymmetric environment of the intraoctahedral Fe^{3+} ions resulting due to local heterogeneities in the compositional ordering of the Fe^{3+} and Nb^{5+} ions. This assumption is supported by the fact that, apart from a doublet, the Mössbauer spectrum of highly ordered ternary perovskite PbFe$_{0.5}$Sb$_{0.5}$O$_3$ contains also a singlet, which is attributed to compositionally ordered regions, whereas the doublet is related to the regions where a long-range ionic order is disturbed [21]. Quadrupole splitting Q of the Mössbauer ^{57}Fe doublet spectra of the mechano-activated PFN powders with small (10–20 nm) mean size D of the X-ray coherent scattering blocks is substantially larger (Fig. 2.6) than that of the single crystal and ceramic samples, in which it is approximately the same (≈ 0.4 mm/s) [22]. As was already mentioned, annealing of the mechanoactivated PFN powders leads to the

Fig. 2.6 Dependences of the mean size D of the X-ray coherent scattering blocks and the value of the quadrupole splitting Q of Mossbauer ^{57}Fe spectra on the annealing temperature T_a for the mixture of PbO and FeNbO$_4$ mechanically activated for 15 min
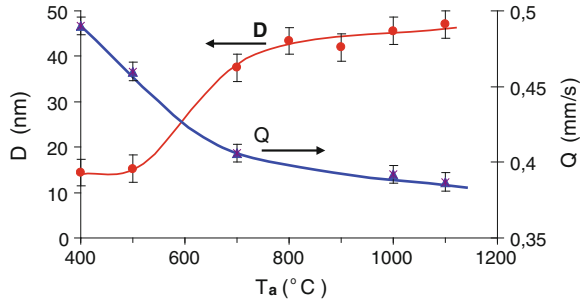
growth of D values. This growth is accompanied by gradual decrease of Q values with increasing the annealing temperature T_a (Fig. 2.6). At $T_a > 800$ °C, the quadrupole splitting reaches the level typical of PFN single crystals and ceramics. It is worth noting that large values of quadrupole splitting were reported for the amorphous PFN and they also decreased as a result of annealing leading to the crystallization of the sample [23].

Now, we turn to the temperature dependence of the Mössbauer spectrum. Below T_N, at cooling, the Mossbauer spectrum transforms from the doublet to a sextet. This transformation is accompanied by a dramatic decrease of the doublet intensity normalized to its value measured at room temperature (Fig. 2.7). The position of the abrupt drop in the temperature dependence of the doublet intensity allows one to obtain the value of T_N from the Mössbauer experiment. This method was successfully used to determine values of T_N in several multiferroics and their solid solutions and the results obtained were very similar to the data got by traditional methods such as the magnetization or magnetic susceptibility measurements (see Ref. [22] and references therein). Thus, we have employed this opportunity to detect the temperature of magnetic phase transition in mechanically activated powders with the help of Mössbauer spectroscopy.

Temperature dependencies of the normalized intensity of doublet in Mössbauer spectra for the powders of the stoichiomentic mixture of PbO and FeNbO$_4$ mechanically activated for 15 min and subsequently annealed at different temperatures are shown in Fig. 2.7. The steps on these dependencies correspond to the temperature of magnetic phase transition. For comparison, results for the PFN crystal that was chosen as a reference are shown. One can see that there are two steps on these dependencies for the powders annealed at 400 and 500 °C: one of the steps is at about 40–50 K, and the second one is at higher temperature which depends on annealing temperature T_a and shifts upward with an increase in T_a. The powders annealed at 700 °C and at higher temperatures exhibit only one step. The highest temperature of magnetic phase transition possesses the powder annealed at 700 °C. With an increase in T_a above 700 °C, T_N starts to decrease, that is, the effect of mechanical activation is annealing, so that for $T_a = 1000$ and 1100 °C, the T_N value almost coincides with the one for the PFN crystal.

The low temperature of magnetic phase transition in the unannealed mechanically activated powder is likely to be connected with its «amorphization». The
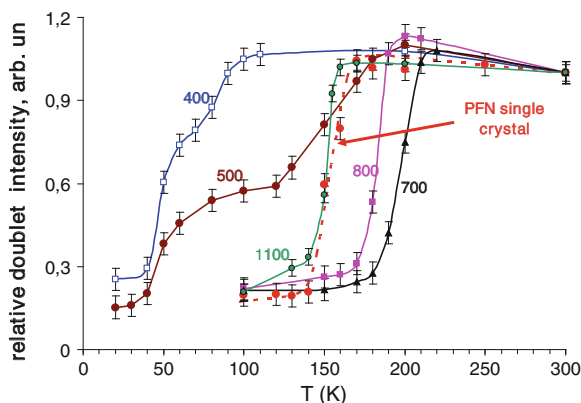
Fig. 2.7 Dependences of the doublet intensity in the Mössbauer ^{57}Fe spectrum normalized to its value measured at room temperature for the powders of the stoichiomentic mixture of PbO and FeNbO$_4$ mechanically activated for 15 min and subsequently annealed at different temperatures. Numbers near the curves represent the corresponding annealing temperature. The dashed line shows the data for PFN single crystal
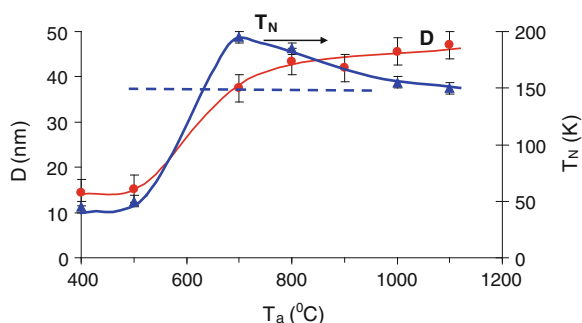
Fig. 2.8 Dependences of the mean size D of the X-ray coherent scattering blocks and the Neél temperature T_N on the annealing temperature T_a for the mixture of PbO and FeNbO$_4$ mechanically activated for 15 min. The dashed line marks T_N value for PFN single crystal

magnetic state in this powder is, most probably, of the spin-glass type, which means that the magnetic order is only short-range. Actually, as this powder gives a normal diffraction pattern, though with broadened lines, this most likely means that the sizes of the regions of the perovskite phase are very small. Annealing is accompanied by an increase in the size of these regions, and the temperature of magnetic transition increases; the formation of long-range antiferromagnetic order is likely to occur. As we suppose, the T_N value depends also on the degree of iron clustering. Presently it seems that this degree varies comparatively slightly during annealing at temperatures below 700 °C, while at higher T_a the degree of iron clustering starts to decrease (Fig. 2.8).

Fig. 2.9 Temperature
dependence of the normalized
second harmonic generation
signal for the powder of PbO
and $FeNbO_4$ stoichiometric
mixture mechanically
activated for 15 min and
subsequently annealed at
700 °C for 2 h
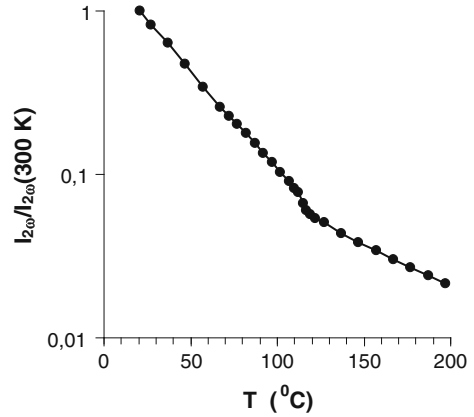
Thus, the present hypothesis explaining the experiment is as follows: for $T_a < 700$ °C the major factor determining the magnetic phase transition temperature is the coherent length, while for $T_a > 700$ °C, it is the decrease in the degree of iron clustering with an increase in T_a.

In order to study if the changes of magnetic phase transition temperature observed for mechanically activated and subsequently annealed PFN powders are accompanied by the changes of the ferroelectric phase transition temperature, we studied the temperature dependence of the second harmonic generation intensity for the powder annealed at 700 °C and showing the largest increase of T_N as compared to PFN crystal. The experimental setup used was described in details elsewhere [24]. The results obtained are shown in Fig. 2.9. One can see that there is a distinct anomaly in the temperature dependence of the second harmonic generation intensity at about 110 °C. This temperature nicely correlates with the literature data for the ferroelectric-paraelectric phase transition temperature both in single crystals and ceramics of PFN [1, 7, 25]. The character of the dependence of the second harmonic generation intensity on temperature for the PFN powder studied shows some differences as compared to the similar dependencies for $BaTiO_3$ powders [24, 26]. However it is known that the shape of this curve may be changed crucially by changing the conditions of pressing the powders and their subsequent annealing [26].

2.4 Summary

The use of the high-energy planetary-centrifugal ball mill AGO-2 enables one to perform the mechanically activated synthesis of PFN at much shorter time (15 min instead of 20–30 h).

Mössbauer studies have shown that the temperature of magnetic phase transition in $PbFe_{0.5}Nb_{0.5}O_3$ powders can be changed by mechanical activation and

subsequent annealing. In particular, the increase by more than 50 K was achieved in the mechanically activated powder of stoichiometric PbO and $FeNbO_4$ mixture annealed at 700 °C. These results are in line with the model assuming that the temperature of magnetic phase transition in $PbFe_{0.5}Nb_{0.5}O_3$ depends substantially on the degree of Fe^{3+} and Nb^{5+} ions clustering [13]. At the same time the second harmonic generation studies did not reveal any substantial changes of the ferro-electric phase transition temperature in this powder.

References

1. W. Kleemann, V.V. Shvartsman, P. Borisov, A. Kania, Phys. Rev. Lett. **105**, 257202 (2010)
2. I.P. Rayevsky, M.S. Novikov, L.A. Petrukhina, O.A. Gubaidulina, A.Ye. Kuimov, M.A. Malitskaya, Ferroelectrics **131**, 327 (1992)
3. A.A. Bokov, L.A. Shpak, I.P. Rayevsky, J. Phys Chem. Solids **54**, 495 (1993)
4. VYu. Shonov, I.P. Raevski, A.A. Bokov, Tech. Phys. **41**, 166 (1996)
5. E.I. Sitalo, YuN Zakharov, A.G. Lutokhin, S.I. Raevskaya, I.P. Raevski, M.S. Panchelyuga, V.V. Titov, L.E. Pustovaya, I.N. Zakharchenko, A.T. Kozakov, A.A. Pavelko, Ferroelectrics **389**, 107 (2009)
6. E.I. Sitalo, I.P. Raevski, A.G. Lutokhin, A.V. Blazhevich, S.P. Kubrin, S.I. Raevskaya, YuN Zakharov, M.A. Malitskaya, V.V. Titov, I.N. Zakharchenko, IEEE Trans. Ultrason. Ferroelectr. Freq. Control **58**, 1914 (2011)
7. D.A. Sanchez, N. Ortega, A. Kumar, G. Sreenivasulu, R.S. Katiyar, J.F. Scott, D.M. Evans, M. Arredondo-Arechavala, A. Schilling, J.M. Gregg, J. Appl. Phys. **113**, 074105 (2013)
8. V.M. Yudin, A.G. Tutov, A.B. Sherman, V.A. Isupov, *Izv. Akad. Nauk SSSR, Ser. Fiz.* **31**(11), 1798 (1967) (in Russian)
9. A.A. Bokov, V.Y. Shonov, I.P. Rayevsky, E.S. Gagarina, M.F. Kupriyanov, J Phys Condens Matter **5**, 5491 (1993)
10. I.P. Raevski, S.A. Prosandeev, S.M. Emelyanov, F.I. Savenko, I.N. Zakharchenko, O.A. Bunina, A.S. Bogatin, S.I. Raevskaya, E.S. Gagarina, E.V. Sahkar, L. Jastrabik, Integr Ferroelectr **53**, 475 (2003)
11. G.-M. Rotaru, B. Roessli, A. Amato, S.N. Gvasaliya, C. Mudry, S.G. Lushnikov, T.A. Shaplygina, Phys. Rev. B **79**, 184430 (2009)
12. V.V. Laguta, J. Rosa, L. Jastrabik, R. Blinc, P. Cevc, B. Zalar, M. Remskar, S.I. Raevskaya, I.P. Raevski, Mater. Res. Bull. **45**, 1720 (2010)
13. I.P. Raevski, S.P. Kubrin, S.I. Raevskaya, D.A. Sarychev, S.A. Prosandeev, M.A. Malitskaya, Phys. Rev. B **85**, 224412 (2012)
14. V.V. Laguta, M.D. Glinchuk, M. Maryško, R.O. Kuzian, S.A. Prosandeev, S.I. Raevskaya, V.G. Smotrakov, V.V. Eremkin, I.P. Raevski, Phys. Rev. B **87**, 064403 (2013)
15. I.P. Raevski, S.P. Kubrin, S.I. Raevskaya, V.V. Titov, D.A. Sarychev, M.A. Malitskaya, I.N. Zakharchenko, S.A. Prosandeev, Phys. Rev. B **80**, 024108 (2009)
16. I.P. Raevski, S.P. Kubrin, S.I. Raevskaya, V.V. Titov, S.A. Prosandeev, D.A. Sarychev, M.A. Malitskaya, V.V. Stashenko, I.N. Zakharchenko, Ferroelectrics **398**, 16 (2010)
17. E.G. Avvakumov, L.G. Karakchiev, Chem Sustain Dev **12**, 287 (2004). (in Russian)

18. L.B. Kong, T.S. Zhang, J. Ma, F. Boey, Prog. Mater Sci. **53**, 207 (2008)
19. X.S. Gao, J.M. Xue, J. Wang, T. Yu, Z.X. Shen, J Am Ceram Soc **85**(3), 565 (2002)
20. D. Bochenek, G. Dercz, D. Oleszak, Arch. Metall. Mater. **56**(4), 1015 (2011)
21. I.P. Raevski, N.M. Olekhnovich, A.V. Pushkarev, Y.V. Radyush, S.P. Kubrin, S.I. Raevskaya, M.A. Malitskaya, V.V. Titov, V.V. Stashenko, Ferroelectrics **444**, 47 (2013)
22. I.P. Raevski, S.P. Kubrin, S.I. Raevskaya, V.V. Stashenko, D.A. Sarychev, M.A. Malitskaya, M.A. Seredkina, V.G. Smotrakov, I.N. Zakharchenko, V.V. Eremkin, Ferroelectrics **373**, 121 (2008)
23. L.N. Korotkov, S.N. Kozhukhar, V.V. Posmet'ev, D.V. Urazov, D.F. Rogovoi, Y.V. Barmin, S.P. Kubrin, S.I. Raevskaya, I.P. Raevskii, Tech. Phys. **54**(8), 1147 (2009)
24. A.M. Pugachev, V.I. Kovalevskii, N.V. Surovtsev, S. Kojima, S.A. Prosandeev, I.P. Raevski, S.I. Raevskaya, Phys. Rev. Lett. **108**, 247601 (2012)
25. I.P. Raevski, S.P. Kubrin, S.I. Raevskaya, S.A. Prosandeev, M.A. Malitskaya, V.V. Titov, D.A. Sarychev, A.V. Blazhevich, I.N. Zakharchenko, IEEE Trans. Ultrason. Ferroelectr. Freq. Control **59**,1872 (2012)
26. V.I. Kovalevskii, V.K. Malinovskii, A.M. Pugachev, I.P. Raevski, S.I. Raevskaya, P.D. Rudych, N.V. Surovtsev, Phys. Solid State **54**(5), 920 (2012)

Chapter 3
Preparation and Investigation of ZnO Nanorods Array Based Resistive and SAW CO Gas Sensors

**A. L. Nikolaev, G. Ya. Karapetyan, D. G. Nesvetaev,
N. V. Lyanguzov, V. G. Dneprovski and E. M. Kaidashev**

Resistive sensors of carbon monoxide based on zinc oxide nanorod arrays were investigated. ZnO nanorods were produced by pulsed laser deposition (PLD) method at high pressure of argon and carbothermal synthesis. Several constructions of resistive carbon monoxide sensors are obtained. Their resistive properties are investigated. The passive wireless CO sensor on surface acoustic waves (SAW) was studied. The dependence of SAW reflection factor for unidirectional inter-digital transducers (IDT) loaded by impedance on its resistance value was investigated. It is shown that the reflection factor varied in linear way versus the value of the resistance in the range from 50 to 400 Ω. The total resistance value for one of the sintered sample lied in the range from 50 to 250 Ω in the case of parallel junction of ZnO nanorods in array by top electrode. This result corresponds to the linear range in the dependence of IDT reflection factor from resistance value. This can be used for determination of small concentrations of CO gas by IDT loaded with impedance based on ZnO nanorod array, because their resistance value depends on CO concentration.

3.1 Introduction

ZnO nanorod arrays are considered as the basic elements for a wide range of new nanoelectronic and nanophotonic devices. In particular, such structures could be used in photodetectors, light emitting diodes, lasers, energy converters, solar cells, electron emitters and chemosensors [1]. Current area of research is the development of wireless CO sensors on surface acoustic waves. As a sensor for CO adsorption, oriented arrays of zinc oxide nanorods currently obtained with laser sputtering [2] or carbothermal synthesis [3] can be used.

A. L. Nikolaev · G. Ya. Karapetyan · D. G. Nesvetaev ·
N. V. Lyanguzov · V. G. Dneprovski · E. M. Kaidashev (✉)
Vorovich Mechanics and Applied Mathematics Research Institute, Southern Federal
University, 200/1, Stachki Ave, Rostov-on-Don, Russia 344090
e-mail: kaidashev@mail.ru
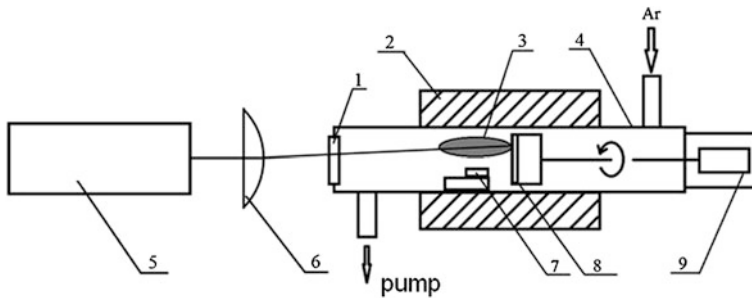
Fig. 3.1 Schematic of the experimental setup for the PLD growth ZnO nanorods

3.2 Experiments and Results

3.2.1 PLD ZnO Nanorods Growth

In our study we investigated the growth of ZnO nanocrystal arrays on sapphire substrates by pulsed laser deposition (PLD) at high pressure of argon [2]. Deposition was carried out in the vacuumized quartz cell with an external resistive heater (Fig. 3.1). Laser radiation of KrF laser ($\lambda = 248$ nm, $E = 300$ mJ) was focused on the surface of rotating ZnO ceramic target. The power density on the target surface was 2 J/cm^2. Target-substrate distance was 5–35 mm. The repetition frequency of the laser pulses was 3–10 Hz. Synthesis of micro-and nanocrystals was carried out at 12000–24000 laser pulses. The substrate temperature was varied in the range of 850–950 °C. The argon flow was 50 sccm at a pressure of 75–300 mbar. Single crystal substrates of c- and a-sapphire size $10 \times 10 \times 0.5$ mm^3 with buffer layer of ZnO are parallel to the laser plasma plume. To improve the vertical orientation of ZnO nanorods was deposited buffer sub-layer film of zinc oxide. ZnO film was deposited at 10,000 laser pulses, the oxygen pressure was 2×10^{-2} mbar, the substrate-target distance was 70 mm and temperature was 670 °C [4].

Isolated gold nanoparticles were deposited on the surface of the ZnO buffer layer and used as a catalyst for the growth of self-organized ZnO nanorods. Gold nanoparticles (Fig. 3.2) was also obtained by laser deposition in an argon atmosphere ($\lambda = 248$ nm, $Q = 2$ J/cm^2, $f = 10$ Hz) at $P_{Ar} = 70$ Pa, $T = 25$ °C, target-substrate distance was $l = 3.5$ cm, the number of laser pulses was $N = 500$). This technique is similar to those reported in [5] and allows one to receive the samples controlling both particle size and number density, virtually without limitations by the nature of the substrate. As seen in Fig. 3.2, gold nanoparticles are isolated from each other and uniformly distributed over the surface of the ZnO buffer layer. The size of Au nanoparticles is about 5–7 nm.

Au nanoparticles were used as a catalyst in PLD of ZnO nanorods under the high pressure of argon [2]. As a result, vertically aligned ZnO nanorods were obtained (see Fig. 3.3). Diameter of nanorods grown via the vapor–liquid–solid process was 60–150 nm, height was 1–2 µm.
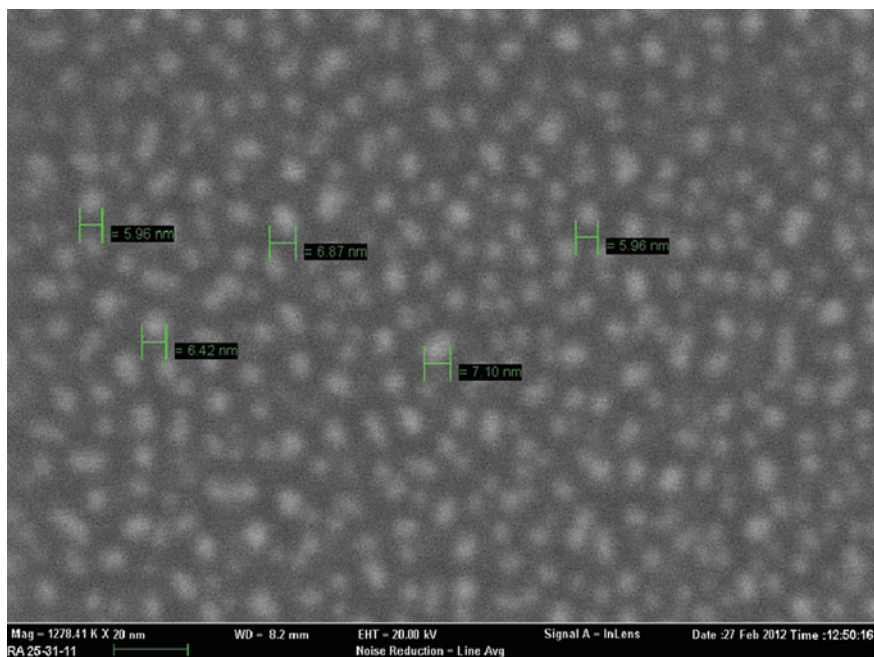
Fig. 3.2 SEM image of gold nanoparticles. *Top* view of the surface. $P_{Ar} = 70$ Pa, $N = 500$ pulses
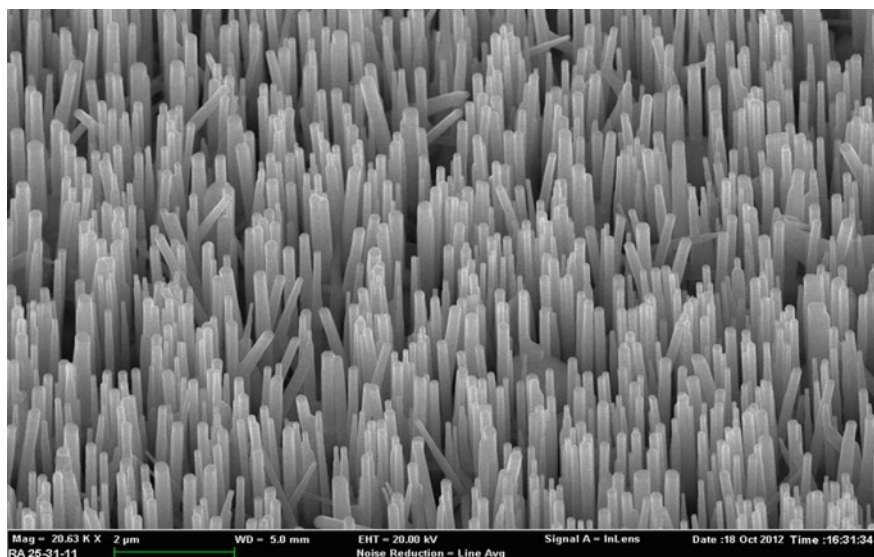
Fig. 3.3 SEM image of ZnO nanorods array, obtained by pulsed laser deposition

Fig. 3.4 Schematic diagram of the wireless SAW CO gas sensor system
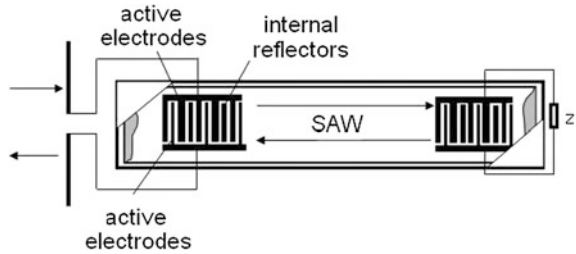
3.2.2 Fabrication of the ZnO Nanorods Sensitive Element of SAW Sensor for CO Detection

We have demonstrated the possibility to construct the SAW wireless and passive sensors based on hold-up line comprising two unidirectional IDT for parameter determination of atmosphere [6].

SAW sensor [6] is a delay line (DL) on a surface acoustic wave (SAW) having two unidirectional interdigital transducers (IDT). Firstly, it is connected to the transmitter and receiver antenna, and secondly to reflective IDT–IDT, loaded on the impedance of the sensitive element of the sensor (Fig. 3.4).

Unidirectional IDT produced on substrates (YX/128°-cut lithium niobate) has 17 internal reflectors, and the set of overlapping electrodes with size of 20 lengths of SAW on the frequency of the acoustic matching. IDT on the central frequency of 95 MHz has a width of electrodes equals 10 mm and the set of overlapping electrodes with size of 40 lengths of SAW. As a sensing element for CO we used zinc oxide nanorods array. Reflection coefficient is determined by the frequency dependence of the IDT impedance, followed by Fourier transformation. Figure 3.5 shows the dependence of the reflection coefficient on value of the load resistance. It is seen that this dependence has a minimum of reflection, due to impedance matching of IDT with a 50 Ω load, i.e. most of the energy of SAW is released at the load resistor. This dependence shows that the reflection coefficient for shorted and open unidirectional IDT tends to 1.

The sensing element of SAW sensor consists of a parallel combination of zinc oxide nanorods. Increasing the area of the upper electrode can reduce the total resistance of the associated array of zinc oxide nanorods. The load value Z depends on CO concentration. If you change the resistance of the sensor, then due to the adsorption of CO changes the reflection coefficient of SAW from the reflective IDT. However, as shown in Fig. 3.5, dependence of the reflection coefficient of the unidirectional interdigital transducer on the value of R, connected to an interdigital transducer, is linear load at the site of resistance from 50 to 400 Ω.

Therefore, we developed new design-related arrays of nanorods of zinc oxide having a low total resistance. We have developed a new design of parallel-connected zinc oxide nanorods, the total resistance of which can be varied by changing the area of the upper electrode. The sensors are designed in several phases and the final version of the structure is shown schematically in Fig. 3.6.
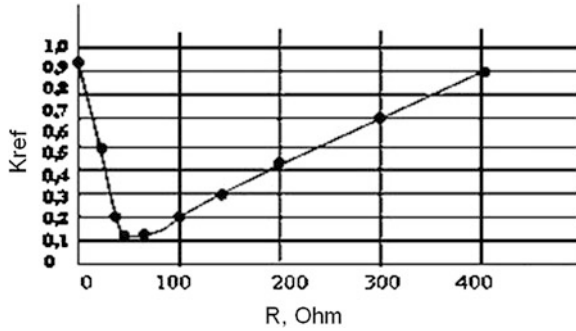
Fig. 3.5 Dependence of reflection coefficient of the unidirectional IDT on load resistance
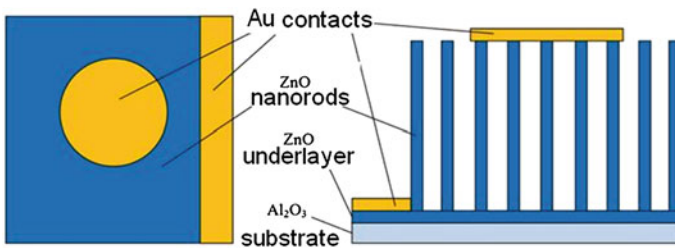
Fig. 3.6 Schematic view of SAW sensing element of CO sensor. *Left top* view and *right side* view

Then the Au electrodes (upper and lower) were deposited by means of PLD for the further investigation of gas-sensing properties of this structure. The lower electrode was deposited on the sample part free from nanorods and the upper one on the top of nanorods. PLD of the upper electrode was carried out at the angle of 45°.

To complete processing the sensor, it was sprayed a nanostructure contact after growth. This sample was placed in a vacuum chamber and lock to the target at the angle of 45° to the target surface. It was also used a masking pattern with a round hole for the deposition of gold contacts on the limited surface area of the sample. Deposition of contact was extended obliquely to gold particles settled on the top of nanorods and not fell to their base. Nanorods screen each other and prevent covering of nanowires base because of its density. Thus, the gold contact is created in the upper part of the nanorods and combines them together.

3.2.3 Resistive CO Sensor Characterization

The sensor design was a series of parallel connected with the nanorods "islands" of Au underlayer. On a quartz substrate was deposited thin-film underlayer by

Fig. 3.7 Sensor's photo obtained by ZEISS Axioskop 40 microscope
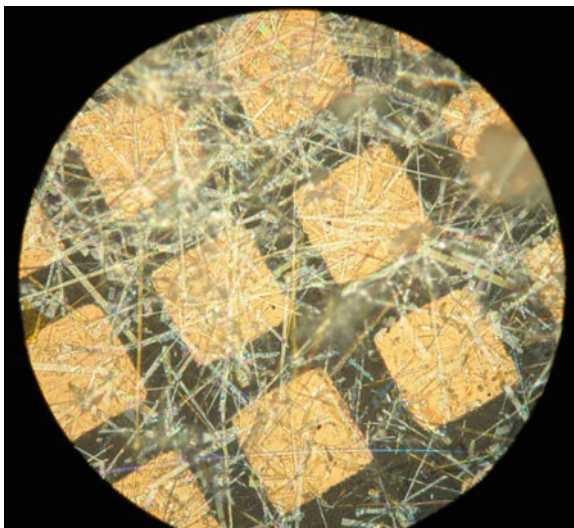
pulsed laser deposition through a mask with square holes of the size $a = 90$ μm. The distance between the "islands" was $b = 40$ μm. ZnO nanorods were removed by sonication in a solution of ethanol. The resulting solution of nanorods was applied on the sample surface. Nanorods were annealed in the Au conductive underlayer in Ar atmosphere at $t = 200$ °C to achieve better electrical contact between rods and sublayer.

The photo given above clearly shows that the individual ZnO nanorods, deposited on the surface of the sample overlap the neighboring gold islands. Thus, as in the case of the above construction sensor of CO, conduction channel from island to island passes through nanorods. Thus, any change in the conductivity of the rods associated with a change in the composition of the surrounding atmosphere, can not affect the total resistance of the sample (Fig. 3.7).

Resistance measurement was carried out using a multimeter Keithley 2000 at constant temperature $t = 250$ °C. CO desorption from the surface of the sample was carried out by blowing measuring chamber with nitrogen gas and continuous UV irradiation of the sample after the measurement. Mutually reversible redox reaction, adsorption–desorption on the semiconductor surface at a constant concentration of CO are in the equilibrium state some time after the lapping CO (Fig. 3.8). By decreasing the concentration of carbon monoxide, the equilibrium shifts toward desorption.

The calculation of the gas sensor's sensitivity occurred by the formula $((R_a - R_b)/R_a) \times 100\%$ where R_a and R_b is the sensor resistance in the presence of CO and in pure air, respectively. Great gas sensor resistance, however, is caused by poor contacts of nanorods with the deposited Au islands. Thus, the sensitivity of the sample was about 250 %. Gas-sensitive properties of the samples are highly dependent on the number of oxygen vacancies [7].

Fig. 3.8 Time dependence
of CO sensor sensitivity
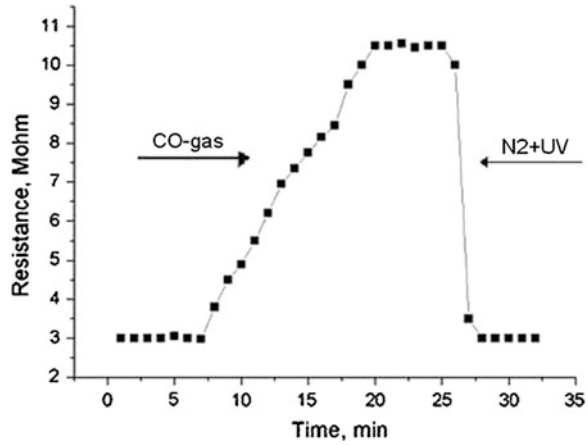
Fig. 3.9 Photoluminescence
spectra of the sensor
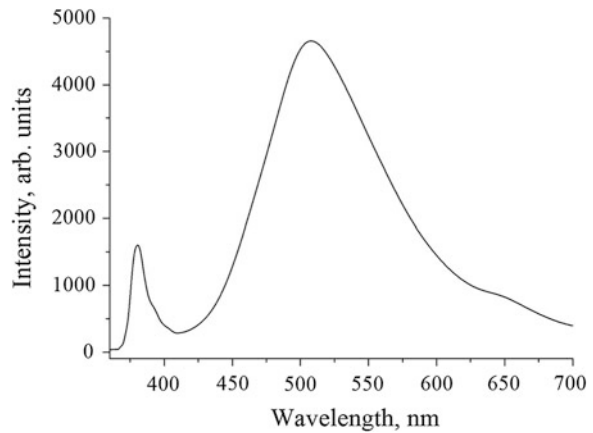
The ratio of the intensities of the exciton/green regions of the PL spectrum
(Fig. 3.9.) was 0.3 for the ZnO nanorods on the surface of the gas-sensitive ele-
ment. From this ratio, it follows that the concentration of oxygen vacancies in the
sample is high. As discussed by authors of the article [7], with increasing the
oxygen vacancies sensitivity of the sensor to CO is greatly increased. Chemi-
sorption of O_2^-, O^{2-} and O^- substantially depends on temperature. At low tem-
peratures, mainly occurs O_2^- chemisorption. At a high temperature begins
O^- chemisorption, while O_2^- disappears.

3.2.4 SAW CO Sensor Characterization

ZnO nanorods array is the load impedance of one of the ITDs. We have obtained
the SAW reflection coefficient dependence on the value of load impedance which

is connected to reflective ITD. This dependence could be used to determine low concentration of gas, for instance, of carbon monoxide. The main goal of our research was fabrication and study of ZnO nanorods sensitive element of SAW sensors for CO detection.

The SAW sensor element sensitive to CO consists of parallel connected ZnO nanorods. In order to decrease the total resistance of ZnO nanorods array we changed the area of upper electrode. The impedance value Z depends on CO concentration. CO absorption influences on the sensitive element resistance resulting in the change of SAW reflection coefficient.

The authors of [7] have studied cathodoluminescence spectra of ZnO nanorods in the visible and ultraviolet regions of the spectrum. Obtained at different temperatures nanorods had a different intensity of the broad band in the green-yellow region of the spectrum of cathodoluminescence associated with oxygen defects in ZnO. By comparing the luminescence intensity in visible and UV region of spectrum, it is possible to make a conclusion about O vacancies in ZnO nanostructures. The photoluminescence spectra (Fig. 3.10) demonstrate the correlation between the sensitivity of samples and the number of O vacancies in nanorods.

By varying nanorods growth temperature from 850 to 915 °C can be produced nanorods with different defectness of oxygen. Because the maximum sensitivity of ZnO at 250 °C [8], the sensitivity measurements were carried out at room temperature and at 250 °C. During heating nanorods to 250 °C from room temperature, the resistance of the connected arrays of ZnO nanorods fell to 6 kΩ. ZnO nanorods array had the load impedance of the reflective ITDs and their total resistance was $R = 6$ kΩ at operational temperature $T = 250$ °C of the sensor. The time dependence of response difference for SAW sensor was obtained. The first response was recorded without CO, the second one—through 8 min after the inflow of gas. These values were normalized with respect to differential response recorded at the end of the first minute after CO inflow (see Fig. 3.11). This dependence indicated that the reflection coefficient had changed. Thus, the ZnO nanostructure obtained could be applied for development of wireless SAW sensors for CO detection.

The low resistance of ZnO nanorods array leads to the maximum value of ITD reflection coefficient. This fact allows us to use this nanostructure as a gas-sensing element of passive noncontact SAW sensor for CO detection. CO was filled with air in the cell capacity of 500 cm^3. Gas was fed from the gas cylinder through a regulator with flow rate of 50 cm^3/min. The reflection coefficient varied in accordance with the increase of resistance of the nanorods. It happened, apparently, because of the adsorption of carbon monoxide surface of the nanorods. Dependence of the reflection coefficient on the reflective IDT loaded with an array of ZnO nanorods in the first 9 min of the inlet CO recorded by the meter complex transfer «Overview-304/1» with a 1 min interval. To increase the sensitivity of the measurements were taken differential impulse responses. Figure 3.11 shows the difference in response time ($T = 250$ °C without CO and through 8 min after lapping CO) relative normalized difference of response removed after 1 min after lapping CO.
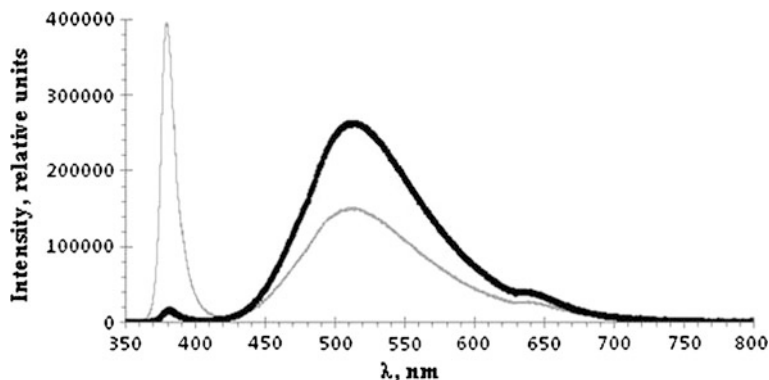
Fig. 3.10 Room-temperature photoluminescence spectra from samples which were grown at different temperatures. Spectrum of the sample grown at 850 °C (*gray line*) and spectrum of the sample grown at 915 °C (*black line*)
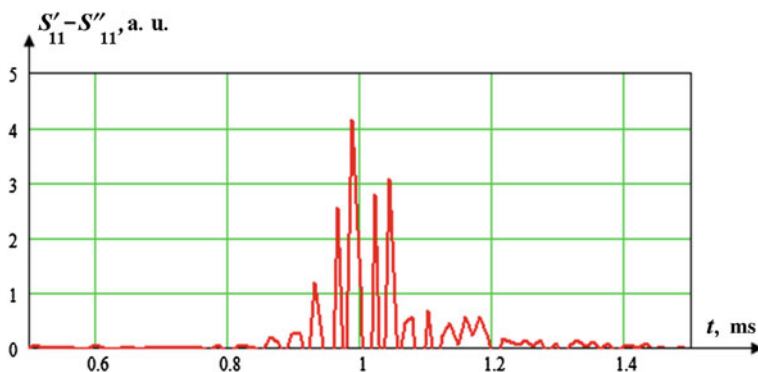
Fig. 3.11 Time dependence of response difference of SAW sensor. The first response was recorded without CO, the second one—through 8 min after the inflow of gas. These values were normalized with respect to differential response recorded at the end of the first minute after CO inflow

If get the resistance values of the nanorods within the maximum sensitivity of the reflection coefficient loaded on IDT resistance [6], it is possible to increase the sensitivity of the sensor to CO. This can be done either by parallel connection of a large number of nanorods, either by increasing the radiation resistance of reflective IDT. However there is a limit, when it is reached the aperture of IDT is decreased. The resistances of a few $k\Omega$ would be so small that it will lead to significant diffraction of SAW and to inability of correct sensor operation.

However, as shown by the measurements, even when the resistance of the nanorods is 6 $k\Omega$, change in the difference signal is sufficient to remove the dependence of the reflection coefficient of the resistance change on the nanorods, which is defined as the maximum amplitude of S_{11} parameter.

3.3 Conclusions

ZnO nanorods array with *c*-axis perpendicular to the substrate was grown by pulsed laser deposition at high pressure of argon and carbothermal synthesis. It was fabricated and tested sensing element of SAW sensor of CO being an array of parallel connected zinc oxide nanorods. It is proposed to use the photoluminescence method for the optimization of ZnO nanorods growth with maximum sensitivity to CO. We used this method to find synthesis temperature at which the sensitivity of the device is the highest.

References

1. S.K. Youn, N. Ramgir, C. Wang, K. Subannajui, V. Cimalla, M. Zacharias, J. Phys. Chem. C **114**, 10092 (2010)
2. M. Lorenz, E.M. Kaidashev, A. Rahm, Th Nobis, J. Lenzner, J.G. Wagner, D. Spemann, H. Hochmuth, M. Grundmann, Appl. Phys. Lett. **86**, 143113 (2005)
3. N.V. Lyanguzov, V.E. Kaydashev, E.M. Kaidashev, K.G. Abdulvakhidov, Tech. Phys. Lett. **37**(3), 193 (2011)
4. E.M. Kaidashev, M. Lorenz, H. Wenckstern, G. Benndorf, A. Rahm, H.-C. Semmelhack, K.-H. Han, H. Hochmuth, C. Bundesmann, V. Riede, M. Grundmann, Appl. Phys. Lett. **82**(22), 3901 (2003)
5. C.D. Andrea, F. Neri, P.M. Ossi, N. Santoand, Nanotechnology **20**, 245606 (2009)
6. G.Y. Karapetyan, V.G. Dneprovski, A.S. Bagdasaryan, S.A. Bagdasaryan, A.L. Nikolaev, E.M. Kaidashev, *Ingenerny Vestnik Dona* **2**, (2012) (in Russian)
7. T.-J. Hsueh, Y.-W. Chen, S.-J. Chang, S.-F. Wang, C.-L. Hsu, Y.-R. Lin, T.-S. Lin, I.-C. Chene, J Electrochem Soc **154**(12), 393 (2007)
8. J.X. Wang, X.W. Sun, H. Huang, Y.C. Lee, O.K. Tan, M.B. Yu, G.Q. Lo, D.L. Kwong, Appl. Phys. A **88**, 611 (2007)

Chapter 4
Carbothermal Synthesis and Characterization of ZnO Nanorod Arrays

N. V. Lyanguzov, D. A. Zhilin and E. M. Kaidashev

An influence of buffer Ar gas pressure and substance-to-source distance on morphometric parameters of vertically aligned ZnO nano- and the microrod arrays synthesized by a carbothermal reduction process on Si (100) substrates covered by ZnO sub-layer is determined. Systematical researches of catalyst-free growth, as well as influence of catalytic agent type (such, as Au and Cu) on formation process and the morphometrical parameters of the produced rods are carried out. It is shown that the catalytic agent plays a role only at the initial stage, and does not participate in the further growth of rods in applied synthesis conditions. Possibility to control the average diameters, lengths and surface distribution density of the rods in the ranges of 100–300 nm, 1.5–9 μm and 2.8×10^8–5.3×10^8 cm^{-2}, respectively, is shown.

4.1 Introduction

Arrays of ZnO filament-like nanocrystals and the nanorods are considered now as basis element of highly efficient electrooptical devices, electrons emitters, sensors for chemical and biological substances, micro- and nanoelectromechanical systems. Morphometric characteristics, such as the characteristic sizes of single elements, the dispersive level, density and homogeneity of surface distribution, mutual spatial orientation are defining for the majority of applications. So far in many presented annuals the possibility to produce the vertically aligned ZnO nano- and microrods arrays with differing morphometric parameters via a very simple gas-phase-technique, such as carbothermal reduction process, is shown. However, comparing these results, it is impossible to create complete and single-digit idea, at least at empirical level, about influence of temperature of synthesis [1],

N. V. Lyanguzov (✉) · D. A. Zhilin · E. M. Kaidashev
Vorovich Mechanics and Applied Mathematics Research Institute, Southern Federal University, 200/1, Stachki Ave, Rostov-on-Don, Russia 344090
e-mail: n.lianguzov@mail.ru

concentration in a gas phase [2], operating pressure [3], existence and type of the catalytic agent [4], etc. on morphologies of formed products.

Considering above-mentioned features, the purpose of this work was to research the opportunities of control of the morphometric parameters of ZnO nano- and microrods arrays during their preparation via carbothermal reduction process. As the tasks, we studied the influence of such technological parameters of synthesis, as operating pressure and substrate-to-source distance, on lengths and diameters, on dispersive level, on surface distribution density and homogeneity of produced ZnO nano- and microrod arrays on exact values of level.

4.2 Experiment

ZnO nano- and microrod arrays were produced by a carbothermal reduction process on Si (100) substrates with use of Cu and Au as growth catalyst agents, and also without catalytic agent, respectively, the technique offered in [1, 2, 5, 6]. Substrates were initially exposed to chemical cleaning. Before the catalytic agent deposition and nanorods synthesis the substrates were covered by 80 nm-thick ZnO thin film sub-layers via pulsed laser deposition (PLD) technique under temperature about of 500 °C. The thickness of the catalytic agent layers deposited by magnetron sputtering was about 2–3 nm. Three area-equal fields were distinguished on each sample: the first one was covered with Cu, the second one covered with Au, and the third one without any catalytic agent covering. The pumped quartz tube with inner diameter of 30 mm placed in the horizontal furnace was used as a reaction chamber for synthesis of ZnO-rod arrays. Source of material, or precursor (compacted mixture of ZnO and graphite powders in a weight ratio of 1:1) and the prepared substrates were loaded in the chamber by so way that the precursor was located at the center of furnace. Further the reactor was evacuated and heated up to working temperature. Pressure value (P) in the chamber was regulated by means of changing pumping rate and introducing buffer gas (argon) with the fixed flow of 200 cm^3/min. The substrate-to-source distance (L) was varied stepwise during synthesis, too. Values of substrate temperatures decreased within range 940–920 °C with increasing distance L. The precursor was heated up to 950 °C for 35 min, and duration of the synthesis was 10 min. After synthesis the reactor was naturally cooled down to room temperature. So, the 12 experimental samples of the ZnO rods for $L = 3, 4, 5, 6$ cm and for $P = 150, 50, 15$ Torr were produced.

The morphology of the sintered samples was studied by scanning electronic microscopy on the instrument FE-SEM Zeiss SUPRA 25. Values of average length of rods were determined from micrographs of cross-sections (Fig. 4.1a) under shooting at the angle of 90° to an axis of rods. For determination of average value of rod diameters, the micrographs were registered parallel to a surface (i.e. at the angle of 0° to an axis of rods) (Fig. 4.2). Further, micrographs were computationally processed in ImageJ program [7]. The diameter of circle, whose area was
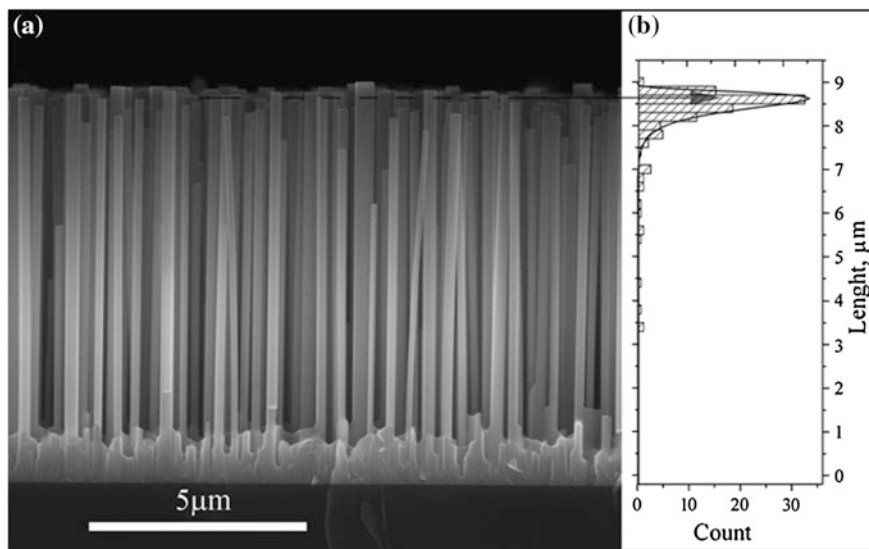
Fig. 4.1 The SEM image of cross-sections of the ZnO-rod array synthesized on Si (100) substrate with pressure of 50 Torr at substrate-to-source distance of 4 cm without the catalytic growth agent (**a**). The histogram of statistical distribution of rods on length for this sample (**b**)

equal to the area of cross-section of the rod, was selected as a value of diameter. Based on obtained data, the histograms of statistical distribution of rods on lengths (Fig. 4.1b) and on diameters (Fig. 4.3) were plotted. These histograms were approximated by logarithmically normal distribution function. As average length or diameter of rods for each sample the maximum of approximating distribution function was accepted. The dispersion level of length or diameter of rods was defined as the expressed in a percentage ratio of FWHM value for correspondent approximating distribution function to the average value.

The XRD studies of the synthesized samples were carried out on the Rigaku ULTIMA IV Theta–Theta Type diffractometer (Cu Kα_1 radiation).

4.3 Result and Discussion

Electron microscopy showed that all of the samples were the arrays of ZnO-rods, which vertically aligned to the substrate. The average length of the rods varied in a non-linear way with increasing substrate-to-source distance, reaching the maximum values at $L = 4$–5 cm. Similar regularity is observed for dependence of the rod length on pressure, namely the rods produced at $P = 50$ Torr have the greatest average length. So, values of average lengths of ZnO-rods sintered without the catalytic growth agent under pressure of 15 Torr, reached of 4.5, 7, 8.7 and

Fig. 4.2 SEM images (*top view*) of ZnO-rod array synthesized on Si (100) substrate at substrate-to-source distance of 4 cm without the catalytic growth agent with pressure of 150 Torr (**a**), 50 Torr (**b**), and 15 Torr (**c**)
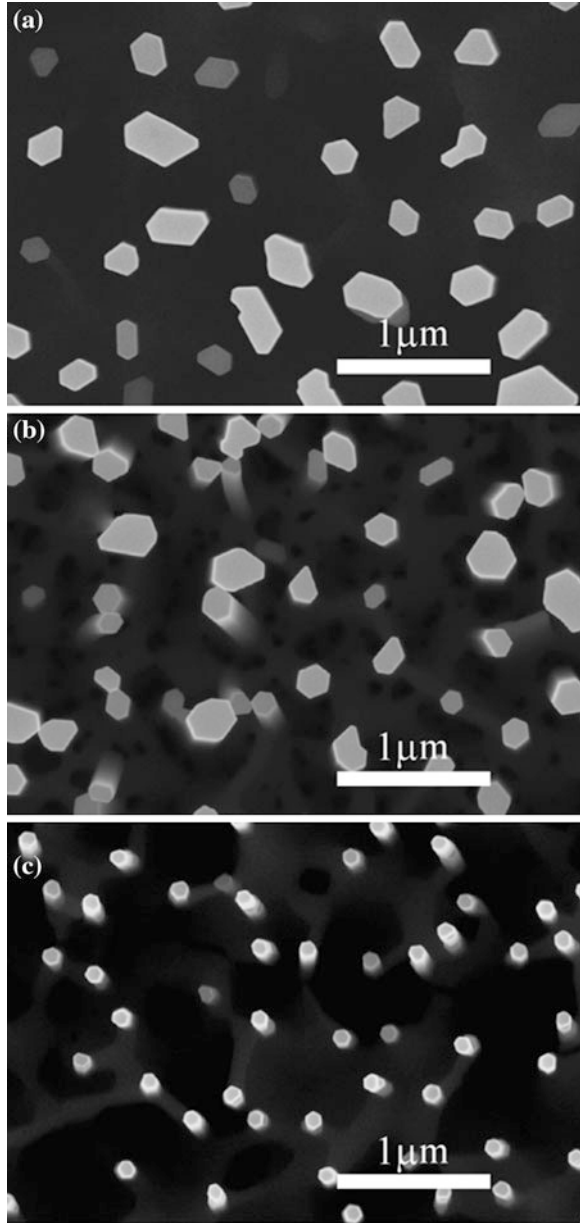
5.9 μm, with the dispersion level of 13, 7, 4 and 2.5 %, for distances of $L = 3$, 4, 5, and 6 cm, respectively. In the case of the same values of L, average lengths of the rods synthesized with $P = 50$ Torr, reached of 7.5, 8.7, 6.7 and 2.1 μm, with

Fig. 4.3 The histogram of statistical distribution on diameters for the ZnO-rods produced with pressure of 50 Torr at substrate-to-source distance of 4 cm without the catalytic growth agent
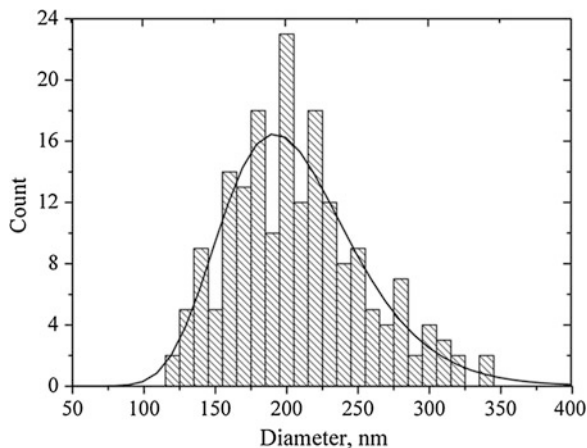
the dispersion level of 2, 3, 3.5 and 7 %, and with $P = 150$ Torr they were 3.2, 5.6, 2.9 and 1.3 μm, with the dispersion level of 5, 4.5, 3.5 and 3 %, respectively.

Average diameter of rods increases with evaluation pressure and increasing substrate-to-source distance. So, average diameters of ZnO-rods produced with the pressure of 15 Torr, reached of 100, 110, 155 and 195 nm, with a dispersion level of 5, 4.5, 3 and 33 % for distances of $L = 3, 4, 5,$ and 6 cm, respectively. For the same values of L, diameters of the rods synthesized with a pressure of 50 Torr, reached of 180, 195, 225 and 240 nm, with a dispersion level of 8, 28, 29 and 25 %, and with $P = 150$ Torr, they reached of 225, 230 (Fig. 4.2a), 270 and 300 nm, with a dispersion level of 24, 28, 30, 32 %, respectively. The average length and diameter of the rods depending on pressure value and substrate-to-source distance are plotted in Fig. 4.4. In the presence of catalytic growth agents, Au or Cu, the increase of average length on 7–15 % and reduction of average diameter of rods on 2–10 % (depending on specific conditions for each sample) were observed.

Surface distribution density of rods for all fabricated samples changed in the range from 2.7×10^8 to 8×10^8 cm^{-2}, being homogenous for each sample along the surface. The rods in the transverse sections have a shape of the close-to-regular hexagons, if their diameters are no more than 150 nm, and of more complex polygons formed by combination of hexagon-like figures in the case of bigger diameters.

In $\theta/2\theta$-patterns (Fig. 4.5) there are only the reflexes relating to Si (100) substrate, and reflexes like (00 l) attributed to zinc oxide, such as (002) and (004). This unambiguously testifies to mutual crystallographic orientation of [001] ZnO ‖ [100] Si in the normal to the substrate direction. The FWHM of rocking curve for ZnO-(002) reflex is obtained about 0.5°. The φ-scans for asymmetrical ZnO-(114) reflex approved that the ZnO-rods showed full azimuthal disorientation in the plane.

Fig. 4.4 The graphical
representation of
dependences of average
length (**a**), and average
diameter (**b**) on pressure
value and substrate-to-source
distance
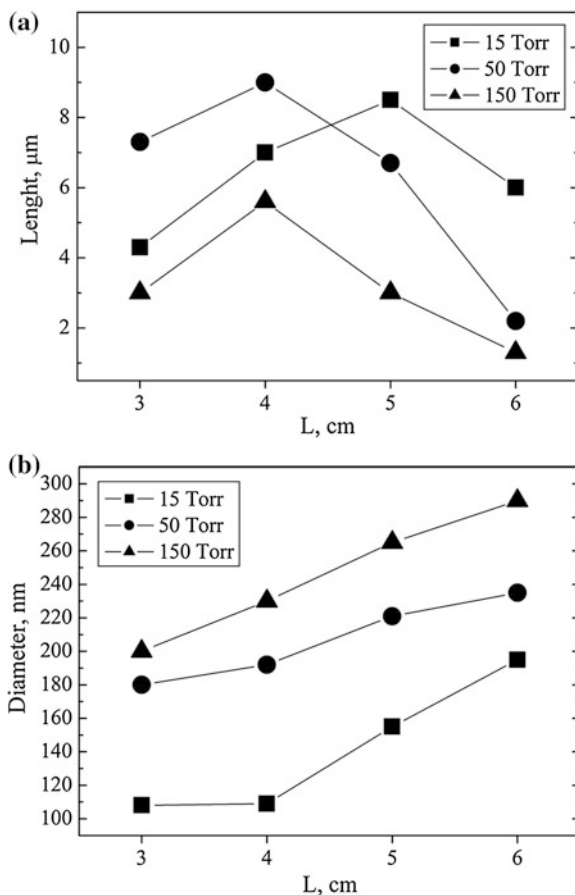
From electron microscopy data for Au-covered areas of the samples it might be supposed the presence of gold nanoparticles with average diameter about of 30 nm concentrated near the interface of ZnO-rods with ZnO-sublayer. XRD also confirmed the existence of gold nanoparticles. In the areas covered with Cu, metal particles were absent. This may confirm that copper is evaporated, or embed into crystalline structure of the ZnO-rods during their formation. Also metal particles were absent on lateral surfaces and peaks of rods in the case of use both Au, and Cu as catalyst. These results, along the facts, that rods grow in absence of the catalytic agent, and only insignificant difference of morphometric parameters, argue that the catalytic agent plays a role only at the initial stage (forming preferential growth centers), and does not participate in the further growth of rods under existing synthesis conditions.

Also, an additional series of samples was synthesized with pressure of 50 Torr at distances of $L = 3, 4, 5$ and 6 cm, when the temperature was lowered by 50 degrees, i.e. the precursor was been heated up to 900 °C. Preparation of substrates

Fig. 4.5 $\omega/2\theta$-pattern array of the rods ZnO on Si. In insertion, it is shown a pole figure of a reflex ZnO-(103)
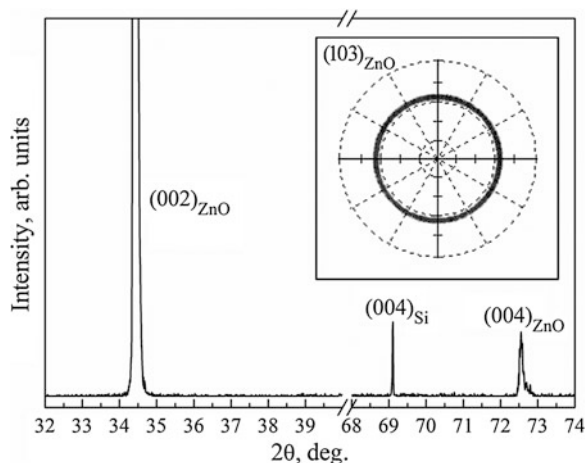
here was carried out in a way similar explained earlier. ZnO-rods were not produced on each of these samples. A zinc oxide layer (no more than 20 nm thick) formed on surface of the initial ZnO-sublayer was only one resulting product formed during this experiment.

From the facts of the dependence of rod length and their average diameter on changing substrate-to-source distance and buffer Ar pressure, it is evident to assume that by varying with distance and pressure, the gas-phase parameters and the rate of surface-related processes on a substrate might be changed. Such values, as partial pressure of Zn vapors, rate of diffusion, oxidation of Zn adatoms and pressure of residual oxygen in each point of the reaction chamber might depend on two technological parameters: substrate-to-source distances and buffer pressure of Ar. By changing and manipulating these two parameters, it is obviously possible to change and control the kinetic and thermodynamic conditions of growth and, therefore, the morphometric parameters of formed structures.

4.4 Conclusion

The possibility to control the average diameters, lengths and surface distribution density of ZnO-nanorod arrays produced by carbothermal reduction process (or carbothermal synthesis) is shown in the ranges of 100–300 nm, 1.5–9 μm, 2.8×10^8–5.3×10^8 cm^{-2}, respectively. The dispersion level of the synthesized rods did not exceed of 33 % in diameter and 13 % in length. The growth of rods was observed in both cases of Cu or Au existence, and without of the growth catalytic agent. The morphometric parameters of ZnO-rod arrays varied no more than on 15 % in dependence on the one of these two cases. From the existence of gold nanoparticles near the interface of ZnO-rods with ZnO-sublayer, it is concluded that the catalytic agent plays a role only at the initial stage of growth.

References

1. Chun Li et al., J Cryst Growth **292**, 19 (2006)
2. Gang Meng et al., Appl Surf Sci **256**, 6543 (2010)
3. G.D. Yuan et al., Nano Lett. **8**, 2591 (2008)
4. H.J. Fan et al., *Small* **2**, 561 (2006)
5. B.D. Yao, Y.F. Chan, N. Wang, Appl. Phys. Lett. **81**, 757 (2002)
6. Wu Weiwei et al., Sci Adv Mater **2**, 402 (2010)
7. M.D. Abramoff, P.J. Magelhaes, S.J. Ram, Biophot. Int. **11**, 36 (2004)

Chapter 5
Electro-Deposition of Cu_2ZnSnS_4 Solar Cell Materials on Mo/SLG Substrates

Min Yen Yeh, Yu-Jheng Liao, Dong-Sing Wuu, Cheng-Liang Huang and Chyi-Da Yang

Cu_2ZnSnS_4 (CZTS) absorber layers, treated with post sulfurization, were successfully grown on Mo/soda lime glass substrates by electro-deposition at room temperature. Electro-deposition is such a method that has the advantages of high quality, low-cost, high-efficiency, high production, vacuum-less and good void fill ability. In this work, a two-electrode arrangement system was used and worked at galvanostat setting. The CZTS was electro-deposited through single-step processes using sodium citrate ($Na_3C_6H_5O_7$) and tartaric acid ($C_4H_6O_6$) as the complexing agents. The as electro-deposited CZTS films were treated with post sulfurization using sulfur vapor. The crystallinity of the as electro-deposited CZTS was improved through the post-sulfurization. The as-formed CZTS was analyzed using FE-SEM, XRD and Raman Spectrometer. The CZTS films exhibit polycrystalline kesterite structures with preferred XRD orientation on (112), (220), (312) planes. The optical band gap energy was ~ 1.25 eV which was a suitable value for solar cell application.

5.1 Introduction

Humans have achieved a level of material progress based on continuous invention in science and technology. The endeavor on developing science and technology to meet the need of comfortable live consumes lots of energy resources. The conventional energy resources include oil, gas, coal, etc. The increase of energy usage exhausts the storage of conventional energy resources year by year. It is a suffering

M. Y. Yeh (✉) · Y.-J. Liao · C.-L. Huang · C.-D. Yang
Department of Microelectronics Engineering, National Kaohsiung Marine University,
No.142, Haijhuan Rd., Nanzih Dist., Kaohsiung City 81157, Republic of China (Taiwan)
e-mail: minyen@webmail.nkmu.edu.tw

D.-S. Wuu
Department of Materials Science and Engineering, National Chung Hsing University, 250,
Kuo Kuang Rd., Taichung 40227, Republic of China (Taiwan)

experience of oil crisis happened in 1970s. Today we face more serious global energy problems which involve not only the shortage of conventional energy, but the impact to the environment. The insurmountable energy problems challenge people to find out suitable alternative resources. The choices and development of alternative resources urge the requirement of recycle and green to our environment. Nowadays, development of solar energies, wind and hydrogen fuel cells are the popular subjects.

The application of solar energy is based on the developments of solar cells. Common use of solar cell devices include silicon based (single, multiple, amorphous crystalline), compound (GaAs, CdTe, CuInSe$_2$), and dye-sensitized (TiO$_2$) solar cells. Since silicon material is abundant in the Earth crust and Si process is a high developed technology, silicon solar cells are dominant in the commercial photovoltaic market. Most of the commercial Si solar cells are made of crystalline Si based on Si bulk substrates. The solar cell structures only occupy few micrometers of thickness onto bulk Si. Most of raw bulk Si material is wasted and causing high cost production. High-efficiency thin-film solar cells may hold the key to the cost consideration.

The development of thin-film compound semiconductor such as CIGS, and CZTS has the potential to meet the requirements of solar cells. Though, the ZnO/CdS/CIGS thin-film solar cells had reached 19.2 % efficiency [1], lower reserve of indium (In) in the earth's crust and toxic element of Se to our environment would become the barrier for mass production. In recent years, Cu$_2$ZnSnS$_4$ is the most promising absorber layer material for solar cell to replace CIGS, although CZTS solar cells have less efficient than CIGS solar cells reported by the National Renewable Energy Laboratory 19.9 % [2] and the German solar and hydrogen energy research institutions 20.3 % [3]. Since CZTS constituents of copper, zinc, tin and sulfur are plenty in the earth and non-toxic, and this makes it a suitable candidate for replacing CIGS solar cells. Nowadays, non-toxic, low-cost and high efficiency CZTS thin film solar cells have been developed by IBM 8.4 % [4] and 11.1 % in 2012 [5].

CZTS can be prepared by various methods, such as spray-pyrolysis deposition [6], electron-beam evaporation [7], radio-frequency magnetron sputtering deposition [8], electroplated deposition [9], pulsed laser deposition [10], and sol-gel deposition [11]. The advantages of low cost materials, large area deposition, low temperature process and easy equipment, make electro-deposition an attractive technique as compared to vacuum system processes like e-beam evaporation, rf-sputtering, and pulse laser deposition. Generally it is easier to deposit mono-element by electro-deposition in a single-step. A quaternary compound is more difficult to deposit in one-step through electro-deposition. Single-step electro-deposition of CZTS thin films from aqueous is difficult since the reduction potential range of these metal ions is considerably large [12]. CZTS films prepared by single-steps electro-deposition remain still a challenge to obtain stoichiometry composition [12–14]. For obtaining stoichiometric CZTS, complexing agents are used to decrease the gap in the reduction potentials of species and improve the lifetime of deposition bath as well as the adhesion of the deposited film on the

Fig. 5.1 Flow chart of Cu$_2$ZnSnS$_4$ electro-deposition process
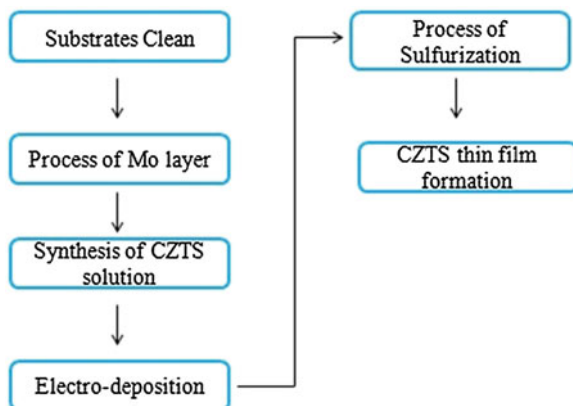
substrate [12, 15]. Tri-sodium citrate (Na$_3$-citrate) was used as the complexing agent in quaternary electrolytic bath for electro-deposition of CZTS thin films [14]. In this work, tri-sodium citrate was used as the agent for single-step electro-deposition on Mo/SLG substrate. The structural properties of the as-electro-deposited and sulfurized thin films were investigated using X-ray diffractometry (PANalytical X'pert Pro with CuKα radiation, $\lambda = 1.5406$ Å). The morphological and compositional characteristics of the as-prepared CZTS thin films are characterized using field emission scanning electron microscopy (JEOL, JSM-6700F), and energy dispersive X-ray spectroscopy (EDX, OXFORD INCA). Raman spectral analysis was performed by using 532 nm laser exited line. Optical transmittance & reflectance spectra are performed using N&K UV-visible analyzer in the range of 190 $\sim$ 1000 nm.

5.2 Experimental Methods

CZTS thin film was prepared by electro-deposition technique through a single-step process in a non-vacuum system at room temperature. The processes have several advantages, such as low cost source materials, large area deposition, cheap capital equipment, solution synthesis and room temperature growth. Molybdenum (Mo) widely used in industry is suitable used as the back contact for CZTS solar cells. Most of CZTS thin films deposited on Mo/SLG substrate may encounter the problems of adhesion and contact resistance between CZTS layer and Mo metal. The interface quality often affects the solar cell performance. Poor interface quality will increase series resistance of solar cells, and deteriorate the device efficiency. Direct electrochemical growth of CZTS onto Molybdenum surface may be a possible way to improve the interface quality and access higher-quality CZTS film.
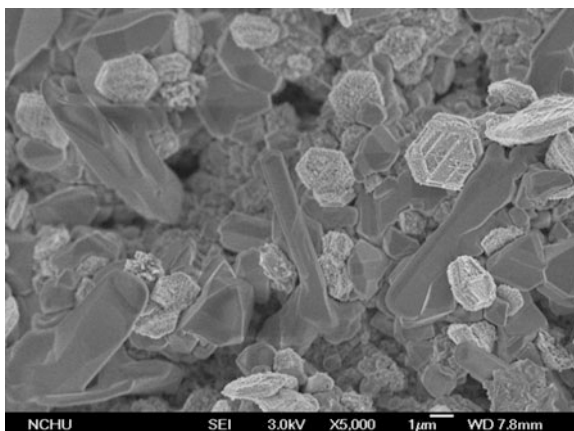
In this work, the deposition process of Cu_2ZnSnS_4 thin film is shown in Fig. 5.1. Soda lime glass (SLG) with 2×4 cm^2 dimension was used as substrates. SLG substrates were cleaned in ultrasonic bathes of acetone and D.I. water, successively, and dried flown nitrogen. Molybdenum layers were chosen as the starting layer for electro-deposition and prepared on SLG substrates by D.C. sputtering. The sputtering chamber was pumping down to a back ground pressure of 5×10^{-6} torr, and working pressure was kept at 6 mtorr. A 2-inch diameter and 6-mm thickness Molybdenum with 99.95 % purity was used as the target. A rotatable substrate holder was fixed at 10 cm from the Molybdenum target. The electrolyte aqueous for CZTS electro-deposition was prepared using metal sulfates ($CuSO_4$, $ZnSO_4$, $SnSO_4$) at 2 : 1 : 2 mol ratios mixed in D.I. water. Sodium citrate ($Na_3C_6H_5O_7$) and tartaric acid ($C_4H_6O_6$) were used as the complexing agents. The electro-deposition was carried out at room temperature using a double-electrode configuration in galvanostat with a maximum current of 3 mA. The working and counter electrodes dipped into electrolyte were 1×1 cm^2. After electro-deposition, the obtained CZTS thin films were treated with sulfurization using a conventional tube furnace filled with nitrogen. Sulfur vapor sublimated from sulfur powder was used for the CZTS sulfurization process at 400 °C for 10 min.

5.3 Results and Discussion

The surface morphology of the as-deposited and sulfurized CZTS thin films was investigated by using scanning electron microscopy (SEM). CZTS thin films were electrochemically deposited in galvanostat at 3 mA. Figure 5.2 presents SEM surface micrographs of as-deposited CZTS thin films onto Mo/SLG substrate. It is observed that the film shows non-uniform distribution of agglomerated particles with dense packing. The agglomerated particles with well-defined boundary reveal

Fig. 5.3 XRD patterns of as electro-deposited CZTS treated with post sulfurization
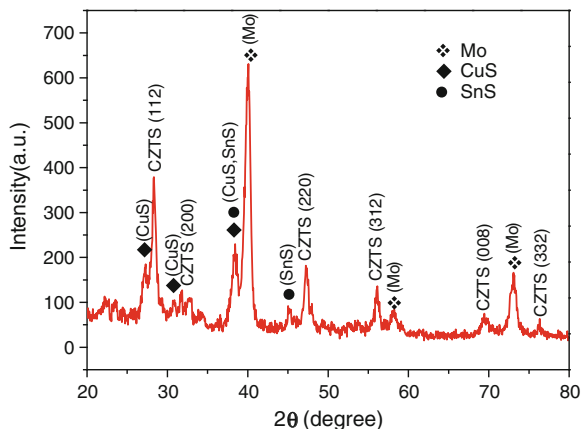
Fig. 5.4 Raman shift spectrum of as electro-deposited CZTS treated with post sulfurization
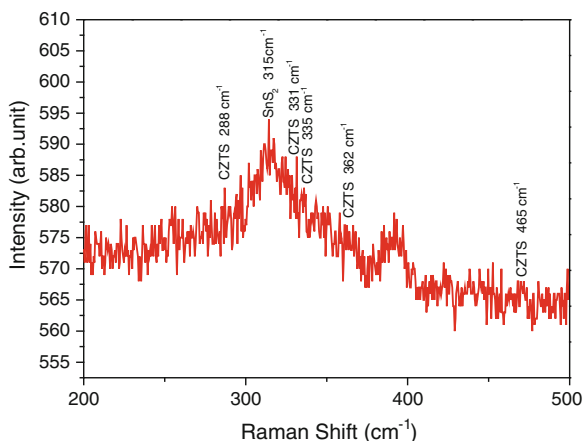
rectangle and pebble shapes have a size range of 1 $\sim$ 8 μm. The obtained grain sizes seem to be larger than those reported in literatures [12, 14]. The larger size of particles might be the effect of sulfurizing process using sulfur vapor in this work, as comparing to other's annealing works using ambient gas of nitrogen or Ar. It had been found that surface morphologies of prepared CZTS thin films were affected by annealing condition [12].

Structural properties of as electro-deposited CZTS treated with post-sulfurization at 400 °C were analyzed using XRD measurement with 2θ scanning from 20 to 80°. The XRD spectrum of as sulfurized CZTS thin films electro-deposited from quaternary electrolyte aqueous containing sodium citrate and tartaric acid on Mo/SLG substrates are presented in Fig. 5.3. The XRD peaks diffracted at the positions indexed as (112), (200), (220), (312), (008), and (332) attribute to different crystallographic planes of Cu$_2$ZnSnS$_4$. The XRD pattern of the as electro-deposited CZTS treated with post-sulfurization reveals polycrystalline and

Element	Weight%	Atomic%
S K	34.02	59.30
Cu L	15.07	13.26
Zn L	9.02	7.71
Sn L	41.89	19.73
Totals	100.00	
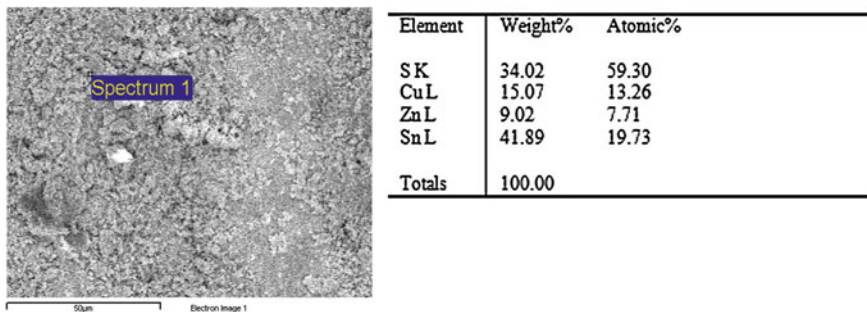
Fig. 5.5 EDS analysis of as electro-deposited CZTS treated with post sulfurization

kesterite structure. Besides polycrystalline CZTS, other secondary phases such as CuS and SnS are found in the films. The secondary phases of copper sulfides and tin sulfides were also frequently observed in CZTS films in other reports [12, 16].

As we can see that it is hard to distinguish some of the XRD diffraction peaks of CZTS from secondary phases such as CuS, SnS and ZnS since they stand too close. XRD seems no a very precise way to distinguish CZTS and its secondary phases. Raman spectroscopy may become an alternative method to identify the structure of the as-deposited CZTS and secondary phases. Figure 5.4 shows Raman spectroscopy results of as electro-deposited CZTS treated with sulfurization. From the Raman spectrum, we can observe scattering peaks at 288, 331, 335, 362 and 465 cm^{-1} defined as the characteristic peaks of Cu_2ZnSnS_4 [17–21]. The existence of SnS peak scattering at 315 cm^{-1} is also found in the as electro-deposited CZTS thin films treated with sulfurization by the Raman test [22–24]. From the XRD and Raman test we know that there are still numerous challenges to electro-deposit CZTS in which no secondary phase is accompanied.

The composition of the CZTS film was analyzed by EDS. Figure 5.5 shows that the content of sulfur in the as electro-deposited CZTS film is compensated enough through the sulfurization treatment. The constituent of copper seems poor in the film. The content of Zn seems to be lost a little during high temperature process (sulfurization) similar to the report [17]. It can be seen that the as deposited CZTS film treated with sulfurization does not reveal a close stoichiometric composition. A close stoichiometric composition was found to relate to an optimal volume of complexing agent added into the quaternary electrolyte for single-step electro-deposition [12].

The transmittance and reflectance of the CZTS films were examined using UV-visible spectra from 200 to 1000 nm. Optical absorption coefficients were then calculated as [27]

$$\alpha = \frac{1}{t}[\ln(1 - R_\lambda) - \ln T_\lambda], \tag{5.1}$$

where t is the film thickness, R_λ and T_λ are reflectance and transmittance coefficients, respectively.

Fig. 5.6 Absorption spectrum of CZTS as a function of photon energy, the CZTS is electro-deposited on Mo/SLG and treated with post sulfurization
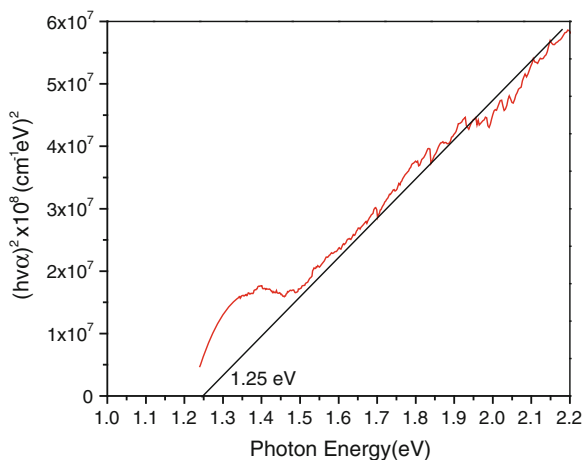
The absorption coefficients of the CZTS are higher than 1×10^4 cm^{-1} in the visible range. A high absorption property over the solar radiation band is thought to be an attractive candidate for solar cells applications. The as electro-deposited CZTS film treated with post-sulfurization, has a high absorption spectrum over a larger photon energy region. From [27], we know that the absorption coefficient related to direct transitions has the following spectral dependence:

$$\alpha = A(h\nu - E_g)^{1/2}, \tag{5.2}$$

where A is a constant, $h\nu$ is the photon energy and E_g is the energy band gap. A direct transition can then be found by the linear dependence of $(\alpha h\nu)^2$ versus $h\nu$. Thus optical-energy gap can be determined by extrapolating the linear part of the spectrum of the square absorption coefficients of the CZTS to zero absorption coefficient as a function of photon energy. As shown in Fig. 5.6, the CZTS optical energy gap is ~ 1.25 eV which is suitable to be the absorber layer for solar cells [25, 26].

5.4   Conclusion

Cu$_2$ZnSnS$_4$ thin films were successfully prepared on Mo/SLG substrates at room temperature by Galvanostat electro-deposition method. The as electro-deposited CZTS films were treated with post sulfurization using sulfur vapor in a conventional tube furnace filled with nitrogen. The one-step electro-deposited processes use sodium citrate (Na$_3$C$_6$H$_5$O$_7$) and tartaric acid (C$_4$H$_6$O$_6$) as the complexing agents to decrease the gap in the reduction potentials of species. Non-uniform agglomerated particles with well-defined boundary rectangle and pebble shapes in a size of $1 \sim 8$ μm were observed from the as prepared CZTS SEM surface

morphology. The obtained grain sizes larger than other's work might be the effect of sulfurizing. The as electro-deposited CZTS treated with post-sulfurization reveals polycrystalline and kesterite structure from XRD test. Secondary phases such as CuS and SnS are found in the CZTS films from XRD and Raman examination. Using an optimal volume of complexing agent may be a way to improve the secondary phases, and this may be also useful to obtain a close stoichometric CZTS. The as electro-deposited CZTS films are suitable to be the absorber layer for solar cells, since they have high absorption efficiencies in the visible range with the optical energy gap of ~ 1.25 eV.

References

1. K. Ramanathan, M.A. Contreras, C.L. Perkins, S. Asher, F.S. Hasoon, J. Keane, D. Young, M. Romero, W. Metzger, R. Noufi, J. Ward, A. Duda, Prog. Photovolt. Res. Appl. **11**, 225 (2003)
2. I. Repins, M.A. Contreras, B. Egaas, C. DeHart, J. Scharf, C.L. Perkins, B. To, R. Noufi, Prog. Photovolt. Res. Appl. **16**, 235 (2008)
3. P. Jackson, D. Hariskos, E. Lotter, S. Paetel, R. Wuerz, R. Menner, W. Wischmann, M. Powalla, Prog. Photovolt. Res. Appl. **19**, 894 (2011)
4. B. Shin B, O. Gunawan, Y. Zhu, N.A. Bojarczuk, S.J. Chey, S. Guha, Prog. Photovoltaics Res. Appl. **21**, 72 (2013)
5. T.K. Todorov, J. Tang, S. Bag, O. Gunawan, T. Gokmen, Y. Zhu, D.B. Mitzi, Adv. Energy Mater. **3**, 34 (2013)
6. N. Kamoun, H. Bouzouita, B. Rezig, Thin Solid Films **515**, 5949 (2007)
7. H. Katagiri, Thin Solid Films **480–481**, 426 (2005)
8. K. Jimbo, R. Kimura, T. Kamimura, S. Yamada, W.S. Maw, H. Araki, K. Oishi, H. Katagiri, Thin Solid Films **515**, 5997 (2007)
9. A. Ennaoui, M. Lux-Steiner, A. Weber, D. Abou-Rus, I. Kotschau, H.W. Schock, R. Schurr, A. Holzing, S. Jost, R. Hock, T. Voβ, J. Schulze, A. Kirbs, Thin Solid Films **517** (7), 2511 (2009)
10. S.M. Pawar, A.V. Moholkar, I.K. Kim, S.W. Shin, J.H. Moon, J.I. Rhee, J.H. Kim, Curr. Appl. Phys. **10**(2), 565 (2010)
11. M.Y. Yeh, C.C. Lee, D.S. Wuu, J. Sol-Gel. Sci. Technol. **52**, 65 (2009)
12. M. Jeona, Y. Tanakab, T. Shimizub, S. Shingubara, Energy Procedia **10**, 255 (2011)
13. S.M. Pawar, B.S. Pawar, A.V. Moholkar, D.S. Choi, J.H. Yun, J.H. Moon, S.S. Kolekar, J.H. Kim, Electrochim. Acta **55**, 4057 (2010)
14. B.S. Pawar, S.M. Pawar, S.W. Shin, D.S. Choi, C.J. Park, S.S. Kolekar, J.H. Kim, Appl. Surf. Sci. **257**, 1786 (2010)
15. A. Ghazali, Z. Zainal, M.Z. Hussein, A. Kassim, Sol. Energy Mater. Sol. Cell **55**, 237 (1998)
16. P.A. Fernandes, P.M.P. Salomé, A.F. daCunha, Thin Solid Films **517**, 2519 (2009)
17. C. Gao, H. Shen, F. Jiang, H. Guan, Appl. Surf. Sci. **261**, 189 (2012)
18. D. Dumcenco, Y.S. Huang, Opt Mater **35**, 419 (2013)
19. H. Yoo, J. Kim, Sol Energy Mater Sol Cells **95**, 239 (2011)
20. L. Sun, J. He, H. Kong, F. Yue, P. Yang, J. Chu, Sol. Energy Mater. Sol. Cells **95**, 2907 (2011)
21. F. Jiang, H. Shen, W. Wang, J Electron Mater **41**, 2204 (2012)

22. I.P. Parkin, L.S. Price, T.G. Hibbert, K.C. Molloy, J. Mater. Chem.**11**, 1486 (2001)
23. Y. Wang, H. Gong, J. Alloy. Compd. **509**, 9627 (2011)
24. P.A. Fernandes, P.M.P. Salomé, A.F. da Cunha, Thin Solid Films **517**, 2519 (2009)
25. K. Ito, T. Nakazawa, J. Appl. Phys. **27**, 2094 (1988)
26. S.M. Pawar, A.V. Moholkar, I.K. Kim, S.W. Shin, J.H. Moon, J.I. Rhee, J.H. Kim, Curr. Appl. Phys. **10**, 565 (2010)
27. J.I. Pankove, *Optical Processes in Semiconductors* (Dover Publication, New York, 1975)

Chapter 6
Complex Investigations of Sapphire Crystals Production

S. P. Malyukov and Yu V. Klunnikova

The problem of optimum conditions choice for processing sapphire substrates was solved with optimization methods and with combination of analytical simulation methods, experiment and expert system technology. The experimental results and software give rather full information on features of real structure of the sapphire crystal substrates and can be effectively used for optimization of technology of the substrate preparation for electronic devices.

6.1 Introduction

The sapphire crystals have a complex of the certain physical properties so it can be widely used in microelectronics, quantum electronics, optics of high accuracy, nanotechnology. The requirements to sapphire structure quality grow with development of technologies. It is known that sapphire quality is determined by a set of criteria, and first of all it is the growth conditions. This concept also includes a set of others, such as temperature distribution in the crystallization camera, temperature gradient and its change, the processes arising on the interphase crystal-liquid boundary and their influence on total crystal structure, crystal annealing process when cooling takes place after growth and the chemical, thermal and mechanical treatment.

In recent years the certain successes have been achieved in research and development of crystal formation mechanisms, morphological stability of crystallization front and the role of impurity, the thermal and concentrated streams and other factors in crystal structure formation. However determination of functional dependences for real crystal parameters based on conditions of crystal growth remains the main task because the problem solution of processing a crystal

S. P. Malyukov (✉) · Y. V. Klunnikova
Southern Federal University, Taganrog, Russia
e-mail: malyukov@fep.tsure.ru

material with the set of properties depends on it. The detailed analysis of processes and environment structure from which crystals grow up is necessary for the solution of this problem. It is necessary also to develop the mathematical and information support for fabrication of products from sapphire crystals.

6.2 Growth Methods of Sapphire Crystals

There are many growth methods of sapphire crystals [1, 2]. The most promising method is the growth method from the melt by horizontal directed crystallization (HDC), allowing one to obtain large-size crystals (e.g., $350 \times 150 \times 45 \text{ mm}^3$) with high growth rates if we compare them with crystallization rates from solutions or gaseous media. There are growth methods with crystallization in the crucible (Verneil's method) or crystallization without it (Kiropoulos's method, Bridgmen-Stokbarger's method, Stepanov's method, Czochralsky's method, HDC method, and zone melting method).

The crystal growth methods from the melt can be divided into two groups:

(i) the methods with small volume of the melt (Stepanov's method, Verneil's method, and zone melting method),
(ii) the methods with large volume of the melt (Kiropoulos's method, Bridgmen-Stokbarger's method, Czochralsky's method, HDC method).

The melt volume influences on crystallization character and there are many methods of sapphire crystals growth [1, 2]. The most promising method from viewpoint of intensity of the crystal physical and chemical processes in melt is the HDC method [3–5], which allows one to obtain large-size crystals with high growth rates. The melt can dissociate, and dissociation products can evaporate in the atmosphere. For these substances the time of staying into melt is limited, so the crystals are grown from the small volume of the melt. The similar conditions have to be applied for substances which interact with container material and atmosphere. It is necessary to pay attention on differences of convection conditions for the both groups of the growth methods. In the large melt volume the convective streams develop early, and the convective transfer plays a noticeable role [6, 7]. In the small volume convection cannot play such role, and the weight is transferred by diffusion.

It should be noted that Kiropoulos's and Czochralsky's methods are brought to the high technological level. But they also have some features which do not promote reduction of crystal prices. First of all there are: (i) the high cost of growth equipment, (ii) the technological difficulties during large diameter sapphire growth with crystallographic orientation (0001) which is optimal for optics and opto-electronics on the nitride-gallium structures, (iii) the necessity of expensive use of the raw materials with high degree of purity (99.996 % Al_2O_3). Many of these problems are not characteristic for HDC method. This method does not demand the complex and expensive equipment, and allows one to grow the large-size crystals of any crystallographic orientation and to use the cheap raw materials with
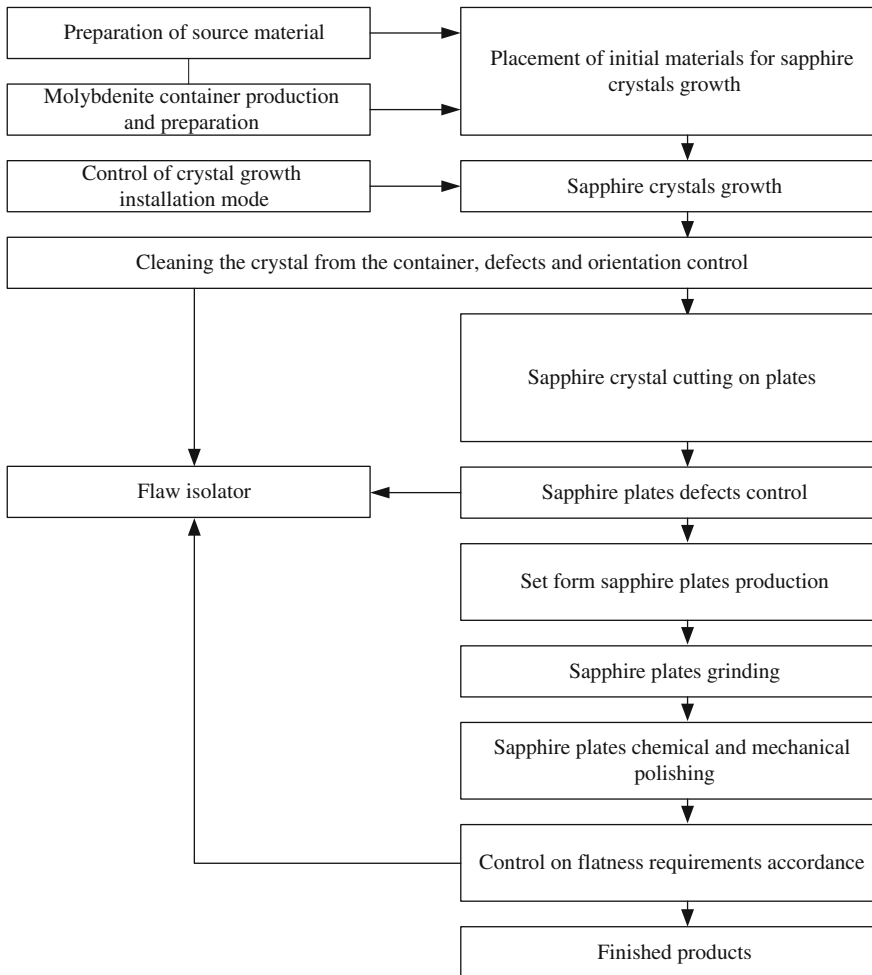
Fig. 6.1 Technological scheme of sapphire crystal production by HDC method

higher impurity concentration because of their effective evaporation in the melt crystallization process. It has allowed one to increase the crystal sizes and to expand their application. The common scheme of Al_2O_3 substrate production by HDC method [8] is presented in Fig. 6.1. It includes crystals growth and substrate production.

The HDC method has some advantages in comparison with other methods. First of all consists in that the melt height and its square are constant during a whole process (see Fig. 6.2). The large melt volume allows one to provide the effective impurities evaporation. The fuse process and boundary of phase division can be controlled visually or by means of optical devices. It creates the grounds for automation process [9, 10].
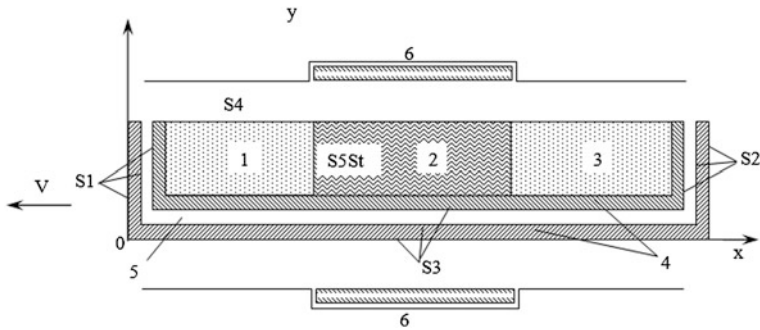
Fig. 6.2 The model for temperature distribution calculation in the system crystal-melt: *1* crystal, *2* melt, *3* powder, *4* molybdenite container and pallet, *5* gap between pallet and crucible, *6* heater, *S1*, *S2*, *S3*, *S4* emitting surfaces, *S5St*—crystallization boundary

6.3 Simulation of Heat Transfer Processes During the Sapphire Crystal Growth by Horizontal Directed Crystallization Method

In real conditions of sapphire crystal growth by HDC method the temperature of fuse decreases that defines the temperature gradient in growth crystal. The simulation of heat transfer processes in the crystal-melt system was carried out for definition of influence of the sapphire growth parameters on the crystal quality [8].

The pallet and the crucible with powder (see Fig. 6.2) move relatively to the heater with the speed of 6–10 mm/h. Therefore it is possible to consider the all process as occurring in the quasi-steady state.

Two stationary positions of crucible with material relatively to the heater were considered: (i) the crystal, melt and powder be in crucible, (ii) the finish of the technological process took place, when the crystal and melt were in the crucible (see Fig. 6.2). The process occurred in the vacuum, so the heat transfer between free surfaces is caused by radiation [8].

The problem of temperature distribution determination in the system "crystal-melt-powder" consists of equations set solution [11] including the thermal conductivity equation:

$$-\nabla k \cdot \nabla T = q, \tag{6.1}$$

with the boundary condition for S5St [12]:

$$-\lambda_{\kappa p}\frac{\partial T_{kp}}{\partial x}\bigg|_{x=0} = \rho_{\kappa p} \cdot L \cdot V - \lambda_p \frac{\partial T_p}{\partial x}\bigg|_{x=0}, \tag{6.2}$$

and the heat balance equation, written in accordance with the Stefan-Boltzmann law for radiation surfaces S_1, S_2, S_3, S_4 [11]:

(a) h, m

(b) T, K
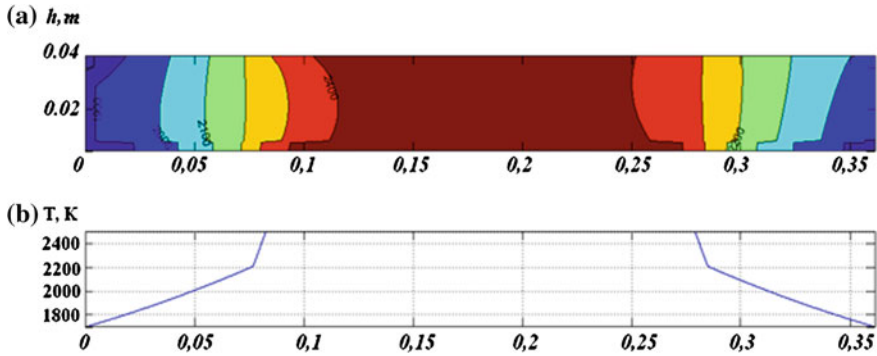
Fig. 6.3 The crystal, melt and powder disposed in the container: **a** The temperature distribution in the system "crystal-melt-powder", **b** The heater temperature

$$-k\frac{\partial T}{\partial n} = \sigma \cdot \beta \cdot (T^4 - T_0^4), \tag{6.3}$$

where k is the material heat conductivity, T is the temperature in the system "crystal-melt-crystal powder", q is the heat release on the boundary "melt-crystal", ρ is the material density, L is the hide crystallization heat, σ is the Stephan-Boltzmann constant, β is the coefficient of reflection.

The heat balance equation at the boundary S5St, written in accordance with the Stefan-Boltzmann law for radiation surfaces and Lambert law for an absorbing medium has the form [11]:

$$q_\psi = E_0 \int \cos \psi \cdot \exp(-\alpha \cdot r(\psi)) \cdot d\omega, \tag{6.4}$$

where q_ψ is the heat stream density due to radiation, $E_0 = \beta \cdot \sigma \cdot (T^4 - T_0^4)$ is the stream density emitted by the melt in crystal, $d\omega$ is the angle under which from the point of emitting it can be visible the elementary crystal surface area, ψ is the angle between the normal to the surface and the emission direction, α is the medium absorbance, r is the distance between the radiation point and the crystal surface.

The system of differential equations (6.1)–(6.4) is solved by the numerical method based on the finite differences method [13]. The two-dimensional numerical model was developed. It includes the translucent crystal area and the opaque melt area, separated by a diffuse boundary [8].

This model allowed us to conduct the calculation for estimation of effects of the thermo-physical material properties and external temperature conditions on the crystallization process in rectangular system "crystal-melt-powder" in the quasi-stationary approximation.

The results of temperature field calculation in the system "crystal-liquid–powder" are presented in Fig. 6.3. The results indicate that the temperature in the container

has the non-linear distribution. The heat streams in the upper part of the crystal are substantially different from the thermal streams in the bottom part. The pallet-vacuum gap-container play a role of screen and change the form of crystallization front making it inclined to the growth direction (see Fig. 6.3).

The crystallization front changes the form with the crystal length increase. It becomes convex in the melt. This fact embarrasses the bubbles emersion on the melt surface so the bubbles accumulate at the bottom part of container. The simulation results showed that the small sapphire absorbance in the solid phase, α, was the explanation for this solidification front distortion.

The model allows us to calculate the temperature distribution in the system "melt-crystal" for sapphire crystallization by the method of horizontal directed crystallization. It takes into the account the radiation from crystal surface and diffusive front boundary.

Thus the results showed that the sapphire crystal transparency in the solid phase for thermal radiation made the radiating component prevailing in the thermal stream from front along the crystal. For this reason the crystal growth rate enlarges with crystal length increase and the crystallization front form changes also. These factors are the principal causes of defects formation in crystals.

It is necessary to calculate the temperature distribution in the growth equipment of sapphire crystals by the HDC method in three-dimensional case for more exact defect diagnostics. The temperature distribution determination in the system "crystal-melt-crystal powder" includes solution of the heat conductivity equations [14, 15]:

$$\frac{\partial T_i(x,y,z,\tau)}{\partial \tau} = \left(\frac{\partial}{\partial x} a_i \frac{\partial T_i(x,y,z,\tau)}{\partial x} + \frac{\partial}{\partial y} a_i \frac{\partial T_i(x,y,z,\tau)}{\partial y} + \frac{\partial}{\partial z} a_i \frac{\partial T_i(x,y,z,\tau)}{\partial z} \right)$$
$$- W \frac{\partial T_i(x,y,z,\tau)}{\partial x},$$
$$0 < x < x_L, \ \ 0 < y < y_L, \ \ 0 < z < z_L, \tag{6.5}$$

here $i = 1, 2, 3$ is the crystal, melt and crystal powder, respectively, a_i is the heat diffusivity coefficients ($a_i = \frac{\lambda_i}{\rho_i \cdot C_i}$, where λ_i is the thermal conductivity coefficient; ρ_i is the material density; C_i is the specific heat); W is the container movement speed.

The container movement speed is small enough, so we can conclude that the growth process is quasi-steady and the temperature distribution can be found by the following formula [11]:

$$\mathrm{div}(\lambda_i \mathrm{grad} T_i(x,y,z)) = 0. \tag{6.6}$$

The boundary conditions for system of (6.6), reflecting continuity of thermal fields and streams on bounds of media section, can be found by using the following expressions:

(a)

(b)

| 1799 | 1977 | 2155 | 2333 | 2511 | | 2422 | 2244 | 2066 |

Fig. 6.4 Temperature fields in the system "crystal-liquid-powder"

$$\lambda_1 \frac{\partial T_1(x_T, y, z)}{\partial x} = \lambda_2 \frac{\partial T_2(x_T, y, z)}{\partial x}, \tag{6.7}$$

$$\lambda_2 \frac{\partial T_2(x_T + \Delta x, y, z)}{\partial x} = \lambda_3 \frac{\partial T_3(x_T + \Delta x, y, z)}{\partial x}, \tag{6.8}$$

$$q_{s_1} = q_{s_2} = q_{s_3} = \sigma\beta(T^4 - T_{hot}^4), \tag{6.9}$$

where σ is the Stephan-Boltzmann constant, β is the radiation coefficient, T_{hot} is the function with the heat temperature distribution.

The final volume method on the unstructured grid was used for simulation. The discrete analog of heat conductivity equation for the final volume (tetrahedron) is:

$$\sum_j \frac{\lambda(T_j - T_i)A_{ij}}{(x_j - x_i)n_{jx} + (y_j - y_i)n_{jy} + (z_j - z_i)n_{jz}} = 0, \tag{6.10}$$

where volume i is the volume for which the heat conductivity equation is solved, volume j is the volume next for volume i, A_{ij} is the area of common face for i and j volumes, $\overrightarrow{n_j}(n_{jx}, n_{jy}, n_{jz})$ is the normal to the next i and j tetrahedrons, $\overrightarrow{l_j}(x_j - x_i, y_j - y_i, z_j - z_i)$ is the direction along which the thermal stream is defined.

The results of temperature calculation in the system "crystal-liquid-powder" are presented in Fig. 6.4. The temperature fields in the system "crystal-liquid-powder" are showed in Fig. 6.4a. The temperature fields in vertical cross-section of the crystal are presented in Fig. 6.4b.

The calculation results showed that sapphire crystals transparency in the crystal phase and the opacity in the melt influenced directly on the radiation streams in the system. Considering their large influence on the common heat exchange, this factor affects also on the temperature field and the crystallization front location. The temperature fields influence on the radiation heat transfer intensity. For this influence estimation, the calculations with temperature increase on 200–300 K in the system "crystal-liquid-powder" were carried out. The results showed that the

melt width increased and as result the crystallization front location changed. So we can conclude that we have possibility to control the crystallization front location owing to heat temperature increase.

In parallel with consideration of temperature fields, the analysis of mechanical stresses in the crystal was carried out. The calculations of the heater construction parameters should be fulfilment on the base of the strain, displacement and stress fields in the crystal. It means that mathematical simulation and calculations should be carried out for all equations which are included in system, namely: the equations of heat conductivity and thermal elasticity. So these equations [15–17] can be written as

$$
\begin{cases}
\mu\Delta u + (\lambda + \mu)\dfrac{\partial\delta}{\partial x} = -\dfrac{\partial(\alpha T)}{\partial x} - F_x, \\[2mm]
\mu\Delta v + (\lambda + \mu)\dfrac{\partial\delta}{\partial y} = -\dfrac{\partial(\alpha T)}{\partial y} - F_y, \\[2mm]
\mu\Delta w + (\lambda + \mu)\dfrac{\partial\delta}{\partial z} = \dfrac{\partial(\alpha T)}{\partial z} - F_z, \\[2mm]
\dfrac{\partial}{\partial x}\left(a_i\dfrac{\partial T}{\partial x}\right) + \dfrac{\partial}{\partial y}\left(a_i\dfrac{\partial T}{\partial y}\right) + \dfrac{\partial}{\partial z}\left(a_i\dfrac{\partial T}{\partial z}\right) = 0,
\end{cases}
\tag{6.11}
$$

where F_x, F_y, F_z are the components of volume sources; u, v, w are the components of displacements; $\phi = \{u, v, w\}$; α is the coefficient of volume heat expansion; λ and μ are the Lamé coefficients; Δ is the Laplace operator; $i = 1, 2, 3$ is the crystal, melt and crystal powder, respectively; a_i is the thermal diffusivity coefficients.

The boundary conditions for the system (6.11) are written in the form of relations [15].

The model allows us to make the numerical experiments and to study the influence of input parameters on the crystals quality. This approach allows one to improve the crystal growth process and to receive the crystals with reduced defects level.

6.4 Research of Stages of the Sapphire Crystal Treatment

Reviews [14, 18–20] showed that for the sapphire surface, corresponding to the substrate requirements for heteroepitaxy, it is necessary to carry out processing in several stages with the abrasive size decrease. In this case the fixed abrasive tool is applied on the initial treatment stages, and then the free abrasive with different granularity is used. The transitions number and the abrasive size are defined experimentally. The research of different tools and influence of treatment methods on sapphire surface was carried out for development of treatment method of the sapphire surface. After cutting the sapphire crystals, the plates were treated sequentially by three diamond grinding tools which allowed making the roughing
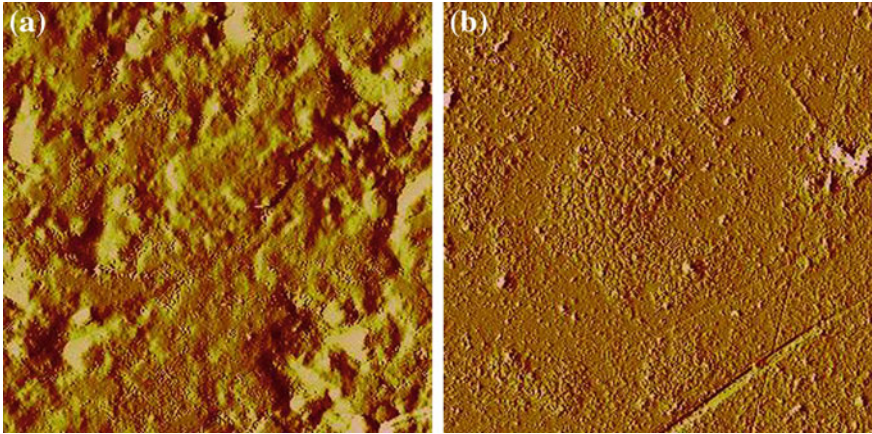
Fig. 6.5 Photomicrographs of sapphire surface after treatment with diamond powder ACM 28/20 and ACM 1/0

and finishing surface treatment. The problems of sapphire substrates processing such as oriented crystal cutting on the plates, substrates grinding, and finishing chemical and mechanical wafers polishing are considered. The two-sided grinding technology was investigated for the stage of mechanical treatment. After study of plates grinding by the free abrasive it was found [8] that these plates had the smooth matted surface without processing line traces. The free abrasive grinding provides the better surface quality. The roughness of surfaces is reduced, and their texture and purity are improved with decreasing diamond powder grain size in the tool or abrasive suspension (deionized water—66.7 %, glycerol—11.11 %) after the transition from hard grinding tools to the elastic and soft polishing tools in the final stages of processing (see Fig. 6.5).

The possibility to use the dependences of crystal microfracture on the singular abrasive grain for estimation of processing mass abrasive grains was investigated in [14]. In the real conditions, when the large amount of abrasive grains influence on the crystal, the final surface dislocation structure is defined by the dynamic balance between the crystal grinding rates and speed of new dislocations formation. On the basis of relation between the plasticity zone and depth of grain implantation into the crystal, it should be noticed that hardness increase of the abrasive and grinding tools will enlarge the layer with high dislocation density.

The dependences of material grinding tool and the abrasive radius on the depth of the surface damaged layer and the depth of formed lateral cracks in sapphire are presented in Fig. 6.6.
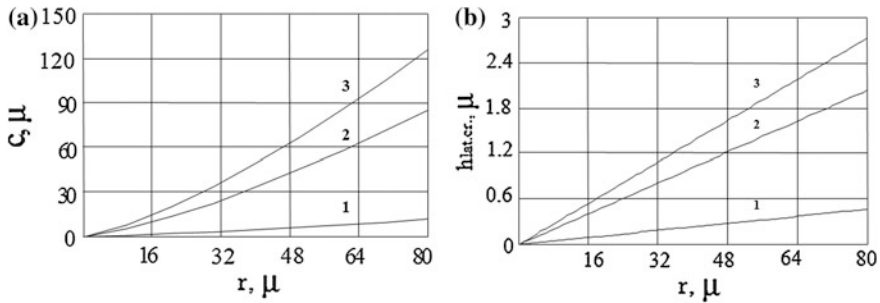
Fig. 6.6 The dependences of material grinding tool (*1*—brass, *2*—cast iron, *3*—glass) and the abrasive radius on the depth of the surface damaged layer (**a**), and the depth of formed lateral cracks in sapphire (**b**)

6.5 Method of Development of the Mathematical and Information Support for Sapphire Crystals Processing

Now, there is the intensive development of information technologies. It gives the unlimited possibilities to use computer possibilities in the crystal production. The complexity of use these methods is defined by incompleteness of mathematical description of the technological models for crystallization processes and absence of information support, which allow optimization of the technology [21].

For successful use of the information technology in the crystal production, it is necessary to develop new approaches and to improve the existing methods.

The main differences of technique applied in the work are: (i) the use of the expert estimation and experiment planning methods with the purpose of model creation. It allows one to receive dependences of the output parameters (levels of defects, etc.) on basic data (growth rate, heater power, etc.); (ii) the use of specific crystal growth and treatment database allows us to consider more adequately technological features; (iii) the complex consideration of three main stages of production (crystal growth, grinding and polishing) of the sapphire substrates.

As a work result, the method of mathematical and information support for designing growth of the sapphire crystals was developed. The algorithm is presented in Fig. 6.7.

The optimization can be divided into three main parts: (i) input data for the calculation (this process is the most time-consuming), (ii) calculations of parameters and defects, (iii) technological process optimization. After receiving the data, the models of dependence of the defect level on growth parameters of the sapphire crystals are built. The final part is the construction of model for growth optimization of the sapphire crystals. The objective function (time, defect level, etc.) is determined and restrictions (temperature, defect levels, speed, etc.) are entered.

Input

| Preparation of input data for calculation | Sapphire growth simulation | Technological process optimization |

| Preparation of requirements for quality | Initial data input | Reception dependencies between defects level and the most important technological parameters |

| Setting the thermal conditions for sapphire growth | Systematization of calculations intermediate results (defects level dependences table and others at the different modes) | Development of optimization model for sapphire crystals production |

| Choice the initial data in the database | Changing the most significant initial data | Conditions choice and solution of received optimal model |

| Expert analysis of the sapphire crystals significant technological parameters influence on quality | | Optimal parameters for sapphire growth technology |

Optimal parameters

Fig. 6.7 The algorithm of mathematical and information support for the sapphire production process

The purposes of the sapphire production process and optimization criterions are based on the key process indicators, determining the production efficiency and competitiveness. These indicators are grouped in two categories: (i) quality indicators, (ii) process cost indicators.

In the modern market the sapphire production should be directed to the realization of the following objective function:

$$F(KK, P) \;\; \rightarrow \;\; \mathrm{opt}, \tag{6.12}$$

where KK is the quality criteria for sapphire products, P is the product price.

Fig. 6.8 The algorithm of
the expert system for
selection of decision for
optimal technical solutions
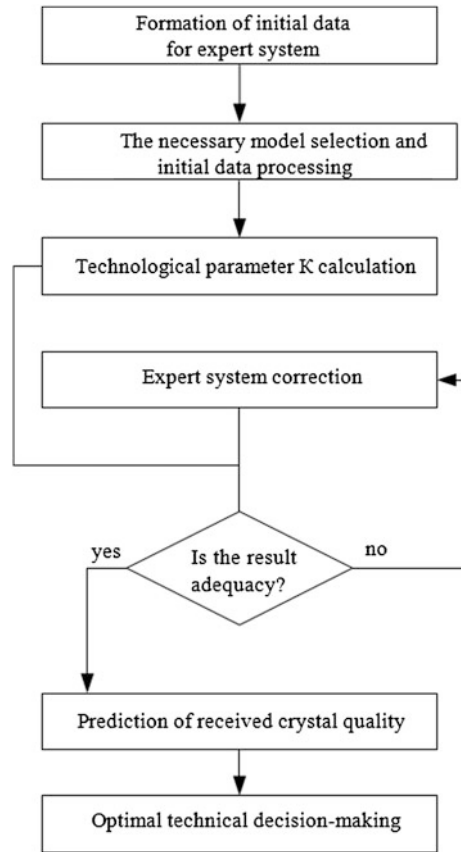
The quality indicator is the multifaceted product property. The total estimation of number of quality indicators is defined by the formula:

$$y = \sum_{i=1}^{n} k_n a_n, \tag{6.13}$$

where k is the factor taking into account the relative importance of process parameters on the crystal quality ($\sum_{i=1}^{n} k_n = 1$), a is the factor taking into account importance of the processing parameters, n is the number of the considered processing parameters.

The formula for translation of the technological parameters [16]:

$$K = \frac{y - y_{min}}{y_{max} - y_{min}}, \tag{6.14}$$
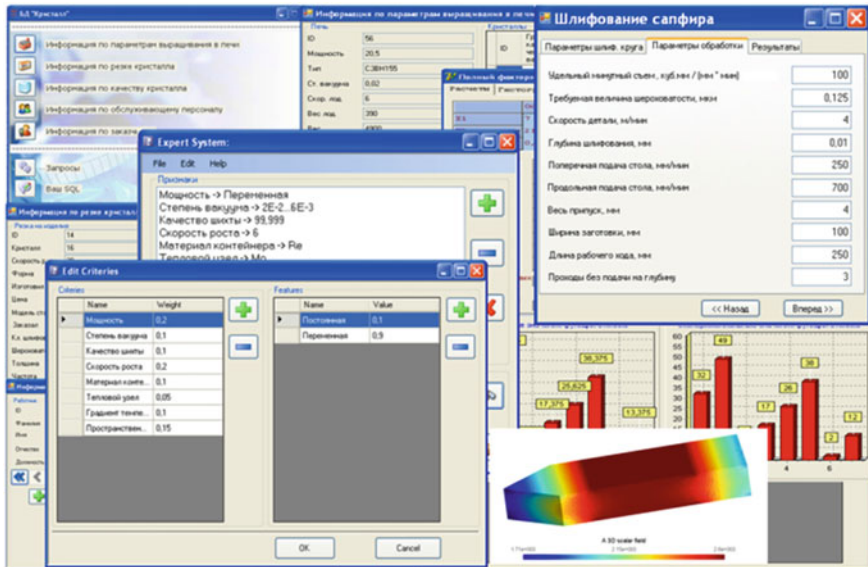
Fig. 6.9   Program interface for intellectual support during sapphire growth and treatment

where y, y_{min}, y_{max} are the current, minimum and maximum values of the processing parameters influence characteristic of the crystal quality, K changes from 0 to 1.

The range of values of the parameters and their importance were identified on the basis of experimental research [15] carried out in the equipment for the sapphire growth by HDC method. The correspondence between the real processing parameters and the parameters received by us was obtained.

These principles are used in the expert system for sapphire crystal production. The algorithm of the expert system for selection of decision on optimal solutions is presented in Fig. 6.8.

The expert system allows us to estimate the obtained crystal quality. The expert system includes database and knowledge base. It allows one to systematize the large information volumes. On the basis of the suggested models and algorithms the computer programs were developed. The interface of developed programs is presented in Fig. 6.9.

In total, the system consists of three calculating modules: (i) database of crystals and their parameters, (ii) information system allowing one to define optimum parameters of the technological process for receiving the best crystal quality, (iii) expert system allows one to make the expert analysis of an initial technological situation, to estimate the current technological situation concerning the database, to present the prediction of category of the processed crystal quality.

The system has the following purposes: (i) to give the exhausting information on crystals, (ii) to order the scattered information on crystallization processes,

(iii) to help the engineer-technologist in choice of growth parameters, (iv) to receive mathematical model for estimation of influence of the parameters on crystal quality, (v) to receive a prediction of crystal quality.

6.6 Conclusion

The complex investigations of sapphire crystals production for electronic equipment were carried out.

The favourable opportunity to control the crystallization parameters is one of the HDC method advantages. So the HDC method has the high reproducibility of growth conditions. It gives a possibility to grow the same crystals according to qualitative characteristics of serial crystallization experiments.

It was developed the model allowing one to investigate the temperature gradient influence on the position and crystallization front shape. On the basis of this model the temperature distribution in the system "melt-crystal" at different growth stages of sapphire production by the HDC method was studied. The three-dimensional numerical model for solution of the heat transfer problem in sapphire crystals allows one to develop computer programs for calculation of the temperature fields. The developed numerical model allows one to study the influence of thermal and physical material properties on sapphire crystallization.

In this work, the treatment processes of sapphire surface and investigation of influence of the different tools and treatment methods on the sapphire surface were studied.

On the basis of the suggested models and algorithms the computer programs were developed. The computer programs were based on intellectual support at decision-making for sapphire growth and treatment. It allowed us to increase the efficiency of substrate production. The experimental results and software give rather full information on features of real sapphire crystal substrate structure and can be effectively used for optimization of the substrate preparation technology for electronic devices.

References

1. K.T. Vilke, *Crystals Growth* (Nedra, Leningrad, 1977). (in Russian)
2. Yu. M. Tairov, V. F. Tsvetkov, *Technology of Semiconductor and Dielectric Materials*. Lan, St. Petersburg (2002) (in Russian)
3. R. Lodiz, R. Parker, *The Growth of Single Crystals* (Englewood Cliffs, New Jersey, 1970)
4. G. Bakly, *Crystals Growth* (Publishing of Foreign Affairs, Moscow, 1954). (in Russian)

5. V.D. Kyznetsov, *Crystals and Crystallization* (Gosgeoltechizdat, Moscow, 1954). (in Russian)
6. E.R. Dobrovinskaya, L.A. Litvinov, V.V. Pishchik, *Corundum Crystals* (Naukova Dumka, Kiev, 1994). (in Russian)
7. E.R. Dobrovinskaya, L.A. Litvinov, V.V. Pishchik, *Sapphire & Other Corundum Crystals* (Institute for Single Crystals Press, Kharkov, 2002). (in Russian)
8. S.P. Malyukov, S.N. Nelina, V.A. Stefanovich, *Physicotechnological Aspects of Sapphire Production* (Lap Lambert Academic Publishing, Germany, 2012)
9. V.P. Monastirsky, A.V. Logunov, J. Phys. Chem. Mater. Process. **4**, 60 (1984)
10. V.V. Pishchik, B.I. Birman, J. Monocrystals Technics **5**, 26 (1971)
11. A.V. Lykov, *Heat Conductivity Theory* (Higher School, Moscow, 1967). (in Russian)
12. S.P. Malyukov, V.A. Stefanovich, D.I. Cherednichenko, J. Semiconductors **42**, 1508 (2008)
13. S. Patankar, *Numerical Solution of Heat Conduction and Convection Heat Transfer in the Flow in the Channels* (MEI, Moscow, 2003). (in Russian)
14. D.I. Cherednichenko, S.P. Malyukov, Yu.V. Klunnikova, *Sapphire: Structure, Technology and Applications (chapter in book)* (Nova Science Publishers, New York, 2013)
15. S.P. Malyukov, Yu.V. Klunnikova, *Optimization of Sapphire Production for Electronic Equipment* (Lap Lambert Academic Publishing, Germany, 2012)
16. I. M. Pershin, *Analysis and Synthesis of Systems with Distributed Parameters*. Pyatigorsk, (2007) (in Russian)
17. S.P. Malyukov, Yu.V. Klunnikova, J. Prog. Prod. Syst. **2**, 240 (2013)
18. O.I. Bochkin, V.A. Bruck, S.N. Nickiphorova-Denisova, *Semiconductor Materials Mechanical Processing* (High School, Moscow, 1977). (in Russian)
19. A.N. Reznikova, *Abrasive and Diamond Material Processing* (Engineering, Moscow, 1977). (in Russian)
20. V.I. Karban, YuI Borzakov, *Crystals Treatment in Microelectronics* (Radio and Connection, Moscow, 1988). (in Russian)
21. N.A. Kuznetsov, V.V. Kulba, S.S. Kovalevskii, S.A. Kosyachenko, *Methods of Analysis and Synthesis of Modular Information Management Systems* (Physmathlit, Moscow, 2002). (in Russian)

Chapter 7
Multi-Objective Optimization of Distributed RTM (Resin Transfer Molding) Process for Curing the Large Composite Structures with Varied Thickness

S. N. Shevtsov, M. B. Flek, J.-K. Wu, I. V. Zhilyaev and J.-P. Huang

At the producing of high loaded composite structures by the autoclave or closed mould processes a curing schedule includes a pre-warming to the resin viscosity reaches a minimum, further applying of pressure, and finally consolidation of resin at elevated temperature to its full polymerization. To ensure the uniformly state of the composites across the thick-walled products, we propose a mathematical model for curing an epoxy-based composite structure with varied thickness. The PDE system linking a kinetic equation with heat transfer equation which takes into account an exothermic heat, a phase transition of resin from liquid to gel and further to the solid state, well describes the cure process which is controlled by independent heat sources. To synthesize the multi-objective optimal control law, we perform the transient analysis of the developed model using the Pareto points in the 8-dimensional space of design variables.

7.1 Introduction

Closed mould processes are widely used in the composites and aircraft industry for the fabrication and manufacturing of three-dimensional high loaded components. This process begins by the placing of a pre-weighted amount of premixed compound

S. N. Shevtsov (✉) · I. V. Zhilyaev
South Center of Russian Academy of Science, Rostov-on-Don, Russia
e-mail: aeroengdstu@list.ru

M. B. Flek
Rostvertol Helicopters, Rostov-on-Don, Russia

J.-K. Wu
National Kaohsiung Marine University, Kaohsiung, Republic of China (Taiwan)
e-mail: kirkwu@webmail.nkmu.edu.tw

J.-P. Huang
Formoza Plastics Co, Taipei, Republic of China (Taiwan)

in a heated mould. As the mould closed and heated, the resin matrix material flows and fills the mould cavity and the fine crevasses between the fibers in a composite part. The application of pressure and elevated temperature causes the prepreg material to make the desired shape, defined by geometry of the mould. Simultaneously with the flow stage, curing takes place and it continues while pressure is applied when the mould is in a closed position. At the first stage of curing the resin viscosity reaches a minimum, caused by outside heat and the heat of reaction of the functional groups, and then increases rapidly due to molecular chain extension. The next step in the reaction is gelation—when the chains start to cross-link, the resin no longer flows and most individual reaction rates decrease markedly. The third step at high cross-linking is vitrification, at which point-chain motion stops [1–3]. On the last step the molded product is cooled down and ejected from the mould.

The dies of the mould, generally made of tool steel, are heated by the set of electric elements, and their temperature is monitored and controlled by the automatic control loop [4]. Heat-up rates, cool-down rates, and applied pressure are controlled together to ensure even curing throughout the part and to reduce the possibility of residual stresses causing structural deficiencies or distortions. The need for complex heating/pressure cycles is necessary to accommodate the requirements of the chemical reactions and to ensure that the resin viscosity is optimum when pressure is increased. So, because the viscosity of the resin falls with increasing temperature until the resin begins to chemically cross-link (gel), it is important that pressure is applied before gelation occurs to allow removal of entrapped gases and excess resin. This would avoid the severe porosity due to solvents and moisture liberation, and also resin-rich areas [1].

In an industrial process, it is economically advantageous to minimize the cure time by increasing the cure temperature and providing a faster cross-linking reaction. But this can lead to significant loss of the composite product quality, which appears in the forms of large shape distortions and delaminations. In general, residual stresses and shape distortions will increase with increased cure temperature [2]. Moreover, at some conditions, in the thick-walled epoxy based composite pieces that are at high cure temperature, the cracks in the resin can be observed due to cure shrinkage [2, 3]. To avoid this problem, instead of using a single step cure schedule, in the some cases gelled the resin at low temperature and slowly increased the temperature by a linear ramp up to its maximal value [2, 3, 5–7]. The temperature–time law usually incorporates the dwell sections (isothermal hold) to prolong the time for consolidation and volatile removal. This hold also pre-reacts the resin and reduces the danger of intensive exothermic reactions that can occur in thick laminates, and also allow the temperature to become more uniform; this is very important in components with large variations in thickness.

In this article we consider the problem of optimizing the cure cycle on an example of a composite spar of the helicopter rotor blade. The manufacturing technology of fiberglass reinforcement with epoxy resin matrix composite spar includes the winding of a pre-impregnated unidirectional glass-fiber tape on a steel mandrel; polymerization of a prepreg in a mould within several hours. After complete cure,

the mould is slowly cooled and opened, and the component released and removed from a mandrel.

The complexity of the spar quality assuring is due to liberation of considerable exothermal heat [8], large variations in the wall thickness near root and main long part of the spar, and inability monitoring of temperature in the body spar inside the mould. The presented model of the epoxy based composites curing processes incorporates the kinetics of the thermoset resin reactions, changing its phase state, thermal capacitance during cure, heat transfer in the whole technological system and multi-input control of the heaters. On the basis of this model we formulate and solve the problem of optimal temperature schedule using the Pareto frontier approach. The main advantage of Pareto approach as compared with genetic algorithm, direct search and other methods that minimize one objective which incorporate two or more functions of quality is a possibility to independently consider an influence of several design variables on each quality criterion. We parameterize the time dependencies of the external heat inflow by the eight parameters (design variables), and we use two objectives—averaged along and across the cured piece degree of cure, and its standard deviation. The optimization problem has been formulated and solved in MATLAB—Comsol Multiphysics environment where simulated in Comsol thermal/kinetics finite element model of cure is called from MATLAB by an optimization algorithm. The proposed approach largely eliminates the effect of "unobservability" of high-strength composites technology, improves process control system, and, thereby, provides improved quality and reliability of composite structures.

7.2 The Kinetics Model of Epoxy Based Resin Cure

The temperature schedule of a thermoset resin is determined by a triple diagram "temperature–time–state", which links the resin state during cure (liquid–gel–glass) with temperature and time of chemical reactions. Change the phase state of resin, which occurs in the form of an initial liquefaction and reducing the viscosity of the liquid transition to the gel-like state (gelation), and the subsequent transition to the solid state. It is important that, unlike crystalline materials, all epoxy based polymers change its state at certain temperature range, and location of this range can be different at variation of thermal—temporal schedule for the same resin material. Therefore, accepted in the scientific literature and used herein the terms "gel transition", "glass transition" refers to a range of temperatures rather than to a strictly fixed temperature, as is the case in crystalline solids. Another feature of the thermoset cure reaction is the discharge of the exothermal heat, and the maximum of the exothermic heat can occur at single (one-step reaction) or more (two-stage reaction) temperatures.

We use the definition of degree of cure (i.e. conversion) as an amount of evolved heat during the exothermic reaction $\alpha \equiv Q(t)/Q_0;\quad \alpha \in [0;1]$, where $Q(t),\quad Q_0$ are an actual and the total heat during the polymerization of unit mass, respectively

Fig. 7.1 Kinetic curves
calculated from (7.1) for
different heating rates
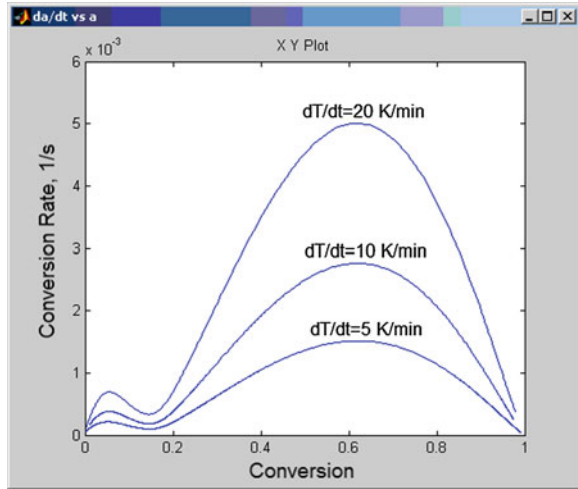
[9, 10]. The dependence of conversion rate on conversion is given by the kinetic
equation. The first description of the cure process given by the kinetic equation is
applied by Kamal [9] for epoxy resin and used with some extensions in many
works, e.g. [12–15]. This generalized kinetic model, which is presented in [3], has
9 constants, allowing a good flexibility for description of cure kinetics. For some
kinds of thermoset plastics, different forms of kinetic equations have been pro-
posed and derived using Differential Scanning Calorimetry (DSC) (see e.g. [16]).

Using DSC the authors of presented work established that studied epoxy resins
have two-modal kinetic dependencies $d\alpha(\alpha, T)/dt$ (see Fig. 7.1), and new kinetic
model and empirical dependence for heat capacity $C_r(\alpha)$ have been proposed [17] as

$$\frac{d\alpha}{dt} = \left[A_1 \cdot \exp\left(\frac{-E_1}{RT}\right) \cdot e^{-\frac{\alpha}{\alpha_t}} + A_2 \cdot \exp\left(\frac{-E_2}{RT}\right) \cdot \alpha^m\right] \cdot (1 - \alpha)^n; \qquad (7.1)$$

$$C_r(\alpha) = \left[C_f - \left(C_f - 1.15C_s\right) \cdot H(\alpha - \alpha_t, \delta\alpha)\right] \cdot (0.8 + 0.2e^{-\alpha}), \qquad (7.2)$$

where A_1, A_2, E_1, E_2 are the kinetic model parameters defined by smoothing the
kinetic curve; C_f and C_s are the specific heats of uncured (liquid) and fully poly-
merized (solid) resin respectively; conversion α_t corresponds to the jump of heat
capacity at the phase transition; and the width of the jump in the smoothed Heaviside
function H for the studied resin have been defined by the empirical relationships:

$$\alpha_t = 0.05 + 0.45 \tanh^2(T_t/12); \qquad (7.3)$$

$$\delta\alpha = 0.1 + 0.4[1 - \exp(T_t/15)]. \qquad (7.4)$$

Equation (7.2) describes the jump of the heat capacity at the phase transition,
and "broadening" of this jump with increasing heating rate. Relation similar to
(7.2) is used for the value of resin thermal conductivity. To do this, simply replace
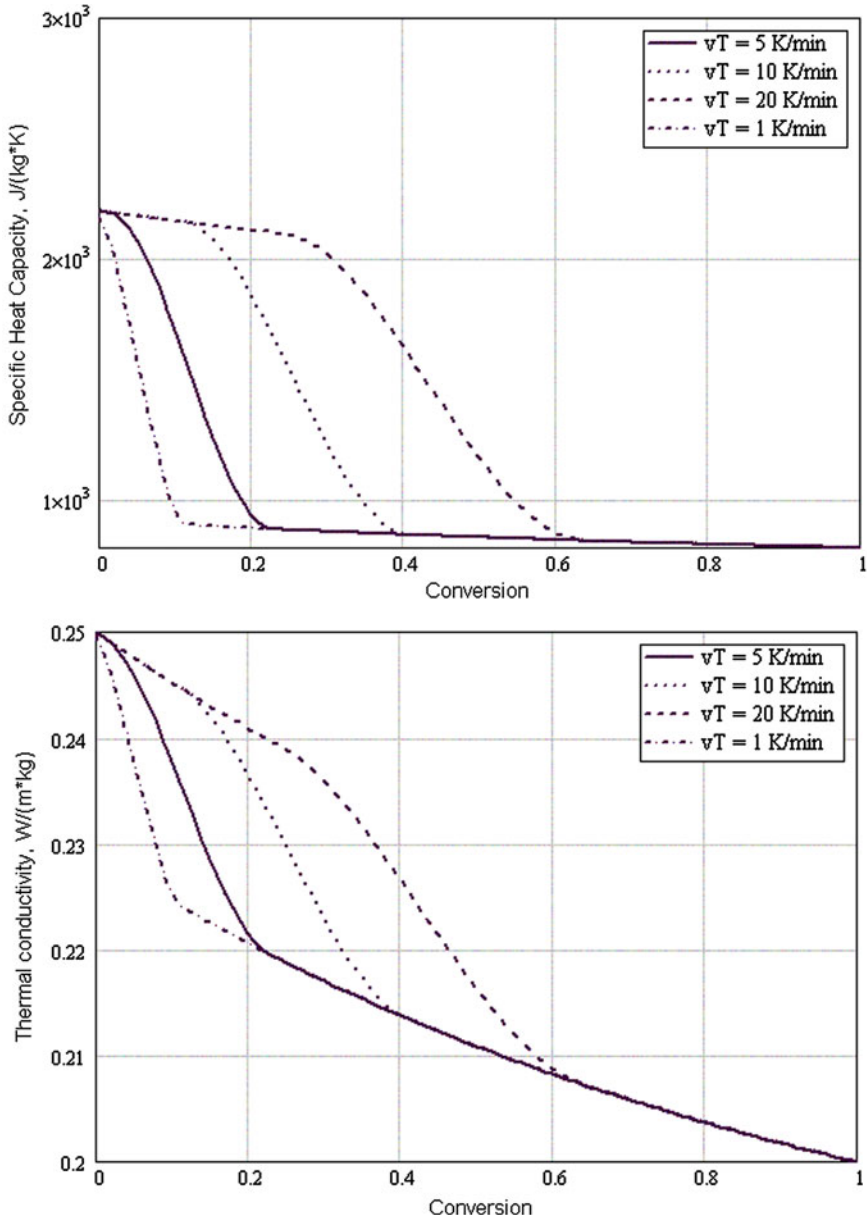
Fig. 7.2 Dependencies of specific heat (*top*) and thermal conductivity (*bottom*) on the conversion at different heating rate

$k_r \rightarrow C_r$; $k_f \rightarrow C_f$; $k_s \rightarrow C_s$. The empirical dependencies of the specific heat and thermal conductivity on the degree of cure for investigated epoxy resin calculated according to (7.3) are shown in Fig. 7.2.

7.3 Equations for Coupled Cure Kinetics and Heat Transfer in Epoxy Composite

Due to difficulties of in situ curing process monitoring described in detail in [6, 7], significant efforts of experts are aimed to the development of model based control methods, and necessary part of these methods is a model of controlled curing system [6–8, 11]. Known approaches (e.g. [8, 10]) to the derivation and further to the analytical solving of the distributed resin transfer molding problem encountered significant mathematical difficulties. More efficient finite element (FEM) approaches were used in [3, 18, 19] for solving problems related to the coupled thermo-kinetic processes at composites curing. This approach was also used in our earlier paper [17].

The prototype for the problem formulation is the curing of composite spar for helicopter tail rotor blades in the mould, which has described above. Consideration of the finished product cooling and formation of the residual thermal stress is beyond the scope of the presented work, and not discussed below. Coupled heat transfer—thermal kinetics problem is formulated for an arbitrary subdomain of a composite body placed inside a heated mould and exchanges heat with the steel mandrel. The problem statement for the cured composite body is presented by the following constitutive equations and governing expressions:

(i) the heat transfer equation

$$\rho_c C_c \partial T/\partial t + \nabla(-k_c \nabla T) = Q_{exo}; \tag{7.5}$$

(ii) the kinetics (7.1) for conversion $\alpha(\mathbf{r}, T, t)$ which is a function of space coordinates, temperature, and time;

(iii) density of composite material

$$\rho_c = \rho_{fb} v_{fb} + \rho_r (1 - v_{fb}); \tag{7.6}$$

(iv) the heat transfer coefficient of filled composite [8, 9, 15]

$$k_c = k_r \cdot \frac{(1 + v_{fb}) \cdot k_{fb} + (1 - v_{fb}) \cdot k_r}{(1 - v_{fb}) \cdot k_{fb} + (1 + v_{fb}) \cdot k_r}, \tag{7.7}$$

where actual value of the resin matrix heat transfer coefficient k_r is defined by a function of conversion

$$k_r = \left[k_f - (k_f - 1.145 k_s) \cdot H(\alpha - \alpha_t, \delta\alpha) \right] \cdot (0.8 + .02 e^{-\alpha}), \tag{7.8}$$

(v) the specific thermal capacity of composite

$$C_c = C_{fb} v_{fb} + C_r (1 - v_{fb}), \tag{7.9}$$
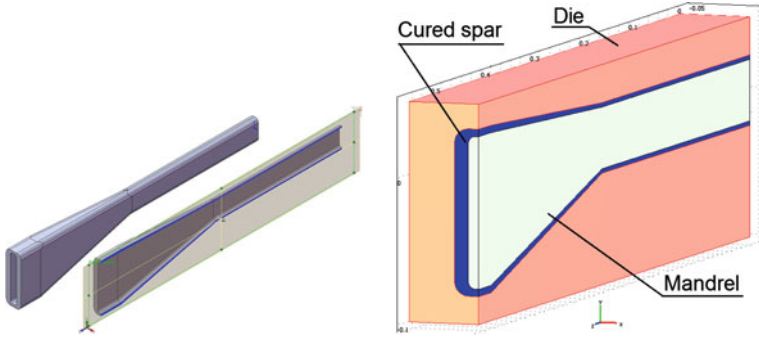
where C_r is defined by (7.3–7.5);

Fig. 7.3 CAD model of cured spar (*left*) and FEM model of the whole curing system (*right*)

(vi) an intensity of the internal heat sources

$$Q_{exo} = Q_{tot}(\partial T/\partial t) \cdot (\partial \alpha/\partial t). \tag{7.10}$$

In the above equations indices indicate the followings: c is the composite material, *fb* relates to the reinforcing fibers, and the index r relates to the resin matrix.

Equations (7.1–7.4) and (7.6–7.10) are active in the spar body only, and heat transfer (7.5) with appropriate coefficients is active everywhere. All boundary conditions depend on the cured piece and mould geometry (see Fig. 7.3) and also on the scheme of controlled heating. On the end surfaces the insulation boundary conditions have the form:

$$-\mathbf{n} \cdot (-k\nabla T) = 0; \quad -\mathbf{n} \cdot (-\nabla \alpha) = 0, \tag{7.11}$$

at the interfaces between metal and cured composite are used the continuity boundary conditions:

$$-\mathbf{n}_s \cdot (-k_c \nabla T) - \mathbf{n}_m \cdot (-k_m \nabla T) = 0, \tag{7.12}$$

where lower indices indicate the followings: s is the composite spar, m is the metallic bold and mandrel, and $\mathbf{n}$ is the unit normal vector to the boundary.

Because cross-section of the spar sufficiently changes along its span, the mould is heated by the set of independently controlled electric heaters to ensure the homogeneity of the thermal-kinetic state of the cured composite material, as far as possible. In the presented case, we consider the transition area of the spar where the thickness varies by about 4 times. Synthesis of proper control law for heaters is the most difficult here. Two heated areas on the external boundary are presented in Fig. 7.4, and adopted boundary conditions for generated heat flux are

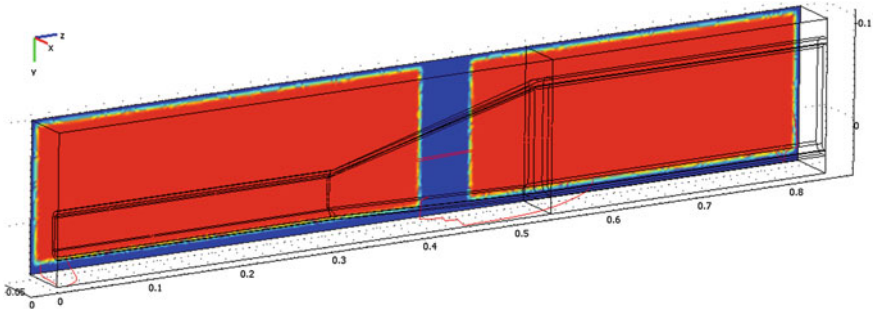$$-\mathbf{n} \cdot (-k\nabla T) = q(y, z, t), \tag{7.13}$$

Fig. 7.4 Spatial distribution of the heated area on the external boundary of the mould (heated areas painted by *red*)

where spatial distribution of incoming heat flux match to the red areas shown in Fig. 7.4.

For all other boundaries, we assumed the infrared radiation boundary conditions according to the Stefan–Boltzmann law:

$$-\mathbf{n} \cdot (-k\nabla T) = \varepsilon\sigma\left(T_{amb}^4 - T^4\right), \tag{7.14}$$

where T_{amb} is ambient temperature, σ is the Stefan–Boltzmann constant, and ε is the surface emissivity taken to be equal 0.5.

To create a complete FEM model, we used geometry of previously created CAD model of the mould assembled with the cured composite products and the mandrel. Due to almost symmetrical cross sections of the cured spar, it is appropriate to consider only half of structure. Conversion from *.x_t CAD format to the FEM format were performed by Comsol Multiphysics built-in converter. The built FEM model was formulated by two coupled working modes—Heat Transfer and Partial Differential Equation (PDE) where the kinetics equation (7.1) were formulated in standard PDE form. The ready model can be simulated for performing of static and transient analyses in a real time.

7.4 Optimization of Distributed Thermal Control

In order to ensure the uniform distribution of conversion inside the cured composite piece immediately before applying of compressive pressure as well as at the end of full curing cycle, both electric heaters should be controlled by its own law. In order to stabilize the process in these moments, the spatial distribution of the temperature and degree of cure must form the dwell sections on temperature–time dependence (see Sect. 7.1). Such two stages of isothermal holds can be performed by using the appropriate temporal dependence of the heaters performance (7.13). To incorporate the built FEM model into the control optimization problem, it is

Fig. 7.5 Two examples of time-dependence for the heaters performance
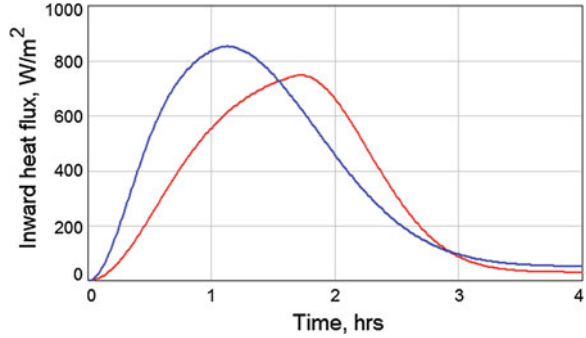
important to choose a good parameterization of the problem. Namely, the dependencies which determine the heaters performance should have the minimal number of parameters, and objective functions (which to be determined) should be enough sensitive to the variations of these parameters. It has been established that good parameterizations for the one step heating (to the gelation or full curing states) is the following (see Fig. 7.5):

$$Q(t) = \begin{cases} Q_1(t) = Q_1^0 \cdot \tanh^2(t/\tau_1) & \text{at} \quad t \le 2\tau_1; \\ Q_1(t) - Q_2^0 \cdot \left[1 - e^{-[(t-2\tau_1)/\tau_2]^2} \right] & \text{at} \quad t > 2\tau_1; \end{cases} \tag{7.15}$$

where Q_1^0, Q_2^0 are the parameters determining the peak and stable values of the generated heat flux, and τ_1, τ_2 are the time constants. According such a law, the heat flux gradually increases and reaches its maximum value, then decreases and moves to the stationary value, which depends only on the heat energy radiated from the mould surfaces. The state of the controlled plant (cured spar) can be identified using only data of indirect measurements of the temperature on the surface of the mold, and our FEM model allows us to predict a future plant response to the acting control signal at open loop conditions. The feedback formed from the indirect temperature measurements can compensate relatively small perturbations. Therefore, an optimization algorithm should find the parameters of controlled input (7.15) that optimize future plant performance, i.e., desired distribution of conversion and its standard deviation inside the spar.

Obviously, such optimization can be implemented independently for the stage of gelation and applying pressure and further for the stage of fully polymerized solid state starting from the optimal state that has been founded in the previous step. Below we present the developed approach on example of most important first stage of gelation state. For the considered case of two electric heat sources there are 8 parameters (or equivalently, design variables) $\{Q\}_{i=1,..4}$ and $\{\tau\}_{i=1,..4}$, which fully determine the control input signals. In our previous work [19], we constructed the target functional in a form of weighted sum:

$$J = w_1 \cdot \langle \alpha - \bar{\alpha} \rangle + w_2 \cdot \langle \Delta\alpha \rangle + w_3 \cdot \langle \Delta T \rangle, \tag{7.16}$$

where

$$\langle \alpha - \bar{\alpha} \rangle \equiv \sqrt{\int\limits_{\Omega} (\alpha - \bar{\alpha})^2 d\omega \Big/ V}; \qquad (7.17)$$

$$\langle \Delta \alpha \rangle \equiv \sqrt{\int\limits_{\Omega} \left[\alpha - \sqrt{\langle \alpha - \bar{\alpha} \rangle} \right]^2 d\omega \Big/ V}; \qquad (7.18)$$

$$\langle \Delta T \rangle \equiv \sqrt{\int\limits_{\Omega} [T - \langle T \rangle]^2 d\omega \Big/ V}; \qquad (7.19)$$

$$\langle T \rangle \equiv \int\limits_{\Omega} T d\omega \Big/ V, \qquad (7.20)$$

$\bar{\alpha}$ is the desired degree of cure at the end of monitored curing stage, and all integrations spread over the composite body which volume is V. Due to a large number of varied parameters, an optimization process has been implemented using live-link of Genetic Algorithm Toolbox MATLAB and Comsol Multiphysics, which performed transient analysis of the FEM model, spreading the simulation time T_F on the given fixed interval that depended on the temperature inertia (i.e., mass and thermal capacitance) of the mould. However, such approach does not allow one to recognize a sensitivity of each component of objective to the variation of design variables. In the considered case, the desired value of averaged conversion $\bar{\alpha}$ is reached easily, while providing variation $\langle \Delta \alpha \rangle$ within a restricted interval encounters difficulties. We use here the Pareto approach, supposing assignment a set of choices for all components of objective that are Pareto-efficient. By restricting attention to the set of choices that are Pareto-efficient, we can make trade-offs within this set, rather than considering the full range of every parameter. We have a designed space with 8 real parameters, and for each designed space point there used 2 different quality criteria $\langle \alpha - \bar{\alpha} \rangle$ and $\langle \Delta \alpha \rangle$. The function $f : \Re^n \to \Re^2$ which assigns to each designed space point $\mathbf{x}$ a criteria space point $f(\mathbf{x})$. So, let $\mathbf{X}$ be a set of feasible designs in $\Re^8$, then the set which represents the feasible criterion points is $f(\mathbf{X})$, and the image of the set $\mathbf{X}$ under the action of f is $\mathbf{Y}$. The Pareto set was constructed as a subset of $\mathbf{Y}$ of the feasible criterion points.

Due to large dimension of the design space $\Re^8$, the number of simulated design variants can be very big, and will require significant computation time. To reduce it, we constructed only half of the mould geometry and performed calculation consistently narrowing the range of the design variables and approaching the area of acceptable values. The subset $\mathbf{Y}$ of the feasible criterion points were assumed as rectangle

Fig. 7.6 Scatter plot for
points of the feasible criteria
subset
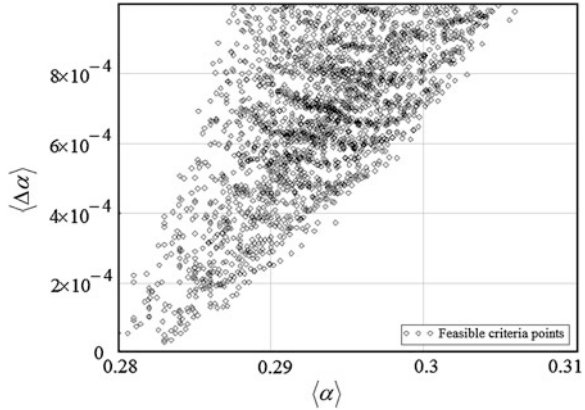
$$\mathbf{Y} = \{\ \langle\alpha\rangle \in [0.28;\ 0.31];\quad \langle\Delta\alpha\rangle \leq 0.001\ \},\qquad\qquad (7.21)$$

where constraint on $\langle\Delta\alpha\rangle$, calculated by integration over the composite body, corresponds to the maximum dispersion of α equal to 0.005. The maximum performance of both heaters is bounded by its real magnitude.

To reconstruct topology of the Pareto set, the number numerical experiments at the curing time $T_F = 3$ h has been performed. The structure of subset of the feasible criteria points is presented in Fig. 7.6.

Some reconstructed projections of set of the criteria points on the subspaces of design variables are presented in Fig. 7.7. All presented plots were calculated at the values of $\langle\alpha\rangle$, that satisfy (7.21), i.e. these values belong to the Pareto set or to the Pareto frontier. To improve a visibility of plots, all calculated values $\langle\Delta\alpha\rangle$ have been transformed according to the rule:

$$\overline{\langle\Delta\alpha\rangle} = \begin{cases} -\log(\langle\Delta\alpha\rangle), & \text{if } \langle\Delta\alpha\rangle > 0; \\ 0, & \text{otherwise}. \end{cases}$$

So, contour lines on level '3' depict projections of the boundaries of Pareto feasible set on the designed subspaces of $\Re^8$, which are projections of Pareto frontier.

Legends of the coordinate axes in Fig. 7.7 correspond to the parameters in (7.15). The parameters $\{Q\}_{i=1,2}$ depicted as Q1_w, Q1_n, Q2_w, and Q2_n, where indices '1' and '2' correspond to the stages of growing heat flow and reducing heat flow, respectively. Here and below index 'w' relates to the heater installed against thick-walled part of the spar, whereas index 'n' corresponds to the heater that heats the thin-walled part. Time constants $\{\tau\}_{i=1,2}$ were expressed in terms of accepted unit of time equal to $T_F/18$, and the coefficients kτ1_w, kτ1_n, kτ2_w, and kτ2_n, so that, for instance

$$\tau_1^w = k\tau1\_w \cdot T_F/18.$$
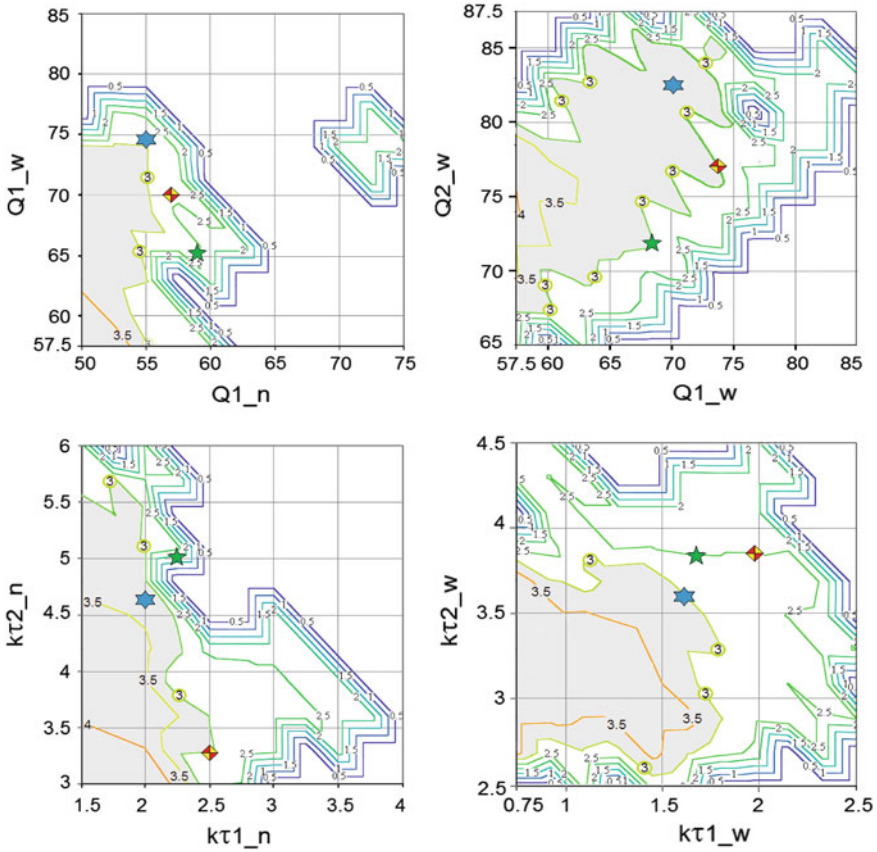
Fig. 7.7 Projections of the criterion $\overline{\langle \Delta\alpha \rangle}$ points set on the subspaces of design variables. *Gray areas represent the projections of subset of the feasible criterion points*

7.5 Results and Discussion

First analysis of results presented in Fig. 7.7 shows that maximum heat flow for thick-walled part should be more intensive at relatively slow rate of heating. To ensure the dwell section on the temperature schedule, the rate of decreasing heat flow for the thin walled section must be reduced. This choice allows one to eliminate an undercooling of thin part. The locations of the level lines corresponding to the best values of the criterion $\overline{\langle \Delta\alpha \rangle}$ on two lower plots suggest the feasibility of the slower process may be contrary to the requirements of the fastest technology. It is obvious, for the shorter cycle T_F the Pareto set will be less than presented here.

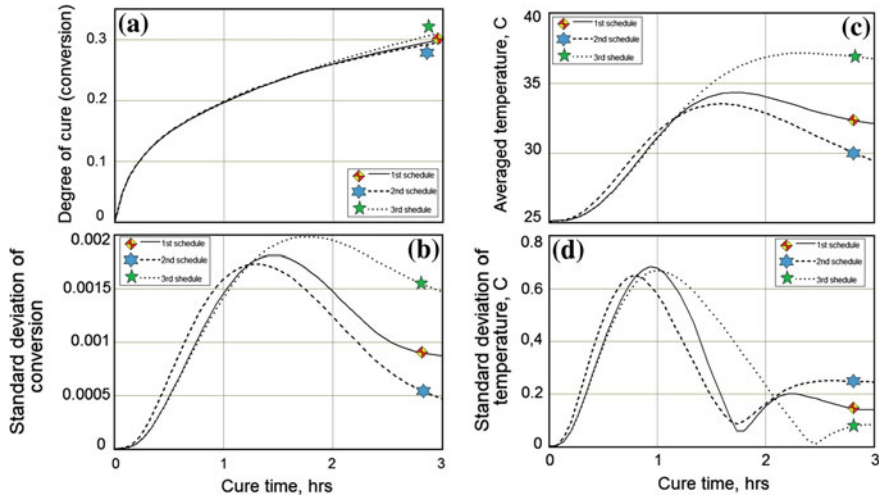**Fig. 7.8** Time dependencies of the process parameters averaged over the cured composite piece: degree of cure (**a**), its standard deviation (**b**), temperature (**c**), and temperature's standard deviation (**d**) for three different curing schedules

To quantitatively estimate the obtained optimization results, we have simulated our cure system at three different schedules with the values of parameters suggested by Pareto analysis and depicted in Fig. 7.7 by the own markers. These simulation results are presented in Figs. 7.8 and 7.9, where dependencies for the first schedule are drawn by solid lines and marked by a diamond, for the second schedule—by dashed lines with a hexagram marker, and for the third schedule— by dotted lines with a pentagram marker. In Fig. 7.9 the bold lines relate to the heaters installed against thick walled (root) part of a spar, whereas the fine lines depict the dependencies of an inward heat flow generated by the heaters installed against the thin walled (tip) parts.

All three schedules provide a required value of conversion after three hours of curing, but standard deviation of conversion for the third schedule (pentagram marker) exceeds a predetermined value of 0.001. The parameters of heating laws (see 7.15) for this schedule are outside the Pareto set.

The second schedule (marked by a hexagram) provides the best uniformity of a conversion distribution, but this uniformity is achieved by cooling the outer walls of the mold (see Fig. 7.9). Such a solution encounters the difficulties and may not be appropriate due to technical conditions of manufacturing. However, the required value of $\overline{\langle \Delta \alpha \rangle}$ criterion is achieved after 2.1 h, although the minimum conversion level 0.28 is not reached. This suggests the possibility of modifying the schedule parameters for faster achieving the desired state of the composite.

Fig. 7.9 Time dependencies of the heaters performance for three different curing schedules
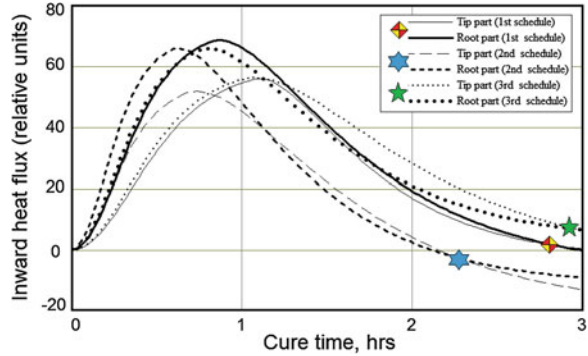
The most suitable schedule for the 3 h process duration is the first, whose parameters are located near Pareto frontier. It is quite obvious that many appropriate schedules constructed in a Pareto set area can be applicable taking into account various kinds of constraints (technological, economical, etc.).

So, Pareto optimization approach has demonstrated a good flexibility satisfying the optimization criteria together with other constraints. Evidently a similar analysis is necessary for a new developed technology and at any changes of components and desirable curing schedule.

7.6 Conclusions

The model of spatially distributed curing process of epoxy matrix polymeric composite was developed and implemented using FEM. The model implementation allowed one to identify the factors determining the homogeneity of resin matrix conversion and temperature inside the cross-section of products, which affected on the material elastic and long-life mechanical properties. To avoid formation of defects such as the internal peel and cavities due to overgrowth heating rate, a problem of optimal heating control was formulated and solved using proposed parameterization of heater's temporal performance, the developed FEM model, and Pareto optimization approach. To synthesize the multi-objective optimal control law, we performed the transient analysis of the developed model using the projections of Pareto points set on the 8-dimensional space of design variables. Effectiveness and eventual way to use in practice of the proposed method was illustrated on example of optimal control synthesis for the closed mould curing of composite spar, where the mould heated by two independently controlled heaters.

References

1. G. Akovali, *Handbook of Composite Fabrication* (RAPRA Technology LTD., Shawbury, 2002)
2. A. Baker, S. Dutton, D. Kelly, *Composite Materials for Aircraft Structures*, 2nd edn. (AIAA, Reston, 2004)
3. A. Koorevaar, in *Proceedings of ISCM 2002 Conference*, Vollenhove, Nedherland (2002)
4. R. Franke, J. Doppelhamer, *Lecture Notes in Control and Information Sciences*, vol. 358 (Springer, Berlin, 2007)
5. J. Rocks, M. Halter, G. George, F. Vohwinkel, in *Proceedings of the Applied Polymeric Technology Conference*, Brisbane, Australia (2003)
6. C. Garschke, C. Weimer, P.P. Parlevliet, B.L. Fox, Compos. Part A Appl. Sci. Manufact. **43**(6), 935 (2012)
7. R. Hardis, J.L.P. Jessop, F.E. Peters, M.R. Kessler, Compos. Part A Appl. Sci. Manufact. **49**, 100 (2013)
8. C. Heinrich, M. Aldridge, A.S. Wineman et al., Int. J. Eng. Sci. **53**(4), 85 (2012)
9. M.R. Kamal, S. Sourour, Polym Eng. Sci. **13**(1), 59 (1973)
10. R. Aboulaich, S. Boujena, J. Pousin, J. Condens Matter **5**(1), 4 (2004)
11. P.M.J. Hof, C. Scherer, P.S.C. Heuberger, *Model-Based Control: Bridging Rigorous Theory and Advanced Technology* (Springer, Berlin, 2009)
12. C. Garschke, P.P. Parlevliet, C. Weimer, B.L. Fox, Polym. Test **32**(1), 150 (2013)
13. M. Harsch, J. Karger-Kocsis, M. Holst, Eur. Polym J. **43**, 1168 (2007)
14. G. Van Assche, S. Swier, B. Van Mele, Thermochim. Acta **388**(1), 327 (2002)
15. P. Canamero-Martinez, M. Fernandez-Garcia, J.L. de la Fuente, React. Funct. Polym. **70**(10), 761 (2010)
16. M.J. Yoo, S.H. Kim, S.D.Park et al., Eur. Polym. J. **46**(5), 1158 (2010)
17. S. Shevtsov, I. Zhilyaev, A. Soloviev, I. Parinov, V. Dubrov, Adv. Mater. Res. **569**, 185 (2012)
18. R.V.N. Melnik, Model. Simul. Mater. Sci. Eng. **10**, 341 (2002)
19. G. Liang, K. Chandrashekhara, J. Appl. Polym. Sci. **916**, 3513 (2004)

Part II
Physics of Advanced Materials

Chapter 8
Relations Between Domain States and Phase Contents in Perovskite-Type Ferroelectric Solid Solutions

V. Yu. Topolov

We develop and generalise crystallographic concepts on the role of non-180° domain (twin) types in the stress relief and phase coexistence in perovskite-type ferroelectric solid solutions near the morphotropic phase boundary. Elastic matching of ferroelectric phases is analysed to show a role of specific domain types in the forming of the phase content. A correlation between volume fractions of the domain types and the composition of the ferroelectric solid solution is discussed.

8.1 Introduction

Ferroelectric (FE) solid solutions are important objects for basic research of interrelations in the dependency triangle of 'composition–structure–properties' [1–4]. In the last decades the FE solid solutions with the perovskite-type structure have been the most studied FE materials with a complex of important physical properties that are important for various applications [5–7]. The perovskite family of FEs stems from the mineral perovskite $CaTiO_3$, however the most known regular FE single crystals are $BaTiO_3$, $PbTiO_3$ and $KNbO_3$ [5, 9, 10]. The perovskite family covers a vast group of compositions with the general formula ABO_3, where A (or B) may be a cation element or mixture of two or more such elements or vacancies [5, 7–9]. An important feature of FE perovskites and related solid solutions is a nearly unlimited isomorphism of the perovskite structure [1, 5, 7, 9] that promotes a continuous change in the composition and properties at a substitution of different elements at equivalent positions in ABO_3. The isomorphism leads to the formation

V. Yu. Topolov (✉)
Department of Physics, Southern Federal University, 5 Zorge Street, Rostov-on-Don, Russia344090
e-mail: vutopolov@sfedu.ru

V. Yu. Topolov
Scientific Design and Technology Institute "Piezopribor", Southern Federal University, 10 Milchakov Street, Rostov-on-Don, Russia 344090

of a great number of the FE solid solutions with the physical properties, Curie temperatures and other characteristics which can be varied within a wide range [1, 3, 6–8]. Depending on the composition and cationic ordering, the perovskite-type solid solutions may be FE, relaxor-FE, multiferroic or exhibit non-FE competing types of the order.

An important feature of the FE solid solutions with the perovskite-type structure and compositions near the morphotropic phase boundary (MPB) consists in various heterophase states that are observed in specific molar-concentration [4, 7, 10–13], temperature [4, 11–13] and electric-field ranges [4, 14, 15]. The physical properties of many FE solid solutions considerably depend on the heterophase states therein, and FE phases coexisting close to the MPB are sensitive to changes in temperature, mechanical and electric fields [5–8, 10], etc. The heterophase states are caused by jumps in unit-cell parameters [6, 7, 11–15] at a first-order phase transition that may proceed in specific ranges of temperature T, electric field E and/or pressure. A coexistence of the FE phases split into non-180° domains (or twin components) [4–6, 12] and various modes of the unit-cell parameters jumps [11–15] close to the MPB makes the interrelations between the crystal structure and physical properties in the perovskite-type FE solid solutions intricate.

A problem of the stress relief in a heterophase structure [4, 16, 17] is of an academic interest due to the presence of the phases from different symmetry classes, with different domain types, under external fields, and so on. The stress relief in the heterophase structure means decreasing the elastic energy of the system as a whole [4, 16, 17] and plays an important role in the kinetics of structural phase transitions, in the forming of the domain (twin) structures and their rearrangement [10, 18].

Studies on the widespread perovskite-type solid solutions of $Pb(Zr_{1-x}Ti_x)O_3$ (PZT) [4, 12] $(1-x)Pb(Mg_{1/3}Nb_{2/3})O_3-xPbTiO_3$ (PMN$-x$PT) [4, 11, 13], $(1-x)Pb(Zn_{1/3}Nb_{2/3})TiO_3-xPbTiO_3$ (PZN$-x$PT) [4, 19], $(1-x)Pb(Fe_{1/2}Nb_{1/2})O_3-xPbTiO_3$ (PFN$-x$PT) [20, 21], $(1-x)BiFeO_3-xPbTiO_3$ (BF–xPT) [22, 23], etc. show that the heterophase states therein are of particular interest due to the presence of the intermediate FE phases near the MPB. These phases considerably influence the physical properties, phase coexistence and stress relief in the studied solid solutions. Two- and three-phase coexistence variants and conditions for the complete stress relief in the presence of the intermediate phases were studied, for instance, in PMN$-x$PT and PZN$-x$PT [4]. Despite structural distinctions, the intermediate FE phases in PMN$-x$PT and PZN$-x$PT favour an elastic matching of the adjacent phases either at the complete stress relief (i.e., along the so-called *zero-net-strain plane*) [4] or at the significant stress relief.

The present paper is devoted to the crystallographic interpretation of the phase coexistence in the FE solid solutions at the first-order phase transitions. We consider examples of heterophase states near the MPB to show the role of domain types in the elastic matching of the coexisting phases and in the forming of the phase content. These examples are concerned with various modes of ion substitutions in the perovskite-type solid-solution systems.

8.2 Heterophase States and Crystallographic Interpretation

8.2.1 Solid Solutions of $(1-x)Pb(Fe_{1/2}Nb_{1/2})O_3-xPbTiO_3$

The perovskite-type solid solutions of PFN$-x$PT [20, 24–26] are of great interest because of a favourable combination of the components. $Pb(Fe_{1/2}Nb_{1/2})O_3$ exhibits multiferroic and relaxor properties [25], and $PbTiO_3$ is a typical regular ferroelectric [5, 10]. A coexistence of the monoclinic (*Cm* symmetry) and tetragonal (*P4mm* symmetry) phases of the ferroelectric nature is observed near the MPB at $x \approx 0.07-0.08$ and room temperature [24]. The tetragonal phase of PFN$-x$PT near the MPB at room temperature is characterised by the moderate unit-cell distortion (ratio of the perovskite unit-cell parameters $c_t/a_t \approx 1.01$ [24]) in comparison to $PbTiO_3$ with the relatively large distortion of the perovskite unit cell ($c_t/a_t \approx 1.065$ [5–7, 18]).

8.2.1.1 Crystallographic Description of Domain and Heterophase States

It is assumed that the coexisting phases (polydomain phases in a general case) are characterized by distortion matrices $\|M\|$ and $\|N\|$, and these matrices are expressed in terms of distortions of several domain types, their volume fractions and angles of mutual rotation of the crystallographic axes of the adjacent domains [4, 27]. Interfaces between the coexisting phases are represented as second-degree surfaces that obey equation $\sum_{a,b=1}^{3} D_{ab}x_a x_b = 0$ in the rectangular co-ordinate system $(X_1 X_2 X_3)$. These interfaces are classified taking into account signs of invariants

$$I = D_{11} + D_{22} + D_{33}, D = \det\|D_{ab}\| \text{ and}$$
$$J = \begin{vmatrix} D_{11} & D_{12} \\ D_{21} & D_{22} \end{vmatrix} + \begin{vmatrix} D_{22} & D_{23} \\ D_{32} & D_{33} \end{vmatrix} + \begin{vmatrix} D_{33} & D_{31} \\ D_{13} & D_{11} \end{vmatrix}, \tag{8.1}$$

where

$$D_{ab} = \sum_{k=1}^{3} (N_{ak}N_{bk} - M_{ak}M_{bk}), \tag{8.2}$$

$a = 1, 2, 3$, and $b = 1, 2, 3$. The interfaces oriented parallel to the zero-net-strain planes at the complete stress relief obey conditions [4]

$$DI = 0 \text{ and } J < 0, \tag{8.3}$$

where D, I and J are taken from (8.1).

To study examples of the phase coexistence in PFN$-x$PT, we consider a single-crystal sample (ceramic grain) that contains the tetragonal and monoclinic phases separated by planar interfaces (Fig. 8.1) in regions v_1 and v_2. As follows from our analysis of the elastic matching of the phases of PFN$-x$PT with the unit-cell parameters from work [24], the complete stress relief in regions v_1 and v_2 and validity of conditions (8.3) take place even in the presence of the single-domain monoclinic phase. Hereafter in Sect. 8.2.1 we consider the single-domain monoclinic phase with perovskite unit-cell vectors a_m, b_m and c_m which are oriented almost parallel to the co-ordinate axes OX_2, OX_1, and OX_3 (Fig. 8.1), respectively. In the tetragonal phase the perovskite unit-cell vector c_T (that shows the spontaneous polarisation direction) is almost parallel to either OX_3 (90° domains with the volume fraction m) or OX_1 (90° domains with the volume fraction $1-m$). We assume that domain walls separating the adjacent domains are permissible and oriented in accordance with concepts [28]. For example, in the tetragonal phase split into the 90° domains, the domain walls between them are stress-free, non-charged and oriented along the {110} planes of the perovskite unit cell.

Distortion matrices of the monoclinic and tetragonal phases coexisting in PFN$-x$PT are represented in the rectangular co-ordinate system $(X_1X_2X_3)$ as

$$
||M|| = \begin{pmatrix} \eta_b & 0 & 0 \\ 0 & \eta_a & \eta \\ 0 & \eta & \eta_c \end{pmatrix} \quad \text{and}
$$

$$
||N(m)|| = m \begin{pmatrix} \varepsilon_a & 0 & 0 \\ 0 & \varepsilon_a & 0 \\ 0 & 0 & \varepsilon_c \end{pmatrix} \tag{8.4}
$$

$$
+ (1-m) \begin{pmatrix} \cos\varphi_T & 0 & -\sin\varphi_T \\ 0 & 1 & 0 \\ \sin\varphi_T & 0 & \cos\varphi_T \end{pmatrix} \begin{pmatrix} \varepsilon_c & 0 & 0 \\ 0 & \varepsilon_a & 0 \\ 0 & 0 & \varepsilon_a \end{pmatrix},
$$

respectively. In (8.4) η_a, η_b, η_c, and η are unit-cell distortions in the monoclinic phase, ε_a and ε_c are unit-cell distortions in the tetragonal phase, and $\varphi_T = \arccos[2\varepsilon_a\varepsilon_c/(\varepsilon_a^2 + \varepsilon_c^2)]$ is the angle of the rotation of the crystallographic axes of the adjacent 90° domains in the tetragonal phase. The unit-cell distortions from (8.4) are expressed in terms of the unit-cell parameters (see details, e.g., in monograph [4]), and the co-ordinate axes OX_j are parallel to the unit-cell vectors in the cubic ($Pm3m$ symmetry) paraelectric phase. Taking into account conditions (8.3) for the complete stress relief in the heterophase state, we find the optimal volume fractions of the 90° domains. There are two possible solutions, $m = m_{opt,1}$ and $m = m_{opt,2}$, with values of $m_{opt,j}$ that obey condition $0 \leq m_{opt,j} \leq 1$ ($j = 1$ and 2), i.e., between 0 and 100 % for each domain type in the tetragonal phase (see inset in Fig. 8.1).

Validity of conditions (8.3) for the complete stress relief at the elastic matching of regions v_1 and v_2 (Fig. 8.1) is examined by using the distortion matrices $||M^*|| = (1-x_T)||M|| + x_T||T(m_{opt,k})||$ [instead of matrix elements of $||M||$ in (8.2)] and $||N^*|| = (1-n_T)||M|| + n_T||T(m_{opt,k})||$ [instead of elements of $||N||$ in (8.2)].
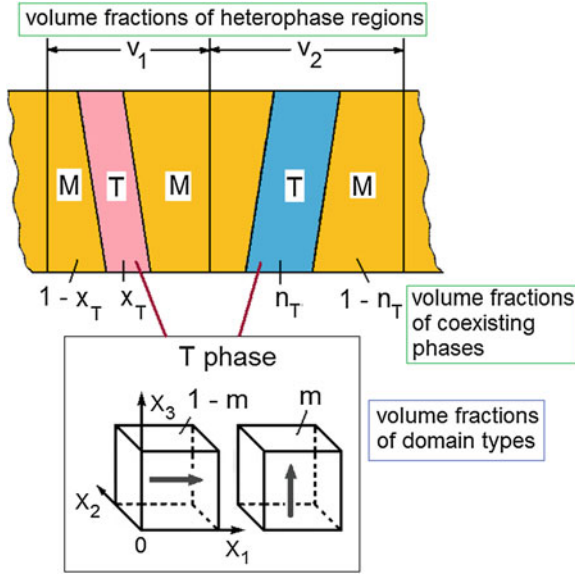
Fig. 8.1 Schematic arrangement of the tetragonal (T) and monoclinic (M) phases. Spontaneous polarization vectors of 90° domains in the tetragonal phase are shown with *arrows* in inset, and m and $1-m$ are volume fractions of these domains. The tetragonal phase is characterized by volume-fraction parameters x_T (region v_1) and n_T (region v_2). Co-ordinate axes OX_j are parallel to the unit-cell vectors in the paraelectric cubic phase (reprinted from paper by Topolov [20], with permission from Elsevier)

This examination enables us to study a link between the volume-fraction parameters x_T and n_T at the complete stress relief in the heterophase state. Assuming that the regions v_1 and v_2 are characterized by equal volume fractions and distributed uniformly in the heterophase sample, we represent the volume fractions of the coexisting phases (Fig. 8.1) as

$$v_{fr,T} = (x_T + n_T)/2 \qquad (8.5)$$

(polydomain tetragonal phase) and

$$v_{fr,M} = 1 - v_{fr,T} \qquad (8.6)$$

(single-domain monoclinic phase).

8.2.1.2 Volume Fraction of the Tetragonal Phase

Based on the experimental unit-cell parameters [24] of PFN−xPT with $0.05 \le x \le 0.08$ at room temperature, we find the optimal volume fractions of the 90° domains ($m_{opt,1}$, lower value and $m_{opt,2}$, upper value) in the tetragonal phase and build the $x_T - n_T$ diagrams for $m = m_{opt,j}$ [20]. For example, at $x = 0.06$ we have
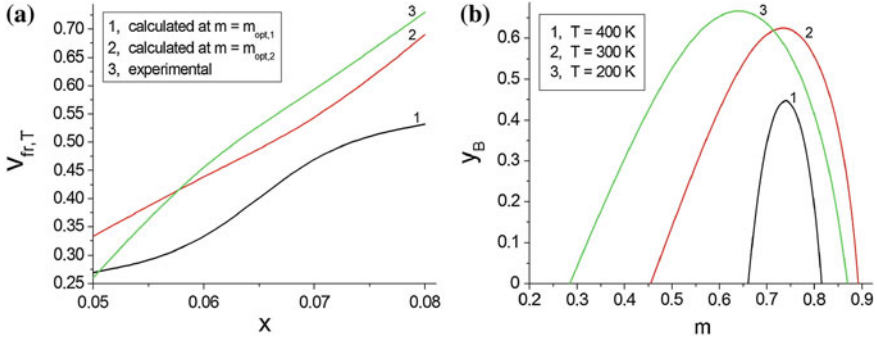
Fig. 8.2 Diagrams that describe heterophase states in PFN–xPT: **a** calculated (curves *1* and *2*) and experimental (curve *3* built using data [24]) volume fractions of the tetragonal phase $v_{fr,T}$ of PFN–xPT in the MPB region at room temperature, and **b** link between the volume fractions m and y_B of the domain types at the tetragonal-monoclinic phase coexistence in PFN–0.08PT. Relations between m and y_B obey conditions (8.3) for the complete stress relief (reprinted from paper by Topolov [21], with permission from Taylor and Francis)

$m_{opt,1} = 0.547$ and $m_{opt,2} = 0.776$. Calculating $v_{fr,T}$ from (8.5) at $m = m_{opt,j}$, we omit cases of $x_T = n_T = 0$ (monoclinic phase everywhere) and $x_T = n_T = 1$ (tetragonal phase everywhere), see Fig. 8.1. A dependence of the volume fraction $v_{fr,T}$ on the molar concentration x is shown in Fig. 8.2a. A difference between the calculated and experimental $v_{fr,T}$ values (Fig. 8.2a) is accounted for by an internal stress field in PFN$-x$PT ceramic grains, by fluctuations of the molar concentration x in the grains, by the presence of additional (not considered above) domain types in the monoclinic phase and by deviations from the complete stress relief in some polydomain regions, at the tetragonal–monoclinic interface, etc. Our results on $v_{fr,T}(x)$ (see curves 1 and 2 in Fig. 8.2a) are consistent with experimental data [24, 25].

8.2.1.3 Phase Coexistence in a Wide Temperature Range

It is assumed that the tetragonal phase in PFN$-x$PT is split into the domains as shown in Fig. 8.1 (inset), and the unit-cell vectors $\boldsymbol{a_m}$, $\boldsymbol{b_m}$ and $\boldsymbol{c_m}$ of the domains in the monoclinic phase are oriented almost parallel to either the co-ordinate axes OX_1, OX_2 and OX_3 (volume fraction y_B) or to OX_2, OX_1 and OX_3 (volume fraction $1-y_B$), respectively. Based on experimental data [29] on PFN-0.08PT and satisfying conditions (8.3), we build the $m-y_B$ diagram for $T = (200-400)$ K (Fig. 8.2b). We remind that m is the volume fraction of the 90° domains with the spontaneous polarization vector parallel to OX_3 (see inset in Fig. 8.1). It should be noted that temperature changes in the unit-cell parameters of PFN-0.08PT [29] favour the complete stress relief at the cubic-tetragonal phase transition (Curie temperature $T_C \approx 425$ K) in the presence of the single-domain tetragonal phase, i.e., at either $m = 0$ or $m = 1$ (Fig. 8.1). However curve 1 related to the phase coexistence in the vicinity of the cubic-tetragonal phase transition is located away from the points

$m = 0$ and 1 (Fig. 8.2b). In general the arrangement of curves 1–3 in Fig. 8.2b can be a reason for a stress field that influences the tetragonal–monoclinic phase coexistence [29] and the stress-accommodation rearrangement of the domain (twin) structure in the wide temperature range. According to experimental data [29], this range covers about 200 K. Thus, the studied elastic matching of the morphotropic FE phases in PFN$-x$PT at the complete stress relief plays the key role in the wide temperature range wherein the phase coexistence is observed.

8.2.2 Solid Solutions of $(1 - x)BiFeO_3 - xPbTiO_3$

8.2.2.1 Heterophase States at a Large Tetragonality

Experimental results [30, 32–37] on the multiferroic solid solutions of BF–xPT near the MPB show that this system is of interest due to various heterophase states. The system of BF–xPT is regarded as an advanced material with a large distortion [30, 37] of the perovskite unit cell in the FE tetragonal phase (often termed T_1) with $P4mm$ symmetry. The tetragonal unit-cell distortion is characterized by the ratio $c_t/a_t = 1.187$ ($x = 0.31$) or $c_t/a_t = 1.170$ ($x = 0.40$) at room temperature. The very large tetragonality ($c_t/a_t = 1.192$) [30] is reached in the stress-induced tetragonal phase at $x = 0.20$. We mention for comparison that at $x = 1$, i.e., in PbTiO$_3$, $c_t/a_t \approx 1.065$ [5–7, 18] at room temperature.

The system of BF–xPT is also of interest due to the coexistence of the FE tetragonal and monoclinic (Cc symmetry) phases [30, 37] near the MPB. The MPB is almost vertical in the (T, x) diagram of BF–xPT and separates regions of thermodynamic stability of the tetragonal and monoclinic phases at $x \approx 0.30$ [37]. Experimental results [30] show that the monoclinic phase at $0.20 \leq x \leq 0.28$ can be partially transformed to the tetragonal phase by the application of a stress field however tetragonal compositions of BF–xPT with $x > 0.29$ remain stable against the external stress. Such behavior enables us to surmise that the role of the 90° domains of the tetragonal T_1 phase in the stress relief would be more active in comparison to the role of the non-180° domains of the adjacent monoclinic phase.

The presence of the FE phases with various domain (twin) structures [33–37] implies possibilities of the stress relief [4, 31] even in the presence of the large tetragonality of the perovskie unit cell. In Sect. 8.2.2 we discuss examples of the phase coexistence at the complete stress relief in BF–xPT.

8.2.2.2 Heterophase States at x = 0.27 and 0.31

Some examples of the coexistence of the T_1 and monoclinic phases in BF–xPT are analyzed taking into account domain types shown in Fig. 8.3. The T_1 phase in the two-phase region (see the left part of Fig. 8.3) is split into the 90° domains with
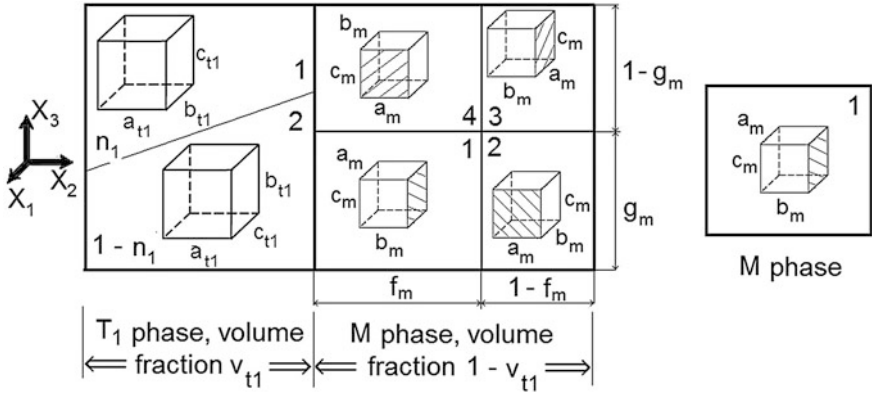
Fig. 8.3 Schematic arrangement of the tetragonal (T_1) and monoclinic (M) phases. a_{t1}, b_{t1}, and c_{t1} are unit-cell parameters in the tetragonal phase, and a_m, b_m, and c_m are unit-cell parameters in the monoclinic phase. n_1 is the volume fraction of domains of the type 1 in the tetragonal phase, and f_m and g_m characterize relative widths of twins in the monoclinic phase. In inset a single-domain region of the monoclinic phase is shown (reprinted from paper by Topolov [31], with permission from the American Institute of Physics)

volume fractions n_1 and $1-n_1$. The monoclinic phase is split into domain types 1–4 with volume fractions m_i written in terms of parameters f_m and g_m [31] as follows:

$$m_1 = f_m g_m, m_2 = (1-f_m)g_m, m_3 = (1-f_m)(1-g_m), \quad \text{and} \quad m_4 = f_m(1-g_m). \quad (8.7)$$

We assume that the volume fraction of the single-domain monoclinic phase (see the right part of Fig. 8.3) is small, i.e., an effect of this region on the ratio $v_{t1}/(1-v_{t1})$ in the heterophase sample is negligible. Distortion matrices of the domain types 1–4 in the monoclinic phase (Fig. 8.3) are written in the co-ordinate system ($X_1X_2X_3$) as

$$\|\mu_1\| = \begin{pmatrix} \eta_a & 0 & \eta \\ 0 & \eta_b & 0 \\ \eta & 0 & \eta_c \end{pmatrix}, \quad \|\mu_2\| = \begin{pmatrix} \eta_b & 0 & 0 \\ 0 & \eta_a & -\eta \\ 0 & -\eta & \eta_c \end{pmatrix},$$

$$\|\mu_3\| = \begin{pmatrix} \eta_a & 0 & -\eta \\ 0 & \eta_b & 0 \\ -\eta & 0 & \eta_c \end{pmatrix}, \quad \text{and} \quad \|\mu_4\| = \begin{pmatrix} \eta_b & 0 & 0 \\ 0 & \eta_a & \eta \\ 0 & \eta & \eta_c \end{pmatrix}, \quad (8.8)$$

and the volume fractions of these domain types are m_1, m_2, m_3, and m_4, respectively [see (8.7)]. In (8.8), η_a, η_b, η_c and η are unit-cell distortions in the monoclinic phase. Distortion matrices of the polydomain T_1 and monoclinic phases are given by

$$\|N_{1-2}\| = n_1 \left\| \tau_1^{(1)} \right\| + (1 - n_1) \left\| R_{1-2}^{(1)} \right\| \cdot \left\| \tau_2^{(1)} \right\| \quad (8.9)$$

and

$$\|M_{1-4}\| = m_1 \|\mu_1\| + m_2 \left\| R_{1-2}^{(m)} \right\| \cdot \|\mu_2\| + m_3 \|\mu_3\| + m_4 \left\| R_{3-4}^{(m)} \right\| \cdot \|\mu_4\|, \quad (8.10)$$

respectively. In (8.9) distortions of the domain types 1 and 2 in the T_1 phase (see

the left part of Fig. 8.3) are characterized by $\left\|\tau_1^{(1)}\right\| = \begin{pmatrix} \varepsilon_a & 0 & 0 \\ 0 & \varepsilon_a & 0 \\ 0 & 0 & \varepsilon_c \end{pmatrix}$

and $\left\|\tau_2^{(1)}\right\| = \begin{pmatrix} \varepsilon_c & 0 & 0 \\ 0 & \varepsilon_a & 0 \\ 0 & 0 & \varepsilon_a \end{pmatrix}$, and volume fractions are n_1 (domain type 1) and

$1-n_1$ (domain type 2). In (8.10), m_i and $\|\mu_i\|$ $(i = 1, 2, 3, \text{ and } 4)$ are taken from (8.7) and (8.8), respectively. $\left\|R_{1-2}^{(1)}\right\|$ from (8.9) and $\left\|R_{1-2}^{(m)}\right\|$ and $\left\|R_{3-4}^{(m)}\right\|$ from (8.10) describe rotations of the crystallographic axes of the adjacent domains [4, 27] in the FE phases. The distortion matrix of the two-phase region shown in the left part of Fig. 8.3 is $\left\|P_{left}\right\| = v_{t1}\left\|P_{1-2}^{(1)}\right\| + (1 - v_{t1})\|M_{1-4}\|$ where $\|N_{1-2}\|$ and $\|M_{1-4}\|$ are taken from (8.9) and (8.10), respectively. Hereafter elements of $\|N_{1-2}\|$ and $\|M_{1-4}\|$ are regarded as N_{ak} and M_{ak}, respectively, and substituted into (8.2). Conditions (8.3) for the complete stress relief are examined for an interface separating the phases coexisting in BF–xPT.

To characterize features of the phase coexistence and stress relief, we use values of the unit-cell parameters measured on annealed samples [30] of BF–0.27PT and BF–0.31PT at room temperature. As follows from our study [31], the domain types 1–4 in the monoclinic phase slightly influence the ratio $n_1/(1-n_1)$ of volume fractions of the domains of types 1–2 in the T_1 phase, and this tendency holds near the MPB. The single-domain monoclinic phase represented by one of the domain types 1–4 (Fig. 8.3) can coexist with the polydomain T_1 phase at the complete stress relief, and any change in the domain type of the monoclinic phase will give rise to minor changes in the volume fraction n_1, and condition $n_1 \approx 0.25-0.29$ holds [31] at various volume fractions of the domains in the monoclinic phase. As seen from Fig. 8.4, the studied phase coexistence in BF–xPT is observed in a relatively narrow n_1 range. In this case the polydomain T_1 phase plays the key role in the stress relief and considerably influences the phase content in the studied system. In our opinion, this role is also important in a case of an external stress field, while the 90° domains in the T_1 phase with the large tetragonality could promote a more effective stress relief and decreasing the width of the molar-concentration range Δx related to the phase coexistence. Domains of types 1–4 in the monoclinic phase (Fig. 8.3) can influence the phase coexistence in BF–xPT to a lesser extent, mainly owing to the shear unit-cell distortion. Taking into account data for $x = 0.31$ and $n_1 = 0.278$ [31], we find two values of the volume fraction of the T_1 phase, $v_{t1} = 0.538$ and $v_{t1} = 0.310$ (see curves 1 and 4 in Fig. 8.4b). We remind that curves 1–4 in Fig. 8.4 obey conditions (8.3) for the complete stress relief in heterophase samples. The average value $v_{fr,T} = (v_{t1} + v_{t2})/2 = 0.434$ is in agreement with experimental results [30] on the phase content at $x \approx 0.30$.
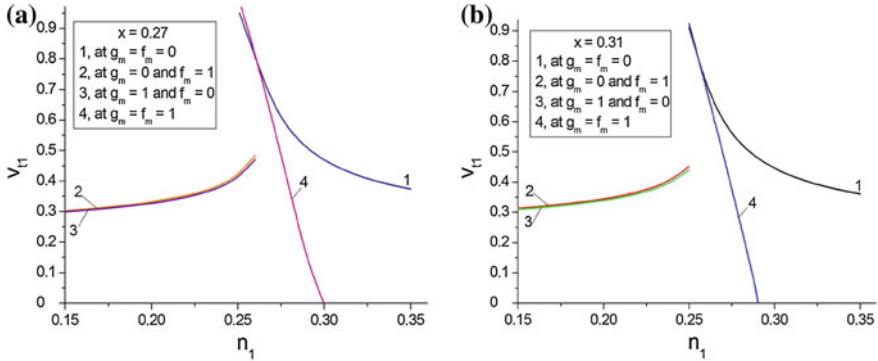
Fig. 8.4 Link between n_1 (volume fraction of domains of the type 1 in the T_1 phase) and v_{t1} (volume fraction of the T_1 phase) in heterophase samples of BF–0.27PT (**a**) and BF–0.31PT (**b**). Domain orientations in the T_1 and monoclinic phases are shown in Fig. 8.3 (reprinted from paper by Topolov [31], with permission from the American Institute of Physics)

8.2.2.3 Heterophase States at x = 0.35

As is known from experimental results [22], by cooling BF–0.35PT undergoes the first-order phase transition from the paraelectric cubic ($Pm3m$ symmetry) phase to the stable ferroelectric tetragonal ($P4mm$ symmetry) phase via the minority of monoclinic (Pm symmetry) phase. The tetragonal-monoclinic phase coexistence is detected in a wide temperature range covering a few tens of Kelvin degrees. The same composition is characterised by the large tetragonality of the perovskite unit cell ($c_t/a_t = 1.19$ [22]) at room temperature. Ranjan and Appala Raju emphasised an original way of stabilisation of the tetragonal phase in BF–xPT near the MPB [22]. This stabilisation is associated with a very large number of domains and interfaces which promote a stress relief [4] in the heterophase system.

   We assume that the tetragonal and monoclinic phases are split into domains with orientations shown in the left part of Fig. 8.3, and this heterophase region coexists with a single-domain tetragonal phase in an interlayer. The orientation of its crystallographic axes coincides with the orientation in the domain type 1 in the tetragonal phase (Fig. 8.3). The single-domain tetragonal phase in the interlayer is regarded as a counterpart and, according to our results, promotes the effective stress relief at the tetragonal-monoclinic phase coexistence. An optimal volume fraction of the domain type 1 in the polydomain tetragonal phase of BF–0.35PT is $n_1 = 0.586$. This value is found from conditions (8.3) for the complete stress relief at the cubic-tetragonal phase transition, and the unit-cell parameters at this phase transition ($T \approx 910$ K) were measured in work [22]. At $T < 910$ K we assume $n_1 = $ const and consider examples of the elastic matching of the polydomain tetragonal and monoclinic phases. Simplest variants of this elastic matching at the complete stress relief in BF–0.35PT are related to $g_m = 0$ and 1 [see g_m in Fig. 8.3 and (8.7)], i.e., in the presence of two domain types in the monoclinic phase.

Table 8.1 Temperature dependence of the volume fraction of the tetragonal phase $v_{fr,T}(T)$ and ratios of unit-cell parameters a_t/c_t and a_m/c_m of BF–0.35PT

T, K	Volume fraction, $v_{fr,T}$		Experimental $v_{fr,T}$ [22]	Experimental a_t/c_t [22]	Experimental a_m/c_m [22]
	Calculated for $g_m = 1$	Calculated for $g_m = 0$			
803	0.521	0.540	0.44	0.947	0.904
828	0.651	0.644	0.65	0.963	0.913
853	0.681	0.676	0.77	0.966	0.918
873	0.744	0.739	0.76	0.975	0.916
893	0.825	0.823	0.88	0.978	0.929
913	0.892	0.890	0.94	0.980	0.933

Analyzing the phase coexistence, we find two branches of the volume fraction of the polydomain tetragonal phase $v_{fr,T}(T)$ (Table 8.1). Differences between the related values of $v_{fr,T}(T)$ at $g_m = 1$ and $g_m = 0$ are small and accounted for by a passive role of the monoclinic phase in the stress relief. The calculated values of $v_{fr,T}$ are consistent with experimental data (4th column in Table 8.1). Changes in the ratios of unit-cell parameters a_t/c_t (tetragonal phase) and a_m/c_m (monoclinic phase) correlate with the $v_{fr,T}(T)$ branches (see Table 8.1) in the wide temperature range. In contrast to these changes, the a_m/b_m ratio in the monoclinic phase remains almost constant: in the same temperature range, according to experimental data [22], $| a_m/b_m-1 | \approx 5 \times 10^{-4}$. Data from Table 8.1 suggest that inequality

$$c_m/a_m > c_t/a_t \qquad (8.11)$$

holds at $T = $ const and provides favorable conditions for the complete stress relief in the heterophase sample within the wide temperature range. Condition (8.11) plays a decisive role in the unconventional mechanism [22] of the stabilization of the tetragonal phase.

8.2.3 Solid Solutions of $(1-z)Pb(Zr_wTi_{1-w})O_3-zPb(Zn_{1/3}Nb_{2/3})O_3$

FE-relaxor solid solutions of $(1-z)Pb(Zr_wTi_{1-w})O_3-zPb(Zn_{1/3}Nb_{2/3})O_3$ (PZT$-$zPZN) with $z = 0.1$ and 0.2 were studied [38] at specific values of w that would characterize the Zr/Ti ratio [5–7] in the well-known system of PZT. Of particular interest are changes in z and w near the MPB and various heterophase states in PZT$-$zPZN at these changes. As follows from experimental data [38] on PZT$-$zPZN, this system is characterised by the coexistence of the tetragonal and monoclinic phases of the FE nature. Below we describe examples of the phase coexistence in PZT$-$zPZN at $z = $ const and $w = $ const.

The elastic matching of the polydomain tetragonal and monoclinic phases is analyzed for the domain orientations shown in the left part of Fig. 8.3. As in

Sect. 8.2.2.3, we assume that the single-domain tetragonal phase is present in the interlayer instead of the single-domain monoclinic phase. Like the elastic matching discussed in Sect. 8.2.2.3, the minimum number of the domain types in the monoclinic phase at the complete stress relief is two, e.g., at $g_m = 1$ or $g_m = 0$. Taking into account conditions (8.3), we find a set of permissible values of the volume fraction of the tetragonal phase $v_{I,k}$ at the volume fraction of the domain type 1 in the tetragonal phase $n_{1,k} = $ const ($k = 1, 2, 3, \ldots$). Finally the volume fraction of the tetragonal phase $v_{fr,T}$ in a two-phase sample is found as a result of averaging the values of $v_{I,k}, v_{I,k+1}, \ldots$

Results related to $g_m = 1$ are graphically represented in Fig. 8.5. The tetragonal phase with the fairly large unit-cell distortion considerably influences the domain content in the monoclinic phase (see curves 1 in Fig. 8.5a–e). Curves 2 in Fig. 8.5a–e show that the volume fraction of the tetragonal phase $v_{I,k}$ can vary in wide ranges at variations of the volume fraction $n_{1,k}$ of the domain type 1. The wider volume-fraction range is achieved in a composition with $z = 0.1$ and $w = 0.49$ (Fig. 8.5b): for this composition inequality $0.03 < v_{I,k} < 0.97$ holds. The similar volume-fraction behaviour is observed at $g_m = 0$, and this fact also testifies to the active role of the tetragonal phase in the stress relief in PZT$-z$PZN. Data from Table 8.2 suggest that the volume fraction $v_{fr,T}$ (average value) predicted for either $g_m = 0$ or $g_m = 1$ is consistent with experimental data [38] on heterophase PZT$-z$PZN.

8.2.4 Solid Solutions of $(1-x)BiScO_3-xPbTiO_3$

An interesting example of the correlation between the volume fraction of the intermediate monoclinic phase and ratios of its unit-cell parameters b_m/c_m and a_m/c_m was discussed [39] for the FE solid solutions of $(1-x)BiScO_3-xPbTiO_3$ (BS–xPT) near the MPB ($0.60 \leq x \leq 0.64$). Physical properties of these solid solutions are concerned with various heterophase states studied in experimental work [40–42]. A two-phase model of BS–0.64PT was put forward [43] to show the role of the monoclinic phase (*Pm* symmetry) in BS–xPT single crystals. An example of the twin-free nanocrystal of BS–0.61PT, wherein the monoclinic (*Cm* symmetry), rhombohedral (*R3m* symmetry) and tetragonal (*P4mm* symmetry) phases coexist [42], is of value to study an adaptive phase in a heterophase structure.

According to experimental results [40], depending on the molar concentration x, the following paths of the first-order phase transitions take place in BS–xPT by cooling:

(i)   at $x < 0.60$ the transition from the paraelectric cubic $Pm\overline{3}m$ phase to the FE rhombohedral $R3m$ phase is observed,

(ii) at $x > 0.70$ the transition from the paraelectric cubic $Pm\overline{3}m$ phase to the FE tetragonal $P4mm$ phase is observed,
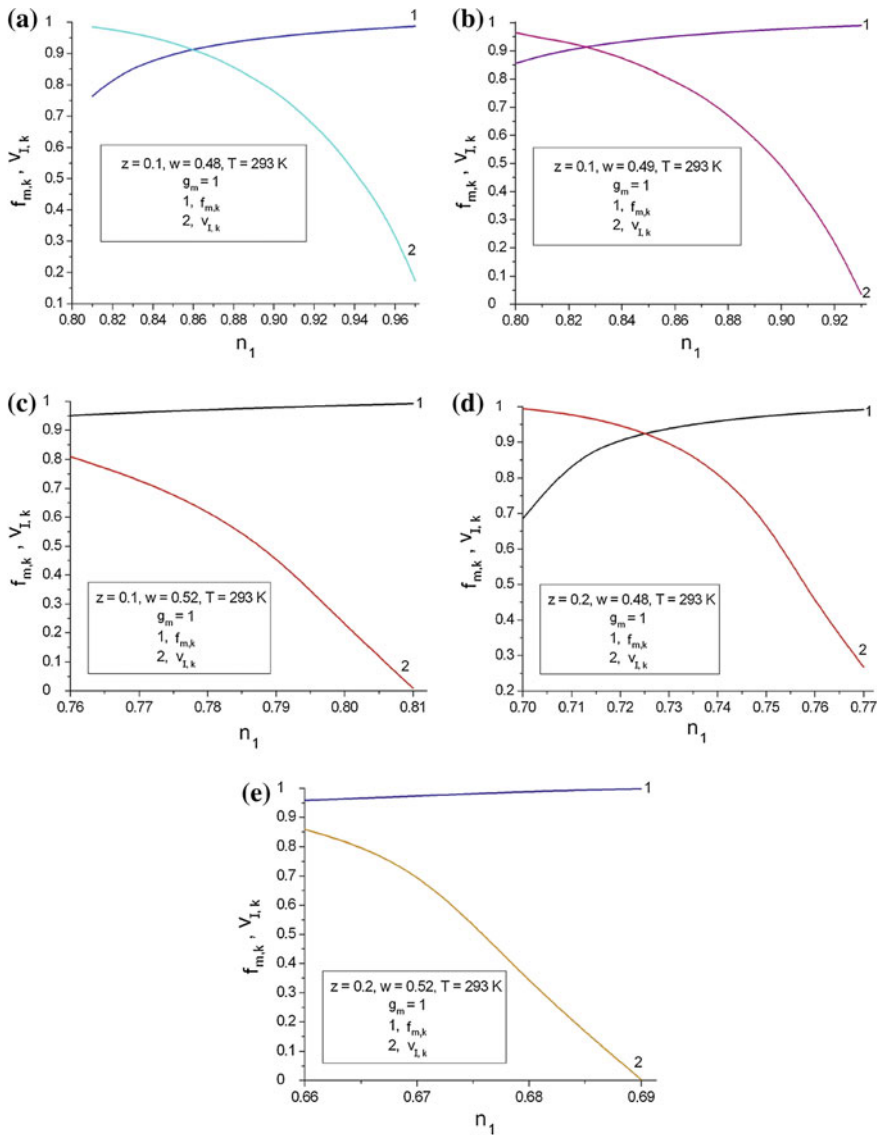
Fig. 8.5 Volume fraction of domain pairs (twins) $f_{m,k}$ in the monoclinic phase and volume fraction of the polydomain tetragonal phase $v_{I,k}$ with changing the volume fraction n_1 of the domain type 1 in PZT–zPZN

(iii) at $0.60 \leq x \leq 0.70$ the transition from the paraelectric cubic $Pm\overline{3}m$ phase to the FE tetragonal $P4mm$ phase and then the transition from the $P4mm$ phase to the FE monoclinic Cm phase are observed.

Table 8.2 Average and experimental values of the volume fraction of the FE tetragonal phase in heterophase samples of PZT–zPZN at $T = 293$ K

z	w	Average volume fraction, $\langle v_{fr,T} \rangle$		Experimental value of $v_{fr,T}$ [38]
		Calculated for $g_m = 1$	Calculated for $g_m = 0$	
0.1	0.48	0.737	0.764	0.67
0.1	0.49	0.670	0.667	0.65
0.1	0.52	0.479	0.470	0.44
0.2	0.48	0.755	0.754	0.80
0.2	0.52	0.687	0.681	0.68

The intermediate monoclinic phase studied in work [40] is similar to that observed in the FE solid solutions of PZT [12, 44] near the MPB. Below we discuss examples of the heterophase states where the monoclinic phase plays the role of the bridging phase and promotes the effective stress relief in BS–xPT.

It is assumed that a single-crystal sample (or a ceramic grain) of BS–xPT contains two FE phases, tetragonal and monoclinic, and these phases are separated by planar interfaces (Fig. 8.6). The two-phase region coexists with an interlayer of the single-domain monoclinic phase (see the right side in Fig. 8.6), and different orientations of domains in this phase are shown as Mi and Mj in Fig. 8.6. Perovskite unit-cell vectors a_m, b_m and c_m of domains in the monoclinic phase are oriented almost parallel to the co-ordinate axes OX_k, and deviations from the parallel orientation are accounted for by the distortion of the perovskite unit cell [4, 12, 44].

The interlayer of the single-domain monoclinic phase (Mj in Fig. 8.6) is regarded as a counterpart to the two-phase region. Such an interlayer may be a stimulus for the effective stress relief over the heterophase sample and can be elastically matched with the two-phase region. It is assumed that the volume fraction of these interlayers is relatively small, i.e., inequalities

$$v_m^* \ll v_m \quad \text{and} \quad v_m^* \ll v_t \tag{8.12}$$

are valid for the phase coexistence shown in Fig. 8.6. It is also assumed that the two-phase regions with the domains M1, M2 and M3 therein (see Fig. 8.6) are characterized by equal volume fractions, distributed uniformly in the sample and the interfaces separating the adjacent phases obey conditions (8.3). In this case the volume fraction of the monoclinic phase is represented as

$$\langle v_m \rangle = \left(v_{m,1} + v_{m,2} + \cdots + v_{m,f} \right)/f, \tag{8.13}$$

where f is the number of variants of the elastic matching of the phases at the complete stress relief.

Table 8.3 contains data on the phase coexistence in BS–xPT near the MPB. The optimal volume fraction t_{opt} is determined from conditions (8.2) for the elastic matching of the polydomain tetragonal and single-domain monoclinic phase. It is seen that two domain types in the monoclinic phase, M2 and M3, promote the
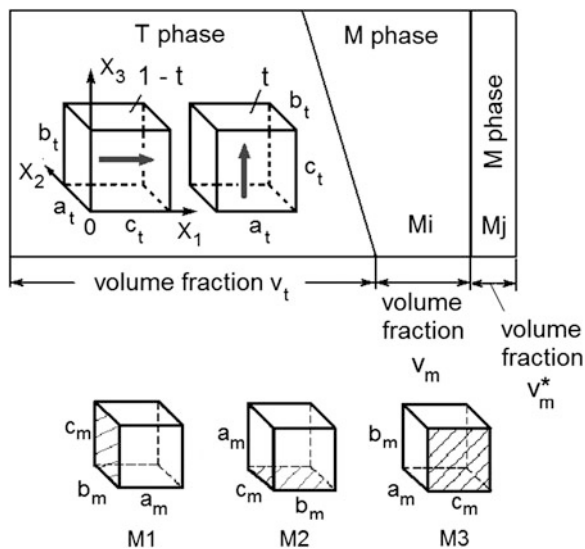
Fig. 8.6 Schematic of the tetragonal–monoclinic phase coexistence. Co-ordinate axes OX_k are parallel to the unit-cell vectors in the paraelectric cubic phase. Spontaneous polarization vectors of 90° domains in the tetragonal (T) phase are shown with *arrows*, and t and $1-t$ are volume fractions of these domains. The single-domain monoclinic (M) phase is represented by one of the domain types (M1, M2 or M3), and $i \neq j$ in the adjacent regions; a_t, b_t and c_t are linear perovskite unit-cell parameters in the tetragonal phase, and a_m, b_m and c_m are linear perovskite unit-cell parameters in the monoclinic phase (reprinted from paper by Topolov [39], with permission from Wiley–VCH Verlag)

complete stress relief in the heterophase structure in accordance with conditions (8.3). However conditions (8.2) are not valid in the presence of the single-domain M1 phase. Such behavior can be accounted for by a specific anisotropy of spontaneous strains of the pereovskite unit cell in the coexisting phases. In general average values of $\langle v_m \rangle$ from (8.13) are consistent with experimental data [41] on the volume fraction of the monoclinic phase at $0.62 \leq x \leq 0.64$ (cf. data from 6th and 7th columns in Table 8.3).

The system of BS–xPT is also of interest because of a correlation between the average volume fraction of the monoclinic phase $\langle v_m \rangle$ and ratios of its perovskite unit-cell parameters (Fig. 8.7). As follows from experimental data [41], at room temperature a_m/c_m is characterized by a slight maximum near $x = 0.64$, while b_m/c_m is almost constant at $0.61 \leq x \leq 0.62$ and decreases at $0.62 < x \leq 0.64$. The correlation shown in Fig. 8.7 may shed light on features of the phase content in BS–xPT. It should be mentioned for comparison that the unit-cell distortion in the perovskite-type solid solutions is often characterized [5, 24] by the ratio of the unit-cell parameters c_t/a_t in the FE tetragonal phase, and this ratio can also influence [31] the phase coexistence near the MPB.

Table 8.3 Optimal volume fractions of 90° domains in the tetragonal phase, optimal volume fractions of the monoclinic phase, average volume fractions of the monoclinic phase, and experimental values of the volume fraction of the monoclinic phase in BS–xPT at room temperature (reprinted from paper by Topolov [39], with permission from Wiley–VCH Verlag)

x	Domain type in the mono–clinic phase (Mi in Fig. 8.6)	Optimal volume fraction[a] of 90° domains t_{opt} in the tetragonal phase	Domain type in the inter-layer (Mj in Fig. 8.6)	Optimal volume fraction[a] of the mono-clinic phase $v_{m,n}$	Average volume fraction[b] of the mono–clinic phase $\langle v_m \rangle$	Volume fraction of the monoclinic phase $v_{m,exp}$ from experimental work [41]
0.62	M1	—[c]	M2	—		
			M3	—		
	M2	0.872	M1	0.242		
			M3	0.936		
	M3	0.128	M1	0.790		
				0.460		
			M2	—		
					0.607	0.653
0.63	M1	—[c]	M2	—		
			M3	—		
	M2	0.280	M1	0.433		
			M3	0.876		
		0.743	M1	0.555		
			M3	0.928		
				0.276		
	M3	0.257	M1	—		
			M2	0.161		
		0.647	M1	—		
			M2	—		
					0.538	0.495
0.64	M1	—[c]	M2	—		
			M3	—		
	M2	0.330	M1	0.446		
			M3	0.884		
		0.729	M1	0.589		
			M3	0.417		
	M3	0.272	M1	—		
			M2	0.186		
		0.586	M1	—		
			M2	—		
					0.504	0.494

[a] Conditions (8.3) are valid for the phase coexistence listed in the 2nd column

[b] Conditions (8.3) are valid for the phase coexistence '(Tetragonal + Mi)–Mj', see the 2nd and 4th columns, and $\langle v_m \rangle$ is calculated from (8.13)

[c] Elastic matching of the polydomain tetragonal and single-domain M1 phases does not obey conditions (8.3)

Fig. 8.7 Correlation
between the average volume
fraction of the monoclinic
phase $\langle v_m \rangle$ and ratios of
perovskite unit-cell
parameters in the monoclinic
phase of BS–xPT at room
temperature (reprinted from
paper by Topolov [39], with
permission from Wiley–VCH
Verlag)
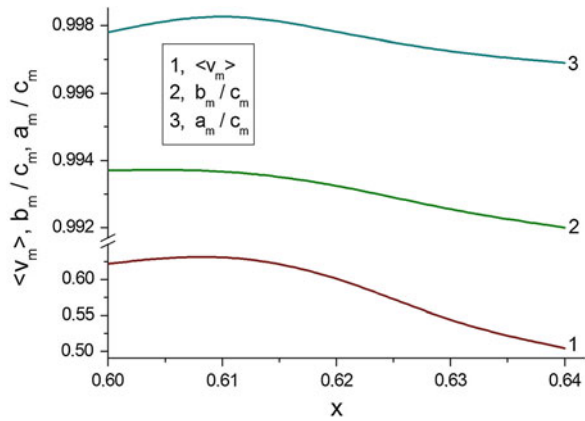
8.3 Conclusions

In the present paper the role of the elastic matching of phases with different
symmetry and domain types has been analysed for a few systems of the FE solid
solutions with the perovskite-type structure. The crystallographic method devel-
oped by the author [20, 21, 31, 39] has been applied to show important inter-
connections between the non-180° domain (mechanical twin) types and the
volume fraction of the tetragonal (or monoclinic) phase at a minimum number of
the domain types in the morphotropic phases under conditions for the complete
stress relief in a heterophase sample. Some heterophase structures and examples of
the phase content near the MPB have been studied in PFN–xPT (Sect. 8.2.1), BF–
xPT (Sect. 8.2.2), PZT–zPZN (Sect. 8.2.3), and BS–xPT (Sect. 8.2.4). Changes in
the phase content and physical properties in these systems are associated with
modes of ion substitutions in the perovskite-type structure.

  The diagrams (Figs. 8.2, 8.4 and 8.5) have been put forward to study various
heterophase states and stress-relief conditions in the FE solid solutions near the
MPB and to show the role of the intermediate phase in the stress relief. In the
diagrams shown in Figs. 8.2, 8.4 and 8.5 relations between the volume fractions of
the domain types and phases have been revealed to describe possibilities of the
complete stress relief in some ranges of molar concentrations and temperatures.
Examples of the elastic matching of the tetragonal and monoclinic phases show,
that different variants of the single-domain intermediate monoclinic phase can be
present (see Table 8.3) and influence the phase content in the system near the
MPB.

  The very wide range of permissible volume fractions of the polydomain
tetragonal phase (for instance, $0.03 < v_{I,k} < 0.97$ at $z = 0.1$ and $w = 0.49$ in PZT–
zPZN, see Fig. 8.5b) at the complete stress relief is an important sign of the
dominating role of this phase in the studied systems. The large tetragonality of the
perovskite unit cell influences the heterophase structures, but does not put

obstacles to the stress relief. Furthermore, the relatively narrow molar-concentration range of the thermodynamic stability of the monoclinic phase and features of the anisotropy of spontaneous strains of its unit cell promote the complete stress relief at a restricted number of the non-180° domain types in this phase.

The correlation between the ratios of the unit-cell parameters of the intermediate monoclinic phase and its volume fraction in the MPB region (Fig. 8.7) may be a stimulus for a further independent study. In addition we underline that the predicted data on the volume contents in various heterophase states are consistent with experimental results on the studied FE solid solutions.

References

1. E.G. Fesenko, *Perovskite Family and Ferroelectricity* (Atomizdat, Moscow, 1972). (in Russian)
2. R.E. Newnham, *Properties of Materials: Anisotropy, Symmetry, Structure* (Oxford University Press, New York, 2005)
3. G.H. Haertling, J. Am. Ceram. Soc. **82**, 797 (1999)
4. VYu. Topolov, *Heterogeneous Ferroelectric Solid Solutions. Phases and Domain States* (Springer, Berlin, 2012)
5. Y. Xu, *Ferroelectric Materials and their Applications* (North-Holland, Amsterdam, 1991)
6. H. Schaumburg (ed.), *Keramik* (B. G. Teubner, Stuttgart 1994)
7. G. Helke, K. Lubitz, in *Piezoelectricity, Evolution and Future of a Technology*, ed. by W. Heywang, K. Lubitz, W. Wersing (Springer, Berlin, 2008) p. 89
8. L.E. Cross, *ibid.*, p. 131
9. K.M. Rabe, M. Dawber, C. Lichtensteiger, et al., in *Physics of Ferroelectrics. A Modern Perspective*, ed. by K.M. Rabe, C.H. Ahn, J.-M. Triscone (Springer, Berlin, 2007)
10. G.A. Smolensky, V.A. Bokov, V.A. Isupov, et al., in *Physics of Ferroelectric Phenomena*, ed. by G.A. Smolensky (Nauka, Leningrad 1985), (in Russian)
11. B. Noheda, D.E. Cox, G. Shirane, Phys. Rev. B **66**, 054104 (2002)
12. B. Noheda, D.E. Cox, Phase Trans. **79**, 5 (2006)
13. A.K. Singh, D. Pandey, O. Zakharko, Phys. Rev. B **74**, 024101 (2006)
14. B. Noheda, Z. Zhong, D.E. Cox et al., Phys. Rev. B **65**, 224101 (2002)
15. H. Cao, J. Li, D. Viehland, Phys. Rev. B **73**, 184110 (2006)
16. A.L. Roitburd, Sov. Phys. Uspehi **17**, 326 (1974)

17. A.L. Roytburd, Phase Trans. **45**, 1 (1993)
18. E.G. Fesenko, V.G. Gavrilyachenko, A.F. Semenchev, *Domain Structure of Multiaxial Ferroelectric Crystals* (Rostov University Press, Rostov-on-Don, 1990). (in Russian)
19. D. La-Orauttapong, B. Noheda, Z.-G. Ye et al., Phys. Rev. B **65**, 144101 (2002)
20. V.Yu. Topolov, Mater. Lett. **66**, 57 (2012)
21. V.Yu. Topolov, Ferroelectrics **428**, 8 (2012)
22. R. Ranjan, K. Appala Raju, Phys. Rev. B **82**, 054119 (2010)
23. V. Kothai, A. Senyshyn, R. Ranjan, J. Appl. Phys. **113**, 084102 (2013)
24. S.P. Singh, D. Pandey, S. Yoon et al., Appl. Phys. Lett. **93**, 182910 (2008)
25. Y. Yamashita, Y. Hosono, in *Piezoelectricity, Evolution and Future of a Technology*, ed. by W. Heywang, K. Lubitz, W. Wersing (Springer, Berlin 2008)
26. L.E. Pustovaya, Russ. J. Appl. Chem. **80**, 1036 (2007)
27. G. Metrat, Ferroelectrics **26**, 801 (1980)
28. J. Fousek, V. Janovec, J. Appl. Phys. **40**, 135 (1969)
29. S.P. Singh, S. Yoon, S. Baik et al., Appl. Phys. Lett. **97**, 122902 (2010)
30. S. Bhattacharjee, D. Pandey, J. Appl. Phys. **110**, 084105 (2011)
31. V.Yu. Topolov, J. Appl. Phys. **111**, 094109 (2012)
32. V.F. Freitas, L.F. Cótica, I.A. Santos et al., J. Eur. Ceram. Soc. **31**, 2965 (2011)
33. T.L. Burnett, T.P. Comyn, A.J. Bell et al., J. Phys: Conf. Ser. **26**, 239 (2006)
34. W.-M. Zhu, H.-Y. Guo, Z.-G. Ye, J. Mater. Res. **22**, 2136 (2007)
35. W.-M. Zhu, H.-Y. Guo, Z.-G. Ye, Phys. Rev. B **78**, 014401 (2008)
36. S. Bhattacharjee, D. Pandey, J. Appl. Phys. **107**, 124112 (2010)
37. S. Bhattacharjee, K. Taji, C. Moriyoshi et al., Phys. Rev. B **84**, 104116 (2011)
38. S. Geetika, A.M. Umarji, Mater. Sci. Eng. B, **167**, 171 (2010)
39. V.Yu. Topolov, Cryst. Res. Technol. **47**, 1054 (2012)
40. J. Chaigneau, J.M. Kiat, C. Malibert, C. Bogicevic, Phys. Rev. B **76**, 094111 (2007)
41. K. Datta, D. Walker, P.A. Thomas, Phys. Rev. B **82**, 144108 (2010)
42. T. Hungria, F. Houdellier, M. Algueró, A. Castro, Phys. Rev. B **81**, 100102 (2010)
43. K. Datta, S. Gorfman, P.A. Thomas, Appl. Phys. Lett. **95**, 251901 (2009)
44. B. Noheda, D.E. Cox, G. Shirane et al., Phys. Rev. B **63**, 014103 (2001)

Chapter 9
Studies of Ferroelectric and Magnetic Phase Transitions in Multiferroic PbFe$_{0.5}$B$_{0.5}$O$_3$–PbTiO$_3$ (B = Nb, Ta) Solid Solution Ceramics

I. P. Raevski, S. P. Kubrin, A. V. Blazhevich, M. S. Molokeev, S. V. Misjul, E. V. Eremin, H. Chen, C.-C. Chou, E. I. Sitalo, S. I. Raevskaya, V. V. Titov, D. A. Sarychev, M. A. Malitskaya and I. N. Zakharchenko

Dielectric, X-ray, Mössbauer and magnetization studies of $(1-x)$PbFe$_{0.5}$B$_{0.5}$O$_3$–(x)PbTiO$_3$ (B = Nb, Ta) ceramics from the $0 < x < 0.3$ range have been carried out. Addition of PbTiO$_3$ to PbFe$_{0.5}$B$_{0.5}$O$_3$ increases the temperature T_m of the permittivity maximum, decreases the diffusion of this maximum and lowers the Neél temperature T_N. However above a certain compositional threshold ($x \approx 0.1$) fast lowering of T_N stops and a new magnetic state stable in a rather wide compositional range appears. Large difference between the zero-field cooled and field-cooled magnetization-temperature curves as well as between the temperatures of magnetic phase transition determined from Mössbauer and magnetization studies for compositions with $x > 0.1$ implies that this state is a spin glass phase.

I. P. Raevski · S. P. Kubrin · A. V. Blazhevich · E. I. Sitalo · S. I. Raevskaya (✉) · V. V. Titov · D. A. Sarychev · M. A. Malitskaya · I. N. Zakharchenko
Research Institute of Physics, and Physical Faculty, Southern Federal University, Rostov-on-Don, Russia
e-mail: sveta.raevskaya@mail.ru

M. S. Molokeev · E. V. Eremin
Kirensky Institute of Physics, SB RAS, Krasnoyarsk, Russia

S. V. Misjul
Siberian Federal University, Krasnoyarsk, Russia

H. Chen
University of Macau, Macau, China

C.-C. Chou
National Taiwan University of Science and Technology, Taipei, Republic of China (Taiwan)

9.1 Introduction

Lead iron niobate $PbFe_{0.5}Nb_{0.5}O_3$ (PFN) and lead iron tantalate $PbFe_{0.5}Ta_{0.5}O_3$ (PFT) are ternary perovskite multiferroic oxides possessing simultaneously ferroelectric and magnetic properties [1–8]. Recent burst of interest to multiferroics has the aim to find materials, which can be used to convert the magnetic signals to electric responses and *vice versa*. From this point of view, PFB–Pb(Zr, Ti)O$_3$ (B = Nb, Ta) solid solutions are among the best candidates as they were reported to possess a large magnetoelectric response at room-temperature, which is a great advantage for magnetoelectric devices [9].

At cooling, both PFN and PFT undergo the same sequence of phase transitions: from the cubic paraelectric to tetragonal ferroelectric phase at $T_{CT} \approx 380$ (270) K, then to the monoclinic ferroelectric phase, at $T_{TM} \approx 350$–360 (200–220) K, and, finally, to the G-type antiferromagnetic phase at $T_N \approx 150$ (180) K [1–8]. Here the data in the parenthesis correspond to PFT. Besides the AFM phase transition both PFN and PFT exhibit also the lower-temperature magnetic anomaly at $T_g \approx 10$–20 K [6, 8, 10–12]. This anomaly was at first attributed to superexchange interaction taking place via –Fe–O–Nb(Ta)–O–Fe– pathways caused by local short range chemical ordering of Fe^{3+} and $Nb^{5+}(Ta^{5+})$ ions on the nanoscale [13]. However, experiments on the temperature and magnetic field dependence of the magnetic susceptibility have shown that this anomaly marks the magnetic glass transition rather than the AFM of FM phase transition [6, 8, 10–12]. Recently a coexistence of AFM and spin glass states was approved for PFN by neutron diffuse scattering at temperatures below ≈ 20 K [12]. Studies of magnetization [2], ^{57}Fe Mossbauer spectra [14], as well as ^{93}Nb and ^{17}O NMR spectra [15] have led to the conclusion that PFN is a chemically inhomogeneous system and long range AFM order appears in Fe-rich-Nb-poor regions while, a low-temperature magnetic relaxor spin-glass state can arise from the Fe-poor-Nb-rich regions [2, 14, 15]. These data are confirmed by the results of first principles calculations showing that in PFN and PFT Fe^{3+} and Nb^{5+} (Ta^{5+}) ions are distributed in the lattice not randomly, but exhibit a sort of clustering [14]. This heterogeneity explains why the experimental values of T_N, for PFN and PFT (≈ 150 K) are located approximately halfway between calculated values of this temperature for the fully ordered ($T_N = 0$ K) and completely disordered ($T_N \approx 300$ K) states [16].

In the present paper, we study ferroelectric and magnetic phase transition temperatures in $(1-x)$PFB–(x)PbTiO$_3$ solid solutions which are the cross-sections of the PFB–Pb(Zr, Ti)O$_3$ (B = Nb, Ta) system.

9.2 Experimental

PFT powder for X-ray studies was obtained by solid-state reaction route using high-purity Fe_2O_3, $PbCO_3$ and Ta_2O_5. These oxides were batched in stoichiometric proportions and mixed thoroughly together with 10 wt.% excess of $PbCO_3$ for lead

loss compensation in an agate mortar in the presence of ethyl alcohol. Then synthesis was carried out for 4 h at 850 °C. After the synthesis, the product of reaction was crushed by pestle in an agate mortar for several minutes and then annealed for 2 h at 450 °C to remove the residual mechanical stresses.

Ceramic samples of $(1-x)$PFB–(x)PbTiO$_3$ (PFB–xPT) have been obtained by solid-state reaction route using high-purity Fe$_2$O$_3$, Nb$_2$O$_5$, PbO, TiO$_2$ and Ta$_2$O$_5$. These oxides were batched in stoichiometric proportions, and 1 wt.% Li$_2$CO$_3$ was added to the batch. This addition promotes formation of the perovskite modifications of both PFN and PFT and reduces their conductivity [17–19]. After mixing thoroughly in an agate mortar under ethyl alcohol and subsequent drying, the green ceramic samples were pressed at 100 MPa in the form of disks of 10 mm in diameter and of 2–4 mm in height using polyvinyl alcohol as a binder. The sintering was performed at 1050–1150 °C for 2 h in a closed alumina crucible. The density of the obtained ceramics was about 90–95 % of the theoretical one. The electrodes for measurements were deposited to the grinded disks of 9 mm in diameter and of 0.9 mm in height by firing on silver past. Dielectric studies were carried out in the 10^2–10^6 Hz range in the course of both heating and cooling at a rate of 2–3 K/min with the aid of the computer-controlled E7-20 and Novocontrol Alpha-A impedancemeters. The piezoelectric coefficient, d_{31}, was measured using the standard resonance–antiresonance technique. The resonance and antiresonance frequencies were obtained using the maximum and minimum of admittance spectra. From these values, the d_{31} values were determined. Mössbauer spectra were measured with the aid of the MS-1104E rapid spectrometer of the latest design and analyzed using the original computer program UNIVEM. Magnetic measurements were performed using the PPMS-9 physical property measurement system (Quantum Design) in the temperature range 2–300 K and under magnetic field up to 90 kOe.

The X-ray diffraction study of the PFT powder was performed on a D8-ADVANCE diffractometer (Cu$K\alpha$ radiation, θ–2θ scan mode) using a VANTEC linear detector and a TTK 450 Anton Paar temperature chamber in the 130–300 K temperature range. The scan step in the angle 2θ was 0.016°. The unit cell parameters were determined and refined during fitting of the profiles using the WTREOR and DDM programs [20].

9.3 Results and Discussion

X-ray diffraction studies have shown that all the investigated compositions were single-phase and had a structure of the perovskite type. For PFT powder the unit cell parameters in all the temperature points in the 135–360 K range were obtained by fitting the X-ray diffraction profiles using the set of codes TOPAS 4.2 [19]. Some data necessary for fitting: space groups, orientation and the initial parameters of the Bravais cells as well as the coordinates of the atoms were taken from [4]. Thus obtained temperature dependence of the PFT unit cell parameters is

Fig. 9.1 Temperature dependences of the unit cell parameters for PFT powder in the monoclinic Cm, tetragonal $P4\,mm$ and cubic $Pm\overline{3}m$ phases: 1—c_{mon}; 2—$a_{mon}/\sqrt{2}$; 3—$b_{mon}/\sqrt{2}$; 4—c_{tetr}; 5—a_{tetr}; 6—a_{cub}. The inset shows temperature dependence of the monoclinic angle β
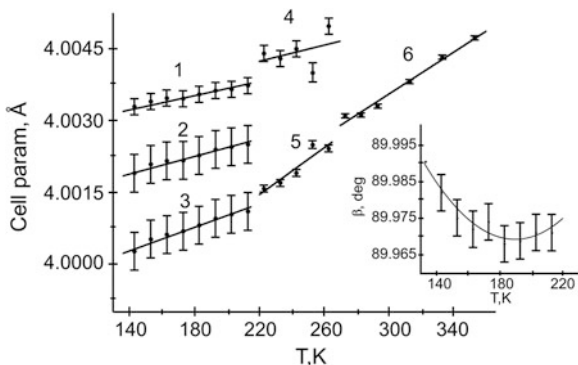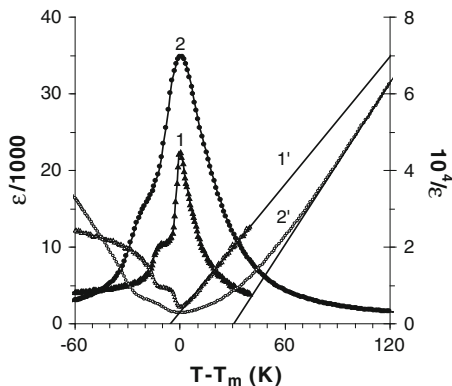

Fig. 9.2 Dependences of dielectric permittivity (1, 2) and reciprocal permittivity ($1'$, $2'$) on the reduced temperature $T - T_m$ for PFN single crystal (1, $1'$) and Li-doped PFN ceramics (2, $2'$)

shown in Fig. 9.1. One can see the anomalies of the unit cell parameters at $T_{CT} \approx 270$ K and $T_{TM} \approx 220$ K. It should be mentioned that the monoclinic angle β shows unusual temperature dependence. At cooling its value at first remains nearly constant or even lowers, but below approximately 180 K it begins to increase and becomes close to 90° (see the inset in Fig. 9.2). This unusual behavior will be discussed in detail further.

Recently we have shown that, in contrast to a commonly adopted view, ferroelectric phase transition in PFN single crystals is non-diffused and usually observed in ceramic samples diffusion of the permittivity ε maximum has an extrinsic origin [7]. As one can see in Fig. 9.2 the $\varepsilon(T)$ anomalies corresponding to the monoclinic-tetragonal phase transition are well seen both in PFN single crystals and highly-resistive Li-doped PFN ceramics. However in ceramics, the extrapolated Curie–Weiss temperature T_{CW} is substantially higher than the temperature T_m of the $\varepsilon(T)$ maximum. Such behavior is typical of ferroelectrics with diffuse phase transition and may be induced in PFN ceramics by dopants (e.g. Li) and/or defects (e.g. lead and oxygen vacancies).

Figure 9.3 shows the temperature dependences of dielectric permittivity ε and loss tangent $\tan \delta$ for highly-resistive Li-doped PFT ceramics measured at several
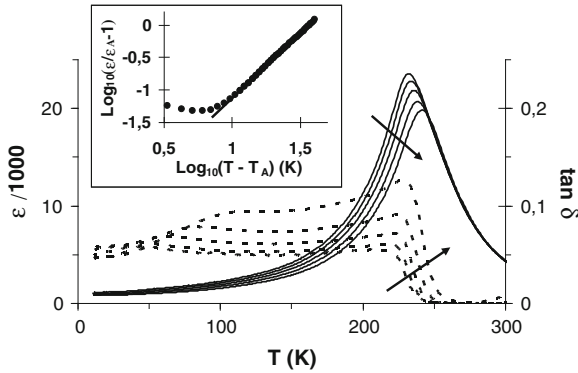
Fig. 9.3 Temperature dependences of permittivity (*solid lines*) and loss tangent (*broken lines*) measured at frequencies 10^2, 10^3, 10^4, 10^5 and 10^6 Hz for highly-resistive Li-doped PFT ceramics. The arrows show the direction of the frequency increase. The inset shows approximation of the high-temperature slope of the experimental $\varepsilon(T)$ peak (*points*) based on formula (9.2) (*straight line*)

frequencies. This ceramics exhibits a very large dielectric response and a pronounced frequency dispersion of both ε and $\tan\delta$. Temperature T_m of the $\varepsilon(T)$ maximum is similar to that reported in the literature for PFT ceramics and single crystals [3, 6, 21–23]. The T_m frequency shift, $\Delta T = T_m\,(10^6\ \text{Hz})$–$T_m\,(10^2\ \text{Hz})$ is much smaller than that for more conducting PFT single crystals [3], but is comparable with ΔT values reported for PFT ceramics studied in Refs. [21, 23]. The increase of T_m with the frequency is well fitted with the Vogel–Fulcher relation, typical of relaxors [24, 25]:

$$f = f_0 \exp[-E/k(T_m - T_0)] \tag{9.1}$$

where f_0 is the attempt frequency, E is the activation energy (the potential barrier height) and T_0 is the Vogel–Fulcher temperature, which is often associated with the freezing of relaxators and transition into the polar glass state. The Vogel–Fulcher freezing temperature $T_0 = 217$ K is close to the temperature of tetragonal-monoclinic phase transition. Other parameters of the Vogel–Fulcher relation for PFT ceramics, namely the attempt frequency $f_0 = 5 \cdot 10^{11}$ Hz and activation energy $E = 0.018$ eV, are very close to the ones reported for similar ternary perovskites $PbSc_{0.5}Ta_{0.5}O_3$ [24] and $PbSc_{0.5}Nb_{0.5}O_3$ [25] exhibiting spontaneous relaxor-ferroelectric transition.

At temperatures above T_m the $\varepsilon(T)$ of Li-doped PFT ceramics follows a quadratic law typical of relaxors and ferroelectrics with a diffuse phase transition [26]:

$$\frac{\varepsilon_A}{\varepsilon} = 1 + \frac{(T - T_A)^2}{2\delta^2} \tag{9.2}$$

with the parameters $T_A = 230$ K, $\varepsilon_A = 2.3 \cdot 10^4$ and $\delta = 26$ K. The value of the $\varepsilon(T)$ diffusion parameter δ for Li-doped PFT ceramics is somewhat larger than the
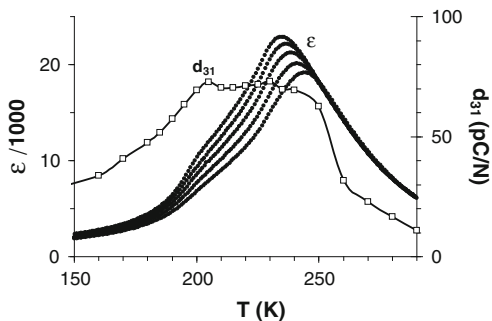
Fig. 9.4 Temperature dependences of piezoelectric modulus d_{31} and permittivity measured at frequencies 10^2, 10^3, 10^4, 10^5 and 10^6 Hz for poled Li-doped PFT ceramics in the zero field heating after field cooling ($E = 5$ kV/cm) mode

one for PFT single crystal ($\delta = 20$ K [26]). As one can see from Fig. 9.3, the $\varepsilon(T)$ maximum for PFT ceramics does not coincide with the $T_{CT} \approx 270$ K and there are no anomalies in the $\varepsilon(T)$ curve corresponding to $T_{TM} \approx 220$ K.

However after cooling under a bias field $E = 5$ kV from 250 K down to 50 K, there appears a step in the $\varepsilon(T)$ curve at about 200 K, its temperature does not depend on frequency (Fig. 9.4). It seems that this step corresponds to the tetragonal-monoclinic phase transition. This assumption is confirmed by the fact that temperature dependence of piezoelectric modulus exhibits a plateau in the 200–250 K range (Fig. 9.4) which approximately coincides with the range of the tetragonal phase determined from the structural studies (Fig. 9.1). Thus the tetragonal-monoclinic phase transition in PFN is not a spontaneous relaxor-ferroelectric transition, because the piezoelectric response does not disappear above T_{TM}. It seems that in the 220–270 K range both tetragonal and cubic phases coexist. This supposition explains the presence of diffuse frequency-dependent $\varepsilon(T)$ maximum between T_{TM} and T_{CT}.

For both PFN–xPT and PFT–xPT compositions T_m increases, as x grows (Fig. 9.5). The $\varepsilon(T)$ maximum diffusion does not change substantially with x for PFN–xPT ceramics [27]. In contrast to this for PFT–xPT compositions the $\varepsilon(T)$ maximum becomes sharper (Fig. 9.6) and its frequency shift ΔT diminishes (Fig. 9.5b). These results corroborate the data reported earlier for PFT–xPT system [28]. For all the PFT–xPT compositions studied, Curie–Weiss law is fulfilled at temperatures exceeding T_m by 40–50 K, but the extrapolated Curie–Weiss temperature T_{CW} appears to be substantially higher than T_m (Fig. 9.6). Similar behavior is observed for Li-doped PFN ceramics (Fig. 9.2). Addition of PbTiO$_3$ leads to decrease of the difference between T_{CW} and T_m. In PFN–xPT ceramics $T_{CW}(x)$ and $T_m(x)$ dependences converge at $x \approx 0.1$ and for compositions with $x > 0.1$ at larger x values $T_{CW} < T_m$ (Fig. 9.5a), as in usual ferroelectrics with a sharp phase transition. Thus Li-doped PFN–xPT ceramics with $x < 0.1$ and all the PFT–xPT ceramic compositions studied exhibit, from one side, the features typical of usual ferroelectrics (slightly diffused $\varepsilon(T)$ maximum, absence of the frequency shift of T_m, structural phase transition near T_m) and, from the other side, properties characteristic
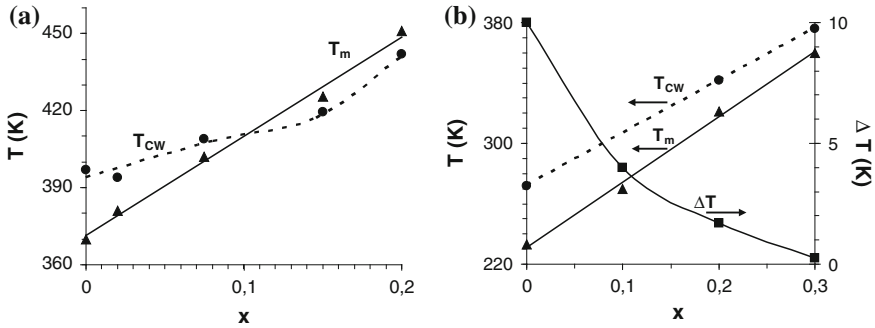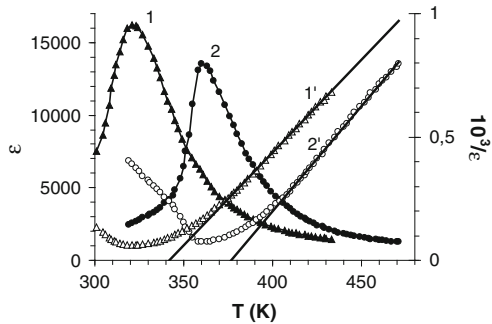
Fig. 9.5 Dependence of permittivity maximum temperature T_m, extrapolated Curie–Weiss temperature T_{CW} and T_m frequency shift ΔT on the composition for Li-doped PFN–xPT (**a**) and PFT–xPT (**b**) ceramics

Fig. 9.6 Temperature dependences of permittivity (1, 2) and reciprocal permittivity (1′, 2′) measured at 1 kHz, for Li-doped PFT–0.2PT (1, 1′) and PFT–0.3PT (2, 2′) ceramics

of relaxors and ferroelectrics with diffuse phase transition (ε follows a quadratic law just above T_m, and the linear Curie–Weiss law is valid only at temperatures much higher than T_m with $T_{CW} > T_m$). Similar combination of contradictory properties was observed for $0.5PbMg_{1/3}Nb_{2/3}O_3$–$0.5PbTiO_3$ single crystals [29] where the structural phase transition takes place at T_m and neither conventional relaxor dispersion, nor the frequency shift of T_m are observed. Nevertheless, the universal relaxor dispersion still persists in these crystals and T_m corresponds no to the ferroelectric–paraelectric but rather to the ferroelectric-relaxor phase transition.

At room temperature Mössbauer ^{57}Fe spectra of all the compositions studied appeared to be doublets with quadrupole splitting of ≈ 0.4 mm/s and isomer shift of ≈ 0.4 mm/s (relative to metallic iron), corresponding to the Fe^{3+} ions occupying the octahedral sites of perovskite lattice. This result is in a good agreement with the data of the X-ray photoelectron studies showing for PFN single crystals and ceramics the presence of only trivalent iron within the sensitivity of the method [30]. When cooling below the Néel temperature, T_N, the Mössbauer spectrum transforms from doublet to sextet [7, 14, 21, 31]. This transformation is accompanied by a dramatic decrease of the magnitude η of doublet intensity normalized to its value at 300 K (Fig. 9.7). This abrupt drop in the temperature dependence of
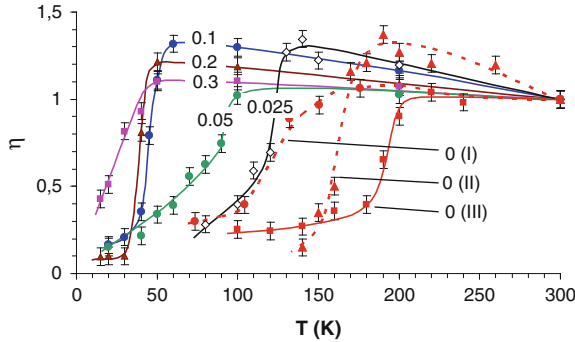
Fig. 9.7 Temperature dependences of η-maximal intensity of the doublet in Mössbauer spectrum related to its value at 300 K for some Li-doped PFT–xPT compositions. Numbers at the curves correspond to x values; 0(I) and 0(II)—Li-doped PFT ceramics sintered at different temperatures [21]; 0(III)—PFT powder, used for X-ray studies

η allows one to obtain T_N from the Mössbauer experiment. This method was successfully used previously to determine values of T_N in several multiferroics and their solid solutions and the results obtained were very similar to the data obtained by traditional methods such as the magnetization or magnetic susceptibility measurements (see [21, 31] and references therein). Li-doping is known to stimulate the compositional ordering in ternary $PbB_{0.5}^{3+}Nb_{0.5}O_3$ perovskites [32]. Such ordering may decrease dramatically the T_N values due to reducing the number of the neighboring magnetic Fe^{3+} ions around the given Fe^{3+} ion. Indeed, Li-doped PFT ceramics, exhibit a large scatter of T_N values, depending on the sintering temperature (curves 0(I) and 0(II) in Fig. 9.7). This scatter can also originate from the changes in the degree of Fe clustering in the lattice [14]. Ceramics sintered at high enough temperature, usually have $T_N \approx$ 160–170 K which corresponds well to the majority of the data published for PFT [6, 22]. The largest $T_N \approx$ 180–190 K was observed for PFT powder (curve 0(III) in Fig. 9.7) used for X-ray studies. It is worth noting this T_N value coincides well with the temperature at which the minimum in the $\beta(T)$ dependence is observed for the same PFT powder (inset in Fig. 9.1). At the same temperature one can see some small anomalies in the temperature dependence of the monoclinic unit cell parameters (Fig. 9.1, curves 1–3), however these anomalies are within the experimental error. It seems that the minimum in the $\beta(T)$ dependence and tiny anomalies of unit cell parameters are due to the magnetoelastic coupling which is believed to maximize in the vicinity of T_N. Note, that anomalies in the temperature dependence of the unit cell parameters in the vicinity of T_N have been already observed in PFN ceramics [33].

There are a lot of literature data on the temperature dependences of magnetization (M) for PFN and PFT single crystals and ceramics [1, 6, 8, 10, 11, 22]. These dependences were also reported for PFN–xPT single crystals [8] and ceramics [11] in the composition range $0 \le x \le 0.2$ and $0 \le x \le 0.15$, respectively. In the present work we studied the $M(T)$ dependences for Li-doped PFT–xPT ceramics
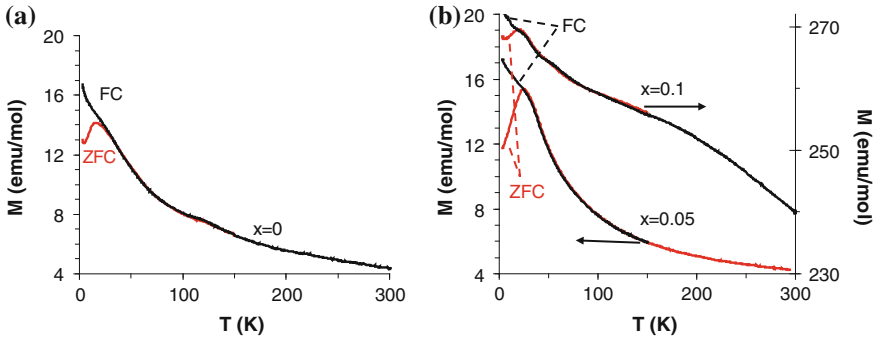
Fig. 9.8 Temperature dependences of magnetization M measured under a magnetic field of 1 kOe in the ZFC and FC modes for Li-doped PFT–xPT ceramics: **a** $x = 0$; **b** $x = 0.05$ and $x = 0.1$

(Fig. 9.8). For this ceramics, the $M(T)$ dependence is very similar to the one observed for PFN and PFT single crystals: during heating under a magnetic field of 1 kOe after zero field cooling (ZFC) it has a maximum at 16 K (Fig. 9.8a). Besides this maximum there is also a bump on the $M(T)$ curve at about 130 K corresponding to AFM–PM transition. As was already mentioned above, the T_N values of Li-doped PFT ceramics are often lower than those of undoped ceramics and single crystals due to possible partial ordering or/and a change in the degree of Fe-ions clustering. The $M(T)$ dependence measured in the field-cooled (FC) mode nicely coincides with the one measured in the ZFC mode except a low-temperature region where the FC curve does not show a maximum. Such a difference between the $M(T)$ curves measured in the ZFC and FC modes is typical of a spin-glass state [2, 8]. For compositions with $x \geq 0.05$ only the low-temperature maximum is observed in the $M(T)$ curves measured in the ZFC mode (Fig. 9.8b). This is typical of solid solutions of multiferroics, where a small bump corresponding to T_N duffuses and finally disappears on increasing the concentration of the nonmagnetic component [8, 11]. For example in the PFN–xPT ceramics a bump corresponding to T_N is observed only for compositions with $x \leq 0.04$ [11]. However the anomalies of the doublet intensity in the Mössbauer spectrum are well seen for all the PFN–xPT and PFT–xPT compositions studied (Fig. 9.7). One of the samples ($x = 0.1$) exhibited unusually high M values which were more than an order of magnitude larger as compared to the other compositions studied. Both the ZFC and FC $M(T)$ curves of this sample were much more diffused than the ones for the other samples studied. Moreover the PFT–0.1PT sample exhibited the well-defined magnetic hysteresis $M(H)$ loops even at room temperature. It is worth noting that very similar M values as well as $M(T)$ and $M(H)$ dependences were reported recently for PFT ceramic sample studied in [6]. We suppose that such unusual behavior is due to the presence in the PFT–xPT sample with $x = 0.1$ a small quantity of ferromagnetic impurity, presumably $PbFe_{12}O_{19}$.

In the PFT–xPT compositions studied, the temperature T_g of the $M(T)$ maximum at first increases with x but at larger x values begins to decrease (Fig. 9.9). It
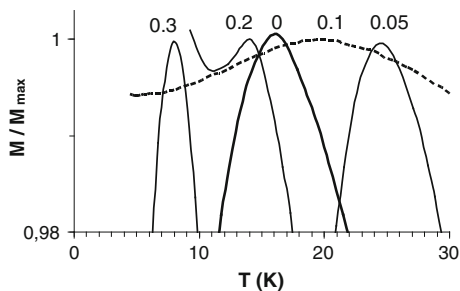
Fig. 9.9 Temperature dependences of magnetization M normalized to its maximal value M_{max} for Li-doped PFT–xPT ceramics. Measurements were carried out under a magnetic field of 1 kOe in the ZFC mode. Numbers at the curves correspond to x values
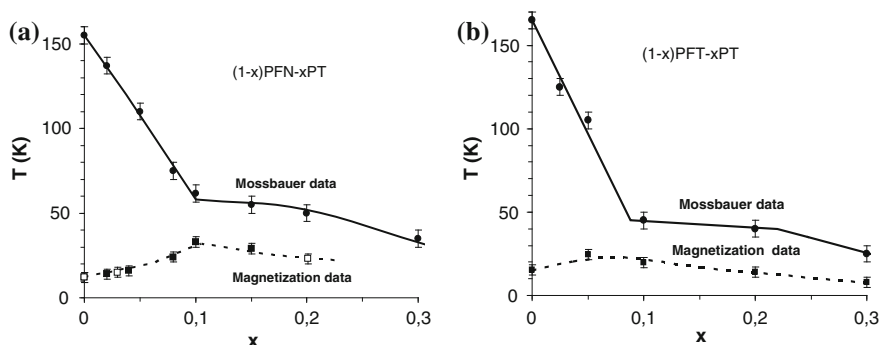

Fig. 9.10 Compositional dependences of the temperatures of $\eta(T)$ anomaly (*filled circles*, *solid lines*) and the maximum of the $M(T)$ dependence in the ZFC mode (*squares*, *broken lines*) for PFN–xPT and PFT–xPT ceramics. Magnetization data for PFN–xPT are plotted using the data of [11] for ceramics (*filled squares*) and [8] for single crystals (*open squares*)

is worth noting that a similar increase of T_g was observed previously in the PFN–xPT ceramics in the $x < 0.1$ compositional range [11]. This increase was attributed to a slight decrease of the lattice parameter with x and a subsequent increase of the magnetic coupling. However the similar character of the $T_g(x)$ dependence was observed in the PFN–xBaFN solid solution system, where the lattice parameter increases with x [8]. We suppose that the observed increase of T_g in both PFN–xPT and PFT–xPT solid solution systems is a result of the increase of the average size of the confined percolation clusters, with x, because of the decrease of strength of the infinite cluster [8].

The results of Mössbauer and magnetization studies for both PFN–xPT and PFT–xPT solid solution systems are summarized in Fig. 9.10. According to Mössbauer data at $x < 0.1$, T_N rapidly decreases as x grows. Lowering of T_N with x in both systems is quite expectable due to dilution of the magnetic subsystem. However above a certain compositional threshold ($x \approx 0.1$) fast lowering of T_N with the increase of the Ti concentration stops and a new magnetic state with

comparatively high (~ 50 K) transition temperature becomes stable in a rather wide compositional range (Fig. 9.10). According to magnetization data, in this compositional range ($x > 0.1$) the magnetic state is a spin-glass-like. In both PFN–xPT and PFT–xPT systems, the T_g values are lower by about 20 K than the temperatures of magnetic phase transition determined from the Mössbauer studies. This difference seems to be caused by the fact that the upper limit of the spin relaxation rates in these samples is above the characteristic Mössbauer time [34]. Similar behavior was reported e.g. for $PbFe_{12-x}Cr_xO_{19}$ hexaferrites [35].

9.4 Summary

In summary, highly-resistive Li-doped $(1-x)PbFe_{0.5}B_{0.5}O_3$–$(x)PbTiO_3$ ($B = $ Nb, Ta) ceramics were obtained by conventional sintering with high density and pure perovskite phase. Dielectric, X-ray, Mössbauer and magnetization studies of ceramics with the $0 < x < 0.3$ composition range have been carried out. Addition of $PbTiO_3$ to $PbFe_{0.5}B_{0.5}O_3$ increases the temperature T_m of the permittivity maximum, decreases the diffusion of this maximum and lowers the Neél temperature T_N. However above a certain compositional threshold ($x \approx 0.1$) fast lowering of T_N stops and a new magnetic state stable in a rather wide compositional range appears. Large difference between the zero-field cooled and field-cooled magnetization curves as well as between the temperatures of magnetic phase transition determined from Mössbauer and magnetization studies for compositions with $x > 0.1$ implies that this state is a spin glass phase.

We suppose that both the maximum of the $T_g(x)$ dependence and a sharp change of the slope of $T_N(x)$ dependence at $x \approx 0.1$ are the fingerprints of a percolation phase transition in the $(1-x)PbFe_{0.5}B_{0.5}O_3$–$(x)PbTiO_3$ solid solution systems. As soon as such a (geometrical) phase transition is a critical phenomenon, one may expect an enhancement of all physical responses in the crystal matrix, and, in particular, the enhancement of the magnetoelectric response.

References

1. V.A. Bokov, I.E. Mylnikova, G.A. Smolenskii, Sov. Phys. JETP. **15**, 447 (1962)
2. W. Kleemann, V.V. Shvartsman, P. Borisov, A. Kania, Phys. Rev. Lett. **105**, 257202 (2010)
3. I.P. Raevskii, V.V. Eremkin, V.G. Smotrakov, M.A. Malitskaya, S.A. Bogatina, L.A. Shilkina, Kristallogr. Rep. **47**, 1007 (2002)
4. N. Lampis, P. Sciau, A.G. Lehmann, J. Phys.: Condens. Matter **12**, 2367 (2000)
5. N. Lampis, C. Franchini, G. Satta, A. Geddo-Lehmann, S. Massidda, Phys. Rev. B **69**, 064412 (2004)

6. R. Martinez, R. Palai, H. Huhtinen, J. Liu, J.F. Scott, R.S. Katiyar, Phys. Rev. B **82**, 134104 (2010)

7. I.P. Raevski, S.P. Kubrin, S.I. Raevskaya, S.A. Prosandeev, M.A. Malitskaya, V.V. Titov, D.A. Sarychev, A.V. Blazhevich, I.N. Zakharchenko, IEEE Trans. Ultrason. Ferroelect. Freq. Contr. **59**, 1872 (2012)

8. V.V. Laguta, M.D. Glinchuk, M. Marysko, R.O. Kuzian, S.A. Prosandeev, S.I. Raevskaya, V.G. Smotrakov, V.V. Eremkin, I.P. Raevski, Phys. Rev. B **87**, 064403 (2013)

9. D.A. Sanchez, N. Ortega, A. Kumar, G. Sreenivasulu, R.S. Katiyar, J.F. Scott, D.M. Evans, M. Arredondo-Arechavala, A. Schilling, J.M. Gregg, J. Appl. Phys. **113**, 074105 (2013)

10. A. Falqui, N. Lampis, A. Geddo-Lehmann, G. Pinna, J. Phys. Chem. B **109**, 22967 (2005)

11. S.P. Singh, S.M. Yusuf, S. Yoon, S. Baik, N. Shin, D. Pandey, Acta Mater. **58**, 5381 (2010)

12. G.-M. Rotaru, B. Roessli, A. Amato, S.N. Gvasaliya, C. Mudry, S.G. Lushnikov, T.A. Shaplygina, Phys. Rev. B **79**, 184430 (2009)

13. H. Schmid, Ferroelectrics **162**, 317 (1994)

14. I.P. Raevski, S.P. Kubrin, S.I. Raevskaya, D.A. Sarychev, S.A. Prosandeev, M.A. Malitskaya, Phys. Rev. B **85**, 224412 (2012)

15. V.V. Laguta, J. Rosa, L. Jastrabik, R. Blinc, P. Cevc, B. Zalar, M. Remskar, S.I. Raevskaya, I.P. Raevski, Mater. Res. Bull. **45**, 1720 (2010)

16. V.M. Yudin, A.G. Tutov, A.B. Sherman, V.A. Isupov, Izv. Akad. Nauk SSSR Ser. Fiz. **31**(11), 1798 (1967) (In Russian)

17. I.P. Raevskii, S.T. Kirillov, M.A. Malitskaya, V.P. Filippenko, S.M. Zaitsev, L.G. Kolomin, Izv. AN SSSR. Neorg. Mater. **24**, 286 (1988) (In Russian) [English translation: Inorg. Mater. **24**, 217 (1988)]

18. V.Y. Shonov, I.P. Raevski, A.A. Bokov, Zhurnal Tekhnicheskoi Fiziki. **66**, 98 (1996) (In Russian) [English translation: Tech Phys. **41**, 166 (1996)]

19. I.P. Raevski, S.P. Kubrin, S.A. Kovrigina, S.I. Raevskaya, V.V. Titov, A.S. Emelyanov, M.A. Malitskaya, I.N. Zakharchenko, Ferroelectrics **397**, 96 (2010)

20. Bruker AXS TOPAS V4, *General Profile and Structure Analysis Software for Powder Diffraction Data* (User's Manual, Bruker AXS, Karlsruhe, Germany, 2008)

21. I.P. Raevski, S. Kubrin, S.I. Raevskaya, V.V. Stashenko, D.A. Sarychev, M.A. Malitskaya, M.A. Seredkina, V.G. Smotrakov, I.N. Zakharchenko, V.V. Eremkin, Ferroelectrics **373**, 121 (2008)

22. S. Nomura, H. Takabayashi, T. Nakagawa, Jpn. J. Appl. Phys. **7**, 600 (1968)

23. W.Z. Zhu, A. Kholkin, P.Q. Mantas, J.L. Baptista, J. Eur. Ceram. Soc. **20**, 2029 (2000)

24. F. Chu, N. Setter, A.K. Tagantsev, J. Appl. Phys. **74**, 5129 (1993)

25. I.P. Raevski, V.V. Eremkin, V.G. Smotrakov, E.S. Gagarina, M.A. Malitskaya, Fizika Tverd. Tela. **42**, 154 (2000) (In Russian) [English translation: Phys. Solid State **42**, 161 (2000)]

26. A.A. Bokov, Y.-H. Bing, W. Chen, Z.-G. Ye, S.A. Bogatina, I.P. Raevski, S.I. Raevskaya, E.V. Sahkar, Phys. Rev. B **68**, 052102 (2003)

27. E.I. Sitalo, I.P. Raevski, A.G. Lutokhin, A.V. Blazhevich, S.P. Kubrin, S.I. Raevskaya, Y.N. Zakharov, M.A. Malitskaya, V.V. Titov, I.N. Zakharchenko, IEEE Trans. Ultrason. Ferroelect. Freq. Contr. **58**, 1914 (2011)

28. S.Y. Cho, J.S. Kim, M.S. Jang, J. Electroceram. **16**, 369 (2006)

29. A.A. Bokov, H. Luo, Z.-G. Ye, Mater. Sci. Engin. B **120**, 206 (2005)

30. A.T. Kozakov, A.G. Kochur, K.A. Googlev, A.V. Nikolsky, I.P. Raevski, V.G. Smotrakov, V.V. Yeremkin, J. Electron Spectrosc. Relat. Phenom. **184**, 16 (2011)

31. I.P. Raevski, S.P. Kubrin, S.I. Raevskaya, V.V. Titov, D.A. Sarychev, M.A. Malitskaya, I.N. Zakharchenko, S.A. Prosandeev, Phys. Rev. B **80**, 024108 (2009)

32. A.A. Bokov, V.Y. Shonov, I.P. Rayevsky, E.S. Gagarina, M.F. Kupriyanov, J. Phys. Condens. Matter. **5**, 5491 (1993)

33. S.P. Singh, D. Pandey, S. Yoon, S. Baik, N. Shin, Appl. Phys. Lett. **90**, 242915 (2007)

34. I.A. Campbell, Hyperfine Interact. **27**, 15 (1986)

35. G. Albanese, B.E. Watts, F. Leccabue, S. Diaz Castanon, J. Magn. Magn. Mater. **184**, 337 (1998)

Chapter 10
Characteristics of Schottky Tunneling Barrier InP MOSFET with TiO_2/Al_2O_3 as Gate Oxides

Yong-Cheng Lu, Chih-Feng Yen, Jung-Chan Lee, Hao Cheng, Tzu-Hsien Tang and Ming-Kwei Lee

The characteristics of Schottky tunneling barrier diodes and corresponding MOSFET with atomic layer deposited TiO_2/Al_2O_3 stacked gate oxides were investigated. The Schottky barrier height is lowered from Schottky tunneling barrier. For Schottky tunneling barrier MOSFET with TiO_2/Al_2O_3 gate oxides, good drain current-voltage and sub-threshold characteristics were obtained. This enhancement mode MOSFET has fairly good gate control and low gate leakage. The drain current is 18 μA/μm at $V_{DS} = 3$ V, $V_{GS} = 2$ V.

10.1 Introduction

Due to higher electron mobility compared with Si, much attention has been focused on Indium Phosphide (InP) high-speed devices. Usually, the metal-semiconductor field effect transistor (MESFET) is the main structure of InP high-speed devices. However, the MESFET lacks stable and high quality oxides and therefore suffers from a high gate current of Schottky contact under a positive bias of several tenths of a volt, which severely limits the maximum drain current, noise margin and flexibility of circuit design. The metal-oxide-semiconductor field effect transistor (MOSFET) with an insulating gate layer has the potential to address these drawbacks.

Compared with MESFET, the gate insulating layer of metal-oxide-semiconductor field effect transistor (MOSFET) can improve these disadvantages. Gate dielectrics with low interface state density (D_{it}), and good thermal stability are essential for

Y.-C. Lu · C.-F. Yen · M.-K. Lee (✉)
Department of Electronic Engineering, Chung Yuan Christian University, Chung Li, 32023 Republic of China (Taiwan)
e-mail: mklee@cycu.edu.tw

J.-C. Lee · H. Cheng · T.-H. Tang
Department of Electrical Engineering, National Sun Yat-sen University, Kaohsiung, 80424 Republic of China (Taiwan)

high quality MOSFETs. Many high-k dielectrics, such as TiO_2 [1], Al_2O_3 [2] and HfO_2 [3] are currently being explored on InP substrate. TiO_2 has a relatively high dielectric constant (k value of 35–100) and MOSFET with high transconductance is expected. However, the thermionic emission of low band-gap TiO_2 (3.5 eV) [4] is high. The stack of a high band-gap Al_2O_3 (9 eV) under TiO_2 can improve it. In addition, Al_2O_3 has self-cleaning ability, and it can reduce interface density state (D_{it}) on oxide semiconductor interface.

Schottky barrier MOSFET can reduce short channel effects by ultra-shallow junction depth with Schottky contact [5]. And no latch-up phenomenon is induced by n-p-n and p-n-p structures in CMOS because it does not have diffusion p-n junctions. It also can promote quality of the gate oxides because of no high-temperature implant annealing.

But the Al/InP Schottky contact resistance is about of 2.1×10^9 Ω. It's much larger than conventional MOSFET. From previous studies, the Schottky barrier height can be reduced by inserting thin dielectric films, that would create dipoles from differences in the electronegativity (χ) or oxygen area density (σ) (number of oxygen atoms per unit area) of two materials [6]. In this study, the characteristics of InP MOSFET with Al_2O_3/TiO_2 gate oxides and source and drain Schottky tunneling barrier of Al_2O_3/TiO_2 were investigated.

10.2 Experimental

Zinc (Zn)-doped p-type InP (100) with a carrier concentration of 5×10^{16} cm^{-3} was used as the substrate in this study. The InP substrate was degreased in solvent and followed by chemical etching in a solution (H_2SO_4: H_2O_2: $H_2O = 5 : 1 : 1$) for 3 min and then rinsed in deionized water. After cleaning, the InP substrate was immediately dipped into a $(NH_4)_2S$ solution for 40 min at 50 °C and then blown dry with nitrogen gas. After the $(NH_4)_2S$ treatment, the InP substrate was thermally annealed at 220 °C in a N_2 atmosphere for 10 min to desorb the excess of weakly bonded sulfide and ready for n-channel InP Schottky tunneling barrier MOSFET fabrication.

TiO_2 and Al_2O_3 were deposited by ALD on S-InP for Schottky tunneling barrier oxides then aluminum was evaporated on dielectric films.

The source and drain regions were defined by photolithography. Then, ALD-TiO_2/Al_2O_3 was deposited to be gate oxides, and evaporated Al as the gate electrode. The gate region was also defined by photolithography.

DC characteristics of MOS capacitor and the 8×100 μm^2 enhancement mode Schottky tunneling barrier InP MOSFET were measured by Agilent B1500A semiconductor device analyzer.

Fig. 10.1 Leakage current densities of TiO$_2$/InP, TiO$_2$/S-InP, TiO$_2$/Al$_2$O$_3$/InP and TiO$_2$/Al$_2$O$_3$/S-InP MOS structures
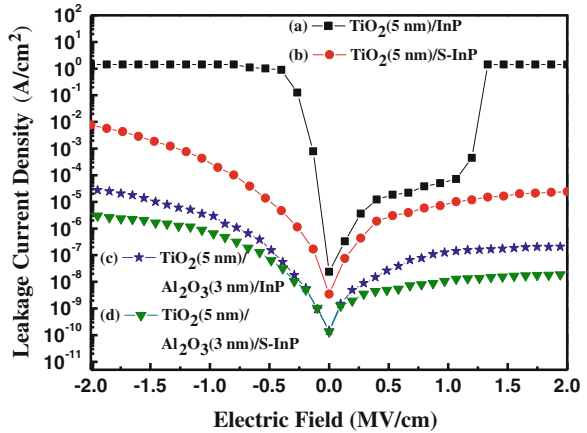
10.3 Results and Discussion

Figure 10.1 curve (a), (b) shows the leakage current of TiO$_2$ films on InP substrate without and with (NH$_4$)$_2$S treatment (identified as TiO$_2$/InP and TiO$_2$/S-InP, respectively). For TiO$_2$/InP, the leakage currents are 1.41 and 1.41 A/cm^2 at ± 2 MV/cm shown in curve (a). For TiO$_2$/S-InP, the leakage currents are obviously improved to 7.6×10^{-3} and 2.4×10^{-5} A/cm^2 at ± 2 MV/cm shown in curve (b). TiO$_2$/S-InP has the magnitudes of 3 and 5 orders improvements at the positive and negative biases, respectively.

Figure 10.2 shows the Schottky barrier MOSFET used Al as the source/drain. High Schottky barrier in on-state cause large source resistance, low drain current and small on-off ratio, and therefore need to lower Schottky barrier height in on-state, which can improve electrical characteristics in our study.

For enhancement mode devices, the I_D-V_D characteristic is induced by Schottky barrier changing and created the inversion channel. The transfer characteristics of MOSFET in Fig. 10.3 show an enhancement mode device with fairly good control and low gate leakage. The variation of drain current is a function of the drain voltage. The physical gate length is 8 μm and the channel width is 100 μm. Drain voltage varies from 0 to 1 V and the gate voltage varies from 0 to 2 V with 1 V step. The measured current-voltage characteristics show typical transistor behaviors. The saturation current at the gate of 2 V is 18 μA/μm. The high saturation current is attributed to the low parasitic source and drain resistance. The gate voltage varies from 0 to 2 V. The increase of the drain current is mainly attributed to the tunneling current component. Tunneling current dominates over the thermionic one as the gate voltage increases. This behavior originates from the decrease of the tunneling distance with the increase of drain voltage. If the barrier lowering is the major mechanism in the increase of drain current, the drain current should be determined by the thermionic current. But the drain current is mainly determined by the tunneling current. The increased tunneling current gives the

Fig. 10.2 I_D-V_D of e-mode
S-InP n-SB MOSFET with
ALD-TiO$_2$/Al$_2$O$_3$ as gate
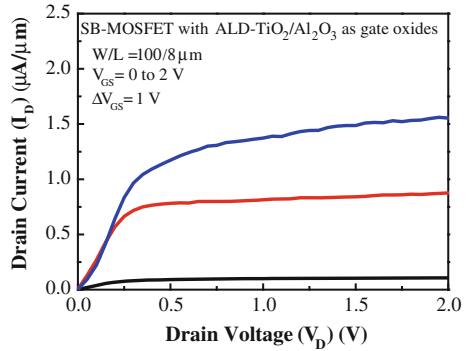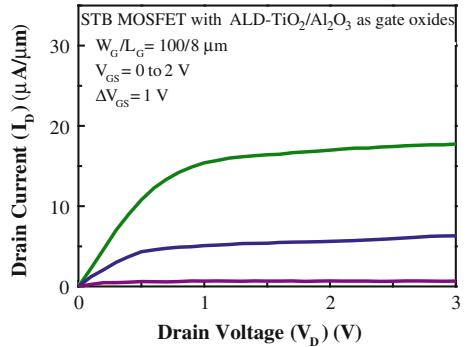oxides

Fig. 10.3 I_D-V_D of e-mode
S-InP n-STB MOSFET with
ALD-TiO$_2$/Al$_2$O$_3$ as gate
oxides

increase of drain current. Apparently, this phenomenon is similar with the drain
induced barrier lowering (DIBL) effect in conventional MOSFET. However, the
major mechanism of the increase of drain current is not only from the lowering of
Schottky barrier height but also the thinning of Schottky barrier thickness.

10.4 Conclusion

The (NH$_4$)$_2$S treatment is essential for III–V InP MOSFET fabrication. Al$_2$O$_3$ with
high bandgap and high k stacked on TiO$_2$ can reduce the leakage current and keep
relatively higher k value. Al$_2$O$_3$/TiO$_2$ bilayer dielectric Schottky diode is fabri-
cated on p-InP and the electrical characteristics are analyzed by using the I–V and
C–V measurements. The current of bilayer dielectric Schottky diode is greater than
Al Schottky diode for five orders. Schottky tunneling barrier MOSFET shows
larger drain current than Schottky barrier MOSFET. Obviously, the contact
resistance and the saturation current have been improved by tunneling barrier.

References

1. M.K. Lee, C.F. Yen, S.H. Lin, J. Electrochem. Soc. **154**(10), G229 (2007)
2. Y.Q. Wu, Y. Xuan, T. Shen, P.D. Ye, Z. Cheng, A. Lochtefeld, Appl. Phys. Lett. **91**(2), 022108 (2007)
3. Y. Hwang, R.E. Herbert, N.G. Rudawski, S. Stemmer, Appl. Phys. Lett. **96**(10), 102910 (2010)
4. S.A. Campbell, D.C. Gilmer, X.C. Wang, M.T. Hsieh, H.S. Kim, W.L. Gladfelter, J.H. Yan, IEEE Tran. Electron Devices **44**(1), 104 (1997)
5. S.M. Sze, K.K. Ng, *Physics of Semiconductor Devices*, 3rd edn. (Wiley, New York, 2006)
6. K. Kita, A. Toriumi, Appl. Phys. Lett. **94**, 132902 (2009)

Chapter 11
Influence of Magnetic Field on Thermoelectric Coefficient Value and Peltier Factor in InSb

G. Ya. Karapetyan, V. G. Dneprovski and P. C. Wu

The original setup for measuring effect of magnetic field on thermo EMF and the Peltier factor in InSb has been developed and fabricated. It has been shown that the magnetic field changes 7 times thermo EMF in InSb, and the Peltier factor at 5 %. It is also shown that in the circuit consisting of an electromagnet and a capacitor in the presence of the temperature gradient could be created continuous waves.

It is well known, that thermo EMF under the influence of magnetic fields may increase [1]. The paper [2–5] show, that thermo EMF in the InSb monotonically increases with increase of the magnetic field induction, does not depend on the sign, and at the fields of about 1 T it is observed saturation. Moreover, thermo EMF $\alpha(B)$ differs from the thermo EMF in zero field (α_0) on 20–40 µV/K at $\alpha_0 = 440$ µV/K. By creating a temperature gradient in the transverse magnetic field, in addition to a longitudinal electric field (thermal EMF), the transverse electric field (Nernst–Ettingshausen effect) and transverse gradient of temperatures (Righi-Leduc effect) arise. The electric field and temperature gradient are parallel one to other and perpendicular to the vector of the magnetic induction. As shown in [9], the transverse electric field is equal to 3 µV/cm at the room temperature and $B = 0.1$ T, and the transverse gradient of temperatures does not exceed of 10^{-3} K/cm.

For studies of this phenomenon, we have chosen the crystal of InSb. For the measurement of thermo EMF, the InSb sample was fabricated in the disc shape with diameter of 3 mm and thickness of 0.5 mm. It had gold–nickel electrodes, sprayed on the upper and lower surfaces of the disk. The sample was fixed between two copper rods, so that between the rods and the disc was a good thermal contact. One of the rods was connected to the heater, representing the spiral coiled on the

G. Ya. Karapetyan (✉) · V. G. Dneprovski
Vorovich Mechanics and Applied Mathematics Research Institute, Southern Federal University, Rostov-on-Don, Russia
e-mail: jorichkaka@yandex.ru

P. C. Wu
Nanoscience and Nanotechnology Center, National Chung Hsing University, Taichung, Taiwan
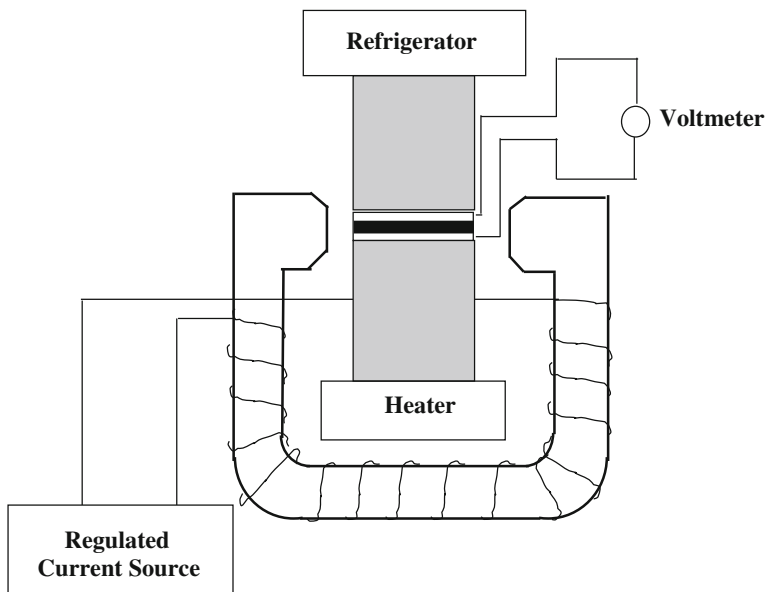
Fig. 11.1 Scheme of the experimental setup for measuring of the magnetic field influence on thermo EMF

rod through isolator, and other rod was connected to the Peltier cooler. In the gap between the rods, besides the InSb disc, the resistance thermometer was attached to measure the temperature and its changes. The rods together with the InSb disk were placed in the gap of the electromagnet, representing itself a coil with steel core. The electromagnet could rotate so that the orientation of the magnetic field changed relative to the crystallographic axes, remaining perpendicular to the gradient of temperature all the time as shown in Fig. 11.1.

The gradients of the electric field and the temperature were negligibly small in the gold–nickel electrodes because of low mobility of electrons and good thermal conductivity in metals. Due to this the gradients of the electric field and the temperature were shorted in the contact area of electrodes and they can be neglected. Thus, the longitudinal thermo EMF was only measured in this setup.

The following measurements were conducted:

(i) the dependence of thermo EMF from the orientation of the magnetic field relative to the crystallographic axes in the InSb specimen at constant magnitude of the magnetic field induction,

(ii) the dependence of thermo EMF on the magnetic field at which was observed maximal change of thermo EMF.

Upper and lower surfaces of InSb disc coincided with InSb planes (111). The disc cut was perpendicular to the x-axis. The dependence of thermo EMF from the magnetic field orientation is shown in Fig. 11.2 at $B = 0.1$ T. The measurements were carried out at the different signs of magnetic induction B, i.e. the orientation
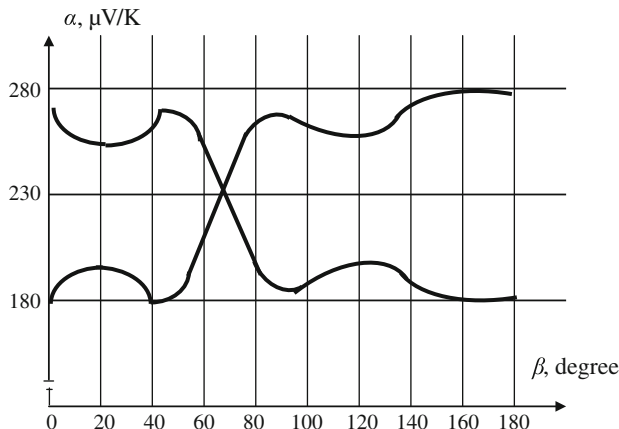
Fig. 11.2 Dependence of thermo EMF on orientation of the magnetic field at $B = 0.1$ T

of B changed by 180° at each angle considered between the direction B and crystallographic axes.

It was stated that thermo EMF depends significantly on the sign of B. Maximal change of thermo EMF was obtained when the vector of B was perpendicular to the cut on the InSb disc.

Figure 11.3 shows the dependence of thermo EMF on the magnetic field at the fixed orientation. As it can be seen from this dependence, α depends not only on magnitude, but also on the sign of B and is almost linear. The $\alpha_{\min} = 50$ μV/K (at $B = -0.25$ T), $\alpha_{\max} = 380$ μV/K (at $B = 0.25$ T), $\alpha(0) = 200$ μV/K.

Thus, under influence of the magnetic field, thermo EMF changed more than 7 times and increased almost 2 times compared to the thermo EMF at $B = 0$.

The experimental data, confirmed in the works [1, 7], differ significantly from the results obtained in the papers [2–5], which indicate that α does not depend on the sign of the field and changes in the fields of lesser than 2 T not more than 10–20 % (significant change of α occurs only in strong magnetic fields more than 5 T).

This fact can be explained, apparently, by the fact that in these works the measurements were carried out at temperatures below 160 K, while our measurements were carried out at the room temperature.
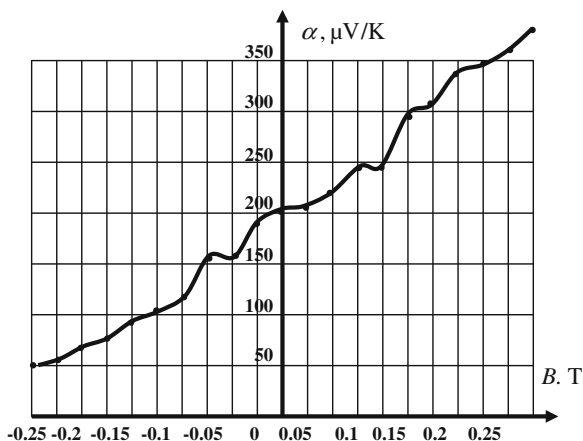
As it follows from the kinetic equations [6] under the assumption: $\nabla T_z = 0$, where ∇T_z is the temperature gradient, which is perpendicular to the electric field intensity E_x.

$$E_x = \nabla T_x \frac{\alpha'(1 + \mu^H B) + \beta' \mu^H B}{1 + (\mu^H B)^2}. \tag{11.1}$$

Then

$$\alpha = \frac{\alpha'(1 + \mu^H B) + \beta' \mu^H B}{1 + (\mu^H B)^2}, \tag{11.2}$$

Fig. 11.3 Dependence of
thermo EMF on the induction
of magnetic field

where μ^H is the mobility of electrons in the presence of magnetic field, α' is the thermo EMF without magnetic field, ∇T_x is the temperature gradient parallel to the electric field intensity E_x. From (11.2), it follows that $\alpha(B)$ depends on the sign of the magnetic induction B, i.e. the dependence of B follows from solution of the kinetic equations.

As it follows from (11.2), in the presence of temperature gradient, the specific thermo EMF α depended on the magnetic field significantly, but it did not subject to the expression of $\Pi = \alpha T$. This equation was valid for the thermo EMF with $B = 0$ ($\Pi = \alpha'/T$). Thus, the thermal EMF under influence of the magnetic field changed very strongly (almost 7 times), and the Peltier changed only slightly (as shown in [2] not more than 37 μV/K, i.e. not more than 10 %).

Therefore, in the case of a thermoelectric generator, the transmission of heat from the hot end to the cold due to the Peltier effect does not correspond to the maximum coefficient of thermo EMF. One is equal to coefficient of thermo EMF at the absence of magnetic field (Fig. 11.3), which is almost two times smaller, that lead to increased efficiency of the generator. Indeed, the useful electric power $W_{el} = \alpha \Delta T I$, where I is the current in the circuit, and the thermal power transferred is $W_{transmit} = \alpha'/(T_h - T_c)I = \alpha'/\Delta T I$. Then the ratio of these powers (excluding losses on heat conductivity) is equal to $\alpha/\alpha' = 1.75 > 1$, while in the absence of magnetic field, this ratio is equal to 1, that means increase of efficiency (at the absence of the losses caused by the thermal conductivity, the coefficient of efficiency would increase 1.75 times). In the case of a refrigerator arises a parasitic thermo EMF because of the temperature difference due to cooling. Therefore, it is necessary to select the value and sign of the magnetic field in such a way that thermo EMF would be minimal. Then the parasitic thermo EMF will decrease, that leads to reduction of power consumption. So for example, if magnetic field of 0.1 T is applied, thermal EMF decreases to 50 μV/K, while the Peltier effect, which responsible for the cooling, almost does not change. So the power, required to overcome the parasitic thermo EMF, reduces almost 5 times, that lead to a

considerable increase in the efficiency of the refrigerator, as the power, required to overcome the parasitic thermo EMF, is one of the main factors determining the refrigerator power consumption.

Thus, the application of a permanent magnetic field allows us to significantly improve the performance of thermoelectric devices, if semiconductor with high electron mobility is used, that leads to a strong dependence of thermo EMF on magnetic field.

Obviously, if the magnetic field is variable $B = B(t)$, then $\alpha(B)$ also depends on time. Since the time of electron scattering on the thermal phonons is the order of 10^{-11} s [8], then with every change of the magnetic field the new equilibrium distribution of electrons is also stated during this time. This means that change of thermo EMF with B will occur with a delay of 10^{-11} s. Therefore, at times of change of the magnetic field $\tau \gg 10^{-11}$ s, this delay can be neglected and consider changes of $\alpha(B)$ occurring synchronously with the changing magnetic field.

This assumption was checked by using setup, shown in Fig. 11.1, at supplying the sinusoidal voltage alternating with frequency of 50 Hz in electromagnet. In this case, the losses of hysteresis in the core of the electromagnet can be neglected.

Change of thermo EMF was observed in the screen of two-channel oscilloscope with high-impedance input. Change $B(t)$ was observed in the second channel. As expected, dependence $\alpha[B(t)]$ almost coincided with the form of the dependence $B(t)$. This confirmed a synchronization between $\alpha[B(t)]$ and $B(t)$. Some insignificant deviations are explained by the fact, that the dependence $\alpha(B)$ is slightly different from linear.

We further assume that the magnetic coil (see Fig. 11.1) connects in series with a thermocouple through the capacitor C. Thus, in series LC circuit arises. In this circuit, magnetic field changes total thermo EMF synchronously with current $i(t)$, flowing through the circuit, because $B(t) \sim i(t)$. The voltage on the thermal element is defined as $U_T = \alpha[B(t)]\Delta T$. Because the dependence $\alpha(B)$ is close to linear (see Fig. 11.3, solid line), then we can write $U_T = \alpha[B(t)]\Delta T = \gamma i(t)\Delta T + U_{T0}$.

Then the differential equation describing fluctuations in the circuit is

$$L\frac{d^2q}{dt^2} + R\frac{dq}{dt} + \frac{q}{C} = U_T(t) = U_{T\sim} + U_{T0}, \quad (11.3)$$

where q is the charge on the capacitor, therefore, $i(t) = \dfrac{dq}{dt}$ and (11.3) takes the form:

$$L\frac{d^2q}{dt^2} + R\frac{dq}{dt} + \frac{q}{C} = \gamma i(t)\Delta T + U_{T0}, \quad (11.4)$$

or

$$L\frac{d^2q}{dt^2} + (R - \gamma\Delta T)\frac{dq}{dt} + \frac{q}{C} = U_{T0}. \quad (11.5)$$

Obviously, the continuous oscillations will arise in the circuit at $R - \gamma\Delta T < 0$. Thus, by using thermocouples disposed in a magnetic field, we can directly obtain

AC. It is very convenient, because with the secondary winding can get voltage, and its value depends on the number of turns in the coil, i.e. voltage can change in wide limits. The magnetic field in the gap of electromagnet when $\mu \gg 1$ is determined by the formula:

$$B(t) \approx \frac{i(t)N\mu_0}{l}, \tag{11.6}$$

where N is the number of turns, l is the gap width, $\mu_0 = 12.56 \cdot 10^{-7}$ H/m. At $N = 1000$ и $l = 0.5 \cdot 10^{-3}$ m. Then

$$B(t) = i(t)\frac{1000 \cdot 12.56 \cdot 10^{-7}}{5 \cdot 10^{-3}} \approx 0.25 i(t)\, \text{T}. \tag{11.7}$$

As it follows from Fig. 11.3 the dependence $\alpha(B)$ can roughly consider as

$$\alpha(B) = 1520 \cdot B(t) + 200, \mu\text{V/K},$$

then $$U(t) = \Delta T(1520 \cdot 0.25 \cdot i(t) + 200) \times 10^{-6}$$
V $= \Delta T(380 \cdot i(t) + 200) \times 10^{-6}$ V.

Suppose that $\Delta T = 10\,°\text{C}$, then

$$U_T = [3800 \cdot i(t) + 2000] \times 10^{-6}\,\text{V} = [3.8 \cdot i(t) + 2] \times 10^{-3}\,\text{V}.$$

Then (11.3) takes the form:

$$L\frac{d^2q}{dt^2} + (R - 3.8 \cdot 10^{-3})\frac{dq}{dt} + \frac{q}{C} = 2 \cdot 10^{-3}\,\text{V}.$$

Evaluate the resistance of a circuit, which is composed mostly of resistance of an electromagnet winding, and losses on hysteresis can be neglected.

By using copper wire with cross-section of 0.2 mm^2 and $N = 1000$, we obtain resistance $R = 3.4\,\Omega$, i.e. $R \gg 3.8 \times 10^{-3}\,\Omega$. Therefore, in such circuit fluctuations do not arise. In order to the fluctuations appear, it is necessary to increase the temperature difference ΔT and apply the serial connection of thermocouples.

At $\Delta T = 100\,°\text{C}$ and number of thermocouples $n = 100$, we obtain $U(t) = 3.8 \cdot i(t)$ V, $R - 3.8\,\Omega < 0$, i.e. continuous oscillations arise in the circuit.

The frequency of oscillations is determined from the condition: $\omega_0 = \frac{1}{\sqrt{LC}}$. Due to appropriate selection of capacity C, it can be obtained the frequency of oscillation $f_0 = 50$ Hz. Then electromagnet inductance can be defined as

$$L \approx \frac{N^2 S \mu \mu_0}{\mu l_g + l_l},$$

where l_g is the gap width of magnetic circuit, l_l is the length of magnetic circuit.

If $S = 0.5$ cm^2 (square of the electromagnet cross-section), $\mu = 2000$, $l_g = 5$ mm, $l_l = 100$ mm, we obtain

$$L = \frac{12.56 \cdot 10^{-7} \text{H/m} \cdot 10^6 \cdot 0.5 \cdot 10^{-4} \text{m}^2 \cdot 2 \cdot 10^3}{2000 \cdot 5 \cdot 10^{-3} \text{m} + 0.1 \text{m}} = 1.24 \cdot 10^{-2} H = 12.4 \text{ mH}.$$

Finally, for $f_0 = 50$ Hz we have

$$C = \frac{1}{\omega_0^2 L} = \frac{1}{6.28^2 \cdot 1.24 \cdot 10^{-2} \cdot 2500} \approx 804.1 \mu\text{F}.$$

Since the magnetic field varies in time, it produces a vortex electric field in the disc of InSb, and therefore vortex EMF $E_{vort} = d\,\Phi/dt = \omega_0 B_0 S_{sec}$, where Φ is the magnetic flux, S_{sec} is the square of disc cross-section in the direction perpendicular to the magnetic field lines. At the frequency of 50 Hz for the disc with thickness of 0.5 mm and diameter of 3 mm, this voltage is approximately of 4 mV, which is much lesser than the thermo EMF at $\Delta T = 100°$, and vortex EMF can be neglected.

Thus, by using an electromagnet with a consistently connected capacity, and forming an oscillatory contour in the gap, which is the thermocouple, we can obtain directly alternating current in thermoelectric converters that is very important for many practical applications.

References

1. W. Ure Ronald, IEEE **51**(5), 702 (1963)
2. M.M. Gadgilaev, Izvestiya Vuzov, Ser. Phys. **3** (1993)
3. M.M. Gadgilaev, Tech. Phys. Lett. **34**(5), 541 (2000)
4. F.M. Gashimzade, A.M. Babaev, H.A. Hasanov, Solid State Phys. **43**(10), 1776 (2001)
5. M.M. Gadgilaev, Tech. Phys. Lett. **36**(3), 282 (2003)
6. P.S. Kireev, *Physics of Semiconductors* (Higher School, Moscow, 1969) (in Russian)
7. D.V. Gitzu, Thermoelectricity **2**, 13 (2000)
8. Weldok, IEEE **51**(5), 697 (1963)
9. G. Weiss, *Physics of Galvanomagnetic Semiconductor Devices and Their Application* (Energy, Moscow, 1974) (in Russian)

Part III
Mechanics of Advanced Materials

Chapter 12
Determination of Elastic and Dissipative Properties of Material Using Combination of FEM and Complex Artificial Neural Networks

A. N. Soloviev, N. D. T. Giang and S.-H. Chang

This paper describes the application of complex artificial neural networks (CANN) in the inverse identification problem of the elastic and dissipative properties of solids. Additional information for the inverse problem serves the components of the displacement vector measured on the body boundary, which performs harmonic oscillations at the first resonant frequency. The process of displacement measurement in this paper is simulated using calculation of finite element (FE) software ANSYS. In the shown numerical example, we focus on the accurate identification of elastic modulus and quality of material depending on the number of measurement points and their locations as well as on the architecture of neural network and time of the training process, which is conducted by using algorithms RProp, QuickProp.

A. N. Soloviev (✉) · N. D. T. Giang
Department of Strength of Materials, Don State Technical University, Rostov-on-Don, Russia 344000
e-mail: solovievarc@gmail.com

A. N. Soloviev
Vorovich Mechanics and Applied Mathematics Research Institute, Southern Federal University, Rostov-on-Don, Russia

A. N. Soloviev
Department of Mathematics, Mechanics and Computer Sciences, Southern Federal University, Rostov-on-Don, Russia

A. N. Soloviev
Department of Mechanics of Active Materials, Southern Scientific Centre of Russian Academy of Sciences, Rostov-on-Don, Russia

N. D. T. Giang
Department of Information Technology, Vietnam Maritime University, HaiPhong, Vietnam

S.-H. Chang
Department of Microelectronics Engineering, National Kaohsiung Marine University, Kaohsiung, Taiwan

12.1 Introduction

The artificial neural networks (ANN) [1] are widely used in different regions of science and industry. One of their applications in mechanics is solving the coefficient inverse problem of identifying elastic [2–6] and dissipative properties of solids [7–11]. In the early 1990s, the complex artificial neural networks (CANN) were proposed in the works of T. Nitta [12, 13], which then have been widely used for various applications [14–16]. The CANN parameters (weights, threshold values, inputs and outputs) are complex numbers, which used in various fields of modern technology, such as optoelectronics, filtering, imaging, speech synthesis, computer vision, remote sensing, quantum devices, spatial–temporal analysis of physiological neural devices and systems. Application of CANN in mechanics is a new research area, which has been developed over the last few years.

This paper describes the application of CANN in solving coefficient inverse problem of identifying elastic (Young's modulus) and dissipative (quality factor) properties of solids. Additional information for solving this inverse problem serves the components of the displacement vector measured at the boundary of the body (in a discrete set of points), which performs harmonic oscillations in the vicinity of the first resonant frequency. The process of displacement measurement in this paper is simulated using calculation of finite element (FE) software ANSYS. In the numerical example shown below, the accuracy of identifying mechanical properties of the material depends on the number of measurement points and their locations, as well as on the architecture of neural network and time of the training process (which is conducted by using algorithms CBP)

12.2 Formulation of Identification Inverse Problems for Mechanical Properties

In the plane problem of elasticity theory, the steady-state harmonic oscillations of a rectangular area ($a \times b$) with the angular frequency ω are considered (Fig. 12.1). The rectangle is fixed on the left side boundary S_u, the vertical force F_0 is applied to the lower right corner, the rest of the right boundary S_t is free from mechanical stresses. The mechanical properties of the material are described by Young's elastic modulus, E, Poisson's ratio, v, and quality factor, Q.
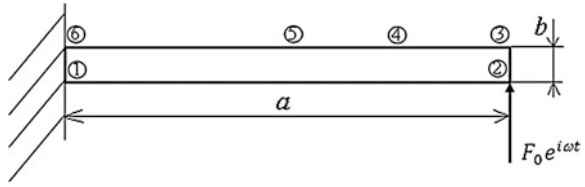
The vibration equations of the solid have the form [18]:

$$\sigma_{kj,j} = -\rho(\omega^2 - i\omega\alpha)u_k; \quad k, j = 1, 2;$$

$$\sigma_{kk} = c_{kj}(1 + i\omega\beta)\varepsilon_{jj}, \ \sigma_{12} = c_{44}(1 + i\omega\beta)\varepsilon_{12}, \ \varepsilon_{kj} = \frac{1}{2}\left(u_{k,j} + u_{j,k}\right). \tag{12.1}$$

The boundary conditions suppose the presence of a force at the point 2 (Fig. 12.1) and similar conditions in the rest of the boundary:

Fig. 12.1 Statement of the problem, the designations are interpreted into text

$$u_k\big|_{S_u} = 0, \quad \sigma_{kj}n_j\big|_{S_t} = 0. \tag{12.2}$$

The additional information to solve the inverse problem are the displacements, measured at the points 2–5 (Fig. 12.1):

$$u_1 = U_{mr} + iU_{mi}, \quad u_2 = V_{mr} + iV_{mi}, \quad m = 2, 3, 4, 5. \tag{12.3}$$

Here σ_{kj}, ε_{kj} are the stress and strain tensor components, respectively, ρ is the density. The elastic coefficients correspond to the isotropic body: $c_{11} = c_{22} = \lambda + 2\mu$, $c_{12} = c_{21} = \lambda$, $c_{44} = \mu$, λ, μ are the Lamé coefficients. The applied vibration frequency ω is matched with proper first resonance frequency, which does not take into account the dissipation of mechanical energy. Coefficients α, β characterize dissipation calculated according to the method [17].

12.3 Structure of CANN

Structure of CANN in solving coefficient inverse problem of identification of the elastic (Young's modulus) and dissipative (quality factor) properties of solids (Fig. 12.2).

This CANN is formed in three layers, called the input layer, hidden layer, and output layer. Each of layers consists of one or more nodes, represented in the diagram by the small circles, as shown in Fig. 12.2. The lines between the nodes indicate the flow of information from one node to the next (with weights W, $\breve{W}$).

When neural networks are trained, they works basically in the following way.

(1) The first step in training a network is to initialize the network connection weights by small random values $(-1.0, 1.0)$.
(2) The input pattern $(X_1 = X_{1r} + iX_{1i}, X_2 = X_{2r} + iX_{2i}, X_n = X_{nr} + iX_{ni})$ on the base of which the network will be trained are presented at the input layer of the net and the net is run normally to see what output pattern it actually produces.
(3) The actual output pattern are compared to the desired output pattern for corresponding input pattern. The differences between actual and desired patterns form the error pattern:
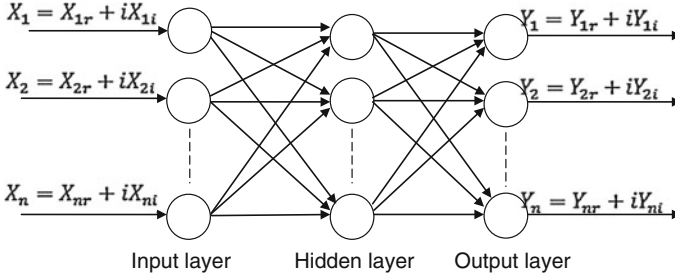
$$Y_n = \sum_m W_{nm}X_m = X + iY = Z; \tag{12.4}$$

$X_1 = X_{1r} + iX_{1i}$

$X_2 = X_{2r} + iX_{2i}$

$X_n = X_{nr} + iX_{ni}$

$Y_1 = Y_{1r} + iY_{1i}$

$Y_2 = Y_{2r} + iY_{2i}$

$Y_n = Y_{nr} + iY_{ni}$

Input layer   Hidden layer   Output layer

Fig. 12.2 Structure of CANN

$$O_n = F_c(z) = F(x) + iF(y) = \frac{1}{1 + \exp(-X)} + i\frac{1}{1 + \exp(-Y)}; \qquad (12.5)$$

$$Ep = \left(\frac{1}{N}\right) \sum_{n=1}^{N} |T_n - O_n|^2$$
$$= \frac{1}{2} \sum_{n=1}^{N} \left(|Re(T_n) - Re(O_n)|^2 + |Im(T_n) - Im(O_n)|^2\right), \qquad (12.6)$$

where W_{nm} is the (complex-valued) weight connecting neuron n and m, X_m is the (complex-valued) input signal from neuron m, F is the sigmoid function, Ep is the square error for the pattern p, O_n are the output values of the input neuron, T_n is the target pattern.

(4) The error pattern is used to adjust the weights on the output layer so that the error pattern reduced the next time if the same pattern was presented at the inputs:

$$W_{nm} = W_{nm} + \Delta W_{nm} = W_{nm} + \overline{H_m}\Delta\lambda_n; \qquad (12.7)$$

$$\Delta\lambda_n = \varepsilon\{Re[\delta^n](1 - Re[O_n])Re[O_n] + iIm[\delta^n](1 - Im[O_n])Im[O_n]\}, \qquad (12.8)$$

where λ_n is the threshold value of the output neuron n, $\delta^n = T_n - O_n$ is the difference (error) between the actual pattern and the target pattern, H_m are the output values of the hidden neuron.

(5) Then the weights of the hidden layer are adjusted similarly, it is stated in this time what they actually produce the neurons in the output layer to form the error pattern for the hidden layer:

$$\breve{W}_{lm} = \breve{W}_{lm} + \Delta\breve{W}_{lm} = \breve{W}_{lm} = \overline{I_l}\Delta\theta_m; \qquad (12.9)$$

$$\begin{aligned}
\Delta\theta_m = &\varepsilon\{(1 - Re[H_m])Re[H_m] \sum_n (Re[\delta^n](1 - Re[o_n]) Re[W_{nm}] \\
&+ Im[\delta^n](1 - Im[o_n])Im[o_n]Im[W_{nm}])\} - i\varepsilon\{(1 \\
&- Im[Hm])Im[Hm] \sum_n (Re[\delta^n](1 - Re[o_n])Re[o_n]Im[W_{nm}] \\
&- Im[\delta^n](1 - Im[o_n])Im[o_n]Re[W_{nm}])\}
\end{aligned} \qquad (12.10)$$

Table 12.1 Data from problem of modal and harmonic analysis using ANSYS

No	Input data		ω	Output data (m)			
	E (Pa)	Q		U_{2r}	U_{2i}	V_{2r}	V_{2i}
1	5×10^9	10	206.35	4.82×10^{-7}	-5.2×10^{-6}	1.09×10^{-6}	-7.3×10^{-5}
2	10×10^9	20	291.83	2.41×10^{-7}	-2.6×10^{-6}	5.46×10^{-7}	-3.6×10^{-5}
3	15×10^9	30	357.41	1.60×10^{-7}	-1.7×10^{-6}	3.64×10^{-7}	-2.4×10^{-5}
4	20×10^9	40	412.7	1.20×10^{-7}	-1.3×10^{-6}	2.73×10^{-7}	-1.8×10^{-5}
5	25×10^9	50	461.42	9.64×10^{-8}	-1×10^{-6}	2.18×10^{-7}	-1.5×10^{-5}
6	30×10^9	60	505.46	8.03×10^{-8}	-8.6×10^{-7}	1.82×10^{-7}	-1.2×10^{-5}
7	35×10^9	70	545.96	6.89×10^{-8}	-7.4×10^{-7}	1.56×10^{-7}	-1×10^{-5}
8	40×10^9	80	583.65	6.02×10^{-8}	-6.5×10^{-7}	1.36×10^{-7}	-9.1×10^{-6}
9	45×10^9	90	619.06	5.35×10^{-8}	-5.8×10^{-7}	1.21×10^{-7}	-8.1×10^{-6}
Etc.							

where $\breve{W}_{lm}$ is the weight between input neuron l and hidden neuron m, I_l are the output values of the input neuron l, θ_m is the threshold value of the hidden neuron m.

(6) The network is trained by presenting each input pattern in turn at the inputs and propagating forward and backward, followed by the next input pattern. Then this cycle is repeated many times. The training stops when any of these conditions occurs: the maximum number of epochs (repetitions) is reached or the error has an acceptable training error threshold.

After network training, a stable network structure is established. The network then can be used to predict output values from new input values, i.e. to solving coefficient inverse problem of identifying elastic and dissipative properties of solids.

12.4 Application of CANN to Solve Coefficient Inverse Problem for Identification of Elastic (Young's Modulus) and Dissipative (Quality Factor) Properties of Solids

In order to identify Young's modulus and quality factor as it was described above used CANN, in which they were output data. As input data, we used displacement amplitudes (12.3), measured on solid surfaces. By training the CANN with a set of input and output data, the first step of the computation process was calculation of natural resonance frequencies, and following definition of steady oscillations of the solid at these frequencies or in their neighborhood with the mechanical energy dissipation.

Figure 12.1 shows four points 2, 3, 4, 5, where displacement amplitudes were measured. The process of the displacement measurements is simulated using

Table 12.2 The results of training and testing for CANN with two and six input values at the different points (with the same number of epochs)

No	Number of data	CANN architecture	Epoch	Error	Accuracy (%)	Notes
1	2000	2-4-1	5000	0.01918	91.18	at the point 2
2	2000	2-4-1	5000	0.01856	93.52	at the point 3
3	**2000**	**2-4-1**	**5000**	**0.01853**	**93.88**	**at the point 4**
4	2000	2-4-1	5000	0.01872	92.95	at the point 5
5	2000	6-4-1	5000	0.01870	92.97	at the three points (x_1, y_1), (x_2, y_2), (x_3, y_3)
6	2000	6-4-1	5000	0.01883	93.64	for three frequencies (ω_{r-k}, ω_r, ω_{r+k}) at the point 2

Table 12.3 The results of training and testing for CANN with two input values at the point 4 (with different epochs)

No	Number of data	CANN Architecture	Epoch	Error	Accuracy (%)	Notes	Time (second)
1	2000	2-4-1	1000	0.02953	91.85	at the point 4	365.5
2	2000	2-4-1	5000	0.01853	93.88	at the point 4	1949.3
3	**2000**	**2-4-1**	**20000**	**0.01390**	**94.89**	**at the point 4**	**13735.5**

Table 12.4 The results of training and testing for CANN with two input values at the point 5 (with different numbers of hidden layers)

No	Number of data	CANN Architecture	Epoch	Error	Accuracy (%)	Notes	Time (second)
1	2000	2-2-1	1000	0.03012	89.72	at the point 5	269.5
2	**2000**	**2-4-1**	**1000**	**0.02653**	**91.85**	**at the point 5**	**365.5**
3	2000	2-6-1	1000	0.02955	89.50	at the point 5	476.5
4	2000	2-8-1	1000	0.02683	91.52	at the point 5	629.8
5	2000	2-10-1	1000	0.02761	91.20	at the point 5	739.1

Table 12.5 The results of training and testing for CANN with six input values at the points 3, 4, 5 (with different numbers of hidden layers)

No	Number of data	CANN architecture	Epoch	Error	Accuracy (%)	Notes	Time (second)
1	2000	6-2-1	1000	0.02485	91.17	at three points	364.6
2	2000	6-4-1	1000	0.02163	90.32	at three points	495.8
3	**2000**	**6-6-1**	**1000**	**0.02056**	**93.83**	**at three points**	**659.3**
4	2000	6-8-1	1000	0.02283	91.52	at three points	830.0
5	2000	6-10-1	1000	0.03763	85.89	at three points	3912.0

Fig. 12.3 Relationship between time of training and testing for CANN with different epochs
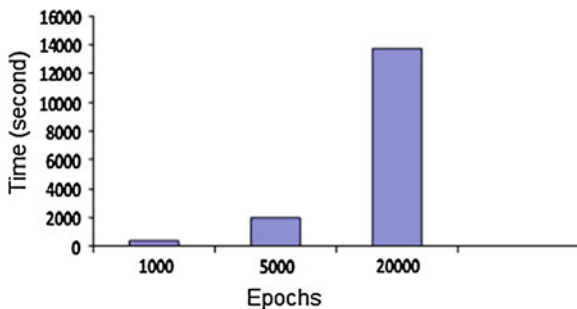
Fig. 12.4 Relationship between time of training and testing for CANN with different architecture
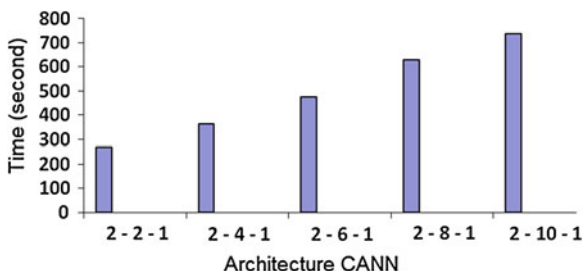
Fig. 12.5 Relationship between time of training and testing in CANN with different architecture
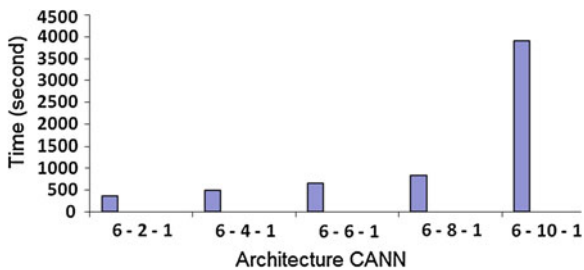
calculation of finite element software ANSYS. Table 12.1 presents the input and output data for the "measurement" at the point 2.

CANN has the following configuration in dependence on number of points and the frequency "measurement":

(i) at one measurement point and one frequency, this neural network consists of two neural input values: $U_{2r} + iU_{2i}$, $V_{2r} + iV_{2i}$ and one neural output value: $E + iQ$;

(ii) at one measurement point and three frequencies, this neural network consists of six neural input values: $U_{1r} + iU_{1i}$, $V_{1r} + iV_{1i}$, $U_{2r} + iU_{2i}$, $V_{2r} + iV_{2i}$, $U_{3r} + iU_{3i}$, $V_{3r} + iV_{3i}$ and one neural output value: $E + iQ$;

Fig. 12.6 Results of testing
E at the threshold error of
20 %
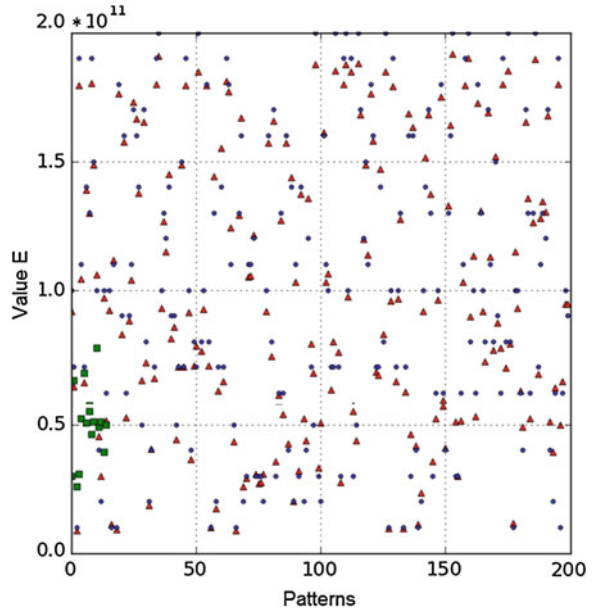
Fig. 12.7 Results of testing
Q at the threshold error of
20 %
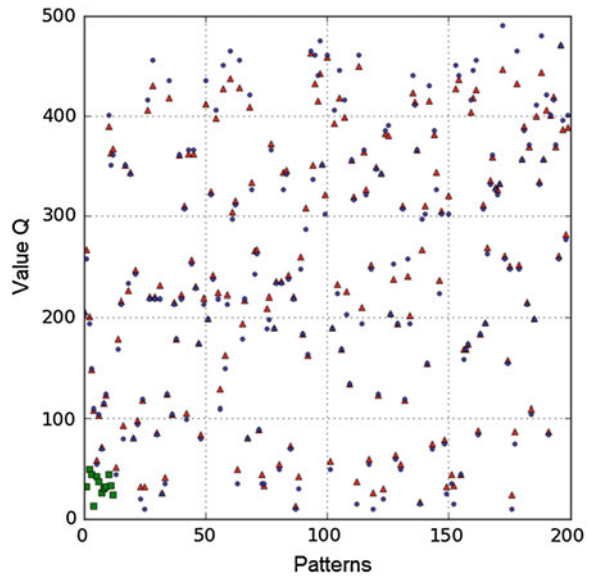
(iii) at three measurement points and one frequency, this neural network consists
of six neural input values: $U_{1r} + iU_{1i}, V_{1r} + iV_{1i},\ U_{2r} + iU_{2i}, V_{2r} + iV_{2i},$
$U_{3r} + iU_{3i}, V_{3r} + iV_{3i}$ and one neural output value: $E + iQ$.

Fig. 12.8 Results of testing *E* at the threshold error of 10 %
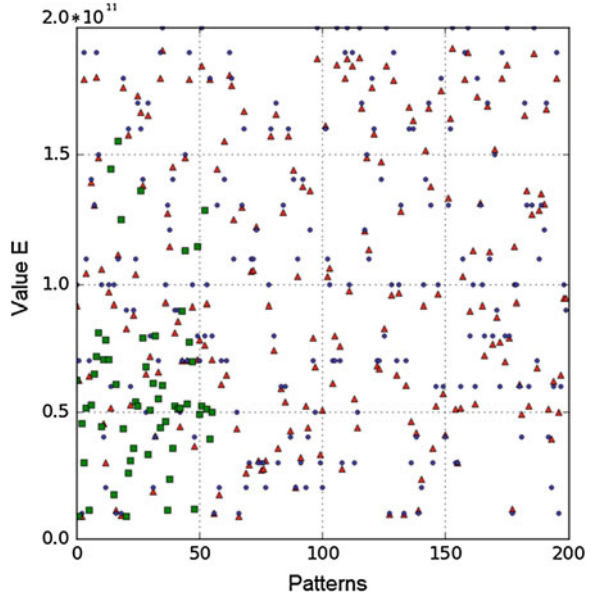
Fig. 12.9 Results of testing *Q* at the threshold error of 10 %
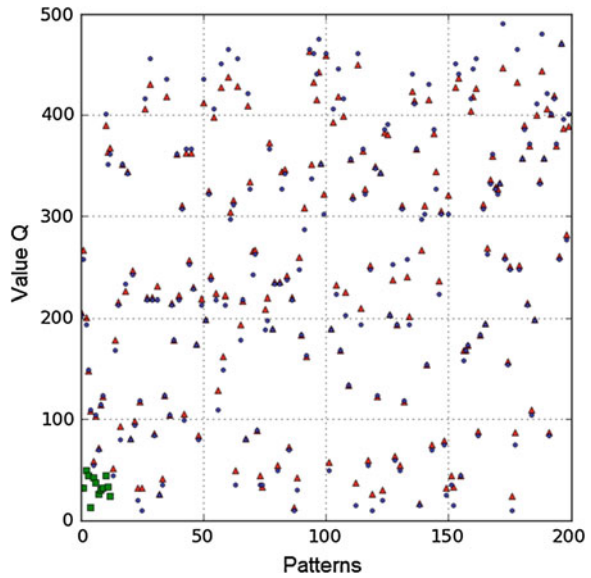
The results of the computer experiments, conducted by using CANN with 2000 patterns, in which, 1800 patterns were used for training and 200 for testing, are show in Tables 12.2, 12.3, 12.4 and 12.5.
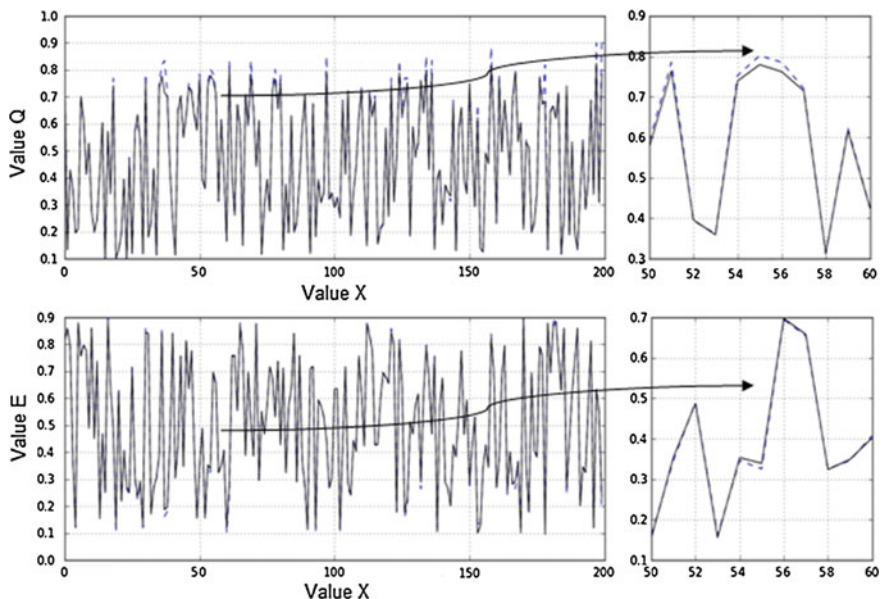
Fig. 12.10 Prediction of results obtained by using CANN

Fig. 12.11 Graph of training error
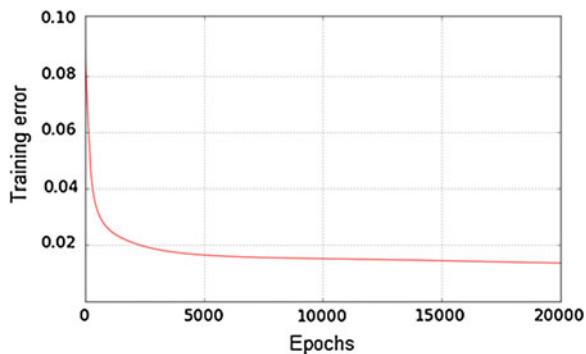
Time of training for CANN with different epochs (Table 12.3) is shown in Fig. 12.3. Time of training and testing for CANN with different number of neurons in hidden layer is shown in Fig. 12.4. The relationship between time of training and testing for CANN with different architecture is shown in Fig. 12.5 (data from Table 12.5).

Figures 12.6, 12.7, 12.8 and 12.9 show the results of testing with 200 patterns in CANN (with architecture 2-4-1, see Table 12.2, the row 3). The circles present the data of test E, triangles and squares describe the forecast data E_c, obtained by using

CANN. The relative errors δ_E, δ_Q are calculated in the forms: $\delta_E = |E_c - E|/E$, $\delta_Q = |Q_c - Q|/Q$. In this case, corresponding triangles and squares with the identification error no exceeding of 20 %, are shown in Figs. 12.6 and 12.7.

The similar results for threshold error of 10 % are shown in Figs. 12.8 and 12.9.

Figure 12.10 demonstrates the results of identification in dependence on number of test data in the form of two curves, the solid curves correspond to the required data, and the dashed lines define the forecast data obtained by using CANN. The graph of training error (12.6) with 20,000 epochs is shown in Fig. 12.11.

12.5 Conclusion

In this paper, we developed a method for determination of material elastic and dissipative properties by using data for harmonic oscillations on the resonance frequency based on a combination of the finite element method and CANN. The results of the experiments showed that CANN with one of the following architectures:

2 (input neurons)—4 (hidden neurons)—1 (output neuron)
or
6 (input neurons)—6 (hidden neurons)—1 (output neuron)

gives the best result of identification. The time expenses caused by the CANN training were also estimated in this paper. The developed method and computer program could be used to determine the dissipative properties on different frequencies (not only on the first one), as well as in anisotropic elastic solids.

References

1. H. Simon, *Neural Network a Comprehensive Foundation*, 2nd edn. (Prentice Hall, New Jersy, 1998)
2. A.A. Krasnoschekov, B.V. Sobol, A.N. Soloviev, A.V. Cherpakov, Russ. J. Nondestruct. Test. **6**, 67 (2011)
3. S.W. Liu, J.H. Huang, J.C. Sung, C.C. Lee, Comput. Methods Appl. Mech. Eng. **191**(4), 2831 (2002)
4. Hasan Temurtas, Feyzullah Temurtas, Expert Syst. Appl. **38**(4), 3446 (2011)
5. V. Khandetsky, I. Antonyuk, NDT&E Int. **35**, 483 (2002)
6. Y.G. Xu, G.R. Liu, Z.P. Wu, X.M. Huang, Int. J. Solids Struct. **38**(8), 5625 (2001)
7. P. Korczak, H. Dyja, E. Łabuda, J. Mater. Process. Technol. **80–81**(8), 481 (1998)
8. T. Mira, S. Zoran, L. Uros, Polymer **48**(8), 5340 (2007)
9. J. Ghaisari, H. Jannesari, M. Vatani, Adv. Eng. Softw. **45**(3), 91 (2012)

10. P. Iztok, T. Milan, K. Goran, Expert Syst. Appl. **39**(4), 5634 (2012)
11. Y. Sun, W. Zeng, Y. Han, X. Ma, Y. Zhao, P. Guo, G. Wang, Comput. Mater. Sci. **60**(7), 239 (2012)
12. T. Nitta, in *Proceedingsof the International Joint Conference on Neural Networks*, IEEE, p. 1649. Nagoya, 1993
13. T. Nitta, Neural Network **10**, 1391 (1997)
14. A. Hirose (ed.), *Complex-Valued Neural Networks: Theories and Applications*. The Series on Innovative Intelligence. (World Scientific, Singapore 2003)
15. C. Li, X. Liao, J. Yu, J. Comput. Syst. Sci. **67**, 623 (2003)
16. T. Nitta, *Complex-Valued Neural Networks: Utilizing High-Dimensional Parameters* (Information Science Reference, New York, 2009)
17. A.V. Belokon, A.V. Nasedkin, A.N. Soloviev, Appl. Math. Mech. **66**(3), 491 (2005)
18. W. Nowacki, *Theory of Elasticity* (MIR Publishers, Moscow, 1976). (in Russian)

Chapter 13
Study of Piezo-Excited Lamb Waves in Laminated Composite Plates

A. Karmazin, E. Kirillova, P. Syromyatnikov and E. Gorshkova

The solution of the wave propagation problem in plate-like composites in the case of excitation by *piezoelectric actuators* modelled using a pin-force model is obtained as a sum of propagating Lamb wave modes. It is calculated in the frequency-wavenumber domain and then transformed into the time–space domain. The harmonic wave responses of *composite plates* and corresponding energy flows are analyzed for various excitation sources at the surface of some composites.

13.1 Introduction

In recent years composites become to be widely used in civil, mechanical, and aerospace engineering due to their high strength and lightness in comparison with metals. Due to the sensitivity of composites to impact actions small damages in the form of cracks or delaminations are practically unavoidable. These small damages could potentially result in the destruction of the construction. In the field of *structural health monitoring* (SHM) [1] there has been a growing interest in the recent decade in developing computer-aided systems for the detection of mechanical defects and the forecasting of destruction [2] in composite structures. It is hoped that SHM systems will be able to regularly scan high-duty structural components (e.g. wind power rotor blades, aircraft panels and wings) and issue warnings concerning the formation of defects as well as provide an estimate of the remaining useful life. The use of SHM systems can increase safety and can allow

A. Karmazin · E. Kirillova (✉)
Department of Applied Mathematics, RheinMain University of Applied Sciences,
Kurt-Schumacher-Ring 18, 76185, Wiesbaden, Germany
e-mail: evgenia.kirillova@hs-rm.de

P. Syromyatnikov
South Scientific Center of Russian Academy of Sciences, Rostov-on-Don, Russia

E. Gorshkova
Kuban State University, Krasnodar, Russia

for a change of the maintenance procedure for aircraft from schedule-driven to condition-based, can reduce the fuel costs and the costs of maintenance significantly, and decrease the time required for the structure to be off-line [3].

One of the promising approaches for SHM consists of applying guided elastic waves since the waves excited or reflected by damages provide significant information on the nature and properties of the defect. An improved inspection potential of *guided waves* over other ultrasonic methods is due to their sensitivity to different type of flaws, their propagation over long distances and their capability to follow curvature and to reach hidden and/or buried parts. The level of understanding which has been reached in an application of elastic waves for NDT (non-destructive testing) and SHM is documented in review works [2] and [4], respectively. A clear understanding of quantitative connections between the waves and their sources is essential for the development of algorithms to detect defects. Moreover, information about the structure in its undamaged state is required since by relating the measured response with one in the same but undamaged structure allows the considerable improvements in the precision of quantitative damage detection. This is shown in case of the application of an approach based on damage influence maps in [5].

Due to the finite dimensions of structural components the waves reflect from the structural boundaries, i.e. the waves guide through the structure. Such structures in many cases can be considered as infinite layers (beams) or plates. The first numerical results which relate to the characteristics of normal waves in a layer can be found in Lamb's work [6]. He was the first to obtain a dispersion equation linking frequencies and wave numbers. Hence, the waves in layer-like and plate-like structures are usually called (guided) *Lamb waves*. Theoretical principles of wave propagation in isotropic, anisotropic and layered materials, as well as principles of wave excitation with standard ultrasonic transducers for nondestructive evaluation, are described in many works, e.g. in [7, 8]. The application of elastic waves for NDT was first studied by Viktorov [9]. However, in these works the waveguides are modelled in two dimensions (plane strain problem), i.e. it is assumed that waves are excited by sources whose distribution is infinitely expanded in the direction perpendicular to the cross-section. To accurately model finite source induced wave propagation in anisotropic composite plates, a 3D formulation is required [10]. *Dispersion relations* for waves in *multilayered media* with an arbitrary number of flat layers were derived for a plain strain (2D) problem using a transfer [11] and a global [12] matrix method and then extended by Nayfeh [13] to the case of 3D-models of composites in which the layers can have as low as monoclinic symmetry. Up to date, there are many methods for the computation of dispersion properties of laminated composites [14]. Analysis of dispersion properties of Lamb waves in anisotropic composites shows that in addition to the frequency dispersion the angular dispersion of waves should be taken into account. Moreover, some directions are privileged for the transport of energy of the guided waves, i.e. the waves are focussed [15].

Taking into account the dispersion properties of waves the problem of wave propagation excited by surface sources can be studied. For in situ monitoring of structures low-cost surface-coupled [1] or embedded piezoelectric actuators [5] are used. Due to the piezoelectric effect the wafers can be used not only as actuators

but also as sensors. The corresponding forced wave propagation problem can be resolved by applying direct numerical methods: conventional FEM [16], spectral FEM [5], strip element method (SEM) [14] and finite difference technique (FD) [17]. A good review of all these direct numerical approaches is given in [18]. The application of direct numerical methods for the modelling of constructions made of composites is the most universal approach, as these yield approximate solution for objects of any form. However, they are also the most expensive with regard to computational resources and do not take into account the wave structure of the solution. An increase in the number of elements is unavoidable in regions of rapid changes of the solutions or characteristics of the medium (angular points, inter-faces between contrast layers etc.) and especially in the case of high frequencies. In some papers the FEM is used only for that part of a construction which has a complex form and comparable sizes in all directions, whereas for the part of the construction which is a typical waveguide the solution is constructed as a sum of propagating waves using the mode expansion technique (NME) [19].

The most time-efficient approach for the simulation of piezo-excited wave propagation is the semi-analytical *integral approach*. The corresponding solutions of wave propagation problem are obtained for 2D-models for isotropic and anisotropic laminates [20] and 3D-models for isotropic laminates under excitation by axis-symmetric sources [21]. The solution of the general 3D-problem for anisotropic laminates is obtained for the far-field area of the excitation source [22] and well approximated for the middle field to the source [23] by applying the integral approach.

In this work the integral approach is used for time-efficient simulations of steady-state piezo-excited Lamb wave propagation in composites and for the investigation of the anisotropy-induced properties of guided waves by computing the peak-to-peak amplitude curves and the power flow corresponding to each Lamb wave mode.

13.2 Mathematical Background

13.2.1 Modeling of the Wave Propagation Problem

In the absence of body forces the *harmonic steady-state* motions in each layer of *composite plate* (Fig. 13.1) after omitting the factor $\exp(i\omega t)$ are expressed in terms of stress and displacement components:

$$\frac{\partial \sigma_{ij}}{\partial x_j} = -\rho\omega^2 u_i. \tag{13.1}$$

The stresses in (13.1) are found using Hooke's law:

$$\sigma_{ij} = C_{ijkl}\varepsilon_{kl}, \qquad \varepsilon_{ij} = \frac{1}{2}\left(u_{i,j} + u_{j,i}\right), \tag{13.2}$$

where C_{ijkl} are the components of the stiffness tensor.

Fig. 13.1 *N*-layered plate under an excitation by a ring-shaped source (inner radius A_i, outer radius A_o)
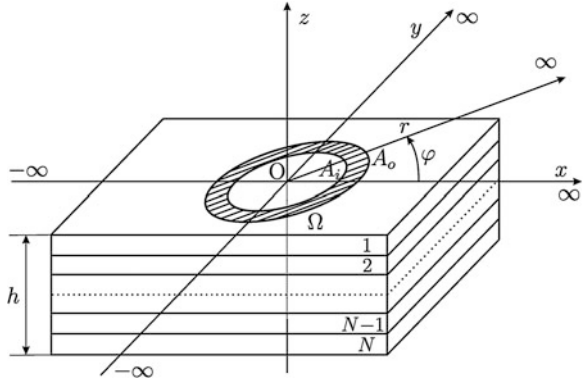
The waves are excited in a *laminated plate* by the force $q(x, y)$ applied in the domain Ω at the upper surface of the plate, whereas the lower boundary is traction-free:

$$\sigma_{i3}|_{z=0} = q(x, y), \qquad \sigma_{i3}|_{z=-h} = 0. \tag{13.3}$$

As surface excitation sources, a *circular* piezoelectric *actuator* (Fig. 13.2a), a *CLoVER sector* (Fig. 13.2b) and *MFC actuator* (Fig. 13.2c) are considered. A nearly ideal bonding of the actuators to the composite plate is assumed, i.e. the thickness of the glue layer is supposed to satisfy $h_b \to 0$ (see Fig. 13.3). The force is transferred over an infinitesimal region at the edges of the patch. The induced strain is assumed to be given by concentrated forces applied at the region ends. This model is also called the *pin-force model* [24] and was originally derived for isotropic structures under excitation by piezoelectric patches. However, this model proved itself applicable also in *3D-model*s of piezo-structure interaction and is therefore used in this work.

Then, the corresponding surface load vectors for the first two piezoactuators considered (Fig. 13.2a and b) are given as follows

$$q_x = \tau_0 \cdot q_r \cdot \cos \varphi, \quad q_y = \tau_0 \cdot q_r \cdot \sin \varphi, \quad q_z = 0, \tag{13.4}$$

where for a *circular actuator* (Fig. 13.2a) q_r is represented by

$$q_r = \delta(r - A_o), \quad \forall(r, \varphi), \tag{13.5}$$

and for a *CLoVER sector* (Fig. 13.2b) by

$$q_r = \delta(r - A_o) - \delta(r - A_i), \quad \forall r, \varphi \in [\varphi_R, \varphi_L], \tag{13.6}$$

respectively.

For *MFC actuator* (Fig. 13.2c) the load vector is given by

$$q_x = \tau_0[\delta(x - a_1) - \delta(x + a_1)], \quad q_y = 0, \quad q_z = 0, \quad y \in [-a_2, a_2] \tag{13.7}$$
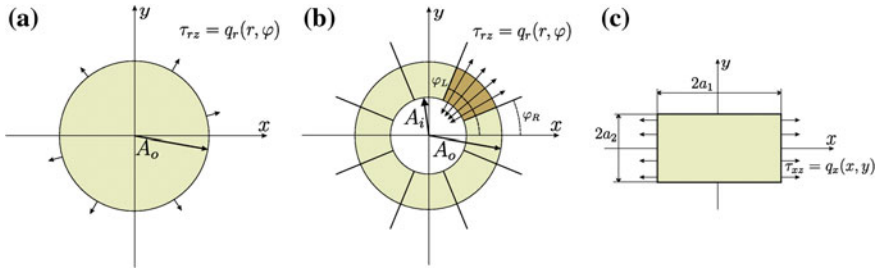
Fig. 13.2 **a** Circular piezoactuator, **b** CLoVER sector, **c** MFC actuator

Fig. 13.3 2D-Model of *piezoactuator* bonded by a *layer of glue* to the plate
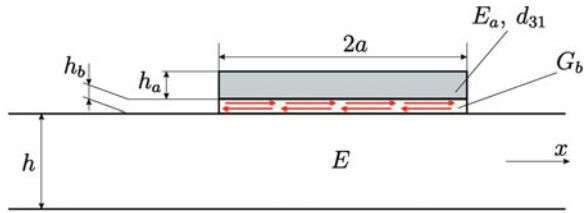
The value of τ_0 is obtained as [24]

$$\tau_0 = G_b \varepsilon_{ISA} / h_b \Gamma^2 a^2, \tag{13.8}$$

here

$$\Gamma^2 = \frac{G_b}{E_a} \frac{1}{h_a h_b} \frac{\alpha + \psi}{\psi}, \qquad \psi = \frac{Eh}{E_A h_a}, \qquad \varepsilon_{ISA} = d_{31} \frac{V(t)}{h_a}, \tag{13.9}$$

where d_{31} is the piezoelectric strain coefficient (in m/V) describing the coupling between the vertically polarized electric field and the in-plane induced strains, h_a is the thickness of the piezoactuator, E_a is its Young's modulus, G_b is the shear modulus of the bonding (adhesive) layer, h_b is the thickness of the adhesive layer, h is the thickness of the structure under excitation, E is the Young's modulus of the structure. Outside of the interval $|x| < a$, the surface stresses are zero. The *modal repartition number* α in (13.8) depends on the stress, strain, and displacement distributions across the plate thickness [24] and at low frequencies $\alpha = 1$ for wave mode S_0, $\alpha = 3$ for wave mode A_0 and $\alpha = 4$ in case of simultaneous excitation of both modes. For the accurate calculation of this parameter at high frequencies the readers are referred to the work [3].

13.2.2 Solution of the Wave Propagation Problem

The problem (13.1–13.3) can be relatively easy solved in the wavenumber-frequency domain [26]. In cylindrical coordinates the displacement vector of the

corresponding steady-state problem can be found as the inverse *Fourier transform* of the product of the *Green's matrix* $k(r, \varphi, z, \omega)$ and the load vector $q(r, \varphi)$ in wavenumber-frequency domain $K(\alpha, \gamma, z, \omega)$ and $Q(\alpha, \gamma)$, respectively:

$$u(r, \varphi, z, \omega) = \frac{1}{4\pi^2} \int_0^{2\pi} \int_{\Gamma_+} K(\alpha, \gamma, z, \omega) Q(\alpha, \gamma) e^{-i\alpha r \cos(\gamma - \varphi)} \alpha \, d\alpha \, d\gamma. \quad (13.10)$$

where the contour Γ_+ is chosen so that it encloses all the real poles of the integrand in accordance with the principle of limiting absorption. There are two possible time-efficient approaches for the evaluation of the double integral (13.10): the *far-field residue integration technique* (FFRIT) and the *asymptotic expansion* (AE). The FFRIT gives an approximate solution in the middle field and an exact solution in the far-field of the excitation source for all types of sources in the following form [23]:

$$u(r, \varphi, z, \omega) = \sum_{m=1}^{\infty} \left[u_m^+ + u_m^- \right] - d(r, \varphi, z, \omega), \quad (13.11)$$

$$u_m^\pm(r, \varphi, z, \omega) = \pm \frac{i}{2\pi} \int_{\varphi \pm \pi/2}^{\varphi + \pi \pm \pi/2} b_m^\pm(\gamma, z, \omega) e^{-ik_m^\pm(\gamma)r \cos(\gamma - \varphi)} d\gamma, \quad (13.12)$$

$$d(r, \varphi, z, \omega) = \frac{1}{2\pi r} \sum_{m=1}^{\infty} \left[\left. \frac{b_m^\pm(\gamma, z, \omega)}{k_m^\pm(\gamma)} \right|_{\gamma = \varphi + \frac{3\pi}{2}} + \left. \frac{b_m^\pm(\gamma, z, \omega)}{k_m^\pm(\gamma)} \right|_{\gamma = \varphi + \frac{\pi}{2}} \right] + O(r^{-2}), \quad (13.13)$$

$$b_m^\pm(\gamma, z, \omega) = \text{res } K(\alpha, \gamma, z, \omega)|_{\alpha = k_m^\pm(\gamma)} Q(k_m^\pm(\gamma), \gamma) k_m^\pm(\gamma), \quad (13.14)$$

where $k_m^\pm(\gamma)$ are the dependencies of the wave numbers on the angle γ for the fixed frequency ω.

The *asymptotic expansion* (AE) represents the solution of the wave propagation problem for the far-field points to the excitation source as follows [22]

$$u(r, \varphi, z, \omega) = \sum_{m=1}^{N_r} \sum_{p=1}^{N_{mp}^+(\varphi)} G_{mp}(r, \varphi, z, \omega) + O(r^{-3/2}), \quad (13.15)$$

$$G_{mp}(r, \varphi, z, \omega) = \pm \frac{i}{2\pi} \sqrt{\frac{2\pi}{r}} \frac{b_m^\pm\left(\gamma_{mp}^\pm(\varphi), z, \omega\right)}{\sqrt{-i \cdot P_{m,\gamma\gamma}''^\pm\left(\gamma_{mp}^\pm(\varphi), \varphi\right)}} e^{irP_{m,\gamma\gamma}^\pm\left(\gamma_{mp}^\pm(\varphi), \varphi\right)}, \quad (13.16)$$

$$P_m^\pm(\gamma, \varphi) = -k_m^\pm(\gamma) \cos(\gamma - \varphi), \quad P_{m,\gamma\gamma}''^\pm\left(\gamma_m^\pm(\varphi), \varphi\right) \neq 0, \quad (13.17)$$

where $\gamma_{mp}^\pm(\varphi)$ are the *stationary points* of the phase function (13.16) for the *wavenumber* curve $k_m^\pm(\gamma)$.

13.2.3 Energy Fluxes Corresponding to Lamb Waves

The energy brought into the structure by a surface source and its radiation through the structure to infinity is studied using the definitions of values of *power flow* and the vector of its power density usually called *Poynting* (or frequently called Umov-Poynting) *vector*. The energy brought into a composite plate by the surface source $q(x^*, y)$ acting in the domain Ω is obtained as

$$E_0^\omega = -\frac{\omega}{2} \text{Im} \int\limits_0^{2\pi} \int\limits_{\Gamma_+} (K(\alpha, \gamma, z, \omega) Q(\alpha, \gamma), Q(\alpha^*, \gamma)) \varkappa d\alpha d\gamma. \qquad (13.18)$$

The density of energy flux through the surface S in the direction of its normal n at a point $x \in S$ is given by the scalar product of the displacement vector and the complex stress vector calculated in direction of normal n

$$E(R, \varphi, z, \omega) = (u(R, \varphi, z, \omega), \sigma_n(R, \varphi, z, \omega)) \text{ with } \sigma_{n,i}(R, \varphi, z, \omega) = \sum_{j=1}^{3} \sigma_{ij} \cdot n_j. \qquad (13.19)$$

The energy propagating from the source to infinity can be evaluated in the same way. A cylinder is taken outside of the source, which is located inside the circle with a minimum radius A_o, i.e. the radius of the cylinder satisfies $R > A_o$ while its center is located at the origin. The height of the cylinder is equal to the thickness of the laminated plate h. The total through-thickness power flow for $r = R$ is given by

$$E_{R,\varphi}^\omega(R, \varphi, \omega) = -\frac{\omega R}{2} \text{Im} \int\limits_{-h}^{0} E(R, \varphi, z, \omega) dz. \qquad (13.20)$$

While computing the energy flow for different values of R, φ and z using both approaches (13.11–13.13) and (13.15–13.17) the total power density of the energy propagating from the source to infinity can be obtained as

$$E(R, \varphi, z, \omega) = \left(\sum_j u_j(R, \varphi, z, \omega), \sum_k \sigma_{n,k}(R, \varphi, z, \omega) \right) = \sum_j \left(u_j(R, \varphi, z, \omega), \sigma_{n,j}(R, \varphi, z, \omega) \right)$$
$$+ \sum_{j,k, j \neq k} \left[\left(u_j(R, \varphi, z, \omega), \sigma_{n,k}(R, \varphi, z, \omega) \right) + \left(u_k(R, \varphi, z, \omega), \sigma_{n,j}(R, \varphi, z, \omega) \right) \right], \qquad (13.21)$$

i.e. as the sum of contributions to the power density corresponding to wave modes solely and some mixed values of power density.

13.3 Numerical Results and Discussion

In this section some results of numerical computations of piezo-excited Lamb wave propagation and the corresponding power flows in composite plates are presented. As *waveguides* three composite specimens are considered. The first one is a cross-ply composite with stacking sequence [0/90]s and all plies manufactured of fiber-reinforced polymer (CFRP-T700GC/M21), whose elastic moduli and density are given in Table 13.1. The second plate is a hybrid plate with stacking sequence [I90/C45/C-45]$_s$, where "I" stands for layers made of IM7-Cycom-977-3 (see Table 13.1) and "C" stands for layers manufactured of CFRP-T700GC/M21. The third plate is a quasi-isotropic plate [0/45/-45/90]$_{2s}$ with layers manufactured of CFRP-T700GC/M21. All values of stiffness for both materials CFRP-T700GC/ M21 and IM7-Cycom-977-3 given in Table 13.1 correspond to the well-known Voigt notation for the stiffness tensor C_{ijkl} (13.2). All of the composite plates considered have a total thickness of 1 mm.

In the following example (Fig. 13.4a) the total through-thickness power density of the energy flow is analyzed in dependence of the direction φ. Here the power flow (13.20) is calculated for $r = 100$ mm and $r = 220$ mm evaluated using FFRIT for [0/90]$_s$ made of CFRP-T700GC/M21 under excitation by the circular source ($A_o = 10$ mm) for $f = 300$ kHz. In Fig. 13.4a some differences between the distributions of power flow are observed in directions, in which the power flow has its maxima. This is explained by the fact that the distribution in the near-field of the source is mostly formed by the shape of the actuator and the near-field terms, whereas in the far-field the distribution of power flow is mostly conditioned by the anisotropy-induced *energy focusing* in directions $\varphi = 0°$, $\varphi = 7°$, etc. [23]. Note that the asymptotic expansion (AE) by its definition gives a distribution of power flow with respect to propagation direction independently of the distance to the excitation source. This means that for a good quantitative description of the wave phenomena in the middle-field for strong focusing of waves the FFRIT has to be used. However, for qualitative analysis the AE is usually enough even for the middle-field area.

The focusing of waves in Fig. 13.4a in directions $\varphi = 0°$, $\varphi = 7°$ is due to the focusing of the wave modes S_0 and SH_0 in these directions. However, the behavior of the corresponding distribution is frequency-dependent, e.g. for lower frequencies it is mostly influenced by the A_0 wave mode. Moreover, as can be observed in Fig. 13.4b, the distribution of amplitudes and hence of the power flow for S_0 and SH_0 wave modes is also frequency-dependent. For frequencies above 150 kHz these wave modes are strongly focused in directions $\varphi = 0°$ and $\varphi = 90°$, while at lower frequencies this effect is negligible.

Another phenomenon occurring in composite plates under excitation by some types of piezoelectric actuators is the presence of frequency- and direction-dependent *anti-resonances*. They occur due to the anti-phase action of the boundaries of the piezoactuator, where the interface stresses are concentrated. Since the wavenumbers are frequency- and direction-dependent, resonances and

Table 13.1 Properties of materials (elastic constants in 10^{11} Pa, density in 10^3 kg/m^3)

	C_{11}	$C_{12} = C_{13}$	$C_{22} = C_{33}$	C_{23}	C_{44}	$C_{55} = C_{66}$	ρ
A	1.528	0.11	0.232	0.176	0.028	0.033	1.558
B	1.234	0.055	0.115	0.064	0.026	0.045	1.6

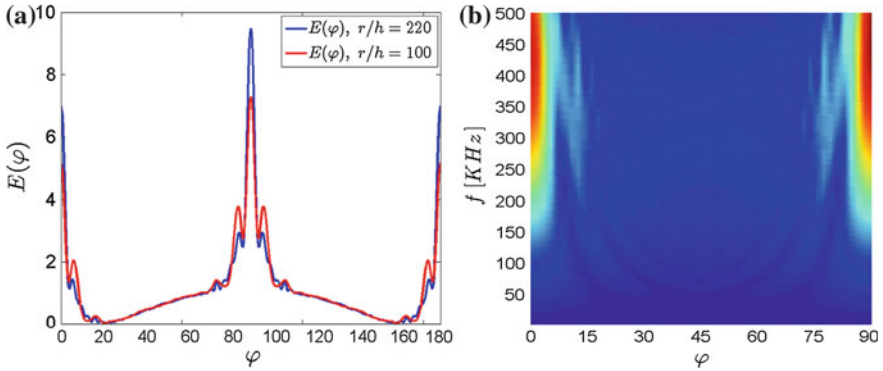A corresponds to IM7-Cycom-977-3 [25], B corresponds to CFRP-T700GC/M21 [15]

Fig. 13.4 a The total through-thickness *power flow* in dependence on φ for $r = 100$ mm and $r = 220$ mm calculated using FFRIT for [0/90]$_s$ made of CFRP-T700GC/M21 under excitation by the circular source ($A_o = 10$ mm) for 300 kHz. **b** Out-of-plane amplitudes in dependence on φ and $f = \omega/2\pi$ calculated using FFRIT in a cross-ply [0/90]$_s$ plate under an excitation by the *circular source* ($A_o = 5$ mm) at $r = 46$ mm for the sum of S_0 and SH_0 wave modes

anti-resonances occur for the different directions not simultaneously. This phenomenon is well observed in Fig. 13.5a for the logarithmical surface out-of-plane displacements corresponding to the A_0 wave mode, excited in a cross-ply [0/90]$_s$ made of CFRP-T700GC/M21 by a circular actuator of radius $A_o = 5$ mm. Comparing the corresponding logarithmical displacements in the directions of $\varphi = 0°$, $\varphi = 45°$ and $\varphi = 90°$ (Fig. 13.5b), it is clearly seen that the difference between the anti-resonance frequencies is about 45 kHz. This implies that if the waves are excited for one direction at the anti-resonance, in some other directions no anti-resonance occurs at the given frequency. Moreover, in the case of strong *anisotropy of wavenumbers* of wave modes in such directions the amplitudes of observed waves can be high. It is concluded that for excitation at frequency higher than the first anti-resonance frequency it is nearly impossible to suppress (or to amplify) the wave propagation of the wave mode in all directions of the composite simultaneously. Note that such a suppression (or amplification) can be easily carried out for isotropic structures [1].

The anti-resonances observed in Fig. 13.5 for the A_0 wave mode for the whole considered frequency range [0, 500] KHz are not observed in this frequency range for the two other fundamental wave modes S_0 and SH_0. The total through-thickness power flow corresponding to the S_0 wave mode is represented in Fig. 13.6a for an
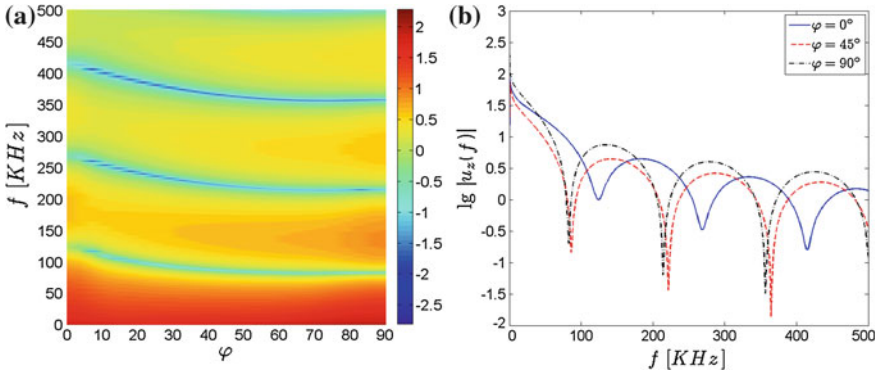
Fig. 13.5 **a** Surface out-of-plane logarithmic displacements ($\lg|u_z(\varphi, \omega)|$) at $r = 46$ mm for the wave mode A_0 calculated using AE for the case of wave excitation by a *circular actuator* ($A_o = 5$ mm) in a $[0/90]_s$ plate with layers made of CFRP-T700GC/M21, **b** The same displacements in some fixed directions

excitation by the *CLoVER sector* ($A_i = 4$ mm, $A_o = 5$ mm, $\varphi_R = 22.5°$, $\varphi_L = 67.5°$). The power flow is despite of the use of the CLoVER sector is focussed in the whole range of frequencies below the 500 kHz in the directions $\varphi = 4°$ and $\varphi = 86°$. Comparing Fig. 13.6a with the similar Fig. 13.4b for the circular piezoactuator lets us conclude that the use of a CLoVER sector slightly shifts the maxima of amplitudes (and energy too). For a circular piezoactuator they are $\varphi = 0°$ and $\varphi = 90°$.

Another interesting numerical example is shown in Fig. 13.6b. The distribution of the total through-thickness power flow for the S_0 wave mode in a hybrid [$I90/C45/C - 45]_s$ plate under an excitation by a circular source ($A_o = 5$ mm) has *focusing directions* too, but they vary with the frequency. For example, for a frequency of 200 kHz the focusing direction is $\varphi = 50°$, whereas for 500 kHz the main focusing direction in the first quarter changes to $\varphi = 60°$ and, moreover, the power flow in the direction of $\varphi = 50°$ for a frequency of 500 kHz is quite low. Similarly to the case of a cross-ply plate the focusing of the S_0 wave mode is not observed for low frequencies (below 100 kHz).

The effects of *energy focusing* observed in composite plates with strong influence of anisotropy are also present in *quasi-isotropic composites*, however for high frequencies or for the case of the non-axis-symmetric source. In Fig. 13.7a and b the total through-thickness power flows are shown for S_0 (Fig. 13.7a) and for SH_0 (Fig. 13.7b) excited in a quasi-isotropic $[0/45/–45/90]_{2s}$ plate under an excitation by an MFC source ($A_1 = 8$ mm, $A_2 = 2$ mm). Here an MFC actuator produces for the S_0 wave mode a power flow mostly in fiber direction in MFC ($\varphi = 0°$), i.e. the highest values of amplitudes (power flow) are usually between the directions $\varphi = [-\text{atan}(2/8), \text{atan}(2/8)] \approx [-15°, 15°]$. However, the energy distribution for S_0 has its frequency- and direction-dependent anti-resonances. For a considerable frequency range [320, 420] KHz the maxima of power flow values
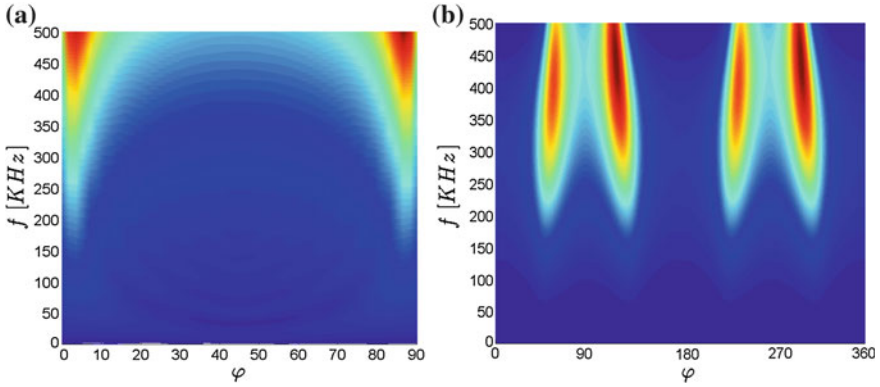
Fig. 13.6 Total through-thickness *power flow* for $r = 150$ mm calculated using AE in dependence on φ and f, calculated for the S_0 wave mode in a *cross-ply* $[0/90]_s$ plate **a** Under an excitation by a *CLoVER sector* ($A_i = 4$ mm, $A_o = 5$ mm, $\varphi_R = 22.5°$, $\varphi_L = 67.5°$) and a hybrid $[I90/C45/C–45]_s$ plate **b** Under an excitation by a circular source ($A_o = 5$ mm)
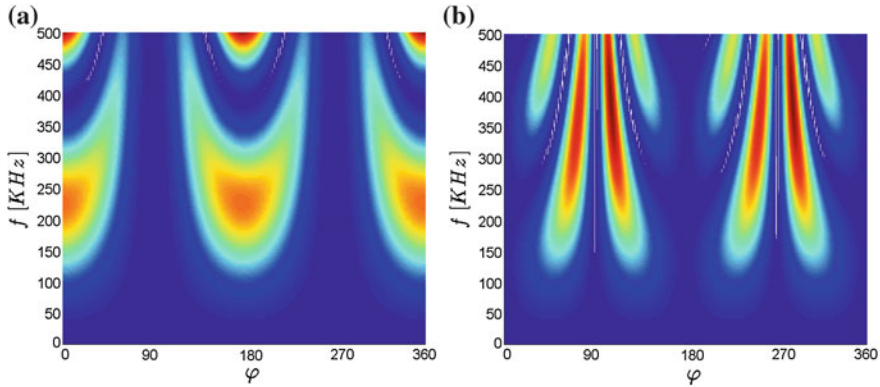
Fig. 13.7 Total through-thickness energy flow in dependence of φ and f calculated using AE in a *quasi-isotropic* $[0/45/−45/90]_{2s}$ *plate* with layers of IM7-Cycom977-3 under an excitation by an *MFC source* ($A_1 = 8$ mm, $A_2 = 2$ mm). Values of energy flow for $r = 150$ mm for S_0 (**a**) and for SH_0 (**b**) wave modes

are found to be in the direction $\varphi = 60°$ instead of the normal focusing direction $\varphi = 0°$. The focusing properties of power flow for the SH_0 wave mode are much more complicated. The corresponding distribution (Fig. 13.7b) shows that for different values of frequency-thickness the main focusing direction is different. Its value changes from $\varphi = 50°$ at 100 kHz to $\varphi = 85°$ at 500 kHz.

13.4 Conclusion

In this paper, displacements and the density of power flow excited in composite plates by harmonic surface-bonded sources of finite size are analyzed with the help of the residue theorem based on far-field residue integration technique (FFRIT) and of the asymptotic expansion (AE). Then, the application of these methods is studied using numerical examples. Results of computations show that these methods admit an efficient analysis of the directivity of the excitation source at different excitation frequencies and provide a tool for selective wave mode excitation and for the study of optimal design of the excitation source(s). Due to the complicated distributions of amplitudes and power flows in composite plates, such procedures are of great importance for the practical application of *elastic waves* for SHM systems and for the understanding of *wave phenomena* occurring in composites under excitation by piezoelectric sources.

References

1. V. Giurgiutiu, *Structural Health Monitoring with Piezoelectric Wafer Active Sensors*. (Elsevier Academic Press, New York, 2008)
2. Z. Su, L. Ye, *Lecture Notes in Applied and Computational Mechanics. Identification of Damage Using Lamb Waves. From Fundamentals to Applications*, vol. 48. (Springer, Berlin, 2009)
3. G. Santoni, *Fundamental Studies in the Lamb-Wave Interaction between Piezoelectric Wafer Active Sensor and Host Structure During Structural Health Monitoring*. Dissertation, University of South Carolina, 2010
4. D. Chimenti, Appl. Mech. Rev. **50**, 247 (1997)
5. P. Kudela, W. Ostachowicz, A. Zak, Mech. Syst. Signal Process. **22**, 1327 (2008)
6. H. Lamb, in *Proceedings of the Royal Society of London. Series A*, vol. 93, p. 293. (1917)
7. J. Achenbach, *Wave Propagation in Elastic Solids* (North-Holland Publishing Company, Amsterdam, 1973)
8. J. Rose, *Ultrasonic Waves in Solid Media* (Cambridge University Press, Cambridge, 1999)
9. I. Viktorov, *Rayleigh and Lamb Waves* (Plenum Press, New York, 1970)
10. A. Velichko, P. Wilcox, J. Acoust. Soc. Am. **121**(1), 60 (2007)
11. W. Thomson, J. Appl. Phys. **21**, 89 (1950)
12. L. Knopoff, Seismol. Soc. Am. **54**(1), 431 (1964)
13. A. Nayfeh, J. Acoust. Soc. Am. **89**, 1521 (1991)
14. G. Liu, Z. Xi, *Elastic Waves in Anisotropic Laminates* (CRC Press, London, 2002)
15. B. Chapuis, N. Terrien, D. Royer, J. Acoust. Soc. Am. **127**(1), 198 (2010)
16. C. Ng, M. Veidt, Smart Mater. Struct. **18**, 074006 (2009)
17. F. Schubert, Ultrasonics **42**, 221 (2004)
18. B. Lee, W. Staszewski, Smart Mater. Struct. **12**, 804 (2003)

19. B. Auld, *Acoustic Fields and Waves in Solids*, 2nd edn. vol. I & II. (R.E. Kreiger Publishing Co., Florida, 1990)
20. E. Glushkov, E. Kirillova, J. Appl. Math. Mech. **62**(3), 419 (1998)
21. A. Raghavan, C. Cesnik, Smart Mater. Struct. **14**, 1448 (2005)
22. A. Karmazin, E. Kirillova, W. Seemann, P. Syromyatnikov, Ultrasonics **53**, 283 (2013)
23. Karmazin A. *Time-Efficient Simulation of Surface-Excited Guided Lamb Wave Propagation in Composites*. Schriftenreihe des Instituts für Technische Mechanik, Band 18, Karlsruher Institut für Technologie, KIT Scientific Publishing (2012)
24. E. Crawley, J. de Luis, AIAA J. **25**(10), 1373 (1987)
25. K. Salas, C. Cesnik, Smart Mater. Struct. **19**, 015014 (2010)
26. A. Karmazin, E. Kirillova, W. Seemann, P. Syromyatnikov, Ultrasonics **51**, 17 (2011)

Chapter 14
Modeling Methods of Stress–Strain State in Layered Constructions from Anisotropic Materials at Pulsed Loading

I. P. Miroshnichenko

The methods and techniques are described which develop the generalized method of scalarization for dynamic elastic displacements, stresses and strains in transverse-isotropic media. The proposed scientific and methodological apparatus is intended for analysis of stress–strain state in layered elliptic constructions with transverse-isotropic layers at pulsed loading with the given space–time distribution on the inner and outer surfaces of the considered constructions.

14.1 Initial Equations, Expressions and Assumptions

Consider a multilayered structure, containing N layers, rigidly fastened one with others (Fig. 14.1). The layers are numbered from 1 to N, starting from the inner layer, the internal boundary of each of the n-th layer is marked as S_{n-1} and external one as S_n ($n = 1,\ldots, N$).

The layers could be of arbitrary thickness and made from different isotropic and transverse-isotropic construction materials with their individual physical and mechanical characteristics, and also possess the properties of liquid and gaseous mediums.

Some areas (V_1, V_2, V_3, …) of the construction are subjected to external loading, which depends on time and coordinates. The loads may be of pulsed character (single pulse or several pressure pulses). The restrictions on the form of these pulses and zones of their applications are absent. In these conditions, a complex stress–strain state arises in the construction, formed not only primary perturbation, but perturbations caused by multiple wave re-reflections from heterogeneities (boundaries of layers), interference phenomena and diffraction.

I. P. Miroshnichenko (✉)
Don State Technical University, Rostov-on-Don, Russia
e-mail: ipmir@rambler.ru

Fig. 14.1 Considered multilayered structure with applied loads
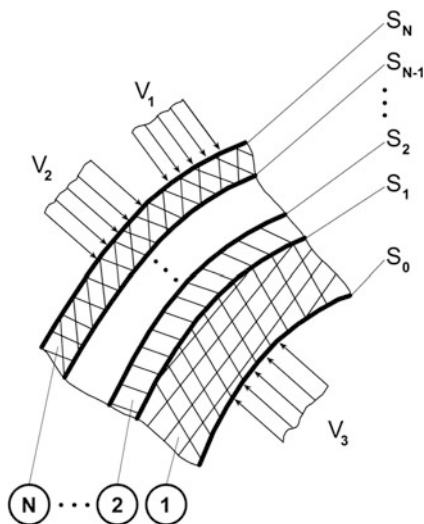
It is required to define this stress–strain state in the construction, i.e. find the fields of displacements, stresses and strains in arbitrary given areas of the construction at any time as in the process of loading as after its completion.

The required displacements, stresses and strains in elastic statement of the problem are described in each layer without sources by using the following set of equations written into invariant form [1, 2]:

(i) the homogeneous equations of motion for the element of a continuous medium in stresses:

$$\rho \frac{\partial^2 U^i}{\partial t^2} = \nabla_j \sigma^{ij}; \tag{14.1}$$

(ii) the Hook's law relations:

$$\sigma^{ij} = C^{ijrs} \varepsilon_{rs}; \tag{14.2}$$

(iii) the Cauchy relationships (geometric relations):

$$\varepsilon_{rs} = \frac{1}{2} (\nabla_r U_s + \nabla_s U_r). \tag{14.3}$$

In (14.1) and relationships (14.2, 14.3), are used the following designations: ρ is the density of the construction material of layer, U^i are the contravariant components of the displacement vector, ∇_j is the covariant derivative, σ^{ij} are the contravariant components of the stress tensor; C^{ijrs} are the contravariant components of the elastic moduli tensor of the construction material of layer, ε_{rs} are the

covariant components of tensor of the small deformations, U_i are the covariant components of the displacement vector, and i, j, r, s are the tensor indices.

By substituting (14.3) into (14.2) and then into (14.1), we obtain a set of the motion equations in displacements:

$$\rho \frac{\partial^2 U^i}{\partial t^2} = \nabla_j C^{ijrs} \nabla_{(r} U_{s)}, \tag{14.4}$$

where on indices r and s, enclosed in parentheses, is conducted a symmetrization.

In order to define displacements from (14.4), it is necessary to formulate the initial and boundary conditions, to which must satisfy the stress–strain state in the considered layered construction.

The solution of the motion (14.4), satisfying the given boundary and initial conditions, fully describes the stress–strain state in the considered construction layer. Definition of this solution in general case of arbitrary geometry and anisotropy presents considerable difficulties caused by the vector nature of the equations, when for the description of field is not enough one numeric value (for example, as in the case of liquid environments, where the vector of velocity of the fluid is defined by the gradient of one value, namely scalar potential) [4].

In the present case, in every point of space, we need in calculation of three numeric values. It is important to select correctly three scalar functions that define a vector field. So, if as these functions, we select Cartesian components of the vector U_x, U_y, U_z, then the satisfaction of the obtained solutions to the boundary conditions will be difficult, because the Cartesian components depend on the curved (cylindrical or elliptic) surface boundary by the complex manner. If we express the vector $\bar{U}$ through the components in the coordinate system corresponding to the boundary, then arises another difficulty caused by that the scalar equations do not divide into three equations, each of which contains only one component. As a result, we obtain the set of three equations, each of which contains all three functions, this leads to solution of the sixth order differential equation [5].

The classic method of solution of the vector value-boundary problems in dynamical theory of elasticity for isotropic environments, when (14.4) transforms into the motion equation of Lamé, consists in the division of the vector field into two parts (longitudinal and transverse). The simplification of the problem is conducted only by using orthogonal coordinate systems in which it is possible to divide the variables, and which satisfy the Bromwich conditions [5]. The resulting, in this case three scalar wave equations describe respectively longitudinal waves and transverse waves of two mutually perpendicular polarizations. The difficulty connected with transformation of these waves one into other at the boundaries, is overcome in the cases when the construction surface coincides with some coordinate surface.

In [6], this method is generalized to the case of transverse isotropic media, and the coordinate systems with admissible transformations of the type:

$$\tilde{x}^J = x^J; \quad \tilde{x}^K = f^K\left(x^K, x^N\right); \quad \tilde{x}^N = f^N\left(x^K, x^N\right), \tag{14.5}$$

where the indexes indicated by capital letters J, K, N are fixed and correspond to local affine basis $\bar{e}_J, \bar{e}_K, \bar{e}_N$, and $f^K(x^K, x^N)$ and $f^N(x^K, x^N)$ are continuously differentiable single-valued functions, the tilde signs show new coordinates, without such a mark these coordinates are old (they can be rectangular Cartesian coordinates).

Group of transforms (14.5) includes orthogonal transforms, which are their subgroup relatively of the "multiplication".

By combining the main axis of symmetry for the considered medium with invariant vector $\bar{e}_J$, (14.4) in the case of monochromatic waves, could be represented as

$$
\begin{aligned}
-&\left\{\left[-\left(\frac{C_{11}-C_{12}}{2}\right)+C_{44}\right]\nabla_J\nabla_J+\omega^2\rho\right\}U_i = C_{11}\nabla_i\nabla^s U_s - \left(\frac{C_{11}-C_{12}}{2}\right)\delta_{ijk}^{rsk}\nabla^j\nabla_s U_s \\
+&\left[-\left(\frac{C_{11}-C_{12}}{2}\right)+C_{13}+C_{44}\right]\nabla_i\nabla_J U_J + \delta_i^J\left\{\left[-\left(\frac{C_{11}-C_{12}}{2}\right)+C_{13}+C_{44}\right]\nabla_J\nabla^s U_s\right. \\
+&\left.\left[-\left(\frac{C_{11}-C_{12}}{2}\right)+C_{44}\right]\nabla^s\nabla_s U_J + \left[C_{13}+C_{33}-2(C_{13}+2C_{44})\right]\nabla_J\nabla_J U_J\right\},
\end{aligned}
\tag{14.6}
$$

where ω is the frequency, C_{ij} are the elements of the matrix of elastic constants, written on the convoluted index [7], and δ_i^J is the Kronecker symbol.

The dependence of the wave motion on coordinate x has the form $\exp[ihx^J]$ and therefore

$$\nabla_J = \nabla^J = \frac{\partial}{\partial x^J} = ih, \tag{14.7}$$

where h is the projection module of the wave vector on the direction $\bar{e}_J$.

The solution of (14.6), as shown in [5] is reduced to solution of three scalar wave equations relatively functions φ, ω, v, describing, respectively, quasi-longitudinal, quasi- transverse and transverse waves:

$$\nabla\begin{pmatrix}\phi \\ \omega \\ v\end{pmatrix} + g^2\begin{pmatrix}\varphi \\ \omega \\ v\end{pmatrix} = 0. \tag{14.8}$$

To find the wave numbers $g = \omega/v_\Phi$, where v_Φ is the phase velocity of propagation of the corresponding waves, we use the following dispersive equations [6]:

$$
\begin{aligned}
2v_\Phi^2\rho = (C_{11}-C_{33})\sin^2 Q + (C_{33}+C_{44}) \\
\pm\left(\left[(C_{11}+C_{33}-2C_{44})\sin^2 Q - (C_{33}-C_{44})\right]^2 + \left[2(C_{13}+C_{44})\sin Q\cos Q\right]^2\right)^{\frac{1}{2}},
\end{aligned}
\tag{14.9}
$$

where the upper sign before the braces relates to the quasi-longitudinal waves, and the lower sign defines the quasi-transverse waves.

To find the wave number of transverse waves $\chi = \omega/v_t$, where v_t is the phase speed of propagation of the transverse waves, the dispersion relation has the form:

$$v_1^2 \rho = 1/2(C_{11} - C_{12})\sin^2 Q + C_{44}\cos^2 Q. \tag{14.10}$$

In (14.9 and 14.10), Q is the angle between the wave vector and direction of $\bar{e}_J$. From (14.9 and 14.10), the wave numbers are defined as

$$g^2 = A_1 \pm \sqrt{A_1^2 - A_2^2}; \tag{14.11}$$

$$\chi^2 = 2(\omega^2 \rho - C_{44}h^2)/(C_{11} - C_{12}) + h^2, \tag{14.12}$$

where

$$A_1 = \left\{(C_{11} + C_{44})\omega^2\rho - [C_{11} - (C_{33} - 2C_{44}) - C_{13}(C_{13} + 2C_{44})]\,h^2\right\} / (2C_{11}C_{44})\;;$$
$$A_2 = [C_{13}(C_{13} + C_{44}) + C_{44}(C_{11} + C_{13}) + C_{33}(C_{44} - C_{11})]\,h^4$$
$$- (C_{33} - C_{11})\,h^2\omega^2\rho + \omega^4\rho^2/(C_{11}C_{44}).$$

The sign of minus in relation (14.11) relates to the wave number $\overset{(L)}{g}$ of the quasi-longitudinal waves, and sign of plus defines the wave number $\overset{(T)}{g}$ of the quasi-transverse waves.

The common solution of the differential (14.8) at the values of the wave numbers determined by the relations (14.11) and (14.12) are used to find displacements U_i, stresses σ_{ij} and strains ε_{ij}, which are written in the forms [6]:

$$U_i = \left(\overset{(L)}{D_1}\nabla_i + \delta_i^J\overset{(L)}{D_2}\nabla_J\right)\varphi + \left(\overset{(T)}{D_1}\frac{1}{\overset{(T)}{g}}\nabla_i\nabla_J + \overset{(T)}{g}\,\delta_i^J\right)\omega$$
$$+ \sqrt{g}\left(\delta_i^K\nabla^N - \delta_i^N\nabla^K\right)v\;; \tag{14.13}$$

$$\sigma_{ij} = \left(\overset{(L)}{d_1}g_{ij} + \overset{(L)}{d_2}\delta_i^J\delta_j^J + \overset{(L)}{d_3}\delta_{(i}^J\nabla_{j)}\nabla_J + \overset{(L)}{d_4}\nabla_i\nabla_j\right)\varphi$$
$$+ \left(\overset{(T)}{d_1}g_{ij}\nabla_J + \overset{(T)}{d_2}\delta_i^J\delta_j^J\nabla_J + \overset{(T)}{d_3}\delta_{(i}\nabla_{j)} + \overset{(T)}{d_4}\nabla_i\nabla_j\nabla_J\right)\omega$$
$$+ 2\sqrt{g}\left[a_2\left(\nabla_{(i}\delta_{j)}^K\nabla^N - \nabla_{(i}\delta_{j)}^N\nabla^K\right) + a_4\left(\delta_{(i}^J\delta_{j)}^K\nabla^N - \delta_{(i}^J\delta_{j)}^N\nabla^K\right)\nabla_J\right]v; \tag{14.14}$$

$$\varepsilon_{ij} = \left(\overset{(L)}{D_1} \nabla_i \nabla_j + \overset{(L)}{D_2} \nabla_{(i} \delta^J_{j)} \nabla_J \right) \varphi + \left(\overset{(T)}{D_1} \frac{1}{\overset{(T)}{g}} \nabla_i \nabla_j \nabla_J + \overset{(T)}{g} \nabla_{(i} \delta^J_{j)} \right) \omega$$
$$+ \sqrt{g} \left(\nabla_{(i} \delta^K_{j)} \nabla^N - \nabla_{(i} \delta^N_{j)} \nabla^K \right) v, \tag{14.15}$$

where

$$\overset{(L)}{d_1} = - \overset{(L)}{g^2} a_1 - h^2 a_3 \left(\overset{(L)}{D_1} + \overset{(L)}{D_2} \right); \quad \overset{(L)}{d_2} = - \overset{(L)}{g^2} a_3 - h^2 \left(2a_4 \overset{(L)}{D_2} + a_5 \overset{(L)}{D_1} + a_5 \overset{(L)}{D_2} \right);$$

$$\overset{(L)}{d_3} = 2a_2 \overset{(L)}{D_2} + 2a_4 \left(2 \overset{(L)}{D_1} + \overset{(L)}{D_2} \right); \quad \overset{(L)}{d_4} = 2a_2 \overset{(L)}{D_1};$$

$$\tag{14.16}$$

$$\overset{(T)}{d_1} = a_1 \overset{(T)}{g} \left(1 - \overset{(T)}{D_1} \right) + a_3 \left(\overset{(T)}{g} - \frac{h^2}{\overset{(T)}{g}} \overset{(T)}{D_1} \right); \quad \overset{(T)}{d_2} = a_3 \overset{(T)}{g} \left(1 - \overset{(T)}{D_1} \right) + 2a_4 \overset{(T)}{g} + a_5 \left(\overset{(T)}{g} - \frac{h^2}{\overset{(T)}{g}} \overset{(T)}{D_1} \right);$$

$$\overset{(T)}{d_3} = 2a_2^{(T)} + 2a_4 \left(\overset{(T)}{} - 2 \overset{(T)}{D_1} \frac{h^2}{\overset{(T)}{g}} \right); \quad \overset{(T)}{d_4} = 2a_2 \overset{(T)}{D_1} \frac{1}{\overset{(T)}{g}};$$

$$\tag{14.17}$$

$$a_1 = C_{12}; \qquad a_2 = (C_{11} - C_{12})/2; \qquad a_3 = C_{13} - C_{12};$$
$$a_4 = C_{44} - (C_{11} - C_{12})/2; \qquad a_5 = C_{11} + C_{33} - 2(C_{13} + 2C_{44}); \tag{14.18}$$

$$\overset{(L)}{D_1} = \frac{\overset{(L)}{g^2} b_4}{b_3 - \left(\overset{(L)}{g^2} - \overset{(L)}{h^2} \right)(1 - b_4)}; \quad \overset{(L)}{D_2} = \frac{\overset{(L)}{g^2}}{\overset{(L)}{h^2}} \frac{b_3 - \left(\overset{(L)}{g^2} - \overset{(L)}{h^2} \right) - b_4 \overset{(L)}{h^2}}{b_3 - \left(\overset{(L)}{g^2} - \overset{(L)}{h^2} \right)(1 - b_4)}; \tag{14.19}$$

$$\overset{(T)}{D_1} = - \frac{\overset{(T)}{g^2} b_4}{b_3 - \left(\overset{(T)}{g^2} - \overset{(T)}{h^2} \right) - b_4 \overset{(T)}{h^2}}; \tag{14.20}$$

$$b_3 = (\omega^2 \rho - h^2 C_{44})/C_{11}; \qquad b_4 = (C_{13} + C_{44})/C_{11}. \tag{14.21}$$

The functions found satisfy the motion (14.6), the solution of which is reduced to the solution of the three well-studied scalar (14.8) with eigen-values (14.11) and (14.12).

To solve the specific problem, it is necessary to find a particular solution corresponding to the given boundary conditions.

Solutions of problems for layered plane and cylindrical constructions have been obtained on the base of relations (14.13 and 14.15) of the generalized method of scalarization of the dynamic elastic fields in transverse isotropic media [6] in the works [8–10] and [10–14], respectively, in which the scientific-methodical apparatus was proposed for determination of displacements, stresses and strains in above-mentioned constructions. Moreover, the features of wave processes were considered at the various types of external non-stationary loading, for various physico-mechanical characteristics of layer materials, and opened the possibilities of the scalarization method for solution of different applied problems.

14.2 Determination of Elastic Fields in Problems of Excitation of Elliptic Cylinder

For constructions with the boundaries in the form of elliptic cylinders, it is convenient to use the system of elliptic cylindrical coordinates ξ, η, z connected with Cartesian coordinates x, y, z through transform formulae:

$$x = f \cdot ch\xi \cdot \cos\eta; \quad y = f \cdot sh\xi \cdot \sin\eta; \quad z = z, \tag{14.22}$$

where $0 \le \xi < \infty$, $0 \le \eta \le 2\pi$, $-\infty < z < \infty$, $2f$ is the inter-focus distance (see Fig. 14.2a, b).

Such constructions include elliptical rod, space with a hole in the form of an elliptic cylinder, thick elliptical tube and layered construction, like to layered circular cylinder.

The law of change in time is accepted as $e^{-i\omega t}$, and transit to other temporal dependence is conducted by using the Fourier transform.

In accordance with introduced previously bench mark $\overline{e_J}$, $\overline{e_K}$, $\overline{e_N}$, we denote

$$x^J = z; \qquad x^K = \xi; \qquad x^N = \eta. \tag{14.23}$$

By using the metric tensor g_{ij} matrix corresponding to the transform (14.22), the values of Christoffel symbols [2] and technique of the covariant differentiation, we specify the differential operators for the considered coordinate system, included in the formulae for tensor fields of displacements (14.13) and stresses (14.14). As a result, we obtain the expressions of covariant components for the tensor of elastic field through scalar functions φ, w, v in the coordinates of elliptic cylinder:

(a)

(b) z=const
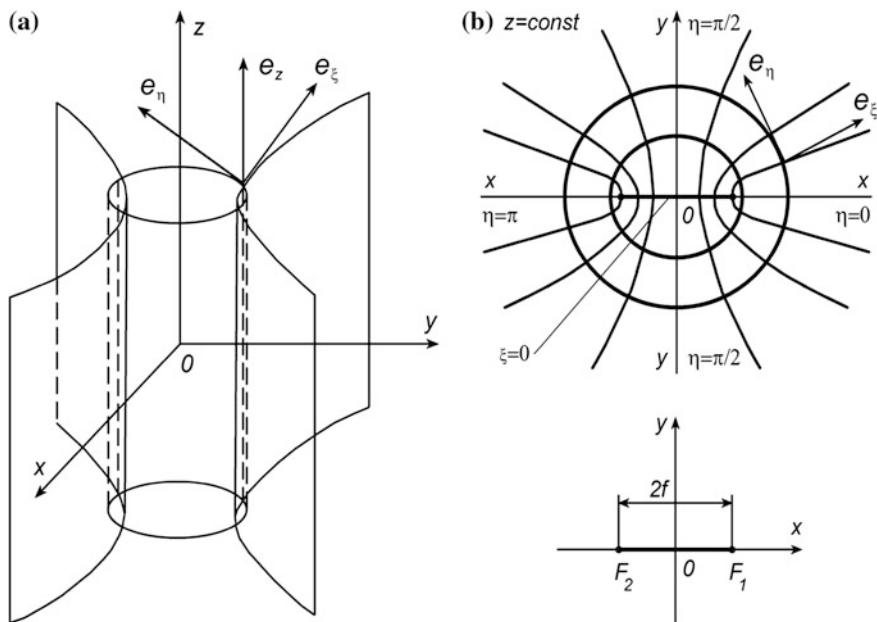
Fig. 14.2 Statement of the problem

$$U_z = ih\left(\overset{(L)}{D_1} + \overset{(L)}{D_2}\right)\varphi + \left(\overset{(T)}{g} - \overset{(T)}{D_1}\frac{h^2}{\overset{(T)}{g}}\right)w;$$

$$U_\xi = \overset{(L)}{D_1}\frac{\partial\varphi}{\partial\xi} + ih\frac{\overset{(T)}{D_1}}{\overset{(T)}{g}}\frac{\partial w}{\partial\xi} + \frac{\partial\gamma}{\partial\eta}; \tag{14.24}$$

$$U_\eta = \overset{(L)}{D_1}\frac{\partial\varphi}{\partial\eta} + ih\frac{\overset{(T)}{D_1}}{\overset{(T)}{g}}\frac{\partial w}{\partial\eta} + \frac{\partial v}{\partial\xi};$$

$$\sigma_{zz} = \left[\overset{(L)}{d_1} + \overset{(L)}{d_2} - h^2\left(\overset{(L)}{d_3} + \overset{(L)}{d_4}\right)\right]\varphi + ih\left(\overset{(T)}{d_1} + \overset{(T)}{d_2} + \overset{(T)}{d_3} - h^2\overset{(T)}{d_4}\right)w;$$

$$\sigma_{z\xi} = ih\left(\frac{1}{2}\overset{(L)}{d_3} + \overset{(L)}{d_4}\right)\frac{\partial\varphi}{\partial\xi} + \left(\frac{1}{2}\overset{(T)}{d_3} - h^2\overset{(T)}{d_4}\right)\frac{\partial w}{\partial\xi} + ih(a_2 + a_4)\frac{\partial v}{\partial\eta};$$

$$\sigma_{z\eta} = ih\left(\frac{1}{2}\overset{(L)}{d_3} + \overset{(L)}{d_4}\right)\frac{\partial\varphi}{\partial\eta} + \left(\frac{1}{2}\overset{(T)}{d_3} - h^2\overset{(T)}{d_4}\right)\frac{\partial w}{\partial\eta} - ih(1 + a_4)\frac{\partial v}{\partial\xi};$$

$$\sigma_{\xi\xi} = \left[\overset{(L)}{d_1} f^2(ch^2\xi - \cos^2\eta) + \overset{(L)}{d_4}\left(\frac{\partial^2}{\partial\xi^2} - \frac{1}{2}\frac{sh2\xi}{ch^2\xi - \cos^2\eta}\frac{\partial}{\partial\xi} + \frac{1}{2}\frac{\sin 2\eta}{ch^2\xi - \cos^2\eta}\frac{\partial}{\partial\eta}\right)\right]\varphi$$
$$+ ih\left[\overset{(T)}{d_1} f^2(ch^2\xi - \cos^2\eta) + \overset{(T)}{d_4}\left(\frac{\partial^2}{\partial\xi^2} - \frac{1}{2}\frac{sh2\xi}{ch^2\xi - \cos^2\eta}\frac{\partial}{\partial\xi} + \frac{1}{2}\frac{\sin 2\eta}{ch^2\xi - \cos^2\eta}\frac{\partial}{\partial\eta}\right)\right]w$$
$$+ 2a_2\left(\frac{\partial^2}{\partial\xi\partial\eta} - \frac{1}{2}\frac{\sin 2\eta}{ch^2\xi - \cos^2\eta}\frac{\partial}{\partial\xi} - \frac{1}{2}\frac{sh2\xi}{ch^2\xi - \cos^2\eta}\frac{\partial}{\partial\eta}\right)v;$$

$$\sigma_{\xi\eta} = \overset{(L)}{d_4}\left(\frac{\partial^2}{\partial\xi\partial\eta} - \frac{1}{2}\frac{\sin 2\eta}{ch^2\xi - \cos^2\eta}\frac{\partial}{\partial\xi} - \frac{1}{2}\frac{sh2\xi}{ch^2\xi - \cos^2\eta}\frac{\partial}{\partial\eta}\right)\varphi$$
$$+ ih\,\overset{(T)}{d_4}\left(\frac{\partial^2}{\partial\xi\partial\eta} - \frac{1}{2}\frac{\sin 2\eta}{ch^2\xi - \cos^2\eta}\frac{\partial}{\partial\xi} - \frac{1}{2}\frac{sh2\xi}{ch^2\xi - \cos^2\eta}\frac{\partial}{\partial\eta}\right)w$$
$$+ a_2\left(\frac{\partial^2}{\partial\eta^2} - \frac{\sin 2\eta}{ch^2\xi - \cos^2\eta}\frac{\partial}{\partial\eta} - \frac{\partial^2}{\partial\xi^2} + \frac{sh2\xi}{ch^2\xi - \cos^2\eta}\frac{\partial}{\partial\xi}\right)v;$$

$$\sigma_{\eta\eta} = \left[\overset{(L)}{d_1} f^2(ch^2\xi - \cos^2\eta) + \overset{(L)}{d_4}\left(\frac{\partial^2}{\partial\eta^2} + \frac{1}{2}\frac{sh2\xi}{ch^2\xi - \cos^2\eta}\frac{\partial}{\partial\xi} - \frac{1}{2}\frac{\sin 2\eta}{ch^2\xi - \cos^2\eta}\frac{\partial}{\partial\eta}\right)\right]\varphi$$
$$+ ih\left[\overset{(T)}{d_1} f^2(ch^2\xi - \cos^2\eta) + \overset{(T)}{d_4}\left(\frac{\partial^2}{\partial\eta^2} + \frac{1}{2}\frac{sh2\xi}{ch^2\xi - \cos^2\eta}\frac{\partial}{\partial\xi} - \frac{1}{2}\frac{\sin 2\eta}{ch^2\xi - \cos^2\eta}\frac{\partial}{\partial\eta}\right)\right]w$$
$$- 2\left(\frac{\partial^2}{\partial\xi\partial\eta} - \frac{1}{2}\frac{sh2\xi}{ch^2\xi - \cos^2\eta}\frac{\partial}{\partial\eta} + \frac{1}{2}\frac{\sin 2\eta}{ch^2\xi - \cos^2\eta}\frac{\partial}{\partial\xi}\right)v;$$

$$(14.25)$$

The factors a_i, $\overset{(L)}{d_i}$, $\overset{(T)}{d_i}$, $\overset{(L)}{D_i}$, $\overset{(T)}{D_i}$ could be found from expressions (14.16–14.20), respectively. The physical components of the elastic field tensors could be obtained from formulae (14.24, 14.25) by the standard way [15].

The potential functions φ, w, v are common solutions of the Helmholtz equations with corresponding wave numbers:

$$\nabla_m\nabla^m F + g^2 F = 0, \qquad (14.26)$$

where g takes a value of $\overset{(L)}{g}$ for quasi-longitudinal waves $F = \varphi$, $\overset{(T)}{g}$ for quasi-transverse waves $F = w$ and χ for purely transverse waves $F = v$.

Following the method of division of variables, the common solution of the wave (14.26), which satisfy the potentials φ, w, v, could be represented as a superposition of particular solutions.

Due to [16, 17], the single-value particular solutions of (14.26) are the wave functions of an elliptic cylinder:

$$
\begin{array}{llll}
Ce_m(\xi,q)ce_m(\eta,q)e^{ihz}; & a=a_m, & m=0,1,\ldots; \\
Se_m(\xi,q)se_m(\eta,q)e^{ihz}; & a=b_m, & m=1,2,\ldots; \\
Me_m^{(1),(2)}(\xi,q)ce_m(\eta,q)e^{ihz}; & a=a_m, & m=0,1,\ldots; \\
Ne_m^{(1),(2)}(\xi,q)se_m(\eta,q)e^{ihz}; & a=b_m, & m=1,2,\ldots,
\end{array}
\tag{14.27}
$$

where

$$
\begin{array}{ll}
Me_m^{(1),(2)}(\xi,q) = Ce_m(\eta,q) \pm iFey_m(\xi,q); & a=a_m \\
Ne_m^{(1),(2)}(\xi,q) = Se_m(\eta,q) \pm iGey_m(\xi,q); & a=b_m
\end{array}
\tag{14.28}
$$

$ce_m(\xi, q)$; $se_m(\eta, q)$ are the odd and even Mathieu functions of the first kind, respectively [17], corresponding to eigen-values a_m and b_m;

$Ce_m(\xi, q)$, $Se_m(\eta, q)$ are the modified Mathieu functions [17] (first particular solutions of the modified Mathieu equation); they are regular inside of the ellipse in the plane of $z = const$ and are similar in their properties with Bessel functions [18];

$Fey_m(\xi, q)$, $Gey_m(\xi, q)$ are the modified Mathieu functions [17] (second particular solutions of the modified Mathieu equation), they are similar to the Neumann functions [18] and have a singularity at $\xi = 0$;

$Me_m^{(1),(2)}(\xi, q)$, $Ne_m^{(1),(2)}(\xi, q)$ are the combined Mathieu functions [17], they satisfy the criterion of radiation and on their properties are similar with Hankel functions of the first and second kind [18], respectively.

So the solution is regular within the cylinder, which is used in "internal problems", has the form:

$$
F(z,\xi,\eta) = \sum_{m=0}^{\infty} \int_{-\infty}^{\infty} \Big[A_m Ce_m(\xi,q)ce_m(\eta,q) + B_m Se_m(\xi,q)se_m(\eta,q) \Big] e^{ihz} dh,
\tag{14.29}
$$

and for "external problems", the total solution must satisfy the condition of radiation and is written as

$$
F(z,\xi,\eta) = \sum_{m=0}^{\infty} \int_{-\infty}^{\infty} \Big[C_m Me_m^{(1),(2)}(\xi,q)ce_m(\eta,q) + D_m Ne_m^{(1),(2)}(\xi,q)se_m(\eta,q) \Big] e^{ihz} dh.
\tag{14.30}
$$

In these series, A_m, B_m, C_m, D_m are the coefficients corresponding to eigen-values m, h, defined in satisfying the boundary conditions of a specific task.

14.3 Fields of Displacements and Stresses in Particular Cases of Two-Dimensional Problems

14.3.1 Expressions for Fields Independent on Coordinate z

If the elastic field is independent on the coordinate z, then $\frac{\partial}{\partial z} e^{ihz} = 0$, that leads to equality 0 of the parameter h, i.e. $h = 0$. The tensors of elastic displacements and stresses are expressed through scalar potentials as

$$U_z = \overset{(T)}{g}\, w; \quad U_\xi = \overset{(L)}{D_1}\frac{\partial \varphi}{\partial \xi} + \frac{\partial v}{\partial \eta}; \quad U_\eta = \overset{(L)}{D_1}\frac{\partial \varphi}{\partial \eta} - \frac{\partial v}{\partial \xi}; \tag{14.31}$$

$$\sigma_{zz} = \left(\overset{(L)}{d_1} + \overset{(L)}{d_2}\right)\varphi; \quad \sigma_{z\xi} = \frac{\overset{(T)}{d_3}}{2}\frac{\partial w}{\partial \xi}; \quad \sigma_{z\eta} = \frac{\overset{(T)}{d_3}}{2}\frac{\partial w}{\partial \eta};$$

$$\sigma_{\xi\xi} = \left[f^2(ch^2\xi - \cos^2\eta)\overset{(L)}{d_1} + \overset{(L)}{d_4}\left(\frac{\partial^2}{\partial \xi^2} - \frac{1}{2}\frac{sh2\xi}{ch^2\xi - \cos^2\eta}\frac{\partial}{\partial \xi} + \frac{1}{2}\frac{\sin 2\eta}{ch^2\xi - \cos^2\eta}\frac{\partial}{\partial \eta}\right)\right]\varphi$$

$$+ 2a_2\left(\frac{\partial^2}{\partial \xi\partial \eta} - \frac{1}{2}\frac{\sin 2\eta}{ch^2\xi - \cos^2\eta}\frac{\partial}{\partial \xi} - \frac{1}{2}\frac{sh2\xi}{ch^2\xi - \cos^2\eta}\frac{\partial}{\partial \eta}\right)v;$$

$$\sigma_{\xi\eta} = \overset{(L)}{d_4}\left(\frac{\partial^2}{\partial \xi\partial \eta} - \frac{1}{2}\frac{\sin 2\eta}{ch^2\xi - \cos^2\eta}\frac{\partial}{\partial \xi} - \frac{1}{2}\frac{sh2\xi}{ch^2\xi - \cos^2\eta}\frac{\partial}{\partial \eta}\right)\varphi$$

$$+ a_2\left(\frac{\partial^2}{\partial \eta^2} - \frac{\partial^2}{\partial \xi^2} + \frac{sh2\xi}{ch^2\xi - \cos^2\eta}\frac{\partial}{\partial \xi} - \frac{\sin 2\eta}{ch^2\xi - \cos^2\eta}\frac{\partial}{\partial \eta}\right)v;$$

$$\sigma_{\eta\eta} = \left[\overset{(L)}{d_1}f^2(ch^2\xi - \cos^2\eta) + \overset{(L)}{d_4}\left(\frac{\partial^2}{\partial \eta^2} + \frac{1}{2}\frac{sh2\xi}{ch^2\xi - \cos^2\eta}\frac{\partial}{\partial \xi} - \frac{1}{2}\frac{\sin 2\eta}{ch^2\xi - \cos^2\eta}\frac{\partial}{\partial \eta}\right)\right]\varphi$$

$$- 2\left(\frac{\partial^2}{\partial \xi\partial \eta} - \frac{1}{2}\frac{sh2\xi}{ch^2\xi - \cos^2\eta}\frac{\partial}{\partial \eta} + \frac{1}{2}\frac{\sin 2\eta}{ch^2\xi - \cos^2\eta}\frac{\partial}{\partial \xi}\right)v;$$

$$\tag{14.32}$$

The factors a_i, $\overset{(L)}{d_i}$, $\overset{(L)}{D_1}$ could be found from the expressions (14.16), (14.18) and (14.19), if you take $h = 0$.

An analysis of the relationships (14.31 and 14.32) shows that quasi-transverse waves w may exist independently of the other types of waves φ, v. They are accompanied by displacements only along the axis $z - U_z$, and cause the stresses $\sigma_{z\xi}$ and $\sigma_{z\eta}$. Other components of the tensors of elastic field arise at the excitation of waves φ and v.

Let's then consider the most simple cases of excitation of the quasi-transverse waves, namely (i) in elliptical cylinder with boundary of $\xi = \xi_0$ (rod), (ii) in space

with a hole in the form of elliptic cylinder with boundary of $\xi = \xi_0$ (tunnel), and (iii) in large elliptical tube with the boundaries of $\xi = \xi_0$ and $\xi = \xi_1$.

The external load in the form of stress is distributed on some law at the boundary $\xi = \xi_0$:

$$\sigma_{\xi z} = \sigma^0_{\xi z}(\eta); \quad \xi = \xi_0. \tag{14.33}$$

14.3.2 Quasi-transverse Waves in Elliptic Rod and in Space of Elliptic Cavity

The solution for the potential function w in the case of quasi-transverse waves in elliptical cylinder (rod) in accordance with (14.29) can be written:

$$w(\xi, \eta) = \sum_{m=0}^{\infty} [w_m^1 Ce_m(\xi, \overset{(T)}{q}) ce_m(\eta, \overset{(T)}{q}) + w_m^2 Se_m(\xi, \overset{(T)}{q}) se_m(\eta, \overset{(T)}{q})], \tag{14.34}$$

where $\overset{(T)}{q} = \frac{1}{4} f^2 \overset{(T)}{g}^2$; $\overset{(T)}{g} = \frac{\omega}{v_\Phi}$; v_Φ is determined from the dispersion equation for the wave lines $\left(\theta = \frac{\pi}{2}\right) v_\Phi^2 = C_{44}/\rho$, w_m^1 and w_m^2 are the amplitudes, respectively of even and odd harmonics, which are defined in satisfying the boundary condition (14.33).

The applied stress $\sigma^0_{\xi z}(\eta)$ can be decomposed into a series of Mathieu functions:

$$\sigma^0_{\xi z} = \sum_{m=0}^{\infty} \left[a_m ce_m(\eta, \overset{(T)}{q}) + b_m se_m(\eta, \overset{(T)}{q}) \right] P_0, \tag{14.35}$$

where

$$a_m = \frac{1}{\pi} \int_0^{2\pi} \sigma^0_{\xi z}(\eta) ce_m(\eta, \overset{(T)}{q}) \, d\eta; \quad b_m = \frac{1}{\pi} \int_0^{2\pi} \sigma^0_{\xi z}(\eta) se_m(\eta, \overset{(T)}{q}) \, d\eta. \tag{14.36}$$

By substituting the expressions (14.35) and (14.34) into relation (14.32) for $\sigma_{z\xi}(\eta)$ and $\xi = \xi_0$, and taking $P_0 = 1$, we get:

$$\sum_{m=0}^{\infty} \left[a_m ce_m(\eta, \overset{(T)}{q}) + b_m se_m(\eta, \overset{(T)}{q}) \right]$$

$$= \frac{\overset{(T)}{d_3}}{2} \frac{\partial}{\partial \xi_0} \sum_{m=0}^{\infty} \left[w_m^1 Ce_m(\xi_0, \overset{(T)}{q}) ce_m(\eta, \overset{(T)}{q}) + w_m^2 Se_m(\xi_0, \overset{(T)}{q}) se_m(\eta, \overset{(T)}{q}) \right]. \tag{14.37}$$

Then we use the orthogonality of angular functions of Mathieu $ce_m(\eta, \overset{(T)}{q})$ and $se_m(\eta, \overset{(T)}{q})$, for that multiply the expression (14.37) on $ce_m(\eta, \overset{(T)}{q})$ and intergrate on η from 0 to 2π, and then multiply by $se_m(\eta, \overset{(T)}{q})$ and intergrate on η.

In this case, the relation (14.37) is divided into a system of algebraic equations for each harmonic n, i. e. on corresponding to even (w_n^1) and odd (w_n^2) parts. By solving this system of algebraic equations, we obtain the formulae for calculating the amplitudes of harmonics as

$$w_n^1 = \frac{2a_n}{\overset{(T)}{d_3} \frac{\partial}{\partial \xi_0} Ce_n(\xi_0, \overset{(T)}{q})}; \qquad w_n^2 = \frac{2b_n}{\overset{(T)}{d_3} \frac{\partial}{\partial \xi_0} Se_n(\xi_0, \overset{(T)}{q})}, \tag{14.38}$$

where a_n and b_n are determined from (14.36).

By substituting the obtained values of the amplitudes in the expression for the potential function (14.34), and using formulae (14.31), (14.32), we obtain the expressions for calculation of arising displacements and stresses at any point of elliptic cylinder with coordinates ξ, η:

$$U_z(\xi, \eta) = \sum_{m=0}^{\infty} \overset{(T)}{g} \left[\frac{2a_m}{\overset{(T)}{d_3} \frac{\partial}{\partial \xi_0} Ce_m(\xi_0, \overset{(T)}{q})} Ce_m(\xi, \overset{(T)}{q}) ce_m(\eta, \overset{(T)}{q}) \right.$$
$$\left. + \frac{2b_m}{\overset{(T)}{d_3} \frac{\partial}{\partial \xi_0} Se_m(\xi_0, \overset{(T)}{q})} Se_m(\xi, \overset{(T)}{q}) se_m(\eta, \overset{(T)}{q}) \right]; \tag{14.39}$$

$$\sigma_{z\xi}(\xi, \eta) = \sum_{m=0}^{\infty} \left[a_m ce_m(\eta, \overset{(T)}{q}) \frac{\frac{\partial}{\partial \xi} Ce_m(\xi, \overset{(T)}{q})}{\frac{\partial}{\partial \xi_0} Ce_m(\xi_0, \overset{(T)}{q})} + b_m se_m(\eta, \overset{(T)}{q}) \frac{\frac{\partial}{\partial \xi} Se_m(\xi, \overset{(T)}{q})}{\frac{\partial}{\partial \xi_0} Se_m(\xi_0, \overset{(T)}{q})} \right];$$

$$\sigma_{z\eta}(\xi, \eta) = \sum_{m=0}^{\infty} \left[a_m \frac{\partial ce_m(\eta, \overset{(T)}{q})}{\partial \eta} \frac{Ce_m(\xi, \overset{(T)}{q})}{\frac{\partial}{\partial \xi_0} Ce_m(\xi_0, \overset{(T)}{q})} + b_m \frac{\partial se_m(\eta, \overset{(T)}{q})}{\partial \eta} \frac{Se_m(\xi, \overset{(T)}{q})}{\frac{\partial}{\partial \xi_0} Se_m(\xi_0, \overset{(T)}{q})} \right]. \tag{14.40}$$

By substituting into the expression for $\sigma_{z\xi}$, value of $\xi = \xi_0$ from (14.40), it could be confirmed that the boundary conditions (14.33) are satisfied.

If the load is concentrated at the point $\eta = \eta_0$ and it could be represented in the form of delta-function $\delta(\eta_0 - \eta)$, then as it follows from (14.36), we obtain:

$$a_m = \frac{1}{\pi} ce_m(\eta_0, \overset{(T)}{q}); \qquad b_m = \frac{1}{\pi} se_m(\eta_0, \overset{(T)}{q}). \tag{14.41}$$

The physical components of the field are determined according to the known rules [2] as

$$U_{(z)}(\xi,\eta) = U_z;$$
$$\sigma_{(z\xi)}(\xi,\eta) = \frac{\sigma_{z\xi}(\xi,\eta)}{f\sqrt{ch^2\xi - \cos^2\eta}}; \quad \sigma_{(z\eta)}(\xi,\eta) = \frac{\sigma_{z\eta}(\xi,\eta)}{f\sqrt{ch^2\xi - \cos^2\eta}}. \tag{14.42}$$

In the case, when the task consists in definition of fields, outside the elliptic cylinder, i.e. in the space with elliptic cavity, the common solution for the potential function w has the form:

$$w(\xi,\eta) = \sum_{m=0}^{\infty}\left[w_m^1 Me_m^{(1)}(\xi, \overset{(T)}{q})ce_m(\eta, \overset{(T)}{q}) + w_m^2 Ne_m^{(1)}(\xi, \overset{(T)}{q})se_m(\eta, \overset{(T)}{q}) \right]. \tag{14.43}$$

The functions of $Me_m^{(1)}\left(\xi, \overset{(T)}{q}\right)$ and $Ne_m^{(1)}\left(\xi, \overset{(T)}{q}\right)$ satisfy the radiation condition at infinity, if it is taken time-dependence in the form of $e^{-i\omega t}$.

The formulae for calculation of the field in this case are coincide with obtained above for the rod, if we replace the function $Ce_m^{(1)}\left(\xi, \overset{(T)}{q}\right)$ on $Me_m^{(1)}\left(\xi, \overset{(T)}{q}\right)$, and the function $Se_m^{(1)}\left(\xi, \overset{(T)}{q}\right)$ on $Ne_m^{(1)}\left(\xi, \overset{(T)}{q}\right)$.

14.3.3 Quasi-transverse Waves in Thick Elliptical Tube

By solving this problem, the inner boundary $\xi = \xi_0$ of the considered construction is subjected to the stress $\sigma_{z\xi}^0(\eta)$, the outer boundary $\xi = \xi_1$ is the free boundary, i.e. on its acts the stress $\sigma_{z\xi}(\xi = \xi_1) = 0$.

In this case, it is convenient to present the fields in the form of waves, running away from the boundaries each to other. Then, the common solution for the function w could be represented as the following decomposition:

$$w(\xi,\eta) = \sum_{m=0}^{\infty}\left[w_m^{+1} Me_m^{(1)}(\xi, \overset{(T)}{q})ce_m(\eta, \overset{(T)}{q}) + w_m^{+2} Ne_m^{(1)}(\xi, \overset{(T)}{q})se_m(\eta, \overset{(T)}{q}) \right.$$
$$\left. + w_m^{-1} Me_m^{(2)}(\xi, \overset{(T)}{q})ce_m(\eta, \overset{(T)}{q}) + w_m^{-2} Ne_m^{(2)}(\xi, \overset{(T)}{q})se_m(\eta, \overset{(T)}{q}) \right]. \tag{14.44}$$

The amplitudes of the running from the boundary $\xi = \xi_0$ even and odd waves w_m^{+1}, w_m^{+2} and waves, running towards them w_m^{-1}, w_m^{-2} (in direction to the boundary), the odd and even respectively, could be found by satisfying the boundary conditions.

With this purpose, we substitute the sum (14.44) and the decomposition (14.35) into expression for $\sigma_{z\xi}$ from (14.40), with $\xi = \xi_0$ and $\xi = \xi_1$, and as a result obtain

$$\sum_{m=0}^{\infty} \left[a_m ce_m\left(\eta, \overset{(T)}{q}\right) + b_m se_m\left(\eta, \overset{(T)}{q}\right) \right]$$

$$= \frac{\overset{(T)}{d_3}}{2} \sum_{m=0}^{\infty} \left[w_m^{+1} \frac{\partial Me_m^{(1)}\left(\xi_0, \overset{(T)}{q}\right)}{\partial \xi_0} ce_m\left(\eta, \overset{(T)}{q}\right) + w_m^{+2} \frac{\partial Ne_m^{(1)}\left(\xi_0, \overset{(T)}{q}\right)}{\partial \xi_0} se_m\left(\eta, \overset{(T)}{q}\right) \right.$$

$$\left. + w_m^{-1} \frac{\partial Me_m^{(2)}\left(\xi_0, \overset{(T)}{q}\right)}{\partial \xi_0} ce_m\left(\eta, \overset{(T)}{q}\right) + w_m^{-2} \frac{\partial Ne_m^{(2)}\left(\xi_0, \overset{(T)}{q}\right)}{\partial \xi_0} se_m\left(\eta, \overset{(T)}{q}\right) \right];$$

$$0 = \frac{\overset{(T)}{d_3}}{2} \sum_{m=0}^{\infty} \left[w_m^{+1} \frac{\partial Me_m^{(1)}\left(\xi_1, \overset{(T)}{q}\right)}{\partial \xi_1} ce_m\left(\eta, \overset{(T)}{q}\right) + w_m^{+2} \frac{\partial Ne_m^{(1)}\left(\xi_1, \overset{(T)}{q}\right)}{\partial \xi_1} se_m\left(\eta, \overset{(T)}{q}\right) \right.$$

$$\left. + w_m^{-1} \frac{\partial Me_m^{(2)}\left(\xi_1, \overset{(T)}{q}\right)}{\partial \xi_1} ce_m\left(\eta, \overset{(T)}{q}\right) + w_m^{-2} \frac{\partial Ne_m^{(2)}\left(\xi_1, {}^{(T)}\right)}{\partial \xi_1} se_m\left(\eta, \overset{(T)}{q}\right) \right].$$

$$(14.45)$$

By using the orthogonality of the Mathieu functions $Ce_m\left(\eta, \overset{(T)}{q}\right)$ and $Se_m\left(\eta, \overset{(T)}{q}\right)$, as in the case of elliptic rod, we obtain a set of equations for finding unknown amplitudes of harmonics w_m as

$$a_m = \frac{\overset{(T)}{d_3}}{2} \left[w_m^{+1} \frac{\partial}{\partial \xi_0} Me_m^{(1)}\left(\xi_0, {}^{(T)}\right) + w_m^{-1} \frac{\partial}{\partial \xi_0} Me_m^{(2)}\left(\xi_0, {}^{(T)}\right) \right];$$

$$b_m = \frac{\overset{(T)}{d_3}}{2} \left[w_m^{+2} \frac{\partial}{\partial \xi_0} Ne_m^{(1)}\left(\xi_0, \overset{(T)}{q}\right) + w_m^{-2} \frac{\partial}{\partial \xi_0} Ne_m^{(2)}\left(\xi_0, \overset{(T)}{q}\right) \right];$$

$$0 = w_m^{+1} \frac{\partial}{\partial \xi_1} Me_m^{(1)}\left(\xi_1, \overset{(T)}{q}\right) + w_m^{-1} \frac{\partial}{\partial \xi_1} Me_m^{(2)}\left(\xi_1, \overset{(T)}{q}\right);$$

$$0 = w_m^{+2} \frac{\partial}{\partial \xi_1} Ne_m^{(1)}\left(\xi_1, \overset{(T)}{q}\right) + w_m^{-2} \frac{\partial}{\partial \xi_1} Ne_m^{(2)}\left(\xi_1, \overset{(T)}{q}\right).$$

$$(14.46)$$

By solving this system relatively unknowns, we can write:

$$w_m^{+1} = \frac{2\frac{a_m}{(T)}\frac{\partial}{\partial \xi_1} Me_m^{(2)}(\xi_1, \overset{(T)}{q})}{-\frac{\partial}{\partial \xi_0} Me_m^{(2)}(\xi_0, \overset{(T)}{q})\frac{\partial}{\partial \xi_1} Me_m^{(1)}(\xi_1, \overset{(T)}{q}) + \frac{\partial}{\partial \xi_1} Me_m^{(2)}(\xi_1, \overset{(T)}{q})\frac{\partial}{\partial \xi_1} Me_m^{(1)}(\xi_1, \overset{(T)}{q})};$$

$$w_m^{-1} = \frac{2\frac{a_m}{(T)}\frac{\partial}{\partial \xi_1} Me_m^{(1)}(\xi_1, \overset{(T)}{q})}{\frac{\partial}{\partial \xi_0} Me_m^{(2)}(\xi_0, \overset{(T)}{q})\frac{\partial}{\partial \xi_1} Me_m^{(1)}(\xi_1, \overset{(T)}{q}) - \frac{\partial}{\partial \xi_1} Me_m^{(2)}(\xi_1, \overset{(T)}{q})\frac{\partial}{\partial \xi_0} Me_m^{(1)}(\xi_1, \overset{(T)}{q})};$$

$$w_m^{+2} = \frac{2\frac{b_m}{(T)}\frac{\partial}{\partial \xi_1} Ne_m^{(2)}(\xi_1, \overset{(T)}{q})}{-\frac{\partial}{\partial \xi_0} Ne_m^{(2)}(\xi_0, \overset{(T)}{q})\frac{\partial}{\partial \xi_1} Ne_m^{(1)}(\xi_1, \overset{(T)}{q}) + \frac{\partial}{\partial \xi_1} Ne_m^{(2)}(\xi_1, \overset{(T)}{q})\frac{\partial}{\partial \xi_0} Ne_m^{(1)}(\xi_1, \overset{(T)}{q})};$$

$$w_m^{-2} = \frac{2\frac{b_m}{(T)}\frac{\partial}{\partial \xi_1} Ne_m^{(1)}(\xi_1, \overset{(T)}{q})}{\frac{\partial}{\partial \xi_0} Ne_m^{(2)}(\xi_0, \overset{(T)}{q})\frac{\partial}{\partial \xi_1} Ne_m^{(1)}(\xi_1, \overset{(T)}{q}) - \frac{\partial}{\partial \xi_1} Ne_m^{(2)}(\xi_1, \overset{(T)}{q})\frac{\partial}{\partial \xi_0} Ne_m^{(1)}(\xi_1, \overset{(T)}{q})}.$$

$$(14.47)$$

By substituting these expressions into (14.44), we determine the values of tensor fields in a certain point of the considered construction on the base of formulae for the displacements and stresses (14.31, 14.32).

14.3.4 The Common Case of Excitation of the Elliptic Constructions

A simple method described above cannot be applied to solve the problems, when in the construction with the form of elliptic cylinder the various types of waves are excited. It is caused by that the angular Mathieu functions, describing above types of waves, are not orthogonal, because the parameter q for quasi-longitudinal, quasi-transverse and transverse waves is different. The same notice takes place in the case, when the considered waves are to be even of the same type in the layered construction, which has different layers with various physical and mechanical characteristics.

In these more difficult cases, it could be applied the decomposition method of the angular functions of Mathieu into Fourier series on the trigonometric functions.

The formal algorithm for the solution of problems for the layered constructions like elliptic cylinders coincides fully with the solution of similar tasks for circular cylinders and is described in detail in [10].

References

1. V. Novatsky, *Theory of Elasticity*. (Mir, Moscow, 1975). (in Russian)
2. A.J. McConnell, *Application of Tensor Analysis* (Dover, New York, 1947)
3. R.M. Christensen, *Mechanics of Composite Materials,* 2nd edn. (Wiley, New York, 1979)
4. V.T. Grinchenko, V.V. Meleshko, *Harmonic Oscillations and Waves in Elastic Bodies* (Naukova Dumka, Kiev, 1981). (in Russian)
5. P.M. Morse, H. Feshbach, *Methods of Theoretical Physics*, Part 2. (McGraw-Hill, New York, 1953)
6. V.P. Sizov, *Mechanics of Solids,* vol. 5. (Izvestiya of USSR Academy of Science, 1988)
7. F.N. Fedorov, *Theory of Elastic Waves in Crystals* (Plenum, New York, 1968)
8. A.G. Nasledyshev, V.P. Sizov, A.A. Chernov, in *Waves and Diffraction-90*, vol. 1. (Physical Society, Moscow, 1990), (in Russian)
9. N.A. Yevtushenko, P.V. Lobzenko, V.P. Sizov, *Mechanics of Solid*, vol. 6. (Izvestiya of Russian Academy of Science, 1996)
10. V.P. Sizov, I.P. Miroshnichenko, *Elastic Waves in Layered Anisotropic Structures* (LAP LAMBERT Academic Publishing, Saarbrucken (Germany), 2012)
11. I.P. Miroshnichenko, V.P. Sizov, *North-Caucases Region. Natural Sciences*,vol. 2. (Izvestia of Higher School, 1999) (in Russian)
12. Miroshnichenko I. P., Sizov V.P. *Izvestia of Higher School. North-Caucases Region. Natural Sciences*, vol. 3. (1999) (in Russian)
13. A.M. Petrov, V.P. Sizov, *Mechanics of Solids*, vol. 3. (Izvestiya of Russian Academy of Science, 2000)
14. I.P. Miroshnichenko, V.P. Sizov, *Mechanics of Solids*, vol. 1. (Izvestiya of Russian Academy of Science, 2000)
15. P.K. Rashevsky, *Riemannian Geometry and Tensor Analysis* (Nauka, Moscow, 1967). (in Russian)
16. E.A. Ivanov, *Diffraction of Electromagnetic Waves on Two Bodies* (Nauka i Tekhnika, Minsk, 1968). (in Russian)
17. N.W. McLachlan, *Theory and Application of Mathieu Functions* (University Press, Oxford, 1947)
18. G.A. Korn, T.M. Korn, *Mathematical Handbook for Scientists and Engineers* (McGraw-Hill, New York, 1968)

Chapter 15
Mathematical Modeling in Problems of Vibration Acoustics of Shells

A. S. Yudin

Small oscillations of shells in the ideal compressible unlimited linear acoustic medium (fluid) under the influence of harmonic loads are studied. In such a statement the acoustics of vibrating constructions are modeled. Different versions of simulation of an environment influence are discussed. In strict statement the boundary-value problem of hydroelasticity on joint oscillations of a fluid and an elastic shell construction contacts with the liquid is considered. Here the integro-differential problem with using of the integral formula of Helmholtz with integration on contact surface of the construction and the medium is solved. More effective method applying the formulae for a dynamic pressure of the fluid, obtained in simpler problems, is offered also. It is discussed application of some iterative processes for obtaining numerical results.

15.1 Equations of Linear Acoustics

The equations of linear acoustics follow from the main hydrodynamic equations including equations of continuity, motion and adiabatic state that leads to wave equation: $\Delta\Phi = c_f^2\Phi_{,tt}$. Here $\Delta = \nabla^2$ is the operator of Laplace, ∇ is the operator of Hamilton, Φ is the velocity potential of medium points: $v_f = -\text{grad}\Phi = -\nabla\Phi$, c_f is the sound speed in the medium. Acoustic pressure, p, and relative change of a liquid density also satisfy the wave equation. The pressure p and potential Φ are coupled by dependence: $p = \rho_f\Phi_{,t}$, where ρ_f is the liquid density in the static state. This dependence fulfills inside and on field boundary. If the field boundary represents an impervious shell, we have on the contact surface the condition: $w_{,t} = \Phi_{,n_o}$, where $w_{,t}$ is the displacement velocity of shell, W is the displacement on normal $\mathbf{n}_o$ (exterior to the shell), $\Phi_{,n_o} = n_o \cdot \nabla\Phi$ is the normal derivative.

A. S. Yudin (✉)
Vorovich Mechanics and Applied Mathematics Research Institute, Southern Federal University, Rostov-on-Don, Russia
e-mail: yudin@math.sfedu.ru

In stationary (harmonic) version of oscillation process, it is fulfilled a time dependence: $\Phi = \Phi_a \cdot \exp(-s_0 i\omega t)$, where $s_0 = -1, +1, \omega$ is the circular frequency. Then the wave equation reduces to the equation of Helmholtz relatively of amplitudes:

$$\Delta\Phi_a + k_o^2\Phi_a = 0, \quad k_o^2 = \omega/c_f. \tag{15.1}$$

Below, for simplification, we shall omit the lower index "a", pointing amplitude, keeping for amplitudes the denotations of considered functions. In this case, the relations (for amplitudes) accept the following forms: $p = -s_0 i\omega\rho_f\Phi$, $\Phi_{,n_o}|_S = -s_0 i\omega w$.

At statement of the problem external to the closed surface for obtainment of the unique solution (taking into account that the waves decrease at infinity), we use Somerfield conditions of radiation in the form: $\lim\limits_{R\to\infty}(\Phi_{,R} - s_0 ik_o\Phi) = 0, \lim\limits_{R\to\infty}\Phi = 0$, where R is the radius of spherical coordinate system with the origin of coordinates in region, bounded by closed surface (shell) O_o. These conditions are equivalent to the requirement of transformation of the waves radiated from a surface into spherical dispersing damping waves at infinite propagation along any ray starting in the restricted field.

Particular solutions of tasks for the Helmholtz equations on propagation of oscillations into fluid from shells (solids) with the given velocity distribution on the contact surface are sufficiently simply determined in spherical and cylindrical coordinate systems for sphere and infinite circular cylinder. More common solutions are constructed in series on effectively computed special functions (of Legendre, Bessel, Neumann, Hankel). Some approximate solutions are obtained in spheroid coordinates for the prolate ellipsoids and slightly oblate spheroids.

Complexity of solution of the radiation and dispersion problem increases in the case of joint oscillations of fluid and shells of sufficiently common form (the shells of revolution which are distinct from canonical forms, with complex connections and others). Here, we develop the corresponding methods based on integral equations and formulae.

Let the surface O_o divides space into the internal finite area O_+ and external one O_-. The following fundamental solution satisfies Helmholtz equation and radiation conditions:

$$\lambda(x, \xi) = \exp(s_0 ik_o\bar{R})/(4\pi\bar{R}), \ \bar{R} = |x - \xi| = \sum_{j=1}^{3}(x_j - \xi_j)^2, \tag{15.2}$$

where $\bar{R}$ is the distance between two points of space. By using solution (15.2) and Green's formula the integrated formula for pressure is deduced [1]:

$$\iint\limits_{O_o} [p(\xi)\lambda(x, \xi)_{,n_o} - \lambda(x, \xi)p(\xi)_{,n_o}] \, dS = K_p p. \tag{15.3}$$

Here $\xi \in O_o$, $(..)_{,n_o} = \partial(..)/\partial n_o$ is the derivative on normal to the surface. For point x in exterior field $K_p = 1$ and integral (15.3) is usually named by an integral of Helmholtz. It can be applied to sound field calculation by using known pressure profile and gradient of pressure (displacements, velocities) on surface O_o. At $x \in O_o$, coefficient $K_p = 0.5$ and the relationship (15.3) becomes an integral equation of Fredholm of the second kind respectively of pressure p. When $x \in O_o$, coefficient $K_p = 0$. Thus in strict statement, the task of calculation of shell oscillations and sound field in the medium is integro-differential (ID) one.

15.2 Equations for Vibrating Shells

The main equations of shell oscillations could be found in [2, 3] and other references. In the case of shell with main surface in the form of closed rotationally symmetric form, the effective algorithms are methods of solution of the boundary-value problem into framework of the Cauchy problem. In this case, trigonometric Fourier series on the peripheral coordinate are applied to two-dimensional equation set. As a result, the prototype set of the two-dimensional equations reduces to one-dimensional one, depending on the remained longitudinal coordinate and number of the peripheral mode as on parameter. Then the equations are led to a normal form of ordinary differential equations sets of the first order, each of which respectively of the mixed group of solving functions. One half of these functions represent power components, other half define the kinematic ones. These components are included into natural boundary conditions following from variational principles of Lagrange (in statics) or Hamilton (in dynamics). From these principles, the matching conditions on lines of breaking meridian and reinforcing discrete ring ridges also are derived. The boundary-value problems for number of resolving sets of equations, including matching and boundary conditions, are solved by using the method of differential sweep with orthogonalization on Godunov at the intermediate points of integrating range. Variability of mechanical characteristics of shells along the meridian is thus admitted. The shells can be multi-connected and preliminary statically stress-strained. In principle, the equations can lead to base functions as displacement components. For compactness of further presentation, it will be assumed.

Symbolically the equations of simple harmonic motions of the reinforced shells we will write respectively of displacement amplitudes by using the compact operator form:

$$C(U) + \omega^2 A(U) + q - p = 0, \qquad (15.4)$$

where C, A are the elastic and inertial operators of the shell reinforced by ribs, $U = \{u, v, w\}$ is the displacement amplitude vector, $q = \{q_1, q_2, q_3\}$ is the amplitude of loading, $p = \{0, 0, p\}$ is the amplitude of dynamic pressure of liquid. We consider, that the operator equation (15.1) includes matching conditions

at discrete ribs and boundary conditions through area of definition of the operators C and A.

Further we shall use the equations with dimensionless quantities, pass to which is conducted by using the following formulae:

$$\{\Phi\}_L = \{\Phi\}_D/(\omega R_*^2); \quad \{\Delta\}_L = \{\Delta\}_D R_*^2; \quad \{\nabla\}_L = \{\nabla\}_D R_*;$$
$$\{n_o, \ R\}_L = \{n_o, \ R\}_D/R_*; \quad \{u, v, w\}_L = \{u, v, w\}_D/h_*;$$
$$\{p, q_j\}_L = \{..\}_D R_*^2 \bar{v}_*/(E_* h_*^2); \quad \{\rho_f\}_L = \{\rho_f\}_D/\rho_*; \tag{15.5}$$
$$\{c_f\}_L = \{c_c\}_D/c_*; \quad c_* = [E_*/(\rho_* \bar{v}_*)]^{1/2}; \quad \bar{v}_* = 1 - v_*^2;$$
$$\varepsilon_1 = h_*/R_*; \quad \Omega = \omega R_*/c_*.$$

Here the subscript "L" corresponds to dimensionless quantities; the index "D" defines the dimensional ones; h_*, R_*, ρ_*, c_* are the proper small and large scales, material density, and sound velocity in the shell; ε_1, Ω are the parameters of thin-wallness and frequency, respectively.

Further in Sect. 15.3, we shall work with dimensionless quantities, but we shall omit subscript "L" with aim of simplification. Then in the dimensionless form above relationships reduce to the following ones:

$$\Delta\Phi + \bar{k}^2\Phi = 0; \quad \bar{k} = \Omega/c_f; \quad p = -s_0 i\rho_c(\Omega/\varepsilon_1)^2\Phi;$$
$$n_o \cdot \nabla\Phi|_{S_o} = s_0 i\varepsilon_1 w; \quad \lim_{R\to\infty} R(\Phi_{,R} - s_0 i\bar{k}\Phi) = 0; \quad \lim_{R\to\infty} \Phi = 0; \tag{15.6}$$
$$p(r_2) = (2\pi)^{-1} \iint\limits_{O_o} [p(r_1)f(R)_{,n_o} - f(R)p(r_1)_{,n_o}] \, dr_1;$$

$$C(\mathrm{U}) + \Omega^2 A(\mathrm{U}) + q - p = 0. \tag{15.7}$$

The integral (15.6) is written for the surface of contact, $f(R) = \exp(i\bar{k}R)/R$, where $\mathbf{r_1}$, $\mathbf{r_2}$ are the radius-vectors of points on the shell surface, $R = |r_1 - r_2|$ is the distance between them.

If necessary to take into account intrinsic losses in fluid, its sound velocity is given as a complex variable [4]. For simulation of intrinsic losses of vibrational energy in construction, the method of complex elastic moduli (or complex stiffnesses) based on Sorokin's hypothesis [5] is used.

15.3 Method of Eigenforms

Method of eigenforms (EF-method) uses integral equation (15.6) and differential equation (15.7) (ID-formulation) and in the case of rotationally symmetric shells contains three stages [6, 7]: (i) calculation of base functions which are eigenforms of shell oscillations in vacuum, (ii) obtainment of pressure and displacement

distributions (forms of forced oscillations) on the shell-medium interface, (i) calculation of acoustic field in the medium.

Basic functions are defined in the process of the solution of eigenvalue problem for the shell equations in which the circumferential coordinate is separated by application of trigonometrical Fourier serieses. Further factors for shell displacements and pressure in liquids on the contact surface further are represented in the form of series on longitudinal eigen-oscillation modes of shell in vacuum. By using the eigenmodes for normal displacement of shell, the set of orthogonal basic functions is found on the base of Gramm-Shmidt's process of orthogonalization. With its help, it is possible to express Fourier factors of pressure through factors of displacements. On the base of boundary integral equation and application of Bubnov-Galerkin's procedure for each n-th circumferential mode, the set of the linear algebraic equations of M-order is formed, where M is the number of the retained longitudinal modes. By this, the orthogonality of vectors of eigenforms is used in power spaces of elastic and inertial operators of the equations for shell oscillations. The equation set solution gives distribution of pressure and pressure gradient at the boundary-contact surface.

Demonstrating a correctness in the solution of the coupled problem for "shell—liquid" system, EF-method is difficult for applications. It also does not possess flexibility to changes of parametres of construction. At multiple calculations, it is necessary to recalculate eigenfunctions (which are required some tens) for ensuring good convergence. A practical applicability of the EF-method is limited by sufficiently average frequencies since natural obstacle for expension EF-method to higher frequencies is the dense spectrum of eigenfrequencies mainly of bending normal forms with zerous circumferential mode of the shell (after frequency of the first radial resonance).

15.4 Method of Local Impedance Modeling

Due to above reason the method of local impedance modelling (LIM-method) is more effective, when a *priori* the dependence of the dynamic pressure on velocity (or amplitudes of displacements) is given on the shell surface. Attractiveness of this method consists in that the fluid account only insignificantly complicates algorithm for "dry" shells with intrinsic vibrational energy dissipation.

The solution of the acoustics equations in cylindrical coordinate system may be deduced by method of variables separation. After that, it is possible to obtain for n-th circumferential mode the impedance linking amplitudes of dynamic pressure and velocities of partticles of the ideal infinite liquid on surface of infinitely long cylindrical shell of radius R_c [4]:

$$p_{n(s)} = Z_{cn}c_{n(s)}; \quad Z_{cn} = \left[s_o i \rho_f c_f \gamma_o H_n^{(s_o)}(\gamma)\right] \Big/ \left[\gamma H_n^{(s_o)'}(\gamma)\right], \quad (15.8)$$

where $\gamma_o = kR_y$; $\gamma = k_r R_y$; $k_r = \sqrt{k^2 - k_z^2}$; $k_o = \omega/c_f$; $k_z = m\pi/L$; $s_o = \pm 1$; k_o, k_r, k_z are the wave numbers; $H_n^{(s_0)}$, $H_n^{(s_0)'}$ are Hankel functions and their derivatives on argument.

For a plane problem when the solution does not depend from z, $k_z = 0$; $k_r = k_o$; $\gamma = \gamma_o$. Hankel functions of the first kind correspond to value of $s_0 = 1$, and Hankel functions of the second kind relate to $s_0 = -1$:

$$H_n^{(s_o)}(\gamma) = J_n(\gamma) + s_o i Y_n(\gamma); \ H_n^{(s_o)'}(\gamma) = n H_n^{(s_o)}(\gamma)/\gamma - H_{n+1}^{(s_o)}(\gamma).$$

Here J_n, Y_n are Bessel functions of the first and second kind, respectively.

By passing in (15.8) from velocities $c_{n(s)}$ to displacements $w_{n(s)}$, taking into account $c_{n(s)} = -s_o i \omega w_{n(s)}$ we obtain

$$p_{n(s)} = Z_{wn} w_{n(s)}; \quad Z_{wn} = \left[\omega \rho_c c_c \gamma_o H_n^{(S_o)}(\gamma)\right] \Big/ \left[\gamma H_n^{(s_o)'}(\gamma)\right], \tag{15.9}$$

where Z_{wn} has a sense of the mechanical stiffness coefficient of medium.

After transition to non-dimensional quantities by means of the relationships:

$$\tilde{p}_{n(s)} = p_{n(s)} v_* / (E_* \varepsilon_1^2); \ \tilde{\rho}_f = \rho_f / \rho_*; \ \tilde{w}_{n(s)} = w_{n(s)}/h_*;$$
$$\tilde{c}_c = c_c/c_*; \ \Omega = \omega R_*/c_*; \ \Omega_1 = \Omega/(\tilde{k}_2 \tilde{c}_2) = \gamma_o;$$
$$\tilde{R}_y = R/R_*, \quad \tilde{L} = L/R_*, \quad \tilde{k}_2 = 1/\tilde{R};$$
$$\varepsilon_1 = h_*/R_*, \ \bar{v}_* = 1 - v_*^2, \ c_* = \sqrt{E_*/(\rho_* \bar{v}_*)};$$
$$\gamma = \Omega_1 \kappa, \ \kappa = \sqrt{1 - \kappa_1^2}, \ \kappa_1 = m\pi c_c/(\omega L) = m\pi \tilde{c}_c/(\Omega \tilde{L});$$
$$c_* = [E_*/(\rho_* \bar{v}_*)]^{1/2}, \ \bar{v}_* = 1 - v_*^2, \ \varepsilon_1 = h_*/R_*, \ \Omega = \omega R_*/c_*$$

the expression of dynamic rigidity takes the form:

$$\tilde{p}_{n(s)} = \tilde{Z}_{wn} \tilde{w}_{n(s)}, \ \tilde{Z}_{wn} = \left[\Omega \tilde{\rho}_c \tilde{c}_c H_n^{(S_o)}(\Omega_1 \kappa)\right] \Big/ \left[\varepsilon_1 \kappa H_n^{(S_o)'}(\Omega_1 \kappa)\right]. \tag{15.10}$$

For $\kappa_1 > 1$, arguments of the Hankel functions becomes purely imaginary, and they can be presented by McDonald functions, or modified Bessel functions of first ($s_0 = 1$) and second ($s_0 = -1$) kind. In this case $\tilde{Z}_{wn}$ is represented as

$$\tilde{Z}_{wn} = \left[\Omega \tilde{\rho}_c \tilde{c}_c K_n^{(s_o)}(\Omega_1 |\kappa|)\right] \Big/ \left[\varepsilon_1 |\kappa| K_n^{(s_o)'}(\Omega_1 |\kappa|)\right] \equiv \tilde{Z}_n^-, \tag{15.11}$$

where $K_n^{(s_o)}$ are McDonald functions, real and positive at the real and positive argument, $K_n^{(s_o)'} = n K_n^{(s_o)}(x) \Big/ x - K_{n+1}^{(s_o)}(x)$.

At $n \neq 0$ and small argument $x = \Omega_1 |\kappa| \to 0$, we obtain

$$K_n^{(s_o)}(x) \to [(n-1)!/2](2/x)^n, \quad K_n^{(s_o)'}(x) \to [n!/4](2/x)^{n+1},$$
$$\tilde{Z}_n^- \to -(\tilde{\rho}_c \Omega^2)/(\varepsilon_1 n \tilde{k}_2).$$

At $n = 0$ and $x \to 0$, we obtain

$$K_0^{(s_o)}(x) \to 0.11593 - \ln x, \quad K_0^{(s_o)'}(x) \to -K_1^{(s_o)}(x) \to 1/x,$$
$$\tilde{Z}_0^- \to -[\tilde{\rho}_c \Omega^2/(\varepsilon_1 \tilde{k}_2)](\ln x - 0.11593).$$

The presented formulae are obtained for cylinder. At their usage for shells of revolution there are alternative versions. In one of them, it is possible to substitute $\tilde{R}_c$ on $\tilde{r}$ being polar radius of shell at the given point on generatrix, and then $\tilde{k}_2 = 1/\tilde{R}_c$. In other version, it is possible to treat $\tilde{k}_2$ as curvature of normal cross-section in circumferential direction, and then $\tilde{k}_2 = (\sin \beta)/\tilde{r}$, where β is the angle of slope of the generatrix normal to rotation axis.

When edges of the shell of revolution are enclosed by rigid plates of radius $\tilde{r}_p$, then at longitudinal oscillations on the zero mode ($n = 0$), the medium response at the edges could be simulated through the impedance of the rigid piston without screen [8]. In the dimensionless form

$$\tilde{p}_0^{(n)} = \tilde{Z}_{w_0}^{(n)} \tilde{w}_0^{(n)}, \quad \tilde{Z}_{w_0}^{(n)} = -\varepsilon_1^{-1} \tilde{\rho}_c \tilde{r}_n \Omega^2 (\Omega_1 \kappa)(2/\pi + s_o i \tilde{r}_n/(2\tilde{c}_c)). \tag{15.12}$$

Calculation of dynamic rigidity of environment is conducted in the form of complex procedure with logic branching. Different formulae are realized on branching in dependence on that where pressure is calculated on the shell or plate. We take into account the mode number and behavior of argument $x = \Omega_1|\kappa|$.

After obtainment of the solution on the shell surface, the field pressure in fluid is determined by Helmholtz integral (15.3) for exterior area O_-.

For shells of revolution, numerical experiments on selection of the longitudinal wave numbers m depending on vibration mode of shell with finite size were executed. Comparison shows possibility to use the plane problem version ($m = 0$, $\kappa = 1$) in sufficiently broad range of frequencies at construction of external field characteristics. Acceptability of such model confirms by comparison with EF-method.

15.5 Iterative Processes

The further development of ID-formulation and LIM-method are iterative methods where given impedance could be used as initial approach of iterative processes (IPs) at the solution of the original equations. For simply connected shells of axisymmetrical geometry (without branching) some variants of IPs, having different areas of convergence, are realized in [9].

15.6 External Field Calculation

In the briefly presented methods (EF, LIM, itterative ones), the exterior acoustic field is calculated at the last stage by using Helmholtz integral (15.3), where $x \in O_-$. The field gives a distribution of dynamic pressure amplitudes (sound) in the fluid. Obsrvation point coordinates $\mathbf{x}$ (radius-vector) are convenient to give in spherical coordinate system $r, \ \varphi = \alpha_2, \ \theta = \theta_1 + \gamma_1$. Here r is the radius, $\varphi \in [0, 2\pi]$ is the circumferential coordinate (longitude), $\theta_1 \in [0, \pi]$ is the coordinate calculated along meridian (latitude). The origin of spherical coordinate system is usually placed at the center of area O_+ (see Fig. 15.1).

Common procedure of calculation allow us to construct the near and far sound field by using repeated integration of the double integral:

$$p(r) = (4\pi)^{-1} \iint\limits_{O_o} \left[p(r_1)f(R)_{,n_o} - f(R)p(r_1)_{,n_o} \right] dr_1 \tag{15.13}$$

on surface O_o with repeated application of Simpson method. Here $\mathbf{r}, \mathbf{r_1}$ are the radius-vectors of points into medium and on the shell surface, respectively, $R = \sqrt{r^2 + r_1^2 - 2r_1 r \cdot \cos(\gamma_1)}$.

For recalculation of levels $|p|$ in decibels two versions of normalizations were used:

(i) in relation to a threshold level of audibility $p_1 = 2 \cdot 10^{-5}$ H/M^2, or $\tilde{p}_1 = 8.84 \cdot 10^{-13}$, where tilde marks non-dimensional value;
(ii) in relation to a maximum level of the field from the force radiating in the liquid half-space (dipole):

$$|p_2| = \Omega Q/(2\pi R c_f), \ L_{|p|}^{(k)} = 20\ln(|\tilde{p}|/|\tilde{p}_k|), \ k = 1, \ 2. \tag{15.14}$$

For constructions with sections such as in Fig. 15.2, some of the eigenmodes are shown in Fig. 15.3. Note that the three-section shell consisted of conical and two cylindrical parts. The shell sections were divided into plates and rigid rings. The last scheme well works and allows us to simplify algorithm. So, instead of using the superelement scheme, it is possible to solve two-dimensional boundary-value problem. Comparison of the applied methods was executed on multi-section long shells with additional masses. The amplitude-frequency characteristics of the field levels in the "illuminated" zones for the same observation points (for these methods) are shown in Fig. 15.4.
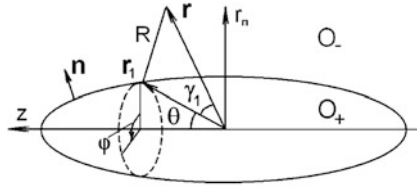
Fig. 15.1 Coordinate system for external field calculation
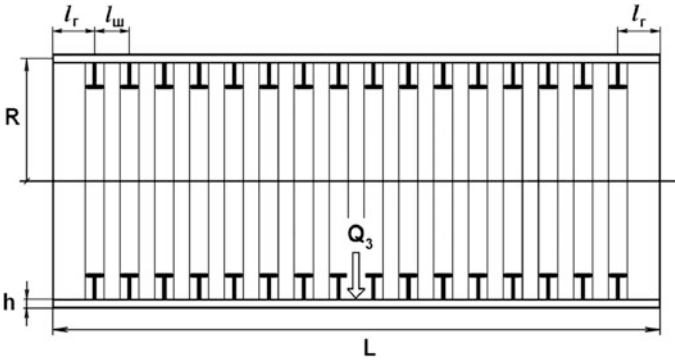
Fig. 15.2 Typical section of shell construction
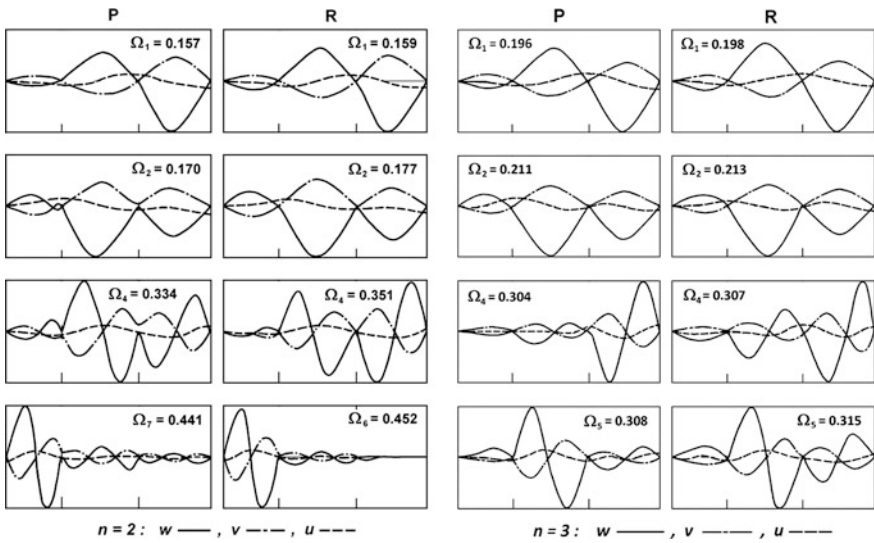
Fig. 15.3 Eigenform of oscillations for three-section shell, divided into plates (*P*) and rings (*R*)
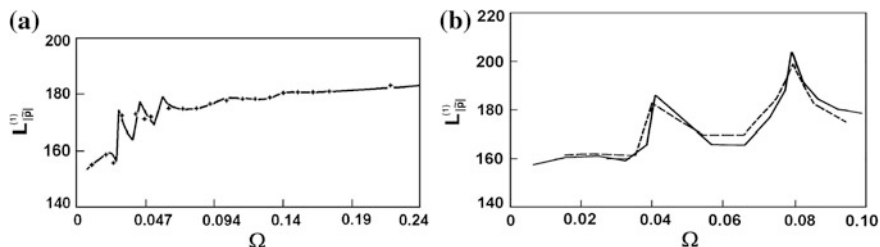
Fig. 15.4 Comparison of methods of eigenforms and local impedance modeling for **a** transverse ($n = 1$) and **b** longitudinal ($n = 0$) oscillations

15.7 Conclusions

Application of the EF-method and methods of iterative processes meets significant challenges for the implementation in algorithms. Therefore, it is expedient to use the LIM-method. On the basis of the LIM-method, there were analyzed the shells with no axisymmetrical rigidities and masses [10, 11], multicoupled [12], coaxial [13, 14] ones, and also the shells with discrete rings of variable stifness [15], incircular cylindrical shells [16] and others.

References

1. N.S. Koshlyakov, M.M. Smirnov, E.B. Gliner, *Differential Equations of Mathematical Physics* (North-Holland Publishers, Amsterdam, 1964)
2. V.I. Myachenkov, I.V. Grigoriev, *Calculation of Composite Shell Constructions on ECM: Handbook* (Mashinostroenie, Moscow, 1981). (In Russian)
3. A.S. Yudin, *Stability and Oscillations of Constructive Anisotropic and Artificated Shells of Revolution* (Southern Federal University Press, Rostov-on-Don, 2011). (In Russian)
4. E. Skudrzyk, *The Foundations of Acoustics, Basic Mathematics and Basic Acoustics* (Springer, Wien, 1971)
5. I.M. Korenev, I.M. Rabinovich (eds.), *Handbook on Dynamics of Constructions* (Stroyizdat, Moscow, 1972). (In Russian)
6. I.I. Vorovich, A. Ya Tsionskii, A.S. Yudin, Acoust. J. **29**(6), 744 (1983). (In Russian)
7. A. Ya. Tsionskii, J. Tech. Acoust. **1**(2), 33 (1994)
8. I.A. Ruminskaya, *Grounds of Hydroacoustics* (Sudostroenie, Leningrad, 1979). (In Russian)
9. O.N. Popov, A. Ya. Tsionskii, A.S. Yudin, Acoust. J. **33**(3), 539 (1987). (In Russian)
10. A.S. Yudin, M.N. Yatsenko, Izvestia AN SSSR. Mech. Solids **2**, 161 (1991). (In Russian)
11. A.S. Yudin, M.N. Yatsenko, Fundam. Appl. Probl. Mech. Deformable Media Construct. **1**, 157 (1993). (In Russian)
12. G.V. Gonchar, A.S. Yudin, M.N. Yatsenko, *Mechanics of Continuum* (Rostov State University Press, Rostov-on-Don, 1988), p. 63. (In Russian)
13. A.S. Yudin, L.M. Yudina, Izvestiay of North-Caucasus Scientific Center of High School: Nat. Sci. **2**, 75 (1988). (In Russian)
14. A.S. Yudin, N.M. Ambalova, Appl. Mech. **25**(12), 63 (1989). (In Russian)

15. A.S. Yudin, M.N. Yatsenko, Fundam. Appl. Probl. Mech. Deformable Media Construct. **2**, 97 (1995). (In Russian)
16. A.S. Yudin, M.N. Yatsenko, in *Proceedings of the III International Science Conference on Modern Problems of Continuum Mechanics*, vol. 195. (Kniga, Rostov-on-Don, 1997). (In Russian)

Chapter 16
On the Problem of Mathematical Modeling in Vibroacoustics of Composite Polymeric Shells

V. G. Safronenko

Forced vibration of thee-layered rotation shells are studied in linear acoustic medium. Physical and mechanical characteristics of a polymer binding are considered in the frameworks of orthotropic thermoviscoelasticity. The shell is being oscillating in linear acoustic media, described by the Helmholtz equation and the equation of continuity for the surface of the shell. To solve the problem the approach based on modeling response of acoustic medium with the help of the local impedance is used. For the numerical solution of the problem the Fourier factorization method is used. The resulting system of equations of the normal type is solved with the sweep method. Forced vibrations in a cylindrical circular shell are considered as a numerical example. Both mode and summary amplitude-frequency and dissipative characteristics of the shell, as well as the far field of sound pressure in acoustic medium are determined.

16.1 Introduction

Development and updating of mathematical models describing the dynamics of stationary composite shells with complex physical and mechanical properties takes one of the central places in the mechanics of thin-walled structures. The problem of reducing vibration levels and improving vibroacoustic and dissipative characteristics of shell structures is crucial for a wide range of applications in advanced technologies. This problem is efficiently solved when composite materials with high coefficients of internal dissipation of vibration energy are used, thus significantly extending the range of issues that need to be considered, taking into account specific characteristics of the materials.

It is well known that the anisotropy of physical and mechanical properties, increased pliability to transverse shear and high nonlinear dependence of

V. G. Safronenko (✉)
Vorovich Mechanics and Applied Mathematics Research Institute, Southern Federal University, 200/1, Stachki Ave, Rostov-on-Don, Russia 344090
e-mail: safron@math.rsu.ru

thermoviscoelastic properties of the polymer binding on the frequency, tempera-
ture and load are typical for polymer composites. The method of mathematical
modeling together with the experiment is the main method of investigation, effi-
ciently and economically feasible in the design of advanced thin-walled structures.

16.2 Methods of Investigation

Forced oscillations of an arbitrary shell of rotation with a three-layer structure,
immersed in an ideal compressible fluid are considered. Let the shell be related to
the orthogonal coordinate system $\{\alpha_1, \alpha_2, \alpha_3\}$, and the coordinate surface $\alpha_3 = 0$
coincide with the middle surface of the filler. Using the hypothesis of a broken line
for such a shell [1], the following kinematic relations are obtained:

$$
\begin{aligned}
u_1^{(1)} &= u_1 + [1 + k_1(\alpha_3 - c)]c\varphi_1 + \alpha_3\vartheta_1; \\
u_2^{(1)} &= u_2 + [1 + k_2(\alpha_3 - c)]c\varphi_2 + \alpha_3\vartheta_2; \\
u_3^{(1)} &= w; \qquad\qquad (c \leq \alpha_3 \leq c + h_1) \\
u_1^{(2)} &= u_1 - [1 + k_1(\alpha_3 + c)]c\varphi_1 + \alpha_3\vartheta_1; \\
u_2^{(2)} &= u_2 - [1 + k_2(\alpha_3 + c)]c\varphi_2 + \alpha_3\vartheta_2; \qquad\qquad (16.1) \\
u_3^{(2)} &= w; \qquad\qquad (-c - h_2 \leq \alpha_3 \leq -c) \\
u_1^{(3)} &= u_1 + \alpha_3(\varphi_1 + \vartheta_1); \\
u_2^{(3)} &= u_2 + \alpha_3(\varphi_2 + \vartheta_2); \\
u_3^{(3)} &= w, \qquad (-c \leq \alpha_3 \leq c)
\end{aligned}
$$

where u_i, w is the displacement of point of the middle surface; φ_1, φ_2 are the
rotation angles of a normal to the filler, additional to the rotation angles ϑ_1 and ϑ_2;
k_i, A_i are the principal curvatures and the Lamé coefficients; h_1, h_2, $2c$ are the
thicknesses of the external layers and the filler, respectively.

In accordance with (16.1) the deformation relations take the form:

$$
\begin{aligned}
\varepsilon_{11}^{(1)} &= E_{11} + \alpha_3 K_{11} + c\varphi_{11} + (\alpha_3 - c)c\eta_{11}; \qquad (1 \Leftrightarrow 2) \\
\varepsilon_{12}^{(1)} &= E_{12} + 2\alpha_3 K_{12} + c\varphi_{12} + 2(\alpha_3 - c)c\eta_{12}; \\
&(c \leq \alpha_3 \leq c + h_1) \\
\varepsilon_{11}^{(2)} &= E_{11} + \alpha_3 K_{11} - c\varphi_{11} - (\alpha_3 + c)c\eta_{11}; \\
\varepsilon_{12}^{(2)} &= E_{12} + 2\alpha_3 K_{12} - c\varphi_{12} - 2(\alpha_3 + c)c\eta_{12}; \qquad\qquad (16.2) \\
&(-c - h_2 \leq \alpha_3 \leq -c) \\
\varepsilon_{11}^{(3)} &= E_{11} + \alpha_3(K_{11} + \varphi_{11}); \\
\varepsilon_{12}^{(3)} &= E_{12} + 2\alpha_3 K_{12} + \alpha_3\varphi_{12}; \\
\varepsilon_{13}^{(3)} &= \varphi_1; \quad \varepsilon_{23}^{(3)} = \varphi_2,
\end{aligned}
$$

where E_{ij} ($i, j = 1, 2$) are deformations of the middle surface, K_{ij} are the changes of curvature and torsion.

$$
\begin{aligned}
&E_{11} = u_1' + k_1 w; \quad E_{22} = u_2^\bullet + \psi u_1 + k_2 w; \\
&E_{12} = u_1^\bullet + u_2' - \psi u_2; \quad \vartheta_1 = -w' + k_1 u_1; \quad \vartheta_2 = -w^\bullet + k_2 u_2; \\
&K_{11} = \vartheta_1'; \quad K_{22} = \vartheta_2^\bullet + \psi \vartheta_1; \quad K_{12} = 1/2(\vartheta_1^\bullet + \vartheta_2' - \psi \vartheta_2); \\
&\varphi_{11} = \varphi_1'; \quad \varphi_{22} = \varphi_2^\bullet + \psi \varphi_1; \quad \varphi_{12} = \varphi_1^\bullet + \varphi_2' - \psi \varphi_2; \\
&\eta_{11} = (k_1 \varphi_1)'; \quad \eta_{22} = (k_2 \varphi_2)^\bullet + \varphi k_1 \varphi_1; \\
&\eta_{12} = k_1 \varphi_1^\bullet + k_2 \varphi_2' - \psi k_2 \varphi_2; \quad \{\ldots\}' = \frac{1}{A_1}\frac{\partial(\ldots)}{\partial\alpha_1}; \quad \{\ldots\}^\bullet = \frac{1}{A_2}\frac{\partial(\ldots)}{\partial\alpha_2}.
\end{aligned}
\tag{16.3}
$$

According (16.1–16.3), the motion equations of the shell take the form:

$$
\begin{aligned}
&L_1(T_{11}, T_{22}, S) + k_1 Q_{11} + X_1 = a_1 \ddot{u}_1 + a_2 \ddot{\vartheta} + a_3 \ddot{\varphi}_1; \\
&L_2(T_{22}, S) + k_2 Q_{22} + X_2 = a_1 \ddot{u}_2 + a_2 \ddot{\vartheta}_2 + a_4 \ddot{\varphi}_2; \\
&L_3(Q_{11}, Q_{22}) - k_1 T_{11} - k_2 T_{22} + X_3 + p = a_1 \ddot{w}; \\
&L_1(M_{11}, M_{22}, H) - Q_{11} = 0; \quad L_2(H, M_{22}) - Q_{22} = 0; \\
&L_1(m_{11} + \overline{M}_{11}\, ck_1; \ m_{22} + \overline{M}_{22}\, ck_1; \ m_{12} + 2\overline{H}\, ck_1) - Q_{13} = 0; \\
&L_2(m_{12} + 2\overline{H}_{11}\, ck_2; \ m_{22} + \overline{M}_{22}\, ck_2) - Q_{23} = 0.
\end{aligned}
\tag{16.4}
$$

Here the differential operators are introduced:

$$
\begin{aligned}
&L_1(f_1, f_2, \varphi) = f_1' + \varphi^\bullet + \psi(f_1 - f_2); \\
&L_2(f_1, f_2) = f_1' + f_2^\bullet + 2f_1 f_2; \\
&L_3(f_1, f_2) = f_1' + f_2^\bullet + \psi f_1; \quad \ddot{f} = \frac{\partial^2 f}{\partial t^2},
\end{aligned}
\tag{16.5}
$$

where X_r ($r = 1, 2, 3$), p are the components of the external load and the normal reaction of the liquid. In (16.5), the generalized forces, moments, shear forces, averaged over the three-layered shell, are introduced. Inertial characteristics a_m ($m = 1, 2, 3, 4$) are expressed in terms of density layers ρ_k ($k = 1, 2, 3$) and the geometric features as the follows:

$$
\begin{aligned}
&a_1 = \rho_1 h_1 + \rho_2 h_2 + 2\rho_3 c; \quad a_2 = \rho_1(ch_1 + h_1^2/2) - \rho_2(ch_2 + h_2^2/2); \\
&a_3 = \rho_1 h_1 c\left(1 + k_1 \frac{h_2}{2}\right) - \rho_2 h_2 c\left(1 - k_1 \frac{h_2}{2}\right); \\
&a_4 = \rho_1 h_1 c\left(1 + k_2 \frac{h_1}{2}\right) - \rho_2 h_2 c\left(1 - k_2 \frac{h_2}{2}\right).
\end{aligned}
\tag{16.6}
$$

Natural boundary conditions for the closed shell with $\alpha_1 = \alpha_{10}$, α_{11} take the form:

$$u_2(1 - \gamma_1) + (S + k_2H)\gamma_1 = 0; \qquad w(1 - \gamma_4) + (Q_{11} + H^\bullet)\gamma_4 = 0;$$
$$\vartheta_1(1 - \gamma_2) + M_{11}\gamma_2 = 0; \qquad \varphi_1(1 - \gamma_5) + (m_{11} + \overline{M}_{11}\, ck_1)\gamma_5 = 0;$$
$$u_1(1 - \gamma_3) + T_{11}\gamma_3 = 0; \qquad \varphi_2(1 - \gamma_6) + (m_{12} + 2H\, ck_2)\gamma_6 = 0,$$

$$(16.7)$$

where $\gamma_1,\ldots,\gamma_6$ are the constants taking values of 0 or 1.

Let the shell be under the periodically varying surface load:

$$X_k(\alpha_1, \alpha_2, t) = q_k(\alpha_1, \alpha_2) \exp(-i\omega t),$$

where q_k is the intensity of the load, ω is the frequency.

All kinematic, deformation and power factors are represented in a similar form. Constitutive relations for each layer of the material can be described in terms of an orthotropic thermoviscoelasticity [2]. In terms of harmonic loading and in the case of small oscillations for k-layer, they take the form:

$$\sigma_{11}^{(k)} = \frac{\overset{*}{E}_1^{(k)}}{1 - \overset{*}{v}_1^{(k)} \cdot \overset{*}{v}_2^{(k)}} \left(\varepsilon_{11}^{(k)} + \overset{*}{v}_2^{(k)} \varepsilon_{22}^{(k)} \right); \quad (1 \Leftrightarrow 2) \tag{16.8}$$
$$\sigma_{12}^{(k)} = \overset{*}{G}_{12}^{(k)} \varepsilon_{12}^{(k)}; \quad \sigma_{i3}^{(3)} = \overset{*}{G}_{i3}^{(3)} \varphi_i$$

where $\sigma_{ij}^{(k)}, \varepsilon_{ij}^{(k)}; \overset{*}{E}_i^{(k)}, \overset{*}{v}_i^{(k)}, \overset{*}{G}_{ir}^{(k)}$ are the complex amplitudes of stress and strain, complex analogues of the Young modules, Poisson coefficients and shear moduli.

By using averaged relations (16.8) on the thickness of the shell, the dependences between amplitudes of the generalized forces, moments, shear forces and characteristics of deformations were obtained:

$$T_{11} = \overset{*}{B}_{11}E_{11} + \overset{*}{B}_{12}E_{22} + \overset{*}{A}_{11}K_{11} + \overset{*}{A}_{12}K_{22} + \overset{*}{F}_{11}\frac{\partial\varphi_1}{\partial\alpha_1} + \overset{*}{F}_{12}\frac{\partial\varphi_2}{\partial\alpha_2} + \overset{*}{F}_{13}\varphi_1;$$
$$M_{11} = \overset{*}{A}_{11}E_{11} + \overset{*}{A}_{12}E_{22} + \overset{*}{D}_{11}K_{11} + \overset{*}{D}_{12}K_{22} + \overset{*}{N}_{11}\frac{\partial\varphi_1}{\partial\alpha_1} + \overset{*}{N}_{12}\frac{\partial\varphi_2}{\partial\alpha_2} + \overset{*}{N}_{13}\varphi_1; \tag{16.9}$$
$$H = \overset{*}{A}_{33}E_{12} + 2\overset{*}{D}_{33}K_{12} + \overset{*}{N}_{33}\frac{\partial\varphi_1}{\partial\alpha_2} + \overset{*}{N}_{44}\frac{\partial\varphi_2}{\partial\alpha_1} + \overset{*}{N}_{55}\varphi_2;$$
$$Q_{i3} = \overset{*}{G}_{i3}\varphi_i.$$

To complete relations (16.1–16.9), it is necessary to determine the dynamic response of the liquid in which the shell is immersed. This can be done with the help of the local impedance modeling method [3, 4]. By using defined the displacement and pressure fields on the surface of the shell, one can define the field of the dynamic pressure in the liquid through the Helmholtz integral:

$$p(\vec{r}) = \frac{1}{4\pi} \int\limits_{S} \left[p(\vec{r}_1) \frac{\partial}{\partial n} \left(e^{ikR_1} / R_1 \right) - \frac{\partial p(\vec{r}_1)}{\partial n} \left(e^{ikR_1} / R_1 \right) \right] dS, \tag{16.10}$$

where S is the middle surface of the shell, k_1 is the wave number, $\vec{r}, \vec{r}_1$ are the radius-vectors of points in the liquid and on the shell, $R_1 = |\vec{r}_1 - \vec{r}|$.

An approach based on the modal representation of the unknown functions in the form of Fourier-series expansion is used for the numerical study:

$$Y(\alpha_1, \alpha_2) = \sum_{n} \left[Y_{n_{(-1)}}(\alpha_1) \sin n\alpha_2 + Y_{n_{(1)}}(\alpha_1) \cos n\alpha_2 \right]. \tag{16.11}$$

By separating coordinate α_2 and leading all relations to the dimensionless form, the quasi-one-dimensional system of the normal type of 12-th order is solved by the orthogonal sweep method:

$$\frac{dy_l}{d\alpha_i} = A_i f_l(\alpha_1, \overline{m}, y); \quad \underline{y} = \{y_1, y_2, \ldots, y_{12}\};$$
$$l = 1, 2, \ldots, 12. \tag{16.12}$$

To evaluate the dissipative properties of the shell, we introduce the energy dissipation coefficient, defined as [5]:

$$k = \frac{\hat{D}}{\hat{\Pi}}; \tag{16.13}$$

where $\hat{D}$ is the energy dissipated from the body of the shell for the oscillation period, $\hat{\Pi}$ is the average value of the total mechanical energy for the oscillation period:

$$\hat{D} = \int\limits_{t}^{t+2\pi/\omega} \int\limits_{V} \mathrm{Re}\, \sigma_{ij} \mathrm{Re}\, \dot{\varepsilon}_{ij}\, dV d\tau = \pi \int\limits_{S} (T_{ij}^R E_{ij}^I - T_{ij}^I E_{ij}^R$$
$$+ M_{ij}^R K_{ij}^I - M_{ij}^I K_{ij}^R + Q_{i3}^R \varphi_i^I - Q_{i3}^I \varphi_i^R) dS;$$

$$\hat{\Pi} = \frac{\omega}{2\pi} \int\limits_{t}^{t+2\pi/\omega} \int\limits_{V} \mathrm{Re}\, \sigma_{ij} \mathrm{Re}\, \varepsilon_{ij}\, dV d\tau = \frac{1}{2} \int\limits_{S} (T_{ij}^R E_{ij}^R + M_{ij}^R K_{ij}^R$$
$$+ Q_{i3}^R \varphi_i^R + T_{ij}^I E_{ij}^I + M_{ij}^I K_{ij}^I + Q_{i3}^I \varphi_i^I) dS.$$

Thus, the method of modal analysis allows us to determine dissipation coefficients which correspond to different modes, as well as the total value of the dissipation coefficient.
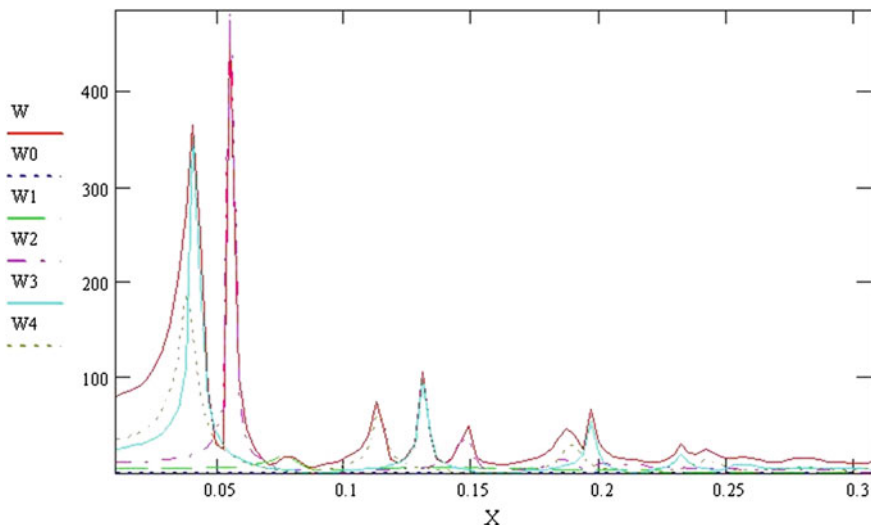
Fig. 16.1 Amplitude-frequency characteristics for normal displacement

16.3 Numerical Experiment

As an example let us consider a three-layered cylindrical shell oscillating in a compressible liquid. Physical and mechanical properties of the external layers correspond to the properties of steel:

$$E^{(1)} = E^{(2)} = 2.1 \cdot 10^{11} \text{ N/m}^2; \quad v^{(1)} = v^{(2)} = 0.3; \quad \rho = 7.8 \ g/cm^3.$$

The constitutive equations of polymer filler correspond to the model of a thermoviscoelastic body [6]. The components of the complex compliance under shear I', I'' in the notation of [6], take the form:

$$
\begin{aligned}
I'(\omega) &= \int_{r_1}^{r_2} \frac{C(r)}{G(r,v,T)} \left[1 - H(r) \frac{\omega^2}{[\varphi(r,v,T)]^2 + \omega^2} \right] dr, \\
I''(\omega) &= \int_{r_1}^{r_2} \frac{C(r)H(r)}{G(r,u,T)} \frac{\varphi(r,v,T)\omega}{[\varphi(r,v,T)]^2 + \omega^2} dr.
\end{aligned}
\tag{16.14}
$$

Such a model excludes bulk relaxation. Boundary conditions correspond to the clamped edges. To determine the response of a liquid to the oscillations of the shell, the impedance of an infinitely long cylindrical shell is used.

Numerical calculations are carried out under the following geometric parameters: $L = 350$ mm, $R = 100$ mm, $h_1 = h_2 = 0.2$ mm, $2c = 1$ mm, $T = 22$ °C.
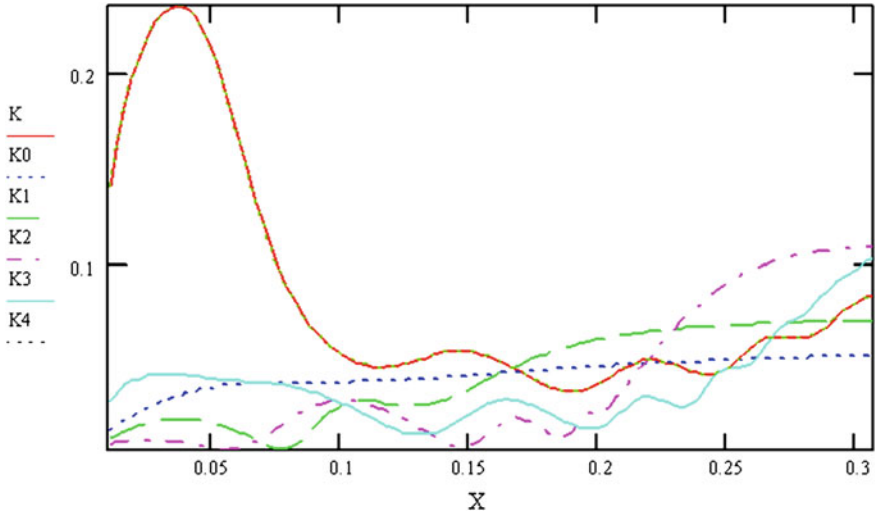
Fig. 16.2 Amplitude-frequency characteristics for dissipation coefficient of the energy
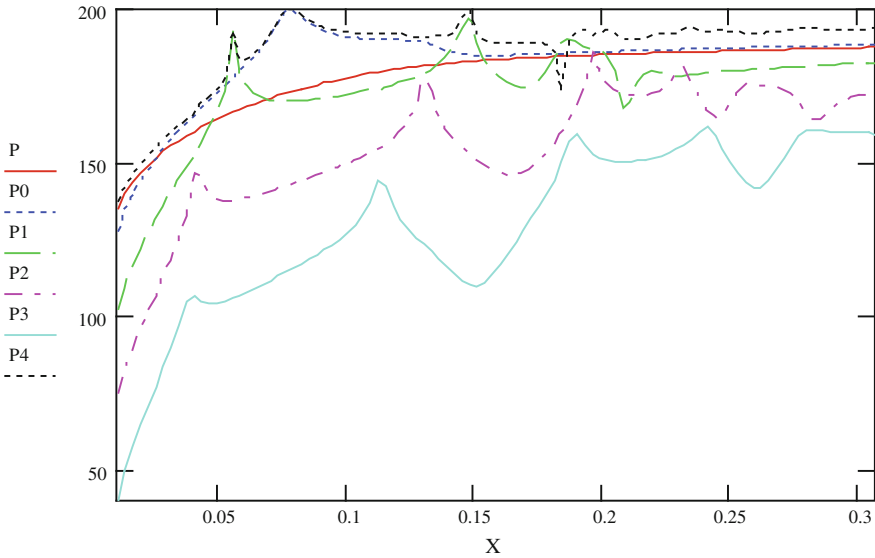
Fig. 16.3 Amplitude-frequency characteristics for acoustic pressure

The load of unit intensity is distributed on a cylindrical panel, located in the middle of the element.

Figures 16.1, 16.2 and 16.3 show the results of calculations for mode and summary values of amplitude-frequency characteristics for the normal

displacement in the center of the loading panel, for the dissipation coefficient of the energy, for the field of acoustic pressure in liquid at the distance, equal to 50 radius of the shell from the axis of its rotation, passing through the center of the loading panel.

16.4 Conclusions

The method of mathematical modeling for vibroacoustics of polymer composite shells of rotation immersed in the acoustic medium has been developed. Numerical and analytical approach based on the Fourier-series method, as well as sweep method were used. The method of local impedance modeling to define the reaction of the surrounding acoustic medium has been applied. Numerical experiment for a cylindrical three-layered shell with a polymeric binder was carried out.

References

1. E.I. Grigolyuk, P.P. Chulkov, *Stability and Vibration of Thee-Layered Shells* (Mashinostroenie, Moscow, 1973). (in Russian)
2. A.A. Ilyushin, B.E. Pobedrya, *Fundamentals of Thermoviscoelasticity Mathematical Theory* (Nauka, Moscow, 1970). (in Russian)
3. G. Chertock, J. Acoust. Soc. Amer. **36**(7), 1305 (1964)
4. A.S. Yudin, N.M. Ambalova, J. Appl. Mech. **25**(12), 63 (1989)
5. V.G. Safronenko, E.N. Donchenko, V.M. Shut'ko, in *Proceedings of XVI International Conference on Modern Problems of Continuum Mechanics*, vol. 2, p. 115. Rostov-on-Don, 2012
6. Yu.P. Stepanenko, K.V. Isaev, A.D. Azarov, in *Proceedings of II International Conference on Modern Problems of Continuum Mechanics*, vol. 1, p.118. Rostov-on-Don, 1996

Chapter 17
Mechanical Testing of Polymeric Composites for Aircraft Applications: Standards, Requirements and Limitations

**Levon Chinchan, Sergey Shevtsov, Arcady Soloviev,
Varvara Shevtsova and Jiun-Ping Huang**

The high-loaded parts of modern aircrafts and helicopters are often produced from polymeric composite materials. Such materials consist of reinforcing fibers, packed by layers with the different angles, and resin, which uniformly distributes the structural stresses between fibers. These composites should have an orthotropic symmetry of mechanical properties to obtain the desirable spatial distribution of elastic moduli consistent to the external loading pattern. Main requirements to the aircraft composite materials are the specified elastic properties (9 for orthotropic composite), long-term strength parameters, high resistance against the environmental influences, low thermal expansion to maintain the shape stability. These properties are ensured by an exact implementation of technological conditions and many testing procedures performed with the fibers, resin, prepregs and ready components. Most important mechanical testing procedures are defined by ASTM, SACMA and other standards. However in each case the wide diversity of components (dimensions and lay-up of fibers, rheological properties of thermosetting resins) requires a specific approach to the sample preparation, testing, and numerical processing of the testing results to obtain the veritable values of tested parameters. We pay the special attention to the cases where the tested specimens

L. Chinchan
Rostvertol Helicopters, Rostov-on-Don, Russia
e-mail: levon-rostvert@yandex.ru

S. Shevtsov (✉)
South Center of Russian Academy of Sciences, Rostov-on-Don, Russia
e-mail: aeroengdstu@list.ru

A. Soloviev · V. Shevtsova
Don State Technical University, Rostov-on-Don, Russia
e-mail: solovievarc@gmail.com

J.-P. Huang
National Kaohsiung Marine University, Kaohsiung City, Rupublic of China (Taiwan)
e-mail: jas3-3@hotmail.com

S. Shevtsov · A. Soloviev
Southern Federal University, Rostov-on-Don, Russia

are cut not from the plates recommended by standards, but from the ready part manufactured with the specific lay-up, tension forces on the reinforcing fiber at the filament winding, and curing schedule. These tests can provide most useful information both for the composite structural design and to estimate a quality of the ready parts. We consider an influence of relation between specimen dimensions and pattern of the fibers winding (or lay-up) on the results of mechanical testing for determination of longitudinal, transverse and in-plane shear moduli, an original numerical scheme for reconstruction of in-plane shear modulus measured by the modified Iosipescu method which use finite element based numerical processing and indicative data preliminary obtained by the short-beam test. The sensitivity and ability to decoupling the values of in-plane and interlaminar shear moduli obtained by the sample twisting test is studied and discussed.

17.1 Introduction

Most often used in aircraft and rotorcraft industry ASTM (American Society for Testing and Materials), SACMA (Suppliers of Advanced Composite Material Association), AGATE (The Advanced General Aviation Transport Experiments consortium) and other standards recommend the detailed technique for the samples preparation. These standards determine the shape and dimensions of specially manufactured plates for cutting the samples intended for elastic and strength properties testing [1–3]. However, the most useful information can be obtained by testing of samples that are cut from the ready part manufactured accordingly the accepted technology with specific schedules, i.e. lay-up, winding forces, curing of prepreg, etc. [4, 5]. Such testing information, especially information about elastic properties, is required to perform a dynamic analysis of any high-loaded aircraft or other composite structure [6, 7], and also to monitor the normalized quality parameters of material [8].

Composite material of high-loaded structures always has the orthotropic symmetry that is determined by the loading pattern. Due to this orthotropic symmetry, the technical problem of the right cutting the specimens for the different testing is important, and solution of this problem depends on the shape of analyzed parts and on the orientation of reinforcing fibers. All above mentioned standards do not give any recommendations for these cases, and decision should be made in each specific case that are considered partially in manuals [1, 2] and in the paper [9] where this problem is solved for the in-plane shear modulus of tested specimens. In particular, the planar zones on the parts should be previously found, and next an orientation of the main axis of orthotropic symmetry on these zones should be determined. As soon such zones are founded, the specimens can be cut along or across the main axis of symmetry. Here and below we assume that this problem is properly solved, and axes of the specimens are oriented in the right directions.

Unfortunately, the samples with the shape recommended by standards cannot be cut from the some parts due to their complicated geometry. In these cases we need to

use the samples with a greater or lesser deviation from the standard shape to obtain no exact data, but some semi-quantitative estimation about the interested elastic modulus. Such case is considered below for the specimens in determination of transverse elastic modulus that are cut in the direction which is normal to the main axis of long composite part. We use here the finite element analysis to estimate location and dimensions of zone on the specimen where tensile stresses are uniform to find a good place for measure a tensile strain. This case is especially studied to determine the effect of the shape deviation on the testing data. To estimate an influence of ends of the reinforcing fibers which come to the cutting surface, we compare the data obtained for the specimens with standard and deviated shapes.

For the V-notched specimen used in standard testing of in-plane shear modulus according to Iosipescu method a detailed study of the shear stress pattern in a working zone was carried out. We established the deviation of the pure shear stress close to the corners of notches, so, the simple dividing of loading force on the cross-sectional area between the notches can results an incorrect value of the shear stress, and therefore to the wrong value of the shear modulus [9, 10]. Using the finite element (FE) analysis we demonstrate how to determine the right dimensions of the pure shear area, and next obtain the refined value of in-plane shear modulus. But FE problem formulation in 3D case requires the exact data about all moduli of orthotropic composite, in particular, the value of the shear modulus to be determined. To resolve this contradiction we propose the iterative FE-based technique, and demonstrate the good convergence of such iterative process.

At this time no standards for determination of the interlaminar shear modulus that is caused by the complexity of its experimental measurement. However, information about this modulus is very important to forecast the torsion deformation of tube-like composite structures. We consider the achievable accuracy of short beam bending test and use these data as preliminary for the numerical processing of torsion test results. Our estimation show the strong dependence of obtained interlaminar test results on the relationship between sides of the specimen's rectangular cross-section.

17.2 Symmetry of Orthotropic Composites, and Standards for Their Elastic Moduli Determination

Composite materials with orthotropic symmetry have three symmetry planes, each normal to others. Such polymeric composites are manufactured by regular symmetrical laying-up of unidirectional tape or fabric. Typical orthotropic structure, formed by proper regular lay-up of the oriented layers, is presented in Fig. 17.1.

For the orthotropic material, which symmetry axes are coincide with the global Cartesian frame, the Hook's law is

(a)

Symmetry axis
of layers

Symmetry axis of
othotropic laminate

(b)

Laminate assembly $[0/\pm 45/90]_s$

0°
$+45^o$
-45°
90°
90°
-45°
$+45^o$
0°
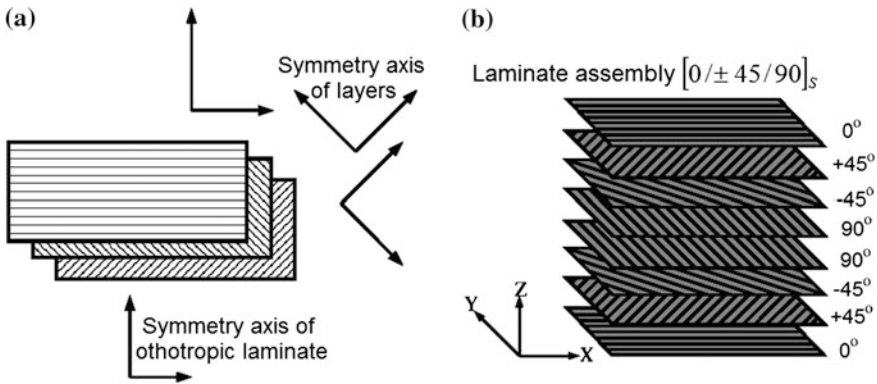
Fig. 17.1 Arrangement of symmetry axes of the layers (**a**) and forming an orthotropic laminate (**b**)

$$
\begin{pmatrix} \sigma_x \\ \sigma_y \\ \sigma_z \\ \tau_{yz} \\ \tau_{zx} \\ \tau_{xy} \end{pmatrix} = \begin{pmatrix} C_{11} & C_{12} & C_{13} & 0 & 0 & 0 \\ C_{21} & C_{22} & C_{23} & 0 & 0 & 0 \\ C_{31} & C_{32} & C_{33} & 0 & 0 & 0 \\ 0 & 0 & 0 & C_{44} & 0 & 0 \\ 0 & 0 & 0 & 0 & C_{55} & 0 \\ 0 & 0 & 0 & 0 & 0 & C_{66} \end{pmatrix} \cdot \begin{pmatrix} \varepsilon_x \\ \varepsilon_y \\ \varepsilon_z \\ \gamma_{yz} \\ \gamma_{yz} \\ \gamma_{yz} \end{pmatrix}, \tag{17.1}
$$

where C_{11}, C_{12}, C_{13}, C_{22}, C_{23}, C_{33}, C_{44}, C_{55}, C_{66} are the independent elastic constants, that fully determine elastic properties of orthotropic material. So, coupling between stresses σ, τ and strains ε, γ is linear, and it is defined by the stiffness elastic matrix, which is symmetrical: $C_{12} = C_{21}$, $C_{13} = C_{31}$, $C_{23} = C_{32}$. More suitable for the engineering applications is an inverted relationship

$$
\begin{pmatrix} \varepsilon_x \\ \varepsilon_y \\ \varepsilon_z \\ \gamma_{yz} \\ \gamma_{yz} \\ \gamma_{yz} \end{pmatrix} = \begin{pmatrix} 1/E_x & -v_{yx}/E_y & -v_{zx}/E_z & 0 & 0 & 0 \\ -v_{xy}/E_x & 1/E_y & -v_{zy}/E_z & 0 & 0 & 0 \\ -v_{xz}/E_x & -v_{yz}/E_y & 1/E_z & 0 & 0 & 0 \\ 0 & 0 & 0 & G_{yz} & 0 & 0 \\ 0 & 0 & 0 & 0 & G_{zx} & 0 \\ 0 & 0 & 0 & 0 & 0 & G_{xy} \end{pmatrix} \cdot \begin{pmatrix} \sigma_x \\ \sigma_y \\ \sigma_z \\ \tau_{yz} \\ \tau_{zx} \\ \tau_{xy} \end{pmatrix}.
$$

$$\tag{17.2}$$

The elements of also symmetrical compliance matrix are expressed through the elastic Young's moduli E_x, E_y, E_z, Poisson's ratios $v_{xy} = v_{yx}$, $v_{xz} = v_{zx}$, $v_{yz} = v_{zy}$, and three shear moduli G_{xy}, G_{zx}, G_{yz}. Equation (17.2) contains 9 independent constants, and from the reciprocity theorem, we have

$$
v_{ij}/E_i = v_{ji}/E_j, \text{ where } i, j = x, y, z. \tag{17.3}
$$

Elements of the stiffness matrix and elements of the compliance matrix are coupled by the relationships:

$$C_{11} = \frac{1}{E_y A}\left(\frac{1}{E_z} - \frac{v_{yz}^2}{E_y}\right); C_{22} = \frac{1}{E_z A}\left(\frac{1}{E_x} - \frac{v_{zx}^2}{E_z}\right); C_{33} = \frac{1}{E_x A}\left(\frac{1}{E_y} - \frac{v_{xy}^2}{E_x}\right);$$

$$C_{12} = \frac{1}{E_z A}\left(\frac{v_{zx}v_{yz}}{E_y} + \frac{v_{xy}}{E_x}\right); C_{13} = \frac{1}{E_y A}\left(\frac{v_{xy}v_{yz}}{E_x} + \frac{v_{zx}}{E_z}\right); C_{23} = \frac{1}{E_x A}\left(\frac{v_{xy}v_{zx}}{E_z} + \frac{v_{yz}}{E_y}\right);$$

$$C_{44} = G_{yz}; C_{55} = G_{zx}; C_{66} = G_{xy},$$

$$(17.4)$$

where

$$A \equiv \frac{1}{E_x E_y E_z}\left(1 - 2v_{xy}v_{yz}v_{zx} - \frac{E_x}{E_z}v_{zx}^2 - \frac{E_y}{E_x}v_{xy}^2 - \frac{E_z}{E_y}v_{yz}^2\right).$$

The simplest form of the symmetrical matrices in the relationships (17.1), (17.2) is valid only if the symmetry axes of material coincide with the Cartesian axes. At the rotation of coordinate axes, the properties of material will be expressed by more complex matrices. Moreover, e.g., tensile stress oriented along the axis, which not coincide with the main axis of material can produce combined tensile with shear deformation.

Poisson's ratio for orthotropic material can vary into a range which is wider compared to isotropic case. The rigorous thermodynamic analysis of orthotropic material deformations [11] states the strong requirements on the elastic moduli and Poisson's ratios:

$$(1 - v_{23}v_{32}), (1 - v_{13}v_{31}), (1 - v_{12}v_{21}), (1 - v_{12}v_{21} - v_{13}v_{31} - v_{23}v_{32} - 2v_{21}v_{32}v_{13}) > 0,$$

$$(17.5)$$

and

$$v_{ij} \leq \left(E_i/E_j\right)^{1/2}; v_{21}v_{23}v_{13} < {}^1\!/_2. \tag{17.6}$$

For example, P. D. Craig and J. Summerscales [12] presented experimentally obtained values for some orthotropic glass fiber composites that vary in the range from 0.1 up to 1.69. Such range is much wider than the allowed range $(-1 \ldots 1/2)$ for isotropic materials.

Structure of (17.2) shows, that determination of all elastic moduli of orthotropic material can be performed by using as minimum 6 independent experiments. Each test should supply in the material the uniform pure tensile/compression or shear strain. It is assumed a synchronous measurement of one Poisson's ratio together with measurement of the corresponding Young's modulus.

Most appropriate and well grounded experimental techniques for determination of above mentioned elastic properties are presented in the following documents.

ASTM D 3039-95 "Test Method for Tensile Properties of Polymer Matrix Composite Materials" regulates all allowed specimens dimensions, strain rates, and order for the Young's modulus and Poisson's ratio determination in the longitudinal and transverse (in plane) directions. SACMA standard SRM 1-94 "Compressive Properties of Oriented Fiber-Resin Composites" presents refined technique for determination of the same material parameters at compression. However, all orthotropic composites are manufactured in the forms of plate, tube-like, and other thin-walled structures. Therefore these documents cannot be used to determine the modulus in the direction normal to the wall (thickness modulus). Due to difficulty to organize a testing load normal to the wall of specimen, this modulus cannot be determined by the static test. Its semi-quantitative determination is possible by the non-standard dynamic testing technique, which consideration is out of framework of our paper.

Next important parameter of material is the in-plane shear modulus, which determination technique is regulated by the following standards: ASTM D 4255-83 (Reapproved 1994) "Guide for Testing In-Plane Shear Properties of Composite Laminates", which contains recommendations about the specimen preparation; ASTM D 3518-94 "Practice for In-Plane Shear Stress–Strain Response of Uni-directional Polymer Matrix Composite Materials" consider the requirements to the testing equipment; and two standards that regulate the testing procedure ASTM D 3846-94 "Test Method for In-Plane Shear Strength of Reinforced Plastics", ASTM D 5379-93 "Test Method for Shear Properties of Composite Materials by V-Notched Beam Method". We consider below last testing method carefully and propose some improvements, which allow us to sufficiently enhance its accuracy.

Other shear modulus (interlaminar) is most difficult for experimental determination. There are some standards intended to estimate its value: ASTM D 2344-84 (Reapproved 1989) "Test Method for Apparent Interlaminar Shear Strength of Parallel Fiber Composites by Short Beam Method", SRM 8-94 "Short-Beam Shear Strength of Oriented Fiber-Resin Composites", but low precision of the short-beam test does not allow us to obtain any well-grounded data about this modulus. We consider the origins of this shortcoming and then propose the supplementary twisting test together with corresponding numerical processing, which also have a serious restriction, but allow one to estimate an accuracy of obtained data.

It is important to note, all of above mentioned standards and methods assume that coordinate axes of material and tested specimen are aligned with maximum allowed accuracy.

17.3 Longitudinal and Transverse Young's Moduli

We consider here some features of tensile test on an example of two specimens derived from ready composite part, which is tube-like with varied cross-section. First type of specimen, which has a standard form, is cut out along a main axis of
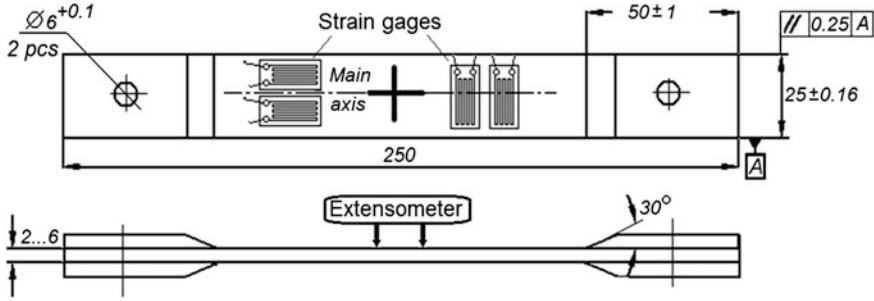
Fig. 17.2 Standard tabbed sample for the longitudinal Young's modulus and Poisson's ratio determination

orthotropic material. Second type specimen, which is cut out across a main axis, is shorter.

The tensile strain is measured by extensometer, whereas tensile force is measured by the testing machine. In order to measure Poisson's ratio simultaneously with the longitudinal Young's modulus the strain gauges were bonded on the sample's surface, and signals from sensor bridges were monitored independently (see Fig. 17.2).

All numerical results have been obtained from the loading diagrams issued by the testing machine (see Fig. 17.3) and the strain gauges circuits (see Fig. 17.4). The Young's modulus is calculated according to the equation:

$$E_i = k/(a \cdot b), \tag{17.7}$$

where k is the slope of the linear region on the loading diagram $F(\varepsilon)$ (see Fig. 17.3), and $a \cdot b$ is the cross-section area of the tested specimen.

A value of Poisson's ratio is calculated using the dependencies of longitudinal and transverse strains, which are recorded from the sensor bridges (see Fig. 17.4), by dividing the slope of linear regions for the transverse contraction into slopes for the longitudinal elongation curves. In Fig. 17.4 this linear region is bounded by two instants (*int* and *out*).

The considered technique is simplest, it always give the good results with minimum experimental dispersion if geometry of the specimens does not have any sufficient deviations from those required by standard. However, if we cannot cut out the samples with required length, two main difficulties will arise. These difficulties are due to necessity to ensure the uniform tensile strain on the measuring base of extensometer, and second difficulty is due to influence of ends of the fibers that exit on the cutting surface. We consider these problems below.

In order to estimate an influence of the specimen shape on the calculated value of the Young's modulus we studied the specimens, which sketch is presented in Fig. 17.5. Before loading the samples in the testing machine we modeled a strain distribution along the working zone whose length was 3.5 times greater than the width. The geometry of FE model and meshing are presented in Fig. 17.6, whereas
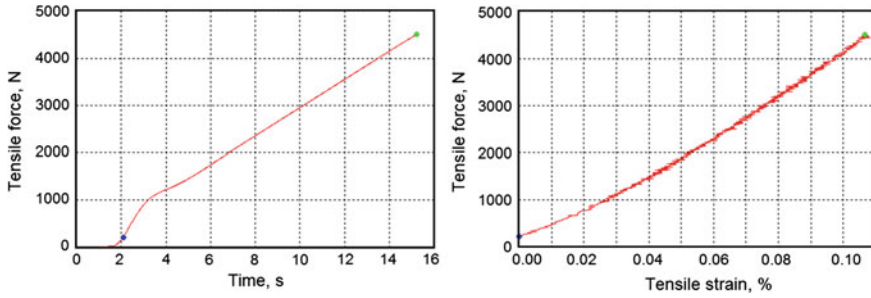
Fig. 17.3 Tensile diagrams from the testing machine

Fig. 17.4 Two time-strain dependencies, which are formed by the strain gauges circuits
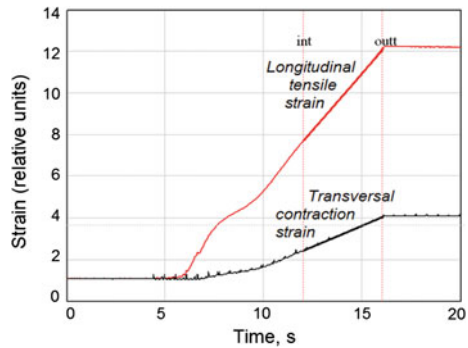
Fig. 17.5 No tabbed shortened specimen with two holes for transmitting a tensile force
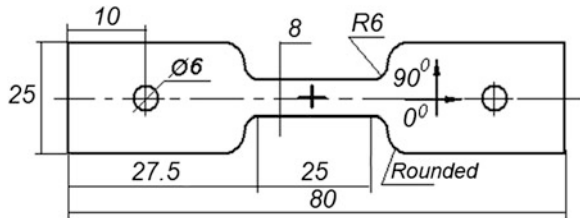
two plots with the normal tensile stress and strain distribution along the specimen axis are presented in Fig. 17.7. At the FE calculation a longitudinal Young's modulus has been used from the experiments with standard samples. Plots in Fig. 17.7 confirm the stress homogeneity on the region with length ∼ 15 mm for the extensometer placing.

Results of longitudinal Young's modulus determination, which were obtained with standard (see Fig. 17.2) and shortened (see Fig. 17.5) samples are presented in Table 17.1. Both types of specimens have been cut out along the main axis of part that has a lay-up scheme ±30°. So, shortened samples demonstrate the value
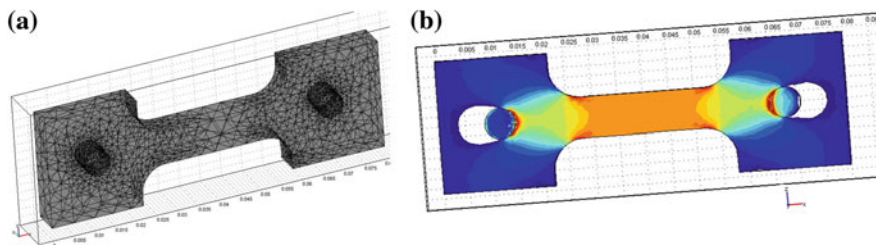
Fig. 17.6 FE model of the shortened specimen: **a** FE mesh, **b** tensile strain distribution
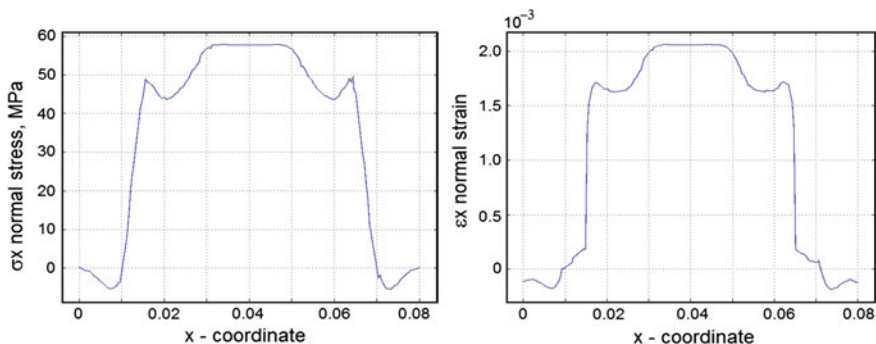
Fig. 17.7 Normal tensile stress and strain distributions along the axis of shortened sample

Table 17.1 Measured values of longitudinal Young's modulus for standard and shortened samples

Specimen shape	Confidence interval (95 %)		Standard deviation (GPa/%)
	Min (GPa)	Min (GPa)	
Figure 17.2	28.3	29.4	0.48/1.6
Figure 17.5	21.0	24.5	2.3/10

of measured Young's modulus 40 % lesser than standard samples. It can be explained by greater relative length of the fibers that approach the cutting surface. For the standard samples, full length of the fiber is 25 mm/ sin(30°) = 50 mm, whereas for the shortened samples this length is equal to 8 mm/ sin(30°) = 16 mm, i.e. 3 times less. If a portion of fibers adjacent to the cutting surface has a weakened coupling with resin, and length of such portion is approximately 2 mm, then 25 % of the fiber's full length does not take the load. For the standard samples such fall of the load capacity is 8 % in a whole.

These results confirm that width of specimen working zone cannot be lesser than some definite size. Otherwise, incorrect result will be obtained. Such results can be used as semi-quantitative estimation, only.

Table 17.2 The measured values of transverse Young's modulus for the shortened samples

Specimen shape	Confidence interval (95 %)		Standard deviation (GPa/%)
	Min (GPa)	Min (GPa)	
Figure 17.5	10.2	11.5	0.65/13

The similar tests have been performed with the shortened samples that were cut out across the main axis of material. The shape of analyzed part did not allow cutting out the standard samples. In these experiments where transverse Young's modulus has been studied, the full length of the fiber is 8 mm/ sin(60°) = 9.2 mm. It is obvious, that an influence of ends of the fibers is more significant for such test. Measured data presented in Table 17.2 show a great decrease of elastic modulus as well as increased scattering of it.

It is accordingly necessary to conclude that width of the samples cannot be lesser than 20–25 mm if lay-up angle relative to the sample axis is greater than 15°. In order to obtain uniform strain/stress distribution in working zone of specimen, the length of this zone should exceed the width 3 times or more. These limitations are very strong, and their scope is not limited by the static tests, but spread also to the Dynamic Mechanics Analysis (DMA) testing.

17.4 In-plane Shear Modulus

Among the known experimental and analytical methods for in-plane shear modulus determination most reliable and direct is the Iosipescu method, which use V-notched prismatic samples (see Fig. 17.8). Vertical motion of cross-arm with speed 100–1000 μm/sec should cause the pure shear in a zone between two notches. This shear strain is determined by using two strain gauges placed in working zone. As soon as the loading force, which is determined by the sensor of testing machine, is known, the shear modulus can be obtained simply by dividing this force on cross-section area between notches and on the measured strain. However, assumption about homogeneity of shear stress between notches is very rough, and can lead to the gross error. Moreover, the geometry and dimensions of the pure shear zone can depend on the scheme of the prepreg lay-up [10].

Other source of experimental error is due to the side reaction from the deformed specimen to the cross-arm, and back to the specimen from the cross-arm. This reaction force can act on the motion of cross-arm and also can distort the measured force values. To eliminate an appearance of the side reaction force we proposed a symmetrical scheme of test presented in Fig. 17.9. Photo of the modified test fixture is presented in Fig. 17.10. A detailed analysis of the shear stress distribution in working zone of symmetrical sample has been studied to refine the value of measured in-plane shear modulus.
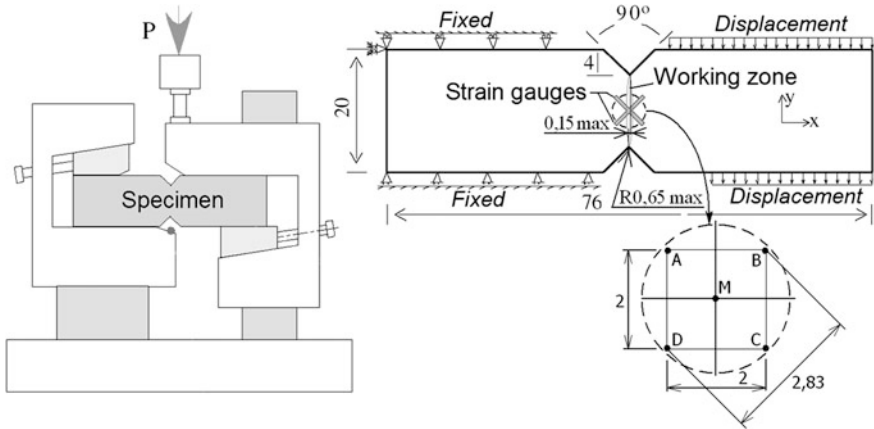
Fig. 17.8 Testing scheme and specimen to determine in-plane shear modulus according to standard ASTM D 5379-93
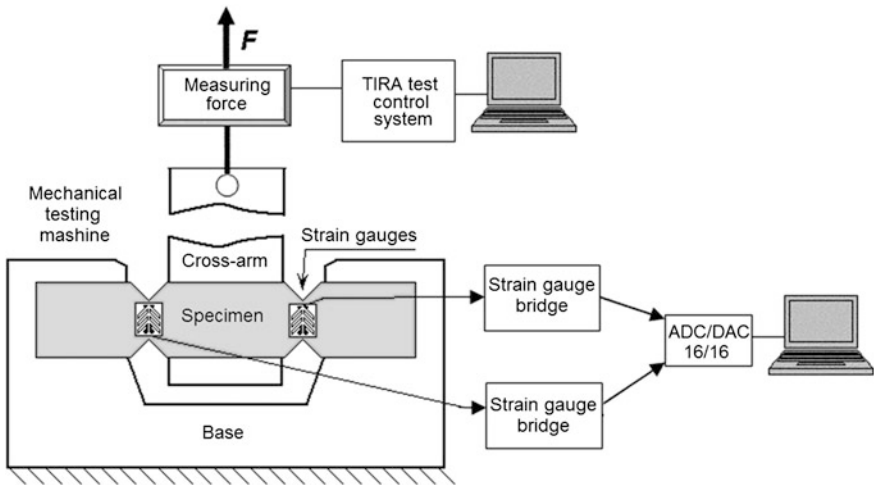
Fig. 17.9 The modified symmetrical testing scheme for in-plane shear modulus determination

Let our sample, which made from orthotropic composite is loaded by the planar stress, and let axes *x, z* are oriented perfectly along and across the main axis of material. According to assumptions of standard ASTM D 5379-93 the pure shear deformation is realized in a zone between notches.

Then interlaminar shear modulus is determined by the shear strain γ_{xz} and by the shear stress τ_{xz}. But in the experiment some averaged strain $\bar{\gamma}$ is determined using the data of the strain gauges (see Fig. 17.8) as

Fig. 17.10 Fixture and symmetrical specimen which tested by the modified Iosipescu method
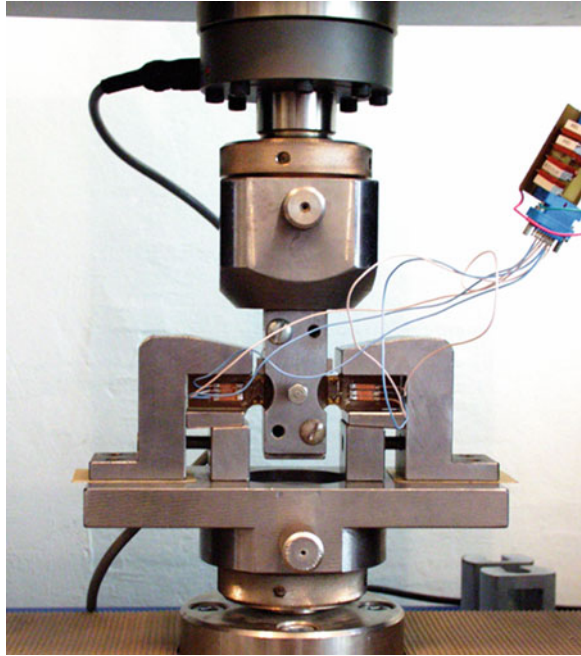
$$\bar{\gamma} = \varepsilon_{45°} - \varepsilon_{-45°}. \tag{17.8}$$

From this value of averaged strain and mean shear stress $\bar{\tau} \equiv P/A$ (where P is applied force, and A is the specimen cross-section between notches) the effective shear modulus $\bar{G}_{xz}$ can be calculated as

$$\bar{G}_{xz} = \bar{\tau}/\bar{\gamma}. \tag{17.9}$$

Because τ is not exact stress value, to determine the stress $\tau° \equiv \tau_{xz}$ in a zone of the pure shear stress, the effective modulus $\bar{G}_{xz}$ should be multiplied by an adjusting coefficient C, which is equal to

$$C = \frac{\tau°}{\bar{\tau}} = \frac{1}{V_0 \bar{\tau}} \int_{V_0} \tau dV, \tag{17.10}$$

where integration is spread over the volume V_0 under area covered by the strain gauges. This adjusting coefficient can be obtained by FE modeling of material state in the working zone of specimen. Because FE problem formulation requires the values of all elastic moduli of the tested composite, the measured value of in-plane shear modulus is determined. To estimate an influence of assumed $\bar{\tau} \equiv P/A$ as the pure shear stress on the calculated value of in-plane shear modulus, we performed the FE modeling whose results are presented below.

Table 17.3 Stiffness matrices elements for two studied virtual orthotropic materials (GPa)

Material	$c_{11} = c_{22}$	c_{33}	c_{12}	c_{13}	c_{23}	$c_{44} = c_{55}$	c_{66}
I	13.4	6.7	4.65	4.65	4.65	1.02	5.37
II	6.7	13.4	4.65	4.65	4.65	4.0	1.02

Note: The matching rule for indexes:
$1 \leftrightarrow x, \quad 2 \leftrightarrow y, \quad 3 \leftrightarrow z, \quad 44 \leftrightarrow yz, \quad 55 \leftrightarrow zx, \quad 66 \leftrightarrow xy$

Table 17.4 Stresses in the central point M and calculated in-plane shear modulus

Material	σ_{xx} (kPa)	σ_{zz} (kPa)	σ_{zx} (MPa)	$\tilde{c}_{55}$ (GPa)	δ (%)
I	-0.350	4.01	-9.18	1.027	0.6
II	-3.480	14.0	-28.8	4.041	1.0

Two virtual orthotropic materials were used in our numerical experiments. The elements of their stiffness matrices are presented in Table 17.3.

According to Fig. 17.8, five points have been separately investigated, namely: the central point $M(x_M, y_M)$ and four points located at the vertices of the square A, B, C, D. Shear stress σ_{xz} is calculated at the center of working zone under point M. The strain $\varepsilon_{45°}, \varepsilon_{-45°}$ measured using strain gauges have been simulated by calculation of displacements of the points A, B, C, D. At the kinematical boundary conditions (left part of the sample is fixed, right part is moved vertically) the values $\bar{\tau}_{FE}$ and $\bar{\gamma}$ were calculated and used in (17.9) to obtain the value of $\bar{G}_{xz}$. These results are presented in Table 17.4. The stress distribution pattern for both studied materials reveals the pure shear stress zone with dimensions $\Delta x \times \Delta z \sim 4 \times 5$ mm^2 that determines the maximum base for the strain gauges.

Data presented in Table 17.4 confirm very good precision of the Iosipescu method for orthotropic materials with different degree of anisotropy. But these data have been obtained with the shear stress, which is calculated by FE technique. This is best achievable precision. In order to estimate an influence of assuming about uniformity of the shear stress between two notches, we compared the values of the stress in central point M, and value of stress obtained by dividing the loading force on the cross-section area. For the studied loading conditions, use of this effective stress leads to the value of in-plane shear module $\tilde{c}_{55} = 1.166$ GPa for the material **I** (adjusting coefficient $C = 0.882$), and to $\tilde{c}_{55} = 4.193$ GPa for the material **II** (adjusting coefficient $C = 0.964$). Hence, rough approximation $\bar{\tau} \equiv P/A$ for the shear stress can result an error at least 5 % and possibly more than 15 % even at the perfect geometry of the samples.

In order to estimate an influence of rounding of the top cuts, the similar numerical experiments were fulfilled. The fillet radius, which is caused by the machining tool geometry, was assumed as 0.7 mm. Some simulation results are presented in Fig. 17.11.
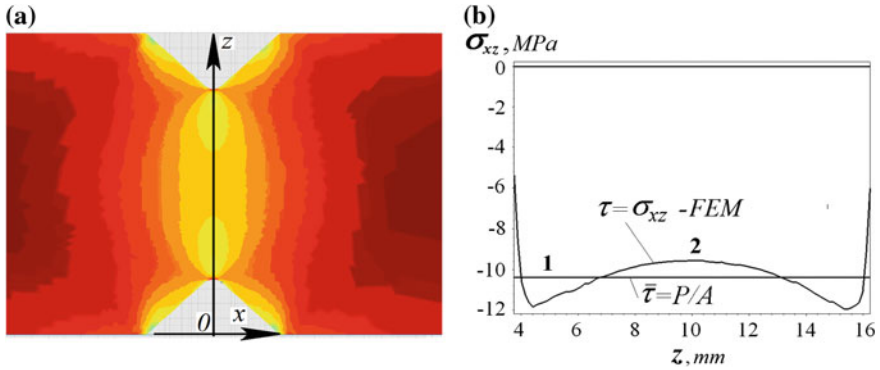
Fig. 17.11 FE simulation results for in-plane shear stress distribution inside the working zone (**a**) and along z-axis (**b**)

As it is presented in Fig. 17.11, the shear stress distribution is very uneven due to a stress concentration near the tops of cuts. In the considered case, the averaged shear stress is $\bar{\tau} = 10.4$ MPa, whereas FE calculated stress in central point is $\sigma_{xz}(x_m, y_m) = 9.56$ MPa. This difference leads to the overestimation of the shear modulus on 9 % ($C = 0.919$). Nevertheless, rounding of corners does not spoil the measurement accuracy.

Above mentioned cases suggest the importance and necessity of refinement the measurement results using FE model of tested specimen. If elastic moduli of material (except for in-plane shear modulus) were previously determined the following iterative procedure can be used. The input data for this iterative process are the loading force P, and experimentally determined shear strain γ_{exp} which allow us to find the initial value $\tilde{c}_{55}$ of the shear modulus. Then the process flowchart is the following:

$$
\begin{aligned}
i &= 0, & c_{55}^{(0)} &= \tilde{c}_{55} \rightarrow & FEA \rightarrow & & \tau^{(0)} &= \sigma_{xz}(x_m, y_m); \\
i &= 1, & c_{55}^{(1)} &= \tau^{(0)}/\gamma_{exp} \rightarrow & FEA \rightarrow & & \tau^{(1)} &= \sigma_{xz}(x_m, y_m); \\
\cdots & & \cdots\cdots\cdots\cdots & \rightarrow & \cdots\cdots\cdots & & \cdots\cdots\cdots & \\
i &= n, & c_{55}^{(n)} &= \tau^{(n-1)}/\gamma_{exp} \rightarrow & FEA \rightarrow & & \tau^{(n)} &= \sigma_{xz}(x_m, y_m).
\end{aligned}
\tag{17.11}
$$

Our experiments show very fast convergence of this procedure. For instance, its use for the material **I** give the following sequence of calculated values for in-plane shear modulus: $c_{55}^{(0)} = \tilde{c}_{55} = 1.166$ GPa $\Rightarrow c_{55}^{(1)} = 1.019$ GPa $\Rightarrow c_{55}^{(2)} = 1.022$ GPa. Even two iterations lead to the value, which differ from the exact value of 1.02 GPa on 0.2 %.

A similar scheme can be effectively used when there are deviations most important dimensions (a mutual displacement of notches, their depth etc.). The described technique used in testing group of the same fiberglass composites can narrow 3–5 times the confidence interval for the measured shear modulus.

Fig. 17.12 Three-point loading of the short beam
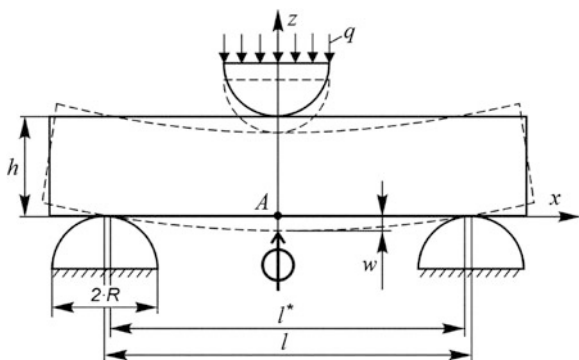
17.5 Interlaminar Shear Modulus

Due to inherent complexity of orthotropic anisotropy and structural features of parts that are made from such composites (relatively thin walls), an experimental determination of interlaminar shear modulus is most difficult and the least accurate. Testing method, described by the standards ASTM D 2344-84 (Reapproved 1989) "Test Method for Apparent Interlaminar Shear Strength of Parallel Fiber Composites by Short Beam Method", and SRM 8-94 "Short-Beam Shear Strength of Oriented Fiber-Resin Composites", is based on the short-beam bending test in the manuals [2, 3], which are referred to the estimation obtained by no determination methods. We analyze below the problem of its correctness, and then we consider and compare the opportunities of method that use twist of prismatic samples with rectangular cross-section.

Short-beam testing method is based on accounting the shear strain component at the transverse bending [13]. The method allow us to estimate two elastic constants of material—longitudinal (or transverse in plane) Young's modulus E_x and interlaminar shear modulus G_{xy}. In Fig. 17.12, l is the beam span, and w is the beam deflection. Other notations are evident.

The beam deflection in a central point is expressed through E_x and G_{xy} as [13]

$$w = \frac{Pl^3}{48E_f I_x} = \frac{Pl^3}{48E_x I_x}\left[1 + \alpha(h/l)^2\frac{E_x}{G_{xy}}\right], \tag{17.12}$$

where α is a coefficient that depends on the beam cross-section (for rectangular cross-section it equals 1.2), I_x is the cross-section moment of inertia, and E_f is the fictitious elastic modulus, which is expressed through E_x and G_{xy} by the following relationship:

$$1/E_f = 1/E_x + \left(1.2/G_{xy}\right)(h/l)^2. \tag{17.13}$$

As one can see from (17.13), an influence of interlaminar shear modulus on the measured deflection will grows for the short and thick beam.

Fig. 17.13 Loading
diagrams for three-point
short-beam test (two lines
were obtained for one
specimen, which has been
loaded on the opposite
surfaces)
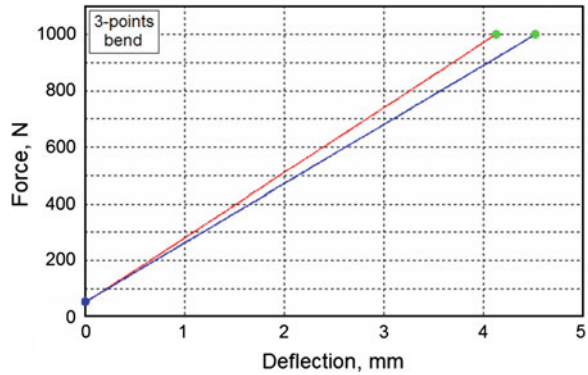
The values of desired maximum stress and strain at testing are defined from the beam theory as [13]

$$\sigma_{\max} = \frac{Plh}{8I_x} = \frac{3Pl}{2bh^2}; \quad \varepsilon_{\max} = \frac{6hw}{l^2\left[1 + 0.6(1+v)(h/l)^2\right]}, \quad (17.14)$$

where h is the beam width. Both experimental dependencies $\sigma(P), \varepsilon(w)$ should be linear as it is presented in Fig. 17.13.

The method includes the following stages. The values P, w are measured at the different ratios of (h/l). For these ratios, fictitious elastic modulus E_f is calculated. The experimental dependence $E_f(h^2/l^2)$, which should be linear, is approximated by the least square method. The values $1/E_f$, $1.2/G_{xy}$ are obtained as a result of the solution of normal equations. Expression for an error of G_{xy} experimental determination by the short-beam test method can be obtained by differentiating (17.13) as

$$\Delta G_{xy} \cong \left(\Delta E_x + \Delta E_f\right) \cdot (l/h)^2. \quad (17.15)$$

At the real test conditions when accuracy of ΔE_x, ΔE_f determination is $\sim 1\%$ the experimental error for G_{xy} at $(l/h) \sim 10$ will be at least $\sim 100\%$. This fact causes the limitations of the considered method.

Below, we illustrate the quality of data obtained for the studied glass–epoxy composite whose specimens have length 200 mm, thickness 6 mm, and two different values of width 25 mm and 60 mm. All specimens have been tested at 8 different distances between cylindrical supports: 40, 50, 60, 70, 80, 100, 140, and 180 mm at the loading force P, that ensures linearity $w(P)$ (see Fig. 17.14). The confidence intervals for E_x and G_{xy} are presented in Fig. 17.15.

As one can see, error in determining the interlaminar shear modulus is greater than 100 %. However, the value found may be used for preliminary FE analysis using more accurate method. This method uses torsion of rectangular prismatic samples with different width to thickness ratios [14, 15], and allow us to

Fig. 17.14 Experimental setup for three-point short-beam test
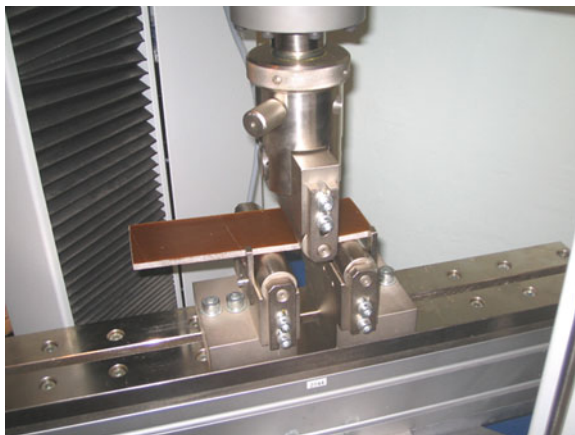
Fig. 17.15 Confidence intervals for the expected values of the longitudinal Young's modulus and interlaminar shear modulus of glass-fiber composite
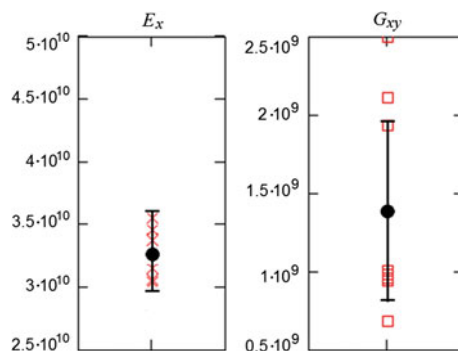
simultaneously determine two shear moduli (in-plane modulus and interlaminar modulus).

Let coordinate surfaces of orthotropic rod with rectangular cross-section are the surfaces of symmetry for the tested material, and z is axis of the specimen torsion. The shear stresses τ_k are expressed through the shear strains $u_{i,j}$ and the linear torsion angle θ by the relationships:

$$\tau_1 = \mu_1\left(u_{3,1} - \theta x_2\right); \quad \tau_2 = \mu_2\left(u_{3,2} - \theta x_1\right), \tag{17.16}$$

where coordinates are depicted as $x \to 1$; $y \to 2$; $z \to 3$, and shear moduli $\mu_1 \equiv E_{1313}$; $\mu_2 \equiv E_{2323}$. By expressing the shear stresses through the stress function

$$\tau_1 = \partial F / \partial x_2; \tau_2 = -\partial F / \partial x_1, \tag{17.17}$$

and introducing the notations:

$$\xi = x_1 \sqrt{(\mu_1 + \mu_2)/2\mu_2}; \eta = x_2 \sqrt{(\mu_1 + \mu_2)/2\mu_1}, \tag{17.18}$$

the Poisson's equation for the stress function is obtained in the form:

$$\frac{\partial^2 F}{\partial \xi^2} + \frac{\partial^2 F}{\partial \eta^2} = -4 \frac{\mu_1 \mu_2}{\mu_1 + \mu_2} \theta. \tag{17.19}$$

Its solution is expressed in the form of the series [15]:

$$F = \mu_1 \theta \cdot \left[\alpha^2 - x_1^2 - 4 \sum_{n=0}^{\infty} \frac{(-1)^n}{\lambda_n^3} \left(1 - \frac{\cosh \lambda_n x_2}{\cosh \lambda_n \beta} \right) \cdot \cos \lambda_n x_1 \right], \tag{17.20}$$

where

$$\alpha = a \sqrt{\frac{\mu_1 + \mu_2}{2\mu_2}}; \quad \beta = b \sqrt{\frac{\mu_1 + \mu_2}{2\mu_1}}; \quad \lambda_n = \frac{2n+1}{2} \cdot \frac{\pi}{\alpha}. \tag{17.21}$$

Equation (17.20) leads to the relationship between linear torsion angle and twisting torque:

$$M = k_1 \mu_1 \theta (2a)^3 (2b), \tag{17.22}$$

where coefficient k_1 depends on the ratio:

$$\chi \equiv \frac{\beta}{\alpha} = \frac{b}{a} \sqrt{\frac{\mu_2}{\mu_1}}, \tag{17.23}$$

and is expressed by the fast converged series

$$k_1(\chi) = \frac{1}{3} - \frac{64}{\pi^5 \chi} \sum_{n=0}^{\infty} \frac{\tanh[(2n+1)\pi\chi/2]}{(2n+1)^5}. \tag{17.24}$$

Both expressions (17.22) and (17.24) are symmetrical with respect to the simultaneous change of $a \leftrightarrow b$; $\mu_1 \leftrightarrow \mu_2$.

Experimental technique involves the following steps. Group of tested samples should have different values of ratio a/b with length at least 5 times exceeding the greatest side of cross-section. At the increased twisting torque the twisting angle is preserved, and slopes $C_i \equiv (k_1\mu_1)_i$ of the linear dependence

$$\frac{M}{(2a)^3 (2b)} = k_1 \mu_1 \theta \tag{17.25}$$

are calculated (see Fig. 17.16).

By using two values C_1, C_2, obtained for two different ratios b/a, two shear moduli μ_1, μ_2 can be calculated from the equation set:

$$\begin{cases} k_1 \left(\frac{b_1}{a_1} \sqrt{\frac{\mu_2}{\mu_1}} \right) \cdot \mu_1 = C_1 \\ k_1 \left(\frac{b_2}{a_2} \sqrt{\frac{\mu_2}{\mu_1}} \right) \cdot \mu_1 = C_2 \end{cases} \Rightarrow k_1 \left(\frac{b_1}{a_1} \eta \right) \cdot C_2 = k_1 \left(\frac{b_2}{a_2} \eta \right) \cdot C_1, \tag{17.26}$$
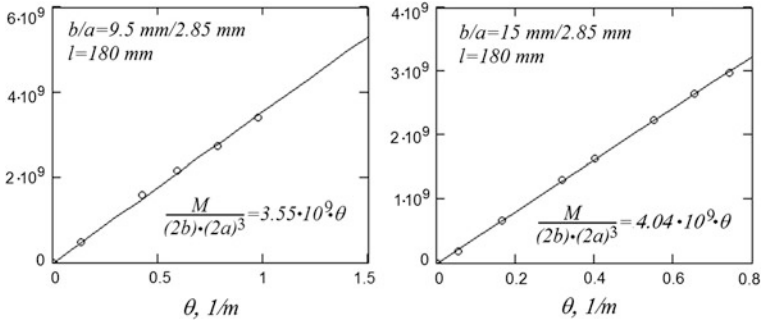
Fig. 17.16 Two dependencies of the ratio $M\left[(2a)^3(2b)\right]^{-1}$ on the linear twisting angle θ

Fig. 17.17 Determination of parameter η from (17.26) with data match to Fig. 17.16
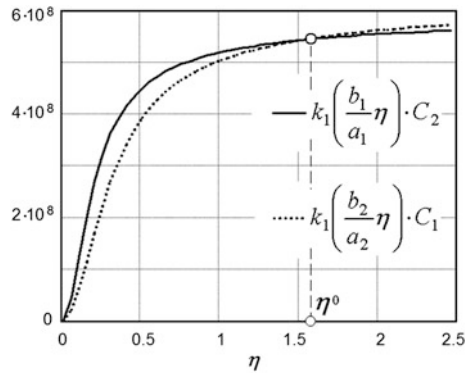
where parameter η denotes the ratio $\sqrt{\mu_2/\mu_1}$. Due to very fast convergence of the series (17.24) numerical solution of (17.26) have not any difficulties. The graphic representation of the solution is shown in Fig. 17.17.

Once the root η° is found, both shear moduli are determined from these two relationships as

$$\mu_1 = C_1 \bigg/ k_1\left(\frac{b_1}{a_1}\eta^\circ\right) \Rightarrow \mu_2 = (\eta^\circ)^2 \cdot \mu_1. \tag{17.27}$$

As it can see from Fig. 17.17, the curves for two different cross-section dimensions are intersected at small angle. This implies a very strong dependence of the root η° on the experimental errors. The first (17.27) and smoothness of the function $k_1(\eta)$ at $\eta \cong \eta^\circ$ imply that the relative error in the μ_1 is of the same order of magnitude as the error in η°. However from the second (17.27), it follows that the error of the μ_2 determination will be two times greater.
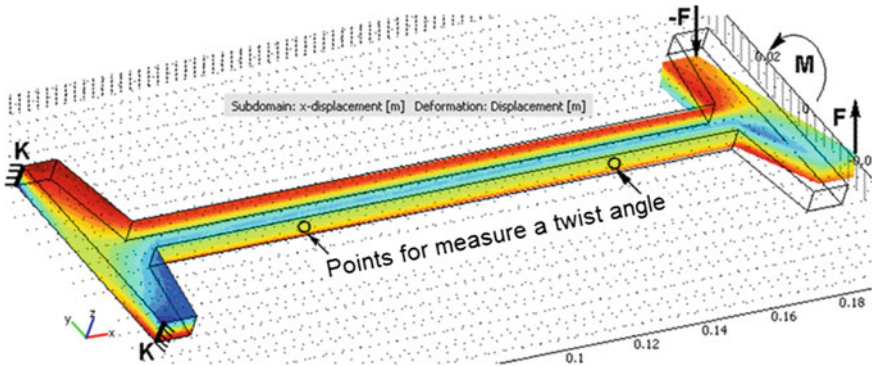
Fig. 17.18 FE model of twisting specimen; the color shows the warping of the rectangular cross-sections

Our experimental results have shown dispersion of calculated moduli 30–50 %. An attempt to reduce the influence of errors by using the symmetry of (17.22) with respect to permutation of the shear moduli μ_1, μ_2 to improve accuracy had no success. The separate determination of interlaminar shear modulus after determination of in-plane shear modulus by short-beam test did not produce improved accuracy also. To clarify the origin of this inaccuracy the FE investigation has been carried out. The required values of all elastic moduli for the test model (see Fig. 17.18) have been accepted from the previously performed tests. The described numerical experiments were carried out for the greater side of cross-section equal to $b = 30$, 18, 12, and 6 mm, with thickness of 5.8 mm, that is, corresponded to aspect ratio $b/a = 5.17$, 3.1, 2.07, and 1.03. All conditions and numerical processing of FE simulation were corresponded to the real-world testing method.

The calculations revealed the following pattern: the calculated value of the modulus μ_1 significantly depended on the aspect ratio of the rectangular cross-section. The named regularity can be described as follows. By increasing the length of the cross-section side, the value of calculated shear modulus (relating to the short side) approaches the value of the shear modulus related to the longer side (see Fig. 17.19). On the contrary, as soon as the lengths of the cross-section become uniform, the calculated value of the modulus deviates from the true value (used in the FE calculation) lesser than 1 %.

The result can be understood after analysis of the stress state of the material in the rectangular cross-section of the sample. Shear stress determined by the shear modulus in the plane xy, occupy substantially a larger space and have a greater value than the stress determined by the shear modulus in the plane corresponding to the thickness of the rod.

The relative contribution of both stresses in the material state for aspect ratio $b/a = 3.1$ is expressed by the ratio:

Fig. 17.19 Influence of aspect ratio of the cross-section on value of the interlaminar shear modulus, which is calculated using results of the numerical experiment
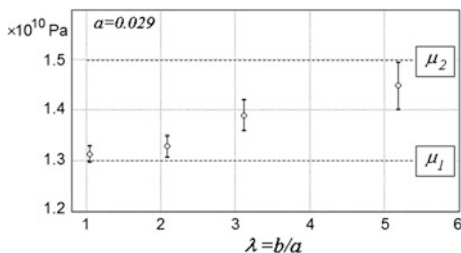
$$\int\limits_{\Omega} |\tau_{xy}|d\omega \bigg/ \int\limits_{\Omega} |\tau_{xz}|d\omega \approx 3.45, \tag{17.28}$$

where integration spreads over the whole cross-section area. This result shows that the stress–strain state of material is determined mostly by in-plane shear modulus. To further study of the error value that is determined by the aspect ratio of rectangular cross-section, the relative torsion stiffness of the rod $S_1(b/a)$ has been calculated at the constant cross-section area as

$$S_1\left(\frac{b}{a}\right) \equiv \frac{M}{16a^2b^2\theta} = k_1\left(\frac{b}{a}\sqrt{\frac{\mu_2}{\mu_1}}\right) \cdot \frac{a}{b}\mu_1, \quad \text{at} \quad a \cdot b = \text{const.} \tag{17.29}$$

Along with the value of S_1 the symmetrical expression of S_2 has been calculated. It was established, that the maximum of these functions is achieved exactly when their argument is equal to 1. Finite element modeling of torsion of the sample with $b/a = 1$ and the subsequent calculation yielded the value of the desired interlaminar shear modulus with an accuracy of 6 characters. Thus, when the in-plane shear modulus is independently determined, the minimum experimental error of the interlaminar shear modulus in the torsional test is achieved when both sides of the cross-section are equal. This fact constitutes a fundamental geometric restriction of the considered methodology. This restriction is especially limiting for the thin material, because an attempt to equalize the sides of the specimen cross-section on the base of limitation caused by effect of the fiber ends is considered above.

17.6 Conclusions

In this paper, we study a possibility to use the specimens that cut out from the ready composite parts to determine some elastic properties of composite material. We considered the applicability of the standard testing methods for determination of the longitudinal, transverse Young's moduli, Poisson's ratios, in-plane and also interlaminar shear elastic moduli. As a result of our investigation, we present some

solutions that improve an accuracy of standard tests, estimate the best achieved accuracy, and determine the test conditions and limitations, which should be taken into account at time of test preparation and their fulfillment. All proposed methods used finite element modeling of testing conditions, and were based on step-by-step determination of tested moduli.

References

1. C.H. Jenkins, *Manual on Experimental Methods for Mechanical Testing of Composites, Society for Experimental Mechanics* (The Fairmont Press Inc., Indiana, 2003)
2. MIL-HDBK-17-1F, *Composite Materials Handbook. Polymer Matrix Composites Guidelines for Characterization of Structural Materials*, vol. 1 (FAA, Washington, 1999)
3. J.S. Tomblin, C.N. Yeow, K.R. Suresh, *Material Qualification and Equivalency for Polymer Matrix Composite Material Systems*, U.S. Department of Transportation; FAA Final Report, DOT/FAA/AR-00/47 (2001)
4. A. Baker, S. Dutton, D. Kelly, *Composite Materials for Aircraft Structures* (AIAA, Reston, 2004)
5. M. Grayson (ed.), *Encyclopedia of Composite Materials and Components*, (Wiley, New York, 1983)
6. D. Hodges, in *Progress in Astronautics and Aeronautics,* vol. 213 (AIAA, Reston, 2006)
7. L. Librescu, O. Song, *Thin-Walled Composite Beams: Theory and Applications* (Springer, Berlin, 2006)
8. R. Wishart, in *ASM Handbook*: *Composites*, ed. by D. B. Miracle, S. L. Donaldson, vol. 21 (ASM International, Novelty, 2001) p. 1765
9. S.N. Shevtsov et al., in *Proceedings of International Conference on the Scientific Computing and Computational Engineering* (2nd IC-SCCE), Athens 2006
10. J. He, M.Y.M. Chiang, D.L. Hunston, C.C. Han, J. Compos. Mater. **36**(23), 2653 (2002)
11. B.M. Lempriure, AIAA Journal **6**(11), 2226 (1968)
12. P.D. Craig, J. Summerscales, Compos. Struct. **9**(3), 173 (1988)
13. J.M. Gere, S.P. Timoshenko, *Mechanics of Materials—Solutions Manual*, 5th edn. (Van Nostrand Company, New York, 2003)
14. F. Fereshteh-Saniee, G.H. Majzoobi, M. Bahrami, J. Mater. Process. Technol **162–163**, 39 (2005)
15. Yu.N. Rabotnov, *Mechanics of Deformable Solids* (Mir Publishers, Moscow, 1979). (in Russian)

Chapter 18
Mathematical Modeling of Interaction of a Circular Plate with an Elastic Inhomogeneous Layer

S. S. Volkov and A. S. Vasiliev

Axisymmetric contact problem about bending of a plate lying on inhomogeneous foundation with complicated structure is considered. The plate is bent under the action of distributed load and elastic response from a foundation. The foundation consists of elastic inhomogeneous soft interlayer and elastic homogeneous half-space. Lamé parameters of interlayer vary with depth by arbitrary law. Both continuously inhomogeneous and stratified interlayers are considered. Also case when layer is significantly softer than an underlying half-space is considered. Bilateral asymptotic method was used to construct an analytical solution of the problem. Analytical expressions for contact stresses and deflection of the plate are provided. The obtained solution is bilaterally asymptotically exact both for large and small ratio of layer thickness to plate radius. Both flexible and stiff plates can be modeled. Numerical results are given which shows that found approximations for kernel transform of integral equation of the problem allow us to construct analytical solution that is effective in the whole range of values of inhomogeneous layer thickness and plate stiffness.

18.1 Introduction

The problem of a plate bending on an isotropic homogeneous elastic foundation was considered in [8] and developed further. Most of the known solutions are applicable only for rigid plates. And very few, in particular those described in

A. S. Vasiliev (✉)
Vorovich Mechanics and Applied Mathematics Research Institute, Southern Federal University, Rostov-on-Don, Russia
e-mail: andre.vasiliev@gmail.com

S. S. Volkov · A. S. Vasiliev
Research and Education Center "Materials", Don State Technical University, Rostov-on-Don, Russia

[5, 6] are applicable either for flexible or rigid plates. There are number of recent investigations in this area [9, 11].

We describe an approach, based on the bilateral asymptotic method of solving the certain type of dual integral equations [2], which allows one to construct analytical solution of the problem in unified form, applicable for any values of geometric and mechanical properties. Similar approach was used for the solution of the problems of torsion and indentation of a rigid punch into the soft inhomogeneous layer [13, 14].

Such problems arise in the calculation of tank bottoms and caissons with enough stiff walls.

The effective technologies of surface engineering, including bioengineering, are based on the development of gradient nanostructured and fine coatings. The geometrical dimensions of the structural members of these materials are under 100 nm. The materials themselves possess qualitative new layer behavior and performance characteristics that traditional materials cannot achieve.

18.2 Formulation of Problem and Construction of Solution

Let us consider circular plate of radius R and constant thickness h lying on the boundary Γ of an elastic half-space Ω, consisting of inhomogeneous soft layer (coating) with thickness H and homogeneous half-space (substrate). We use cylindrical coordinate system $\{r', \varphi, z'\}$, where z' axis is perpendicular to the plane Γ and passes through the center of the plate. The plate is bent under the action of an axisymmetric distributed load $p^*(r')$ and response from the elastic half-space. Function $w^*(r')$ describes the deflection of the plate (Fig. 18.1).

Lamé parameters $\Lambda(z)$, $M(z)$ of the foundation vary with depth according to the following laws:

$$\Lambda(z) = \begin{cases} \Lambda_0(z), & -H \leq z \leq 0; \\ \Lambda_1, & -\infty < z < -H, \end{cases} \tag{18.1}$$

$$M(z) = \begin{cases} M_0(z), & -H \leq z \leq 0; \\ M_1, & -\infty < z < -H. \end{cases} \tag{18.2}$$

Along with the Lamé parameters we introduce Young's modulus $E(z)$ and Poisson's ratio $v(z)$ to specify the elastic properties of the inhomogeneous foundation.

The Young's modulus of the foundation is defined as

$$E_1 = \beta E_0(-H). \tag{18.3}$$

The parameter β indicates stiffness of the substrate.

Due to these conditions, solution of the problem is reduced to following system of equations:
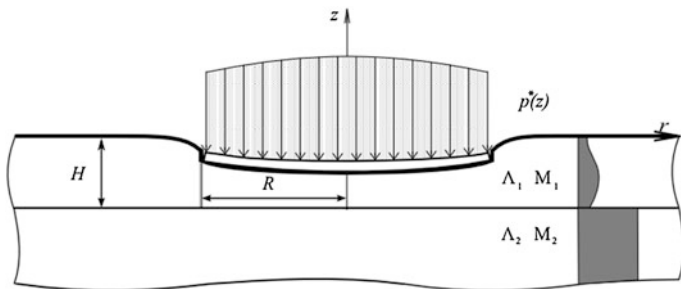
Fig. 18.1 Scheme of the statement of the problem

$$\mathbf{L_0}w(r) = p(r) - q(r), \ 0 \le r \le 1; \tag{18.4}$$

$$\begin{cases} \int\limits_0^\infty Q(\alpha)L(\alpha\lambda)\mathrm{J}_0(\alpha r)\,d\alpha = sw(r), \ 0 \le r \le 1; \\ \int\limits_0^\infty Q(\alpha)\mathrm{J}_0(\alpha r)d\alpha = 0, \ r > 1, \end{cases} \tag{18.5}$$

where $p(r)$ is the applied load, $q(r)$ is the contact stresses under the plate, $w(r)$ is the deflection function, $L(\alpha\lambda)$ is the kernel transform of the integral equation, $\lambda = H/R$, J_0 is the Bessel function, $\mathbf{L_0} = \left(\frac{d^2}{dr^2} + \frac{1}{r}\frac{d}{dr}\right)^2$ is the differential operator.

Function $Q(\alpha)$ is related with the contact stresses $q(r)$ by the Hankel transformation:

$$Q(\alpha) = \int\limits_0^1 q(\rho)\mathrm{J}_0(\alpha\rho)\rho d\rho, \ q(r) = \int\limits_0^\infty Q(\alpha)\mathrm{J}_0(\alpha r)\alpha d\alpha\,.$$

The parameter $s = \Theta R^3 D^{-1}$ indicates the bending stiffness of the plate, where D is the cylindrical stiffness of the plate, Θ is given by

$$\Theta = 2\mathrm{M}_0(\Lambda_0 + \mathrm{M}_0)(\Lambda_0 + 2\mathrm{M}_0)^{-1}.$$

Following substitutions are used above:

$$r = r'/R; \ w^*(r') = w(r)R; \ p^*(r') = p(r)DR^{-3}; \ q^*(r') = q(r)DR^{-3}.$$

Deflection of the plate must satisfy the following boundary conditions:

$$\left(\frac{d^2w}{dr^2} + \frac{v}{r}\frac{dw}{dr}\right)\Bigg|_{r=1} = 0, \ \frac{d}{dr}(\nabla w)\Bigg|_{r=1} = 0. \tag{18.6}$$

Conditions (18.6) correspond to free edges of the plate.

Dual integral equation (18.5) defines the relation between the contact stresses and plate deflection. The kernel transform $L(u)$ is equal to that appearing in the indentation problem and can be constructed numerically [1].

It has been shown [14] that by increasing the value of parameter β, the kernel transforms got closer to the limiting case corresponding to non-deformable foundation.

We represent the deflection function in terms of series with respect to eigenfunctions of oscillations of a circular plate with free edges (similar to [12]) as

$$w(r) = \sum_{m=0}^{\infty} w_m \varphi_m(r); \qquad w_m = \int_0^1 w(\rho)\varphi_m(\rho)\rho d\rho,$$

where $\varphi_0(r) = \sqrt{2}$; $\varphi_m(r) = A_m \left[J_0(k_m r) - \frac{I_0(k_m r)}{I_1(k_m)} J_1(k_m) \right]$; A_m, k_m, $m = 0, 1, \ldots$, 10 are known constants [12], I_0, I_1 are modified Bessel functions.

Due to the linearity of the problem the contact stresses can be represented as

$$q(r) = \sum_{m=0}^{\infty} w_m q_m(r), \qquad 0 \le r \le 1.$$

Dual integral equation (18.5) can be solved using an asymptotic method [2]:

$$q_0^N(r) = \frac{2\sqrt{2}}{\pi} s \left[\frac{L_N^{-1}(0)}{\sqrt{1 - r^2}} + \sum_{i=0}^{N} C_i^0 \Psi(r, a_i \lambda^{-1}) \right];$$

$$q_m^N(r) = \frac{2}{\pi} A_m s \left[\frac{\Psi(r, ik_m)}{L_N(m)} - \frac{J_1(k_m)\Psi(r, k_m)}{I_1(k_m)L_N(i\lambda k_m)} + \sum_{i=0}^{N} C_i^m \Psi\left(r, a_i \lambda^{-1}\right) \right], \, m = 1, 2, \ldots$$

where the special approximation of the kernel transform is used:

$$L(\alpha) \approx L_N(u) = \prod_{i=1}^{N} \frac{u^2 + a_i^2}{u^2 + b_i^2}, \quad a_i, b_i \in C. \tag{18.7}$$

Constants C_i^m are the solution of a set of linear algebraic equations [3]. It has been proved that the solutions were asymptotically exact for $\lambda \to 0$ or $\lambda \to \infty$ [2].

Representing the contact stresses and the applied load in the form:

$$q_m^N(r) = \sum_{j=0}^{\infty} y_j^m \varphi_j(r); \qquad y_j^m = \int_0^1 q_m^N(\rho)\varphi_j(\rho)\rho d\rho;$$

$$p(r) = \sum_{m=0}^{\infty} p_m \varphi_m(r); \qquad p_m = \int_0^1 p(\rho)\varphi_m(\rho)\rho d\rho,$$

and using (18.4) we obtain the infinite system of linear algebraic equation to determine w_m, $m = 0, 1 \ldots$, that can be solved using the reduction method.

Fig. 18.3 Contact stresses for the layers 1, 2 and different values of λ, solid lines corresponds to $s = 0.1$, dashed lines relate to $s = 4$

However, obtaining accurate solution for average values of λ requires high accuracy of the approximation for the kernel transform. By using recent results [4], it is possible to obtain a solution, which is applicable for all possible values of characteristic parameters of the problem.

18.3 Analysis of Contact

Let us consider soft inhomogeneous layers whose Young's moduli vary with depth according to the harmonic function:
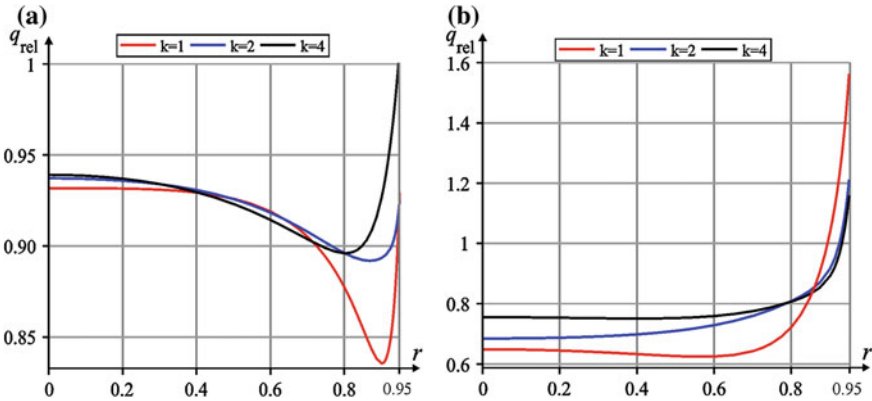
Fig. 18.4 Contact stresses for the layer 1, $k = 1, 2, 4$; $s = 0.1$

$$(\text{Layer 1})\, E_1(z) = 2.25 - 1.25 \cos\left(2\pi k \frac{z}{H}\right);$$

$$(\text{Layer 2})\, E_2(z) = 0.643 + 0.357 \cos\left(2\pi k \frac{z}{H}\right).$$

Layers 1, 2 describe periodic variation of the Young's modulus: soft layers (material 1) alternate hard layers (material 2). Parameter k sets the number of sub-layers. In the layer 1 first sub-layer is stiffer, while in layer 2 one is softer (see Fig. 18.2).

Mechanics of such coatings and their investigation using transmission electron microscopy (TEM) and nanoindentation are described in the work by [7].

Young's modulus in the layers 1, 2 varies in 3.5 times, that corresponds to the combinations of hard (Fe with $E = 217$ GPa, or Cr with $E = 240$ GPa, or Mo with $E = 340$ GPa) and soft metals (Ag with $E = 80$ GPa or Al with $E = 72$ GPa).

The foundation is assumed to be 100 times stiffer than the layer ($\beta = 100$).

It is seen (Fig. 18.3) that the contact stresses appearing on the surfaces of the layers 1 and 2 for flexible plates (small values of s) are higher than that for stiff plates in range of $r < r_0 \approx 0.8$ and lower for $r > r_0$. The maximum difference between them is under the center of the plate ($r = 0$).

Thickness of the inhomogeneous layer greatly influences the contact stresses under the plates (difference between the contact stresses at $r = 0$ for $\lambda = 0.25$ and $\lambda = 4$ is more than 2 times).

For the thick layers (big values of λ) the difference between the contact stresses under the center of the plate and near its edge is bigger than for the thin layers (small values of λ).

Figure 18.4 shows how the number of the sub-layers (parameter k) redistributes the contact stresses appearing on the surface of the layer 1 (similar for layer 2).

References

1. S.M. Aizikovich, V.M. Aleksandrov, Mech. Solids **19**(2), 73 (1984)
2. S.M. Aizikovich, J. Appl. Math. Mech. **54**(5), 719 (1990)
3. S. Aizikovich, A. Vasiliev, I. Sevostianov, I. Trubchik, L. Evich, E. Ambalova, in *Shell-like Structures: Non-classical Theories and Applcations*, ed. by H. Altenbach, V.A. Eremeyev, vol. 15 (Springer, Heidelberg, 2011)
4. S.M. Aizikovich, A.S. Vasiliev, J. Appl. Math. Mech. **77**(1), 91 (2013)
5. V.M. Aleksandrov, M.D. Solodovnik, Sov. Appl. Mech. **10**(7), 749 (1974)
6. S.V. Bosakov, J. Appl. Math. Mech. **72**(1), 59 (2008)
7. P. Dayal, N. Savvides, M. Hoffman, Thin Solid Films **517**, 3698 (2009)
8. M.I. Gorbunov-Posadov, J. Appl. Math. Mech. **4**(3), p. 61 (1940) (in Russian)
9. M. Kashtalyan, M. Menshykova, Compos. Struct. **89**, 167 (2009)
10. G.N. Pavlik, in *Mechanics of Contact Interactions*, ed. by I.I. Vorovich, V.M. Aleksandrov, vol. 73 (Fizmatlit, Moscow, 2001) (in Russian)
11. R.D. Silva Andrea, A.M. Silveira Ricardo, B. Goncßalves Paulo, Int. J. Solids Struct. **38**(10–13), p. 2083 (2001)
12. A.I. Tseitlin, Izvestiya AN USSR. Mech. Solids **1**, 99 (1969). (in Russian)
13. A. Vasiliev, S. Volkov, S. Aizikovich, Y.-R. Jeng, ZAMM—Z. Angew. Math. Mech. (2013). doi:10.1002/zamm.201300067
14. S.S. Volkov, S.M. Aizikovich, Y.-S. Wang, I. Fedotov, Acta. Mech. Sin. **29**(2), 196 (2013)

Chapter 19
Dependence of Displacements on Elastic Properties in Solids of Complex Shape

G. A. Zhuravlev and Y. E. Drobotov

It is studied the influence of material properties of elastic cantilever plate and the longitudinal localization level of transverse load applied to the plate on change of the plate shape. The expediency of using analytical methods based on analysis of each of the main loading factors separately is shown in studies of bending and shear stress concentrations in the solids of complex shapes with loaded ledges.

19.1 Introduction

Due to rapid development of technologies and materials used in mechanical engineering, the need of strength calculations clarification rises for innovative purposes. In our opinion, the application of the theory of elasticity in these cases should be closely connected with the ability to analyze stress–strain state of solids of a complex shape, considering influence of each of the force factors of a load separately.

Theoretical study of the mechanism of stress concentration displaying in elastic solids with ledges of a complex shape, based on the analysis of separate force factors, is the valuable tool for better understanding of the nature of changes in the stress state of such solids. In particular, the discovery of the relationships between the elastic properties of the ledge material and the contribution in creating the effect of stress concentration of each of the main force factors opens up the possibility for a significant improvement of machinery details design.

G. A. Zhuravlev (✉) · Y. E. Drobotov
Vorovich Mechanics and Applied Mathematics Research Institute, Southern Federal University, Rostov-on-Don, Russia 344090
e-mail: zhuravl@math.rsu.ru

Y. E. Drobotov
e-mail: yuedrobotov@sfedu.ru

It is known, that the standardized methods for calculating a set of details of mechanisms and machines with loaded ledges (see, for instance the existing Russian GOST—State Standard No. 21354-87 "Cylindrical Involute Gear Transmissions: Strength Calculations", 1987—for steel teeth) on the bending strength of the ledges do not include the elastic constants of the material. They are based on the analytical solutions (for example, on the method of conformal mapping) of a plane problem of determining the stress state of ledge under the action of uniformly distributed load. In particular, these solutions determine the position of the considered point, regardless of material properties. It is easy to be convinced in absence of account of the material properties by considering Levy's equation for the generalized plane stress state. In addition, standard methods give the exact solution for solids with boundaries of a simple form. In any case, they are very difficult to be used for innovative problems. For example, the Russian GOST 21354-87 has information only for steel involute gears and only for the type of base contour of teeth. The cause of these circumstances is particular assignment of boundary conditions. Registration of the spatial nature of real solid loading in the standard methods of calculation is provided by introduction of approximate values of the correction coefficients (for the level of load concentration), which reduce, as it is believed, plane problem to spatial one.

Spatial nature of a real problem (with estimate of the material properties) is better taken into account by numerical methods. The main advantage of numerical methods (e.g., FEM) is the potential possibility of quantitative estimation of a specific structure or of analysis a certain known effect. However, these methods are characterized by high complexity of the model construction and the difficulty of determination of its accuracy. All these causes, as well as the lack of visibility of the results, makes their use for research purposes (including the problems of synthesis of new knowledge and improved designs) appropriate only in cases where the effect itself is already known or clear at least hypothetically. Furthermore, FEM does not provide an assessment of each of the separated force factors. This makes impossible to complete the analysis of the mechanism of specific effect.

In works [1–3], the research method (the method of local approximation, MLA) has been proposed by G. A. Zhuravlev. MLA was built as a combination of specially selected solutions of two-dimensional problems, to which the problem of determining three-dimensional stress state of loaded ledge was reduced. MLA provided background for definition of the "missing" laws, being deprived of restrictions of the intrinsic solutions, on which it has been based.

As the base of MLA creation, the exact analytical solutions have been selected, which were sufficiently simple in application and ensured separation of operating force factors. First solution was stated for a rod with two hyperbolic recesses under action of pure bending, simple tension and pure shear. This solution was obtained by G. Neuber (*stress concentration*) [4] and used the method of three harmonic functions, developed by N. F. Papkovich and G. A. Grodsky. The second one was the solution for a thin cantilever plate of infinite length, obtained by T. J. Jaramillo [5] for the determination of displacements and force factors at the anchorage line

of a plate in the case of a concentrated force action. It should be noted that this choice provides the definition of each of the three major force factors: bending moment, shear force and compression force. However, in many features these solutions do not satisfy all requirements of MLA.

The first solution has been developed in [1, 2, 6–8]:

- for free form of geometrical concentrator taking into account the effect of the stress damping law,
- for the conditions of loading the rod by transverse bending.

The second solution has been developed in [9, 10], where

- it was shown the opportunity to determine displacements and force factors caused by distributed load,
- the solutions were obtained for three main force factors along and outside the anchorage line.

MLA is based on these and a set of other advanced solutions.
The advantages of MLA are:

- the ability to take into account the properties of material,
- relative simplicity to obtain a large amount of computational results,
- the ability of separate analysis of various force factors,
- the ability to identify the effects of stress state of solids with complex shape,
- the ability to explain the mechanism of detectable effect displaying,
- a broad scope of potential applications—from engineering calculations to theoretical developments and creating innovative designs.

For example, the use of MLA shows, that the position of the dangerous cross-section in geometrical concentrator of elastic solid with loaded ledges and the level of maximum stress strongly depend on elastic properties of the material, features of distribution and degree of localization of the force factors along the ledge. At the same time, standardized methods of calculation (for example, the Russian GOST 21354-81) are based on determining the position of the dangerous section with solution of the plane problem. At the same time, registration of the contact localization in maximum stresses is carried out only for the level of external load concentration along the ledge.

The primary purpose of this chapter is description of some MLA elements, which determine influence of physical and mechanical properties of a material on degree of localization of the external load along ledge.

For better conditions of understanding and possibility to repeat the results, obtained in this study, approximated expressions are used. They give (into framework of used ranges of model parameters) absolute error, that is no exceeding 7 %. The authors consider such accuracy sufficient for the goals of the chapter.

19.2 Determination of Displacements in Cantilever Plate, Arising under Action of Distributed Load

We study an infinitely long cantilever plate of width A. Note that in our case of plate using for approximation of spatial ledge we will call A as the height of the plate. In any case, A is the distance from the anchorage line of the plate to its free edge. In this condition, the considered plate is subjected to the external transverse load, distributed along straight-line segment. This line is called hereinafter the line of action of the external load, and we assume it is located parallel to the anchorage line. The segment of the distributed load action is called the loaded interval. The external distributed load has the resultant F_Σ.

Cartesian coordinate system $Oxyz$ is introduced so that xy-plane coincides with the median plane of the plate, the axis Oy coincides with its fixed side, and the center point of the loaded interval (the latter is symmetrically disposed about the axis Ox) has coordinates $(c, 0)$. By introducing the dimensionless coordinate $\zeta = \frac{c}{A}$, we consider $\zeta = 1$ hereinafter. We assume the parabolic law of distribution of the load, which is located in xz-plane. The calculated point is denoted as $D(x, y)$.

19.2.1 Obtaining the Deflection Function

Before considering displacement field in the plate, we form the approximated function $K^*(\xi, \eta)$ for the displacement components caused by the concentrated load. The function $K^*(\xi, \eta)$ will allow us to find the values of displacements and force factors within a rectangular area of the considered plate.

As such an area, we take the square $S = \{\forall \xi \in R, \eta \in R : \xi \in [0,5; 1], \eta \in [-1; 1]\}$, where $\xi = \frac{x}{A}$ and $\eta = \frac{y}{A}$ are the dimensionless coordinates of the calculated point D. For the chosen square we take an approximate function $K^*(\xi, \eta)$ as

$$K^*(\xi, \eta) = a(\eta)\xi^2 + b(\eta) + c(\eta), \tag{19.1}$$

where

$$a(\eta) = 0,376429 \cdot e^{-1,12174\eta},$$
$$b(\eta) = -0,21788\eta^2 + 0,16657\eta + 0,170357,$$
$$c(\eta) = 0,0370284\eta^2 - 0,032657\eta - 0,0236857.$$

Within the considered region, the function $K^*(\xi, \eta)$ gives the maximum absolute error of 6.1 % which can be assumed satisfactory for our further calculations.

The functions $K^*(\xi, \eta)$ and $W^*(\xi, \eta)$ are related as [5]

$$W^*(\xi, \eta, \zeta) = -\frac{F \cdot A^2}{\pi \cdot N} K^*(\xi, \eta), \tag{19.2}$$

where $N = \frac{Eh^3}{12(1-\mu^2)}$ is the bending rigidity of the plate.
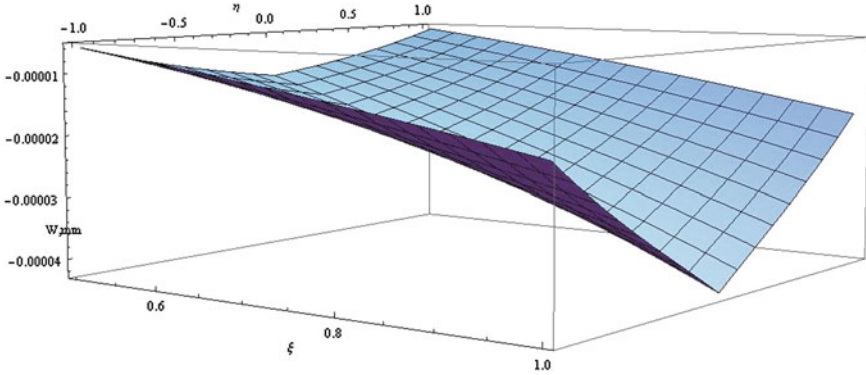
Fig. 19.1 Plot of function (2) with $\zeta = 1$ for the steel plate of height $A = 3.45$ mm and thickness $h = 1.33$ mm, loaded with concentrated load of 1 N

Figure 19.1 shows the plot of function (19.2) with $\zeta = 1$ for the steel plate of height $A = 3.45$ mm and thickness $h = 1.33$ mm, loaded with concentrated load of 1 N.

At transition from the concentrated load to the load distributed over segment with length of $2l$, we use the next algorithm. We divide the loaded interval into n smaller segments, the length of each one is ΔS (i.e. $\Delta S = \frac{2l}{n}$). Let q_i is the specific load on i-th segment then unit force acting on the same segment is

$$F_i = q_i \cdot \Delta S. \tag{19.3}$$

In accordance with [10], we suppose the parabolic law of load distribution:

$$q_i = q_i(A, F_\Sigma, l) = \frac{3 \cdot F_\Sigma \cdot \left(l^2 - \varepsilon_i^2 \right)}{4l^3}, \tag{19.4}$$

where $\varepsilon_i = l + \frac{\Delta S}{2} - \Delta S \cdot i$, $i = 1, \ldots, n$ is the coordinate of the point, located at the center of the considered i-th segment, which is also the application point of the concentrated force F_i. We shall introduce also the dimensionless coordinate $\rho_i = \frac{\varepsilon_i}{A}$.

By using (19.4), we define q_i for all points $i = 1, 2, \ldots, n$ and submitting them in the expression (19.3), we calculate n values of W_i^* in the form:

$$W_i^*(\xi, \eta, \zeta) = -\frac{F_i \cdot A^2}{\pi \cdot N} K^*(\xi, \eta - \rho_i), \, i = 1, \ldots, n. \tag{19.5}$$

Thus, formula (19.4) gives values of displacements at the calculated point $D(\eta)$, caused by corresponding concentrated force F_i, acting on the i-th segment of the loaded interval.

In order to obtain the values of the total displacement at the calculated point, we conduct summing the obtained values of $W_i^*(\eta)$:
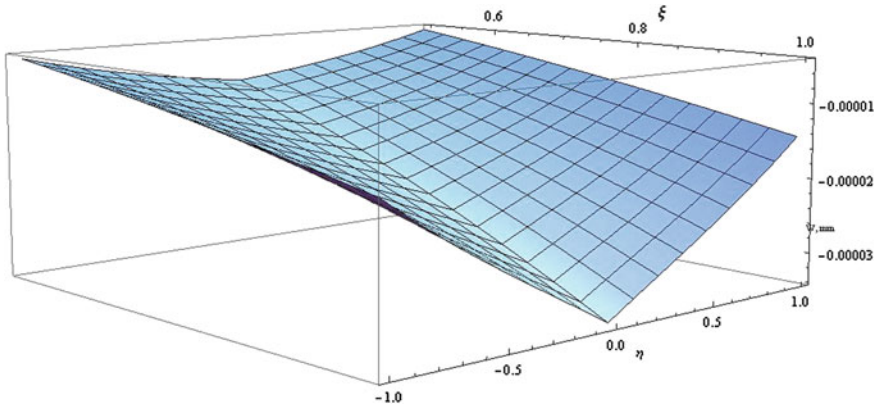
Fig. 19.2 Dynamics of displacement changing

$$W = W(\xi, \eta) = \sum_{i=1}^{n} W_i^*(\xi, \eta). \tag{19.6}$$

Thus, the value of W is the displacement at the calculated point D (η) due to action of the load with resultant F_Σ, distributed along the segment of length $2l$.

19.2.2 Analogy to Concentrated Load

We apply the described algorithm to the steel plate with height of $A = 3.45$ mm under external load, distributed over the segment with length of $2l = 0.001$ mm, divided into 10 ranges. The resultant of the external load is $F_\Sigma = 0.79$ N. Due to the smallness of the loaded interval, this case can be considered as an approximation to the case of concentrated load action. Figure 19.2 shows the dynamics of displacement changing in this case.

Now we calculate the displacements along some line $\xi = $ const on the segment $\eta \in [0; 1]$. Let us choose, for example, a line, that corresponds to overlaying of the calculated segment on the loaded interval. We move on the calculated segment with length step of 0.1. Table 19.1 and Fig. 19.3 present the results of calculations of the displacements on the pointed interval. Due to the symmetry of the acting load, the same values can be obtained for the range $\eta \in [-1; 0]$.

Finally, we compare the values of the displacement function, obtained at different points of the area S by using two different approaches: (i) considering the load distributed over the segment with length of 0.001 mm and having the resultant F_Σ, and (ii) considering the concentrated load equal to F_Σ and applying results of [9]. The correlation coefficient of these values is 0.997.

Table 19.1 Numerical results for displacements

η	W (mm)
0.0	$-3.37 \cdot 10^{-5}$
0.1	$-3.19 \cdot 10^{-5}$
0.2	$-3.19 \cdot 10^{-5}$
0.3	$-2.83 \cdot 10^{-5}$
0.4	$-2.65 \cdot 10^{-5}$
0.5	$-2.47 \cdot 10^{-5}$
0.6	-2.28×10^{-5}
0.7	-2.08×10^{-5}
0.8	-1.88×10^{-5}
0.9	-1.66×10^{-5}
1.0	-1.43×10^{-5}
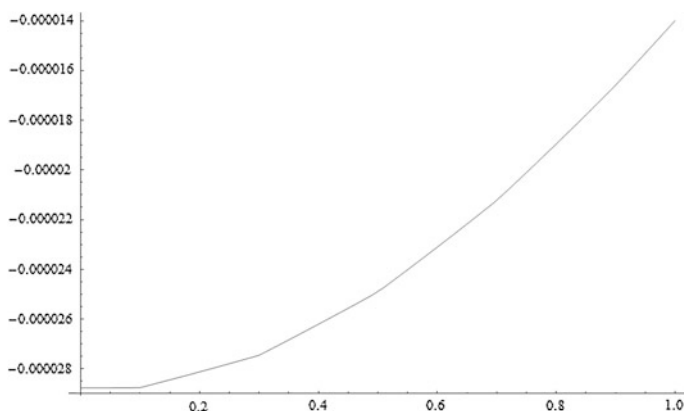
Fig. 19.3 Numerical results for displacements

19.2.3 Effect of Loaded Interval Length

Now let us compute the displacements for the case $l = A \cdot i$, $i = 0.1, 0.2, \ldots, 1$, considering $\eta \in [-1; 1]$ as the calculated segment. Such a definition of the length of the loaded interval will allow us to identify the dynamics of the displacement changing when the length of the loaded interval changes, too. The resultant of the external load is assumed still equal to $F_\Sigma = 0.79$ N. Figure 19.3 present useful illustration of the process of this changing.

Figure 19.4 shows the plots of the function W for the loaded intervals equal to $0.2A$, $0.6A$, $1.4A$ and $2A$. In this case, the smaller length of the loaded interval leads to the lower and sharper plot of function W.

Separately, we study the case of $l = A$. It is especially interesting because the loaded interval coincides with the calculated interval. The plot of the displacement function for this case is shown in Fig. 19.5.
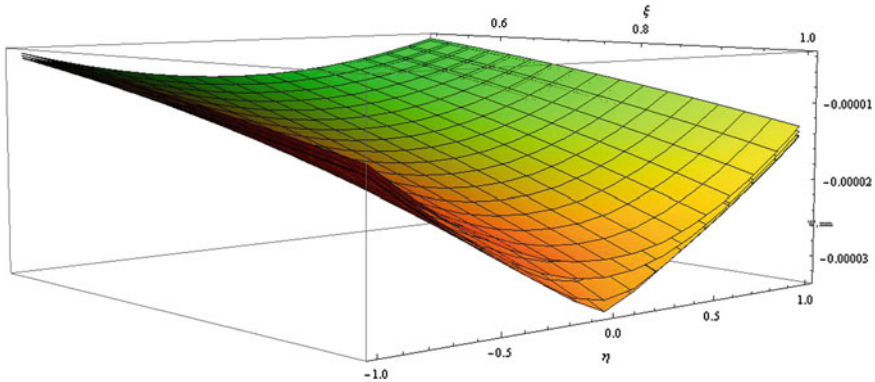
Fig. 19.4 Function W for the loaded intervals equal to $0.2A$, $0.6A$, $1.4A$ and $2A$
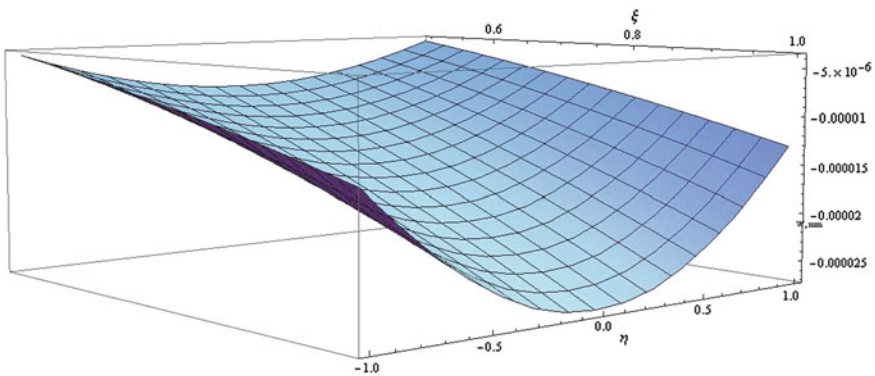
Fig. 19.5 Displacement function for the case of $l = A$

By applying this algorithm to the case of $\xi = \zeta = 1$ with step of 0.2, we obtain the results shown in Fig. 19.6.

19.3 Influence of Material Properties on Stress–Strain State Characteristics

Standard methods for calculation of different machine and mechanisms details with loaded ledges (e.g. gears) on bending strength of the ledges are based on the analytical solutions of the plane problem (such as the method of conformal mapping, for example) of determining the stress state of the ledge under action of concentrated force. In any case (plane strain and plane stress), these solutions do not contain the elastic constants or other characteristics of material properties of
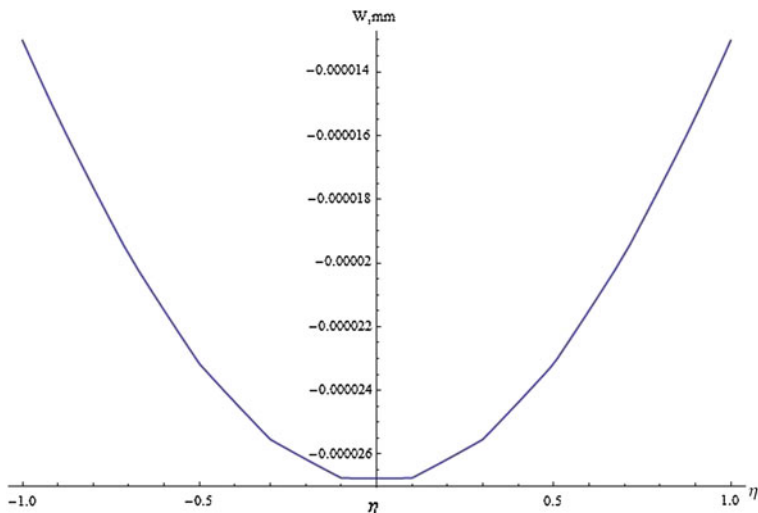
Fig. 19.6 Displacement function for the case of $\xi = \zeta = 1$ with step of 0.2

such solids. In addition, they provide accurate results only for solids with boundaries of a simple shape. Finally, when they are used there are no possibilities of analysis of separated force factors.

The first restriction follows from Levy's equation for generalized plane stress state. The second and third ones follow from the features of the boundary conditions.

Account of spatial nature of actual problem in these cases is based on using of correcting coefficients $K_{H\beta}$ and $K_{F\beta}$ (in calculation on the contact and bending fatigue strength of teeth, respectively) of load concentration along the distribution line of localized external load. It is believed, that this method allows one to reduce the spatial problem to the plane problem of theory of elasticity. This approach almost excludes a satisfactory estimate of material properties.

It is shown that the position of the dangerous cross-section of the geometrical concentrator in elastic solids with loaded ledges and the level of maximum stress strongly depend on the material properties of the solid and nature of the load distribution along the ledge.

Below we show significant influence of physical and mechanical properties of the material of solid with complex shape on the load concentration along the ledge, and also on the levels and ratios of force factors and the corresponding stresses in the region of the solid geometrical concentrator.

Similar to the previous sections, we model the ledges of solids with complex shape by cantilever plate of infinite length subjected to action of external transverse distributed load.

19.3.1 Material Properties Having the Greatest Influence on Change of Force Factors, Operating in Loaded Ledge

Here we give an analysis of the influence of physical and mechanical material properties, such as a Young's modulus (or modulus of elasticity), E, Poisson's ratio, μ, yield strength, σ_T and hardness, H. We present the estimations for each of them precisely in the area where its effect is particularly high.

Thus, the concentration of external load is much more dependent on the parameters σ_T and H, characterizing the ability of material to resist plastic deformation. As a result, the yield strength σ_T and hardness H influence on running-degree of different contact nodes and due to they determine the distribution of force factors along the ledge, changing maximum stress and position of dangerous cross-section in the area of geometrical concentrator of the ledge.

The influence of Young's modulus E and Poisson's ratio μ in the most degree define (e.g., for constant external loading) the change of force factors, maximum stress and position of the dangerous cross-section in the area of geometrical concentrator of the ledge.

To perform this analysis for the influence of yield strength σ_T (hereinafter indicate the hardness of the material H on the Brinell scale), we use the following parameters of low-carbon chromium-nickel steel 12X2M4A [11]:

- $\sigma_T = 1100$ MPa, $N = 200$ (without chemical-heat treatment);
- $\sigma_T > 2500$ MPa, $N = 600$ (with a surface chemical and thermal hardening).

In the case of study of the effect of Young's modulus and Poisson's ratio, we choose three materials (duraluminium, steel and cermet):

- duralumin for $E = 0.74 \times 10^5$ MPa, $\mu = 0.34$;
- for steel $E = 2.0 \times 10^5$ MPa, $\mu = 0.3$;
- for cermet $E = 6.23 \times 10^5$ MPa, $\mu = 0.21$.

19.3.2 Influence of Hardness of Ledge Material

To estimate the degree of localization of the longitudinal loading of ledge (cantilever plate) for the case, when the hardness of its material is changed, we turn to the theory and practice of strength calculations of gear being the most typical representative of solids with complex shape.

A typical teeth contact for heavily-loaded power-consuming gears is characterized by very uneven distribution of the specific load q_{tb} along the nominal line of contact 1 (Fig. 19.7a) with a concentration at the edge of the contact line
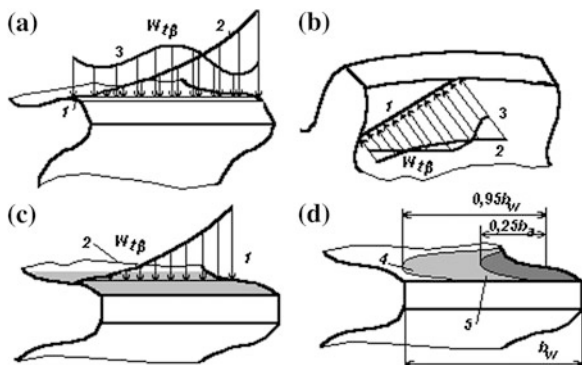
(distribution diagrams 2) or at its middle part (distribution diagrams 3). This effect
displays also at longitudinal or profile modifications of teeth during their wear and
natural barrel-shaped forming especially noticeable in load level fluctuations.

The edge concentration of load (curve 2) can display also at full (over all
surface) contact of teeth (Fig. 19.7c). Nevertheless, incomplete contact is the most
proper for high-deformed gears. In this mean, the technological standards of
accuracy are very important. They restrict relative size of integral (i.e. obtained
after rotation of wheels under some test load) patch of the contact. This size
changes along the length of the teeth (Fig. 19.7d) from 95 % for a high-accurate
gear (area 4 corresponds third degree of accuracy in accordance with Russian
GOST 1643-81) to 25 % (area 5) at the eleventh degree of accuracy.

Moreover, even in the perfectly accurate gear with wear-free teeth and abso-
lutely rigid body (when the teeth contact is close to 100 %),it is also impossible to
avoid stress concentrations due to finite sizes of teeth and inconstant rigidity of
gearing along the contact line.

Real gears of numerous transport machines (e.g.in the traction nodes of rolling
stock) work in very difficult conditions. For instance, the coefficients of non-
uniformity ofthe load distribution $K_{H\beta}$ and $K_{F\beta}$ (in the calculations on the contact
and bending fatigue strength of teeth, respectively) for these gears often are very
large (up to $K_{H\beta} \approx 4 - 5$ and $K_{F\beta} \approx 3 - 4$) and could be reduced during a
special run-in (or long-term work) only to levels of $K_{H\beta} \approx 2 - 3$ and
$K_{F\beta} \approx 1.5 - 2.5$. Such gears are classified as badly run-in ones.

However as it is known, conformability of teeth depends on combination of
such parameters as, for example rigidity of teeth, lubrication conditions, summary
rolling velocity of teeth in the area of their contact and general deformability of the
gear construction, etc. Low-speed gears with small rigidity of teeth can reach
almost uniform distribution of the load as a result of nature run-in. On the contrary,
high-speed gears can maintain high non-uniformity of the load distribution even
almost independently on teeth rigidity.
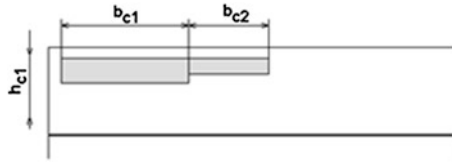
Fig. 19.8 Size of the contact patch in helical gear (where h_{c1} is the active tooth height), obtained by the procedure, established by the UK standard BS 1807, after testing in operational conditions
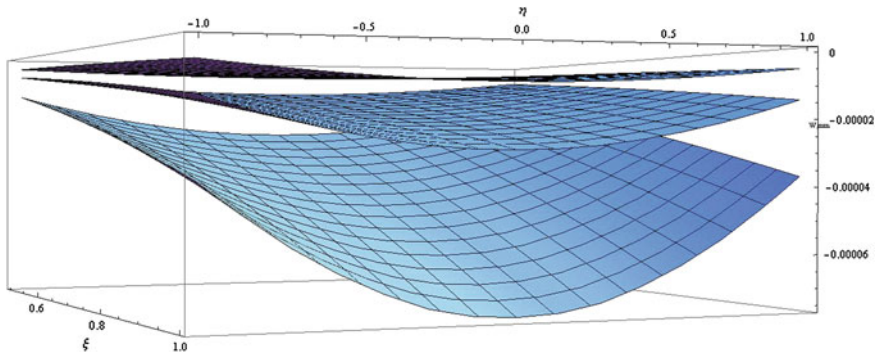
Fig. 19.9 Plots of the displacement function for the whole area of approximation S

Similar regulations are provided also by standards of various countries. The scheme of boundary concentration of teeth contact (in accordance with DIN 3990) and the contact sizes (standard BS1807) are shown in Fig. 19.8.

Therefore, even very accurate (technologically) gears often cannot ensure perfect teeth contact. Experience has shown that the quality of teeth contact often are restricted no so much by technological manufacturing accuracy and gear installation accuracy, but by the level of deformability of construction as a whole.

19.3.3 Influence of Material Elastic Constants on Displacements in Ledge

Now let us study the nature of influence of the elastic material properties on the displacements, rising in the plate body, which simulates a real ledge, at the action of distributed load. As before, we consider the plate with height of $A = 3.45$ mm and thickness of $h = 1.33$ mm. The external load is distributed in parabolic law along segment with length of $2A$ and having the resultant $F_\Sigma = 0.79$ N. We select the value of $\zeta = 1$. On example of above-mentioned three materials (duraluminium, steel and cermet), we discuss influence of the elastic constants of the plate material on arising displacements under above-stated conditions of loading.
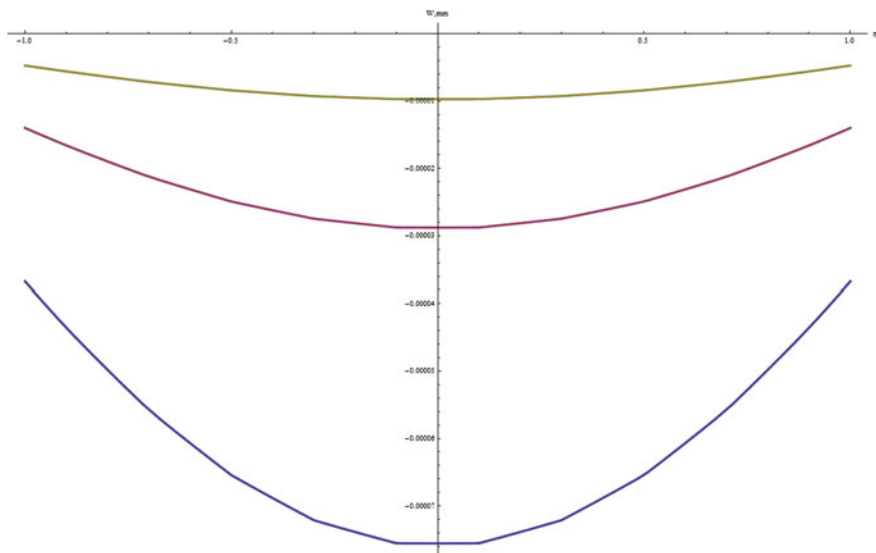
Fig. 19.10 Plots of the displacement function for line $\xi = 1$
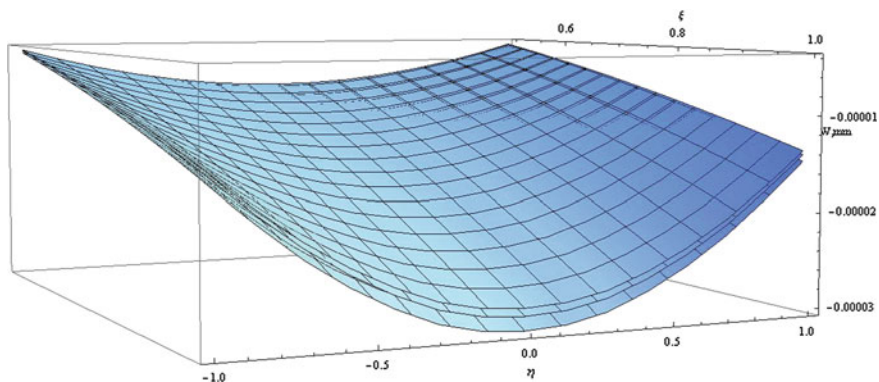
Fig. 19.11 Dependence of displacementson Poisson's ratio on area S

Figures 19.9 and 19.10 show plots of the displacement function for the whole area of approximation S and only one line $\xi = 1$, respectively. By observing from above to down, the first surface in Fig. 19.9 (respectively, the first line in Fig. 19.10) corresponds to cermet, the second one—to steel and the third one—to duraluminium. So, the largest (in absolute value) displacements correspond to duraluminium, the lowest ones relate to cermet. The graphs show a high effect of the elastic material properties.

Table 19.2 Values of the displacements for different Poisson's ratios

	$\eta = 0.0$	$\eta = 0.2$	$\eta = 0.4$	$\eta = 0.6$	$\eta = 0.8$	$\eta = 1.0$
$\mu = 0.21$	$-3.02 \cdot 10^{-5}$	$-2.95 \cdot 10^{-5}$	$-2.75 \cdot 10^{-5}$	$-2.43 \cdot 10^{-5}$	$-1.99 \cdot 10^{-5}$	$-1.47 \cdot 10^{-5}$
$\mu = 0.30$	$-2.88 \cdot 10^{-5}$	$-2.81 \cdot 10^{-5}$	$-2.62 \cdot 10^{-5}$	$-2.31 \cdot 10^{-5}$	$-1.90 \cdot 10^{-5}$	$-1.40 \cdot 10^{-5}$
$\mu = 0.34$	$-2.80 \cdot 10^{-5}$	$-2.73 \cdot 10^{-5}$	$-2.55 \cdot 10^{-5}$	$-2.25 \cdot 10^{-5}$	$-1.84 \cdot 10^{-5}$	$-1.36 \cdot 10^{-5}$

Conditionally considering Young's modulus to be constant and equal to, for example, $E = 2.0 \times 10^5$ MPa, we state dependence of the displacementson Poisson's ratio. The plot of the dependence on the area S is shown in Fig. 19.11.

For the line $\xi = 1$, we calculate the values of the displacement function along the segment $\eta \in [0; 1]$ with step of 0.2 (taking into account the symmetry of the values relatively zero, generated by the parabolic law). For three different values of Poisson's ratio, we obtain the values of the deflections, listed in Table 19.2.

Table 19.2 shows that the values of the displacements for different Poisson's ratios in the range of 0.21–0.34 (and for the same values of Young's modulus) differ by no more than 9 %.

Now, conditionally considering Poisson's ratio to be constant for the three materials and equal to $\mu = 0.3$, we compose similar Table 19.3 for changing the values of Young's modulus.

Conclusions about the existence of the relationship between the elastic properties of the plate material and displacements that arise in it under action of the distributed external load could be transferred by using MLA to an elastic ledge with similar conditions of loading. This circumstance is especially important. It witnesses, for example on arising of the possibility to take into account technological features of real solid (including separate influence of each force factor), which are not identifiable in the solutions of plane problems.

19.3.4 Influence of Teeth Running-in

In accordance with the Russian GOST 21354-87, influence of rigidity of the steel teeth surfaces, which depend on the yield strength of steel, on gears natural running-in can be described by the following formulae:

$$K_{H\beta} = 1 + \left(K_{H\beta}^\circ - 1\right) K_{HW}, \tag{19.7}$$

where

$$K_{HW} = 2 \cdot 10^{-3} H_{HB} + a_{HV}; \tag{19.8}$$

$$K_{F\beta} = 1 + \left(K_{F\beta}^\circ - 1\right) K_{FW}, \tag{19.9}$$

where

$$K_{FW} = 2 \cdot 10^{-3} H_{HB} + a_{FV}; \quad a_{FV} = a_{FV}(v_0). \tag{19.10}$$

Table 19.3 Values of the displacements for different Young's moduli: $E_1 = 0.74 \cdot 10^5$MPa, $E_2 = 2.0 \cdot 10^5$ MPa, $E_3 = 6.225 \cdot 10^5$ MPa

	$\eta = 0.0$	$\eta = 0.2$	$\eta = 0.4$	$\eta = 0.6$	$\eta = 0.8$	$\eta = 1.0$
E_1	$-7.78 \cdot 10^{-5}$	$-7.60 \cdot 10^{-5}$	$-7.08 \cdot 10^{-5}$	$-6.24 \cdot 10^{-5}$	$-5.12 \cdot 10^{-5}$	$-3.78 \cdot 10^{-5}$
E_2	$-2.88 \cdot 10^{-5}$	$-2.81 \cdot 10^{-5}$	$-2.62 \cdot 10^{-5}$	$-2.31 \cdot 10^{-5}$	$-1.9 \cdot 10^{-5}$	$-1.4 \cdot 10^{-5}$
E_3	$-9.24 \cdot 10^{-6}$	$-9.04 \cdot 10^{-6}$	$-8.42 \cdot 10^{-6}$	$-7.42 \cdot 10^{-6}$	$-6.09 \cdot 10^{-6}$	$-4.50 \cdot 10^{-6}$

Here $K_{H\beta}$, $K_{F\beta}$ are the coefficients, taking into account teeth natural running-in in calculations on contact and bending strength, respectively; $K^{\circ}_{H\beta}$, $K^{\circ}_{F\beta}$ are the coefficients, taking into account non-uniformity of the load distribution on width of gear crown in the initial period of gear work at the same calculations; α_{HV}, α_{FV} are the coefficients, taking into account the influence of circumferential speed v_0 of gears on their natural running-in.

Moreover, the effect of teeth conformability is much more complicate and wider than the traditional concepts. Thus, it is shown that the level of gear conformability with initially linear (or close to that law) contact of teeth determines the influence degree of geometrical factors on the possibility to increase the bearing capacity and to select the direction of improving gears. An account of these features has led to creation of gears with fundamentally improved characteristics [13]. Especial influence of level of the gear wheels natural running-in on development of gearings witnesses on that, the change of the yield strength of teeth increases the variation of gears efficiency indexes and reduces the gear reliability.

19.4 Conclusion

Thus, this paper contains study of elastic cantilever plate into framework of MLA and some useful consequences of its application to the calculation of solids with complex shape. In particular, the analysis of influence of the elastic material properties (for example, chromium-nickel steel, cermet and duraluminium) on changes of displacements in the cantilever plate under the action of uniformly distributed transverse load is given. As shown, the level of this influence is essential enough.

Since the nature of the obtained displacement changes defines the mutual relations between separate force factors, it may be concluded on existence of dependence between position of dangerous cross-section in geometrical concentrator of elastic solid with loaded ledge, level of maximum stress and elastic properties of material of the ledge.

Further improvement of MLA and ways of its application can be conducted in the following directions.

Firstly, the study of solids of various shapes and different cases of loading will lead to discovery of new useful reserves, existing in specific details of machines,

mechanisms and constructions. Based on these reserves, the details can be significantly improved and become more reliable, easy and simple to manufacture, thus providing savings the resources and man-hours, durability and safety of the machineries and mechanisms.

Secondly, the use of more complex and precise geometrical models and solutions will clarify MLA.

Thirdly, the consideration of complex tasks, including, for example, estimation of effects of the various material properties, thermal processes, different cases of dynamic loading will enrich MLA with new useful relationships and dependencies, which later will be applied in engineering, similar to contact curvature effects [13, 14] and curvature effects of the geometrical concentrators [1, 2, 7].

References

1. G.A. Zhuravlev, in *Proceedings of ISMM '97 International Symposium on Machines and Mechanisms*. Belgrade, 2–5 September, 1997
2. G.A. Zhuravlev, in *Proceedings of the International Symposium "Theory of Real Gears"*. Kurgan, 30 September–2 October 1997, p. 53–57
3. G.A. Zhuravlev, P.S. Prokopiev. in *Proceedings of the International Conference on Motion and Power Transmissions*, The Japan Society of Mechanical Engineers, Tokyo. 23–26 November 1991, p. 866–870
4. G. Neueber, *Stress Concentration* (State Publishers of Technical and Theoretical Literature, Moscow, 1947)
5. T.J. Jaramillo, J. Appl. Mech. **17**(1), 67 (1950)
6. G.A. Zhuravlev, R.B. Iofis, *Hypoid Gears. Problems and Development*, Rostov State University Press, Rostov-on-Don (1978) (in Russian)
7. G.A. Zhuravlev, vol. 37 (CIAM, Moscow, 1979) (in Russian)
8. G.A. Zhuravlev, in *Proceedings of Ninth World Congress on the Theory of Machines and Mechanisms*, Milano, 30 August–2 September 1995, p. 433–437
9. G.A. Zhuravlev, V.M. Onishkova,*VINITI*, Moscow, No 6266-B87, 17.07.1987 (in Russian)
10. G.A. Zhuravlev, V.M. Onishkova, *VINITI*, Moscow. No 46-B, 02.01.1986 (in Russian)
11. E.I. Fradkin, G.A. Zhuravlev, O.V. Tvarilidze, *Russian Engineering Research*, **30**(3), p. 269 (2010) (in Russian)
12. A.A. Botaki, E.V. Pozdeeva, *Bulletin of the Tomsk Polytechnic University*, **311**(2), p. 98 (2007) (in Russian)
13. G. Zhuravlev, *Gear Drive*, Patent Application PCT/RU2005/000367. July 05, 2005; USA Patent No US 8,061,229 B2, November 22, 2011; Europatent No 1908992, 05.05.2010, Japan Patent No 4838307, October 7, 2011, China Patent No ZL 200580050187.5, June 8, 2011
14. G.A. Zhuravlev, J. Frict Wear **20**(2), 57 (1999)

Part IV
Applications of Advanced Materials

Chapter 20
Optimal Design of Underwater Acoustic Projector with Active Elements Made from Porous Piezoceramics

Andrey Nasedkin, Maria Shevtsova and Shun-Hsyung Chang

Porous piezoceramic materials have received considerable attention due to their successful application in ultrasonic transducers, hydrophones and other piezoelectric devices. In order to formulate and solve the optimization problem for multilayered piezoelectric transducer with active porous piezoelectric layer, the calculation of the effective moduli for porous piezoelectric material has been previously performed. The obtained dependences of material properties on porosity allowed us to decrease the number of design variables. The multi-objective optimization problem based on the Pareto-frontier calculation has been solved using the live-link of finite-element (FE) package Comsol Multiphysics with MATLAB.

20.1 Introduction

Nowadays a lot of investigations are referred to the development of effective structures for acoustic transducers based on the porous piezoelectric materials due to their high piezoelectric sensitivity, extended frequency bandwidth and better matching to the acoustic medium. The aim of present work is the developing of methods to synthesize the optimal structures of the transducers for underwater

---

A. Nasedkin · M. Shevtsova (✉)
Southern Federal University, Rostov-on-Don, Russia
e-mail: mariamarcs@bk.ru

A. Nasedkin
e-mail: andrey.nasedkin@gmail.com

M. Shevtsova
Southern Scientific Center of Russian Academy of Sciences, Rostov-on-Don, Russia

S.-H. Chang
National Kaohsiung Marine University, Kaohsiung, Republic of China (Taiwan)
e-mail: stephenshchang@me.com

applications. On the base of developed numerical method for the porous materials effective moduli determination, the optimization problem statement and solution for a whole device structure have been implemented.

Hydrophones, projectors and combined devices—transceivers are the general types of modern devices used for sonar and underwater transmission. A projector is a transducer used for generating sound and transmitting it to the acoustic medium. In order to effectively fulfill its purpose, underwater acoustic transducers have to meet many requirements, including: low impedance for better acoustic matching with water, durability, high sensitivity, ability to take high mechanical load and hydrostatic pressure.

The most widely used devices in underwater acoustics are the devices based on the piezoelectric effect. The expansion of their effective applications is caused by both the success of the piezoelectric materials science and the development of the micro-electromechanical systems (MEMS). These technologies create devices based on nanoscale multilayer active hydrophones and projectors, arrays of transducers for receipt and radiation of directed sound [1, 2]. One of the problems at realization of such structures is the impedance matching. The use of intermediate layers allows one to overcome this difficulty. However in case of active element made of dense piezoelectric ceramics a number of layers are needed, and this involves big energy losses of the whole structure. The effective method for getting over this difficulty is the use of porous piezoelectric ceramics. This entails both decreased number of intermediate layers and better acoustic agreement between the transducer and medium. Various experimental [3–8] and theoretical [9–13] investigations show, that porous piezoelectric ceramics may significantly improve the desired properties of transducers and expand the use of piezoelectric materials. Porous piezocomposite materials are characterized by lower values of the transverse piezoelectric modulus d_{31} at almost the same values of the thickness piezoelectric modulus d_{33} [14–16] responsible for the efficient conversion of electrical and mechanical energy. Therefore, the use of porous materials in piezoelectric ultrasonic transducers, hydrophone structures and other piezoelectric devices is very promising today.

In previous works [14–16], it was investigated how the properties of piezoelectric material depend on porosity for the ceramics of different connectivity and ferroelectric hardness. Such dependencies have been obtained for a whole set of material constants.

The aim of presented research is a structural optimization of multilayered transducer with the porous piezoelectric active element, all material parameters of which are expressed through the value of porosity. The previously obtained dependencies of effective moduli allow us to sufficiently decrease the number of design variables. For the underwater acoustic projector, structure of which contains such layers as an acoustic window, matching, piezoelectric, backing plate and protective foam layers (see Fig. 20.1), we formulate the coupled problem of acoustics and electric elasticity in axial-symmetric formulation. As the optimization objects, we introduce averaged sound pressure level (SPL), transmitting current response (TCR) and the mean-square value of the SPL irregularity in frequency range from 100 to 400 kHz. The design variables are: Young's moduli

Fig. 20.1 Scheme of multilayered transducer placed in acoustic medium: *1*—acoustic window layer, *2*—matching layer, *3*—active porous piezoelectric layer, *4*—backing plate, *5*—protective foam layer
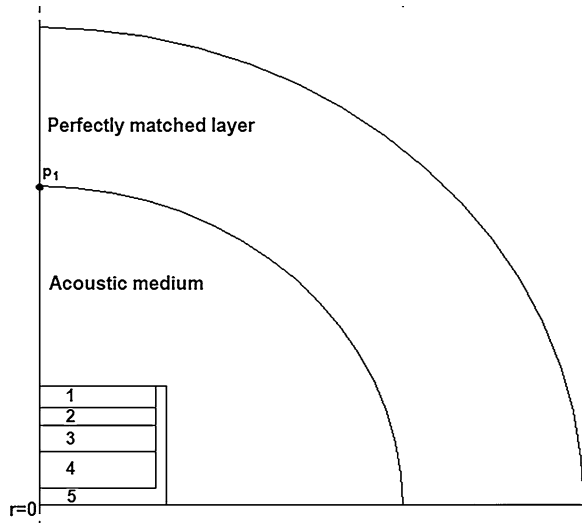
of an acoustic window layer, protective foam layer, and matching layer; mass damping parameter and stiffness damping parameter of layers; porosity of an active layer. In this investigation we use the approach based on the Pareto-frontier calculation, i.e. building the set of points in the 6D space of design variables where all the objects are feasible.

The coupled problem is numerically implemented by the live-link of the FE package Comsol Multiphysics with MATLAB. The best results have been obtained at about 30–40 % of porosity for piezoelectric layer and mechanical and damping parameters of intermediate layers that may characterize a wide range of polymeric materials. Electro-acoustic efficiency, defined by the TCR parameter, is significantly higher for porous material than for the dense ceramics. Obtained data and proposed methods might be effectively used for the structural optimization of enough wide range of transducers.

20.2 Determination of Effective Moduli Dependencies on Porosity

For determination of the effective properties, we used an approach presented in details in [12, 14–16] and based on the effective moduli methods [4, 14, 16, 17], modeling of representative volumes for porous piezoelectric materials and the use of the FE technologies. There are several methods to obtain the structure of a two-phase cubic piezoelectric composite material. At low percent of porosity a simple but an adequate microstructure of porous material is a model of the piezoceramic cubic lattice consisting of unit cells (cubes), some of which are randomly called by

pores [4]. However, this model may lose connectivity of a skeleton at a large number of pores. In order to overcome this problem, the algorithms based on the percolation theory can be used. In case of low porosity the clusters can be built from pores, while at high porosity—from piezoelectric material. One of such methods is Witten-Sander method [18], it has been implemented by V. Remizov and analyzed in [15]. In present work both methods: random method and Witten-Sander method were used.

The experimental data [4, 11, 19–21] were compared with the obtained results for a porous material with medium ferroelectric hardness PZT-4. For all the figures, presented below, the curves, related to the random method, marked by circles, and the Witten-Sander method—by triangles. The dependencies, obtained without taking into account the heterogeneity of the polarization field, correspond to dotted lines, dash-dotted lines correspond to calculations performed at taking into account the non-uniform polarization, and the dashed lines indicate the experimental data.

Figure 20.2 shows the relative dielectric permittivity $r(\varepsilon_{33}^S) = \varepsilon_{33}^S(p)/\varepsilon_{33}^S(0)$ on porosity p in comparison with the experimental data [19, 20]. One can conclude that the dependencies are linear for both random and Witten-Sander methods. The results obtained with the hypothesis of polarization field heterogeneity differ from those obtained without this hypothesis lesser than 1–2 %. It also can be seen that all four dependencies are very close, and numerical results are in better agreement with the data of [19]. The values of dielectric permittivity obtained in [20] strongly decrease with increasing porosity and give about 35 % discrepancy with the calculated data and the results of [19].

After the calculation of full set of the effective moduli $c_{\alpha\beta}^E(p)$, $e_{i\alpha}(p)$, $\varepsilon_{ii}^S(p)$, we obtained such important characteristics of piezoelectric ceramics as piezoelectric coefficients d_{31} and d_{33} ($d_{i\alpha} = d_{i\alpha}(p) = e_{i\beta}(p)s_{\alpha\beta}^E(p)$), where $s_{\alpha\beta}^E$ are the components of the compliance matrix. The comparison of the obtained dependencies with the experimental data [4, 11, 21] are performed for both longitudinal (Fig. 20.3a) and transverse (Fig. 20.3b) piezoelectric moduli.

As can be seen the dependence for coefficient d_{31}, related to the Witten-Sander method, significantly decreases with increasing porosity compared to the random method. It is obvious that the relationship obtained by assuming the polarization field heterogeneity is in a better agreement with the experimental data (Fig. 20.3a). At the same time, the dependencies for the piezoelectric modulus d_{33} are essentially independent of porosity for both methods (Fig. 20.3b). It should be noted that the maximum error is still quite significant and is approximately 10–15 % for the data of [21], and about 3–5 % for the data of [4, 11].

At the second stage of the present investigation, during the simulation of a multilayer transducer structure, the obtained dependencies by assuming the polarization field heterogeneity and related to the Witten-Sander method have been accepted as material properties for the active element.

Fig. 20.2 The dependencies of relative dielectric permittivity on porosity
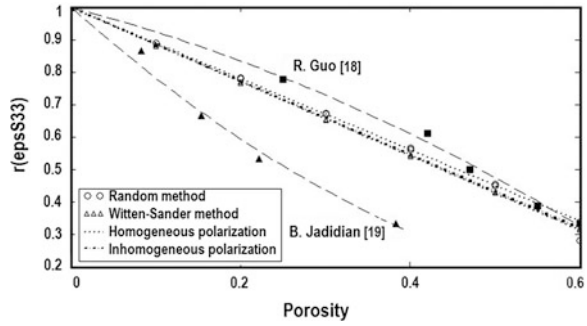
Fig. 20.3 The dependencies of relative piezoelectric coefficients on porosity
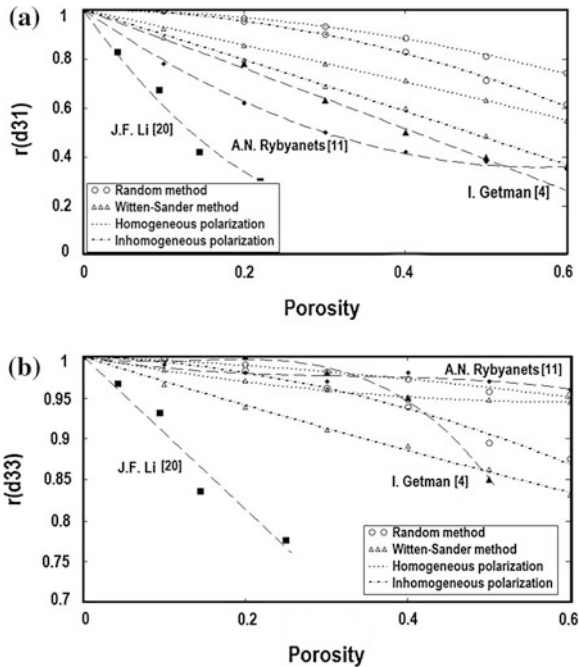
20.3 Formulation of Coupled Acoustics and Electroelasticity Problem for Multilayered Piezoelectric Transducer

In present investigation we consider a model of an ultrasound piezoelectric transducer for underwater applications in its axial-symmetric formulation. Cylindrical surface and the bottom of the transducer are covered with a protective layer made of foam. The transducer consists of four layers, such as: backing plate, piezoelectric active layer, matching layer and acoustic window. The whole

construction is surrounded with an acoustic medium. On the boundary of the acoustic medium the perfectly matched layer (PML) is placed so that the waves, incident upon the PML from a non-PML medium, do not reflect at the interface (Fig. 20.1). The thicknesses of the piezoelectric layer, protective and backing plate layers have been chosen to be approximately a half length of the longitudinal wave at thickness vibration mode, an acoustic window thickness was approximately ¾, and matching layer thickness was ¼ of the longitudinal waves at the same frequency of about 300 kHz. We formulate the coupled problem of acoustics and electric elasticity using the FE package COMSOL Multiphysics and its two application modes: Pressure Acoustics mode (time-harmonic analysis) and Piezo Axial Symmetry mode (frequency response analysis). Sound waves are governed by the inhomogeneous Helmholtz equation for the acoustic pressure, p:

$$\nabla \cdot \left(-\frac{1}{\rho_0} \nabla p \right) - \frac{\omega^2 p}{\rho_0 c_s^2} = 0, \tag{20.1}$$

where $\rho_0 = 1000$ kg/m^3 is the fluid density, $c_s = 1500$ m/s is the speed of sound, $\omega = 2\pi f$ (rad/s) is the angular frequency with f(Hz) denoting the frequency. The boundary conditions are following: sound hard wall (the boundary between an acoustic medium and the PML) and axial symmetry (on the left boundary), (see Fig. 20.1).

The constitutive relations for the piezoelectric active layer are taken in the stress-charge form as follows:

$$\begin{aligned} \boldsymbol{\sigma} &= \mathbf{c}^E \cdot \cdot\, \boldsymbol{\varepsilon} - \mathbf{e}^* \cdot \mathbf{E}; \\ \mathbf{D} &= \mathbf{e} \cdot \cdot\, \boldsymbol{\varepsilon} + \boldsymbol{\varepsilon}^S \cdot \mathbf{E}, \end{aligned} \tag{20.2}$$

where $\boldsymbol{\varepsilon}$ is the strain tensor, $\boldsymbol{\sigma}$ is the stress tensor, $\mathbf{E}$ is the electric field vector, $\mathbf{D}$ is the electric displacement vector, $\mathbf{c}^E$ is the tensor of elastic stiffness moduli at constant electric field, $\mathbf{e}$ is the tensor of piezoelectric moduli (stress coefficients), $\boldsymbol{\varepsilon}^S$ is the tensor of dielectric permittivity moduli at constant mechanical stress.

Coupling between the two equations is provided by the boundary conditions: the top and the sides of the transducer undergo both an acoustic pressure and the inward accelerations.

The bottom of the transducer is fixed; on the left boundary we consider an axial symmetry condition; on the top of piezoelectric layer the constant electric potential with amplitude 100 V in a whole studied frequency band is applied, when the bottom is grounded.

Since the dimensions of the investigated transducer are quite small, this type of projector cannot be used to generate directional sound and therefore we will consider the sound pressure level only in a direct beam. When the transducer is placed into acoustic medium the thickness vibration mode is excited at frequencies from approximately 100–400 kHz. This frequency range was used during the following optimization of the transducer parameters.

20.4 Optimization Problem for Multilayered Piezoelectric Transducer

There is a wide set of materials that can be used as the constituent layers of a transducer. This proves a possibility to vary their mechanical properties within the wide scope. It should be noted that we chose tungsten as a backing plate material to generate the thickness vibration mode of PZT layer because of its large mechanical stiffness and high acoustic impedance.

In order to formulate the optimization problem let us introduce six design variables: porosity of an active layer (por); Young's moduli of acoustic window layer (E_{aw}), matching layer (E_m), and protective foam layer (E_f); mass damping parameter (R_1) and stiffness damping parameter (R_2) of layers.

In our investigation we considered three objectives: sound pressure level (SPL) in direct beam measured at the 1 m-distance from the sound source and transmitting current response (TCR) are maximized, the deviation of SPL is minimized. SPL is represented in decibels as follows

$$p = 20 \lg\big(|p_1|/p_{ref}\big), \tag{20.3}$$

where p_1 is the sound pressure at the measurement point, and $p_{ref} = 2 \times 10^{-5}$ Pa is the threshold of sound pressure.

TCR is the ratio of sound pressure p_1, to the electric current I through the active element:

$$S_I = |p_1|/I. \tag{20.4}$$

There is a wide set of approaches to structural optimization. In the framework of multi-criteria optimization problem (MOO) when several objective functions exist, there is no unique solution, but exists a number of optimum solutions. In this situation the most suitable way to optimization is calculation of so-called Pareto optimum or Pareto-frontier. During the solution of the considered transducer optimization problem, the three integrals were assumed for optimization:

$$\langle p \rangle = \int_{f_1}^{f_2} p(f)df \bigg/ (f_2 - f_1), \tag{20.5}$$

$$\langle \Delta p \rangle = \sqrt{\frac{\int_{f_1}^{f_2} |\langle p \rangle - p(f)|^2 df}{f_2 - f_1}}, \tag{20.6}$$

$$\langle TCR \rangle = \int_{f_1}^{f_2} \frac{p(f)}{I(f)} df \bigg/ (f_2 - f_1), \tag{20.7}$$

where $\langle p \rangle$, $\langle \Delta p \rangle$ and $\langle TCR \rangle$ represent an averaged SPL, deviation of SPL and TCR, respectively; f_1 and f_2 are the boundaries of the frequency range.

Obviously the construction of Pareto-frontier was complicated for the three-dimensional space of objective functions. In order to overcome this difficulty the illustration of Pareto-frontier has been represented using the level lines.

At the numerical problem solution, MATLAB varies design parameters for the transducer, calls the FE model simulated by Comsol Multiphysics, and carries out the multiple computations of the objectives. Then obtained data are being analyzed and illustrated using the set of complimentary procedures, written in MATLAB (see Fig. 20.4a, b).

20.5 Results and Discussion

At the analysis of the simulation results, it was founded that the influence of both damping design variables on the objectives is negligible. So only two obtained projections of the criteria points set on the spaces of other design variables are presented in Fig. 20.4. Figure 20.4a corresponds to the projection on subspace of two design variables: porosity of active layer and Young's modulus of matching layer. Figure 20.4b presents the projection for Young's modulus of side protective layer and Young's modulus of acoustic window. For the studied objectives we used the following bounds for the feasible values: ≥ 150 dB for the SPL, ≥ 1500 dB/A for the TCR, and ≤ 2.5 dB for the deviation of SPL. On the presented figures the areas between solid and dashed lines are the projections of Pareto frontier on the 2D subspaces of the design variables. Green areas represent the intersections of optimum areas. It can be seen from Fig. 20.4a that the energetic efficiency, characterized by TCR, reaches desirable values when the porosity of active layer is greater than 0.3. However the maximum values of SPL are reached at a considerable variation of porosity. One can observe that the optimum SPL value shifts with the growth of Young's modulus of matching layer from about 1.6 to 2.2 GPa at higher porosity. On the other hand the smaller Young's modulus corresponds to lower porosity. The most uniform frequency response of SPL are reached when the percent of porosity is greater than 0.25. It is obvious (Fig. 20.4b) that the Young's modulus of acoustic window significantly influences on the uniformity of the SPL frequency response. The optimum quantities correspond to the values greater than or equal to 2 GPa. At the same time the Young's moduli of protective and acoustic window layers does not influence on TCR in optimum areas.

For clarity, we present below three groups of frequency responses obtained for the three sets of values of the design variables that are contained in Table 20.1. For the first set all the design variables were taken from the obtained optimum areas. The second set contains parameters being outside the Pareto frontier. The last set corresponds to a transducer with an active layer made of dense piezoelectric

Fig. 20.4 Projections of the criteria set presented as the contour lines of objective levels on the subspaces of design variables
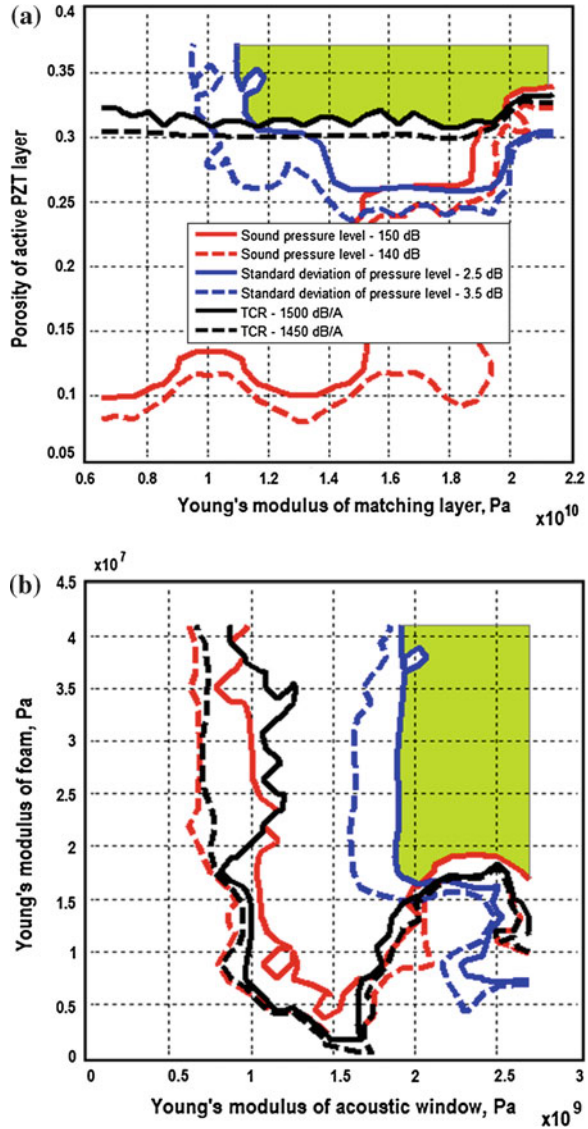
Table 20.1 Design variables for the three examples of simulated projectors

Studied design	E_{aw} (GPa)	E_f (MPa)	E_m (GPa)	R_1	R_2	por
(1) Inside the optimum	2.5	30	16	1.5×10^{-7}	0.6×10^{-7}	0.4
(2) Outside the optimum	0.5	5	20	2.3×10^{-7}	1.2×10^{-7}	0.2
(3) Dense PZT ceramics	0.5	30	16	1.5×10^{-7}	0.6×10^{-7}	0

Fig. 20.5 The frequency
responses of SPL
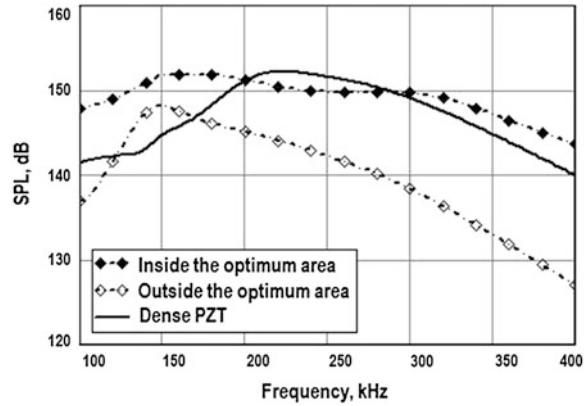
Fig. 20.6 The frequency
responses of TCR
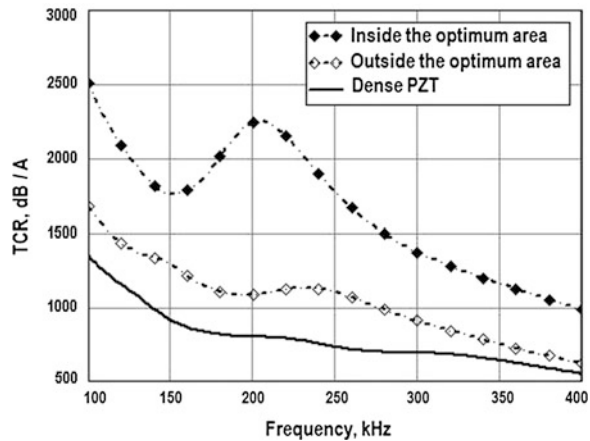
ceramics. The first parameter (Young's modulus of acoustic window) was taken
outside the optimum area the other 4 variables belong to the Pareto frontier.

For each set of design variables the frequency responses for SPL and TCR are
calculated and plotted in Figs. 20.5 and 20.6.

The graphs shown in Fig. 20.5 clearly show that the optimal set of design
parameters provides a much less unevenness of sound pressure level in comparison
to the cases of active element with dense ceramics (20.3) and 20 % porosity. The
maximum deviation of the sound pressure level in the investigated frequency range
for the designs (20.1), (20.2), and (20.3) are 8.5, 21, and 12 dB, respectively. The
sound pressure level inside the whole frequency range is the best. It exceeds the
SPL of projector on the base of dense ceramics on 5 %, and SPL for design (20.2)
on 10 %. The peak observed in the TCR graph (see Fig. 20.6) shows that trans-
ducer (20.1) demonstrates the utmost resonance properties when the design vari-
ables are taken from the optimal area. If the electronic exciting device has

sufficient performance that allows us to maintain constant amplitude of the applied potential in the whole frequency range, the resonance features of TCR do not make worse the uniformity of the frequency response for the sound pressure.

20.6 Conclusions

In order to optimize the hydroacoustic performance of multilayered projector on the base of active layer made from piezoelectric ceramics with varied porosity, ten dependencies of material constants on porosity were successfully obtained for the porous piezocomposite materials of different connectivity. These effective moduli were calculated using finite element method at the assumption of homogeneous and heterogeneous polarization field, and due to best agreement with the experimental data the last dependencies were used at the statement and solution of the optimization problem. Obtained dependencies allowed us to reduce the number of design variables to six (Young's moduli of an acoustic window layer, protective and matching layers; mass and stiffness damping parameters of layers; porosity of an active layer). On the base of the Pareto optimality, the set of feasible designs in six-dimensional design space was reconstructed using three objectives: averaged sound pressure level, transmitting current response and the standard deviation of the SPL in a frequency range from 100 to 400 kHz. A comparative analysis of three examples of the simulated designs has demonstrated the best performance of projector with porosity of active piezoelectric element near 40 % and elastic moduli of intermediate layers tuned to achieve the matching acoustic impedances of the whole structure and acoustic medium.

References

1. R. Sathishkumar, A. Vimalajuliet, J.S. Prasath et al., Indian J. Sci. Technol. **4**(1), 8 (2011)
2. M.I.H. Yaacob, in *Proceedings of the 7th International Symposium on Mechatronics and its Applications (ISMA10)*, Sharjah, UAE, 2010
3. K. Boumchedda, M. Hamadi, G. Fantozzi, J. Eur. Ceram. Soc. **27**, 4169 (2007)
4. I. Getman, S. Lopatin, Ferroelectrics **186**, 301 (1996)
5. S. Marselli, V. Pavia, C. Galassi, E. Roncari, F. Craciun, G. Guidarelli, J. Acoust. Soc. Am. **106**(2), 733 (1999)
6. R. Ramesh, H. Kara, C.R. Bowen, Ultrasonics **43**, 173 (2005)
7. H. Banno, Ferroelectrics **50**, 3 (1983)
8. W. Wersing, K. Lubitz, J. Moliaupt, Ferroelectrics **68**(1/4), 77 (1986)
9. K. Mizumura, Y. Kurihara, H. Ohashi, Jpn. J. Appl. Phys. **32**(1), 2282 (1993)

10. H. Kara, R. Ramesh, R. Stevens, C.R. Bowen, IEEE Trans. Ultrason. Ferroelectr. Freq. Control **50**(3), 289 (2003)
11. A.N. Rybyanets, IEEE Trans. Ultrason. Ferroelectr. Freq. Control **58**(7), 1492 (2011)
12. E. Roncari, C. Galassi, F. Craciun, G. Guidarelli, S. Marselli, V. Pavia, in *Proceedings of the 11th IEEE International Symposium on Applications of Ferroelectrics* (1998)
13. V.Y. Topolov, C.R. Bowen, *Electromechanical Properties in Composites Based on Ferroelectrics* (Springer, London, 2009)
14. A.V. Nasedkin, M.S. Shevtsova, in *Ferroelectrics and Superconductors: Properties and Applications*, ed by I.A. Parinov (Nova Science Publishers, New York, 2011), p. 231
15. T.V. Domashenkina, A.V. Nasedkin, V.V. Remizov, M.S. Shevtsova, in *Proceedings 7th GRACM International Congress* on *Computational Mechanics*, Athens, Greece, 2011
16. A.V. Nasedkin, M.S. Shevtsova, in *Physics and Mechanics of New Materials and their Applications*, ed by I.A. Parinov, S-H. Chang (Nova Science Publishers, New York, 2013), p. 185
17. L.P. Khoroshun, B.P. Maslov, P.V. Leshchenko, *Prediction of Effective Properties of Piezoactive Composite Materials* (Naukova Dumka, Kiev, 1989) (In Russian)
18. T.A. Witten, L.M. Sander, Phys. Rev. Lett. **47**(19), 1400 (1981)
19. R. Guo, C.-A. Wang, J. Appl. Phys. **108**, 124112 (2010)
20. B. Jadidian, N.M. Hagh, A.A. Winder, A. Safari, IEEE Trans. Ultrason. Ferroelectr. Freq. Control **56**(2), 368 (2009)
21. J.F. Li, K. Takagi, M. Ono et al., J. Am. Ceram. Soc. **86**, 1094 (2003)

Chapter 21
Distributed Underwater Sensing: A Paradigm Change for the Future

T. C. Yang

Distributed netted underwater sensors (DNUS) present a paradigm change that has generated high interest all over the world. It utilizes many small spatially distributed, inexpensive sensors, and a certain number of mobile nodes, such as autonomous underwater vehicles (AUVs), forming a wireless acoustic network to relate data and provide real time monitoring of the ocean. Distributed underwater sensors can be used for oceanographic data collection, pollution monitoring, offshore exploration, disaster prevention, assisted navigation and tactical surveillance applications over wide areas. These functions were traditionally accomplished by a cabled system, such as an array of sensors deployed from a platform, or a large number of sensors moored on the ocean bottom, connected by a cable. The cabled systems are not only expensive but often require heavy ocean engineering (e.g., equipment to deploy heavy armored cables). In the future, as fabrication technology advances making low cost sensors a reality, DNUS is expected to be affordable and will become the undersea "OceanNet" for the marine industry like the current "internet" on land. This paper gives a layman view of the system concept, the state of the art, and future challenges. One of challenges, of particular interest to this conference, is to develop technologies for miniature-size sensors that are energy efficient, allowing long time deployment in the ocean.

21.1 Introduction

Ocean is of vital national and international interest to human beings since 70 % of the world is covered by ocean. Ocean affects our weather, food supply and energy since a high percentage of the world energy is buried under the ocean, yet our knowledge about the ocean is very limited. Acoustic methods can be used to invert

T. C. Yang (✉)
Institute of Applied Marine Physics and Undersea Technology, National
Sun Yat-sen University, Kaohsiung 80424, Taiwan
e-mail: tsihyang@gmail.com

oceanographic features (eddies, currents, internal waves, etc.) to aid the weather predictions; monitor the intensities of hurricanes; detect/sense underwater seismic events such as earthquakes and tidal waves; as well as detect, track and classify underwater targets. Traditionally, many of these functions were accomplished by platform (ship) based, and/or centrally connected systems (such as tethered remotely operated vehicles, towed line arrays deployed by the oil companies and Navy, and fixed deployed arrays, e.g., the SOSUS system deployed by the US involving hundreds to thousands of sensors), which are not only expensive but also require heavy ocean engineering (e.g., equipment to deploy heavy armored cables), and thus are unaffordable except by selected parties/countries.

Distributed netted sensing (DNS) is an emerging technology that promises unprecedented ability to monitor and manipulate the physical world. It presents a paradigm change that has generated high interest all over the world [1]. It utilizes many small inexpensive sensors spatially distributed, and a certain number of mobile nodes, such as autonomous underwater vehicles (AUV), forming an underwater wireless acoustic network to conduct environmental sensing and target/event detection. For underwater applications, the technology for producing individual sensor packages is relatively simple, mature and robust. As fabrication technology advances making low cost sensors a reality in the future, DNS will become affordable for widely use.

Distributed netted sensing involves three concepts: distributed detection, communication and networking, and data fusion. Distributed detection has the potential to offer higher probability of detection and lower probability of detection error (false alarm) when observation data from multiple distributed sensors are intelligently fused in a decision making algorithm rather than using a single observation data set (as in conventional systems). Thus information flow is fundamental to DNS. While communication and networking is no different in DNS than an *ad hoc* wireless communication network, DNS involves sensing, communication and processing (data fusion) that are integrated into one system. The study (optimization) of DNS has emerged as a new research field [2, 3].

For underwater applications, environmental sensing, target/event detection and communication and networking rely on acoustic methods as radio frequency (RF) and optical signals travel very limited distances. It is well known that the ocean (sound speed profile) has strong influences on sound propagation. Consequently, to improve the performance of acoustic sensing and acoustic communications and networking one must have a good knowledge of the physical channel. Conversely, as every ocean is kind independent of other oceans and different from itself at different times (winter versus summer), it makes acoustic sensing and understanding of the ocean increasingly more necessary in order to learn the physical channel. In other words, acoustic sensing, communication and processing (data fusion) are all parts of the same equation. Underwater acoustic communications and networking is a relatively new field that has gained attention in many countries; it is an indispensable component of future underwater DNS.

This paper is organized as follows. In Sect. 21.2, one paints a picture of future OceanNet for ocean observation. In Sect. 21.3, a brief review of the underwater

acoustic channel is given, and how it impacts underwater acoustic communications and networking is discussed. The underwater channel has extensive multipaths and short coherence time (due to the complex oceanographic processes), posing various challenges to high data rate communications; the usual techniques used in RF communications do not work here. In Sect. 21.4, one reviews some current efforts using distributed sensors for acoustic sensing, showing some of the benefits of DNS over the conventional systems. Section 21.5 presents a short summary.

21.2 Observing the Oceans through Acoustic Sensing

On a large scale, the ocean influences the weather. For example, abnormal ocean surface temperature is responsible for El Nino and La Nino which have tremendous effect on weather patterns. Ocean is not a homogeneous medium; it contains transatlantic currents, eddies, internal waves in decreasing spatial scales. Our knowledge and ability to monitor the ocean is rather limited, since the measurement data cover a small percentage of the ocean despite thousands of sensors deployed over the years to study the ocean. To study the ocean on a small (regional) scale, many ocean observation systems are under development, such as that deployed by the Monterey bay aquarium research institute, the Norwegian COSMOS project, the Canadian Neptune system and the observatory supported by the US National Science Foundation, shown in Fig. 21.1. These systems are intended to provide long term monitoring using small profiling floats spread over the sea floor (Fig. 21.1) connected by cables to provide critical information for research on biogeochemical cycles, ecosystem assessment, marine resources, and environmental hazards. The (additional) autonomous mobile platforms provide (on-demand) adaptive observing systems to increase access while reducing costs. The observatory will contribute to operational forecasting of natural environmental disasters, climate change and its effects. While such observatories are of great importance to ocean research, they are very expensive and take many years to develop and construct. They are restricted to fixed location and provide information mostly along where the cables are laid.

When small, inexpensive, low power acoustic nodes (Fig. 21.2) are available in the future, one can set up a distributed networked underwater sensing (DNUS) system as shown in Figs. 21.2 (top view) and 21.3 (three-dimensional view). Because of the low cost of the acoustic nodes, many of them will be deployed over a wide area and used/shared by different groups for different purposes. In one set up, the sensors could be the traditional biological and chemical sensors. The data collected by these sensors will be relayed by the wireless acoustic nodes and networked back to office through the OceanNet. The sensors can be deployed by a ship within 1–2 days (compared with years to tens of years for a cabled system) and picked up at the end of their life time, saving the cost and time of laying a cable. In another setup, the sensing nodes can be the acoustic sensors. The acoustic data collected by these sensors can be used to invert for inhomogeneous ocean

Detect and quantify change in Ocean, Earth, and Atmospheric processes
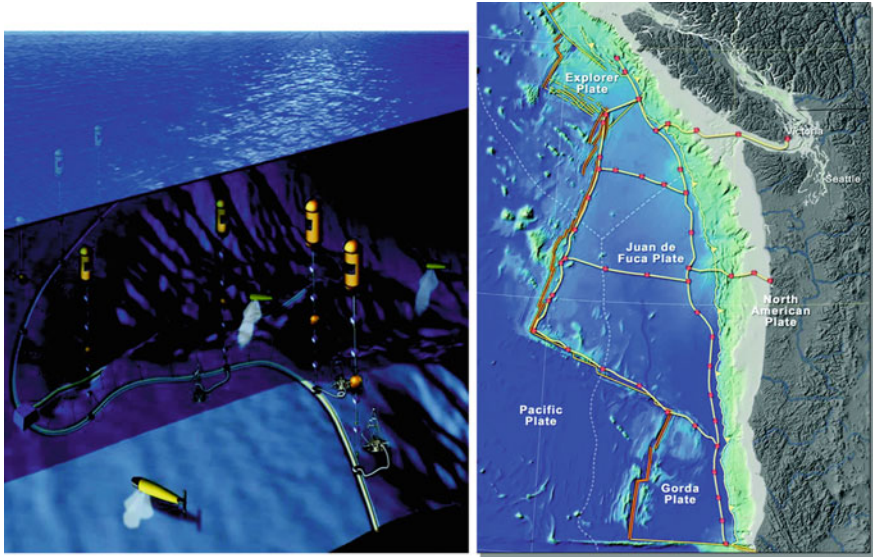
Fig. 21.1 A ocean observatory. Individual sensors and AUVs (L). Planned cable layout (R)

A Self-Organizing Adaptive Underwater Network
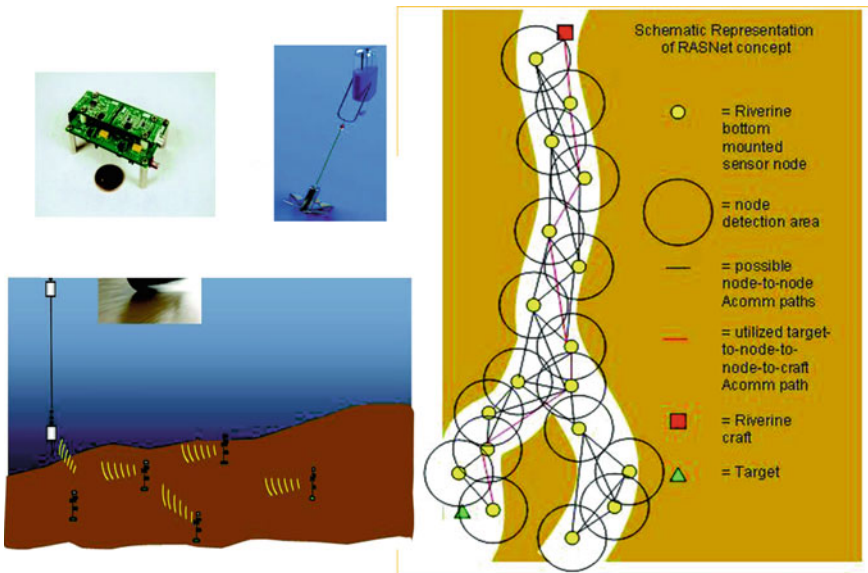
Fig. 21.2 From *top-left* in clock wise order: sensor node electronics, a deployed sensor node, *top view* of a sensor network, and a three dimensional view of a deployed networked underwater sensing system
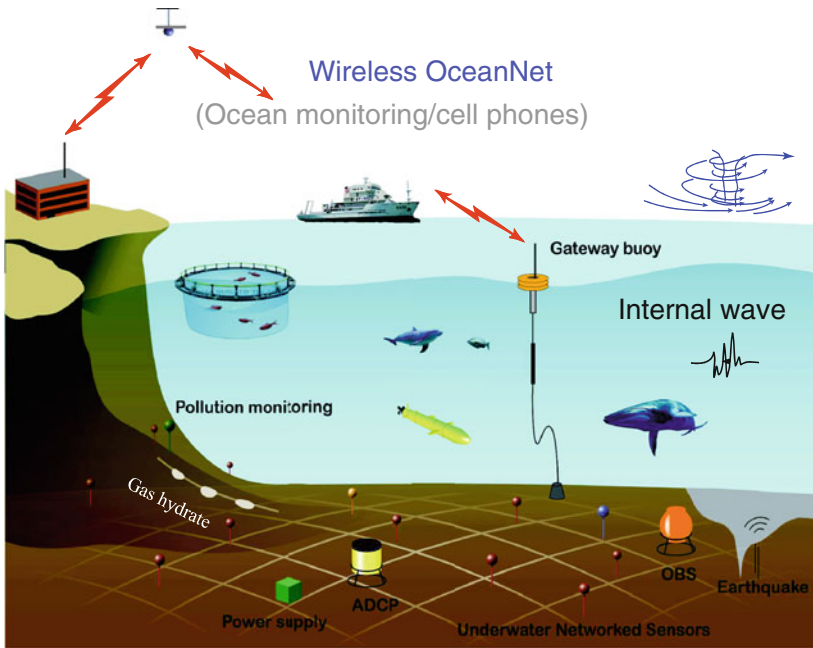
Fig. 21.3 Ocean monitoring with inexpensive nodes forming an OceanNet

structure induced by eddies, internal waves, or ocean currents as in ocean acoustic tomography or ocean current tomography. They can also be used to detect and track an underwater target. Depending on the size of the acoustic sensors, they can be air dropped or deployed by (fishing) boats. Acoustic sensors are usually expendable and are intended to last, say, 6 months. One area of research interest in Taiwan is to acoustically monitor the structure and temporal variation of the Hiroshio current over an extended area which is difficult to do with the point measurements using the relatively expensive Acoustic Doppler Current Profilers (ADCPs). The other is to investigate the feasibility of acoustically monitoring the intensity of an approaching Typhoon using distributed ocean bottom seismotors.

21.3 Underwater Acoustic Communications and Networking

Underwater acoustic communications and networking are much more difficult than their counterparts in radio frequency world. The difficulty comes from:
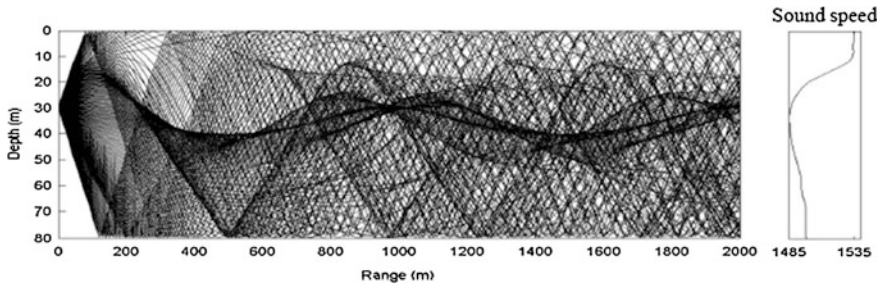
Fig. 21.4 Acoustic rays in a shallow water environment with a sound speed profile shown on the *right*
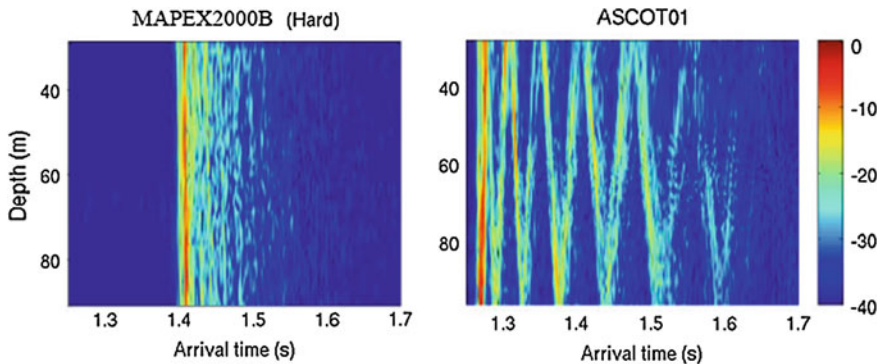
Fig. 21.5 Measured channel impulse response as a function of delay time at different depths based on data collected at two different sites in the Mediterranean

(1) Limited bandwidth due to high attenuation by the medium at high frequencies. This requires development of communication algorithms that fully use the available bandwidth.

(2) Extended multipaths due to the fact that acoustic rays do not travel in a straight line. The depth dependent sound speed profile allows many refracted and reflected rays to travel from the source to the receivers. See an example shown in Fig. 21.4. The arrival structure is dependent on the sound speed profile as shown by two measurements in Fig. 21.5. The number of rays (multipaths) is determined by the medium (e.g., bottom) attenuations. The extended multi-paths create the so-called inter-symbol interference (ISI) which confuses the receiver and must be removed before the communication message can be decoded.

(3) Short coherence time due to time-varying nature of the medium (sound speed profile) and scattering of sound by the (inhomogeneous) medium. Figure 21.6 shows a range dependent sound speed profile on the New Jersey continental shelf showing the cold water on the left coming from the Arctic, and the warm
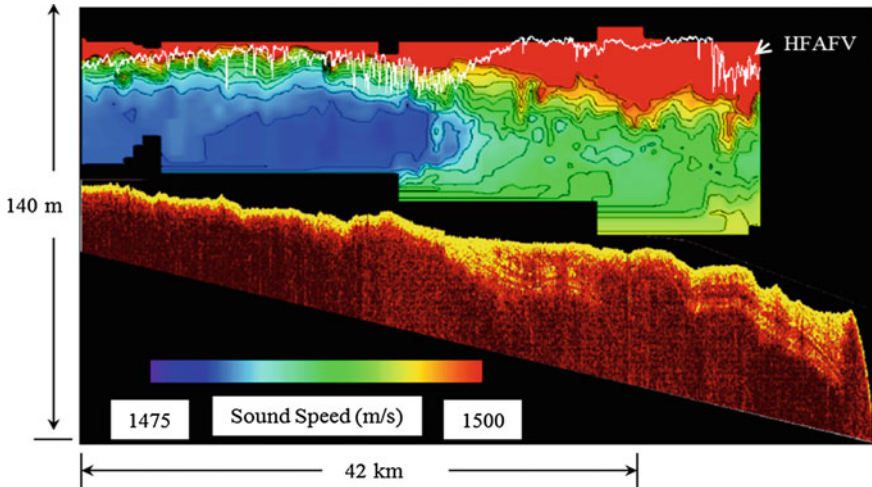
Fig. 21.6 Sound speed profile as a function of range from the source. The white line displays the pycnocline measured with high frequency acoustic visualization showing the presence of solitary internal waves

water on the right due to the Gulf streams, and evidence of solitary internal waves. The time varying environment produces a fading channel with a rapidly changing channel impulse response. It imposes significant challenges to the channel equalizer which must track the channel in order to remove the ISI.

(4) Relatively high Doppler shift due to the low sound speed (compared with the speed of light), which induces symbol phase rotation and symbol timing error. Doppler shift is usually time varying and need to be tracked as a function of time.

(5) The long and time-varying travel time (latency) due to the low sound speed, making networking handshake (medium access control) difficult.

Current approaches to underwater acoustic communications rely on spatial diversity to combat signal fading. With multiple receivers, bit error rate (BER) can be improved using spatial diversity. Two popular modulation schemes use (1) single-carrier (quadrature) phase shift keying, and (2) multi-carrier orthogonal frequency division multiplexing (OFDM). For the single-carrier, two widely used algorithms are (1) the multichannel decision feedback equalizer and (2) passive phase conjugation to the data followed by a single channel equalizer. While the latter method is no different than a multichannel equalizer in principle, it does simplify the processing and decrease the computational burden. The OFDM is simplifier in terms of channel equalization, but it requires precise Doppler estimation and compensation due to the narrowband nature of the carrier frequencies. Both methods have been demonstrated at sea and there are prototype modems built to accommodate user designed algorithms.

For DNUS, the deployed acoustic nodes and the vehicles (i.e., mobile nodes) must possess self-configuration capabilities, i.e., they must be able to coordinate their operation by exchanging configuration, location and movement information, and to relay monitored data to an onshore station. In other words, they must form a network to make these applications viable. A major function of networking is to determine how to efficiently relay the acoustic data; it will determine the optimal paths and adaptively reconfigure the paths when conditions change. While many aspects of underwater acoustic networking are the same as their RF counterpart, what makes underwater acoustic networking difficult is the slow sound speed which causes long delay from the time the message is sent to the time it is received. The travel time latency imposes significant challenges to the medium access control (MAC) protocols since individual nodes generally have no (instant) knowledge of whether the channel is occupied. (The MAC controls which node has access to the channel.) To avoid collision between data packets sent by neighboring nodes, a solution is to allow a clearance time equal to the maximum latency time, before a node transmits a packet. This results in a low network throughput, since the channel is idle (no occupied) for a large percent of time. To improve the network throughput rate, the channel needs to be used all the time, but this increase the probability of data collisions if individual nodes have no knowledge of what is going on in the network (due to the message latency). For a small number of users, when time is not critical, networking can be accomplished without much difficulty. If the number of users is large, or if the end to end transmission time is critical, or when many contact data need to be sent through the network, network MAC becomes difficult and there does not seem to be an agreed upon solution.

One of the bottle necks for DNUS is underwater acoustic communication (ACOMM) data rate and networking throughput rate, since the state of art data rate and throughput rate is orders of magnitude lower than required to transmit raw acoustic data. Multiple-input multiple-output communication using multiple antennas at source and receivers is one way to improve the ACOMM data rate. Multi-hop cooperative communications, using widely distributed nodes to serve as (virtue) antennas, could be used to ensure that the message will be relayed in a timely manner. In-buoy processing will reduce the data to be relayed through the network. This requires algorithms that are simple and do not involve a lot of computations. Many challenges remain and require further research. For practical applications, to make DNUS a reality, their system must last a decent amount of time to be worthwhile. Since most deployed systems are powered by batteries, how to make communication and networking power efficient is another issue that needs to be addressed. On the hardware side, miniature-size transducers and electronics that are power efficient, and batteries that last a long time and/or can be recharged in situ, are critical technologies for DNUS.

21.4 Distributed Sensing and Detection

DNUS can be used for acoustic sensing of the ocean environment, such as current mapping, typhoon intensity monitoring etc., in addition to functioning as a network for relaying data. In this section, we give an overview about acoustic current mapping using distributed sensors, and address potential benefits of DNUS for target detection.

21.4.1 Acoustic Current Mapping Using Distributed Sensors

Ocean acoustic tomography (OAT) uses (the perturbation of) acoustic ray travel time to invert and map mesoscale oceanic disturbance in a deep ocean. To reach long distances (hundreds of kilometers), low frequency (tens to hundreds of hertz) sources and receivers were used; the equipment was heavy and the measurements were costly to conduct, often requiring a ship support, especially for moving ship tomography [4]. Coastal acoustic tomography (CAT) was recently proposed as the application of OAT to coastal seas, with the goal of continuously monitoring the tidal currents in harbors, bays, straits, and inland seas [5], based on travel time differences between reciprocal transmissions. Given inexpensive (thus expendable) underwater sensors distributed over a wide area (e.g., DNUS), one can conduct acoustic current measurements with less power consumption and comparable (or better) spatial resolution, depending on the number of nodes deployed. Examples of distributed sensors are shown in Fig. 21.7b–f. For comparison, a traditional tomographic system with eight sensors is shown in Fig. 21.7a. For a conventional OAT system, given N sensors, there are independent input data. The system is equivalent to a number of virtual nodes, of the order of N^2, for sampling the current field. The distributed systems use physical nodes to sample the current field. For the sensor configurations in Fig. 21.7b–f, there are M triangles providing M independent measurements of the current in each triangle, where M is a function of the number of sensor nodes in each system. Thus, it is expected that for a large enough M, the system should provide equal performance as the conventional OAT system based on the spatial sampling theorem [6]. Note that data from physical nodes are free of extrapolation errors versus data using virtual nodes.

One of the selling point of the DNUS is that it uses much less power than the conventional OAT system, since the acoustic signals in DNUS travel much shorter distances than the counter parts in OAT, as shown the lines connecting the nodes in Fig. 21.7. Using 4 kHz as an example, Fig. 21.4a shows the total power used for each system as a function of the number of nodes N. One observes that the power consumption for the DNUS ($N = 12$, 16, 30, 42 and 49 corresponding to Fig. 21.7b–f) is ~ 7 dB lesser than that of conventional OAT with $N = 8$ (Fig. 21.7a). Furthermore, the power consumption decreases with increasing N for DNUS whereas the power consumption increases with increasing N for OAT.
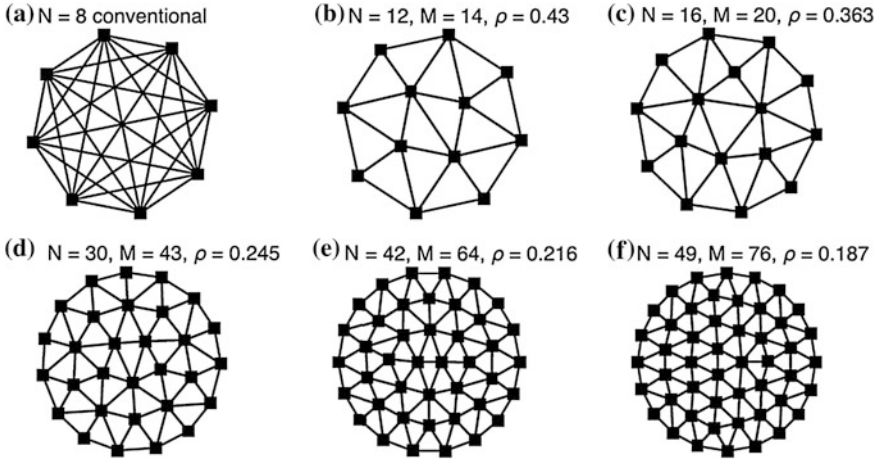
Fig. 21.7 Examples of sensor configurations for: **a** the conventional OAT system and **b–f** DNUS systems. The lines indicate the communication/propagation routes, N is the total number of nodes, M is the total number of triangles for a given DNUS, ρ is the maximum node separation divided by the diameter

Since the node distances are much smaller as N increases (for the same area coverage), one could pick a (higher) frequency to further minimize the power consumption as shown in Fig. 21.8b, c for example. Putting the two together, one finds that DNUS systems can save energy by as much as 15 dB in signal projection compared with the conventional OAT system implying many-fold extension in life time for battery-powered systems. One also finds that (1) better than the OAT performance can achieved by increasing (doubling) the number of sensors, and (2) currents can be deduced using a simple algorithm for the DNUS (without using the computationally intensive tomographic algorithm which generally requires a high power computer) and thus can be carried out by in-buoy processing. The reader is referred to [6] for the technical details.

An experiment was conducted in waters adjacent to the National Sun Yat-sen University to test the concept of DNUS for acoustic ocean current mapping. Nine acoustic nodes were deployed as shown in the upper part of Fig. 21.9. The currents measured along the T2–T4 line using travel time difference measurements are compared with that determined from a nearby ADCP. The results are shown in the lower part of Fig. 21.9 as a function of time. One observes that the acoustic inversion data are generally speaking in good agreement with that measure by ADCP. Considering the cost of an ADCP, the relatively inexpensive acoustic nodes can function as well as an ADCP. It provides measurements of the spatial distribution of currents over a wide area (Fig. 21.9), which will take many ADCP to do the same job.
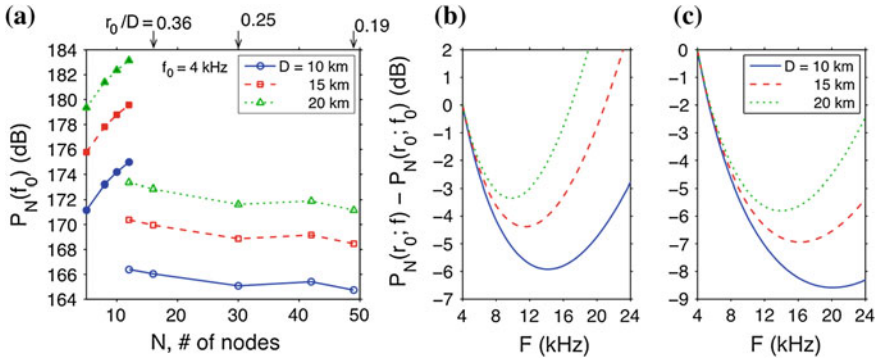
Fig. 21.8 **a** Total transmission power versus the number of nodes N to achieve a minimum 20 dB of SNR at each receiver. The *left* set of curves (*solid symbols*) are for the sensors deployed on the periphery of circle (the conventional OAT system), $N = 5, 8, 10$ and 12. The right sets of curves (*open symbols*) are for the DNUS systems with different N as shown in Fig. 21.7b–f. **b** The frequency dependence of the total transmission power for the sensor configuration given in Fig. 21.7c. **c** The frequency dependence of the total transmission power for the sensor configuration given in Fig. 21.7f
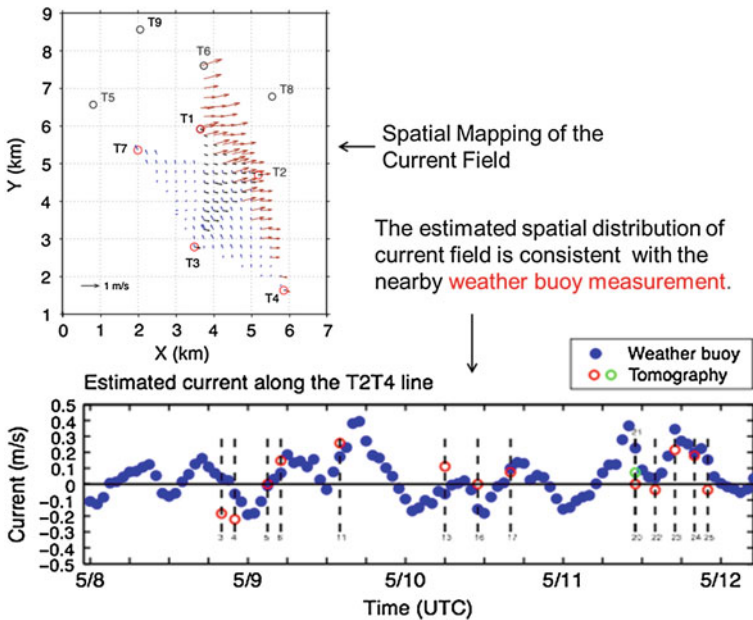
Fig. 21.9 (*Upper*) Inverted spatial distributions of the current field. The circles show the modem positions. The *solid lines* show the ray paths used for the inversion. (*Lower*) Temporal variation of mean current estimated along the T4–T2 path. *Solid* and *open circles* indicate the current measured by the weather buoy and by the reciprocal acoustic method, respectively. Positive value indicates the current moving away from T4

21.4.2 Detection Capacity

DNUS has attracted a great deal of attention recently from the point of view of target detection [1], since the probability of detection increases with the number of sensors N. First, as N increases, there is a high probability that some sensors will be close to the events and will return with high quality (high signal-to-noise ratio) data. Second, higher probability of detection can be achieved when observation data from multiple distributed sensors are intelligently fused in a decision making algorithm rather than using a single observation data set (as in conventional systems). It is based on the hypothesis that while an individual sensor may have a limited detection range, the information fused together can greatly enhance detection. In other words, the whole is greater than the sum of its parts. This concept will be illustrated in this section.

Consider the target detection as a communication problem. For a single target with multiple receivers, one has the single-input multiple-output (SIMO) communication. The receivers may be co-located in the case of an array, and may be spread out over a wide area in the case of distributed sensor. In terms of the information theory, knowledge about the target is bound by the mutual information (relative entropy) between the target source and receivers, which is the maximum information regarding the target that can be learned by the receivers. Consequently, any measure of detection should not violate the information theoretical bound. Treating the target radiated signal as continuous Gaussian-distributed alphabets, the Shannon channel capacity can be applied to calculate the detection capacity and the area of coverage where a target can be detected (for a given detection threshold). This is the approach adapted in this paper.

We shall evaluate the detection capacity for a moving source which can be anywhere in the operation area. We consider five receiver systems, each with a total of 256 sensors. Figure 21.10a shows a system with 256 sensors evenly distributed, spaced at 4 km in the $\{x, y\}$ coordinates, referred to as system 1. Figure 21.10b shows a system of $N = 64$ nodes evenly distributed in the $\{x, y\}$ coordinates, spaced at 8 km; each of nodes contains 4 sensors forming an array. It will be referred to as system 2. System 3 (Fig. 21.10c) contains $N = 16$ nodes, evenly distributed, spaced at 16 km. Each node contains 16 sensors forming an array. System 4 (Fig. 21.10d) contains $N = 4$ nodes spaced at 32 km in x and y coordinates. Each of nodes contains 64 sensors. System 5 contains $N = 1$ node located at the origin, with 256 sensors forming an (planer) array. When a node contains more-than-one sensors, it is assumed that the node will process the signals coherently yielding a perfect array gain (in the target look direction) equal to the number of sensors in the node. For convenience, system 5 will be referred to as the centralized system. System 1, with one sensor per node, is the most-distributed system. Systems 2–4 are hybrid systems, often also referred to as distributed systems. Figure 21.10b shows a target track entering the 100×100 km^2 area from the left at $y_L = -27$ km and exit on the right at $y_R = -14$ km in a straight line. The various systems are also referred to by their system configuration number from 1 to 5.
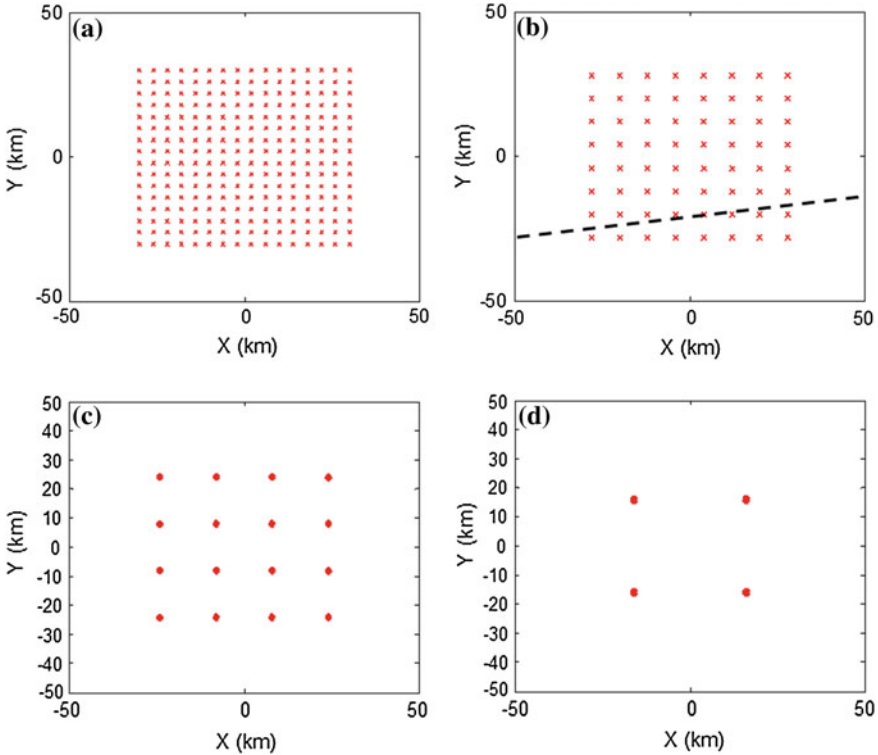
Fig. 21.10 Distributed system configurations

The system performance will be evaluated in a shallow water environment with a downward refractive sound speed profile and a water depth of 70 m. The bottom has a sediment layer of 100 m with a sound speed of 1560 m/s with an attenuation coefficient of 0.15 dB per wavelength, referred to as the high loss bottom. Given that a target can randomly walk (hide) inside the 100×100 km^2 area of surveillance, one calculates the detection capacity per target position based on the SIMO (1 to N) capacity

$$C_i = \int \log_2 \left(1 + \frac{\sigma_S^2}{\sigma_N^2} \sum_{j=1}^{N} |H_{ij}(f)|^2 \right) df, \qquad (21.1)$$

To simulate the detection capacity as a function of target position, we divide the 100×100 km^2 area into 1601×1601 grids. Each grid has a dimension 62.5×62.5 m^2 and an area of ~ 3906 m^2. The target can be randomly placed in each grid, and one evaluates the average detection capacity. One can define an area of coverage as the total area in which the target is considered detected, i.e., when the capacity is above a certain detection threshold (DT). Using the detection capacity per target for the high loss environment, one calculates the area of
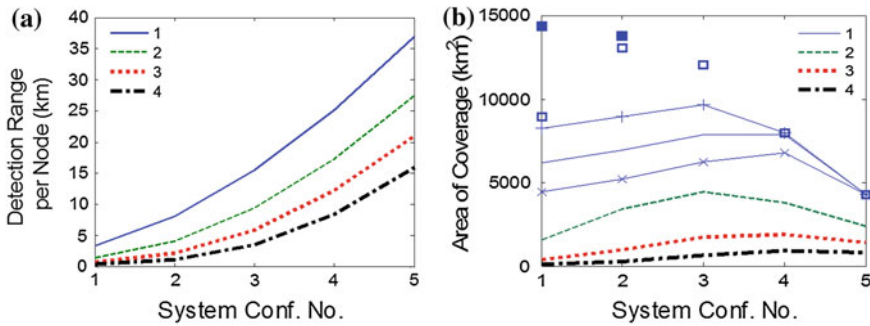
Fig. 21.11 **a** Detection range per node for DT = 1, 2, 3, and 4 bits/s/Hz as given in the legend. **b** Area of coverage for each system. Solid line with "x" denotes $a = 1$, solid line denotes $a = 1.2$, and solid line with "+" denotes $a = 1.4$, all for DT = 1 bit/s/Hz

coverage as a function of the DT (per target) for each system. To study the system performance as a function of the node spacing, we will modify the system configuration by extending the node spacing by a factor of $a = 1.2$ and 1.4 while still keeping the nodes sufficiently away from the boundary of the surveillance area. (System 5 has only one node and is unaffected.) The original system will be denoted by $a = 1.0$. We also calculate the detection area per node for a given DT, and sum over all the nodes. This will be referred to as the cookie cut model.

Figure 21.11a shows the detection range per node for DT = 1, 2, 3, and 4 bits/s/Hz and Fig. 21.11b shows the area of coverage calculated for each system with different scale factors given by a. The open squares denote the area of coverage based on the cookie cut model, where for each system the nodes are spaced by the detection range per code for DT = 1 bit/s/Hz. The filled squares denote the area of coverage based on the detection capacity for system 1 and 2 with node spacing determined by the cookie cut model. It is found that for DT = 1, the distributed systems can achieve in principle an area of coverage two to three times larger than that of a centralized system, and the area of coverage by the entire system can be significantly larger than the sum of detection areas of individual nodes for distributed systems. This implies for real system design, one must ensure sufficient detection per node so that target can detected at DT = 1.

21.5 Summary and Conclusions

Distributed netted sensing involves three concepts: distributed detection, communication and networking, and data fusion. Each task is orders of magnitude harder in underwater than above water because the ocean properties are range and time dependent, and hard to predict in advance. To improve the system performance, one needs to improve acoustic sensing of the channel and incorporate the

channel physics in the detection and communication algorithms. In this paper, we showed how the communication performance is influenced by the channel, and how one can use DNUS to conduct acoustic sensing. We showed the benefit of acoustic sensing compared with the traditional methods and we discussed the challenges that remain before DNUS can become a reality.

References

1. Various authors, session on the design of distributed, surveillance and oceanographic monitoring systems, *J. Acoust. Soc. Am.* **122**, 2997 (2007)
2. R. Viswanathan, P.K. Varshney, Proc. IEEE **85**, 54 (1997)
3. R.S. Blum, S.A. Kassam, V. Poor, Proc. IEEE **85**, 64 (1997)
4. B. Cornuelle, W. Munk, P. Worcester, J. Geophys. Res. **94**, 6232 (1989)
5. J.-H. Park, A. Kaneko, Geophys. Res. Lett. **27**, 3373 (2000)
6. C.-F. Huang, T. C. Yang, J.-Y. Liu, J. Schindall, *J. Acoust. Soc. Am.* **134**(3), 2090–2105 (2013)

Chapter 22
A Prototype of a PDMS-Based Environment for Automated and Parameterized Piping Arrangement Design

Jiing-Kae Wu, Chong-He Yang, Cheng-Yuan Ko and Wen-Kong Horng

To carry out piping system design effectively using complicated CAD systems, such as PDMS or AM Outfitting, engineers needs some customized tool modules. This paper briefly reports the approaches taken in developing a tool system that can be integrated with PDMS, including (22.1) the network approach for equipment peripheral pipe designs and (22.2) the PDMS form development for constructing 3D piping system diagrams. Using these tools in piping system working design, engineers are actually specifying length parameters of pipe segments and orientation parameters of pipe components and let the CAD system to automatically generate the pipe models.

22.1 Introduction

In large shipyards, the working design of a ship is divided into and schedule by ship blocks. In a block, engineers can pre-install as many objects that belong to the block as possible, including ship structure components, equipment sets, cable racks, pipes, and even ventilation trunks. Naturally all working design jobs are grouped by ship blocks, Fig. 22.1. However, such a design area cutting initiates the deficiency of the piping system working design.

With new pipe design automation methods proven to be feasible, such as a trunk based piping arrangement design automation [1], the network based peripheral pipe design of equipment sets [2, 3], and a 3D piping system diagram approach [4], the working design (or detail design) of piping systems of a ship engine room can consider the whole engine room as one integral space, instead of blocks by blocks. Furthermore, with design automation methods available, pipe routes would be searched and constructed by computer codes, what remains for

J.-K. Wu (✉) · C.-H. Yang · C.-Y. Ko · W.-K. Horng
Department of Marine Engineering, National Koahsiung Marine University,
142, Haichuan Rd., Kaohsiung, Nantzu, Taiwan
e-mail: kirkwu@webmail.nkmu.edu.tw
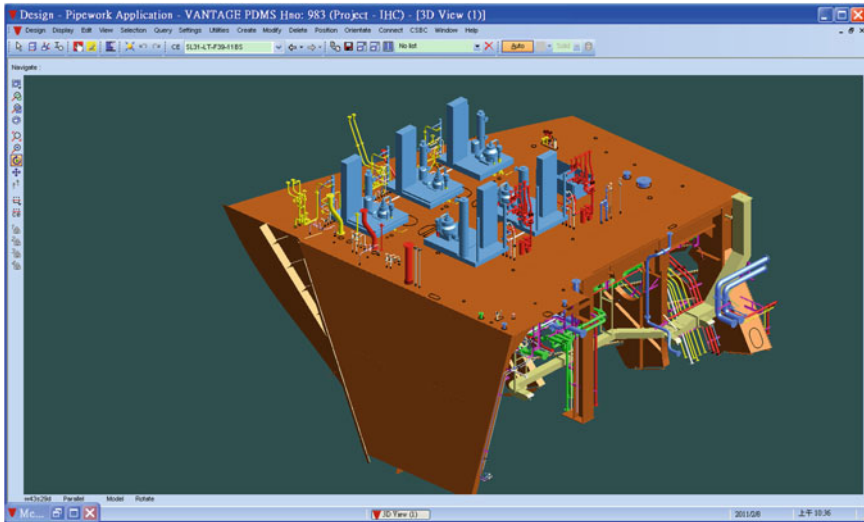
Fig. 22.1 A block of ship engine room design model

engineers to consider is: which pipe route is economic or saves manufacturing jobs/costs.

Each of these pipe route design automation methods has been prototyped and will be implemented as a design tool one by one. The platform to wrap these design automation tools is called Piping Design Assistants (PDA) and can be integrated with CAD environments, for instance, PDMS [5] or its new version—AM Outfitting. This paper briefly reports (22.1) the network (or graph) approach and the tool kit (called Peripheral Pipe Editor) for parameterized equipment peripheral pipe designs and (22.2) the PDMS form developed for specifying dimension and orientation parameters of pipe component to construct 3D piping system diagrams (called Equipment Connectivity Editor).

22.2 Review of Related Literatures

Researches and developments on piping arrangement design were slow. Part of the reasons is either the methods developed were not applicable in industries and then stopped, or industries implemented the methods as software codes in their systems without reporting in the papers.

In one of early research work, a pipe assembly was described as summation of spatial vectors together with coordinate transformations [6]. On such a base, orthogonal routing method was developed to find the pipe route connecting two nozzles in space, with the pipes aligned with the X, Y, or Z coordinate axis and using the least number of elbows [7].

While many researches focus on looking for shortest pipe routes [8–11] and collision avoidance [12, 13], a pipe-trunk based piping arrangement method [1] restricted pipes to go through predefined pipe trunks to reduce the chance of collision and chose the shortest pipe route from the pipe trunk routes searched.

The pipes around the same type of equipment sets are similar in different ships, for instance the peripheral pipes of parallel arranged dual coolers. To reuse the peripheral pipes designed, the network (or graph) concept was used to describe these pipes and form a system of equations [2]. Examples [3] showed that properly set the pipe length according to their minimal values, this approach can be used to find the minimal space needed for the network of pipes.

Recently, efforts were made to replace the traditional piping system diagrams by three-dimensional (3D) models [4]. With 3D model transfer technology [14] available, engineers can navigate the 3D model details and design attributes on regular computers without any CAD system or its database. Due to such a technology development, replacing the piping system diagrams by 3D models becomes feasible, and open many new opportunities in crew training, design concept presentation and exchanging, etc.

This paper demonstrate that to effectively use advanced piping design methods, tool kits need to be developed to wrap the methods for engineers and to integrate the methods with CAD design environment.

22.3 Network and Editor of Peripheral Pipes

The space occupied by some equipment sets installed in commercial ship engine rooms can be very large especially then dual sets of equipment are installed, such as lubricating oil coolers etc. The peripheral pipes of these equipment sets also take significant space when the diameters of the pipes are large. In the equipment arrangement process, if there are no appropriate tools to add the peripheral pipes of equipment sets into the arrangement models, very often insufficient peripheral pipe space would be left, by looking at the space consumed only by the equipment sets in the engine room models. The influence of such a mistake can be very serious, for instance, when the pipe space left between the main engine front end and the engine room bulkhead is insufficient.

Figure 22.2a shows a portion of engine room arrangement drawing, where the positions and orientations of main engine lubricating oil coolers are depicted without cooler peripheral pipes. Figure 22.2b shows the arrangement of the coolers and their peripheral pipes. The later clear illustrates the space needed by the peripheral pipes and space left around the coolers.

Preliminary studies on the computer and mathematic models of peripheral pipes [2, 3] indicates that these peripheral pipes can be captured/stored as a group and reused and adjusted according to the geometries of the new (but same type) equipment sets and the relative position and orientation between the equipment sets.
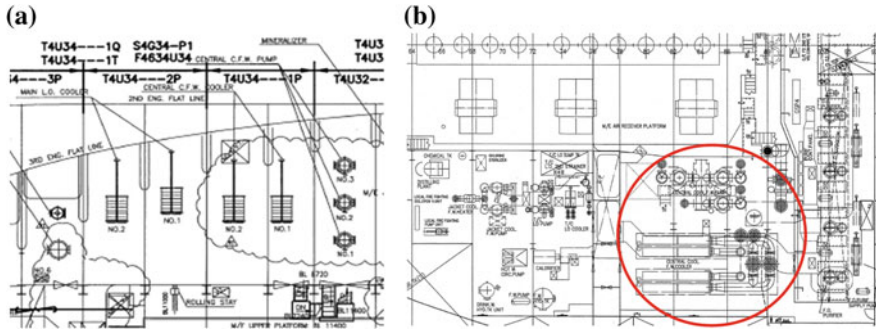
Fig. 22.2 Arrangement design of dual coolers: **a** without showing peripheral pipes, and **b** with both peripheral pipes and coolers shown

Fig. 22.3 Pipes connecting two vertical centrifugal pumps in a ship engine room

In the computer model, the peripheral pipes of dual sets of equipment, such as the main engine jacket cooling fresh water pumps (Fig. 22.3), are a network of nodes, which are elbows (or bends) or Tee-branches in a pipe assembly or nozzle flanges on equipment sets. These nodes are connected by pipe segments, which are treated as edges between a pair of nodes. Figure 22.4 is the CAD model of the pumps shown in Fig. 22.3. Figure 22.5 is the network representation of the peripheral pipes at the inlet side of the dual pumps shown in Fig. 22.4.

In the network of the peripheral pipes, a node whose position is fixed is a fixed node and is represented by a filled circle. A node whose position can be changed along with the pipe length is a floating node and is represented as a hollow circle.

Among the three fixed nodes (1, 6, and 8), there are 3 routes connecting any two of them. For instance, vector from node 1 to node 8 should be equal to the vector sum of edges 1 to 2, 2 to 3, 3 to 7, and 7 to 8. By separating the edge vectors according to X-, Y-, and Z-components, one can obtain the following edge vector relationships, which are the constraint equations of the network:
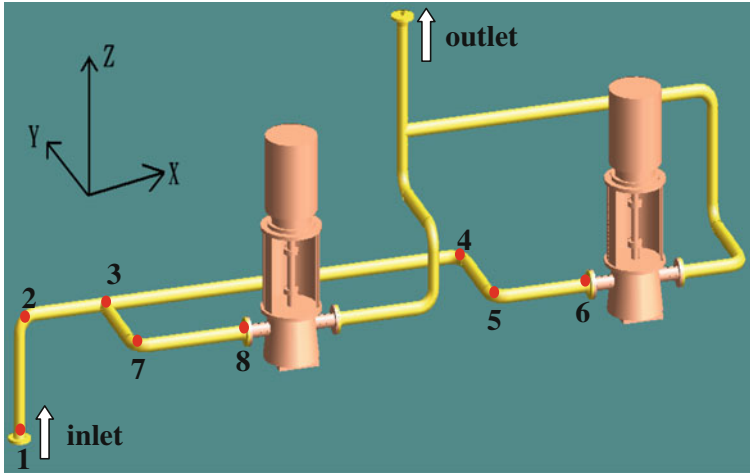
Fig. 22.4 CAD model of the pumps and peripheral pipes shown in Fig. 22.3

Fig. 22.5 Network model of
the peripheral pipes at the
inlet side of the pumps shown
in Fig. 22.4
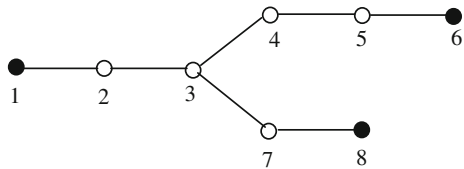
$$\begin{bmatrix} 1 & 1 & 0 & 0 \\ 1 & 0 & 1 & 1 \\ 0 & 1 & -1 & -1 \end{bmatrix} \begin{Bmatrix} X_{2\_3} \\ X_{7\_8} \\ X_{3\_4} \\ X_{5\_6} \end{Bmatrix} = \begin{Bmatrix} r_{1\_8,x} \\ r_{1\_6,x} \\ r_{6\_8,x} \end{Bmatrix} \tag{22.1}$$

$$\begin{bmatrix} 1 & 0 \\ 0 & 1 \\ 1 & -1 \end{bmatrix} \begin{Bmatrix} Y_{3\_7} \\ Y_{4\_5} \end{Bmatrix} = \begin{Bmatrix} r_{1\_8,y} \\ r_{1\_6,y} \\ r_{6\_8,y} \end{Bmatrix} \tag{22.2}$$

$$\begin{bmatrix} 1 \\ 1 \end{bmatrix} \{Z_{1\_2}\} = \begin{Bmatrix} r_{1\_8,z} \\ r_{1\_6,z} \end{Bmatrix} \tag{22.3}$$

In the network constraint equations, X_{i_j} is the edge vector from node i to node j. The root vector $r_{m\text{-}n}$ is from fixed node m to fixed node n.

Through matrix rank analysis [15], one can be sure the network constraint equations are independent or not. If dependence exists, each set of dependent constraint equations can only leave one equation in the constraint equations. The following equations are the independent constraint equations of the network of the inlet side of the peripheral pipes of the pumps shown in Figs. 22.3 and 22.4.

$$\begin{bmatrix} 1 & 0 & 1 & 1 \\ 0 & 1 & -1 & -1 \end{bmatrix} \begin{Bmatrix} X_{2\_3} \\ X_{7\_8} \\ X_{3\_4} \\ X_{5\_6} \end{Bmatrix} = \begin{Bmatrix} r_{1\_6,x} \\ r_{6\_8,x} \end{Bmatrix} \tag{22.4}$$

$$\begin{bmatrix} 1 & 0 \\ 0 & 1 \end{bmatrix} \begin{Bmatrix} Y_{3\_7} \\ Y_{4\_5} \end{Bmatrix} = \begin{Bmatrix} r_{1\_8,y} \\ r_{1\_6,y} \end{Bmatrix} \tag{22.5}$$

$$\begin{bmatrix} 1 \\ 1 \end{bmatrix} \{Z_{1\_2}\} = \begin{Bmatrix} r_{1\_8,z} \\ r_{1\_6,z} \end{Bmatrix} \tag{22.6}$$

Take the X-component of the constraint equations as an example. Equation (22.4) shows 2 independent equations containing 4 unknown edge length parameters, and the dimension of the coefficient matrix is 2×4. Hence, parameters in (22.4) are undetermined. Two edge length parameters (X_{3_4} and X_{5_6}) must by given, and leave the remaining (two) parameters being determined by the 2 constraint equations shown in (22.4).

The edge length parameters whose values need to be assigned by design engineers are called free parameters, and the edge length parameters that will be left in the constraint equations for computers to determine their values are called constraint parameters.

To assist design engineers in reusing existing network of peripheral pipes of equipment sets in CAD environment such as PDMS, a prototype of a graphical user interface has been developed using PML programming language [16]. The purpose of the prototype is to demonstrate required functions when using the network approach to copy (an existing network), past, and adjust the peripheral pipe lengths for a new design.

Figure 22.6 shows the graphical user interfaces developed to design the outlet side of the peripheral pipes of parallel pumps (Fig. 22.7). The top two rows of menu options in the user interface are for commanding the process, including constructing the node connectivity matrix, constructing the coefficient matrices and edge parameter vectors for X-, Y-, and Z-components, fining independent coefficient matrices, solving/determining the constraint edge length parameters (by calling MATLAB [17]), and constructing CAD model input files to let PDMS generate the peripheral pipe models.

Prior to determining the constrained edge length parameters, design engineers need to specify the values for free edge length parameters that they choose, using the lower portion of the user interface fields shown in Fig. 22.6. The variable names in the user interface are corresponding to the edges in the outlet side of the peripheral pipes of the dual pumps and are grouped by X-, Y-, and Z- components, see Fig. 22.7. This lower portion of the user interface would be designed according to the network of the peripheral pipes considered.

As an example, Fig. 22.8 shows the CAD model of the dual pumps and their outlet pipes modified by using the peripheral network and the user interface described above.
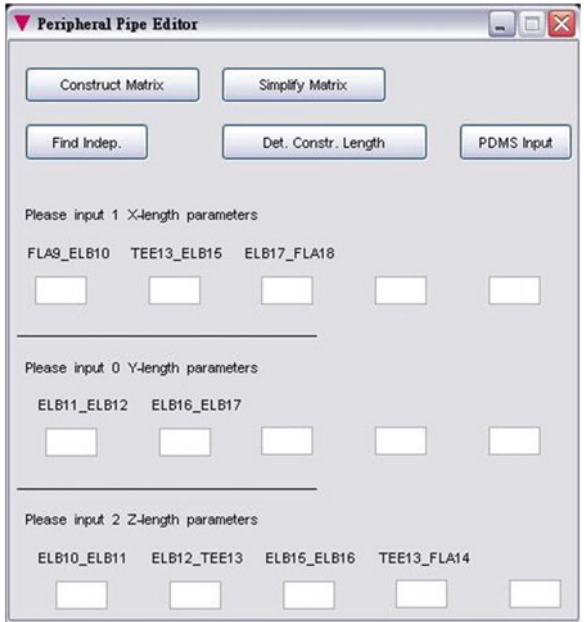
Fig. 22.6 User interface prototyped for modifying the outlet side of the peripheral pipes of two parallel arranged pumps using the network method
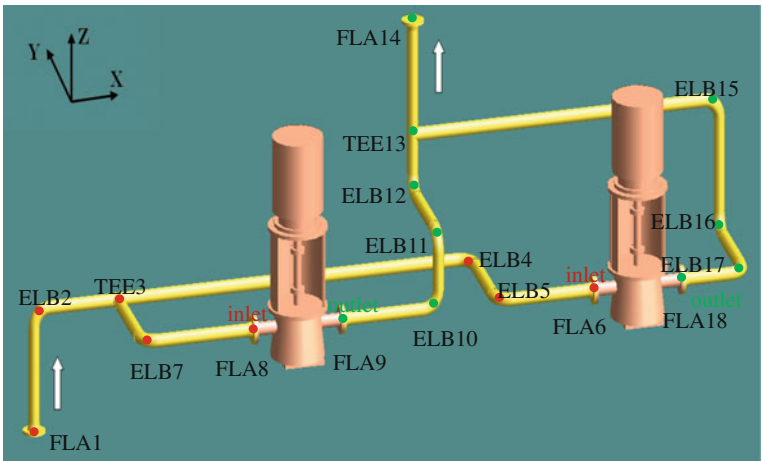
Fig. 22.7 Nodes and names of the peripheral pipes of the dual pumps
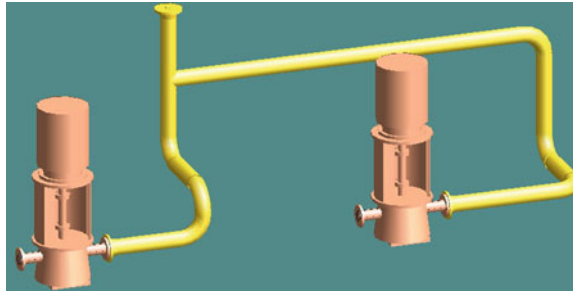
Fig. 22.8 CAD model of the modified outlet side of the peripheral pipes of the dual pumps
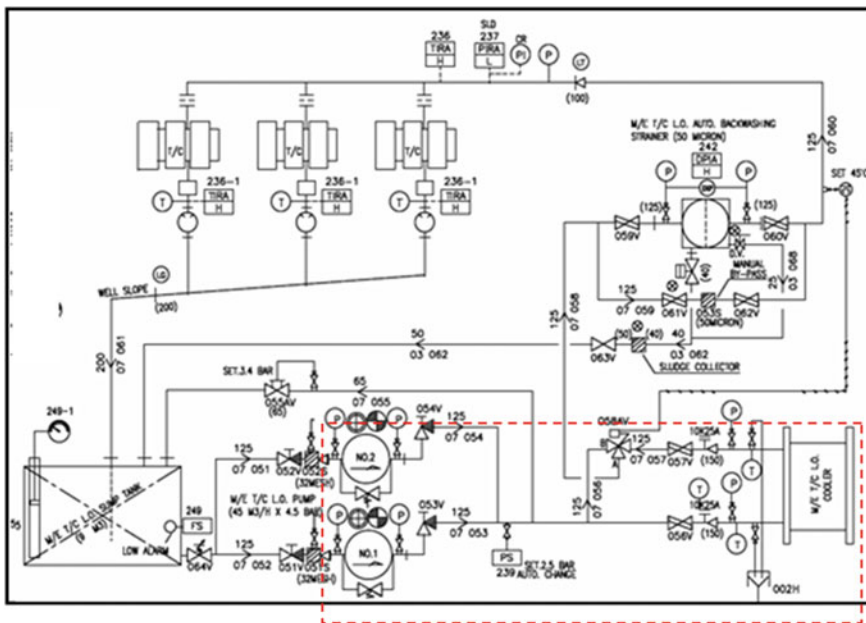
Fig. 22.9 Piping system diagram of a main engine turbocharger lubricating oil

22.4 Tool Kit for Constructing 3D Piping System Diagrams

Two sets of important design information developed in the functional design (or key design) process of a ship engine room are Machinery Arrangement and Piping System Diagrams. Each of the piping system diagrams describes the flow sequence of a specific fluid among equipment sets to exchange heat in the main or auxiliary machines, to transport fluid from a device to another, to increase/reduce the pressure in the fluid, etc. Figure 22.9 is the piping system diagram of a main engine turbocharger lubricating oil.
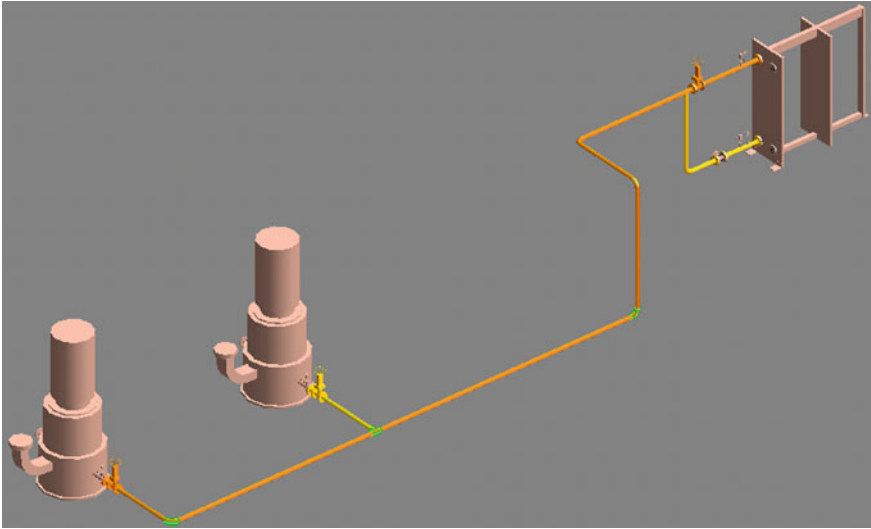
Fig. 22.10 Equipment connectivity model between the lubricating oil pumps and the cooler that are shown in Fig. 22.9

As the main purpose of the piping system diagrams is to describe such sequences, the true positions of the equipment sets are not reflected in the diagrams; the real pipe routes are not shown in the diagrams; and straight lines, symbols, and numbers are used in the diagrams to describe/depict the equipment sets, pipe diameters, connectivity of equipment sets, etc. Therefore, design information shown in the piping system diagrams needs human interpretation, and it is difficult to check, from the connectivity point of view, if the machinery arrangement of the ship engine room is effective (saving manufacturing work and costs) or not.

To overcome such defects, an Equipment Connectivity Model has been developed [4]. A more commonly perceivable name for such a model would be 3D Piping System Diagram. Figure 22.10 is the equipment connectivity model between the lubricating oil pumps and the cooler that are enclosed in the dash rectangle shown in Fig. 22.9. In such a connectivity model, the CAD model of equipment set is located and oriented according to the engine room machinery arrangement design. The pipes connecting the equipment sets are constructed using orthogonal pipe arrangement method (every pipe segment is along X-, Y-, or Z-direction), and whether the pipes collide with equipment sets or structure members are not concerned (since the later objects are not shown in the model).

To resolve the reprint problem encountered by most 3D models, a 3D model transfer tools has been developed [14], and the equipment connectivity model not only can be displayed and navigated as 3D models on any regular computer without installing CAD systems, but also conveying design information no less
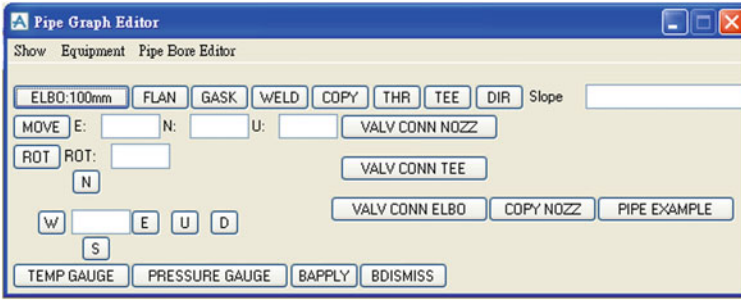
Fig. 22.11 3D piping system diagram editor prototyped

than traditional piping system diagrams, as both text attribute information and 3D geometry models can be re-displayed without any error.

However, several important advantages can be obtained from the equipment connectivity model over the piping system diagrams: (1) engineers can recognize (from the connectivity model) if the equipment arrangement design fits well with the connectivity of the equipment sets; (2) from the model database, engineers can extract bill of material information for constructing the whole piping systems, except the total number of elbows and total length of straight pipes; (3) the connectivity model already complete part of the detail design (or working design) jobs of piping systems. It should be noted that the pipes shown in the equipment connectivity model along X-, Y-, or Z-directions are not the real pipe route between the equipment sets.

To facilitate the construction of the equipment connectivity model, a tool kit has been prototyped and is called Equipment Connectivity Editor [18], see Fig. 22.11. It is actually a customized graphical user interface, developed by using PML, to accelerate the process to construct the equipment connectivity model and to demonstrate tool features needed for constructing the models.

According to the tool kit, the pipe components used in the equipment connectivity models include elbow, nozzle flange, gasket, Tee-branch, etc. Each of these pipe components can be rotate or translated by specifying the amount of translation or rotation or specifying the coordinates to be moved to. Commonly used connections in the model include valve to elbow, valve to Tee-branch, and valve to nozzle (the inlet or outlet of a device), and the commonly used instruments include temperature and pressure gauges. Using the tool kit to construct equipment connectivity models, engineers actually are specifying the pipe length parameters of the orthogonal pipes in the CAD system.

As an example and for comparison, the equipment connectivity model (also called 3D piping system diagram) of the main engine turbocharger lubricating oil system has been developed and shown in Fig. 22.12. The piping system diagram of the same system is shown in Fig. 22.9.
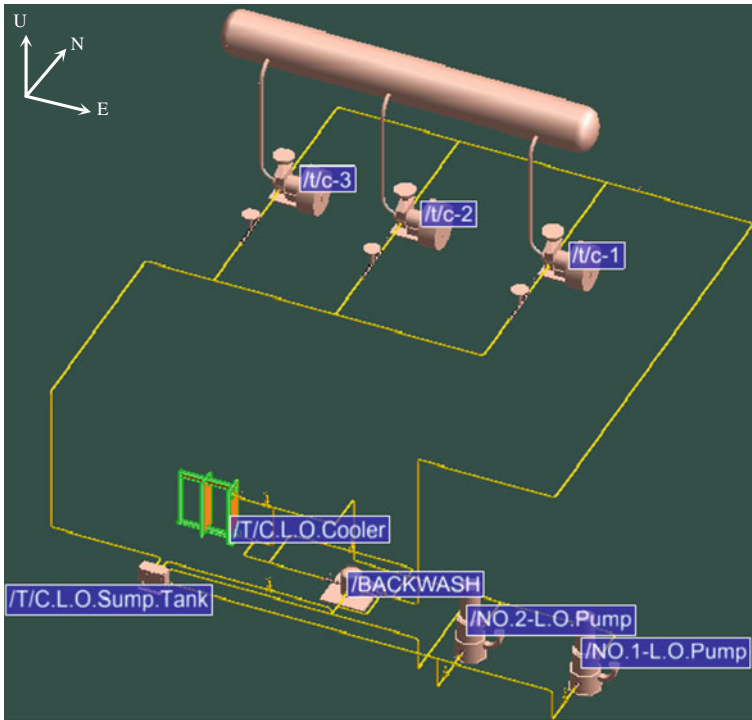
Fig. 22.12 Equipment connectivity model of the main engine turbocharger lubricating oil system

It should be pointed out, the equipment connectivity model can be constructed by using regular piping design CAD systems, the customized tool kit, the Equipment Connectivity Editor, simply accelerates the construction work of the connectivity models.

22.5 Conclusion

The concepts of network approach in parameterizing the design of peripheral pipes of equipment sets have been introduced. The usages of customized tool kits for facilitating engineers in specifying pipe length parameters using the peripheral pipe network approach and for facilitating engineers to specify pipe length parameters in constructing the equipment connectivity models (also called 3D piping system diagrams) have been demonstrated in the paper.

The customized tool kits basically simplifies the process in using advanced technologies developed for piping system working design, hence they also improve the design efficiency of engineers.

References

1. J.K. Wu, W.K. Horng, in *Proceeding of the 20th Taiwan Society of Naval Architecture and Marine Engineering*, Taipei, Taiwan, March 2011
2. J.K. Wu, P.H. Huang, Y.S. Tsai, in *Proceeding of the 23rd Taiwan Society of Naval Architecture and Marine Engineering*, Kaohsiung, Taiwan, March 2011
3. Y.S. Tsai, J.K. Wu, W.K. Horng, in *Proceeding of the 22nd Taiwan Society of Naval Architecture and Marine Engineering*, Taipei, Taiwan, March 2010
4. J.K. Wu, J.P. Wang, W.K. Horng, C.Y. Ko, in *Proceeding of the World Maritime Technology Conference (WMTC2012)*, St. Petersburg, Russia, May 29–June 1 2012
5. *Plant Design Management System (PDMS) Administrator User Guide, Version 12.0 SP6*, Cambridge, England (2010)
6. J.K. Wu, T.C. Yang, *Marit. Res. J.* **10**, 71 (2001)
7. J.K. Wu, *J. Ship Prod.* **16**(3), 173 (2000)
8. E.W. Dijkstra, Numer. Math. **1**, 269 (1959)
9. L.H. Wang, *Study on the Genetic Algorithms Based 3D Pipe Routing*, Master Thesis, Department of Systems and Naval Mechatronic Engineering, National Cheng Kung University (2000)
10. Y. Yamada, Y. Teraoka, Comput. Math. Appl. **35**(6), 137 (1998)
11. G.E. Wangdahl, S.M. Pollock, J.B. Woodward, *J. Ship Res.* **18**(1), 46 (1974)
12. C.C. Kuo, *Study on the Automatic Piping Route System for 3D Piping Arrangement*, Master Thesis, Department of Systems and Naval Mechatronic Engineering, National Cheng Kung University (1999)
13. L.W. Wang, *The Application of Genetic Algorithm with Consideration of Equipment Operability on the Optimal Design of Piping Arrangement in Ship Engine Room*, Master Thesis, Department of Systems and Naval Mechatronic Engineering, National Cheng Kung University (2010)
14. *Design Model Transfer Technology*, Chen-Wei International Co., Kaohsiung, Taiwan (2012)
15. R. Broson, G.B. Costa, *Matrix Methods* (Elsevier, New York, 2009)
16. *Plant Design Management System (PDMS) Customization Guide, Version 12.0 SP6*, Cambridge, England (2010)
17. J. William, I.I.I. Palm, *MATLAB for Engineering Applications* (McGraw-Hill, New York, 1999)
18. C.H. Yang, in *Proceeding of the 23rd Taiwan Society of Naval Architecture and Marine Engineering*, Kaohsiung, Taiwan, March 2011

Chapter 23
VLSI Implementation of Low-Power and High-SFDR Digital Frequency Synthesizer for Underwater Instruments and Network Systems

Ying-Shen Juang, Tze-Yun Sung and Hsi-Chin Hsin

COordinate Rotation DIgital Computer (CORDIC) is an efficient algorithm for computations of trigonometric functions. Scaling-free-CORDIC is one of the famous CORDIC implementations with advantages of speed and area. In this paper, a novel direct digital frequency synthesizer (DDFS) based on scaling-free CORDIC is presented. The proposed multiplier-less architecture with small ROM (4×16-bit) and pipeline data path has advantages of high data rate, high precision, high performance, and less hardware cost. The design procedure with performance and hardware analysis for optimization has also been given. It is verified by Matlab® simulations and then implemented with FPGA (field programmable gate array) by Verilog®. The spurious-free dynamic range (SFDR) is 118.2 dBc, and the signal-to-noise ratio (SNR) is 81.12 dB. The scaling-free CORDIC based architecture is suitable for VLSI implementations for the DDFS applications in terms of hardware cost, power consumption, SNR, and SFDR. The proposed DDFS is very suitable for underwater instruments and network systems.

Y.-S. Juang (✉)
Department of Business Administration, Chung Hua University, Hsinchu City 300-12, Taiwan
e-mail: ysjuang@chu.edu.tw

T.-Y. Sung
Department of Electronics Engineering, Chung Hua University, Hsinchu City 300-12, Taiwan
e-mail: bobsung@chu.edu.tw

H.-C. Hsin
Department of Computer Science and Information Engineering, National United University, Miaoli City 360-03, Taiwan
e-mail: hsin@nuu.edu.tw

23.1 Introduction

Direct digital frequency synthesizer (DDFS) has been widely used in the modern communication systems. DDFS is preferable to the classical phase-locked loop (PLL) based synthesizer in terms of switching speed, frequency resolution, and phase noise, which are beneficial to the high-performance communication systems. Figure 23.1 depicts the conventional DDFS architecture [1], which consists of a phase accumulator, a sine/cosine generator, a digital-to-analog converter (DAC), and a low-pass filter (LPF). As noted, two inputs: the reference clock and the frequency control word (*FCW*) are used; the phase accumulator integrates *FCW* to produce an angle in the interval of $[0, 2\pi)$; and the sine/cosine generator computes the sinusoidal values. In practice, the sine/cosine generator is implemented digitally, and thus followed by digital-to-analog conversion and low-pass filtering for analogue outputs. Such systems can be applied in many fields, especially in underwater instruments and network systems [2–4].

The simplest way to implement the sine/cosine generator is to use ROM lookup table (LUT). However, a large ROM is needed [5]. Several efficient compression techniques have been proposed to reduce the lookup table size [5–10]. The quadrant compression technique can compress the lookup table and then reduce the ROM size by 75 % [6]. The Sunderland architecture splits the ROM into two smaller memories [7]; and the Nicholas architecture improves the Sunderland architecture to achieve a higher ROM-compression ratio (32:1) [8]. The ROM size can be further reduced by using the polynomial approximations [11–18] or CORDIC algorithm [19–27]. In the polynomial approximations based DDFSs, the interval of $[0, \pi/4]$ is divided into sub-intervals, and sine/cosine functions are evaluated in each sub-interval. The polynomial approximations based DDFS requires a ROM to store the coefficients of the polynomials, and the polynomial evaluation hardware with multipliers. In the circular mode of CORDIC, which is an iterative algorithm to compute sine/cosine functions, an initial vector is rotated with a predetermined sequence of sub-angles such that the summation of the rotations approaches the desired angle [28, 29]. CORDIC has been widely used for the sine/cosine generator of DDFS [19–27]. Compared to the look-up table based DDFS, the CORDIC based DDFS has the advantage of avoiding the exponential growth of hardware complexity while the output word size increases [30–33].

In Fig. 23.1, the word length of the phase accumulator is v bits; thus, the period of the output signal is as follows:

$$T_o = \frac{2^v T_s}{FCW}, \qquad (23.1)$$

where *FCW* is the phase increment, and T_s denotes the sampling period. It is noted that the output frequency can be written by

$$F_o = \frac{1}{T_o} = \frac{F_s}{2^v} \cdot FCW. \qquad (23.2)$$
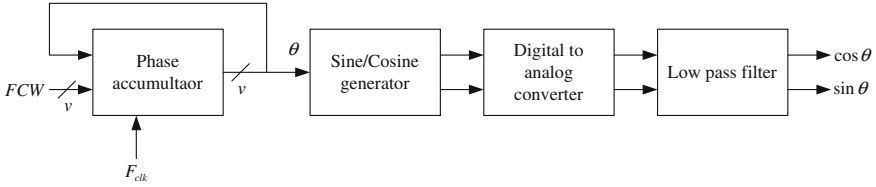
Fig. 23.1 Conventional DDFS architecture

According to the equation above, the minimum change of output frequency is given by

$$\Delta F_{o,\min} = \frac{F_s}{2^v}(FCW + 1) - \frac{F_s}{2^v}FCW = \frac{F_s}{2^v}. \tag{23.3}$$

Thus, the frequency resolution of DDFS is dependent on the word length of the phase accumulator as follows:

$$\Delta F_o \geq \frac{F_s}{2^v}. \tag{23.4}$$

The bandwidth of DDFS is defined as the difference between the highest and the lowest output frequencies. The highest frequency is determined by either the maximum clock rate or the speed of logic circuitries; the lowest frequency is dependent on *FCW*. Spurious-Free Dynamic Range (SFDR) is defined as the ratio of the amplitude of the desired frequency component to that of the largest undesired one at the output of DDFS, which is often represented in dBc as follows:

$$\text{SFDR} = 20\log\left(\frac{A_p}{A_s}\right) = 20\log(A_p) - 20\log(A_s), \tag{23.5}$$

where A_p is the amplitude of the desired frequency component and A_s is the amplitude of the largest undesired one.

In this paper, a novel DDFS architecture based on the scaling-free CORDIC algorithm [34] with ROM mapping is presented. The rest of the paper is organized as follows. In Sect. 23.2, CORDIC is reviewed briefly. In Sect. 23.3, the proposed DDFS architecture is presented. In Sect. 23.4, the hardware implementation of DDFS is given. Conclusion can be found in Sect. 23.5.

23.2 The CORDIC Algorithm

CORDIC is an efficient algorithm that evaluates various elementary functions including sine and cosine functions. As hardware implementation might only require simple adders and shifters, CORDIC has been widely used in the high speed applications.

23.2.1 The CORDIC Algorithm in the Circular Coordinate System

A rotation of angle θ in the circular coordinate system can be obtained by performing a sequence of micro-rotations in the iterative manner. Specifically, a vector can be successively rotated by the use of a sequence of pre-determined step-angles: $\alpha(i) = \tan^{-1}(2^{-i})$. This methodology can be applied to generate various elementary functions, in which only simple adders and shifters are required. The conventional CORDIC algorithm in the circular coordinate system is as follows [28, 29]:

$$x(i+1) = x(i) - \sigma(i)2^{-i}y(i); \tag{23.6}$$

$$y(i+1) = y(i) + \sigma(i)2^{-j}x(i); \tag{23.7}$$

$$z(i+1) = z(i) - \sigma(i)\alpha(i); \tag{23.8}$$

$$\alpha(i) = \tan^{-1} 2^{-i}, \tag{23.9}$$

where $\sigma(i) \in \{-1, +1\}$ denotes the direction of the i-th micro-rotation, $\sigma_i = \text{sign}(z(i))$ with $z(i) \to 0$ in the vector rotation mode [34], $\sigma_i = -\text{sign}(x(i)) \cdot \text{sign}(y(i))$ with $y(i) \to 0$ in the angle accumulated mode [34], the corresponding scale factor $k(i)$ is equal to $\sqrt{1 + \sigma^2(i)2^{-2i}}$, and $i = 0, 1, \ldots, n-1$. The product of the scale factors after n micro-rotations is given by

$$K_1 = \prod_{i=0}^{n-1} k(i) = \prod_{i=0}^{n-1} \sqrt{1 + 2^{-2i}}. \tag{23.10}$$

In the vector rotation mode, $\sin \theta$ and $\cos \theta$ can be obtained with the initial value: $(x(0), y(0)) = (1/K_1, 0)$. More specifically, x_{out} and y_{out} are computed from the initial value: $(x_{in}, y_{in}) = (x(0), y(0))$ as follows:

$$\begin{bmatrix} x_{out} \\ y_{out} \end{bmatrix} = K_1 \begin{bmatrix} \cos \theta & -\sin \theta \\ \sin \theta & \cos \theta \end{bmatrix} \begin{bmatrix} x_{in} \\ y_{in} \end{bmatrix} \tag{23.11}$$

23.2.2 Scaling-Free CORDIC Algorithm in the Circular Coordinate System

Based on the following approximations of sine and cosine functions,

$$\sin \alpha(i) \cong \alpha(i) = 2^{-i}; \tag{23.12}$$

$$\cos \alpha(i) \cong 1 - \frac{\alpha^2(i)}{2} = 1 - 2^{-(2i+1)} \tag{23.13}$$

the scaling-free CORDIC algorithm is thus obtained by using equations (23.6), (23.7), and the above, in which, the iterative rotation is as follows:

$$\begin{bmatrix} x(i+1) \\ y(i+1) \end{bmatrix} = \begin{bmatrix} 1 - 2^{-(2i+1)} & 2^{-i} \\ -2^{-i} & 1 - 2^{-(2i+1)} \end{bmatrix} \begin{bmatrix} x(i) \\ y(i) \end{bmatrix}; \tag{23.14}$$

$$z(i+1) = z(i) - 2^{-i}. \tag{23.15}$$

For the word length of w bits, it is noted that the implementation of scaling-free CORDIC algorithm utilizes four shifters and four adders for each micro-rotation in the first $w/2$-micro-rotations; it reduces two shifters and two adders for each micro-rotation in the last $w/2$-micro-rotations [24, 34, 35].

23.3 Design and Optimization of the Scaling-Free-CORDIC Based DDFS Architecture

In this section, the architecture together with performance analysis of the proposed DDFS is presented. It is a combination of the scaling-free-CORDIC algorithm and LUT; this hybrid approach takes advantage of both CORDIC and LUT to achieve high precision and high data rate, respectively. The proposed DDFS architecture consists of phase accumulator, radian converter, sine/cosine generator, and output stage.

23.3.1 Phase Accumulator

Figure 23.2 shows the phase accumulator, which consists of a 32-bit adder to accumulate the phase angle by FCW recursively. At time n, the output of phase accumulator is $\phi = n \cdot FCW/2^{32}$ and the sine/cosine generator produces $\sin(n \cdot FCW/2^{32})$ and $\cos(\frac{n \cdot FCW}{2^{32}})$. The *load* control signal is used for FCW to be loaded into the register, and the *reset* signal is to initialize the content of the phase accumulator to zero.

23.3.2 Radian Converter

In order to convert the output of the phase accumulator into its binary representation in radians, the following strategy has been adopted. Specifically, an efficient

Fig. 23.2 Phase accumulator
in DDFS
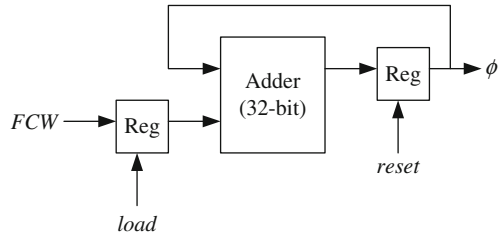
Fig. 23.3 Symmetry-based
map of an angle in either the
second, third, or fourth
quadrant to the corresponding
angle in the first quadrant
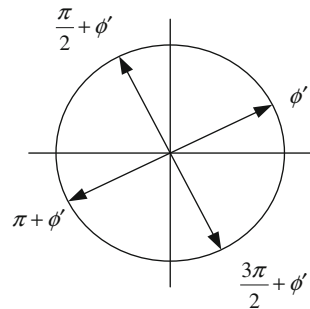
ROM reduction scheme based on the symmetry property of sinusoidal wave can be obtained by simple logic operations to reconstruct the sinusoidal wave from its first quadrant part only. In which, the first two MSBs of an angle indicate the quadrant of the angle in the circular coordinate; the third MSB indicates the half portion of the quadrant; thus, the first three MSBs of an angle are used to control the interchange/negation operation in the output stage. As shown in Fig. 23.3, the corresponding angles of ϕ' in the second, third, and fourth quadrants can be mapped into the first quadrant by setting the first two MSBs to zero. The radian of phi' is therefore obtained by $\theta = \frac{\pi}{4}\phi'$, which can be implemented by using simple shifters and adders array shown in Fig. 23.4.

Note that the third MSB of any radian value in the upper half of a quadrant is 1, and the sine/cosine of an angle γ in the upper half of a quadrant can be obtained from the corresponding angle in the lower half as shown in Fig. 23.5. More specifically, as $\cos\gamma = \sin(\frac{\pi}{2} - \gamma)$ and $\sin\gamma = \cos(\frac{\pi}{2} - \gamma)$, the normalized angle can be obtained by replacing θ with $\theta' = 0.5 - \theta$ while the third MSB is 1. In case the third MSB is 0, there is no need to perform the replacement as $\theta' = \theta$.

23.3.3 Sine/Cosine Generator

As the core of the DDFS architecture, the sine/cosine generator produces sinusoidal waves based on the output of the radian converter. Without loss of

input

| 1-bit shifter | 2-bit shifter | 5-bit shifter | 8-bit shifter | 12-bit shifter | 18-bit shifter |

CSA(3,2)   CSA(3,2)

CSA(4,2)

CLA
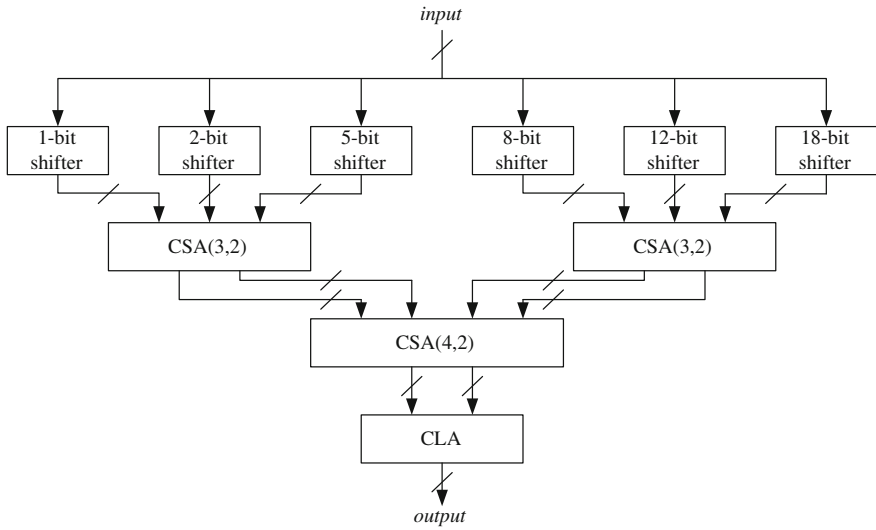
output

Fig. 23.4 Constant ($\pi/4$) multiplier

Fig. 23.5 $\pi/4$-mirror map of an angle γ above $\pi/4$ to the corresponding angle $\pi/2 - \gamma$ below $\pi/4$
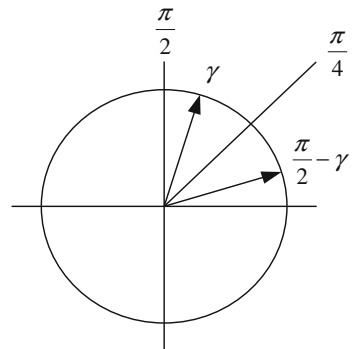
generality, let the output resolution be of 16 bits, for the sine/cosine generator consisting of a cascade of w processors, each of which performs the sub-rotation by a fixed angle of 2^{-i} radian as follows:

$$x(i+1) = (1 - \sigma(i)2^{-(2i+1)})x(i) + \sigma(i)2^{-i}y(i); \tag{23.16}$$

$$y(i+1) = (1 - \sigma(i)2^{-(2i+1)})y(i) - \sigma(i)2^{-i}x(i). \tag{23.17}$$

For $8 \leq i < 16$, we have

$$x(i+1) = x(i) + \sigma(i)2^{-i}y(i); \tag{23.18}$$

Fig. 23.6 CORDIC processor-A
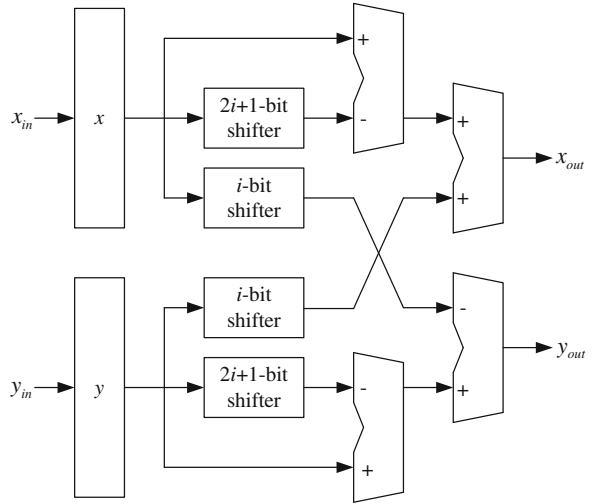
Fig. 23.7 CORDIC processor-B
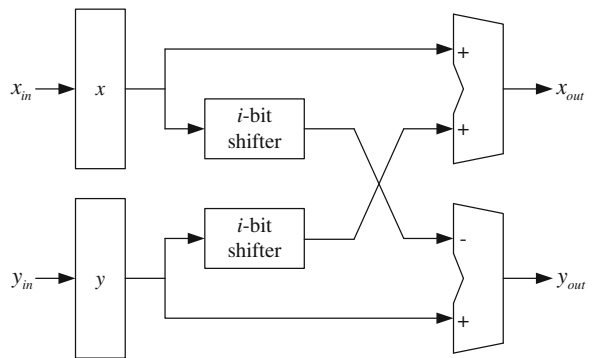
$$y(i + 1) = y(i) - \sigma(i)2^{-i}x(i), \tag{23.19}$$

where $\sigma(i) \in \{1, 0\}$ representing the positive or zero sub-rotation, respectively. Figure 23.6 depicts the CORDIC processor-A for the first 7 micro-rotations, which consists of four 16-bit adders and four 16-bit shifters. The CORDIC processor-B with two 16-bit adders and two 16-bit shifters for the last 9 micro-rotations is shown in Fig. 23.7.

The first m CORDIC stages can be replaced by simple LUT to reduce the data path at the cost of hardware complexity increasing exponentially. Table 23.1 depicts the hardware costs in 16-bit DDFS with respect to the number of the replaced CORDIC-stages, where each 16-bit adder, 16-bit shifter, and 1-bit memory require 200 gates, 90 gates, and 1 gate [36], respectively. Figure 23.8 shows the hardware requirements with respect to the number of the replaced CORDIC-stages [24]. Figure 23.9 shows the SFDR/SNRs with respect to the replaced CORDIC-stages

Table 23.1 The hardware costs in 16-bit DDFS with respect to the number of the replaced CORDIC-stages (*m*: the number of the replaced CORDIC-stages, 16-bit adder: 200 gates, 16-bit shift: 90 gates and 1-bit ROM: 1 gate)

m	0	1	2	3	4	5	6	7
CORDIC Processor requirement								
CORDIC Processor-A	7	5	4	3	2	1	0	0
CORDIC Processor -B	9	9	9	9	9	9	9	8
Hardware cost								
16-bit adders	46	38	34	30	26	22	18	16
16-bit shifters	46	38	34	30	26	22	18	16
ROM size (bits)	4×16	8×16	14×16	26×16	50×16	102×16	194×16	386×16
Total gate counts	13404	11148	10084	9116	8340	8012	8324	10816
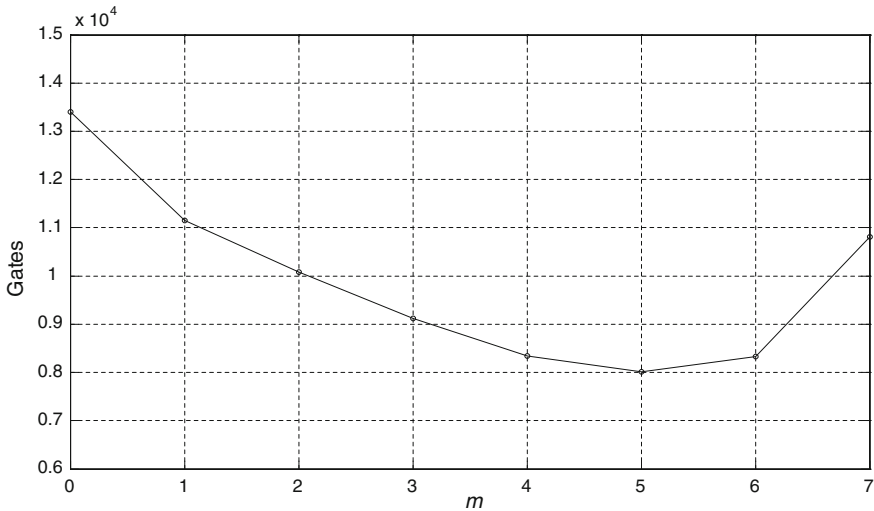
Fig. 23.8 Hardware requirements with respect to the replaced CORDIC-stages

[25]. As one can expect, based on the above figures, there is a trade-off between hardware complexity and performance in the design of DDFS.

23.3.4 Output Stage

Figure 23.10 shows the architecture of output stage, which maps the computed sin θ and cos θ to the desired sin ϕ and cos ϕ. As mentioned previously, the above mapping can be accomplished by simple negation and/or interchange operations. The three control signals: *xinv*, *yinv*, and *swap* derived from the first three MSBs of
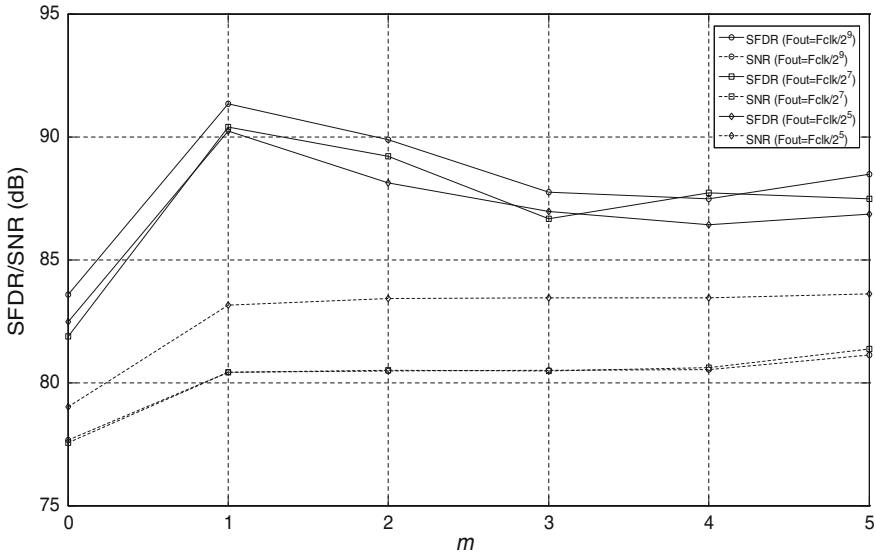
Fig. 23.9 SFDR/SNRs with respect to the replaced CORDIC-stages

Fig. 23.10 Output stage
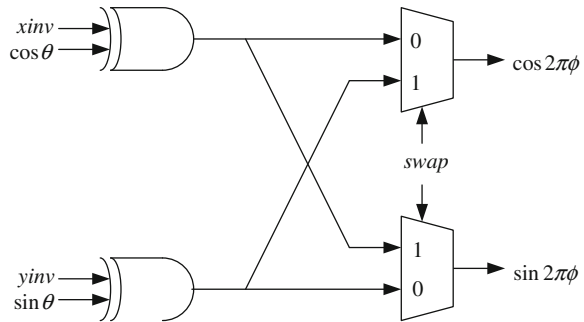
ϕ are shown in Table 23.2. *xinv* and *yinv* are for the negation operation of the output; and *swap* for the interchange operation.

23.4 Hardware Implementation of the Scaling-Free-CORDIC-Based DDFS

In this section, the proposed low-power and high-performance DDFS architecture ($m = 5$) is presented. Figure 23.11 depicts the system block diagram; SFDR of the proposed DDFS architecture at output frequency $F_{clk}/2^5$ is shown in Fig. 23.12. As one can see, the SFDR of the proposed architecture is more than 86.85 dBc.

Table 23.2 Control signals of the output stage

MSB's of ϕ			ϕ	$xinv$	$yinv$	$swap$	$\cos 2\pi\phi$	$\sin 2\pi\phi$
0	0	0	$0 < 2\pi\phi < \frac{\pi}{4}$	0	0	0	$\cos\theta$	$\sin\theta$
0	0	1	$\frac{\pi}{4} < 2\pi\phi < \frac{\pi}{2}$	0	0	1	$\sin\theta$	$\cos\theta$
0	1	0	$\frac{\pi}{2} < 2\pi\phi < \frac{3\pi}{4}$	0	1	1	$-\sin\theta$	$\cos\theta$
0	1	1	$\frac{3\pi}{4} < 2\pi\phi < \pi$	1	0	0	$-\cos\theta$	$\sin\theta$
1	0	0	$-\pi < 2\pi\phi < -\frac{3\pi}{4}$	1	1	0	$-\cos\theta$	$-\sin\theta$
1	0	1	$-\frac{3\pi}{4} < 2\pi\phi < -\frac{\pi}{2}$	1	1	1	$-\sin\theta$	$-\cos\theta$
1	1	0	$-\frac{\pi}{2} < 2\pi\phi < -\frac{\pi}{4}$	1	0	1	$\sin\theta$	$-\cos\theta$
1	1	1	$-\frac{\pi}{4} < 2\pi\phi < 0$	0	1	0	$\cos\theta$	$-\sin\theta$
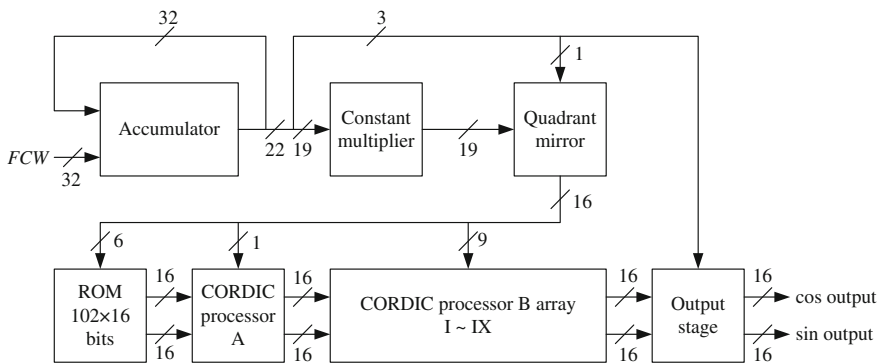
Fig. 23.11 Proposed DDFS architecture

The platform for architecture development and verification has also been designed as well as implemented to evaluate the development cost [37–40]. The proposed DDFS architecture has been implemented on the Xilinx FPGA emulation board [41]. The Xilinx Spartan-3 FPGA has been integrated with the microcontroller (MCU) and I/O interface circuit (USB 2.0) to form the architecture development and verification platform.

Figure 23.13 depicts block diagram and circuit board of the architecture development and evaluation platform. In which, the microcontroller read data and commands from PC and writes the results back to PC via USB 2.0 bus, the Xilinx Spartan-3 FPGA implements the proposed DDFS architecture. The hardware code in Verilog® runs on PC with the ModelSim simulation tool [42] and Xilinx ISE smart compiler [43]. It is noted that the throughput can be improved by using the proposed architecture while the computation accuracy is the same as that obtained by using the conventional one with the same word length. Thus, the proposed DDFS architecture is able to improve the power consumption and computation
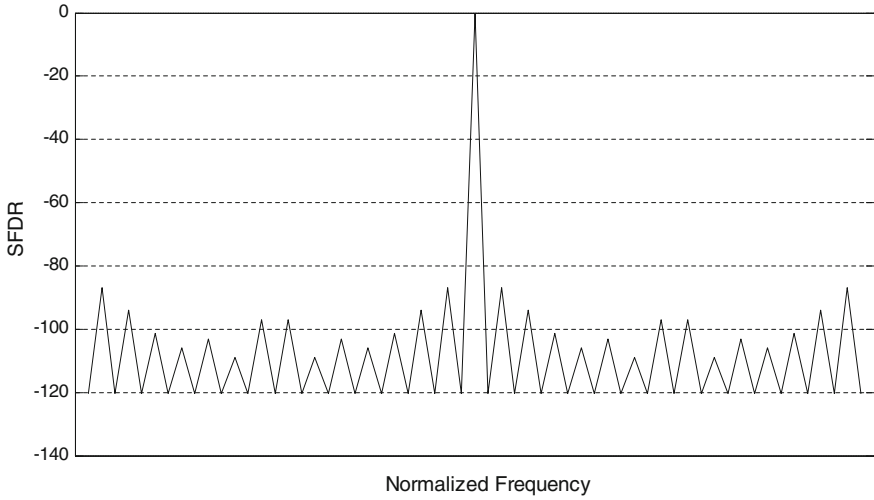
Fig. 23.12 SFDR of the proposed DDFS architecture at output frequency $F_{clk}/2^5$
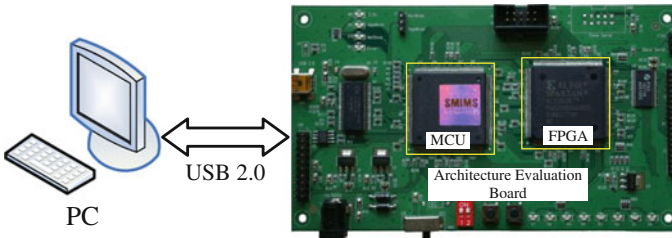
Fig. 23.13 Block diagram and circuit board of the architecture development and verification platform

speed significantly. Moreover, all the control signals are internally generated on-chip. The proposed DDFS provides both high performance and less hardware.

The chip has been synthesized by using the TSMC 0.18 μm 1P6 M CMOS cell libraries [44]. The physical circuit has been synthesized by the Astro® tool. The circuit has been evaluated by DRC, LVS, and PVS [45]. Figure 23.14 shows the cell-based design flow.

Figure 23.15 shows layout view of the proposed scaling-free CORDIC based DDFS. The core size obtained by the Synopsys® design analyzer is 452×452 μm^2. The power consumption obtained by the PrimePower® is 0.302 mW with clock rate of 500 MHz at 1.8 V. The tuning latency is 11 clock cycles. All of the control signals are internally generated on-chip. The chip provides both high throughput and low gate count.

```
┌──────────────┐     ┌──────────────┐     ┌──────────────┐     ┌──────────────┐
│              │     │  Functional  │     │ Hardware code│     │Comprehensive │
│  Algorithm   │────▶│  simulation  │────▶│implementation│────▶│ simulation & │
│              │     │   (Matlab)   │     │  (Verilog)   │     │    debug     │
│              │     │              │     │              │     │  (ModelSim)  │
└──────────────┘     └──────────────┘     └──────────────┘     └──────────────┘
                                                                       │
                                                                       ▼
┌──────────────┐     ┌──────────────┐     ┌──────────────┐     ┌──────────────┐
│CKT evaluation│     │   Physical   │     │Logic synthesis│    │ CKT tracing  │
│ (DRC/LVS/PVS)│◀────│ compilation  │◀────│  (Design     │◀────│  (Debussy)   │
│              │     │   (Astro)    │     │  Compiler)   │     │              │
└──────────────┘     └──────────────┘     └──────────────┘     └──────────────┘
       │
       ▼
   Tape out
```
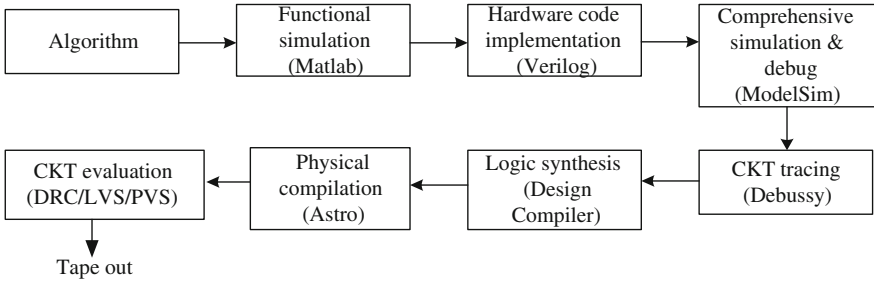
Fig. 23.14 Cell-based design flow

Fig. 23.15 Layout view of
the proposed scaling-free-
CORDIC-based DDFS
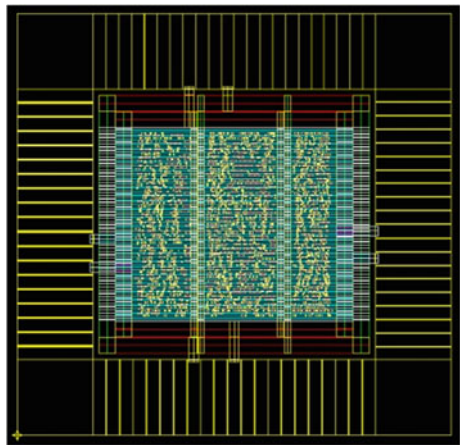
Table 23.3 Comparisons of the proposed DDFS with other related works

DDFS	Kang and Swartzlander (2006), [20]	Sharma et al. (2009), [23]	Jafari et al. (2005), [14]	Ashrafi and Adhami (2007), [15]	Yi et al. (2006), [3]	De Caro et al. (2009), [24]	This work, Juang et al. (2013)
Process (μm)	0.13	–	0.5	0.35	0.35	0.25	0.18
Core area (mm^2)	0.35	–	–	–	–	0.51	0.204
Maximum sampling rate (MHz)	1018	230	106	210	100	385	500
Consumption (mW)	0.343	–	–	112	0.81	0.4	0.302
SFDR (dBc)	90	54	–	72.2	80	90	86.85
SNR (dB)	–	–	–	67	–	70	81.12
Output resolution (bit)	17	10	14	12	16	13	16
Tuning latency (clock)	–	–	33	–	–	–	11

23.5 Conclusion

In this paper, we present a novel DDFS architecture based on the scaling-free CORDIC algorithm with small ROM and pipeline data path. Circuit emulation shows that the proposed high performance architecture has the advantages of high precision, high data rate, and simple hardware. For 16-bit DDFS, the SFDR of the proposed architecture is more than 86.85 dBc. As shown in Table 23.3, the proposed DDFS is superior to the previous works in terms of SFDR, SNR, output resolution, and tuning latency [6, 17, 18, 26, 27]. According to the high performance of the proposed DDFS, it is very suited for underwater instruments and network systems [46–49]. The proposed DDFS with the use of the portable Verilog® is a reusable IP, which can be implemented in various processes with trade-offs of performance, area and power consumption.

References

1. J. Tierney, C. Rader, B. Gold, IEEE Trans. Audio Electroacoust. **19**(1), 48 (1971)
2. S. Chen, M. Zhao, G. Wu, C. Yao, J. Zhang, Comput. Math. Methods Med. **2012**, 101536 (2012)
3. Z. Teng, A.J. Degnan, U. Sadat et al., J. Cardiovasc. Magn. Reson. **13**, 64 (2011)
4. S. Chen, X. Li, Comput. Math. Methods Med. **2012**, AID 613465 (2012)
5. J. Vankka, *IEEE Proceedings of the Frequency Control Symposium*, p. 942, June 1996
6. S.C. Yi, K.T. Lee, J.J. Chen, C.H. Lin, *IEEE Canadian Conference on Electrical and Computer Engineering,* p. 963, May 2006
7. D.A. Sunderland, R.A. Srauch, S.S. Wharfield, H.T. Peterson, C.R. Cole, IEEE J. Solid-State Circ. **19**(4), 497 (1984)
8. H.T. Nicholas, H. Samueli, B. Kim, *IEEE 42nd Annual Frequency Control Symposium*, p. 357, June 1988
9. L.A. Weaver, R.J. Kerr, *High resolution phase to sine amplitude conversion,* U.S. Patent 4 905 177 (1990)
10. A. Bonfanti, D. De Caro, A.D. Grasso, S. Pennisi, S.C. Samori, A.G.M. Strollo, IEEE J. Solid-State Circ. **43**(6), 1403 (2008)
11. A. Bellaouar, M.S. O'Brecht, A.M. Fahim, M.I. Elmasry, IEEE J. Solid-State Circ. **35**(3), 385 (2000)
12. A. Bellaouar, M.S. O'Brecht, M.I. Elmasry, *Low-power direct digital frequency synthesizer architecture,* U.S. Patent 5 999 581 (1999)
13. M.M. El Said, M.I. Elmasry, IEEE Int. Symp. Circuits Syst. **5**, 437 (2002)
14. G.C. Gielis, R. Van de Plassche, J. Van Valburg, IEEE J. Solid-State Circ. **26**(11), 1645 (1991)
15. D. De Caro, E. Napoli, A.G.M. Strollo, IEEE Trans. Circ. Syst. II Express Briefs **51**(7), 337 (2004)
16. Y.H. Chen, Y.A. Chau, IEEE Trans. Consum. Electron. **56**(2), 436 (2010)
17. H. Jafari, A. Ayatollahi, S. Mirzakuchako, *IEEE Conference on Electron Devices and Solid-State Circuits*, p. 829 (2005)
18. A. Ashrafi, R. Adhami, IEEE Trans. Circ. Syst. I Regul. Pap. **54**(10), 2252 (2007)
19. S. Nahm, K. Han, W. Sung, IEEE Int. Symp. Circ. Syst. **4**, 385 (1998)
20. A. Madisetti, A.Y. Kwentus, A.N. Willson, IEEE J. Solid-State Circ. **34**, 1034 (1999)
21. A. Madisetti, A.Y. Kwentus, *Method and apparatus for direct digital frequency synthesizer*, U.S. Patent 5 737 253 (1998)
22. E. Grayver, B. Daneshrad, IEEE Int. Symp. Circ. Syst. **5**, 241 (1998)
23. C.Y. Kang, E.E. Swartzlander Jr, IEEE Trans. Circ. Syst. I Regul. Pap. **53**(5), 1035 (2006)
24. T.Y. Sung, H.C. Hsin, IET Comput. Digital Tech. **1**(5), 581 (2007)
25. T.Y. Sung, L.T. Ko, H.C. Hsin, IEEE International Symposium on Circuits and Systems, p. 249, May 2009
26. S. Sharma, P.N. Ravichandran, S. Kulkarni, M. Vanitha, P. Lakshminarsimahan, *International Conference on Advances in Recent Technologies in Communication and Computing*, p. 266, October 2009
27. D. De Caro, N. Petra, A. Strollo, IEEE Trans. Circ. Syst. I Regul. Pap. **56**(2), 364 (2009)
28. J. Volder, IRE Trans. Electron. Comput. **EC-8**(3), 330 (1959)
29. J.S. Walther, *Proceedings of the Spring Joint Computer Conference*, p. 379 May 1971
30. S. Chen, W. Huang, C. Cattani, G. Altieri, Math. Prob. Eng. **2012**, 732698 (2012)
31. W. Huang, S.Y. Chen, J. Stat. Mech: Theory Exp. (JSTAT) **2011**(12), P12004 (2011)
32. H. Shi, W. Wang, N.M. Kwok, S.Y. Chen, Sensors **12**(7), 9055 (2012)
33. C. Cattani, S.Y. Chen, G. Aldashev, Math. Prob. Eng. **2012**, AID 868413 (2012)
34. Y.H. Hu, IEEE Sig. Process. Mag. **9**(3), 16 (1992)
35. K. Maharatna, A.S. Dhar, S. Banerjee, Sig. Process. **81**(9), 1813 (2001)
36. T.Y. Sung, IEE Proc. Vis. Image Sig. Process. **53**(4), 405 (2006)

37. C. Cattani, Comput. Math. Methods Med. **2012**, AID 673934 (2012)
38. M. Li, Comput. Math. Methods Med. **2012** (2012)
39. S. Chen, Y. Zheng, C. Cattani, W. Wang, Comput. Math. Methods Med. **2012**, 769702 (2012)
40. C. Cattani, Telecommun. Syst. Spec. Issue Traffic Model. Comput. Appl. **2009**, 207 (2009)
41. http://www.smims.com. Accessed SMIMS Technology Corp (2010)
42. http://model.com/content/modelsim-pe-simulation-and-debug. Accessed ModelSim– Simu-
    lation and Debug (2010)
43. http://www.xilinx.com/products/. Accessed Xilinx FPGA Products (2010)
44. TSMC (Taiwan Semiconductor Manufacturing Company), Hsinchu City, Taiwan, and CIC
    (National Chip Implementation Center), National Science Council, Hsinchu City, Taiwan:
    TSMC 0.18 CMOS Design Libraries and Technical Data, v.1.6 (2010)
45. http://www.cadence.com/products/pages/default.aspx. Accessed Cadence Design Systems
    (2010)
46. D. Prutchi, V.M. Norris, *Design and Development of Medical Electronic Instrumentation: A
    Practical Perspective of the Design, Construction, and Test of Medical Devices* (Wiley,
    Hoboken, 2005). doi: 10.1002/0471681849
47. N. Li, J. Guo, H.S. Nie, W. Yi, H.J. Liu, H. Xu, Appl. Mech. Mater. **136**, 396 (2011)
48. K.H. Lin, W.H. Chiu, J.D. Tseng, Comput. Math. Appl. **64**(5), 1400 (2012)
49. J. Guo, P. Dong, Lect. Electr. Eng. **139**, 7 (2012)

Chapter 24
Hilbert-Huang Transform Based Instantaneous Frequency Features for Underwater Voice (I) Transmission

C. F. Lin, K. J. Hsiao, C. C. Wen, S. H. Chang and I. A. Parinov

This paper examines the features of a Hilbert-Huang transform instantaneous frequency for application in underwater voice (I) transmissions. The duration and sampling frequency of the voice (I) sample were 5 s, and 8000 Hz, respectively. The voice (I) sample was inputted into a Matlab-based direct mapping orthogonal variable spreading factor/orthogonal frequency division modulation underwater multimedia communication platform. An underwater actual test channel model was employed in the proposed Matlab-based platform. Applying Hilbert-Huang time–frequency analysis to investigate the IF features of the received voice (I) signal resulted in transmission bit error rates of 0, 10^{-4}, 10^{-3}, 10^{-2} and 10^{-1}. The mean frequencies of the voice sample (I) signal for IF2 were 646.6, 644, 648.3, 625.2, and 669.0 Hz, respectively, for the transmission bit error rates of 0, 10^{-4}, 10^{-3}, 10^{-2} and 10^{-1}. The mean frequencies of the voice sample (I) signal for IF2 were 2.6, -3.7, 21.1 and 22.4 Hz, respectively, for the transmission bit error rates of 10^{-4}, 10^{-3}, 10^{-2} and 10^{-1}.

C. F. Lin (✉) · K. J. Hsiao
Department of Electrical Engineering, National Taiwan Ocean University, Keelung, Republic of China (Taiwan)
e-mail: lcf1024@mail.ntou.edu.tw

C. C. Wen
Department of Shipping Technology, National Kaohsiung Marine University, Kaohsiung, Republic of China (Taiwan)
e-mail: wencc@webmail.nkmu.edu.tw

S. H. Chang
Department of Microelectronics Engineering, National Kaohsiung Marine University, Kaohsiung, Republic of China (Taiwan)
e-mail: shchang@webmail.nkmu.edu.tw

I. A. Parinov
Vorovich Mechanics and Applied Mathematics Research Institute, Southern Federal University, Rostov-on-Don, Russia
e-mail: ppr@math.rsu.ru

24.1 Introduction

Underwater voice transmission is a worthy research topic. Quazi et al. [1], developed an underwater telephone in 1945, and Sari et al. [2], investigated the digital underwater speech communication scheme. Previous studies have proposed the direct-mapping orthogonal variable spreading factor (OVSF) [3], multi-input multi-output orthogonal frequency division modulation (OFDM) underwater multimedia communication scheme [4], and Hilbert-Huang transform (HHT) time–frequency analysis for biomedical signals [5–7]. The intrinsic mode function (IMF) features of the HHT underwater voice (I) transmission were discussed in [8]. The current study, examines HHT instantaneous frequency (IF) and its features for underwater voice (I) transmission. The simulation architecture is shown in Fig. 24.1. The voice sample (I) was inputted into a G.729 encoder. The duration and sampling frequency of the voice (I) sample were 5 s, and 8000 Hz, respectively. The G.729 voice sample (I) bit streams were extracted as outputs, that were then inputted into the Matlab-based direct-mapping OFDM underwater communication platform and G.729 decoder for extracting and decoding the recorded voice sample (I) as an output. An underwater actual test channel model [9] was employed in the Matlab-based platform. The transmission distance, carrier central frequency, and underwater channel bandwidth were 1 km, 11.5 and 4 kHz, respectively. A 2×2 direct-mapping strategy, binary phase shift keying modulation, and $K = 9$ 1/2 (561,753) convolution codes with soft decoding [10] were used in the Matlab-based platform. The fixed adaptive white Gaussian noise, and the transmission power were adjusted to achieve transmission bit error rates of 0, 10^{-4}, 10^{-3}, 10^{-2} and 10^{-1}.

24.2 The Instantaneous Frequency Features for Voice Sample (I)

The parameter of the refereed total energy is defined as follows:

$$E = \sum_{i=1}^{N} E_{imf_i} + E_{rf}, \tag{24.1}$$

where E_{imf_i} is the energy of the i-th intrinsic mode function (IMF), E_{rf_i} is the energy of the i-th residual function (RF).

According to our analysis, the ratios of the energy of the voice sample (I) to its refereed total energy for IMF1, IMF2, IMF3, and IMF4 were 32.10, 34.98, 18.94, and 11.00 %, respectively. Furthermore, the ratios of the energy of the voice sample (I) to its refereed total energy for IMF1, IMF2, IMF3, and IMF4 were 31.82, 34.95, 18.96, and 11.18 %, respectively, at the transmission bit error rate of 10^{-3}. The IFs for the voice sample (I) signal of the transmission bit error rate of 0
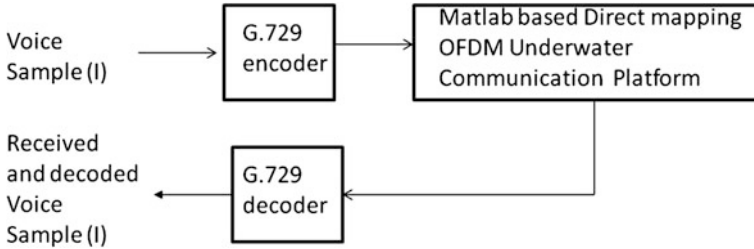
Fig. 24.1 The simulation architecture for the proposed system
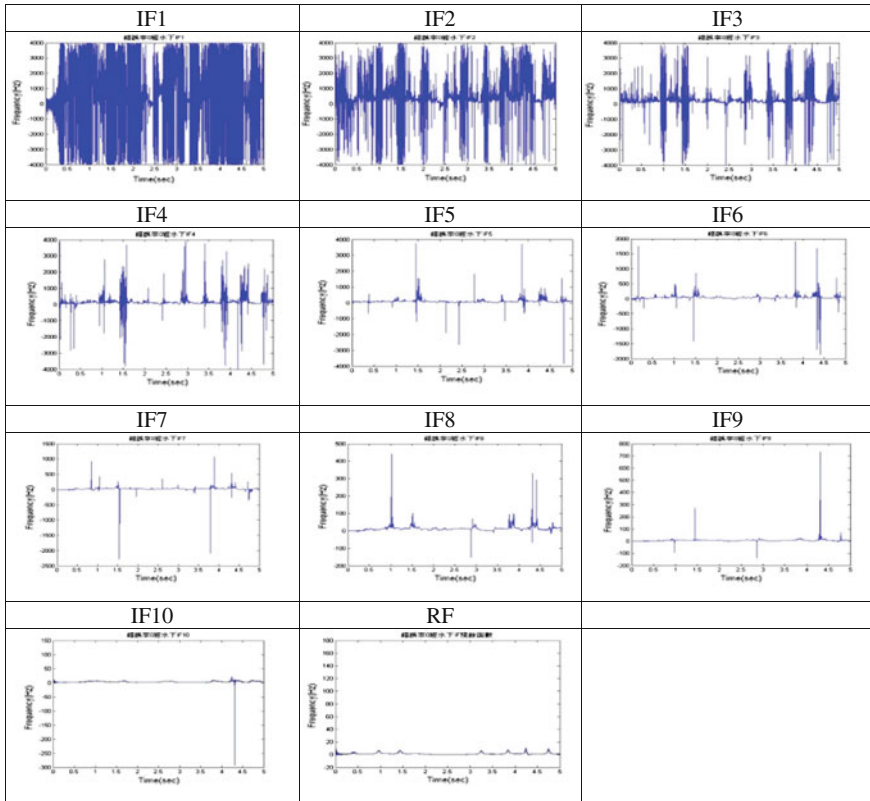
Fig. 24.2 The IFs for the voice sample (I) signal of the transmission bit error rate of 0

and 10^{-3}, respectively, are shown in Figs. 24.2 and 24.3. Table 24.1 shows the statistical characteristics of the IFs for the voice sample (I) signal of the transmission bit error rates of 0, 10^{-4}, 10^{-3}, 10^{-2} and 10^{-1}. The mean frequencies of the voice sample (I) signal for IF1, in the transmission bit error rates of 0, 10^{-4},
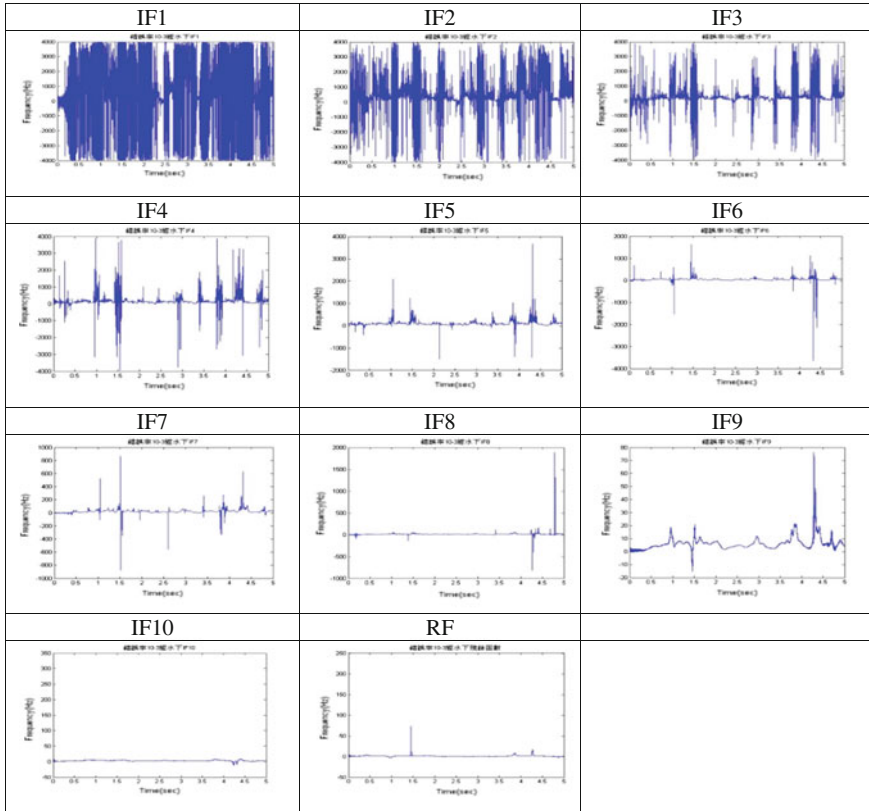
Fig. 24.3 The IFs for the voice sample (I) signal of the transmission bit error rate of 10^{-3}

10^{-3}, 10^{-2} and 10^{-1}, respectively, were 1323.3, 1321.3, 1319.7, 1359.3, and 1560.6 Hz. The mean frequencies of the voice sample (I) signal for IF2, in the transmission bit error rates of 0, 10^{-4}, 10^{-3}, 10^{-2} and 10^{-1}, respectively, were 646.6, 644, 648.3, 625.2, and 669.0 Hz. The mean frequencies of the voice sample (I) signal for IF3, in the transmission bit error rates of 0, 10^{-4}, 10^{-3}, 10^{-2} and 302.4, 299.8, 300.4, 329.1, and 330.5 Hz. The mean frequencies of the voice sample (I) signal for IF4, in the transmission bit error rates of 0, 10^{-4}, 10^{-3}, 10^{-2} and 10^{-1}, respectively, were 169.9, 169.3, 167.9, 164.9, and 163.2 Hz. Compared with the mean frequencies of the voice sample (I) signal for IF2, that of the transmission bit error rates of 10^{-4}, 10^{-3}, 10^{-2} and 10^{-1}, respectively, were 2.6, − 3.7, 21.1 and 22.4 Hz.

Table 24.1 The statistical characteristics of the IFs for the voice sample (I) signal of the transmission bit error rates of 0, 10^{-4}, 10^{-3}, 10^{-2} and 10^{-1}, respectively

	Mean (Hz)	Max (Hz)	Min (Hz)	Std (Hz)
IF1, BER = 0	1323.3	3998.9	−4000	1787.1
IF1, BER = −4	1321.3	4000	−3999.5	1761.2
IF1, BER = −3	1319.7	3999.9	−3999.8	1827.2
IF1, BER = −2	1359.3	4000	−3999.9	1812.4
IF1, BER = −1	1560.6	3999.7	−3999.5	1666.4
IF2, BER = 0	646.6	3994	−3997.8	762.3
IF2, BER = −4	644	3997.9	−3998.8	762.4
IF2, BER = −3	648.3	3989.7	−3999.6	765.9
IF2, BER = −2	625.2	3994.8	−3999.7	764.2
IF2, BER = −1	669	3993.1	−3996.6	678.7
IF3, BER = 0	302.4	3992.2	−3986.4	361.1
IF3, BER = −4	299.8	3994.8	−3968	371
IF3, BER = −3	300.4	3963.1	−3976.3	372.8
IF3, BER = −2	329.1	3984.7	−3968.2	375.2
IF3, BER = −1	330.5	3781.6	−3992.5	300.7
IF4, BER = 0	169.9	3925.9	−3981.1	182
IF4, BER = −4	169.3	3962	−3916	180.1
IF4, BER = −3	167.9	3869.3	−3939.4	181.7
IF4, BER = −2	164.2	3911.2	−3491.7	183.5
IF4, BER = −1	163.2	3924.1	−3809.3	161.6

24.3 Conclusion

This paper investigated the HHT IF features for a received voice (I) signal with transmission bit error rates of 0, 10^{-4}, 10^{-3}, 10^{-2} and 10^{-1}. With variations in the transmission bit error rate, the statistical characteristics of the IFs varied. The HHT IF features for the received voice (I) signal with the transmission bit error rate of 0 were similar to the features of the bit error rates of 10^{-4}, 10^{-3}, etc., respectively.

References

1. A.H. Quazi, W.L. Konrad, IEEE Commun. Mag. **20**(2), 24 (1982)
2. H. Sari, B. Woodward, in *Underwater Acoustic Digital Signal Processing and Communication Systems*, ed. by R.S.H. Istepanian, M. Stojanovic (Kluwer Academic Publishers, New York, 2002), p. 127
3. C.F. Lin, J.Y. Chen, Y.J. Yu, J.T. Yan, S.H. Chang, J. Mar. Sci. Technol. **18**(3), 413 (2010)
4. C.F. Lin, S.H. Chang, W.C. Wu, W.H. Chen, K.H. Chang, C.Y. Lee Jenny, I.A. Parinov, Wireless Pers. Commun. **71**(2), 1231 (2013)

5. C.F. Lin, J.D. Zhu, Proc. Inst. Mech. Eng. [H] **226**, 208 (2012)
6. C.F. Lin, S.W. Yeh, S.H. Chang, T.I. Peng, Y.Y. Chien, *An HHT-Based Time-Frequency Scheme for Analyzing the EEG Signals of Clinical Alcoholics* (Nova Science Publishers, New York, 2010). Online Book
7. C.F. Lin, B.H. Yang, T.I. Peng, S.H. Chang, Y.Y. Chien, J.H. Wang, in *Advance in Telemedicine: Technologies, Enabling Factors and Scenarios*, ed. by G. Graschew, Theo A. Roelofs (Intech Science Publishers, Austria, 2011), p. 149
8. C.F. Lin, K.J. Hsiao, J.D. Zhu, C.C. Wen, S.H. Chang, I.A. Parinov , in *Proceedings of The 15th Underwater Technology Conference*, Keelung, Taiwan (2013)
9. J. Tao, Y.R. Zheng, C. Xiao, T.C. Yang, W.B. Yang, in *Proceedings of International Conference 'OCEANS'08 MTS/IEEE, Kobe* (2008)
10. Technical specification group radio access network—Multiplexing and channel coding (FDD), 3rd Generation Partnership Project (3GPP), p. **7**25 (2007)

Chapter 25
An Improved Dark Channel-Based Algorithm for Underwater Image Restoration

Po-Fang Chen, Jun-Kai Guo, Chia-Chi Sung and Herng-Hua Chang

Underwater imaging is crucial to a wide variety of research and realistic applications in marine biology, water fauna identification and assessment, archaeology, mine detection, oceanic mapping, and autonomous underwater robotics. However, due to specific propagation properties of light in water such as absorption and scattering as well as unstable environment such as light changing and water turbidness, the images captured are highly disturbed with low contrast, blurring, darkness, and color diminishing. This paper proposes a new underwater image restoration algorithm that consists of three major phases: haze removal, color correction, and contrast enhancement. To estimate the transmission coefficient function, we first compute the dark channel map, which is the set of "dark" pixels having very low intensity values in at least one RGB color channel. To accommodate the blue color distortion phenomenon, the red channel value is excluded from the calculation if the peak histogram intensity is smaller than a specified threshold. To optimize the medium transmission map, we adopt the matting Laplacian matrix associated with the sparse linear system to generate a cost function, followed by the guided filtering method to accelerate the computation. Finally, the contrast limited adaptive histogram equalization method is used to enhance the contrast while maintaining the color fidelity. We have applied this new approach to a wide variety of underwater images. Experimental results indicated that this new method is of potential in facilitating the interpretation and perception of underwater images in the fields of ocean engineering, ocean biology, and ocean science.

P.-F. Chen · J.-K. Guo · C.-C. Sung · H.-H. Chang (✉)
Department of Engineering Science and Ocean Engineering, National Taiwan University,
1 Sec. 4, Roosevelt Road, Daan, Taipei 10617, Republic of China (Taiwan)
e-mail: herbertchang@ntu.edu.tw

25.1 Introduction

In recent years, there has been an increasing number of research interest in using underwater remotely operated vehicles (ROVs) and autonomous underwater vehicles (AUVs) for ocean engineering, surveillance, and navigation [1, 2]. These underwater vehicles are typically equipped with optical sensors and/or acoustic sensors for acquiring underwater images. Underwater imaging is crucial to a wide variety of research and realistic applications in marine biology, water fauna identification and assessment, archaeology, mine detection, oceanic mapping, and autonomous underwater robotics [3, 4]. However, due to specific propagation properties of light in water such as absorption and scattering as well as unstable environment such as light changing and water turbidness, the images captured are highly disturbed with low contrast, blurring, darkness, and color diminishing [5–7]. In consequence, the need of restoration of underwater images is fundamental for compensating attenuation effects, increasing image resolution, and retrieving better color balancing.

Many researchers have proposed different approaches to investigate the characteristics of underwater images. The challenge is to obtain clear and color-corrected scene while maintaining detail textures that are important to the interpretation of the images. Pioneering work in underwater optics was developed back in the 1960s by Duntley [8], who initiated the research at the Massachusetts Institute of Technology and pursued at the Visibility Laboratory of the Scripps Institute of Oceanography. He first defined the basic limitations of underwater imaging and has become the foundation of subsequent works. Further experiments in underwater imaging were performed at the Scripps Visibility Laboratory and other research groups in the 1970s. One well-known underwater image formation model has been developed by the Jaffe and McGlamery in the 1990s. McGlamery [9] laid out the theoretical foundations of the optical properties of the light propagation in water while Jaffe [10] extended the image formation model and applied it to design different subsea image acquisition systems. Subsequently, a simplified version of the Jaffe-McGlamery model was proposed by Trucco and Olmos-Antillon [11] to design a self-tuning restoration algorithm without covering a wide spectrum of imaging conditions.

Other research works addressing image formation in underwater image processing include: Li et al. [12] presented a photogram-metric model based on a 3-D optical ray tracing technique which rigorously models imaging systems with multi-lens configurations and multiple refractions. Negahdaripour [13] proposed a general framework to decouple different changes induced by illumination and motion in image intensity. Narasimhan et al. [14] derived physical models for the analysis of light stripe range scanning and photometric stereo in a scattering medium. Hou et al. [15] extended traditional restoration methods by incorporating underwater optical properties into two system response functions namely the point spread function in the spatial domain and modulation transfer function in the frequency domain. Petit et al. [16] described a method based on light attenuation

Fig. 25.1 Flow chart of the proposed algorithm
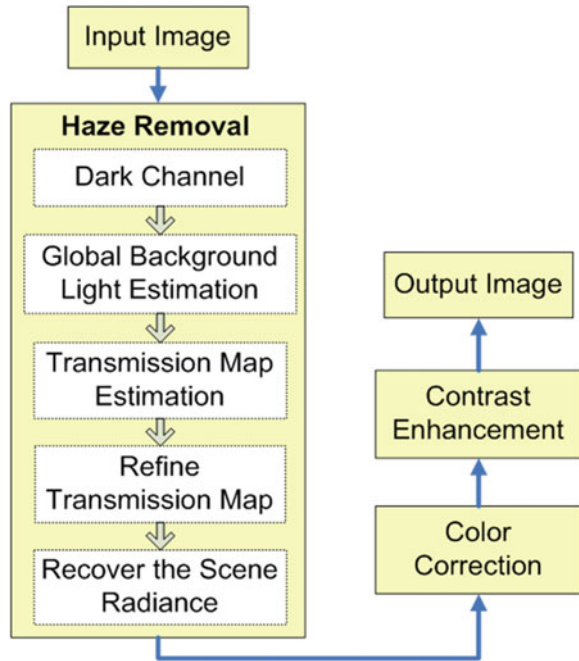
inversion after processing a color space contraction using quaternions. Chao and Wang [1] proposed an efficient restoration method based on the estimation of the depth of the turbid water using a dark channel priori. The ambition of this paper is in an attempt to develop a more effective underwater image restoration system that consists of a series of specific image processing algorithms: haze removal, color correction, and contrast enhancement.

25.2 Methods

Figure 25.1 illustrates the flow chart of the proposed underwater image restoration algorithm. In our approach, the image $I(x)$ that we eventually perceived from the camera can be expressed as

$$I(x) = J(x)t(x) + B(1 - t(x)) \tag{25.1}$$

where $J(x)$ is the scene radiance of the original image, $t(x)$ is the medium transmission coefficient describing the portion of the light that is not backward scattered and reaches the camera, and B is the background light source. In (25.1), the transmission coefficient is an exponentially decayed function with respect to the distance using

$$t(x) = e^{-\eta d_p(x)} \tag{25.2}$$

where η is the attenuation coefficient mainly due to absorption energy decay and $d_p(x)$ is the distance to the target object, which depends on the pixel coordinates (x).

To facilitate the process, we will first find J from (25.1) assuming J the target scene radiance we would like to recover and introducing the dark channel prior [17]. The dark channel prior is based on the statistics of water-free images in our case. It is observed that in most of underwater image patches, there exist some pixels (called "dark" pixels) having very low intensity values in at least one color channel, namely,

$$I_{dark}(x) = \min_{y \in \rho(x)} \left(\min_c I_c(y) \right) \tag{25.3}$$

where I_{dark} is the dark channel of I, I_c is a color channel in RGB, and $\rho(x)$ is a local patch centered at (x). To accommodate the blue color phenomena in most underwater images, the color channel is adaptively selected as follows. In the red channel, if more than s % of the intensity histogram values are below p, $c \in \{g, b\}$, otherwise, $c \in \{r, g, b\}$. After obtaining the dark channel I_{dark}, the background light source B is computed by superimposing the brightest 0.1 % pixels on the input image I.

We assume the transmission in a local patch $\rho(x)$ is constant and denote the corresponding patch transmission coefficient as $t_0(x)$. Taking the min operation in the local patch of underwater images in (25.1) independently for each color channel and divided by B, we obtain

$$t_0(x) = 1 - \varphi \min_{y \in \rho(x)} \left(\min_c \frac{I_c(y)}{B_c} \right) \tag{25.4}$$

where φ is a coefficient used to adjust the opacity of the restored image. Finally, the target scene radiance $J(x)$ is recovered using

$$J(x) = \frac{I(x) - B}{\max(t(x), t_{low})} + B \tag{25.5}$$

where t_{low} is a threshold used to prevent distortion from very low transmission coefficients.

To handle the color distortion problem, we directly work on the each individual channel using

$$J_{e_c}(x) = J_c(x) + (mean_w - J_{mean_c}) \tag{25.6}$$

where J_c is the color component of J in RGB, $J_{mean\ c}$ is the mean intensity of J in each color channel, $mean_w$ is the desired mean intensity, and J_e is the restored image. In the last phase, we use the CLAHE (Contrast Limited Adaptive Histogram Equalization) [18] to enhance the image contrast.

Fig. 25.2 Representative examples of restoration results. *Left column* input images. *Right column* restored images

25.3 Experimental Results

A wide variety of underwater images have been used to evaluate the proposed restoration algorithm. Some representative examples are illustrated in Fig. 25.2. Obviously, the restored images have better clarity and contrast comparing with the input images in all cases. The blue distortion phenomena have been effectively removed and the restored color looks more natural and pleasing.

25.4 Conclusion

In this paper a new underwater image restoration algorithm is introduced. The proposed framework consists of three major phases: haze removal, color correction, and contrast enhancement. We have applied this new approach to a wide variety of underwater images. As consistent with the theory of the proposed model, we found that our method effectively removed the hazing and blurring images while recovering correct color and balanced contrast. We believe that our restoration algorithm is of potential in facilitating the interpretation and perception of underwater images in the fields of ocean engineering, ocean biology, and ocean science.

References

1. L. Chao, M. Wang, in *Proceedings of 2nd International Conference on Computer Engineering and Technology (ICCET)*, V2-35 (2010)
2. Y. Wang, B. Wu, in *Proceedings of International Conference on Computational Intelligence and Software Engineering (CiSE)*, 1 (2010)
3. Y.Y. Schechner, N. Karpel, IEEE J. Oceanic Eng. **30**, 570 (2005)
4. E. Nascimento et al., in *Proceedings of 22nd Brazilian Symposium on Computer Graphics and Image Processing (SIBGRAPI)*, 330 (2009)
5. A.T. Celebi, S. Erturk, in *Proceedings of 2nd International Conference on Image Processing Theory Tools and Applications (IPTA)*, 221 (2010)
6. G. Padmavathi et al., Int. J. Comput. Sci. Netw. Secur. **10**, 58 (2010)
7. S. E. Bazeille et al., in *Caractérisation du Milieu Marin (CMM)* (2006)
8. S.Q. Duntley et al., J. Opt. Soc. Amer. **53**, 351 (1963)
9. B. McGlamery, SPIE Proc. Ocean Optics VI **208**, 221 (1979)
10. J.S. Jaffe, IEEE J. Oceanic Eng. **15**, 101 (1990)
11. E. Trucco, A.T. Olmos-Antillon, IEEE J. Oceanic Eng. **31**, 511 (2006)
12. R. Li et al., IEEE J. Oceanic Eng. **22**, 364 (1997)
13. S. Negahdaripour, IEEE Trans. Pattern Anal. Mach. Intell. **20**, 961 (1998)
14. S.G. Narasimhan et al., in *Proceedings of Tenth IEEE International Conference on Computer Vision*, *ICCV 2005*, **1**, 420 (2005)
15. W. Hou et al., in *Proceedings of IEEE International Symposium on Geoscience and Remote Sensing*, *IGARSS 2007*, 1889 (2007
16. F. Petit et al., in *Proceedings of IEEE International Conference on Acoustics, Speech and Signal Processing, ICASSP 2009*, 1177 (2009)
17. K. He et al., IEEE Trans. Pattern Anal. Mach. Intell. **33**, 2341 (2011)
18. K. Zuiderveld, in *Contrast Limited Adaptive Histogram Equalization, Graphics Gems IV*, ed. by P. Heckbert (Academic Press, New York, 1994), p. 474

Chapter 26
Circuit Synthesis Using Pathological Elements

**Hung-Yu Wang, Nan-Hui Chiang, Quoc-Minh Nguyen
and Shun-Hsyung Chang**

The concept of pathological nullor and mirror elements has proven to be a very valuable tool for circuit analysis, synthesis, circuit transformation and interrelation in the realizations using different active elements. The pathological elements provide a common framework for linear and nonlinear circuits. In this paper, the nullor and nullor-mirror equivalents are reviewed, and several new nullor-mirror equivalents are proposed. The nullor-mirror equivalents are conductive to reducing circuit complexity and synthesizing new functional circuits. Combining the nullor-mirror equivalents with circuit transformation techniques, more useful functional circuits with simpler circuit structures can be generated. The circuit synthesis using the proposed nullor-mirror equivalents is illustrated to demonstrate the usefulness and feasibility.
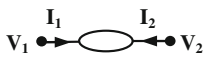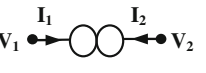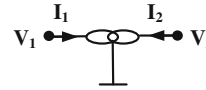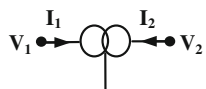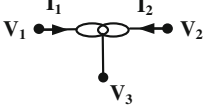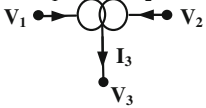
26.1 Introduction

The concept of nullors, i.e. combinations of nullators and norators, was first implicitly introduced by Tellegen [1] under the name of ideal elements and given its present name by Carlin [2]. The terminal behaviors of the nullors cannot be described by any of the existing network descriptions such as Z, Y and H matrices. Such networks usually called pathological networks, are degenerate forms and are needed to complete the domain of network elements. The pathological nullor

H.-Y. Wang (✉) · N.-H. Chiang · Q.-M. Nguyen
Department of Electronic Engineering, National Kaohsiung University of Applied Sciences,
415 Chien Kung Rd, Kaohsiung 807 Taiwan, Republic of China
e-mail: hywang@kuas.edu.tw

S.-H. Chang
Department of Microelectronics Engineering, National Kaohsiung Marine University,
142 Haichuan Rd, Kaohsiung 811 Taiwan, Republic of China

Table 26.1 Symbols and definitions of nullor and mirror elements

(a) Nullator	I_1 I_2 V_1 V_2 $V_1 = V_2$ $I_1 = I_2 = 0$
(b) Norator	I_1 I_2 V_1 V_2 V_1 and V_2 are arbitrary $I_1 = -I_2 =$ arbitrary
(c) Voltage mirror	I_1 I_2 V_1 V_2 $V_1 = -V_2$ $I_1 = I_2 = 0$
(d) Current mirror	I_1 I_2 V_1 V_2 V_1 and V_2 are arbitrary $I_1 = I_2 =$ arbitrary
(e) Floating voltage mirror	I_1 I_2 V_1 V_2 V_3 $V_{13} = -V_{23}$ $(V_1 - V_3 = V_3 - V_2)$ $I_1 = I_2 = 0$
(f) Floating current mirror	I_1 I_2 V_1 V_2 I_3 V_3 V_{13} and V_{23} are arbitrary $I_1 = I_2 = I_3/2 =$ arbitrary

elements have been proven to be very valuable due to their capability of modeling active devices independently of the particular implementation of the active devices and the simplicity with which nodal or loop analysis of these circuits can be carried out [3, 4]. They provide a common framework for circuit analysis, synthesis, circuit transformation and interrelating the realizations using different active devices [5–9]. Despite the ability of nullors to represent all active elements, without the use of resistors, they fail to represent some important analog elements. Therefore, two new pathological elements, i.e. the current mirror and voltage mirror have been defined in 1999 [10]. The new defined pathological mirror elements are basically used to represent active devices with current or voltage reversing properties. Their usefulness to circuit synthesis has been demonstrated in the literature [11–14]. In this article, the properties of pathological elements are

Table 26.2 Some pathological sections and their terminal properties
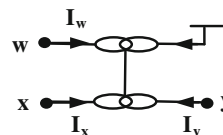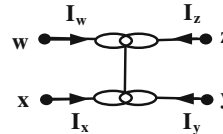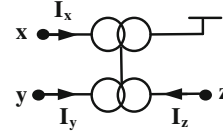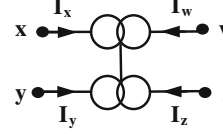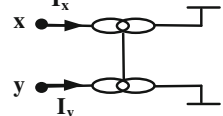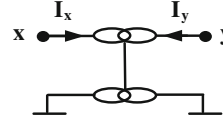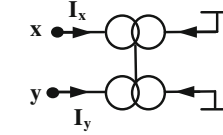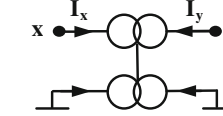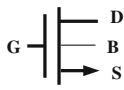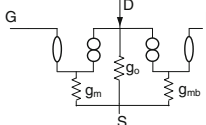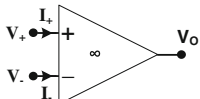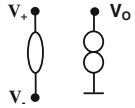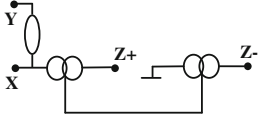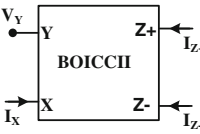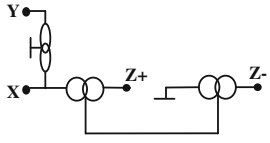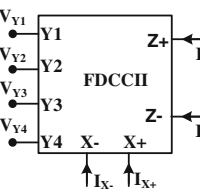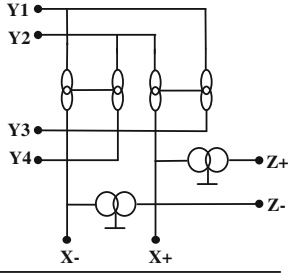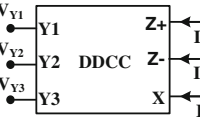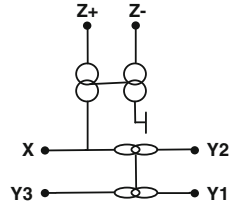
(a) Differential voltage cell	I_w w I_x I_y y	$V_y = V_w - V_x$ $I_w = I_x = I_y = 0$
(b) Differential voltage conveying cell	I_w I_z w z x I_x I_y y	$V_w - V_x = V_y - V_z$ $I_w = I_x = I_y = I_z = 0$
(c) Current replication cell	I_x x y z I_y I_z	$I_z = I_y = -I_x$
(d) Current replication cell	I_x I_w x w y z I_y I_z	$I_z = I_y = -I_x = -I_w$
(e) Equivalent of a nullator	I_x x y I_y	$V_x = V_y$ $I_x = I_y = 0$
(f) Equivalent of a VM	I_x I_y x y	$V_x = -V_y$ $I_x = I_y = 0$
(g) Equivalent of a norator	I_x x y I_y	$I_y = -I_x$
(h) Equivalent of a CM	I_x I_y x y	$I_y = I_x$

Table 26.3 Pathological representations of some ideal active devices

Active Device	Ideal Device Property	Pathological Model
(a)	$I_D = g_m V_{GS} + g_o V_{DS} + g_{mb} V_{BS}$	
(b)	$\begin{bmatrix} V_O \\ I_+ \\ I_- \end{bmatrix} = \begin{bmatrix} 0 & A_v & -A_v \\ 0 & 0 & 0 \\ 0 & 0 & 0 \end{bmatrix} \begin{bmatrix} I_o \\ V_+ \\ V_- \end{bmatrix}$ $A = \infty$	
(c)	$\begin{bmatrix} I_Y \\ V_X \\ I_{Z+} \\ I_{Z-} \end{bmatrix} = \begin{bmatrix} 0 & 0 & 0 & 0 \\ 1 & 0 & 0 & 0 \\ 0 & 1 & 0 & 0 \\ 0 & -1 & 0 & 0 \end{bmatrix} \begin{bmatrix} V_Y \\ I_X \\ V_{Z+} \\ V_{Z-} \end{bmatrix}$	
(d)	$\begin{bmatrix} I_Y \\ V_X \\ I_{Z+} \\ I_{Z-} \end{bmatrix} = \begin{bmatrix} 0 & 0 & 0 & 0 \\ -1 & 0 & 0 & 0 \\ 0 & 1 & 0 & 0 \\ 0 & -1 & 0 & 0 \end{bmatrix} \begin{bmatrix} V_Y \\ I_X \\ V_{Z+} \\ V_{Z-} \end{bmatrix}$	
(e)	$\begin{bmatrix} V_{X+} \\ V_{X-} \\ I_{Z+} \\ I_{Z-} \end{bmatrix} = \begin{bmatrix} 0 & 0 & 1 & -1 & 1 & 0 \\ 0 & 0 & -1 & 1 & 0 & 1 \\ 1 & 0 & 0 & 0 & 0 & 0 \\ 0 & 1 & 0 & 0 & 0 & 0 \end{bmatrix} \begin{bmatrix} I_{X+} \\ I_{X-} \\ V_{Y1} \\ V_{Y2} \\ V_{Y3} \\ V_{Y4} \end{bmatrix}$	
(f)	$\begin{bmatrix} I_{Y1} \\ I_{Y2} \\ I_{Y3} \\ V_X \\ I_{Z+} \\ I_{Z-} \end{bmatrix} = \begin{bmatrix} 0 & 0 & 0 & 0 & 0 & 0 \\ 0 & 0 & 0 & 0 & 0 & 0 \\ 0 & 0 & 0 & 0 & 0 & 0 \\ 1 & -1 & 1 & 0 & 0 & 0 \\ 0 & 0 & 0 & 1 & 0 & 0 \\ 0 & 0 & 0 & -1 & 0 & 0 \end{bmatrix} \begin{bmatrix} V_{Y1} \\ V_{Y2} \\ V_{Y3} \\ I_X \\ V_{Z+} \\ V_{Z-} \end{bmatrix}$	

reviewed and their usage of modeling active devices is illustrated. All the available nullor equivalents are presented and many new nullor and nullor-mirror equivalents are proposed. The nullor-mirror equivalences are conductive to reducing circuit complexity, realizing circuit using convenient structure and synthesizing new functional circuits. Combining the nullor-mirror equivalents with circuit

Table 26.4 Common nullor equivalents
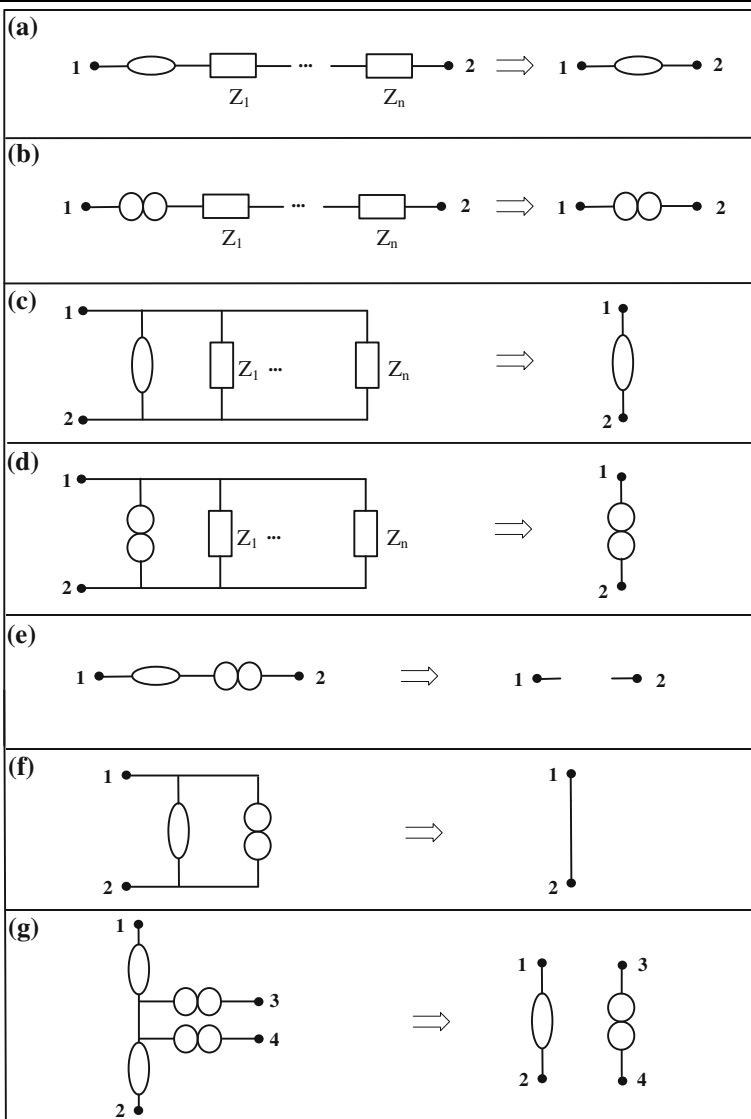
transformation techniques, more useful functional circuits with simpler circuit structures can be generated. The circuit synthesis using the new proposed nullor-mirror equivalents is illustrated to demonstrate their usefulness and feasibility.

Table 26.5 Nullor relocation

(a)	Nullator relocation	
(b)	Norator relocation	
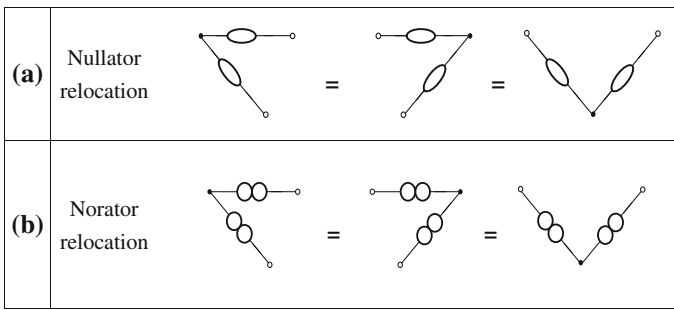
Table 26.6 Nullor-mirror equivalents
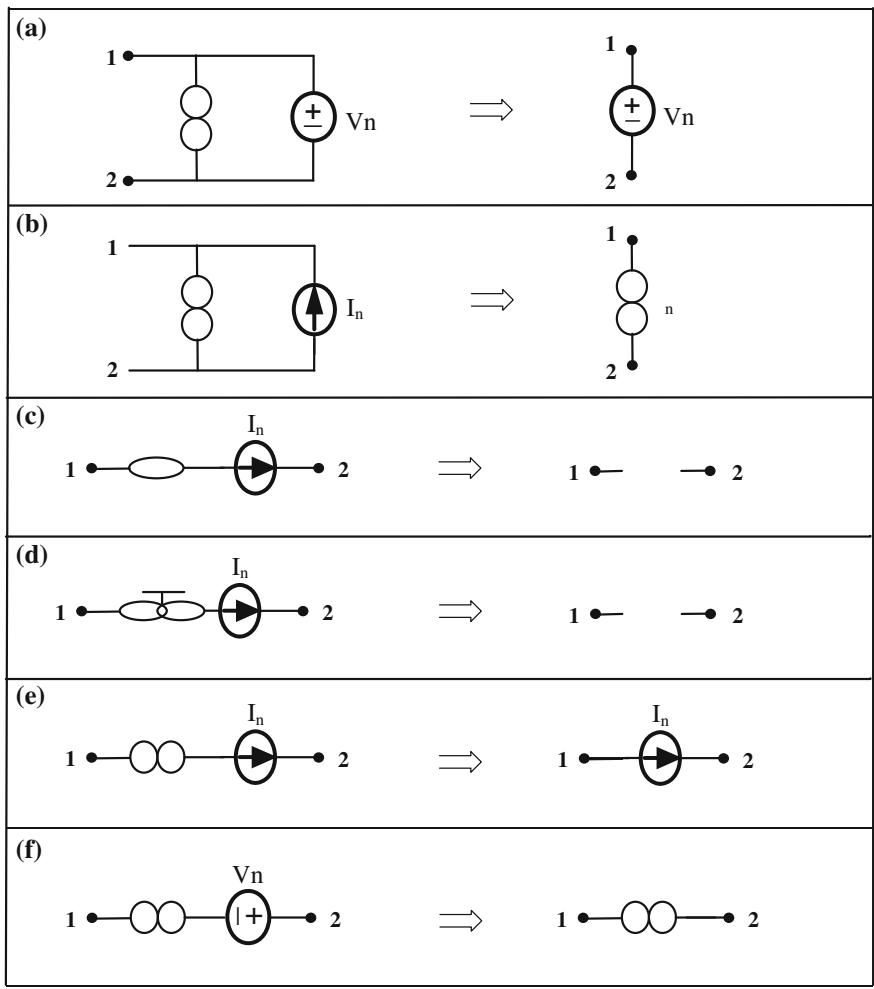
Table 26.7 Series and parallel connections of nullor-mirror elements

26.2 Pathological Elements and Equivalents

The symbols and definitions of the nullor and mirror elements are shown in Table 26.1. The pathological elements in Table 26.1a–d are bi-directional pathological elements that possess ideal characteristics and are specified on the basis of the constraints they impose on their terminal voltages and currents. The pathological nullor elements comprise the nullator and norator, as shown in Table 26.1a and b.

Table 26.8 Proposed nullor-mirror relocations

The pathological voltage mirror (VM) and current mirror (CM), as shown in Table 26.1c and d, are lossless two-port network elements used to represent an ideal voltage reversing property and an ideal current reversing property, respectively. Each of the symbols of the pathological mirror elements has a grounded reference node [11]. Although these two mirror elements are two-port network elements, they can be used as two-terminal elements with the reference node unused [10]. The symbols and definitions of the floating mirror elements are shown in Table 26.1e–f [15]. It is clear that when the reference node of each mirror element in Table 26.1e and f is connected to ground, they can be regarded as the mirror elements in Table 26.1c and d, respectively. In [16], two floating voltage mirrors with a common reference node are used to represent the pathological differential voltage cell and differential voltage conveying cell, as shown in Table 26.2a and b. Also, two floating current mirrors with a common reference node are used to express the pathological current replication cells in Tables 26.2c and d. These two pathological cells can be used to model some popular ideal active devices with differential or multiple single-ended features in concise forms [16]. The terminal properties for the cells consist of two floating mirror elements with a common reference node are shown in Table 26.2. According to the definitions of pathological elements in Table 26.1 and considering the labeled terminals only, the cells in Tables 26.2e,f,g and h can be respectively regard as a nullator, a pathological VM, a norator and a pathological CM.

The nullor elements have been used to model many ideal active devices before. With the new defined mirror elements, the pathological representations of some active devices possess the simpler circuit structures (i.e. circuits with less node number) compared to their nullor representations. The simpler circuit structure is conductive to achieving high-performance symbolic nodal analysis since the less nodal equations are needed to build [17, 18]. Table 26.3 shows the pathological representations of some ideal active devices, including the MOS transistor, the operational amplifier (OP AMP), the balanced-output second generation current conveyor (BOCCII), the balanced-output second generation inverting current conveyor (BOICCII), the fully differential second generation current conveyor (FDCCII) and differential difference current conveyor (DDCC). All the pathological elements in Table 26.1 have been used.

Table 26.9 Nullor-mirror equivalents

Nullor equivalents have received much attention as they can be used to obtain new alternative circuits or reduce the circuit complexity with the identical function [19–22]. Table 26.4 shows seven common nullor equivalents in [19]. The nullor

Fig. 26.1 The simplified procedure of a filter circuit applying nullor-mirror equivalent: **a** the original circuit, **b** the derived circuit applying nullor relocation, **c** the derived circuit applying nullor-mirror relocation, **d** the obtained circuit with simpler circuit structure
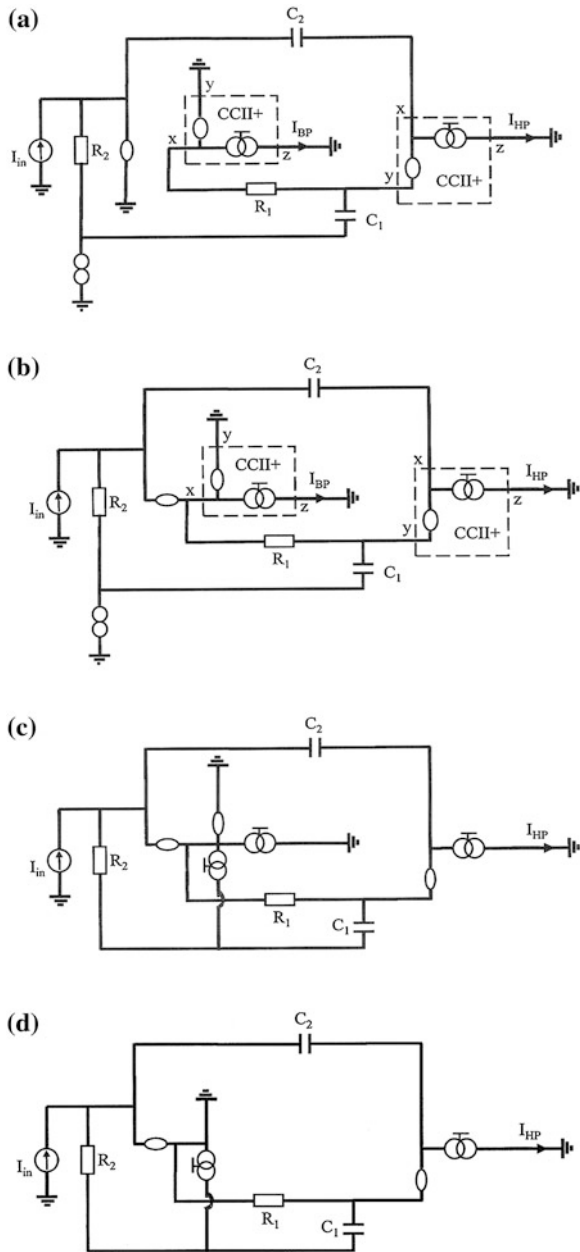
equivalents in Tables 26.4e and f are very useful and they have been applied to many circuit transformations techniques, such as the inverse transformation in [23, 24]. Besides, the nullor equivalents of nullor relocations shown in Table 26.5 are also the popular techniques to obtain different circuit structures with identical

transfer function and perform circuit transformations [20–22]. Due to the appearance of new pathological mirror elements, nullor-mirror equivalents were further investigated recently [25–27]. For the completeness of pathological equivalents, we try to present the available nullor-mirror equivalents and proposed some new equivalents.

Table 26.6 shows some nullor-mirror equivalents. The equivalents in Table 26.6a,b,e and f were proposed in [28] and the equivalents in Table 26.6c and d are the new proposed ones. To investigate the properties of the series and parallel connections of nullor-mirror elements, their equivalences or terminal characteristics according to the element definitions in Table 26.1 are given in Table 26.7 [25]. All the series connections of pathological elements in Table 26.7a–d are equivalent to an open circuit. For the structures in Table 26.7g–j, the V_1 and I_1 beside node 1 are used to denote respectively the voltage from node 1 to ground and the current flowing out of node 1. The relative voltage and current for node 2 are shown beside node 2, according to the element properties. If node 2 in Tables 26.7g–j is adopted as grounded node, all the nodes 1 of parallel conditions can be seen to be a short circuit to ground.

Other new proposed nullor-mirror equivalents of nullor-mirror relocations are presented in Table 26.8. The validity of voltage mirror relocation in Table 26.8a can be observed since the identical electrical property for the three connection circuits according to the element definitions. In addition, from the super-node concept in circuit analysis, the three schemes in Table 26.8b are equivalent as they can be represented by the same nodal equations. Furthermore, the nullor equivalent in Table 26.4g was extended to obtain other new nullor-mirror equivalents, as redrawn in Table 26.9 [27]. Their usefulness was also illustrated in [27].

26.3 The Application Example of the New Proposed Nullor-Mirror Equivalent

To demonstrate the application of new proposed nullor-mirror relocation in Table 26.8, one circuit example is presented below. We consider the current-mode filter circuit in Fig. 1c of [26], which is redrawn in Fig. 26.1a. According to the nullor relocation in Table 26.5a, one can obtain the circuit given in Fig. 26.1b. Applying the equivalence in Table 26.8b, the equivalent circuit in Fig. 26.1c is derived. It can be found that we can realize this circuit with three identical CCII+s. The simplified circuit in Fig. 26.1d can be obtained after applying the equivalent in Table 26.7i. Namely, only two CCII+s are needed to implement the circuit in Fig. 26.1(d). Therefore, the usefulness of the new proposed nullor-mirror equivalent is demonstrated.

26.4 Conclusion

In this paper, the properties of available pathological elements and cells are reviewed. The ideal behaviors of some active devices are modeled with different pathological elements. The available nullor equivalents in the literature are presented and some new pathological equivalents are proposed. The nullor-mirror equivalences are conductive to reducing circuit complexity and facilitating circuit realization. Combining the nullor-mirror equivalences with circuit transformation techniques, more useful functional circuits with simpler circuit structures can be generated. One circuit example using the presented nullor-mirror equivalence is illustrated to demonstrate the usefulness and feasibility.

References

1. B.D.H. Tellegen, Rendiconti del Seminario Matematico e Fisico di Milano **25**, 134 (1954)
2. H. J. Carlin, IEEE Trans. Circuit Theory **CT-11**, 67 (1964)
3. W.K. Chen, *The Circuits and Filters, Handbook*, 3rd edn. (CRC Press, London, 2009)
4. J.A. Svoboda, Int. J. Circuit Theory Appl. **14**(3), 169 (1986)
5. S.M. Chang, G.M. Wierzba, IEEE Trans. Circuits Syst. I. **41**, 699 (1994)
6. S. Celma, P.A. Martinez, J. Sabadell, IEEE Trans. Circuits Syst. I **43**, 61 (1996)
7. C.A. Papazoglou, C.A. Karybakas, IEEE Trans. Circuits Syst. II **45**, 894 (1998)
8. P. Kumar, R. Senani, Analog Integr. Circ. Sig. Process **33**, 65 (2002)
9. H. Schmid, IEEE Trans. Circuits Syst. II, Analog Digit. Sig. Process. **47**(11), 1160 (2000)
10. I.A. Awad, A.M. Soliman, Int. J. Electron. **86**, 413 (1999)
11. A.M. Soliman, R.A. Saad, Int. J. Circuit Theory Appl. **38**(8), 787 (2010)
12. R.A. Saad, A.M. Soliman, Int. J. Circuit Theory Appl. **36**(3), 289 (2008)
13. I.A. Awad, A.M. Soliman, Analog Integr. Circ. Sig. Process **32**, 79 (2002)
14. H.Y. Wang, C.T. Lee, C.Y. Huang, Analog Integr. Circ. Sig. Process **44**, 95 (2005)
15. R.A. Saad, A.M. Soliman, Int. J. Circuit Theory Appl. **38**(9), 935 (2010)
16. R.A. Saad, A.M. Soliman, Int. J. Circuit Theory Appl. **38**(2), 148 (2010)
17. H.Y. Wang, W.C. Huang, N.H. Chiang, IEEE Trans. Circuits Syst. II **57**, 874 (2010)
18. C. Sanchez-Lopez, F.V. Fernandez, E. Tlelo-Cuautle, S.X.D. Tan, IEEE Trans. Circuits Syst. I **58**, 1382 (2011)
19. L.T. Bruton, *RC Active Circuits: Theory and Design* (Prentice-Hall, Englewood Cliffs, 1980)
20. J.A. Svoboda, Proceedings of the Institution of Electrical Engineers Part G **136**, 317 (1989)
21. G.H. Wang, Y. Fukui, K. Kubota, K. Watanabe, Proc. IEEE Int. Symp. Circuits Syst. 1833 (1991)
22. R. Palomera-Garcia, Proc. IEEE Int. Symp. Circuits Syst. 252 (2005)
23. A. Leuciuc, Electron. Lett. **33**, 949 (1997)
24. H.Y. Wang, C.T. Lee, Electron. Lett. **35**, 1889 (1999)
25. H.Y. Wang, C.T. Lee, C.Y. Huang, Analog Integr. Circ. Sig. Process **44**, 95 (2005)
26. H.Y. Wang, S.H. Chang, Y.L. Jeang, C.Y. Huang, Analog Integr. Circ. Sig. Process **49**, 87 (2006)
27. H.Y. Wang, C.Y. Liu, S.H. Chang, Int. J. Electron. Commun. (AEU) **64**, 828 (2010)
28. Wang Z., 信息工程學院學報, **12**(3), 9 (1993)

Chapter 27
On Seismicity Driven Chaotic Model by DWT

Fu-Tai Wang, Chung-Cheng Chen, Jenny Chih-Yu Lee, Shun-Hsyung Chang, Chin-Feng Lin, Hsiao-Wen Tin and Wen-Jin Kao

A new Chaotic Model based on discrete wavelet transformation (DWT) is proposed. DWT is an excellent method for analyzing non-stationary and transient signals. A collection of hierarchically structured decompositions of input signals called approximations and details can be generated based on scaling functions and wavelets of DWT. Based on wavelets properties of compactly supported in a time domain, the instantaneous change (IC) of input signals can be realized. Inspired by the observation of the Gutenberg-Richter (GR) relation having been recognized as the appearance of the self-organized criticality (SOC) state of the dynamics of the seismic faults, the seismicity driven chaotic model (SDCM) based on DWT is successfully obtained The result of real datum examination in this paper shows that the proposed seismicity driven chaotic model (SDCM) can serve as a different seismic monitor for earthquake.

27.1 Introduction

The observation of the Gutenberg-Richter relation has been identified as the manifestation of the self-organized criticality (SOC) state of the dynamics of the earthquake faults [1] since the concept of SOC based on the sand-pile model was introduced by Bak et al. [2]. The Gutenberg-Richter (GR) relation [3] for the frequency-magnitude statistics of earthquakes exhibits the power-law distribution

F.-T. Wang (✉) · C.-C. Chen · W.-J. Kao
Department of Electrical Engineering, Hwa Hsia Institute of Technology, 111 Gong Jhuan Road, Chung Ho, New Taipei City 235, Republic of China (Taiwan)
e-mail: wft@cc.hwh.edu.tw

S.-H. Chang · C.-F. Lin · H.-W. Tin
Department of Electrical Engineering, National Taiwan Ocean University, 2 Pei-Ning Road, Keelung 202, Republic of China (Taiwan)

J. C.-Y. Lee · S.-H. Chang
Department of Microelectronics Engineering, National Kaohsiung Marine University, 142 Haichuan Road, Nantzu, Kaohsiung 811, Republic of China (Taiwan)

and is scale invariant [4, 5]. The scaling exponent, known as the b-value, in the Gutenberg-Richter (GR) relation, $\log N(M) = a - bM$, is discussed in the study of seismicity evolution very often [6–8] To review about the reduction in b-values before a large earthquake is a popular topic. Due to the presence of non-stationary and complexity in seismic faults, it is difficult to derive the seismicity model for earthquake. Discrete wavelet transforms (DWT) is an excellent way to processing non-stationary signals because of wavelets are compactly supported in a time domain [9, 10]. DWT uses scaling functions and wavelets to decompose the input signal into a hierarchically structured collection of approximations and details [11, 12]. The choice of a suitable level for the hierarchy is dependent on the signal [13]. The DWT producing a hierarchically structured decomposition has been shown to be particularly effective in noise reducing, compression, and image processing [14–18]. Recently, an alternative modified long-range connective sand-pile (LRCS) model is proposed to improving the seismicity model to better represent real earthquake activity because of it so repeatedly approaches and retreats from a critical state. The precursory b-value reduction before large earthquakes observed from earthquake catalogues closely mimics the evolution in power-law slopes for the frequency-size distributions of events derived in the LRCS system [19, 20]. Inspired by this observation of b-values, the first step of chaotic modeling for earthquake datum via Wavelet Transform is proposed in [21]. In this paper we show that this approach can be extended to derive a seismicity driven chaotic model (SDCM) for any investigating area and propose different seismicity-based model based on wavelet properties. This paper is organized as follows: Sect. 27.2 presents the hierarchically structured decomposition of DWT. In Sect. 27.3, we perform the b-values of real seismic datum. Section 27.4 explores the seismicity evolution for the temporal variation. Our main DWT-based seismicity driven chaotic model (SDCM) is presented in Sect. 27.6.

27.2 Discrete Wavelet Transforms

In wavelet analysis, the low-frequency, high-scale components of the signal have reference to the approximation A_j, and the high-frequency, low-scale components have reference to the detail D_j, where j is decomposition level. One commonly used series of mother wavelets was constructed by Daubechies [9]. The filtering process [10] in Fig. 27.1a, which includes down-sampling at its most basic level, produces DWT coefficients. The detail coefficient 'cD' contains the high-frequency components, while the approximation coefficient 'cA' consists of the low-frequency components. For the filtering process, the lengths of the 'cD' and 'cA' are slightly more than half the length of the input signal. The high- and low-pass decomposition filters (H_1 and H_0) in Fig. 27.1a, together with their associated reconstruction filters (H'_1 and H'_0) in Fig. 27.1b, form a system of quadrature mirror filters. It is not only possible to reconstruct the original signal from the coefficient 'cD' and the coefficient 'cA', but also capable of reconstructing the approximation 'A' and the detail 'D' themselves from their coefficient 'cA' and
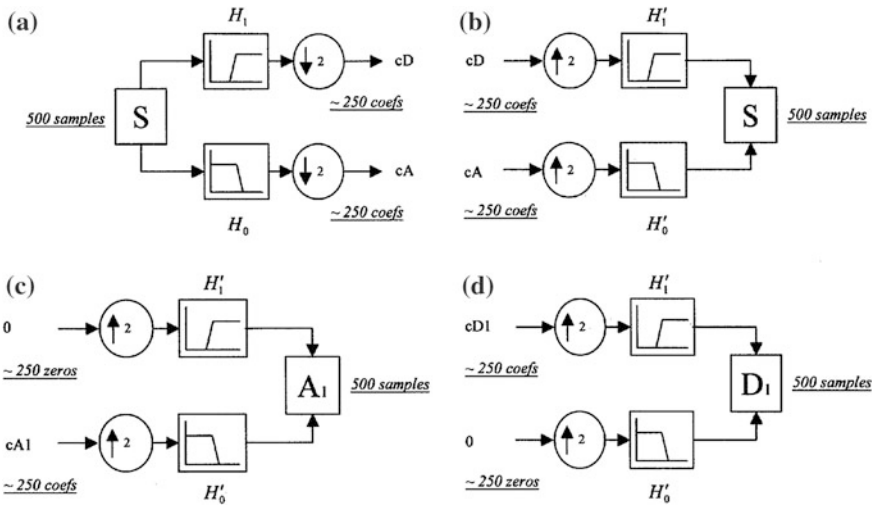
Fig. 27.1 One-stage filtering: approximations and details. **a** Decomposition. **b** Reconstruction. **c** Reconstructed approximation A1. **d** Reconstructed detail D1
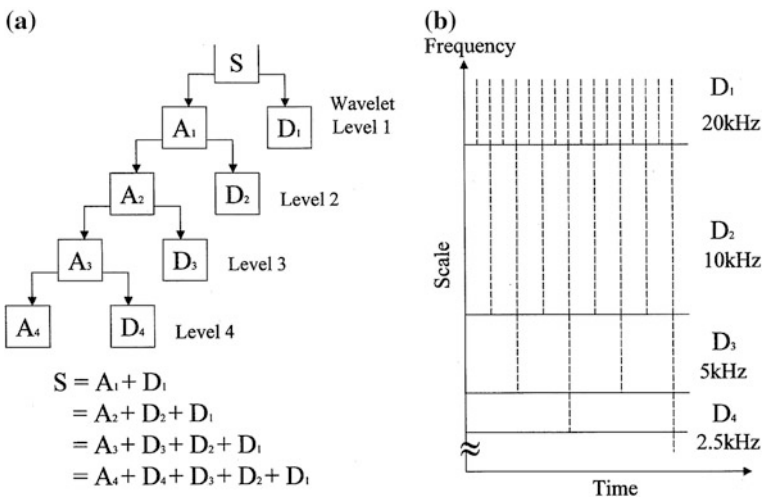
Fig. 27.2 Reconstructing approximations and details. **a** A hierarchically organized decomposition. **b** Time-scale resolution of wavelet transform

'cD', respectively. The process in Fig. 27.1c yields a reconstructed approximation A_1. Similarly, we can reconstruct the first-level detail D_1, using the schematic diagram in Fig. 27.1d. Both A_1 and D_1 have the same length as the original signal S. And they are true constituents of S, $S = A_1 + D_1$. Extending this scheme to the components of a multi-level analysis, as depicted in Fig. 27.2a, there are several ways to combine and reproduce the original signal. Then, DWT decomposition
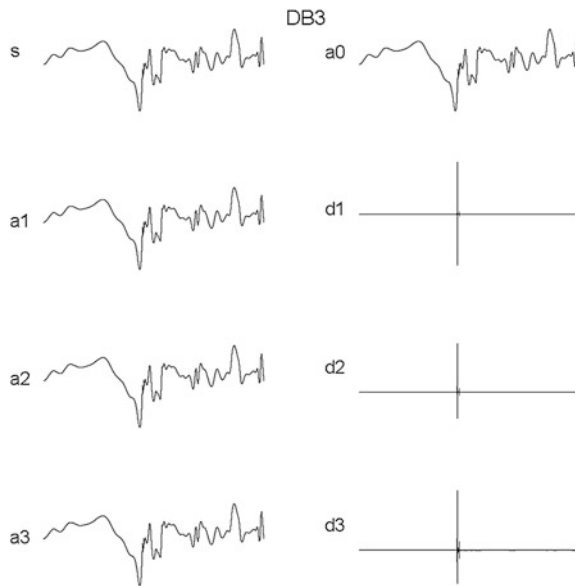
Fig. 27.3 A collection of hierarchically structured decompositions of an input signal based on DWT. Level j for this hierarchy is 3. The original signal s is considered as the approximation a0 at level 0. Approximations a1, a2, a3 and details d1, d2, d3 are generated based on scaling functions and wavelets DB3, respectively. We have s = a0 = a1 + d1, a1 = a2 + d2, a2 = a3 + d3, and s = a0 = a1 + d1 = a2 + d2 + d1 = a3 + d3 + d2 + d1. Based on wavelets properties of compactly supported in a time domain, the instantaneous change (IC) of the input signal s is realized in the details d1, d2, and d3 by DWT

produces a hierarchically structured decomposition. The choice of a suitable level for the hierarchy is dependent on the signal. At each level j, we build the approximation at level j, A_j, and the detail at level j, D_j. The original signal is considered as the approximation A_0 at level 0. The time-scale resolution of wavelet transform, plotted in Fig. 27.2b, shows that the filter analysis of DWT are regularly spread in a logarithmic scale over the frequency axis. If the input signal is sampled at 40 kHz, D_1 at level 1 contains the higher 20 kHz frequency range component of the input signal S, while A_1 contains the lower 20 kHz frequency range component of the signal. D_2 then covers the higher 10 kHz frequency range of A_1 which contains the 10 kHz frequency range component of the signal. D_3 and D_4 contain the followed 5 and 2.5 kHz frequency range components of the dolphin sound, respectively, while A_4 contains the lower 2.5 kHz frequency range component of the input signal S. In the DWT, the low-pass filter $h_0(n)$ fully determines the orthogonal wavelet base. Let $h_0(n)$ and $h_1(n)$ are a class of exactly reconstructing filters called 'conjugate quadrature filter' or CQF's [11]. That is

$$\sum_n h_0(n)h_0(n+2k) = \delta(k) = \begin{cases} 1, & k = 0 \\ 0, & k \neq 0 \end{cases}$$

and $h_1(n) = (-1)^{(n)} h_0(N - n)$, where N is an odd integer. The scaling $\phi_h(t)$ and wavelet functions $\psi_h(t)$ are given by the dilation and wavelet equations

$$\phi_h(t) = \sqrt{2} \sum_n h_0(n) \, \phi_h(2t - n);$$

$$\psi_h(t) = \sqrt{2} \sum_n h_1(n) \, \phi_h(2t - n)$$

Because of the discrete wavelet transforms (DWT) use scales and positions based on powers of two their calculations are much more efficient. A collection of hierarchically structured decompositions of input signals called approximations and details can be generated based on scaling functions and wavelets of DWT. The DWT is an excellent way to processing a transient signal because of wavelets are compactly supported in a time domain. Based on this property of compactly supported in a time domain, the instantaneous change (IC) of input signals can be realized in the details by DWT. An efficient algorithm to implementing this scheme using filters was obtained by Mallat [12]. At each level j, the DWT decomposes the approximation aj − 1 to building the approximation aj and the detail dj, and gets a decomposing relation as aj − 1 = aj + dj. Extending this scheme to the components of a multi-level analysis, there are several ways to combining and reproducing the original signal s. While the original signal is considered as the approximation of a0 at level 0, we have s = a0 = a1 + d1, a1 = a2 + d2, …, S = aj − 1 = aj + dj, and S = a0 = a1 + d1 = a2 + d2 + d1 = a3 + d3 + d2 + d1 = a4 + d4 + d3 + d2 + d1 = …. The choice of a suitable level j for the hierarchy is dependent on the signal. Figure 27.3 shows a collection of hierarchically structured decompositions of input signals based on DWT.

27.3 The *B*-Value

The b-value is discussed in the study of seismicity evolution very often. It is the scaling exponent in the Gutenberg-Richter (GR) relation

$$\log N(M) = a - bM, \tag{27.1}$$

where M is the magnitude of an earthquake, $N(M)$, named as an Event size, is the number of earthquakes with magnitudes greater than or equal to M, and a and b are the a- and b-values of the frequency-magnitude distribution.

The observation of the Gutenberg-Richter (GR) relation has been recognized as the appearance of the self-organized criticality (SOC) state of the dynamics of the seismic faults since the concept of SOC based on the sand-pile model was introduced. The reduction in b-values before a large earthquake is a popular topic to exploring. In this paper, b-values are used to deriving the seismicity driven chaotic model (SDCM). The 2391 earthquake events that are registered in the Taiwan
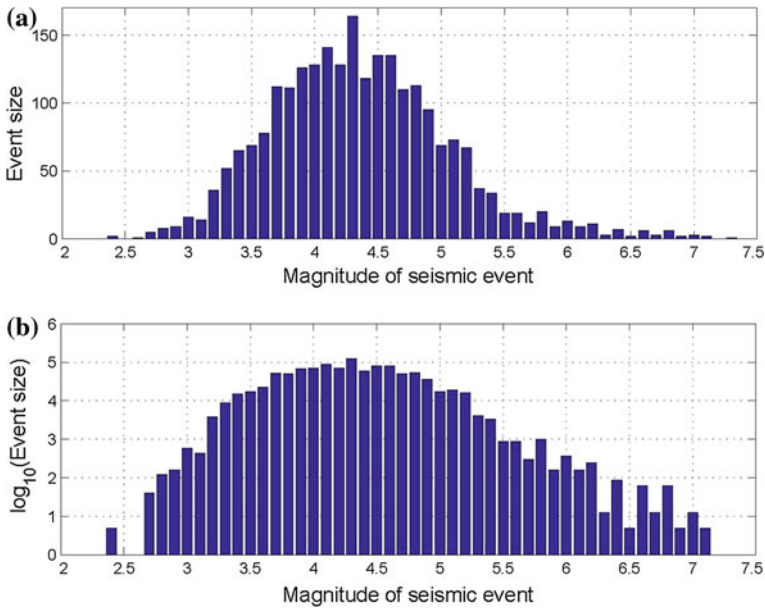
Fig. 27.4 Magnitude/size distribution of earthquakes: **a** event size $N(M)$ of the 2391 earthquake events that have been registered in the Taiwan Central Weather Bureau (CWB) catalogue occurring in the Taiwan for a time span from 1995 to 2012, **b** $\log_{10}$(Event size) of these earthquake events

Fig. 27.5 One sample of b-value is calculated. The b-value is averagely about 0.4588 in this study. The magnitude/size distribution of earthquakes having magnitude of seismic even being larger than 2.4 could fulfill the Gutenberg-Richter relation very well and could be used to calculating the b-values. The b-value is calculated by every 500 earthquake events. Every 500 earthquake events are defined as a window
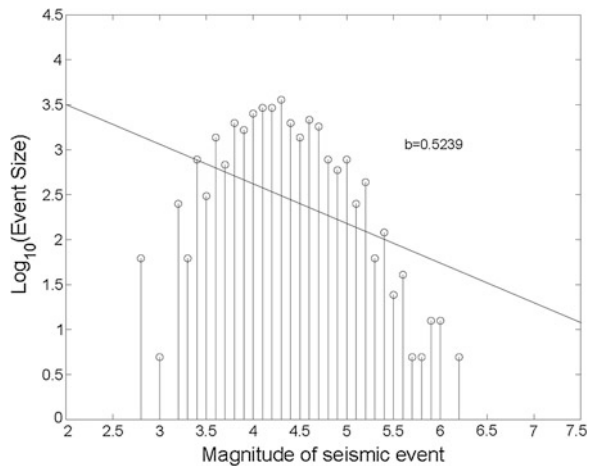
Central Weather Bureau (CWB) catalogue occurring in the Taiwan for a time span from 1995 to 2012 are applied to calculating b-values. Figure 27.4 is the magnitude/size distribution of earthquakes. The event size $N(M)$ and the $\log_{10}$(Event size) of
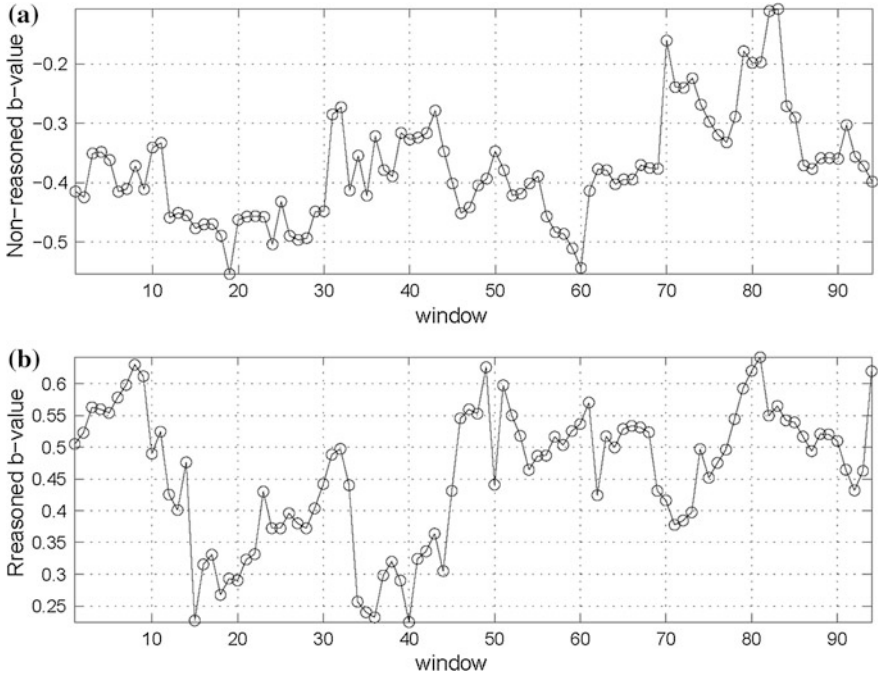
Fig. 27.6 Temporal variations of the b-values correspond to each window. To trace variations in b-value with respect to time, the sliding window technique with an overlap of 480 events is used, which means that we selected 500 events to calculating b-value then shifted 20 events to calculating the next value of b. Figure 27.6a considers all events during the counting and derives non-reasoned b-value. Figure 27.6b considers all events excepting events with $\log_{10}$(event size) $= 0$ and obtains a reasoned b-value
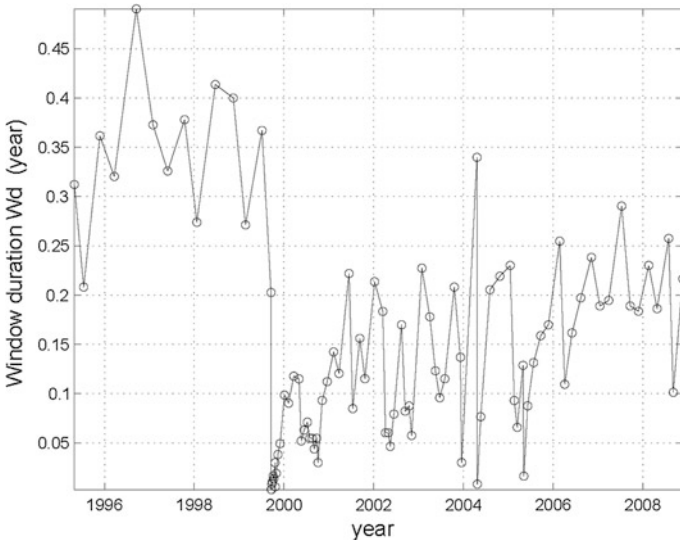
Fig. 27.7 Window duration Wd is the time interval between each two adjacent b-values of the real seismic events
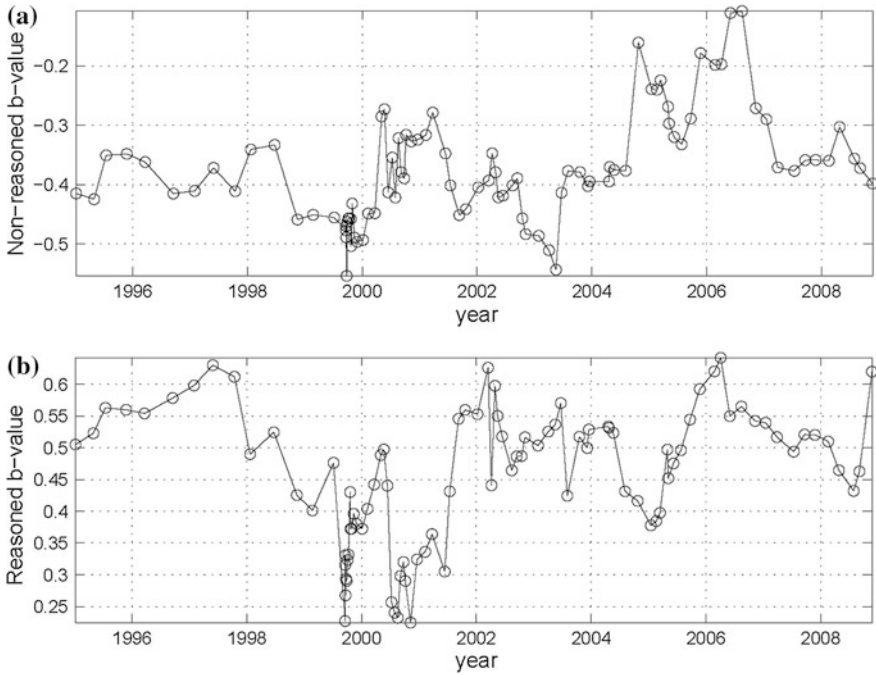
Fig. 27.8 Seismicity evolution is derived from the temporal variations in the *b*-values *versus* to their corresponding time respecting to the window duration. Figure 27.8**a** has non-reasoned *b*-values (with negative *b*-values) when all the events are consider. But when the event with the $\log_{10}$(event size) $= 0$ is omitted in calculating the *b*-values, the reasoned *b*-values (with positive *b*-values) of seismicity evolution is obtained and shown in Fig. 27.8**b**

these earthquake events are shown in Fig. 27.4a and b, respectively. The magnitude/size distribution of earthquakes, having magnitude of seismic even being larger than 2.4, could fulfill the Gutenberg-Richter relation very well and could be used to calculating the *b*-values. One sample of *b*-value is depicted in Fig. 27.5. The *b*-value is averagely about 0.4588 in this study. The *b*-value is calculated by every 500 earthquake events with each magnitude of seismic event being larger than 2.4. Every 500 earthquake events is defined as a window [20]. To trace variations in *b*-value with respect to time, the sliding window technique with an overlap of 480 events is used, which means that we selected 500 events to calculating *b*-value then shifted 20 events to calculating the next value of *b*. Corresponding to each window, the scaling exponent in the Gutenberg-Richter (GR) relation, which is the *b*-value, is calculated for the real seismicity. The temporal variations of the *b*-values corresponding to each window are shown in Fig. 27.6. Figure 27.6a has non-reasoned *b*-values when we consider all the events. But when the *b*-value is calculated omitting the event with the $\log_{10}$(event size) $= 0$, we get a reasoned temporal variation as shown in Fig. 27.6b. In Fig. 27.6, the temporal variation in the *b* values corresponds to each window.
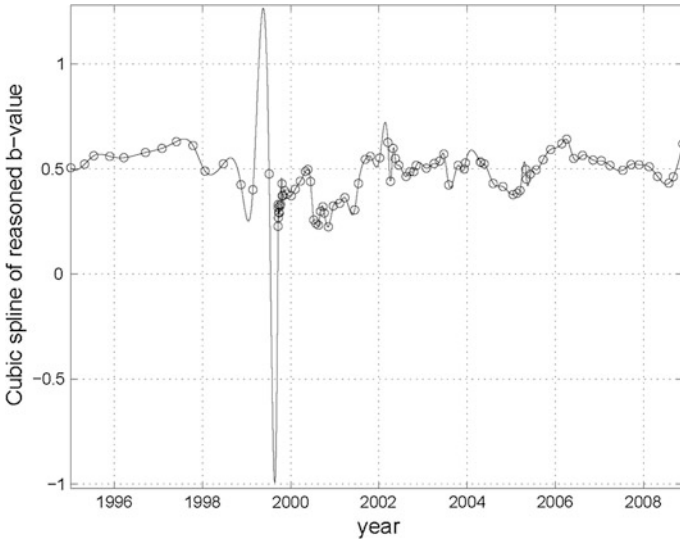
Fig. 27.9 Cubic spline interpolation (*line*) of reasoned *b*-values (*circles*) of seismicity evolution in Fig. 27.8b
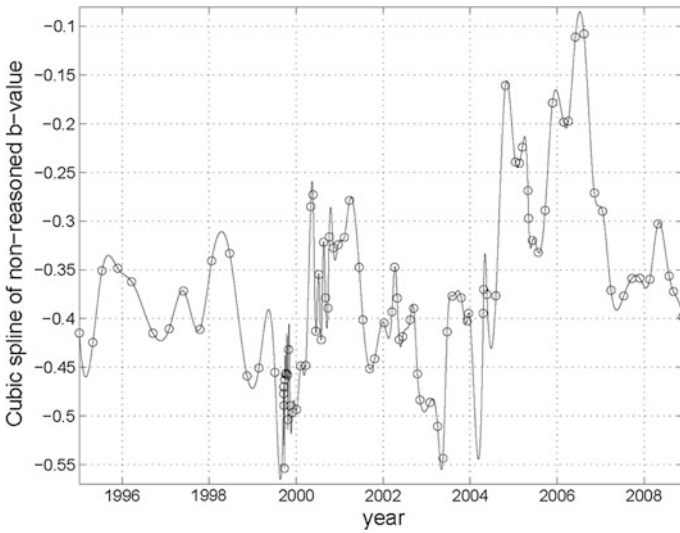
Fig. 27.10 Cubic spline interpolation (*line*) of non-reasoned *b*-values (*circles*) of seismicity evolution in Fig. 27.8a
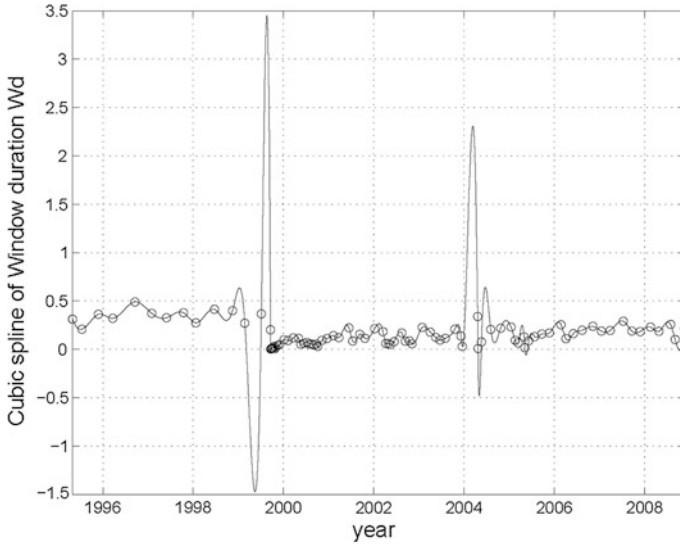
Fig. 27.11 A cubic spline interpolation (*line*) of window duration Wd (*circles*) in Fig. 27.7
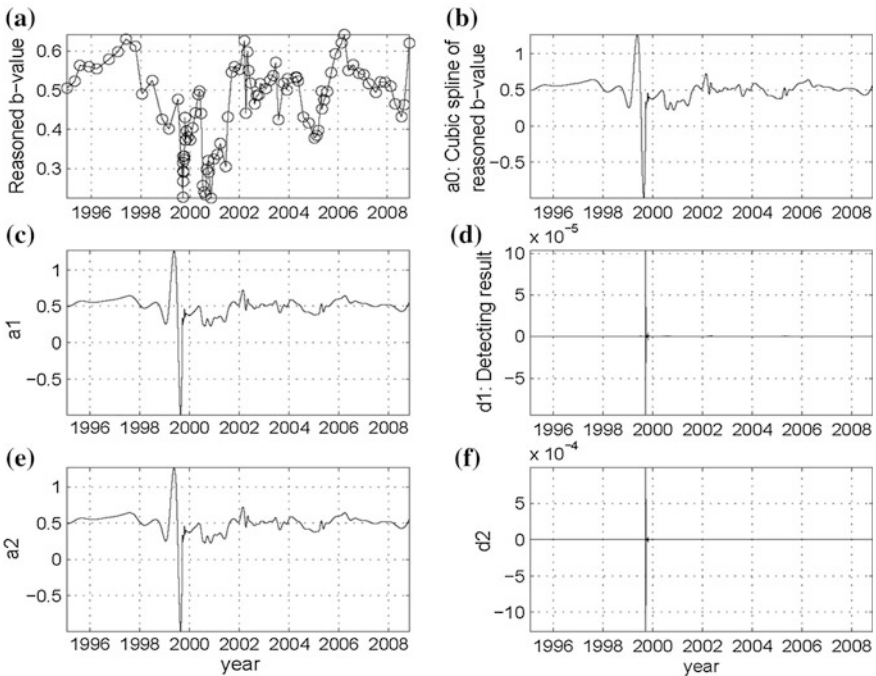
Fig. 27.12 DWT-based major stroke detecting result on the cubic spline of reasoned *b*-values of seismicity evolution in Fig. 27.9: **a** The reasoned *b*-values of seismicity evolution in Fig. 27.8b, **b** The cubic spline of reasoned *b*-values of seismicity evolution in Fig. 27.9, **c** The approximation at level 1, **d** Shows that the major stroke is detected in the detail *d1*, **e** and **f** Are the approximation *a2* and detail *d1* at level 2, respectively
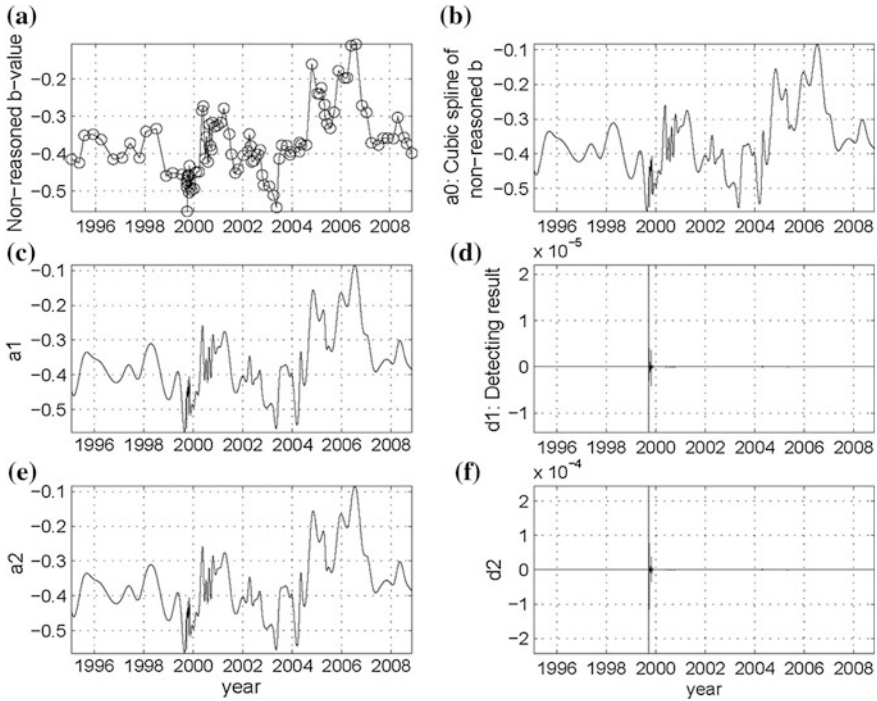
Fig. 27.13 DWT-based major stroke detecting result on the cubic spline of non-reasoned *b*-values of seismicity evolution in Fig. 27.10: **a** The non-reasoned *b*-values of seismicity evolution in Fig. 27.8a, **b** The cubic spline of non-reasoned *b*-values of seismicity evolution in Fig. 27.10, **c** The approximation at level 1, **d** Shows that the major stroke is detected in the detail *d1*, **e** and **f** Are the approximation *a2* and detail *d1* at level 2, respectively

27.4 Seismicity Evolution

In the study of seismicity evolution, the *b*-value in GR relation is considered as a monitoring index related to reveal precursory phenomena according to the time. In Fig. 27.7 window duration Wd is the time interval between each two adjacent *b*-values. According to these window durations, the *x*-axis in Fig. 27.6 is re-ranged and obtains the seismicity evolution of the real seismic events shown in Fig. 27.8, where the *b*-values are related to their corresponding time. Figure 27.8a considers all events during the counting and derives non-reasoned *b*-values (with negative *b*-values). Figure 27.8b considers all events excepting events with $\log_{10}$(event size) $= 0$ and obtains the reasoned *b*-values (with positive *b*-values) of seismicity evolution.
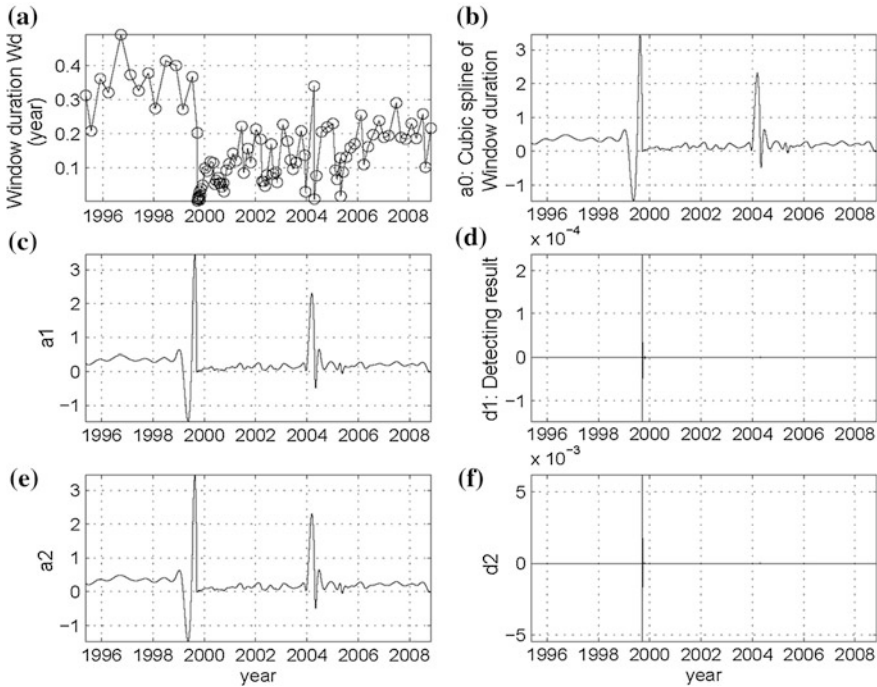
Fig. 27.14 DWT-based major stroke detecting result on the cubic spline of window duration Wd in Fig. 27.11: **a** The window duration Wd in Fig. 27.7, **b** The cubic spline of window duration Wd in Fig. 27.11, **c** The approximation at level 1, **d** Shows that the major stroke is detected in the detail *d1*, **e** and **f** Are the approximation *a2* and detail *d1* at level 2, respectively

27.5 Detection of the Major Stroke

Because of discrete wavelet transform (DWT) produces a hierarchically structured decomposition and is an excellent way to processing a transient signal, the major stroke in seismicity catalogues can be detected by decomposing the seismicity evolution with DWT. We solved this decomposing problem by using a cubic spline function, which interpolates the *b*-values in the seismicity evolution into a sequence of transient signal. A cubic spline interpolation of the reasoned *b*-values of the seismicity evolution in Fig. 27.8b is a sequence of transient signal and shown in Fig. 27.9. A cubic spline interpolation of the non-reasoned *b*-values of seismicity evolution in Fig. 27.8a is another sequence of transient signal and shown in Fig. 27.10. A cubic spline interpolation of the window duration Wd in Fig. 27.7 is also a sequence of transient signal and shown in Fig. 27.11.

After the seismicity evolution and the window duration transform to transient signals via the cubic spline function, the time of the major stroke in seismicity catalogues can be achieved by decomposing these transient signals with DWT. In Figs. 27.12, 27.13 and 27.14, the wavelet db8 of DWT-based detection results are
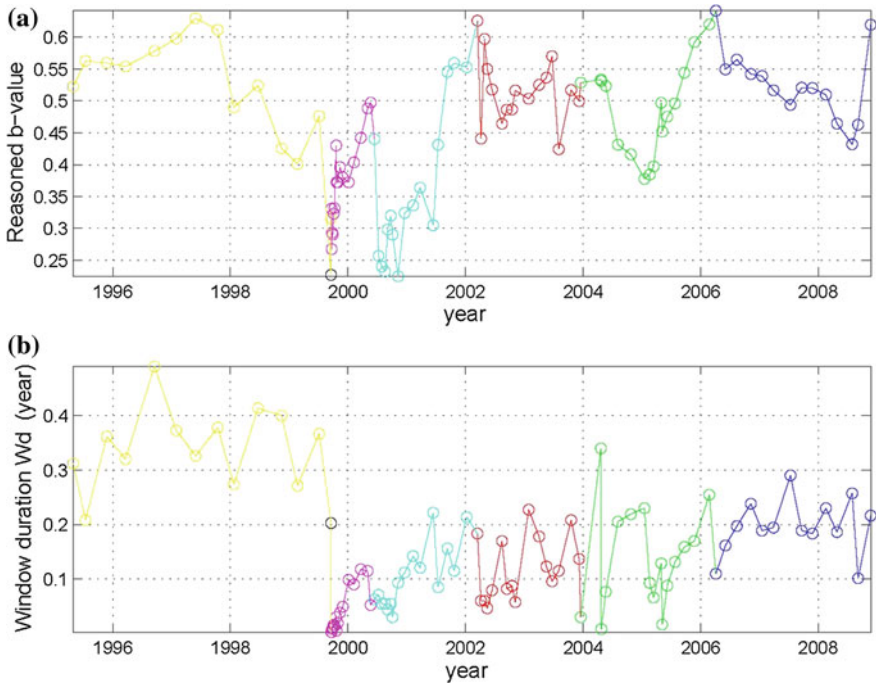
Fig. 27.15 Two elements of the seismicity driven chaotic model (SDCM): **a** The window duration Wd which is the replica of Figs. 27.7 and 27.14a, **b** The reasoned *b*-values of seismicity evolution which is the replica of Figs. 27.8b and 27.12a. The black circles in Fig. 27.15a, b indicate the time of the major stroke in seismicity catalogues detected by DWT shown in Figs. 27.14d and 27.12d, respectively, and which is the time of 1999 Chi-Chi, Taiwan, earthquake occurred. Different colors stand for different periods

demonstrated to detecting the major stroke, which is the 1999 Chi-Chi, Taiwan, earthquake, occurred in seismicity catalogues. Figure 27.12 shows the DWT-based detecting result on the cubic spline of reasoned *b*-values of seismicity evolution. Figure 27.12a is the reasoned *b*-values of seismicity evolution. Figure 27.12b is the cubic spline of reasoned *b*-values of seismicity evolution. Figure 27.12c is the approximation at level 1. Figure 27.12d shows that the major stroke is detected in the detail d1. Figure 27.12e and f are the approximation a2 and detail d1 at level 2, respectively. The DWT-based detecting result on the cubic spline of non-reasoned *b*-values of seismicity evolution is shown in Fig. 27.13. Figure 27.13a demonstrates the non-reasoned *b*-values of seismicity evolution. Figure 27.13d shows that the major stroke is detected in the detail d1. The DWT-based detecting result on the cubic spline of window duration Wd is shown in Fig. 27.14. Figure 27.14a is the window duration Wd. Figure 27.14d shows that the major stroke is detected in the detail d1.
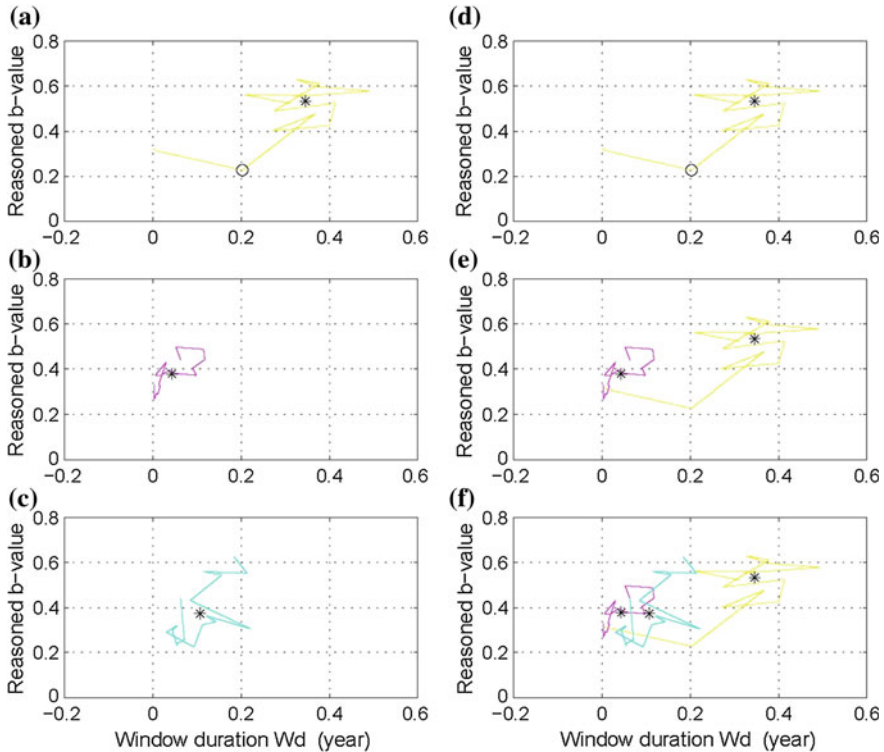
Fig. 27.16 Seismicity driven chaotic model (SDCM) in different periods: **a**, **b**, and **c** Are the SDCM of the first three separate periods in Figs. 27.15, and 27.16**d**–**f** are their cumulative results. The *x*-axis of the SDCM is related to the window duration Wd and the *y*-axis is related to the reasoned *b*-values of seismicity evolution. The *black circles* in Fig. 27.16**a**, **d** indicate the time of the major stroke in seismicity catalogues detected by DWT. The *black stars* indicate the mean values of SDCM in different separate periods. Compare two figures of Fig. 27.16**c**, **f**, it shows that the *black star* moves to the *left hand side* and *lower position* after the major stroke

27.6 Seismicity Driven Chaotic Model

The idea that the seismicity driven chaotic model (SDCM) could be successfully obtained after the time of the major stroke in seismicity catalogues had been detected in the details by DWT and was inspired by the observation of the Gutenberg-Richter (GR) relation having been recognized as the appearance of the self-organized criticality (SOC) state of the dynamics of the seismic faults. The seismicity driven chaotic model (SDCM) is constructed by two elements. They are the window duration Wd in Figs. 27.7 and 27.14a and the reasoned *b*-values of seismicity evolution in Figs. 27.8b and 27.10a. It is convenient for us to explore the idea of the SDCM by plotting both of the window duration and the reasoned *b*-values of seismicity evolution in Fig. 27.15a and b, respectively. The black
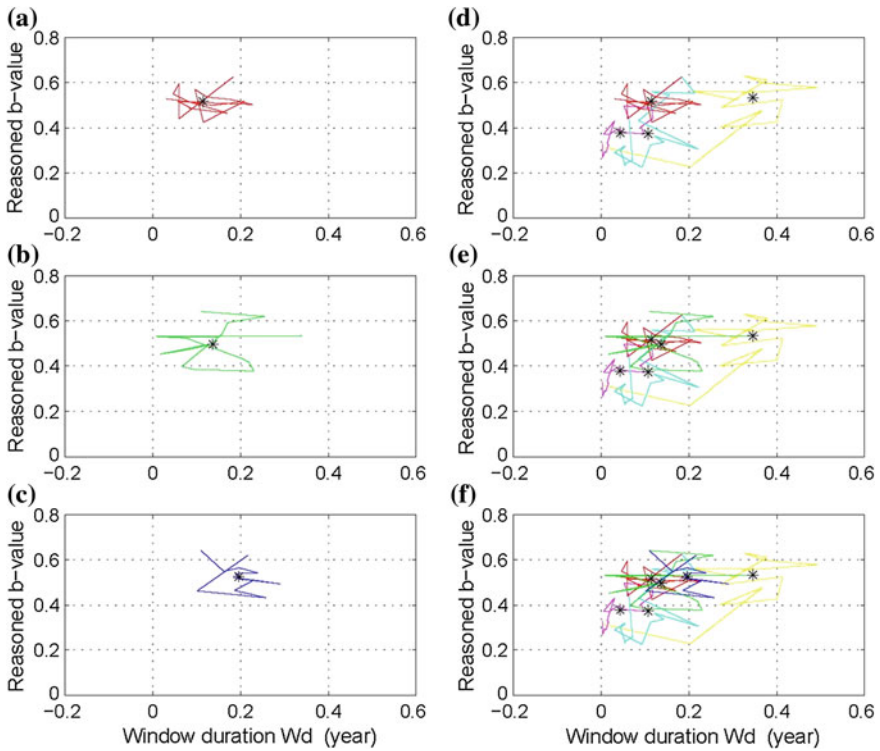
Fig. 27.17 Seismicity driven chaotic model (SDCM) in the following periods: **a**, **b**, and **c** are the SDCM of the following three separate periods in Figs. 27.15, and 27.17**d**–**f** are their all six cumulative results. Figure 27.17**f** shows that the mean values of SDCM in different separate periods after the major stroke are shifting toward to the *black star* at the beginning

circles in Figs. 27.15a, b indicate the time of the major stroke in seismicity catalogues detected by DWT shown in Figs. 27.14d and 27.12d, respectively, and which is the time of 1999 Chi-Chi, Taiwan, earthquake occurred. Different colors stand for different periods. Each subplot in Figs. 27.16 and 27.17 is the seismicity driven chaotic model (SDCM) in different periods. The *x*-axis of the SDCM is related to the window duration Wd and the *y*-axis is related to the reasoned *b*-values of seismicity evolution. Figure 27.16a–c are the SDCM of the first three separate periods in Figs. 27.15, and 27.16d–f are their cumulative results. The black circles in Fig. 27.16a, d indicate the time of the major stroke in seismicity catalogues detected by DWT, which is the time of 1999 Chi-Chi, Taiwan, earthquake occurred. The black stars indicate the mean values of SDCM in different separate periods. In Fig. 27.16d, the mean value of the SDCM is located on the right hand side and near the upper corner before the major stroke. Compare two figures of Fig. 27.16c, f, it shows that the black star moves to the left hand side and lower position after the major stroke. Figure 27.17 shows the seismicity driven

chaotic model (SDCM) in the following periods. Figure 27.17a–c are the SDCM of the following three separate periods. Figure 27.17d–f are their all six cumulative results. Figure 27.17f shows that the mean values of SDCM in different separate periods after the major stroke are shifting toward to the black star at the beginning.

27.7 Conclusion

In this paper a new seismicity driven chaotic model (SDCM) is introduced. Inspired by the observation of the Gutenberg-Richter (GR) relation having been recognized as the appearance of the self-organized criticality (SOC) state of the dynamics of the seismic faults, the seismicity driven chaotic model was successfully obtained after the time of the major stroke in seismicity catalogues is detected in the details by DWT. Based on wavelet properties, the cubic spline function is used to derive the SDCM from the past history of seismicity in Taiwan. The result of real datum examination in this paper shows that the proposed seismicity driven chaotic model can serve as a different seismic monitor for earthquake.

References

1. C.C. Chen, Geophys. J. Int. **155**, F1 (2003)
2. P. Bak, C. Tang, J. Geophys. Res. **94**, 15635 (1989)
3. B. Gutenberg, C.F. Richter, Ann. Geofis. **9**, 1 (1956)
4. D.L. Turcotte, PAGEOPH **131**(1/2), 171 (1989)
5. J.R. Holliday, D.L. Turcotte, J.B. Rundle, Pure Appl. Geophys. **165**, 1003 (2008)
6. W.D. Smith, Geophys. J. R. Astron. Soc. **86**, 815 (1986)
7. M. Wyss, C.G. Sammis, R.M. Nadeau, S. Wiemer, Bull. Seismol. Soc. Am. **94**, 410 (2004)
8. C.C. Chen, L.Y. Chiao, Y.T. Lee, H.W. Cheng, Y.M. Wu, Tectonophysics **454**, 104 (2008)
9. I. Daubechies, Comm. Pure Appl. Math. **41**, 909 (1988)
10. M. Misiti, Y. Misiti, G. Oppenheim, J.M. Poggi, *Wavelet Toolbox User's Guide* (The MathWorks, Natick, 1996)
11. M.J.T. Smith, T.P. Barnwell III, IEEE Trans. Acoust. Speech Sig. Process **ASSP-34**, 434 (1986)
12. S.G. Mallat, IEEE Trans. Pattern Recognit. Mach. Intell. **11**, 674 (1989)
13. S. Mallat, *A Wavelet Tool of Signal Processing: The Sparse Way*, 3rd edn. (Academic, San Diego, 2009)
14. D.L. Donoho, I.M. Johnstone, Biometrika **81**(3), 425 (1994)
15. G. Steidl, J. Weickert, T. Brox, P. Mrazek, M. Welk, SIAM J. Numer. Anal. **42**(2), 686 (2004)
16. U. Kamilov, E. Bostan, M. Unser, IEEE Sig. Process. Lett. **19**(4), 187 (2012)
17. H.L. Chan, Y.C. Siao, S.W. Chen, S.F. Yu, Comput. Methods Programs Biomed. **90**, 1 (2008)

18. M. Guerquin-Kern, M. Haberlin, K.P. Prussmann, M. Unser, IEEE Trans. Med. Imag. **30**(9), 1649 (2011)
19. Y.T. Lee, C.C. Chen, L.Y. Chiao, Y.F. Chang, Phys. A **387**, 5263 (2008)
20. Y.T. Lee, *Modeling precursory seismicity with numerical model*, PhD thesis, National Central University, Taiwan (R.O.C.) (2011)
21. F.T. Wang, C.Y. Lee Jenny, C.F. Lin, S.H. Chang, C.T. Chen, W.J. Kao, C.C. Hwu, Chaotic modeling for earthquake datum via wavelet transform, in *Proceedings of MTS/IEEE YEOSU OCEANS 2012,* Yeosu, Korea, May 2012

Chapter 28
Zinc Oxide and Its Applications

Shun Hsyung Chang, Chih Chin Yang, Ting-hao Hu, Shang yang Chen and Ian Yi-yu Bu

Over the past decades, there have been intensive interests in research on zinc oxide (ZnO). The high electron mobility, high thermal conductivity, wide and direct band gap and large exciton binding energy make ZnO suitable for a wide range of devices, including transparent thin-film transistors, photodetectors, light-emitting diodes and laser diodes that operate in the blue and ultraviolet region of the spectrum. In spite of the recent rapid developments, controlling the electrical conductivity of ZnO has remained a major challenge. While a number of research groups have reported achieving *p*-type ZnO, there are still problems concerning the reproducibility of the results and the stability of the *p*-type conductivity. Even the cause of the commonly observed unintentional *n*-type conductivity in as-grown ZnO is still under debate. In this paper, we will present some of the work on ZnO from our laboratory.

28.1 Introduction

Zinc oxide is an important material for semiconductor applications. It possesses a direct wide band gap 3.37 eV and large free-exciton binding energy 60 meV [1, 2]. Generally, as deposited ZnO shows *n*-type conduction behaviour due to its structure defects and incorporated impurities [3]. Although such *n*-type behaviour has been explored in various optoelectronic applications it presents serious obstacles in its usage in semiconductor industry [4–6]. In other word, the use of ZnO as a semiconductor in electronic devices has been hindered by the difficulty in obtaining stable *p*-type ZnO. So far, two strategies have been developed to synthesis *p*-type ZnO: (i) direct doping through substituting group V elements such as N [7], P [8] or As [9] for O, and (ii) co-doping of N or Li acceptor with reactive

S. H. Chang · C. C. Yang · T. Hu · S. y. Chen · I. Y. Bu (✉)

Department of Microelectronics Engineering, National Kaohsiung Marine University, Kaohsiung, Republic of China (Taiwan)

e-mail: ianbu@webmail.nkmu.edu.tw

donors such as Ga, In or Al [10, 11]. The N/Al combination is preferred due to material abundance and the greater acceptance by the semiconductor manufacturers.

Another emerging research area of ZnO is reducing its dimensions into nanometer scale. Different geometries of ZnO nanomaterials such as, nanowires [12] nanoplates [13], nanoflake [14] and nanoflower [15] have been obtained. ZnO is suitable material for humidity sensor as its resistivity is sensitive to changes in humidity due to adsorption of hydrogen gas molecules [14]. The desired characteristics of a high performance moisture sensor include fast response, high sensitivity, durable and cost effective. It is expected that by adapting ZnO into nanomaterials can offer further enhancement in moisture sensitivity due to increased surface area.

In this paper, we will introduce the latest work on ZnO from National Kaohsiung Marine University.

28.2 Sol–Gel Deposition of *p*-Type ZnO Through Co-doping Method

Sol–gel deposition of *p*-type ZnO : Al : N was obtained by stirring 0.7 M zinc acetate ($Zn(CH_3COO)_2 \cdot H_2O$) in isopropanol IPA, with an 0.7 M of MEA added as a chelating agent to prevent precipitation. The solution was magnetically mixed at 70° C for 1 h until a transparent solution was formed. NH_4Cl (0.03 M) and NH_4OH were selected as the nitrogen source and the co-doping was achieved by adding 1 wt% $AlCl_3$ into the precursor solution. For comparison purposes, a sample without Al co-doping was also synthesized. Depositions were achieved in atmospheric air using a spin coater set at 3000 rpm for 30 s. The deposited thin films were first heated to 250° C, in order to evaporate the solvents, and subsequently sintered to 550° C by a hotplate to crystallize the films.

Figure 28.1 shows SEM image of surface morphology of the NZO films doped with different nitrogen source [1]. Figure 28.1a, b show NZO produced via sol–gel method consists of a wrinkled thin film embedded within smaller grain ZnO particles. Both the films exhibit wrinkle-network on the surfaces. Such "wrinkle" effects have been observed in the past and is usually attributed to stress relaxation during the cooling of the ZnO thin film. The wrinkle effect is only visible on at lower magnification (5 mm scale) (see Fig. 28.1a). Figure 28.1b–d show SEM of the films at higher resolution. The NZO films on glass composed of compact and dense nanoparticles with diameters of 10–50 nm. The grain size of ZnO films are affected by the post annealing temperature. Typically, as the temperature increases the density and grain size of ZnO increase. The *c*-axis oriented and dense packed structure is typical of the films deposited by sol–gel method.

Figure 28.2 shows the XRD patterns of the deposited NZO films. All the films showed preference growth along the (002) plane. The quality of the XRD peaks is
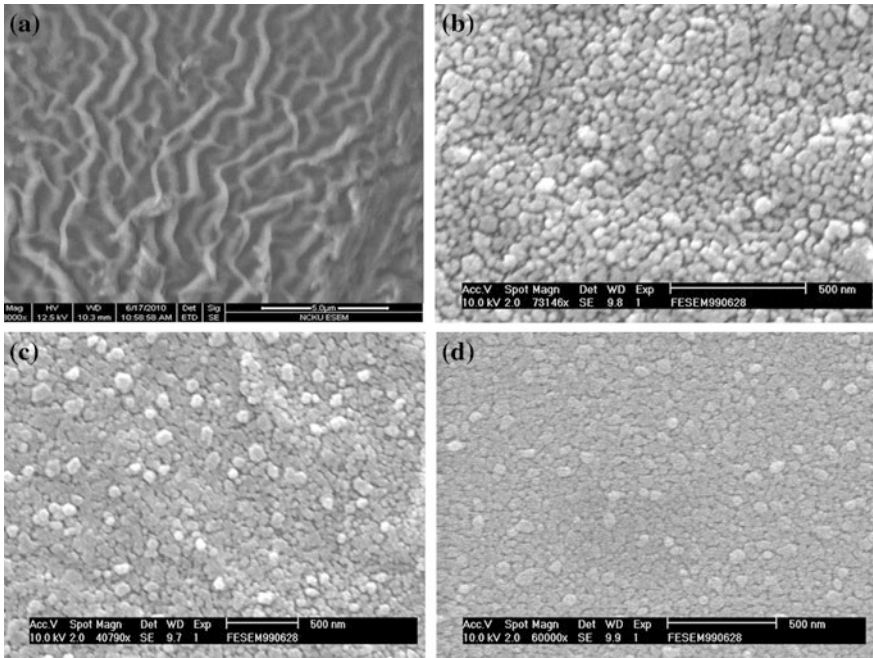
Fig. 28.1 SEM image: **a** typical sol–gel derived NZO film at lower magnification, **b** sol–gel synthesized NZO without Al co-doping, **c** sol–gel produced ZnO : Al : N using NH_4Cl as source of nitrogen, **d** sol–gel produced ZnO : Al : N using NH_4OH as source

Fig. 28.2 XRD of the synthesized NZO films, sol–gel synthesised AZO, sol–gel produced ZnO : Al : N using NH_4Cl as source of nitrogen, sol–gel produced ZnO : Al : N using NH_4OH as source and sputtered ZnO : Al : N [1]
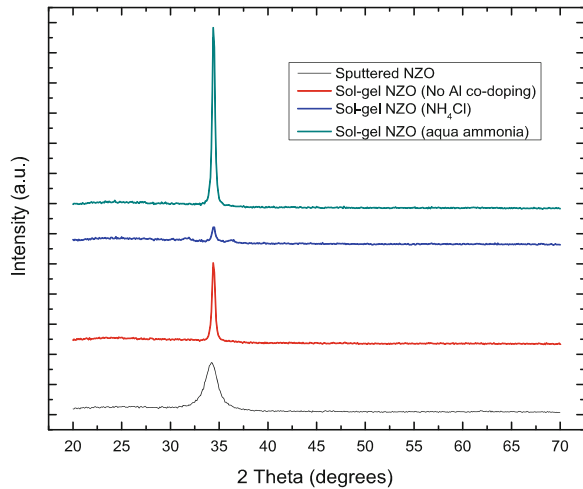
an indication of the degree of crystallinity. As expected, the sputtered ZnO : Al : N showed a broad peak which indicates the amorphous structure of the film. Figure 28.2 illustrates that the XRD pattern for ZnO : Al : N is very sensitive to chemical selection. The films, derived from NH_4Cl, produced weaker XRD signal intensity than NH_4OH. The results are significant and indicate the orientation and quality of p-type ZnO films that can be controlled through chemistry of the sol. The utilisation of NH_4OH produced high quality crystalline film with extreme preference to c-axis. The Hall measurement confirms p-type conductivity of the films. P-type properties of sol–gel processed ZnO films are highly dependent on nitrogen source. Without co-doping we can observe film with high resistivity. Films co-doped with aluminium all have acceptable resistivity with hole concentration in the 10^{17} cm^{-3} and resistivity range between 45–62 cm^2/Vs.

28.3 Effect of NH$_4$OH Concentration on P-Type Doped Zinc Oxide Film by Solution Based Process

In subsequent study, we investigated the effect of ammonia concentration on optoelectronic properties of p-type ZnO : Al : N [4]. Figure 28.3 shows the surface morphology of the films obtained via spin coating of the sol precursor solution with different NH_4OH concentration. In Fig. 28.2, it can be observed from insets of the SEM images, that the calcinated film consists of NZO nanoparticles of around 30–50 nm. Films with 1 ml NH_4OH exhibit smooth surface. As the concentration of NH_4OH increases to 2.5 ml, small patches of agglomerate appeared. This trend continues, as further increase of NH_4OH to 5 ml, yield films with more prevalent agglomeration. The data suggest excessive NH_4OH leads to agglomeration formation in NZO films. The mechanism of agglomeration is discussed at a latter section of this article.

Figure 28.4 shows the crystal orientation of the sol–gel derived NZO films with different concentration of NH_4OH. The results of these films showed preferential orientation towards (002) orientation. The preferred orientation decreases with increasing NH_4OH addition. With the addition of 5 ml of NH_4OH into the precursor, the resultant film consists of crystallites with random orientation. It is well known, that the orientation of the crystallites is strongly dependant on the chemistry of the precursor. The random orientated crystallites synthesized at 5 ml NH_4OH suggest the possibility of other phases, such as AlN or Zn_3N_2 in the doped film. The XRD data correlates the corresponding SEM image where random agglomeration can be clearly seem within the film.

Hall effect measurements for NZO films were measured by the four-probe van der Pauw method. Data were averaged to ensure accuracy. All the films show p-type conduction, indicate N incorporation via Al co-doping. Figure 28.5 shows the resistivity as a function of NH_4OH concentration. It can be observed that, when NH_4OH is introduced to the sol, resistivity of p-type ZnO film is reduced. The minimum resistivity as determined by Hall measurements occurs at around 2.5 ml
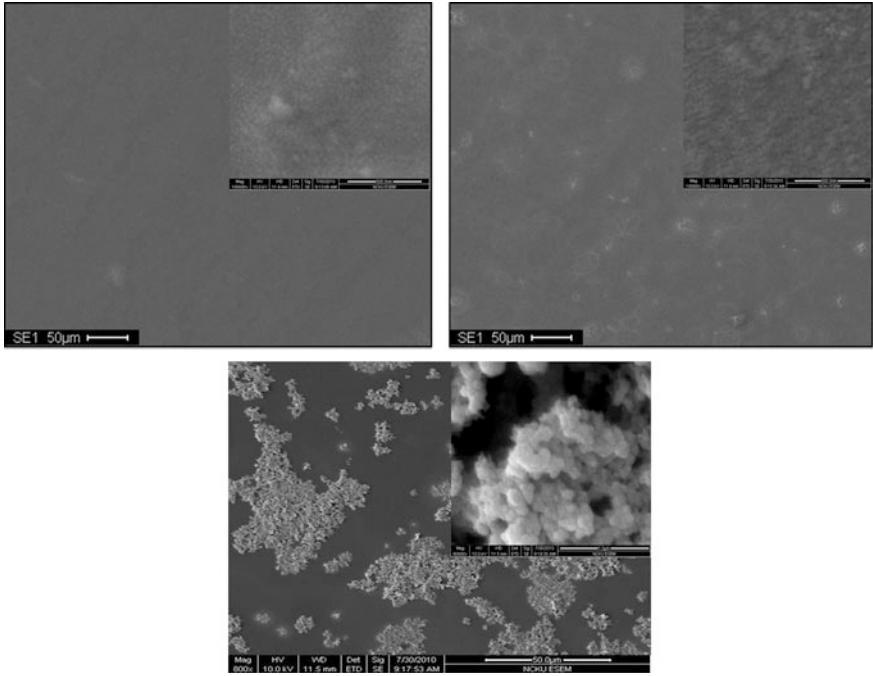
Fig. 28.3 Effect of ammonia concentration on the structure of *p*-type ZnO

Fig. 28.4 Crystal orientation of the sol–gel derived NZO films with different concentration of NH₄OH
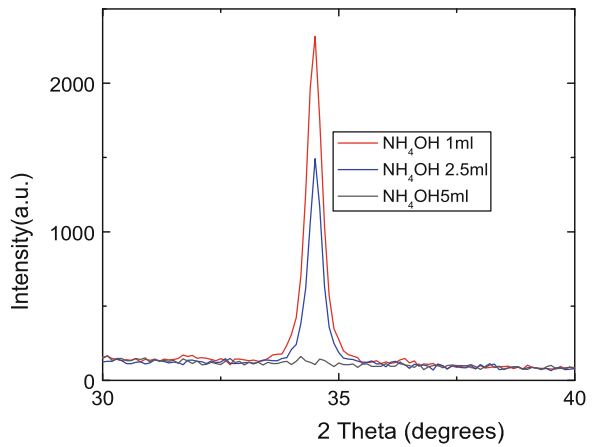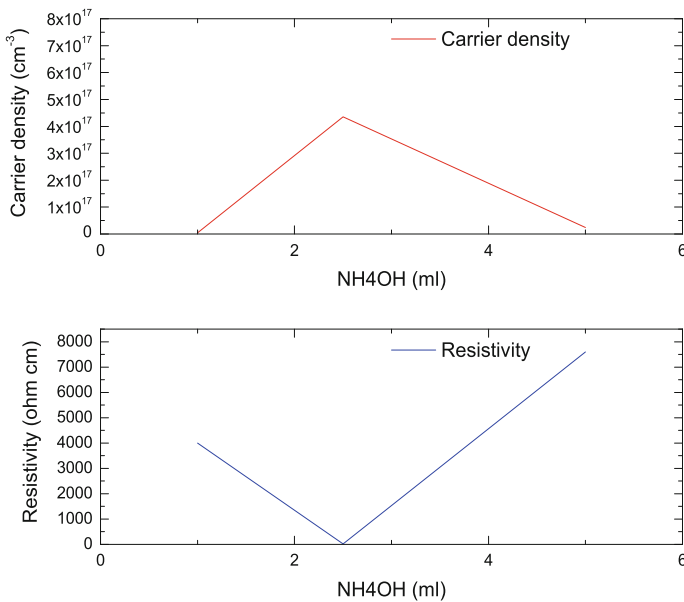
Fig. 28.5 Hall effect measurements for NZO films were measured by the four-probe van der Pauw method

of NH$_4$OH. Further increase in NH$_4$OH concentration resulted in films with higher resistivity. As NH$_4$OH concentration increases, the hole concentration increases and resistivity decreases. The increase of hole concentration is due to an increase in the quantity of N molecules due to an increase in the concentration of NH$_3$ molecules dissociated into N and NO molecules with an increase of NH$_4$OH. Further increase of NH$_4$OH (5 ml), resulted in precipitates in the films, which act as a defect and scattering centers, degrades the carrier mobility and increases resistivity.

Excessive NH$_4$OH concentration results in a large density of oxygen vacancies and zinc interstitials will exist in ZnO crystal due to the absence of oxygen in ambient acting as donors. Therefore, the carrier density of *p*-type ZnO is reduced greatly because of high self compensation. The NH$_4$OH shifts the PH of the solution towards alkaline deposition, which results in accelerated rate of condensation than hydrolysis. This favors agglomeration of larger particles. The incorporation of excessive nitrogen alters the structure and affects its electrical property.

28.4 Conclusion

In this study, *p*-type ZnO was successfully deposited using sol–gel deposition method. It was found that the ammonia concentration has a profound effect on its subsequent structure and optoelectronic properties.

References

1. I.Y. Bu, J. Alloy. Compd. **509**(6), 2874 (2011)
2. C.F. Klingshirn, *Zinc Oxide: From Fundamental Properties Towards Novel Applications* (Springer, Berlin, 2010)
3. A. Janotti, C.G. Van de Walle, Rep. Prog. Phys. **72**(12), 126501 (2009)
4. I.Y. Bu, Appl. Surf. Sci. **257**(14), 6107 (2011)
5. I.Y. Bu, Ceram. Int. **39**(5), 1189–1194 (2013)
6. I.Y. Bu, Superlattices Microstruct. **64**(4), 213–219 (2013)
7. A. Tsukazaki, A. Ohtomo, T. Onuma, M. Ohtani, T. Makino, M. Sumiya, K. Ohtani, S.F. Chichibu, S. Fuke, Y. Segawa, Nature Mater. **4**(1), 42 (2004)
8. K.–K. Kim, H.-S. Kim, D.-K. Hwang, J.-H. Lim, S.-J. Park, Appl. Phys. Lett. **83**(1), 63 (2003)
9. A. Dadgar, A. Krtschil, F. Bertram, S. Giemsch, T. Hempel, P. Veit, A. Diez, N. Oleynik, R. Clos, J. Christen, Superlattices Microstruct. **38**(4), 245 (2005)
10. J. Lu, Z. Ye, F. Zhuge, Y. Zeng, B. Zhao, L. Zhu, Appl. Phys. Lett. **85**(15), 3134 (2004)
11. F. Zhuge, L. Zhu, Z. Ye, D. Ma, J. Lu, J. Huang, F. Wang, Z. Ji, S. Zhang, Appl. Phys. Lett. **87**(9), 092103 (2005)
12. I.Y. Bu, Ceram. Int. **38**(12), 3869–3873 (2012)
13. Y. Qiu, W. Chen, S. Yang, J. Mater. Chem. **20**(5), 1001 (2010)
14. I.Y. Bu, C.–C. Yang, Superlattices Microstruct. **51**(6), 745 (2012)
15. L.–L. Xing, C.-H. Ma, Z.-H. Chen, Y.-J. Chen, X.-Y. Xue, Nanotechnology **22**(21), 215501 (2011)

Chapter 29
Energetic Efficiency of Cantilever Type Piezoelectric Generators

V. A. Akopyan, I. A. Parinov, E. V. Rozhkov, Yu. N. Zakharov and M. S. Shevtsova

The paper presents new estimation criterion of energetic efficiency for the cantilever type piezoelectric generators (PEGs) and its comparison with the known criteria. The generalized form of the proposed criterion allows us to define the energetic efficiency for the several configurations of PEGs in which different oscillation modes of cantilever plate are realized. Analysis of calculated values of the generalized criterion for the cantilever type PEGs of various configurations shows that their maximal output electric power could be reached for PEGs demonstrating most great value of the criterion. It is stated that if the value of generalized characteristic for some PEGs type exceeds its value two times compared to other their types, then its output electric power surpasses the power of others more than one order of magnitude. In particular, it is shown that PEGs with substrates made from high stiffness materials have higher output power comparing to flexible, e.g. fiberglass material. Moreover, the upper boundary is found for resonance oscillation frequencies of cantilever plate, above of which proof mass of PEG does not influence on its output power.

V. A. Akopyan (✉) · I. A. Parinov · E. V. Rozhkov
Vorovich Mechanics and Applied Mathematics Research Institute, Southern Federal
University, Rostov-on-Don, Russia
e-mail: akop@math.rsu.ru

Yu. N. Zakharov
Physics Research Institute, Southern Federal University, Rostov-on-Don, Russia

M. S. Shevtsova
Department of Mathematics, Mechanics and Computer Sciences, Southern Federal
University, Rostov-on-Don, Russia

M. S. Shevtsova
Department of Mechanics of Active Materials, South Scientific Centre of Russian Academy
of Sciences, Rostov-on-Don, Russia

29.1 Introduction

Energetic efficiency of piezoelectric generators (PEGs) and piezoelectric storage devices are characterized by the value of their output electric power per volume of piezoelectric elements and by the parameters influencing on this power. The value of storage output power depends with one hand on output characteristics of the piezoelectric transducer, and with other hand on processing data of electric signals and electric energy harvesting. In the last time, majority studies on energetic efficiency of piezoelectric generators have been devoted to solution of the optimization problem of electric schemes for the processing output signals of piezoelectric transducer and electric energy storage. Reviews of these studies and analysis of different schemes and methods (*standard interface circuit, synchronized switching harvesting with inductor SSHI*, etc.) for the processing output signals are presented by Lefeure E., Badel A., Richard, Guyomar D. [1, 2]. A comparative analysis of different signal processing methods accounting their energetic efficiency is given in the studies of A. Nechibvute, A. Chamanda, P. Luhanda et al. [3], and S. Priya, D. J. Inman [4]. In particular, the last book presents the results of J. M. Renno, M. F. Daqaq, D. J. Inman, D. Guyomar, C. Richard, A. Badel, G. A. Rincon-Mora, M.A. Sodano, C.R. Farrar, G. Park et al. The influence of the transducer materials on energetic efficiency of PEGs has been briefly investigated in [5]. The main aim of this paper is develop the new criterion to estimate an energetic efficiency of the cantilever type PEG. In the final part of the paper we compare the proposed criterion with known criteria.

The generalized criterion, proposed in the paper, allows one to estimate energetic efficiency of PEGs with several configurations, in each of which is realized mainly one specific oscillation mode.

29.2 Analysis of Known Criteria and Approaches for Energetic Efficiency of PEGs Estimation

As such criterion for the cantilever type PEG the known expression for the piezoceramic material (PCM) was proposed in [5]

$$k^2 = \frac{d^2}{\varepsilon^T s^E}, \tag{29.1}$$

where k is the effective coupling coefficient, d is the piezoelectric constant, ε^T is the dielectric permittivity at tension $T = 0$ or const, s^E is the compliance factor of the material at electric field $E = 0$ or const. Expression (29.1) describes known coefficient of electric mechanical coupling for only CH_t mode, presenting the mode of low-frequency oscillations of the transverse-polarized thin plate, whose sizes satisfy the constraints [6]

$$l \gg w; \quad l \gg t, \tag{29.2}$$

where l, w, t are the length, width and thickness of piezoelectric element, respectively.

At the case of low-frequency one-dimensional oscillations of the transversally polarized PEG plate the electromechanical coupling factor k_{31}^2 is presented in the form [6, 7]:

$$k_{31}^2 = \frac{d_{31}^2}{\varepsilon_{33}^T s_{11}^E}, \tag{29.3}$$

where d_{31} is the piezoelectric constant; ε_{33}^T, s_{11}^E are the dielectric permittivity and the compliance factor, respectively.

So, criterion (29.1) can be used for the cantilever PEG configuration with the size constraints (29.2) at the longitudinal low-frequency oscillations. By using the criterion (29.1) with constraints (29.2) for other PEG configurations or other vibration modes, we could obtain incorrect results.

E. Lefeuvre, A. Badel, C Richard et al. proposed other criterion, so-called *global coupling factor* k^2 expressed in the form [8]:

$$k^2 = \frac{(e_{33} S_{cs})^2}{L(c_{33}^D S_{cs} + L K_s) C_0}, \tag{29.4}$$

where e_{33} is the piezoelectric constant at the longitudinal oscillations of rod into longitudinal electric field [6], L and S_{cs} are the height and cross-section area, respectively, c_{33}^D is the compliance factor of piezoelectric material at constant electric displacement $D = 0$ or const, K_s is the stiffness of mechanical system transferring a force to disc- (or rod-like) piezoelectric element, C_0 is the clamped capacitance.

In the expression (29.4), the value of the k^2-criterion is directly proportional to the square of piezoelectric constant e_{33} and inversely proportional to the compliance factor c_{33}^D and capacitance C_0. The k^2-criterion (29.4) is expressed through the parameters defined at thickness oscillations of rod or thick disc along the polarization vector [6]. This means that the estimation criterion of the energetic efficiency is defined in the generalized form while the expression (29.3) contains parameters relating only to one of oscillation modes of the piezoelement. It is known that the different piezoelectric constants for the one piezoceramic material may vary in three or more times. For instance, the following parameters have been obtained for PZT-5: $h_{33}/h_{31} = 21.5 \times 10^{-8}$ (V/m)/7.3×10^{-8} (V/m) ≈ 3, and $e_{33}/e_{31} = 15.8$ (C/m^2)/5.4 (C/m^2) ≈ 3 [7]. Therefore, the values of the k^2-criterion for different PEG configurations, in which are realized various oscillation modes, differ approximately three times. So, the proposed in [8] the global coupling factor k^2 does not allow in a whole one to estimate energetic efficiency of PEG of the different configurations, in which could be excited only one oscillation mode.

The energetic efficiency criterion based on Rayleigh–Ritz method has been proposed by H. A. Sodano et al. [9, 10]. This approach assumes that the process of energy storage by resonator is caused by the sum of different oscillation modes, and energy harvesting could be estimated by a dimensionless, so-called *effective coupling coefficient* δ. Then the efficiency factor of transformation of the electric energy into mechanical one (conversion efficiency) is defined as

$$\eta_{ph} = \frac{\delta\lambda\gamma}{1 + (1+\delta)(\lambda\gamma)^2}, \tag{29.5}$$

where $\lambda = RC_p\omega_n^E$, C_p is the effective capacitance of piezoelectric element, ω_n^E is the eigenfrequency of *n*-th oscillation mode,

$$\gamma = \frac{\omega}{\omega_n^E}, \tag{29.6}$$

ω is the current value of resonance frequency of oscillations, ω_n^E is the natural frequency of oscillations in no short-circuit electrical scheme.

The expression (29.5) shows that the conversion efficiency, i.e. PEG efficiency, in a whole depends on effective coupling coefficient, defined through ratio of short-circuit and open-circuited natural frequencies ω^D and ω^E ($E = 0$ or $E =$ const), respectively [9, 10]:

$$\delta = \frac{(\omega^D)^2 - (\omega^E)^2}{(\omega^E)^2}. \tag{29.7}$$

Thus the approach proposed in [9, 10] allows one to calculate the energetic efficiency of piezoelectric harvester in generalized form, i.e. including both as piezoelectric generator (cantilever plate with bimorph piezoelectric element), as electric block of energy processing and harvesting (standard interface circuit or other).

However the configuration of various type PEGs differ significantly one from other due to the different oscillation modes of the cantilever are realized in them, namely: longitudinal (d_{33}), transverse (d_{31}) and shear (d_{15}). At the same time, the proposed in the approach of H. A. Sodano et al. [9, 10] unification of all these forms, corresponding to various oscillation modes, impedes calculation of the energetic efficiency criterion in common form, due to it does not define this criterion for specific type of PEGs. Moreover, it should be noted that in each of above-mentioned PEGs configuration, besides the dominant oscillation mode, other modes presence also. It is defined by a specific geometry of piezoelectric generator. Therefore, the generalized character of the approach [9, 10] impedes estimation based on energetic efficiency of PEG for concrete its configuration.

Recently, new criterion for cantilever type PEG with bimorph piezoelement and proof mass has been proposed [11], in which the energetic efficiency is estimated by the *total quality factor*, *Q*, calculated as

$$Q = \frac{m\sqrt{\frac{Ywh^3}{4l^3}\left(m_p + 0.24m_c\right)}}{d}, \tag{29.8}$$

where m is the effective mass of cantilever; Y is Young modulus of piezoceramic material of the transducer; w, h, l are the width, thickness and length of cantilever plate with bimorph piezoelement, respectively, m_p is the proof mass, m_c is the cantilever mass with joined bimorph piezoelement, d is the total damping (parasitic damping and electrical damping).

After some algebraic transformations of expressions (29.4) and (29.5), it may be obtained the expression for output electric power, P, of PEG in the form [11]:

$$P = \frac{m^2 A^2 \omega_n^4}{2d}, \tag{29.9}$$

where A is the amplitude of transverse displacement of free edge of the cantilever plate, ω_n is the natural frequency:

$$\omega_n = \sqrt{\frac{Ywh^3}{4l^3(m_p + 0.24m_c)}}. \tag{29.10}$$

In the expression (29.9), the displacement amplitude A is used, but in the work [11], it does not define more precisely in which point of the cantilever this displacement is measured. It may be only to suppose that in this case the authors assumed the free edge of the cantilever plate. Moreover, in [11], it does not included formula for calculation of parameter d. In the presented expression [10]: $d = 2m\omega_n\eta$, where η is the total damping factor (mechanical and electrical), the value of η also is not be defined. Taking into account above arguments, the analysis of PEG energetic efficiency with help of the criterion [11] is presented very problematic.

With purpose to extend a range of applicability the known approaches to estimation of energetic efficiency of the different concrete type PEGs, then we propose new strain criterion for estimation of energy harvesting. It should be noted, that the described below criterion includes only the cantilever parameters with piezoelements glued on it. Influence of characteristics of the electric scheme (interface) for the processing and harvesting of electric energy on the PEG energetic efficiency in the proposed criterion does not take into account.

29.3 New (Strain) Criterion of Cantilever Type PEG Energetic Effectiveness

In the studies [12, 13], we have presented results of finite-element investigations optimal characteristics of the cantilever type PEGs, were we received the following expression for calculation of electrical voltage, generated by piezoplate:

$$|V| = \frac{\omega e_{31} \delta b R}{\sqrt{1 - (\omega R C_{pz})^2}}, \tag{29.11}$$

where ω is the circular frequency, e_{31} is the electric constant of the piezoelectric element, δ is the amplitude of the dynamic displacement of the piezoelectric-plate edge, b is the piezoplate width, R is the load impedance, and C_{pz} is the capacity.

The analysis of the expression (29.11) shows that output voltage for cantilever type PEG depends from several parameters. In particular, output voltage is directly proportional to frequency ω, piezoelectric constant e_{31}, load resistance R, and also amplitude of displacement δ and the width of cantilever plate b. The dependence of output voltage (and hence output power) on the parameters ω, e_{31}, and R have been studied enough, in particular in [2, 4, 6, 8]. At the same time, this dependence on strain (δ) and geometric (b) parameters of PEGs, in our best knowledge was not considered. Therefore, we conducted analysis of this dependence for known configuration of the cantilever type PEGs. Before, we have proposed, so-called *deformation factor* (δb) for estimation of energetic effectiveness of the cantilever type PEGs [12].

Significance of influence of the factor (δb) on output power of the cantilever type PEG could be estimated by comparing of characteristics of known PEGs with different configurations and described by us in [12]. In particular, it has been fulfilled analysis of the cantilever type PEGs characteristics presented in works [8, 11, 12]. As the comparative characteristics, besides the factor (δb), we selected the generalized parameter $\xi = Y^{\frac{1}{2}} \left(\frac{h}{l}\right)^{\frac{3}{2}}$, where Y is Young's modulus of piezoelement material, h and l are the thickness and length of the cantilever plate, respectively.

The selection of the last characteristic is obvious, if we consider the expression (29.10) for natural frequency ω_n. From (29.9) and (29.10), it follows that the output power of PEG is directly proportional to ω_n^4, but the value of ω_n depends significantly on the pointed generalized characteristic ξ. The comparative data on the selected parameters of the known PEGs are presented in Table 29.1.

Table 29.1 shows that the most value of output power equals 65 mW and attains at the deformation factor of 180 mm^2 for the PEG model [8]. As it follows from the expression (29.11), this factor dominates (at other equal characteristics of PEG) in output power, i.e. the piezoelectric generators which have ratio of geometric and deformation parameters close to studies ones in [8], ensure greater energetic effectiveness compared with PEGs of other configurations considered in [11, 12]. Other generalized parameter ξ, taking into account not only geometry of the cantilever plate, but its stiffness, plays also important role in estimation of the energy harvesting. As it follows from Table 29.1, value of the generalized parameter ξ at least two times greater than for other models [11, 12]. As it has been noted above, the output power of PEG for the model [8] is also at least on one order of magnitude higher compared with other models. Therefore, it is not surprising that in other PEGs (they are not presented in this paper) as the material of the cantilever plate are used either stain steel or brass [4].

Table 29.1 Comparative characteristics of cantilever type PEGs

PEG type and dimensions of cantilever plate $l \times b \times h$ (material of the shim)	Displacement of free edge of cantilever plate, δ (at resonance frequency)	Deformation factor, δb (mm²)	Generalized characteristic, ξ	Output power at load resistance (used measurement method)	Reference
Cantilever type PEG without proof mass $180 \times 90 \times 2$ mm³ (steel, $Y = 2.1 \times 10^5$ MPa)	2 mm (56 Hz)	180	0.55×10^2 MPa$^{1/2}$	10 mW at $R_l = 50$ kΩ (standard circuit) 65 mW at $R_l = 70$ kΩ (SCHI circuit)	[8]
Cantilever type PEG with proof mass $220 \times 35 \times 1$ mm³ (flexible material, $Y = 10^4$ MPa)	1 mm (18 Hz)	35	0.17×10^2 MPa$^{1/2}$	0.34 mW at $R_l = 50$ kΩ (N/A)	[11]
	2 mm	70	0.28×10^2 MPa$^{1/2}$		
Cantilever type PEG without proof mass $54 \times 6 \times 0.5$ mm³ (fiberglass plastic, $Y = 0.25 \times 10^5$ MPa)	2 bmm (78 Hz)	18	0.14×10^2 MPa$^{1/2}$	0.28 mW at $R_l = 70$ kΩ (standard circuit)	[12]
	3 mm	18	0.13×10^2 MPa$^{1/2}$		

It should be noted, that in the expressions for estimation of energetic effectiveness (for example, see (29.4), (29.8)), besides above discussed characteristics, presence other important characteristics, e.g. piezoelectric constant e_{33}, cantilever mass m_c and proof mass m_p. Their contribution into output power and energetic effectiveness is also very important. It is connected with form oscillation modes of the cantilever plate, as pointed above. The effects of these factors will be studied in other works.

29.4 Conclusion

1. It has been described new deformation criterion for estimation of PEG energetic effectiveness. Its calculation is conducted by using parameters of cantilever plate with bimorph piezoelement. The proposed deformation and generalized criteria allow for a selection of optimal configuration of the PEG cantilever plate, providing maximal value of output power ceteris paribus of characteristics of the blocks processing and storage of piezoelectric charge.
2. Analysis of constructions of the known cantilever type PEGs and their output characteristics taking into account the proposed generalized criterion showed that PEGs with substrates from materials with high elastic moduli have higher output power, than in the case of using more flexible material of the fiberglass type.
3. Effect of significant increasing output voltage in the cantilever type PEGs with a proof mass, described in [11] displays only into range of low resonance frequencies of the cantilever plate below 15 Hz for the case of application of the flexible cantilever plate with low Young's modulus and corresponding values its mass momentum of inertia and load resistance. The cantilever type PEG with stiffer material of substrate demonstrates this effect on higher resonance frequencies of order 30–40 Hz [14].

References

1. E. Lefeuvre, A. Badel, C. Richard, L. Petit, D. Guyomars, In: *DTIP of MEMS/MOEMS*, Stresa, Italy, 26–28 April 2006
2. A. Badel, D. Guyomar, E. Lefeuvre, C. Richard, J. Intell. Mater. Syst. Struct. **16**, 889 (2005)
3. A. Nechibvute, A. Chawanda, P. Luhanga, A. Akande, Int. J. Eng. Technol. **2**(6), 936 (2012)
4. S. Priya, D.J. Inman (eds.), *Energy Harvesting Technologies* (Springer Science + Business Media LLC, New York, 2009)
5. T. Rodig, A. Schonecker, G. Gerlach, J. Am. Ceram. Soc. **93**(4), 901 (2010)

6. V.A. Akopyan, A.N. Soloviev, I.A. Parinov, S.N. Shevtsov, *Definition of Constants for Piezoceramic Materials* (Nova Science Publishers, NY, 2010)
7. W.P. Mason (eds.), *Physical Acoustics: Principles and Methods*, vol. 1(A) (Academic Press, NY, 1964)
8. E. Lefeuvre, A. Badel, C. Richard, L. Petit, D. Guyomar, Sens. Actuators, A **126**(2), 405 (2006)
9. Y. Liao, H.A. Sodano, J. Intell. Mater. Syst. Struct. **21**(2), 149 (2010)
10. H.A. Sodano, G. Park, D.J. Inman, J. Strain **40**(2), 49 (2004)
11. G.A. Wahied, W.I. Sutrisno, Energy Power Eng. **4**, 496 (2012)
12. S.N. Shevtsov, V.A. Akopyan, in *Piezoceramic Materials and Devices*, ed by I.A. Parinov (Nova Science Publishers, NY, 2010), p. 285
13. V.A. Akopyan, Y.N. Zakharov, I.A. Parinov, E.V. Rozhkov, S.N. Shevtsov, V.A. Chebanenko, in *Nano- and Piezoelectric Technology, Materials and Devices*, ed by I.A. Parinov (Nova Science Publishers, NY, 2013)
14. Yu. Shudong, He Siyuan, Li Wen, J. Mech. Mater. Struct. **5**(3), 427 (2010)

Chapter 30
Closed Axisymmetric Shells as Flat Jacks

S. A. Yudin and T. V. Sigaeva

Buildings during exploitation can be subjected to the external loadings leading to various kinds of heterogeneous strains or tilts. There is engineering technologies of uplift and flattening of multistory buildings by means of steel shells of the closed volume which are named as flat jacks (FJs) [1]. FJ represents two circular close plates which at the outer contour are joined to torus shell. The oil could be introduced into volume by hydraulic station creating a high pressure. As a result the plates diverge and through inserts from thick plywood create powerful force. The construction and working conditions of flat lifting jacks generates a set of problems of the mathematical modeling which are interesting to study. One of the directions is the geometry optimization. In the paper, we analyze variants of the axisymmetric shells modeling FJs. Stress states of shells with different shapes are compared at the initial loading stage.

30.1 Constitutive Equations

In the problems of the radial axisymmetric deformation of the shells all functions depend on the meridian coordinate α_1, only. To solve such boundary-value problems, equations of the axisymmetric stress–strain state of the thin elastic revolution shells in the framework of the geometrically-nonlinear theory of the quadratic approximation are used [2]. In the general shell theory, trihedral of the middle surface is considered as special coordinate system. Displacements and strains are related in this coordinate system as

S. A. Yudin (✉)
Vorovich Mechanics and Applied Mathematics Research Institute, Southern Federal
University, Rostov-on-Don, Russia
e-mail: ysergey@mail.ru

T. V. Sigaeva
Department of Mathematics, Mechanics and Computer Sciences, Southern Federal
University, Rostov-on-Don, Russia

$$\varepsilon_{11}(\alpha_1,\, z) = E_{11}(\alpha_1) + z \cdot K_{11}(\alpha_1);$$
$$\varepsilon_{22}(\alpha_1,\, z) = E_{22}(\alpha_1) + z \cdot K_{22}(\alpha_1);$$
$$E_{11} = u' + k_1 w + \vartheta_1^2/2; \;\; E_{22} = \psi u + k_2 w; \qquad (30.1)$$
$$\vartheta_1 = -w' + k_1 u; \;\; K_{11} = -\vartheta_1'; \;\; K_{22} = \psi \vartheta_1;$$
$$\psi = A_2'/A_2; \;\; (\ldots)' = \mathrm{d}(\ldots)/(A_1 \mathrm{d}\alpha_1).$$

Here u, v are the middle surface displacements, ϑ_1 is the rotation angle of the normal; A_1, A_2 are Lamé coefficients, k_1, k_2 are the principal curvatures. Positive direction of the normal is assumed to be in outward direction with respect to the shell.

Equilibrium equations for the forces and moments are resulted from Lagrange principle based on the kinematic relations (30.1):

$$T_{11}' + \psi(T_{11} - T_{22}) + k_1 Q_{11} + q_1 = 0;$$
$$Q_{11}' + \psi Q_{11} - k_1 T_{11} - k_2 T_{22} + q_3 = 0;$$
$$M_{11}' + \psi(M_{11} - M_{22}) - Q_{11} - T_{11}\vartheta_1 = 0.$$

Constitutive equations for the isotropic shells are given by

$$T_{11} = B(E_{11} + vE_{22}); \;\; T_{22} = B(E_{22} + vE_{11});$$
$$M_{11} = D(K_{11} + vK_{22}); \;\; M_{22} = D(K_{22} + vK_{11});$$
$$B = Eh/(1 - v^2); \;\; D = Eh^3/[12(1 - v^2)],$$

where B and D are effective tension/compression and bending stiffness, respectively, E is Young's modulus, v is Poisson's ratio.

Stresses and stress intensity can be expressed as

$$\sigma_{11} = E_v(\varepsilon_{11} + v\varepsilon_{22}); \;\; \sigma_{22} = E_v(\varepsilon_{22} + v\varepsilon_{11});$$
$$E_v = E/(1 - v^2); \;\; \sigma_{11} = (\sigma_{11}^2 + \sigma_{22}^2 - \sigma_{11}\sigma_{22})^{1/2}. \qquad (30.2)$$

Boundary conditions are found from the requirement stating that contour integrals of the Lagrange functional are equal to zero. In the case of the homogeneous boundary conditions, the generalized displacements or generalized strains are equated to zero:

$$u(1 - \gamma_1) + \gamma_1 T_{11} = 0, \; w(1 - \gamma_2) + \gamma_2 Q_{11} = 0,$$
$$\vartheta_1(1 - \gamma_3) + \gamma_3 M_{11} = 0; \; \alpha_1 = \alpha_{11};$$
$$u(1 - \gamma_4) + \gamma_4 T_{11} = 0; \; w(1 - \gamma_5) + \gamma_5 Q_{11} = 0;$$
$$\vartheta_1(1 - \gamma_6) + \gamma_6 M_{11} = 0, \alpha_1 = \alpha_{12}.$$

Here coefficients γ_j are assumed to be 0 or 1 and allow us to state different boundary conditions.

Let introduce main functions $y_1 = T_{11}$, $y_2 = Q_{11}$, $y_3 = M_{11}$, $y_4 = u$, $y_5 = w$, $y_6 = \vartheta_1$ and establish for them canonical system of the differential equations of the sixth-order:

$$\mathbf{y}' = f(\alpha_1, \mathbf{y}) + \mathbf{p}_1(\alpha_1) = 0;$$
$$\mathbf{y} = (y_1, \ldots, y_6); \quad \mathbf{f} = (f_1, \ldots, f_6);$$
$$\mathbf{p} = (-q_1, -q_3, 0, 0, 0, 0).$$

The right-hand sides (RHS) f_j are given by:

$$f_1 = \psi(T_{22} - y_1) - k_1 y_2; \quad f_2 = -\psi y_2 + k_1 y_1 + k_2 T_{22}; \quad f_3 = \psi(M_{22} - y_3) + y_2 + y_1 y_6;$$
$$f_4 = E_{11} - y_1 - k_1 y_5 - 0.5 y_6^2; \quad f_5 = k_1 y_4 - y_6; \quad f_6 = K_{11},$$

where

$$E_{22} = \psi u + k_2 w; \quad K_{22} = \psi y_6;$$
$$K_{11} = y_3/D - \nu K_{22}; \quad E_{11} = y_1/B - \nu E_{22};$$
$$T_{22} = B(E_{22} + \nu E_{11}); \quad M_{22} = D(K_{22} + \nu K_{11}).$$

In realization of algorithm, these equations are reduced to the dimensionless form by using the following formulae:

$$\{U, W, u, w, h, z\}_U = \{\ldots\}_D/h_*; \quad \{A_1, A_2\}_U = \{\ldots\}_D/R_*;$$
$$\{k_1, k_2, K_{11}, K_{22}\}_U = R_*\{\ldots\}_D; \quad \{\vartheta_1, \varepsilon_{11}, \varepsilon_{22}, E_{11}, E_{22}\}_U = \{\ldots\}_D/\varepsilon_*;$$
$$\{\sigma_{11}, \sigma_{22}, \sigma, \sigma_A, \sigma_T\}_U = \{\ldots\}_D/(E\varepsilon_*); \quad \{T_{11}, T_{22}, Q_{11}\}_U = \{\ldots\}_D R_*/A_*;$$
$$\{M_{11}, M_{22}\}_U = \{\ldots\}_D R_*/D_*; \quad \{q_1, q_3\}_U = \{\ldots\}_D R_*^2/A_*;$$
$$B_U = B_D/B_*; \quad D_U = D_D/D_*; \quad E_U = E_D/E_*,$$

$$(30.3)$$

where $\varepsilon_* = h_*/R_*$; $B_* = E_* h_*/(1 - \nu_*^2)$; $A_* = B_* h_*$; $D_* = B_* h_*^2$. The normalization parameters E_*, ν_*, R_*, h_* have sense and dimension of the Young's modulus, Poisson's ratio, curvature radius or linear size and thickness, respectively. The dimensionless quantities are combined by braces with index "U" in the left-hand side (LHS) of equations. Their dimension analogues are given in the braces with index "D" in the RHS of (30.3). Governing equations in the dimensionless form are given as

$$dy_j/d\alpha_1 = A_1 F_j(\alpha_1, y), \quad j = 1, \ldots, 6; \qquad (30.4)$$

$$F_1 = \psi(T_{22} - y_1) - k_1 y_2 - q_1; \quad F_2 = -\psi y_2 + k_1 y_1 + k_2 T_{22} - q_3; \quad F_3 = \psi(M_{22} - y_3) + y_2/\varepsilon_* + y_1 y_6;$$
$$F_4 = E_{11} - y_1 - k_1 y_5 - 0.5\varepsilon_* y_6^2; \quad F_5 = k_1 y_4 - y_6; \quad F_6 = K_{11}/\varepsilon_*; \quad E_{22} = \psi y_4 + k_2 y_5, \quad K_{22} = \varepsilon_* \psi y_6;$$
$$K_{11} = y_3/D - \nu K_{22}, \quad E_{11} = y_1/B - \nu E_{22}; \quad T_{22} = B(E_{22} + \nu E_{11}), \quad M_{22} = D(K_{22} + \nu K_{11}).$$

$$(30.5)$$

For simplicity, index "U" is not used in the following expressions. In the closed form RHS of (30.5) of the equation set (30.4) is fully determined through independent functions y_j and for isotropic shell are expressed as

$$
\begin{aligned}
F_1 &= \psi[(v-1)y_1 + B(1-v^2)(\psi y_4 + k_2 y_5)] - k_1 y_2 - q_1; \\
F_2 &= -\psi y_2 + (k_1 + vk_2)y_1 + k_2 B(1-v^2)(\psi y_4 + k_2 y_5) - q_3; \\
F_3 &= \psi[(v-1)y_3 + D(1-v^2)\varepsilon_* \psi y_6] + y_2/\varepsilon_* + y_1 y_6; \\
F_4 &= y_1/B - v\psi y_4 - (k_1 + vk_2)y_5 - 0.5\varepsilon_* y_6^2; \\
F_5 &= k_1 y_4 - y_6, \quad F_6 = y_3/(\varepsilon_* D) - v\psi y_6.
\end{aligned}
\tag{30.6}
$$

30.2 Types of Shells

We consider shells of revolution of composed geometry formed by coaxial circular plates (they can be weakly curved) joined by the toroidal shell at the external contours. In addition to the axial symmetry, shell is symmetric with respect to the equidistant plates and, thus, only half of the construction can be considered (e.g., upper part). A prototype for such a construction can be found in [3]. In the prototype, meridian of upper half of the shell consists of three sections: segment of straight line, concave and convex arcs of the circles of the different radii.

Denote main points on the radial axis as r_0 is the radius of the cylindrical pin, r_1 is the radius of the plate, r_2 is the point of the arcs conjugation, r_m is the point of the toroid's maximal ordinate and r_3 is the external radius of the shell middle surface. Then prototype has the following sections of the meridian: segment of straight line at $r \in [r_0, r_1]$, concave arc of the radius R_1 at $r \in [r_1, r_2]$, convex arc of the radius R_2 at $r \in [r_2, r_3]$. The main drawback of this form is a curvature jump followed by change of sign and leading to the stress concentration in the neighborhood of the arcs joint during loading process.

As an alternative, let consider types of the shells, in which meridian consists of segments of the well-known curves [4]:

(1) segment of straight line at $r \in [r_0, r_1]$, Cassini oval at $r \in [r_0, r_1]$;
(2) exponential curve at $r \in [r_0, r_m]$, concave arc of the radius R_2 at $r \in [r_m, r_3]$;
(3) versiera of Agnesi at $r \in [r_0, r_m]$, concave arc of the radius R_2 at $r \in [r_m, r_3]$;
(4) versiera of Agnesi at $r \in [r_0, r_m]$, Pascal's limacon at $r \in [r_m, r_3]$;
(5) versions of the single curve formed by power, fractional, exponential and logarithmic functions, $r \in [r_0, r_3]$.

It should be noted that equations for the curves are used in non-classical form but with modified one with coefficients controlling the shape and scales on coordinates. Selection of these parameters is made in such a way that overall dimensions remain the same, i.e. diameter is $D = 2(r_3 + 1.5) = 520$ mm and toroidal section height is

$H_T = 39$ mm. Other sizes of the prototype are the following: $r_0 = 8$ mm, $r_1 = 204.3$ mm, $r_m = 239$ mm, $r_3 = 258.5$ mm, $R_1 = 24.4$ mm, $R_2 = 19.5$ mm, $h_1 = 3$ mm, where h_1 is the shell thickness. Below we go to the dimensionless quantities, where $R_* = r_1$, $h_* = h_1$ and the used parameters are also dimensionless.

The purpose of our analysis is to find the curves for which the following improvements (optimization criteria) will be: (i) small number of sections is, (ii) smooth meridian curvature as far as is possible, (iii) reduced stresses in the toroidal part of the shell.

Main attention is directed to the toroidal part of the shell due to complexity of its deformation working circle compared with central part, which serves as platform attached to the rigid insert and deforms in its plane as membrane during the main stage of the lifting. The toroidal part is subjected to tangential as well as bending stresses.

Consider first type of the shells based on the equation:

$$(k_x x^2 + k_y y^2)^2 - 2c_k^2(g_x x^2 - g_y y^2) - A_C = 0, \tag{30.7}$$

where $A_C = a_k^4 - c_k^4$. LHS represents odd function with respect to x and y, i.e. it is symmetric with respect to coordinate axis. Central point ($x = 0$) has horizontal tangent to the curve (30.7), and it gives an opportunity to make smooth conjugation between toroid and plate.

Then we will obtain the equation of the curve in the implicit form, given with respect to the vertical ordinate. By assuming $Y = y^2$ and introducing denotations:

$$A_{Kas}(x) = (c_k^2 g_y + k_x k_y x^2)/k_y^2; \ C_{Kas}(x) = (A_C + 2c_k^2 g_x x^2 - k_x^2 x^4)/k_y^2$$

on the basis of (30.7) one can obtain equation:

$$Y^2 + 2A_{Kas}(x)Y - C_{Kas}(x) = 0.$$

The required solution is given by:

$$Y_{K1}(x) = -A_{Kas}(x) + \sqrt{[A_{Kas}(x)]^2 + C_{Kas}(x)}.$$

Let go to the cylindrical coordinates (r, Z), carry out scaling and shear of the curve along r-axis. Then we obtain the function:

$$Z_{0K}(r) = K_{Mz} \cdot \sqrt{Y_{K1}\left(\frac{r - r_1}{K_{Mr}}\right)}. \tag{30.8}$$

The condition of the overall equivalence is satisfied using the following set of the parameters:

$$K_{Mz} = 15.9, \ K_{Mr} = 18.8, \ c_k = 1.423,$$
$$a_k = 1.445, \ k_x = 1.0, \ k_y = 0.5, \ g_x = 2.02, \ g_y = 1.8.$$
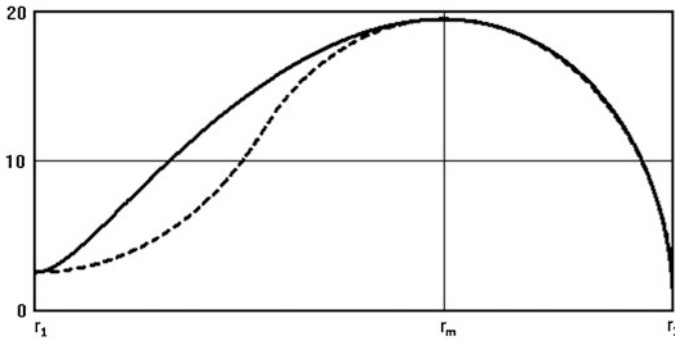
Fig. 30.1 Curves corresponding to the first type of the shells (*solid line*) and the prototype
(*dotted line*)
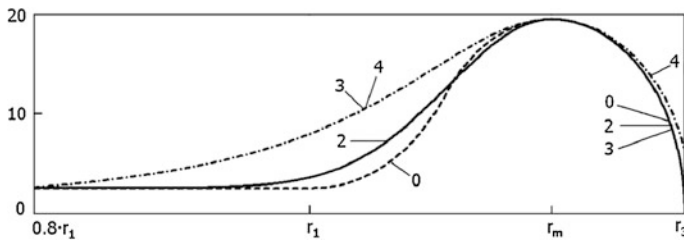
Fig. 30.2 Curves corresponding to the types of the shells (*2*)–(*4*), and the prototype

The curve (8) is shown in Fig. 30.1 by solid line, while the dotted line represents prototype.

Similar approach is used to build other curves. For the types of the shells (2)–(4), the corresponding plots are present in Fig. 30.2, where the digits denote the number of the type, while "0" corresponds to the prototype.

For the type of the shells (5) several curves were analyzed, two of which are given by

$$f_1(r) = A_{1z} \cdot \left[\lambda_{10} - \lambda_{11} \left(\frac{r - r_{1c}}{A_{1r}} \right)^2 \right] \cdot \exp[-\lambda_{1e}(r_{1c} - r)] \log \left(\frac{r_{t1c} - r}{A_{1r}} \right) + B_{1z};$$

$$A_{1z} = 1.1, \ \lambda_{10} = 10, \ \lambda_{11} = 4.8, \ A_{1r} = 20, \ r_{1c} = 230, \ B_{1z} = 3, \ \lambda_{1e} = 0.05.$$

$$(30.9)$$

$$f_2(r) = \frac{-A_{2z}}{r - r_{2c}} \cdot \left(\frac{r_{2c} - r}{A_{2r}} - \lambda_{20} \right)^{n_c} \exp[-\lambda_{21}(r_{2c} - r)^{n_e}] \log \left(\frac{r_{2c} - r}{A_{2r}} - \lambda_{20} \right) + B_{2z};$$

$$A_{2z} = 0.48, \ \lambda_{20} = 2.0, \ \lambda_{21} = 0.12, \ A_{2r} = 0.8, \ r_{2c} = 264, \ B_{2z} = 2.5, \ n_e = 0.95, \ n_c = 2.65.$$

$$(30.10)$$
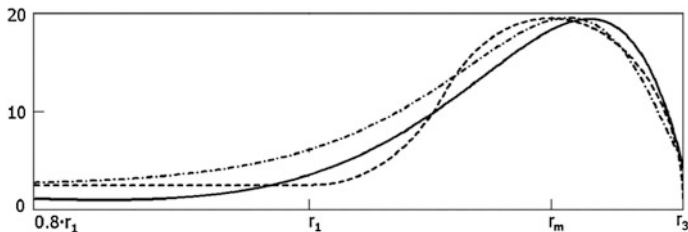
Fig. 30.3 Curves corresponding to the type of the shells (5) and the prototype

These curves are given in Fig. 30.3, in which solid and dash-dotted lines correspond to (30.9) and (30.10), respectively, while dotted line represents prototype again.

The curves similar to Fig. 30.3 can be obtained using retuning of the parameters in (30.9) and (30.10) and ignoring logarithmic functions.

If the meridian ordinate is given by $Z(r)$, then Lame's coefficient A_1, slope angle of the normal to the revolution axis Φ_0, principle curvature k_1, k_2 and function ψ are determined by the following expressions:

$$A_1(r) = \sqrt{1 + (\mathrm{d}Z(r)/\mathrm{d}r)^2}; \quad \Phi_0(r) = -\arctan(\mathrm{d}Z(r)/\mathrm{d}r);$$
$$k_1(r) = [\mathrm{d}\Phi_0(r)/\mathrm{d}r]/A_1(r); \quad k_2(r) = \sin[\Phi_0(r)]/r; \quad \psi(r) = \cos[\Phi_0(r)]/r. \tag{30.11}$$

Some of the considered curves on the right edge can have tangents close to vertical. Therefore it is reasonable to use arc length s as an independent coordinate instead of polar radius. Then, equations of the meridian and all shell parameters should be functions of s. It can be easily done analytically for the initial shell composed of circle arcs. For curves that are more complicated, a numerical approach should be used.

Let consider integral with variable upper limit, which denotes arc length as a function of polar radius:

$$s(r) = \int_{r_0}^{r} \sqrt{1 + Z_{,r}(r)} \mathrm{d}r. \tag{30.12}$$

Calculate the corresponding values of s_i on the grid of values of r_i, $i = 0, \ldots, N$ using formulae (30.12). Then, by using s_i as independent variables, the function $r(s)$ can be obtained by means of locally linear or spline interpolation. By making replacement of r by $r(s)$, we obtain an equation for the meridian as function of s: $z(s) = Z[r(s)]$. The replacement of r by $r(s)$ is also conducted in the geometric functions (30.11).

Material of the shell is assumed to be homogeneous (steel) with corresponding elastic moduli E and v. In transition of the problem to the dimensionless form the

Fig. 30.4 Stress intensity σ at the middle surface of the shells of type (*1*) with Cassini oval (*solid curves*) compared with prototype shell (*dotted line*) at the type *B* loading
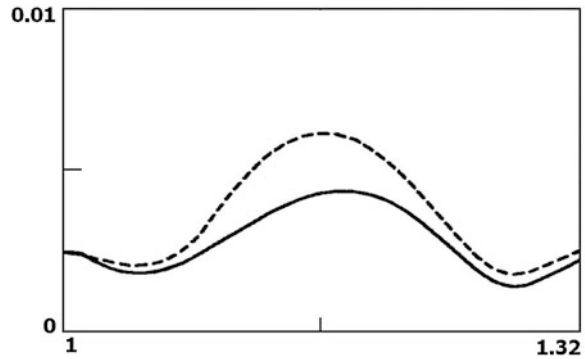
following characteristic parameters were used again: $E_* = E$, $v_* = v$, $R_* = r_1$, $h_* = h_1$.

Boundary-value problems for the system of equation with RHS (30.6) were considered with the following boundary conditions: at the left edge (in the central part of the shell) there is moved clamping allowing a vertical movement, and the right edge (external contour) is clamped. The boundary-value problem was solved by shooting method.

Two types of the loading caused by internal pressure ($q_1 = 0$, $q_3 \neq 0$) have been considered. Type *A* presented the pressure with intensity of 0.1 MPa (dimensionless value was $q_3 = 0.002$) applied to the whole surface of the shell, and type *B* corresponds to pressure with intensity of 0.6 MPa (dimensionless value was $q_3 = 0.012$) applied to the toroidal part only at $r_1 < r < r_3$. These types simulate initial stage of the selection of the gap between load and shell, and in some way characterize the stage of the intimate contact of the shell with insert taking into account resistance of the construction, which compensates internal pressure in the platform zone. Thus, for type *B* of loading, central part of the shell works almost without bending.

To illustrate this, Fig. 30.4 provides information on the stress intensity σ at the middle surface for the toroidal part of the shells of type (1) with Cassini oval (solid curves) compared with prototype shell (dotted line) at the type *B* loading.

30.3 Conclusions

The shells of type (1) and prototype have similar locations of the dangerous points but the stresses for the type (1) are significantly reduced. The same properties are demonstrated for the shells of type (2). Therefore the analysis of different forms is actual for practice with viewpoint of search of the strength reserves. It is clear, that the considered shells work out the limits of elasticity theory at large displacements and strains. It would be interesting to take into account these factors in the more complicated models in the further research. However, experiments under prototype

shell show that the most stressed zones discovered into framework of linear elasticity remain to be the most stressed zones when further increasing of load. During cyclic work, when lifting construction is replaced by return to the nominal initial state, this repetition leads to storage of low-cycle fatigue (initiation of micro-cracks) causing gradual fracture of the construction. So, relatively simple solutions of the elastic problem are useful for providing information on possible zone of damage.

References

1. M.V. Zotov, I.A. Kutasov, in *Proceedings of 13th International Conference on Modern Problems of Mechanics of Solid Medium*, vol. 1 (Southern Federal University Press, Rostov-on-Don, 2009), p. 101 (In Russian)
2. A.S. Yudin, Izvestiya of North-Caucasus Scientific Center of High School. Nat. Sci. **3**, 184 (2000) (In Russian)
3. A.S. Yudin, S.A. Yudin, I.A. Kutasov, in *Proceedings of 13th International Conference on Modern Problems of Mechanics of Solid Medium*, vol. 2 (Southern Federal University Press, Rostov-on-Don, 2009), p. 201 (In Russian)
4. I.N. Bronstein, K.A. Semendyaev, *Handbook on Mathematics for Engineers and Students* (Nauka, Moscow, 1980) (In Russian)

Index